RGNZ/*MGPB*

Rudarsko-geološko-naftni zbornik

The Mining-Geological-Petroleum Engineering Bulletin



Godište XXXVIII, broj 79 / *Anno XXXVIII, number 79*



Rudarski znak na nogostupu grada Bad Ischla u Austriji. Grad Bad Ischl je najvažnije nalazište soli u Austriji a poznat je kao i termalno lječilište (od tuda Bad u imenu grada). Također, iz njega potječu i poznati „išleri“.

Fotografirao: izv. prof. dr. sc. Krešimir Pavlić, 2011

A mining sign on the sidewalk of the town of Bad Ischl in Austria. The town of Bad Ischl is the most important salt mining site in Austria and is also known as a thermal spa (hence the "Bad" in the town's name). It is also the place of origin of the famous "Ischler" pastries.

Photographed by: Assoc. Prof. Krešimir Pavlić, 2011

RGNZ/MGPB

Rudarsko-geološko-naftni zbornik

The Mining-Geological-Petroleum Engineering Bulletin

Hrvatski znanstveni časopis / *Croatian scientific journal*

Godište XXXVIII, broj 79 (vol. 41, sv. 3) / *Anno XXXVIII, number 79 (vol. 41, issue 3)*

Referira se u / *Indexed and abstracted in:*
Chemical Abstracts, Emerging Sources Citation Index (Thomson Reuters, WoS, Core Collection), Compendex + Geo Abstracts (Geobase) + Scopus (Elsevier), GeoRef, Geotechnical abstracts, Google Scholar (via PDFs on http://hrcak.srce.hr/rgn-zbornik), Petroleum Abstracts, Norwegian register for scientific journals, series and publishers.

Akademske baze i pretraživači (otvorena pristupa) / *Academic databases and search engines (open access)*:
DOAJ (received DOAJ Seal), DOI (CrossRef), Geoscience e-journal, Electronic Journals Library, Hrčak, JournalSeek.

Komercijalne baze i pretraživači / *Commercial databases and search engines*:
EBSCO Publishing Services, ProQuest (SciTech, Natural Science, Environmental Science, Earth Science, Technology Collection, Materials Science collections).

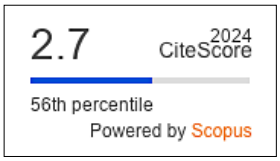
Uvjeti uporabe otvorenoga pristupa časopisu i njegovim arhivama dani su na / *Open access license and archiving is available*:
http://www.sherpa.ac.uk/romeo/search.php?id=2374&format=full&fIDnum=%7c.

UDK/*UDC* 62:66:51-56
Mrežna inačica / *Online:* ISSN 1849-0409
Tiskana inačica / *Print:* ISSN 0353-4529
DOI Prefix: doi.org/10.17794/rgn

Izdavač
Sveučilište u Zagrebu Rudarsko-geološko-naftni fakultet, Pierottijeva 6, HR-10000 Zagreb

Publisher
University of Zagreb Faculty of Mining, Geology and Petroleum Engineering, Pierottijeva 6, 10000 Zagreb, Croatia





2026.





Izjava o recenzentskom postupku/*Peer Review Statement:*

Svi predani rukopisi prolaze jednostruko anonimni postupak recenziranja
koji provode najmanje dva neovisna recenzenta.
Uredništvo donosi konačnu odluku na temelju ocjena recenzenata i općih uredničkih standarda.

All submitted manuscripts undergo a single blind peer review process conducted by at least two independent reviewers.
The editorial board makes the final decision based on reviewers' evaluations and overall editorial standards.

Etika objavljivanja/*Publication Ethics:*

Časopis poštuje najviše standarde akademskog integriteta i etičkog objavljivanja.

The journal upholds the highest standards of academic integrity and ethical publishing.
https://ojs.srce.hr/index.php/rgn/about

Izjava o otvorenom pristupu/*Open Access Statement*:

Svi su članci dostupni u otvorenom pristupu pod licencom CC BY 4.0.
Autorima i čitateljima ne naplaćuju se nikakve naknade.

All articles are open access under a CC BY 4.0 license.
No fees are charged to authors or readers.

Odricanje od odgovornosti/*Disclaimer*:

Stavovi izneseni u člancima objavljenim u časopisu Rudarsko-geološko-naftni zbornik
isključivo su stavovi autora.
Časopisom upravlja neovisni urednički odbor i slijedi međunarodno priznate
najbolje prakse u znanstvenom izdavaštvu.

The views expressed in the articles published in the Mining-Geological-Petroleum Engineering Bulletin are solely those of the authors.
The journal is governed by an independent editorial board and follows internationally recognized best practices in scholarly publishing.

Glavni i odgovorni urednik: Tomislav Korman, Sveučilište u Zagrebu Rudarsko-geološko-naftni fakultet
Zamjenik glavnog i odgovornog urednika: Zoran Kovač, Sveučilište u Zagrebu Rudarsko-geološko-naftni fakultet

Urednici polja:
Lidia Hrnčević (naftno rudarstvo i energetika), Sveučilište u Zagrebu Rudarsko-geološko-naftni fakultet
Zlatko Briševac (rudarstvo), Sveučilište u Zagrebu Rudarsko-geološko-naftni fakultet
Duje Smirčić (geologija), Sveučilište u Zagrebu Rudarsko-geološko-naftni fakultet
Krešimir Pavlić (matematika, fizika, znanosti o svemiru), Sveučilište u Zagrebu Rudarsko-geološko-naftni fakultet

Tehnički urednik: Dubravko Domitrović, Sveučilište u Zagrebu Rudarsko-geološko-naftni fakultet
Zamjenica tehničkog urednika: Josipa Kapuralić, Sveučilište u Zagrebu Rudarsko-geološko-naftni fakultet

Uredнички odbor:
Članovi sa Sveučilišta u Zagrebu Rudarsko-geološko-naftnog fakulteta:
Sanja Bernat Gazibara
Marija Macenić
Šime Bilić
Mario Klanfar

Vanjski članovi:
Moshood Onifade, Federation University, Australija
Manoj Khandelwal, Federation University, Australija
Satria Bijaksana, Institut Teknologi Bandung, Bandung, Indonezija
Maria Alzira Pimenta Dinis, UFP Energy, Environment and Health Research Unit (FP-ENAS), University Fernando Pessoa, Porto, Portugal
Vasyl Hryhorovych Lozynskyi, Dnipro University of Technology, Ukraine, Dnipro, Ukraina
Josip Ivšinović, Vodnikova 17, Zagreb, Hrvatska
Sara Kasmaeeyazdi, University of Bologna, Bologna, Italija
Aleksandar Mezga, Sveučilište u Zagrebu Prirodoslovno-matematički fakultet, Geološki odsjek, Zagreb, Hrvatska
Ivica Skokić, Sveučilište u Zagrebu Geodetski fakultet, Opservatorij Hvar, Croatia
Francesco Tinti, University of Bologna, Department of Civil, Chemical, Environmental and Materials Engineering, Italija
Mojtaba Yari, Isfahan University of Technology Department of Mining Engineering, Isfahan, Iran

Lektura engleskih tekstova:
Dubravka Pleše, Sveučilište u Zagrebu Rudarsko-geološko-naftni fakultet

Lektura hrvatskih tekstova:
Ivana Matas Ivanković, Institut za hrvatski jezik i jezikoslovlje

Izdavački savjet: Fakultetsko vijeće

Za izdavački savjet: Vladislav Brkić, dekan

Adresa na Hrčkovom OJS-u: https://hrcak.srce.hr/ojs/index.php/rgn/index

Adresa na Hrčku (arhiva): https://hrcak.srce.hr/rgn-zbornik

E-pošta glavnoga urednika: tomislav.korman@rgn.unizg.hr

Prijelom
Gredice, Horvaćanska 67, HR-10000 Zagreb

Naklada
elektroničko izdanje, pet brojeva godišnje

Editor-in-Chief:
Tomislav Korman, University of Zagreb Faculty of Mining, Geology and Petroleum Engineering, Croatia

Deputy Editor-in-Chief:
Zoran Kovač, University of Zagreb Faculty of Mining, Geology and Petroleum Engineering, Croatia

***Editors of scientific fields**:*
Lidia Hrnčević (Petroleum Engineering and Energetics),
University of Zagreb Faculty of Mining, Geology and Petroleum Engineering, Croatia
Zlatko Briševac (Mining),
University of Zagreb Faculty of Mining, Geology and Petroleum Engineering, Croatia
Duje Smirčić (Geology),
University of Zagreb Faculty of Mining, Geology and Petroleum Engineering, Croatia
Krešimir Pavlić (Mathematics, Physics, Space Sciences),
University of Zagreb Faculty of Mining, Geology and Petroleum Engineering, Croatia

***Tehnical editor**:*
Dubravko Domitrović, University of Zagreb Faculty of Mining, Geology and Petroleum Engineering, Croatia

***Assistant Technical Editor**:*
Josipa Kapuralić, University of Zagreb Faculty of Mining, Geology and Petroleum Engineering, Croatia

Editorial board:

Members from the University of Zagreb Faculty of Mining, Geology and Petroleum Engineering, Croatia:
Sanja Bernat Gazibara
Marija Macenić
Šime Bilić
Mario Klanfar

Non-Faculty Members of the Editorial Board:
Moshood Onifade,
Federation University, Australia
Manoj Khandelwal,
Federation University, Australia
Satria Bijaksana,
Institut Teknologi Bandung, Bandung, Indonesia
Maria Alzira Pimenta Dinis,
UFP Energy, Environment and Health Research Unit (FP-ENAS), University Fernando Pessoa, Porto, Portugal
Vasyl Hryhorovych Lozynskyi,
Dnipro University of Technology, Ukraine, Dnipro, Ukraine
Josip Ivšinović,
Vodnikova 17, Zagreb, Croatia
Sara Kasmaeeyazdi,
University of Bologna, Bologna, Italy
Aleksandar Mezga,
University of Zagreb Faculty of Science, Geological Department, Croatia
Ivica Skokić,
University of Zagreb Faculty of Geodesy, Observatory Hvar, Croatia
Francesco Tinti,
University of Bologna, Department of Civil, Chemical, Environmental and Materials Engineering, Italy
Mojtaba Yari,
Isfahan University of Technology Department of Mining Engineering, Isfahan, Iran

English proofreading:
Dubravka Pleše,
University of Zagreb Faculty of Mining, Geology and Petroleum Engineering, Croatia

Croatian proofreading:
Ivana Matas Ivanković,
Institute of Croatian Language and Linguistics, Croatia

Publishing council*: Faculty Council*

Chairman of Council*: Vladislav Brkić, Dean*

The Open Journal System web site: *https://hrcak.srce.hr/ojs/index.php/rgn/index*

The Croatian scientific and professional journals archive (Hrčak): *https://hrcak.srce.hr/rgn-zbornik*

E-mail of the Editor-in-Chief: *tomislav.korman@rgn.unizg.hr*

Layout
Gredice, Horvaćanska 67, HR-10 000 Zagreb

Edition
e-publication, five issues per year

Sadržaj/*Contents*

Radovi/*Papers*

1.	Predicting the weight and type of drilling mud by machine learning method *(Amin Tohidi, Alireza Afradi)*	1-20
2.	Integrated Mathematical and Physical Modelling of Salt Ions Leaching from Coal-Mining Waste: Implications for Ecological Safety and Civil Protection *(Vasyl Karabyn, Iryna Kochmar, Oksana Karabyn, Clint Sutherland, Valentyna Loboichenko, Andrii Khorolskyi)*	21-36
3.	Data-driven and knowledge-driven MARCOS method to Cu porphyry prospectivity modelling, a case study, Shahr-e-Babak area, southeastern Iran *(Moslem Jahantigh, Hamidreza Ramazi)*	37-54
4.	Experimental Investigation of the Effects of Temperature and Oil Composition on CO_2-Crude Oil Swelling, Extraction Mechanisms, and Displacement Performance *(Kartika Hartono, Asep K. Permadi, Ucok W. R. Siagia, Andri L. Hakim, Sumadi Paryoto, Ahlul H. Resha, Syaeful A. Satya, Reno Pratiwi, Maman Djumantara, Dina A. Chusniah)*	55-67
5.	Seismogenic Analysis of the 2023 Mw6.9 Murghob Earthquake, Tajikistan, based on Multi-Track InSAR and Modelling *(Rana Jaladara, Naufal Setiawan, Erlan Sumanjaya)*	69-80
6.	Geographic Information System Application for Prospecting the Sandstone-type Uranium Deposit in the Melawi Region, West Kalimantan, Indonesia *(Tyto Baskara Adimedha, Roni Cahya Ciputra, Frederikus Dian Indrastomo, I Gde Sukadana, Heri Syaeful, Yoshi Rachael)*	81-97
7.	Stress Transfer and Seismicity Along the Southern Great Sumatran Fault: Insights from the 1994 Liwa Earthquake *(Andri Kurniawan, Nicolas Silaen, Khalil Ibrahim, Arsy Nurrochman, Ridho Destawan, Nanda Hanyfa Maulida, Irfan Prasetyo, Ahmad Zaenudin, Adhi Wibowo)*	99-113
8.	Enhanced desorption of Cobalt from contaminated sandy silty-clay soils *(Tamás Bacsó, Márton Tóth)*	115-126
9.	Geochemistry and genesis of the manganese ores in the Nawagai ophiolitic melange, Mohmand District, Khyber Pakhtunkhwa, Pakistan *(Irfan Ullah, Aamir Khan, Mohammad Tahir Shah, Liaqat Ali, Asad Khan, Muhammad Mustafa)*	127-141
10.	Enhancing Hypocenter Relocation for Seismic Hazard Evaluation in Central Java and Yogyakarta Indonesia: Findings from the BMKG Earthquake Catalog of August-October 2024 *(Wahyu Hidayat, Nanda Agustina, Ekalia Ardenti, Suharsono, Ardian Novianto, Uli Ulfa, Maman Rohaman, Herry Riswandi)*	143-158
11.	Ore Genesis and Hydrothermal Evolution of the Cheshmeh-Hadi Stratabound (Manto-type) Copper Deposit in the Volcanic-Plutonic Belt North of the Doruneh Fault, East of the Sepid-Sarve copper deposit (NW Bardeskan, Central Iran): Evidence from Geology, Geochemistry, Fluid Inclusions, and Stable S and O Isotopes *(Morteza Esform, Hasan Zamanian, Alireza Zarasvandi, Alireza Almasi, Mahya Manouchehry Nia)*	159-184
12.	Magnetic characteristics and mineralogy of cave sediments from Solek Cave, West Sumatra: Implications for paleoenvironmental processes within the cave *(Hamdi Rifai, Rizaldi Putra, Wilda Febi Rahmadhani, Nilam Sari, Dessupri Niarti, Wardina Nasution, Erni Erni, Christopher M. Wurster)*	185-195
13.	Fall cone test calibration for slope stability analysis *(Chalabi Youssouf, Aissaoui Soufyane, Zadjaoui Abdeldjalil, Aissa Mamoune Sidi Mohammed)*	197-205
14.	Remote sensing of radioactive alteration zones using Sentinel-2 and SPAD chlorophyll measurements in Mamuju, Indonesia *(Nuraisyiah Pertiwi Kamsir, Asep Saepuloh, Very Susanto, Eka Djatnika Nugraha)*	207-218
15.	RAM measure of hydraulic powered roof supports in underground longwall coal mines *(Mohammad Javad Rahimdel)*	219-231

RGNZ/MGPB

Predicting the weight and type of drilling mud by machine learning method

Rudarsko-geološko-naftni zbornik
(The Mining-Geology-Petroleum Engineering Bulletin)
DOI: 10.17794/rgn.2026.3.1

Original scientific paper

CC BY

Amin Tohidi[1]*, Alireza Afradi[2]
[1] *Department of Mining Engineeing, Amirkabir University of Technology, Tehran, Iran.*
[2] *Department of Mining and Geology, QaS.C., Islamic Azad University, Qaemshahr, Iran.*

Abstract
Selecting the optimal drilling fluid, defined by its weight and chemical type, is critical for preventing costly wellbore instability and catastrophic accidents. Traditional methods often rely on trial-and-error, past experience or simplified models that fail to capture the complex rock-fluid interactions. While data mining offers a promising alternative, a research gap exists in simultaneously predicting both mud weight and type. This study introduces a novel machine learning framework that concurrently predicts these essential properties. Utilizing a comprehensive dataset extracted from 50 years of daily drilling reports across 20 oil wells, we trained and compared three nature-inspired algorithms: Ant Colony (ACO), Bee Colony (BCO), and Emperor Penguins Colony (EPC) optimization. The results demonstrate that all models achieved high predictive accuracy, with the Bee Colony Optimization (BCO) algorithm emerging as the most precise, yielding a correlation coefficient (R^2) of 0.9841 and a root-mean-square error (RMSE) of 0.0245. Furthermore, sensitivity analysis revealed that the Rate of Penetration (ROP) is the most influential parameter on mud properties, surpassing other drilling variables. A key practical finding was the consistent model consensus, with 79-87% confidence, that sea water-based mud with polymer and soltex additives (SW-PO-SX) is the optimal fluid for the studied field. This research provides a robust, data-driven solution that enables a systematic and proactive approach to drilling fluid selection, significantly enhancing operational safety and efficiency.

Keywords:
data mining, predictive model, mud weight, mud type, wellbore stability

1. Introduction

The problems of inappropriate drilling fluid are stuck pipe, wellbore instability, slow drilling rates, excess torque and drag, lost circulation, high temperature additive degradation, and corrosion (**Caenn et al., 2011**). The selection of the drilling fluid depends on numerous factor such as economic, and technical issues. Oil and synthetic based mud are expensive relative to water-based mud so used in challenging geological condition. Some of complex geotechnical conditions are salt and active shale rock. The excellent choice for active shale formation is oil-based mud (**Technology Roundtable: Drilling Fluids, 2017**).

Sometimes, the wrong choice of drilling fluid causes a catastrophic accident. For example, in the Rag-Sefid accident, drilling mud was lost into the natural fracture of the formation, and the reduction in the weight of mud caused the gas to be imported into the well and a blow-out took place (**Reuters, 2013**).

* Corresponding author: Amin Tohidi
e-mail address: a.tohidi@aut.ac.ir
Received: 27 April 2025. Accepted: 22 October 2025.
Available online: 14 May 2026

Also, to reach the oil and gas formation, drilling passes through various rocks, in this path some formations have natural fracture and bedding planes and some formations have creep, swelling and dissoluble potential so the stability of a wellbore is critical and makes drilling a challenging phase in the oil and gas industry. Wellbore instability, lost circulation, kick and blowout are examples of what may occur during drilling. Lost circulation is the migration of the drilling fluid into the pores and natural fractures of a rock and is estimated to cost over 2 billion USD annually. Drilling in active shale and salt formations can cause chemical instability, so accurate prediction of the type of mud is the most critical solution to dealing with these difficulties (**Ebadati & Najari, 2016; Gholami et al., 2021; Eppelle and Gerogiorgis., 2019; Nunez et al., 2021; Pao et al., 2016; Sabah et al., 2021**). Wellbore instability can be either of the mechanical or chemical type and can cause financial losses of 1–6 billion USD annually (**Albukhari et al., 2018; Tohidi et al. 2017**).

Mechanical wellbore instability occurs when the mud pressure act on the wellbore wall is too low or too high and causes shear or tensile failure of the rock, respectively (**Freij-Ayoub et al., 2003**). The mud weight can

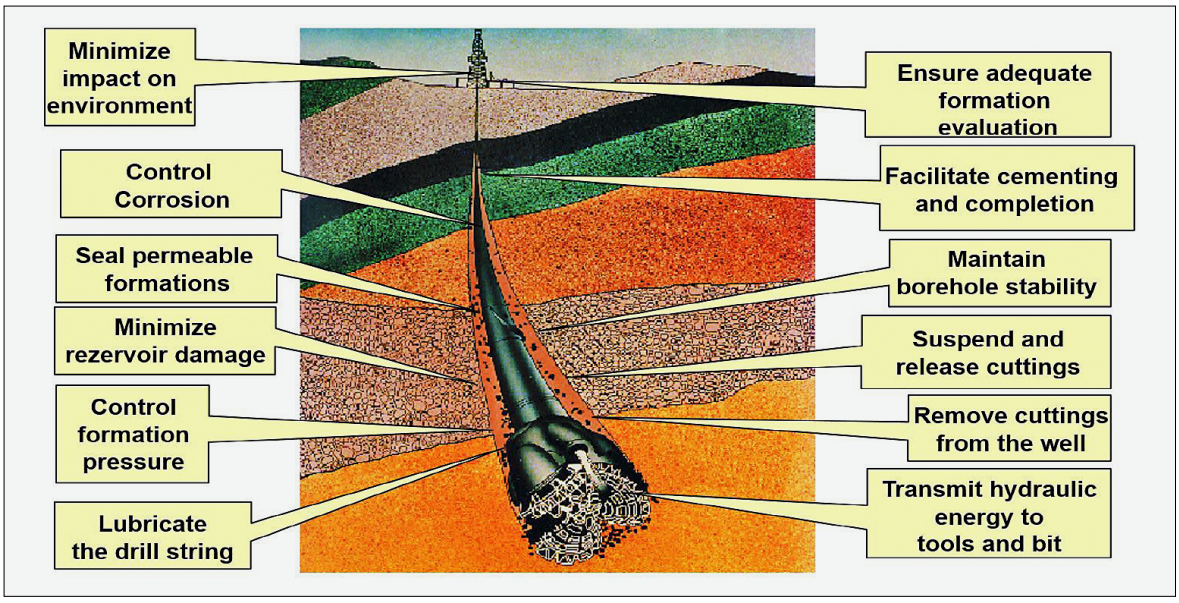


Figure 1. Multi-function of drilling fluid (**Mozie, n.d.**)

be lightened by inserting foam or gas into the mud and the mud can be weighted with an agent such as barite (**Aljubran et al., 2022**). Chemical wellbore instability results from an interaction between the drilling mud and formations such as active shale and salt. When the reason for wellbore stability is mechanical, the mud density is altered. When the reason for the problem is chemical, the mixture of drilling fluid such as clay, polymer, and surfactant changed to achieve the right solutions (**Allawi, 2023**). So, accurate prediction of drilling fluid weight and type is critical and requires simultaneous consideration during drilling operations (**Olson et al., 2005**).

As shown in **Figure 1**, drilling fluid or drilling mud has several advantages (**Aljubran et al., 2022; Deka, 2023**). The mechanical and chemical properties of the drilling fluid must be designed for a specific scenario (**DRILLING FLUID, 2023**).

Figure 2 shows that, for determining the maximum mud density of the fluid, the mud pressure must be below the tensile strength of the rock mass to prevent lost circulation. Two criteria control the minimum density of the mud weight. It must be greater than pore pressure to prevent kick or blowout from occurring and also should be greater than the shear strength of the rock so that wellbore instability does not occur (**Soroush, 2020**). Although the logic for estimating drilling fluid weight is simple, predicting the proper mud weight cannot be straightforward, because the number, dip, and strike of natural fracture control the strength behaviour of rock masses that cannot be estimated with deterministic approaches.

The chemical composition of the drilling fluid can be determined from the formation and interaction requirements. There are three main types of drilling fluid: oil, water and synthetically based fluid (**Aljubran et al., 2022**). The type of drilling fluid is based on the composition and concentration of the fluid components. In the current study, an algorithm is proposed that predicts both the weight and type of the mud in a specific oil field so that the most appropriate fluid can be selected. For clarification, at first, a schematic diagram of wellbore problems (that we extract data from it) during drilling was drawn.

Schematic diagram of problems that occurred during drilling in well 2 and 3 of oil field in south-west of Iran is shown in **Figure 3**.

According to **Figure 3**, when problems such as lost circulation, stuck pipe, and tight hole occur, the remediation actions involve adjusting the mud weight and/or its chemical composition. Mud weight is primarily adjusted to address mechanical wellbore instability (e.g. increasing weight to prevent shear failure or decreasing it to avoid tensile fracture and lost circulation). In contrast, the chemical composition is modified to combat chemical instability; for instance, switching to an inhibitive oil-based mud or adding salts like potassium chloride (KCl)

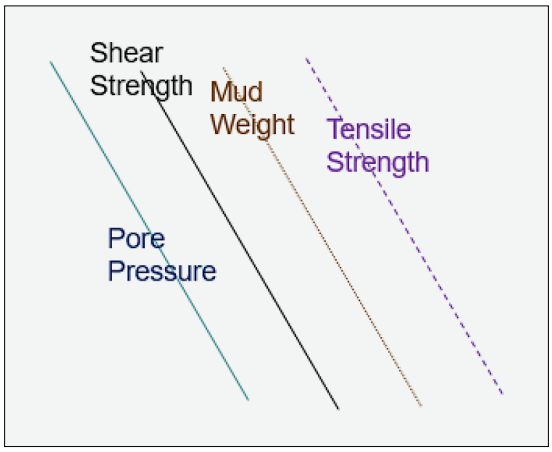


Figure 2. The logic for mud weight selection

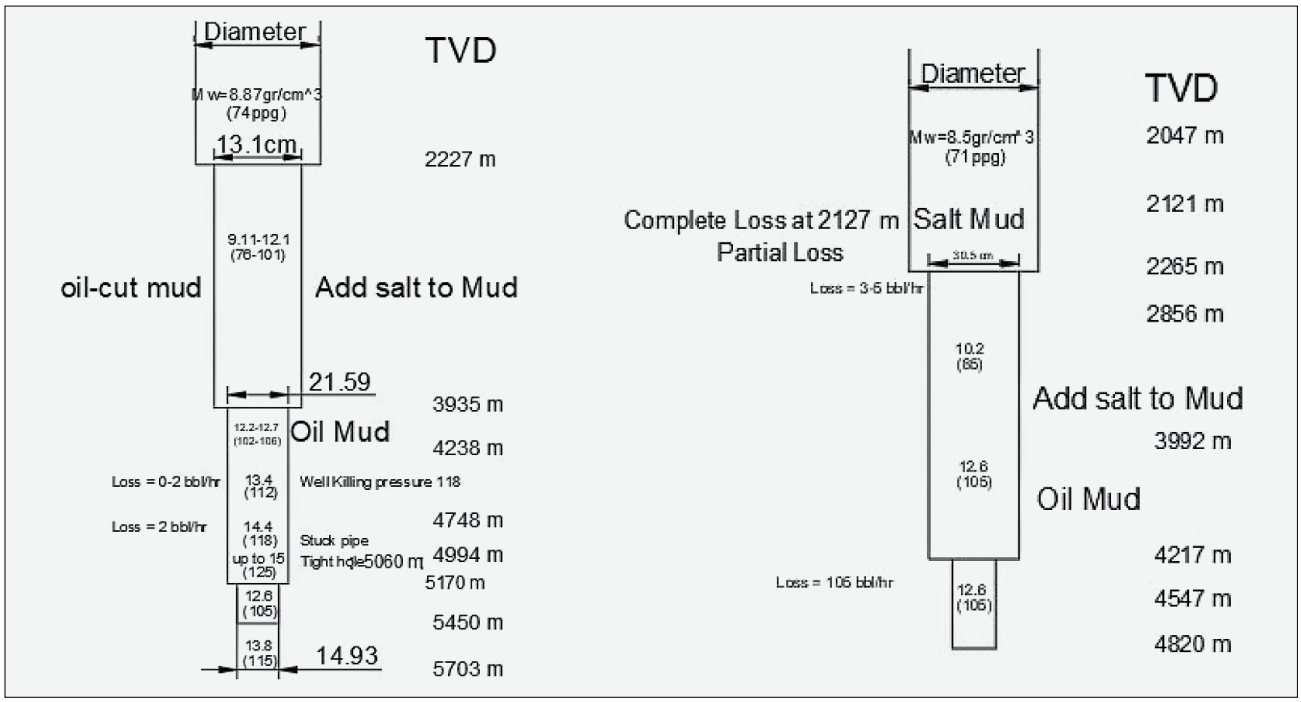


Figure 3. graphical representation of problems during drilling well 2 and well 3

to a water-based mud is a standard practice to prevent shale hydration and swelling that leads to stuck pipe and tight holes. If these remedial actions are unsuccessful in controlling the wellbore instability, a well control operation means killing the well may be required, followed by a workover to restore safe and efficient operations.

Unfortunately, these drilling problems occur for the next wells, in **Figure 4** the schematic drilling problems of well number 4 are shown as the same problems as well number 2 and 3. That means lost circulation and chemical problems of the well occurred during drilling. Thus, we need to find a systematic solution so that the mistake is not repeated. Data-mining techniques were used to learn from previous wells to minimize drilling problems. For this, the parameters such as depth, rate of penetration (ROP), drill string rotation (RPM), weight on a bit (WOB), and flow rate input to model and mud weight and type the output of prediction model.

All engineering efforts can be simplified into two terms, prediction and if the result of the prediction is not suitable the prevention applied, for prediction behaviour researchers have used different approaches. For example, to determine the appropriate drilling fluid properties with analytical methods, only the mechanical instabilities can predict when the stress induced around a wellbore is larger than the strength of the rock. Simplified assumptions used in this method like CHILE (Continues Homogeneous Isotropic Linear Elastic) rock are its main disadvantage (**Albukhari et al., 2018; Tohidi et al., 2017**). Numerical procedures for determining the mud weight depend on input parameters such as the in-situ stress, natural fracture orientation, friction angle, cohesion, etc. which cannot be determined precisely (**Be-**

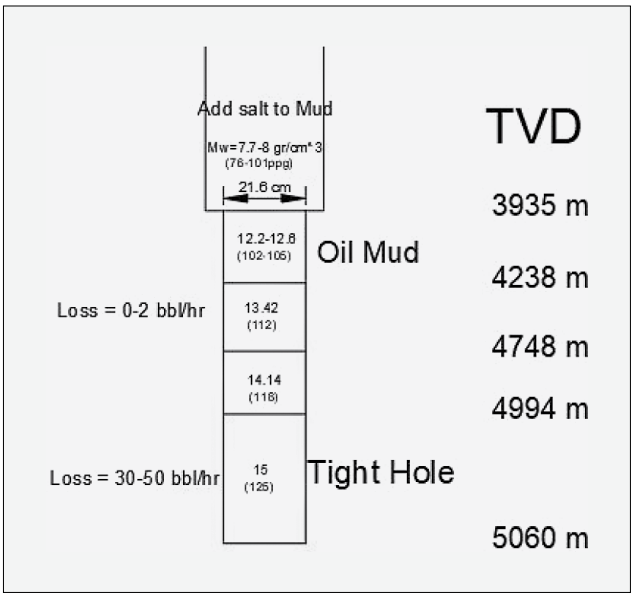


Figure 4. graphical representation of problems during drilling well 4

heshtian et al., 2022; Freij-Ayoub et al., 2003; Gowida et al., 2022; Zahiri et al., 2018). Laboratory simulation is a miniature model of real problems usually conducted on synthetic specimens so it cannot describe the complexity existing in the field (**Agwu et al., 2018; Allawi, 2023**). Mud engineers generally select the weight and type of mud based on previous experience, but this knowledge can be lost if the engineer leaves the company (**Tatar et al, 2015; Ayoub et al., 2019**).

The complex nature of a reservoir, including a natural fracture, high pressure, high temperature, plastic behav-

Table 1. Descriptive statistics of database based on lithology

Lithology	TVD (m)	ROP (m/h)	Diameter (m)	RPM (1/min)	WOB (kN)	Flow Rate (kg/s)	Mud Density (kg/m³)
argillaceous limestone	2482.71	1.07	0.35	188.57	35.90	1237.38	1534.18
argillaceous limestone 80%	3594.00	1.40	0.31	244.00	35.59	1133.98	1774.23
calcareous claystone	2880.50	1.34	0.33	142.28	39.82	1168.71	1666.18
claystone	2204.00	1.98	0.40	166.66	46.71	1533.18	1630.18
dolomite	1766.02	1.51	0.48	104.00	49.82	1669.22	1450.10
limestone	3682.42	1.22	0.27	171.00	33.44	966.17	1774.23
marl	4002.50	0.84	0.26	210.00	33.36	1043.26	2025.07
shale	3986.00	0.49	0.22	60.00	20.02	907.18	2073.40
silty claystone	3626.00	0.49	0.31	244.00	44.48	1133.98	1774.23
Total	2892.22	1.34	0.33	143.15	39.73	1167.07	1676.44
min	17.00	0.03	0.15	10.00	0.00	222.26	1210.44
max	22121.00	10.56	0.61	650.00	122.33	1814.37	2253.33

iour and chemical composition, makes the precise prediction of the mud properties impossible by conventional methods. Hence, the use of data-mining techniques that are trained using the recorded well data is a promising way of predicting the mud properties. Data mining presents a comprehensive solution that is superior to the other methods. The current study used daily drilling reports to extract the mud properties and controllable and non-controllable parameters of 20 oil wells drilled over 50 years for machine learning to predict the mud properties of future wells.

2. Related Work

The efficacy of machine learning (ML) and metaheuristic optimization in solving complex geomechanical challenges is well-documented across various mining and rock engineering domains. For instance, sophisticated ML models have been successfully deployed to predict critical phenomena such as blast-induced ground vibration and flyrock intensity, demonstrating superior accuracy over traditional empirical methods (**Chen et al., 2025; Hasanipanah & Amineh, 2025**). Similarly, deep learning and optimized ensemble techniques have proven highly effective in assessing the intrinsic mechanical and shear strength properties of rock masses, tasks that are fundamental to geotechnical design (**Ding et al., 2025; Ding et al., 2024**). These studies consistently highlight that hybrid models, particularly those enhanced by metaheuristic algorithms, can capture the high non-linearity and complex interactions inherent in rock engineering systems. However, while these intelligent systems have been extensively validated for predicting rock behaviour and the consequences of engineering actions upon it, their application to the proactive optimization of operational inputs – specifically, the properties of drilling fluid – remains comparatively underexplored. Building upon this established precedent of ML success in geomechanics, the present study aims to bridge this gap by adapting and evaluating a suite of optimized metaheuristic algorithms for the simultaneous prediction of mud weight and type, a critical operational parameter in wellbore stability.

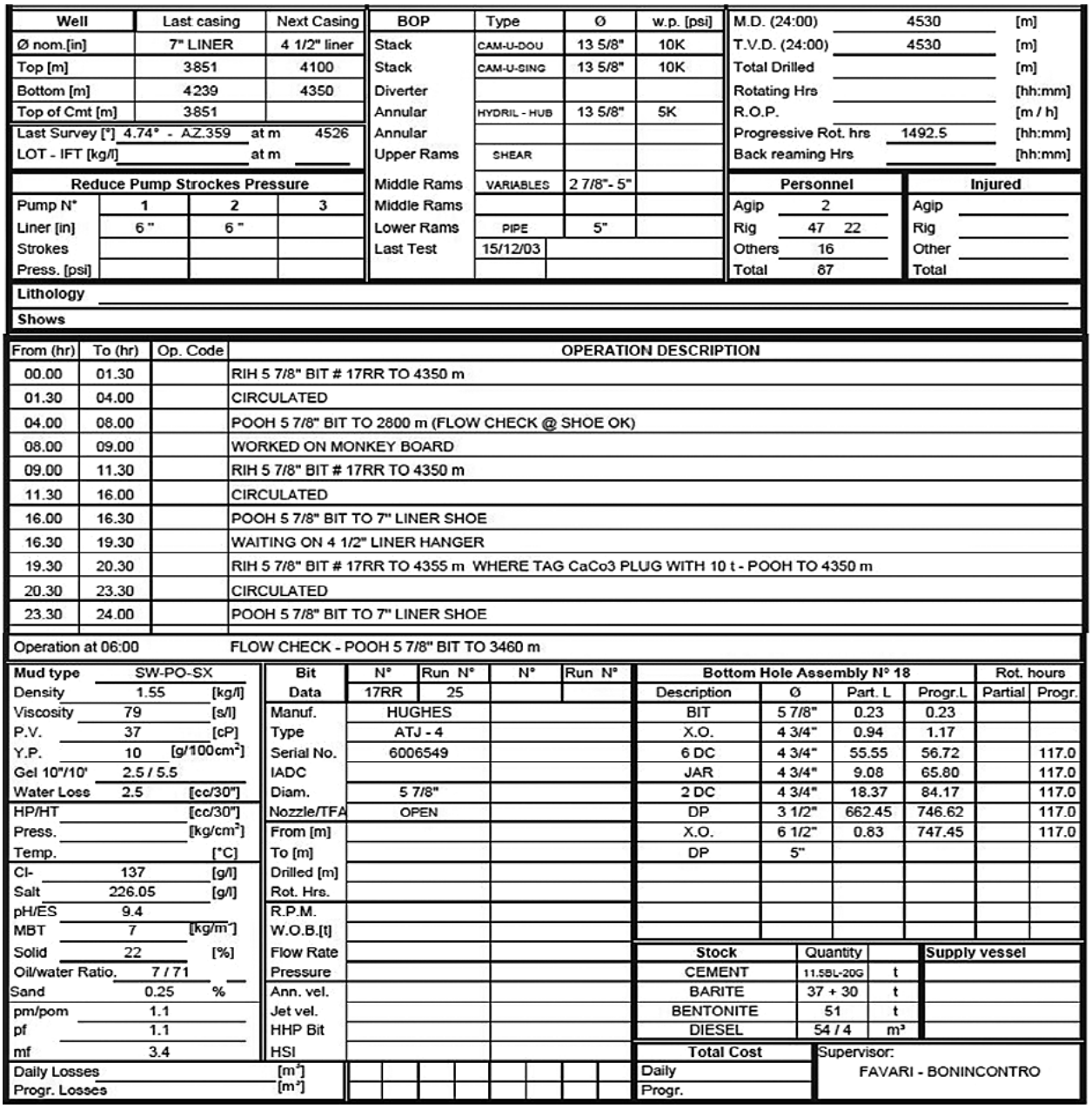
So the challenges of mud prediction include estimation of the mud weight and determination of the chemical properties of the mud. The first part can be named mud-weight window prediction.

2.1. Mud-weight prediction models

In order to determine the mud weight, the induced stress is first calculated and then compared with the failure criteria of the specific rock formation (Mohr-Coulomb, Hoke-Brown, etc.). The upper limit of the mud weight can be determined by substituting the stress induced in tensile failure. If this stress equals the shear strength of the rock, a lower mud weight limit should be estimated.

Researchers used a numerical method and sensitivity analyses to determine a safe mud-weight window (**Ayoub et al., 2019**). The results revealed that, for low-cohesion and friction angle formation, the mud weight window will become narrower. A decrease in the pore pressure and ratio between the maximum and minimum horizontal stresses will widen the mud weight window. This does not simulate the complex nature of the reservoir, such as natural fracture, bedding plane, high pressure and temperature of the reservoir. Additionally, the input parameters of numerical modelling such as the Young's modulus, cohesion and friction angle contain uncertainties.

Zahiri et al first derived the mud-weight window using an analytical approach for three wells and then use an ANN technique to derive a relation between the well-logging data and the mud-weight window. The major disadvantage was that ANN training using the analytical approach included simplified assumptions. It also did not consider chemical instability (**Zahiri et al., 2018**).



Well	Last casing	Next Casing
Ø nom.[in]	7" LINER	4 1/2" liner
Top [m]	3851	4100
Bottom [m]	4239	4350
Top of Cmt [m]	3851	
Last Survey [°] 4.74° - AZ.359	at m	4526
LOT - IFT [kg/l]	at m	

Reduce Pump Strockes Pressure			
Pump N°	1	2	3
Liner [in]	6 "	6 "	
Strokes			
Press. [psi]			

BOP	Type	Ø	w.p. [psi]
Stack	CAM-U-DOU	13 5/8"	10K
Stack	CAM-U-SING	13 5/8"	10K
Diverter			
Annular	HYDRIL - HUB	13 5/8"	5K
Annular			
Upper Rams	SHEAR		
Middle Rams	VARIABLES	2 7/8"- 5"	
Middle Rams			
Lower Rams	PIPE	5"	
Last Test	15/12/03		

M.D. (24:00)	4530	[m]
T.V.D. (24:00)	4530	[m]
Total Drilled		[m]
Rotating Hrs		[hh:mm]
R.O.P.		[m / h]
Progressive Rot. hrs	1492.5	[hh:mm]
Back reaming Hrs		[hh:mm]

Personnel		Injured	
Agip	2	Agip	
Rig	47 22	Rig	
Others	16	Other	
Total	87	Total	

Lithology

Shows

From (hr)	To (hr)	Op. Code	OPERATION DESCRIPTION
00.00	01.30		RIH 5 7/8" BIT # 17RR TO 4350 m
01.30	04.00		CIRCULATED
04.00	08.00		POOH 5 7/8" BIT TO 2800 m (FLOW CHECK @ SHOE OK)
08.00	09.00		WORKED ON MONKEY BOARD
09.00	11.30		RIH 5 7/8" BIT # 17RR TO 4350 m
11.30	16.00		CIRCULATED
16.00	16.30		POOH 5 7/8" BIT TO 7" LINER SHOE
16.30	19.30		WAITING ON 4 1/2" LINER HANGER
19.30	20.30		RIH 5 7/8" BIT # 17RR TO 4355 m WHERE TAG CaCo3 PLUG WITH 10 t - POOH TO 4350 m
20.30	23.30		CIRCULATED
23.30	24.00		POOH 5 7/8" BIT TO 7" LINER SHOE

Operation at 06:00 FLOW CHECK - POOH 5 7/8" BIT TO 3460 m

Mud type	SW-PO-SX
Density	1.55 [kg/l]
Viscosity	79 [s/l]
P.V.	37 [cP]
Y.P.	10 [g/100cm²]
Gel 10"/10'	2.5 / 5.5
Water Loss	2.5 [cc/30"]
HP/HT	[cc/30"]
Press.	[kg/cm²]
Temp.	[°C]
Cl-	137 [g/l]
Salt	226.05 [g/l]
pH/ES	9.4
MBT	7 [kg/m³]
Solid	22 [%]
Oil/water Ratio.	7 / 71
Sand	0.25 %
pm/pom	1.1
pf	1.1
mf	3.4

Bit Data	N°	Run N°	N°	Run N°
	17RR	25		
Manuf.	HUGHES			
Type	ATJ - 4			
Serial No.	6006549			
IADC				
Diam.	5 7/8"			
Nozzle/TFA	OPEN			
From [m]				
To [m]				
Drilled [m]				
Rot. Hrs.				
R.P.M.				
W.O.B.[t]				
Flow Rate				
Pressure				
Ann. vel.				
Jet vel.				
HHP Bit				
HSI				

Bottom Hole Assembly N° 18				Rot. hours	
Description	Ø	Part. L	Progr.L	Partial	Progr.
BIT	5 7/8"	0.23	0.23		
X.O.	4 3/4"	0.94	1.17		
6 DC	4 3/4"	55.55	56.72		117.0
JAR	4 3/4"	9.08	65.80		117.0
2 DC	4 3/4"	18.37	84.17		117.0
DP	3 1/2"	662.45	746.62		117.0
X.O.	6 1/2"	0.83	747.45		117.0
DP	5"				

Stock	Quantity		Supply vessel
CEMENT	11.5BL-20G	t	
BARITE	37 + 30	t	
BENTONITE	51	t	
DIESEL	54 / 4	m³	

Daily Losses	[m³]
Progr. Losses	[m³]

Total Cost	Supervisor:
Daily	FAVARI - BONINCONTRO
Progr.	

Figure 5. Daily drilling report for well 19

Agwu et al. used an ANN model to forecast the density of oil-based mud in high temperature/high pressure (HTHP) wells. They summarized previous empirical and AI approaches to determining the mud density in HTHP wells (**Agwu et al., 2020**). Sabah et al. used machine learning to predict the amount of lost circulation. This parameter was essential for selecting an appropriate lost circulation material to cope with. The data was extracted from 2820 daily drilling reports from 305 oil wells and 18 input parameters were used to predict the amount of circulation lost into the formation (**Sabah et al., 2021**).

Beheshtian et al. gathered 3389 daily drilling reports from three gas wells to predict a safe mud-weight window using several machine learning algorithms (**Beheshtian et al., 2022**). Gowida et al. used the ANN approach to predict the minimum and maximum mud weights (**Gowida et al., 2022**). Phan et al. found that a model was required to predict the real-time mud weight. They reported that analytical and numerical models for this purpose are time consuming and that the AI based method was the best solution for real-time mud-weight prediction (**Phan et al., 2022**). As mentioned earlier prediction drilling fluid is divided into two-part mud weight and mud type. In the next section, the mud-type prediction works were reviewed.

2.2. Mud type prediction models

A greater mud-weight will reduce the tangential stress and increase the normal stress on the wellbore; however,

Table 2. Descriptive statistics of database based on MUD type

Mud Type	TVD (m)	ROP (m/h)	Diameter (m)	RPM (1/min)	WOB (kN)	Flow Rate (kg/s)	Mud Density (kg/m³)
FW-GE	176.46	2.20	0.60	90.71	18.93	1392.87	1339.83
FW-GE SPUD	65.00	1.55	0.61	130.00	6.67	1270.06	1318.44
FW-GE-PO	258.00	3.35	0.61	130.00	20.02	1587.57	1390.44
FW-GEL	201.00	2.14	0.61	100.00	24.47	1723.65	1330.44
FW-GY	2669.11	0.76	0.33	151.87	48.73	1207.73	1600.99
FW-KC	1440.37	2.17	0.42	117.37	39.57	1616.95	1462.99
FW-KC-PC	1491.52	2.38	0.42	137.16	50.28	1605.00	1484.55
FW-LS	4476.00	0.69	0.21	150.00	19.28	718.18	1983.66
FW-PO	2905.80	3.14	0.31	220.00	13.88	1319.95	1618.20
FW-S-PO	1539.67	1.68	0.21	96.67	37.81	801.31	1378.44
FW-SW-GE	1070.10	1.86	0.61	50.00	46.71	1769.01	1246.44
SW	3136.95	0.20	0.31	110.00	6.67	861.83	1744.11
SW-GE	1514.76	2.24	0.43	150.04	63.66	1597.40	1509.33
SW-GE-PO	2114.45	1.53	0.39	162.59	44.18	1480.65	1536.66
SW-LS-LI	4333.72	0.62	0.17	106.41	17.64	490.73	1920.44
SW-PO	2706.99	1.54	0.34	148.78	41.34	1273.12	1647.99
SW-PO-LS	3473.40	0.43	0.31	136.21	37.31	1084.39	1642.77
SW-PO-SX	4030.80	0.87	0.24	145.85	34.28	844.10	1860.00
PO-LS	2492.00	0.16	0.31	129.40	9.34	900.00	1476.66
Total	2892.23	1.34	0.33	143.16	39.73	1167.52	1676.44
min	17.00	0.03	0.15	10.00	0.00	222.26	1210.44
max	22121.00	10.56	0.61	650.00	122.33	1814.37	2253.33

FW = fresh water; SW = sea water; PO = polymer; KC = potassium chloride; GE = gel; LI = lime mud; SX = soltex; LS = lingosulfonate; GY = gypsum base; PC = partially hydrolyzed polyacrylamide.

in some situations this has an adverse effect on wellbore stability. When mechanical solutions are not appropriate, a chemical analysis of the drilling fluid should be carried out. Most chemical analyses are based on an experimental approach by measuring parameters such as the cation exchange capacity (CEC) and x-ray diffraction (XRD) to determine the active clay mineral content. The choice of drilling fluid is based on the composition of the formation. For example, shale swells slightly when sodium silicate is added to polymer mud. However, the addition of potassium chloride to the polymer mud produced significant swelling, indicating that the mud consisted of various chemical constituents which interacted with the formation, especially shale (**Allawi, 2023**).

Swelling shale has low strength and tends toward time-dependent wellbore instability. Traditionally, oil-based mud has been employed in such formations; however, because of its negative environmental impact, other types of mud, such as polymer/KCL/lime/gypsum have been used instead. Few works have used AI to estimate mud type, but some researchers have predicted the rheological properties of mud and the density of its constituents (**Agwu et al., 2020**).

Tatar et al. used pressure, temperature and concentration as inputs to predict the brine density of mud (**Tatar et al, 2015**). Aljubran et al. determined the mechanical-thermal/physico-chemical interaction on wellbore instability. They reported that cooler temperatures and higher salt concentrations in the mud improved the wellbore stability in a shale formation (**Aljubran et al., 2022**).

Due to the lack of research that comprehensively solves drilling fluid prediction, this work used a data mining approach to find mud's physical and chemical properties. In the following, the details of the research are explained.

3. Methods

A sample daily drilling report is shown in **Figure 5**. This report records mud type, bit data, bottom hole assembly, and pressure. Such reports are the most reliable data because of gathering during daily drilling and on the well location.

3.1. Data Analysis

The initial determination of the dataset's descriptive statistics involved a comprehensive examination of each

parameter through mathematical calculations. It was ascertained that the highest correlation with mud density across all parameters was observed when the relationship between them followed a power and linear equation. The selection of this equation in the present research was made to encompass all three algorithms. **Tables 1 and 2** display the descriptive statistics of the database.

The general form of the predictive equation used in this investigation is given by **Equation 1**. In this model, the output (predicted mud density) is a function of six standard drilling parameters, each multiplied by a specific weight coefficient (W~i~) that is optimized by the algorithms. The coefficients determine the relative influence and scaling of each input parameter.

$$\begin{aligned} &\mathrm{TVD} \times \mathrm{W1} + \mathrm{ROP} \times \mathrm{W2} + \mathrm{W3} \times \mathrm{diam} + \\ &+ \mathrm{RPM} \times \mathrm{W4} + \mathrm{W5} \times \mathrm{WOB} + \mathrm{flow\ rate} + \mathrm{W6} \end{aligned} \quad (1)$$

Where:
TVD is the True Vertical Depth (m),
ROP is the Rate of Penetration (ft/h),
diam is the drill bit diameter (inches)
RPM is the drill string Revolutions Per Minute (1/min),
WOB is the Weight On Bit (kip),
flow rate is the mud flow rate (lb/s),
W1, W2, W3, W4, W5, W6 are the weight coefficients optimized by the ACO, BCO, and EPC algorithms.

3.2. Evaluation criteria

This investigation evaluated the accuracy and efficiency of the predictive models using the coefficient of determination (R^2) and the root mean-square error (RMSE), as stipulated in **Equations 2** and **3**. These metrics are well-established in the literature for assessing the performance of machine learning models in geotechnical and mining engineering applications, providing a standardized and interpretable measure of predictive power (**Hasanipanah et al., 2022; Hasanipanah et al., 2015**). The ideal values for R^2 and RMSE are one and zero, respectively. Utilizing distribution diagrams and comparative graphs of observational versus computational data, the results were analyzed and compared.

3.2.1. Coefficient of determination

The coefficient of determination measures the explanatory power of a model by quantifying the percentage of variance in the dependent variable that can be accounted for by the independent variables. Specifically, it represents the total variation in the dependent variable as the sum of the variation explained by the regression and the variation not explained by the regression. This coefficient provides a probabilistic estimate of the correlation between two sets of data in the future, based on a defined mathematical model that conforms to existing data (**Allawi & Al-Jawad, 2021**).

The R^2 is utilized as a key measure for evaluating the precision of the regression model in depicting variables, with a higher value denoting a more suitable fit. It demonstrates the concordance between the recorded and anticipated values, which can be assessed using parsing and fitting techniques. The coefficient of determination delineates a segment of the overall variance in the recorded values that can be explained by simulated values, ranging from zero to one, where an ideal value of one signifies impeccable alignment between the simulated and recorded values (**Phan et al., 2022**). Its robustness and intuitive interpretation have made it a standard metric in intelligent systems developed for geotechnical prediction, such as forecasting rock mass properties and environmental hazards (**Hasanipanah et al., 2022; Hasanipanah et al., 2015**).

Equation 2 defines the relationship between the computational value $x\ i$ and the observational value $y\ i$ for time-step i. The variables N, $\bar{x}$, and $\bar{y}$ denote the total number of time-steps and the average computational and observational values, respectively.

$$R^2 = \frac{\sum_{i=1}^{N}(x_i - \bar{x})(y_i - \bar{y})}{\sqrt{\sum_{i=1}^{N}(x_i - \bar{x})^2 \ \sum_{i=1}^{N}(y_i - \bar{y})^2}} \quad (2)$$

3.2.2. Root mean square error (RMSE)

The RMSE is a function of the fit or objective function and is defined as the square root of the mean squared error value. The RMSE serves as a measure of the absolute error between predicted and observable values. The range of this statistical index is from zero to infinity, with lower values indicating better simulation performance. The optimal value of the RMSE is zero. The mathematical expression for the RMSE is:

$$RMSE = \sqrt{\frac{1}{N}\sum_{i=1}^{N}(x_i - y_i)^2} \quad (3)$$

3.3. Ant Colony Optimization (ACO)

Ant colony optimization can be modeled as P= (S, Ω, f), where S is the set of all finite sets of discrete decision variables, and Ω represents the constraints between these variables and a target function f: $S \longrightarrow R0+$, subject to minimization or maximization (**Dorigo & Blum, 2005**). Ant colony optimization incrementally generates solutions by considering the likelihood of solution components, with probabilities determined by pheromone levels (**Dorigo & Blum, 2005**). When applied to hybrid optimization problems, a set of solution components is defined based on the problem formulation. During solution construction, ants select ci from $N(s^p)$ using **Equation 4** at each step.

$$p(\mathrm{c}_{ij}|\mathrm{s}^p) = \mathrm{c}_{ij}{}^p \cdot \frac{\eta(cij)^\beta}{\sum c_{il \in N(s^p)} \tau ij^\alpha . \eta(cij)^\beta}, \ \forall \mathrm{c}_{ij} \in N(s^p) \quad (4)$$

In pheromone-based optimization, τij represents the pheromone level on edge cij. A weight function, $\eta(0)$, updates edges $cij \in N(s^p)$ at each iteration, producing values termed "apocalyptic information." Positive parameters α and β govern the relationship between pheromone and heuristic information. A Gaussian kernel, used for sampling, is defined as the sum of weighted one-dimensional Gaussian functions, $Gi(x)$.

$$G^i(x) = \sum_{l=1}^{k} \omega_l g_l^i(x) = \sum_{l=1}^{k} \omega_l \frac{1}{\sigma_l^i \sqrt{2\pi}} e^{-\frac{\left(x-\mu_l^i\right)^2}{2\sigma_l^{i^2}}} \quad (5)$$

Multi-core probability density functions determine a single probability density function based on the problem's dimension (i = 1,…, n). Each $Gi(x)$ is represented using three parametric vectors: ω (weights), μi (means), and δi (standard deviations), along with one-dimensional Gaussian functions, g_l^i (x). These vectors have cardinality equivalent to the number of Gaussian functions (denoted by k) in the Gaussian kernel.

$$| \omega | = | \mu i | = | \delta i | = k \quad (6)$$

Ant Colony Optimization (ACO) is governed by several control parameters. α controls the influence of pheromone trails, with higher values favoring exploitation. β controls the influence of heuristic information, with higher values favoring exploration. ρ represents the pheromone evaporation rate, preventing premature convergence; higher values increase exploration. The number of ants affects search thoroughness, with more ants increasing computational cost. Q is a constant related to pheromone deposition. These parameters are typically tuned empirically, using literature-based values, or through computationally expensive meta-optimization.

3.4. Bee Colony Optimization (BCO)

The freak algorithm utilizes a freak colony with three groups hired, hunt, and watch notions. Each food source represents a implicit result, and its quencher volume indicates result quality (**Karaboga, 2005**). Originally, a population of results, corresponding to food source locales, is generated.' SN' denotes the number of hired/ hunt notions. Each result (j = 1.2.3.. SN) is a D- dimensional vector, where' D' is the number of optimization parameters. Search notions elect food sources grounded on quality; the probability of opting a source is calculated using **Equation 7**.

$$P_{i=\frac{fit_i}{\sum_{N-1}^{SN} fit_N}} \quad (7)$$

In the context of statistical analysis, the variable $fiti$ represents the fitness value of the i^{th} observation.

The process of selecting a novel food source (Vij) is determined by **Equation 8**, which is contingent upon the preceding food source (Xij). This approach is adopted within an academic context.

$$Vij = Xij + (Xij - Xkj) \quad (8)$$

Random pointers j and k, where j and k are rudiments of the set{ 1.2.. SN}, are named. It's important to note that k is named aimlessly, but must be distinct from j. In the environment of the freak algorithm, a food source that fails to recover after a specified replication is supposed an abandoned food source. In similar cases, the notions cover the situation in agreement with **Equation 9** and latterly replace the abandoned food source with a new one named at arbitrary (**Karaboga & Basturk, 2008**).

$$X_i^j = X_{min}^j + \text{rand}[0.1](X_{max}^j - X_{min}^j) \quad (9)$$

The variable j denotes the quantity of optimization variables.

In BCO, key control parameters include colony size (SN), representing the number of food sources or solutions, and Limit, which dictates when an unproductive food source is replaced by a scout bee to escape local minima. The maximum cycle number (MCN) serves as the stopping criterion, defining the maximum number of iterations.

In the ABC algorithm, foundational literature (**Karaboga, 2005**) typically suggests setting the Limit parameter to SN * D, where D represents the number of dimensions. Here, D=6 (TVD, ROP, Diam, RPM, WOB, Flowrate). We systematically varied SN and Limit to optimize performance for this specific problem. The omission of this detail regarding the Limit parameter is significant, as it plays a crucial role in balancing exploration and exploitation within the ABC algorithm.

3.5. Emperor Penguins Colony (EPC)

The foundational premise of the Emperor Penguin algorithm posits that penguins are distributed across the examined environment. Consequently, at the outset, prior to the introduction of more complex procedures, it is essential to assess the relative positions of each penguin in relation to one another. It is important to note that a penguin typically gravitates towards another that presents a lower absorption cost. Thus, the second critical measurement involves determining the absorption cost for each penguin, which is influenced by both heat intensity and distance. Throughout the execution of this algorithm, each phase of absorption entails the evaluation of a new potential solution to the problem at hand, accompanied by an update of the heat intensity. Following this, all potential solutions are organized, and the optimal one is identified. Additionally, a damping ratio is calculated for each penguin, which is influenced by various factors, including the individual penguin's movement, heat radiation, and heat absorption. A lower damping ratio indicates a more favorable solution (**Harifi et al., 2019**).

Emperor Penguin Colony (EPC) is a metaheuristic algorithm that mimics the huddling behaviour of emperor penguins seeking warmth.

Table 3. ACO results for six models

Model	Training Dataset	Testing Dataset	Coefficient of weighting						Model evaluation	
			W1 TVD	W2 ROP	W3 diameter	W4 RPM	W5 WOB	W6 flow rate	R^2	RMSE
1	P2-P3-P4	P1	-0.0078	0.0432	-0.4567	0.1324	-2.3456	0.8765	0.6589	0.1245
2	P1-P3-P4	P2	-0.0089	0.0456	-0.5678	0.1234	-2.8765	0.7654	0.7890	0.1434
3	P1-P2-P4	P3	-0.0086	0.0567	-0.4433	0.1259	-2.1234	0.6890	0.8896	0.1278
4	P1-P2-P3	P4	-0.0085	0.0642	- 0.4567	0.1347	-2.0987	0.8976	0.7644	0.1239
5	Entire training dataset.	P1	-0.0064	0.0778	-0.6555	0.1447	-1.3364	0.7651	0.9176	0.0987
		P2	-0.0064	0.0778	-0.6555	0.1447	-1.3364	0.7651	0.9034	0.0876
		P3	-0.0064	0.0778	-0.6555	0.1447	-1.3364	0.7651	0.9078	0.0912
		P4	-0.0064	0.0778	-0.6555	0.1447	-1.3364	0.7651	0.9025	0.0789
6	80% of all dataset	20% of all dataset	-0.0012	0.047	-0.5824	0.2234	-1.1345	0.5612	0.9649	0.0364

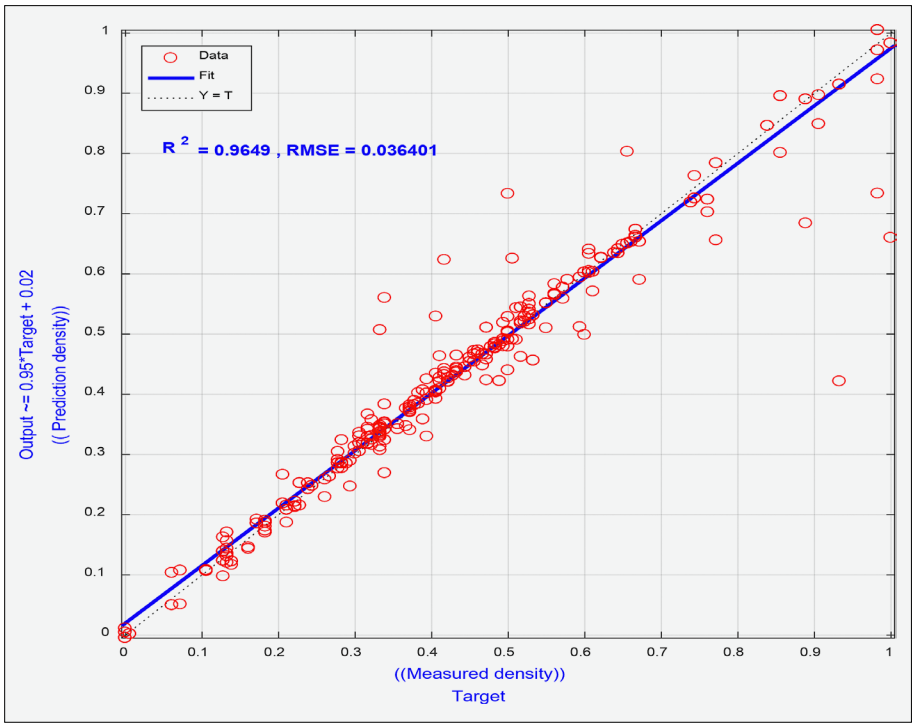


Figure 6. Distribution of top model by ACO

Key control parameters include:

- Population Size (N): the number of penguins in the colony.
- Heat Absorption Cost Function Parameters (A, B): these parameters govern penguin movement and huddling behaviour based on metaphorical temperature and distance calculations.
- Damping Ratio (R): simulates reduced heat loss during huddling, influencing convergence.
- Maximum Iteration Number: the stopping criterion.

Parameter Value Selection based on the algorithm's recent development, the original paper (**Harifi et al., 2019**) is often consulted for default values. Sensitivity analysis may also be performed to assess the impact of parameter variations on model output for specific applications like drilling fluid prediction.

4. Results

This section presents the comprehensive results of applying the three nature-inspired optimization algorithms – Ant Colony Optimization (ACO), Bee Colony Optimization (BCO), and Emperor Penguins Colony (EPC) – to predict drilling mud weight and identify the optimal mud type. The performance of each algorithm is evaluated based on the coefficient of determination (R^2) and root mean square error (RMSE), as defined in the methodology. Furthermore, the final weighting coefficients (W1 to W6) derived from the optimal model for each algorithm are presented, revealing the relative influence of the input parameters (TVD, ROP, Diameter, RPM, WOB, Flow Rate) on the predicted mud density. The results are systematically organized to first detail the predictive performance and derived equations for each al-

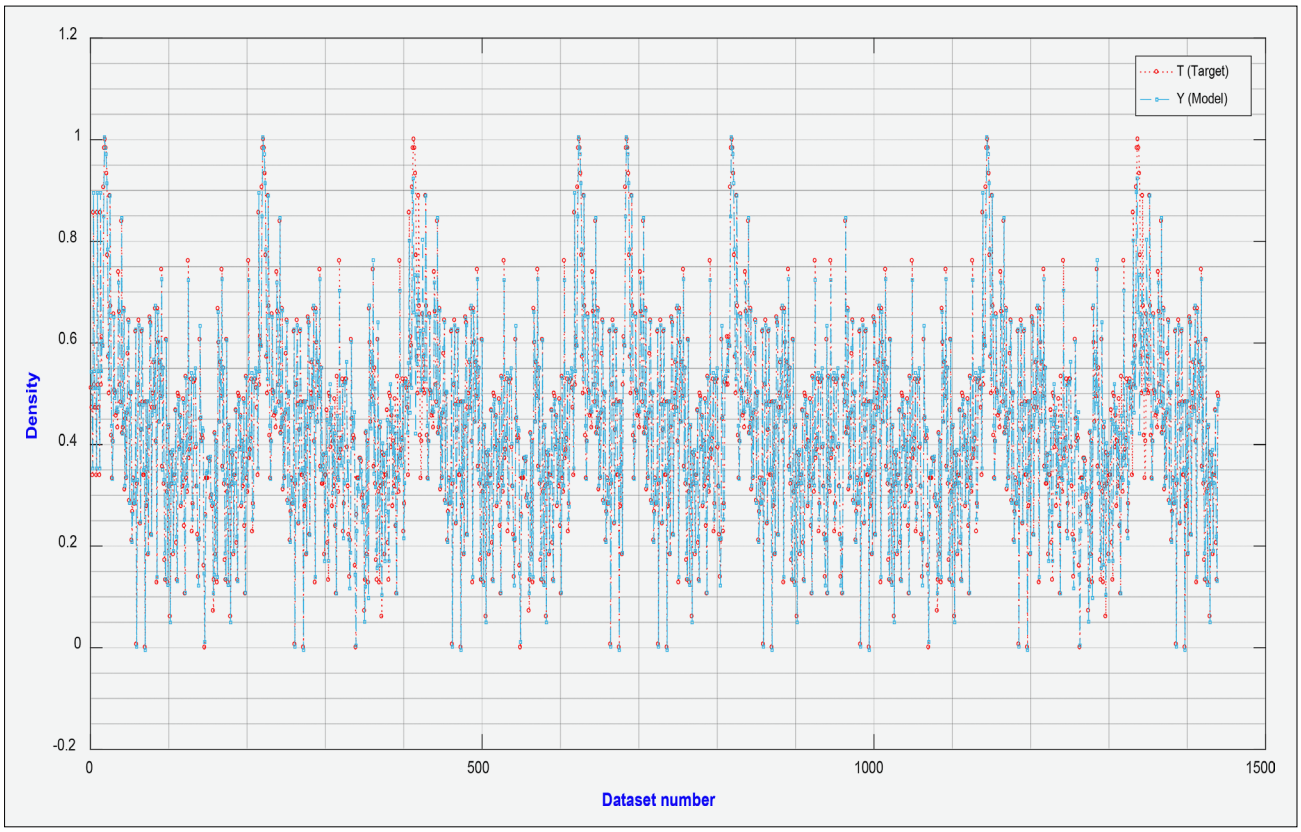


Figure 7. Matching of top model by ACO

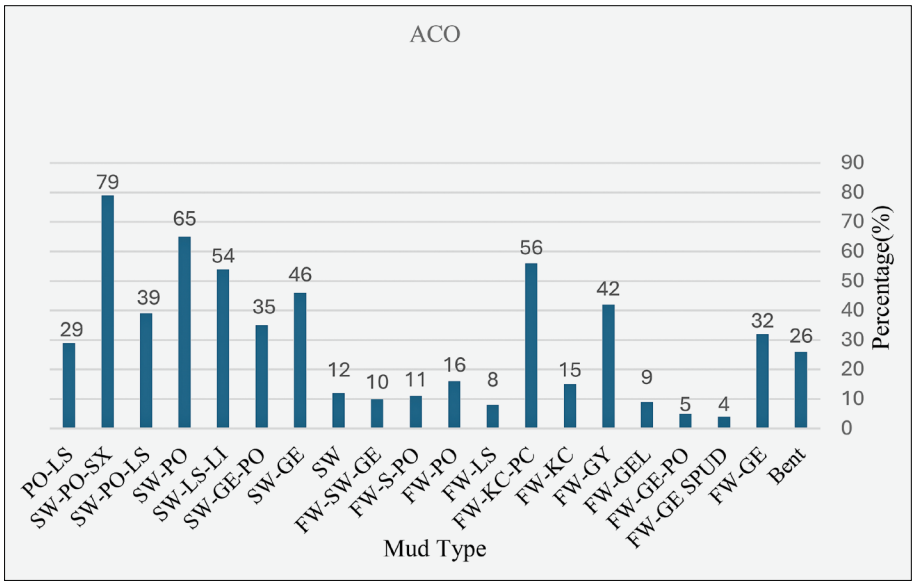


Figure 8. Best mud type by ACO

gorithm individually, followed by a comparative analysis that highlights the most effective model and its practical implications for optimal fluid selection in the studied field.

4.1. Ant colony optimization Result (ACO)

Models 1-4 used a four-fold cross-validation approach, training on three steps and testing on the remaining one. Model 5 trained on the entire dataset and was then tested on datasets P1-P4. Model 6 trained on 80% of the data and tested on the remaining 20%. Model 6 demonstrated sufficient accuracy, achieving an R2 of 0.9649 and RMSE of 0.0364. **Table 3** presents R2, RMSE, and coefficient weighting across all models. **Figures 6** and **7** illustrate the distribution and correlation between measured, target, and predicted values for the top-performing model. **Figure 8** identifies the optimal mud type according to ACO.

Table 4. BCO Algorithm Results: Six Models

Model	Training Dataset	Testing Dataset	Coefficient of weighting						Model evaluation	
			W1 TVD	W2 ROP	W3 diameter	W4 RPM	W5 WOB	W6 flow rate	R^2	RMSE
1	P2-P3-P4	P1	-0.0023	0.0876	-0.3321	0.4567	-3.7654	0.6543	0.9086	0.3421
2	P1-P3-P4	P2	-0.0014	0.0789	-0.3346	0.3257	-2.4532	0.8976	0.8765	0.4456
3	P1-P2-P4	P3	-0.0015	0.0456	-0.5567	0.5678	-2.5643	0.6532	0.7864	0.3245
4	P1-P2-P3	P4	-0.0054	0.0897	- 0.7864	0.3245	-2.9543	0.9986	0.8324	0.4478
5	Trained on 100% of dataset.	P1	-0.0022	0.0332	-0.4567	0.2223	-1.1123	0.4532	0.9132	0.1265
		P2	-0.0022	0.0332	-0.4567	0.2223	-1.1123	0.4532	0.9543	0.1870
		P3	-0.0022	0.0332	-0.4567	0.2223	-1.1123	0.4532	0.9325	0.1032
		P4	-0.0022	0.0322	-0.4567	0.2223	-1.1123	0.4532	0.9143	0.0989
6	80% of all dataset	20% of all dataset	-0.0019	0.0664	-0.2365	0.2987	-1.9433	0.2137	0.9841	0.0245

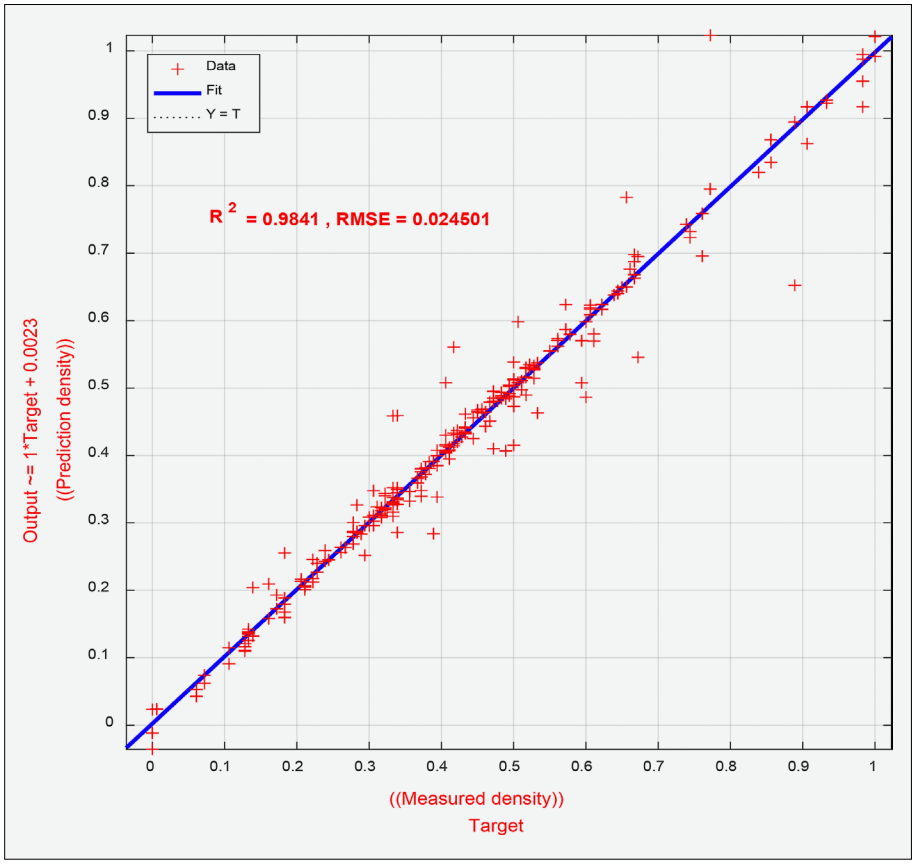


Figure 9. Distribution of top model by BCO

The equation obtained using ACO was:

$$-0.0012 \times TVD + ROP^{0.047} - 0.5824 \times diam + RPM^{0.2234} - 1.1345 \times WOB + flowrate^{0.5612} \quad (10)$$

4.2. Bee colony optimization results (BCO)

BCO algorithm Models 1-4 used a four-step partition: each step tested the targets while the remaining steps trained the sets. Model 5 trained on the entire dataset, then each step (P1-P4) was used for testing. Model 6 trained on 80% of the dataset and tested on the remaining 20%. The results showed Model 6 to be sufficiently accurate, yielding an R2 of 0.9841 and RMSE of 0.245 for the best prediction. **Table 4** presents the R2, RMSE, and weighting coefficients for all BCO models. **Figures 9** and **10** display the distribution and matching charts, respectively, of measured and predicted values for the top model. **Figure 11** identifies the best mud type according to the BCO.

The equation obtained using BCO was:

$$-0.0019 \times TVD + ROP^{0.0664} - 0.2365 \times diam + RPM^{0.2987} - 1.9433 \times WOB + flowrate^{0.2137} \quad (11)$$

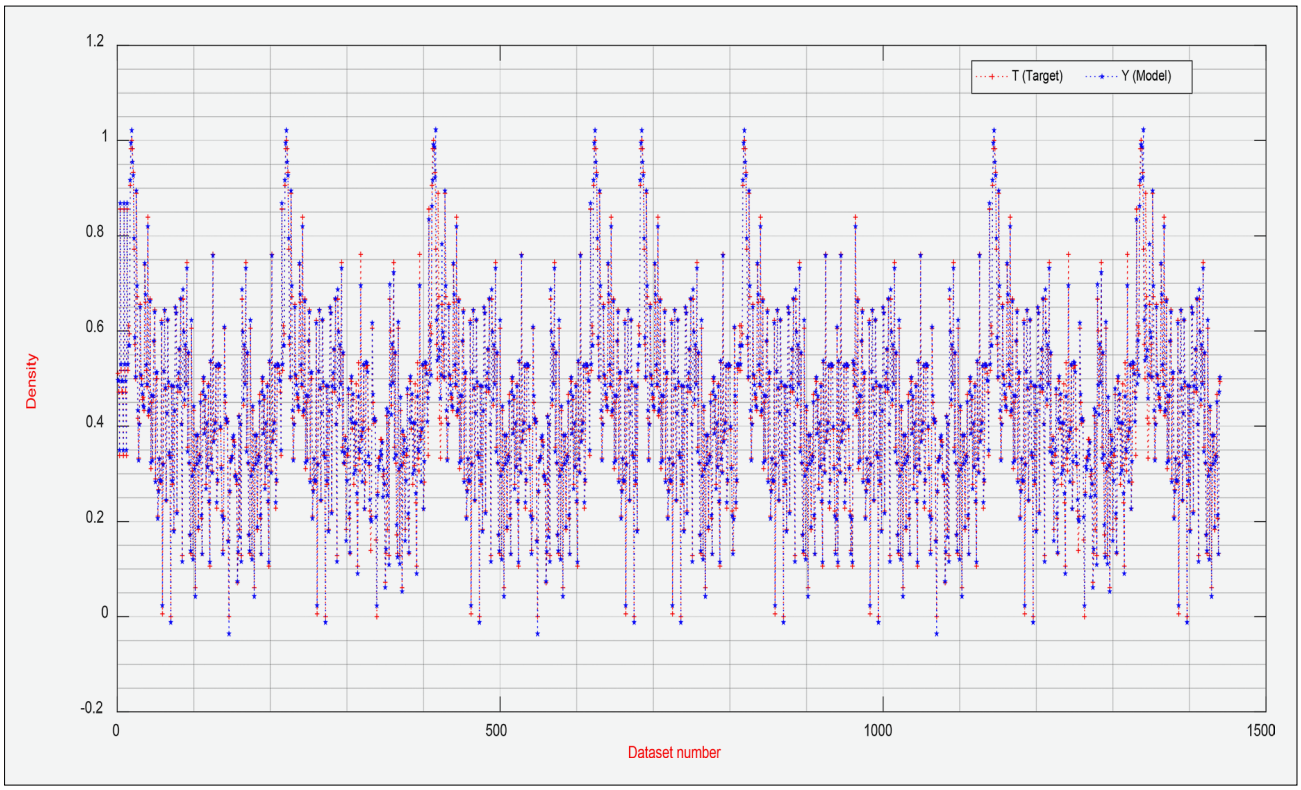


Figure 10. Matching of top model by BCO

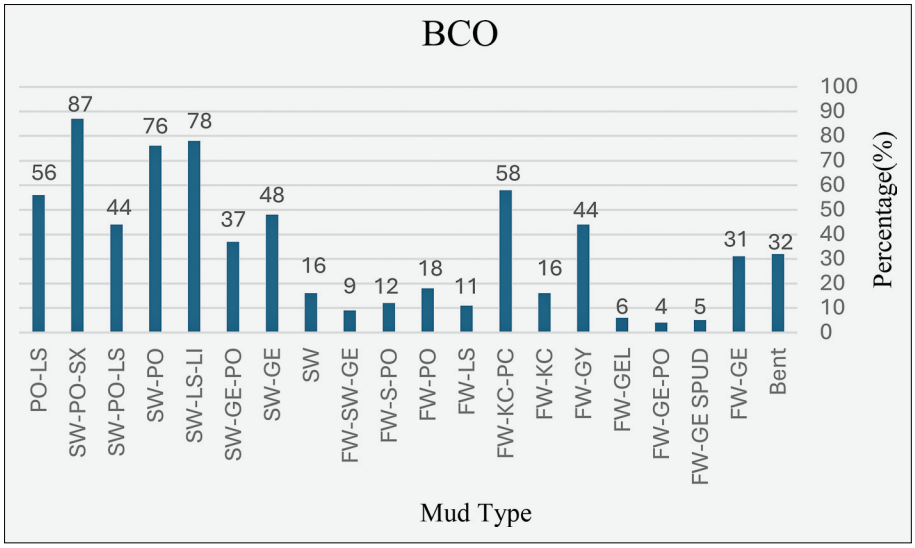


Figure 11. Best mud type by BCO

4.3. Results of Emperor Penguins Colon (EPC)

Models 1- 4 of the EPC algorithm used a four-step partitioning, employing one step for testing and the remaining three for training. Model 5 trained on the full dataset and also tested each step (P1-P4) across all models. Model 6 employed 80 of the dataset for training and 20 for testing. The results demonstrated that Model 6 and its associated equation displayed high delicacy, achieving an R2 of 0.9707 and an RMSE of 0.0332 in the stylish model. **Table 5** presents the R2, RMSE, and weighting portions for all EPC algorithm vaticination models. **Figures 12** and **13** illustrate the distribution and correlation, independently, between measured and prognosticated target values for the top- performing model. **Figure 14** identifies the optimal slush type grounded on the EPC.

The equation using EPC was:

$$-0.0056 \times TVD + ROP^{0.432} - 0.2223 \times diam + \\ + RPM^{0.3254} - 1.3456 \times WOB + flowrate^{0.3317} \quad (12)$$

An investigation was conducted on the modelling process and the outcomes are presented in **Table 6** and

Table 5. EPC Six models' algorithm results

Model	Training Dataset	Testing Dataset	Coefficient of weighting						Model evaluation	
			W1 TVD	W2 ROP	W3 diameter	W4 RPM	W5 WOB	W6 flow rate	R^2	RMSE
1	P2-P3-P4	P1	-0.0055	0.0666	-0.7787	0.4567	-4.2246	0.4321	0.8765	0.1789
2	P1-P3-P4	P2	-0.0065	0.0876	-0.8876	0.6543	-4.5678	0.3456	0.8790	0.1897
3	P1-P2-P4	P3	-0.0067	0.0654	-0.7654	0.3245	-2.5678	0.7896	0.7890	0.1765
4	P1-P2-P3	P4	-0.0076	0.0897	- 0.6543	0.3456	-2.7654	0.6542	0.8765	0.1123
5	Entire dataset used for model training.	P1	-0.0044	0.0556	-0.2345	0.3345	-2.1346	0.4567	0.9234	0.0779
		P2	-0.0044	0.0556	-0.2345	0.3345	-2.1346	0.4567	0.9345	0.0987
		P3	-0.0044	0.0556	-0.2345	0.3345	-2.1346	0.4567	0.9214	0.0543
		P4	-0.0044	0.0556	-0.2345	0.3345	-2.1346	0.4567	0.9123	0.0635
6	80% of all dataset	20% of all dataset	-0.0056	0.0432	-0.2223	0.3254	-1.3456	0.3317	0.9707	0.0332

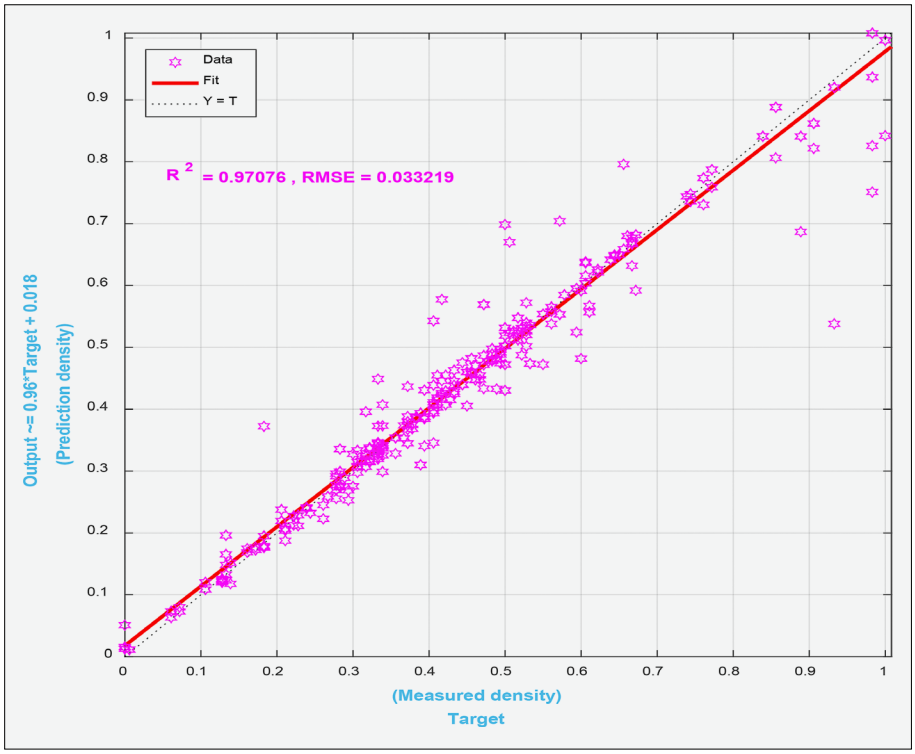


Figure 12. Distribution of top model by EPC

Figures 15 and **16** The results (predicted values) from the use of ACO, BCO and EPC were compared with the measured values (targets). These predicted values also were compared with the obtained values.

5. Discussion

The findings of this study underscore the transformative potential of machine learning in revolutionizing drilling fluid engineering. By successfully predicting both mud weight and type – a dual challenge often addressed in isolation – our framework provides a holistic, data-driven solution to a complex geomechanical problem. The following discussion elaborates on the performance of the algorithms, the critical influence of input parameters, the practical significance of the optimal mud type, and the broader implications for the industry.

5.1. Comparative Algorithm Performance and Robustness

The superior performance of the Bee Colony Optimization (BCO) algorithm (R^2 = 0.9841, RMSE = 0.0245) over Ant Colony Optimization (ACO) and Emperor Penguins Colony (EPC) can be attributed to its intrinsic search mechanisms. BCO employs a balanced combination of employed, onlooker, and scout bees, which allows for robust exploitation of promising solutions while simultaneously exploring new regions of the search space to avoid local optima. This is particularly advantageous for the high-dimensional, non-linear relationship

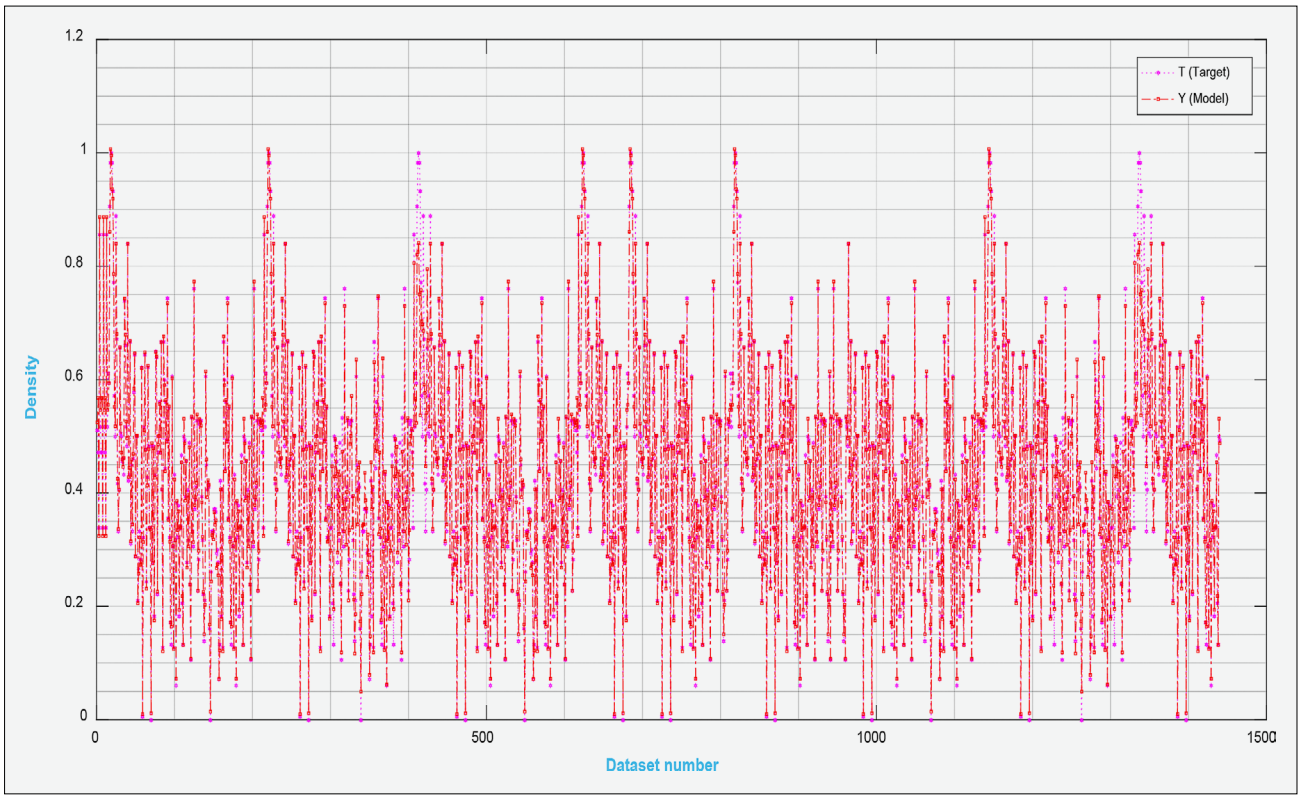


Figure 13. Matching top models by EPC

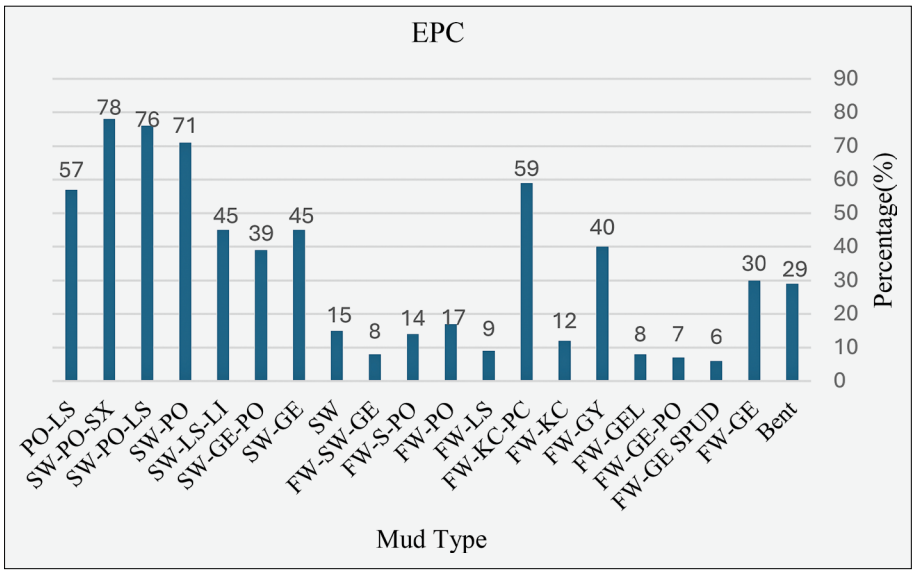


Figure 14. Best mud type by EPC

between drilling parameters and mud properties, where the risk of convergence to suboptimal solutions is high.

While ACO and EPC also delivered highly accurate results ($R^2 > 0.96$), their slightly lower performance may stem from their specific convergence behaviours. ACO's reliance on pheromone trails can sometimes lead to premature stagnation if the evaporation rate (ρ) is not optimally tuned. EPC, inspired by huddling behaviour, is effective for continuous optimization but might be less agile than BCO in discretely navigating the complex weight space for each parameter in our predictive equation. The consistent high performance across all three nature-inspired algorithms, however, validates the fundamental premise that metaheuristic-driven ML models are exceptionally well-suited for capturing the intricate rock-fluid interactions that elude traditional analytical methods.

5.2. Sensitivity Analysis and Parameter Influence

A critical step in validating any data-driven model is to interpret its inner workings. To this end, we conducted

Table 6. Comparison of models

Model	R^2	RMSE	Best Mud Type	Best Mud Type (%)
ACO	0.96	0.03	SW-PO-SX	79
BCO	0.98	0.02	SW-PO-SX	87
EPC	0.97	0.03	SW-PO-SX	78

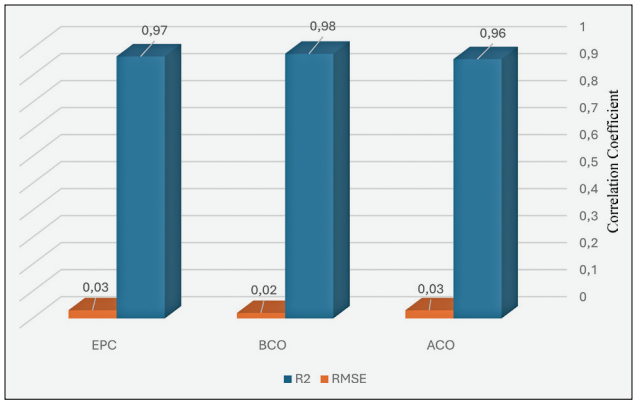


Figure 15: Comparison of models

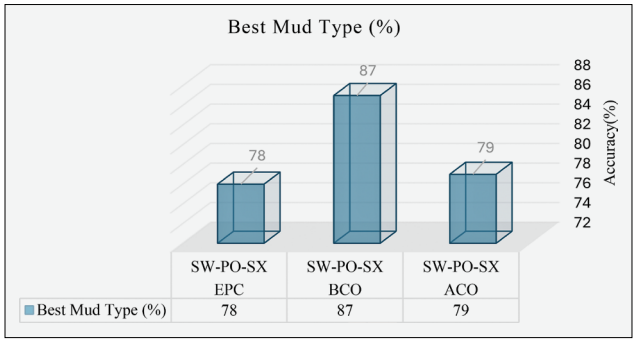


Figure 16. Best mud type from models

a comprehensive sensitivity analysis based on the final weight coefficients (Wi) from the optimal BCO model (Equation 11). The relative importance of each input parameter was quantified and is presented in **Figure 18**.

According to **Figure 18**, ROP (W2): 100% (Normalized Importance): as indicated by its high positive weight (0.0664), ROP emerged as the most influential parameter. This is mechanistically sound; ROP is a direct manifestation of the drill bit's interaction wth the formation. A high ROP often indicates softer, more porous, or fractured rock, which may require a different mud weight to stabilize and a specific chemical type to inhibit interaction. The strong correlation suggests that ROP acts as a real-time proxy for in-situ rock strength and lithology.

Weight on Bit (WOB) (W5): ~65% Importance - the significant negative weight (-1.9433) of WOB indicates an inverse relationship with mud density. Higher WOB typically leads to higher ROP and generates more cuttings, potentially necessitating mud system adjustments. Its high importance underscores its role as a primary controlled variable affecting the drilling process's mechanical efficiency.

Diameter (W3): ~35% Importance - the negative coefficient (-0.2365) suggests that larger boreholes may require slightly lower mud weights, possibly due to the reduced hoop stress and different cuttings load.

Flow Rate (W6): ~30% Importance - flow rate is crucial for hole cleaning. Its positive influence (0.2137) aligns with the need for adequate hydraulic energy to lift cuttings, which influences the effective mud density and rheology downhole.

RPM (W4): ~25% Importance - while important, RPM's lower influence suggests its effect might be partially captured by its correlation with ROP.

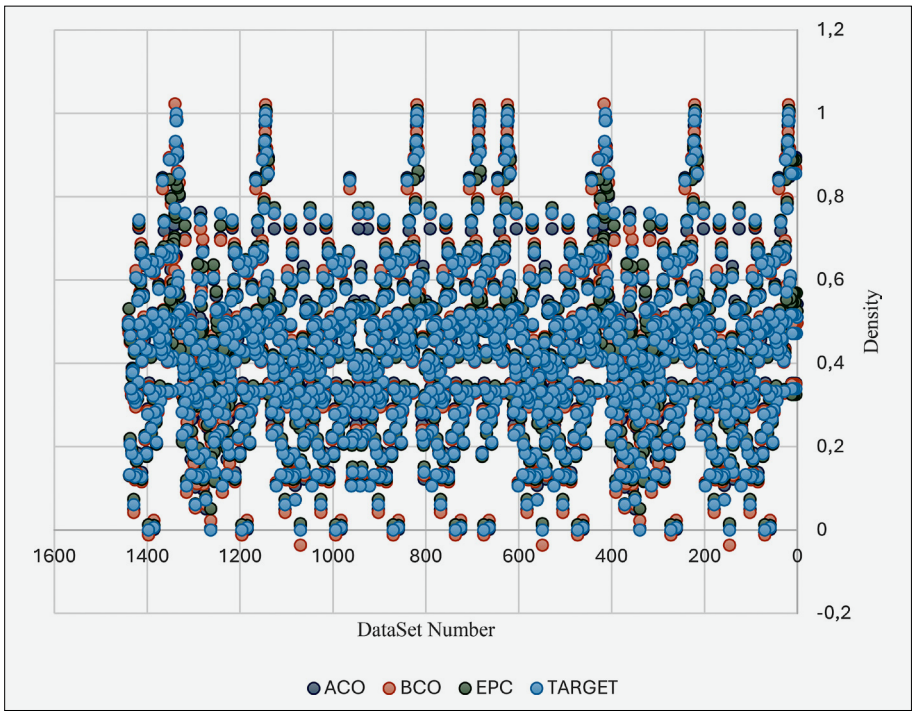


Figure 17. Comparison of results from ACO, BCO and EPC and target

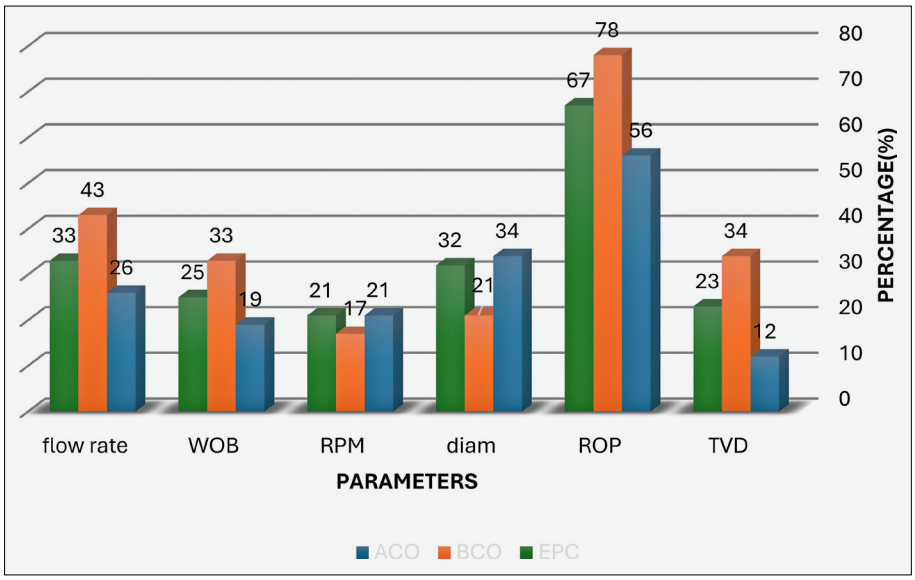


Figure 18. Parameter sensitivity analysis diagram

TVD (W1): ~3% Importance - surprisingly, TVD had the least direct influence in this model. This could be because the critical changes in mud properties are more directly linked to lithological changes and drilling mechanics at a specific depth rather than the depth itself, and this lithological information is indirectly captured by parameters like ROP and WOB.

This sensitivity analysis moves beyond mere prediction, offering valuable interpretability. It informs mud engineers that, for proactive mud management, real-time monitoring of ROP and WOB is paramount. The ROP model among all models is shown in **Figure 19**.

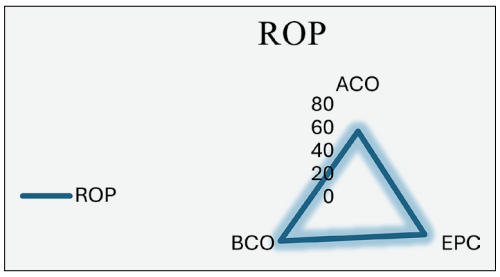


Figure 19. ROP in all models

Moreover, a 3D modelling approach illustrated the non-linear thresholds where ROP alterations necessitate immediate changes in mud composition. This finding corroborates the premise that real-time data integration with ML models enhances decision-making processes as opposed to relying solely on deterministic models, which may not account for the complexities of subsurface conditions, as shown in **Figure 20**.

5.3. *Practical Implications and Model Consensus on Mud Type*

A key practical outcome of this research is the strong, cross-model consensus identifying Sea Water-based mud

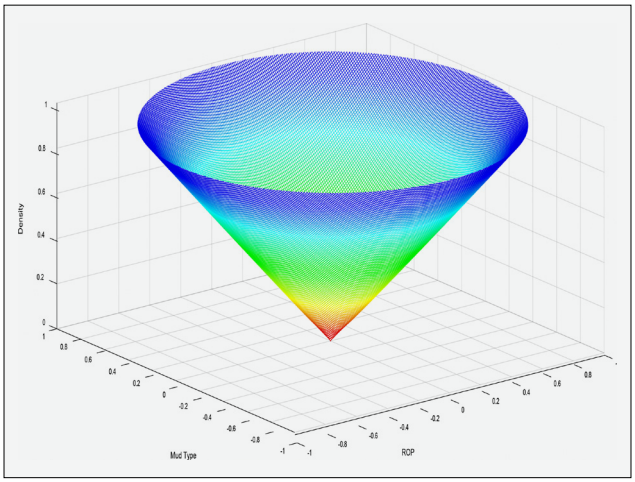


Figure 20. ROP in all models

with Polymer and Soltex (SW-PO-SX) as the optimal fluid for the studied field, with a confidence level of 79-87%. This recommendation is not a black-box output but a data-driven conclusion derived from 50 years of operational experience encoded in the daily drilling reports.

The SW-PO-SX system offers a balanced solution:

- Chemical Stability: the polymer and Soltex additives provide excellent shale inhibition, controlling clay swelling and dispersion in the active shale formations encountered, thereby mitigating chemical wellbore instability.
- Mechanical Stability: the model has learned the appropriate density range for this mud type to maintain wellbore pressure within the safe window.
- Environmental and Economic Advantage: as a water-based mud, SW-PO-SX presents a lower environmental footprint and is more economical than synthetic or oil-based alternatives, aligning with the industry's push towards more sustainable operations.

The high confidence level across three different algorithms significantly de-risks the fluid selection process for future wells in this field, transforming it from an experience-based art to a systematic, repeatable science.

6. Conclusions

This study successfully developed and validated a novel machine learning framework for the simultaneous prediction of drilling mud weight and mud type, a critical dual objective for ensuring wellbore stability and operational safety. By leveraging a comprehensive dataset extracted from 50 years of daily drilling reports across 20 oil wells, three nature-inspired optimization algorithms were employed and rigorously compared.

The key findings conclusively demonstrate that:

1. Data-driven prediction is a viable and superior paradigyym: machine learning models can effectively capture the complex, non-linear relationships between standard drilling parameters (TVD, ROP, RPM, WOB, diameter, flow rate) and the required mud properties, overcoming the simplifications inherent in traditional analytical and numerical methods.

2. Bee Colony Optimization (BCO) is the most effective algorithm: among the models tested, BCO emerged as the most precise predictor, achieving a correlation coefficient (R^2) of 0.9841 and a root-mean-square error (RMSE) of 0.0245 for mud density, highlighting its superior capability in navigating the complex solution space of this problem.

3. Rate of Penetration (ROP) is the dominant parameter: sensitivity analysis revealed that ROP is the most influential input variable, underscoring its role as a real-time indicator of formation characteristics and its critical importance for proactive mud management.

4. A consensus optimal mud type exists: all models converged with high confidence (78-87%) on Sea Water-based mud with Polymer and Soltex additives (SW-PO-SX) as the optimal fluid for the studied field, providing a robust, data-backed recommendation that reduces reliance on subjective experience.

6.1. Limitations of the Study

Despite the promising results, this research is subject to several limitations:

- Data Dependency and Quality: the model's performance is inherently tied to the quality, consistency, and comprehensiveness of the historical Daily Drilling Reports (DDRs). Inconsistencies in data recording, missing values, or human error in the original reports could propagate into the model.
- Feature Set Scope: the current model utilizes a set of common drilling parameters. It does not incorporate real-time mud logging data (e.g. gas units, cuttings morphology), lithology-specific logs (e.g. gamma ray, sonic), or precise downhole pressure measurements, which could further enhance predictive accuracy.
- Geological Specificity: the model was trained and validated on data from a specific oil field in South-West Iran. Its direct applicability to other fields with different geological settings, stress regimes, and formation fluids may be limited without retraining or transfer learning.
- Algorithmic Scope: the study focused on three nature-inspired metaheuristics. While they performed excellently, other powerful machine learning families (e.g. ensemble methods like Gradient Boosting or deep learning networks) were not explored for comparative benchmarking.

6.2. Suggested Improvements

To address the above limitations and strengthen the current model, the following immediate improvements are suggested:

1. Data Pre-Processing Enhancement: implement more advanced data imputation and cleansing techniques to handle missing or anomalous data points in the DDRs. Incorporating a domain-expert review to label data quality could also be beneficial.

2. Feature Engineering and Expansion: expand the input feature set to include mud rheological properties (e.g. plastic viscosity, yield point), lithology codes from mud logs, and estimated pore pressure and fracture gradient curves where available.

3. Hybrid Model Development: create a hybrid model that combines the global search capability of BCO with the strong predictive performance of an ensemble method (e.g. using BCO to optimize the hyperparameters of an Extreme Gradient Boosting (XGBoost) model).

6.3. Future Research Directions

This work opens several avenues for future research:

- Real-Time Integration and Deployment: the most critical future direction is the development of a real-time advisory system. This would involve integrating the trained model with a live data stream from the rig, enabling dynamic mud recommendations as drilling progresses.
- Generalizability and Transfer Learning: investigate the model's transferability to other oil and gas fields. Research could focus on developing a foundational model that can be fine-tuned with a smaller dataset from a new field, reducing the data requirement for deployment.
- Multi-Objective Optimization for Economics and Environment: expand the optimization objective beyond technical success to include economic and environmental factors. A future model could simultaneously optimize wellbore stability, drilling cost (e.g. mud cost, non-productive time), and the envi-

ronmental impact score, recommending the most sustainable and economical fluid.

- Causal Analysis: move beyond correlation to causality by exploring how the model's predictions change with specific geological events (e.g. entering a salt section, encountering a fault), enhancing interpretability and engineer trust.

In conclusion, this research provides a robust, data-driven foundation for systematic drilling fluid selection. By acknowledging its limitations and pursuing the outlined future directions, the industry can move closer to fully automated, adaptive, and optimized drilling fluid management, significantly enhancing safety, efficiency, and sustainability in hydrocarbon exploration.

7. References

Tatar, A., Halali, MA.,Mohamadi, AH. (2016). On the Estimation of the Density of Brine with an Extensive Range of Different Salts Compositions and Concentrations. *Journal of Thermodynamics & Catalysis*, *7*(2). https://doi.org/10.4172/2157-7544.1000167

Agwu, O. E., Akpabio, J. U., Alabi, S. B., & Dosunmu, A. (2018). Artificial intelligence techniques and their applications in drilling fluid engineering: A review. *Journal of Petroleum Science and Engineering*, *167*(February), 300–315. https://doi.org/10.1016/j.petrol.2018.04.019

Agwu, O. E., Akpabio, J. U., & Dosunmu, A. (2020). Artificial neural network model for predicting the density of oil-based muds in high-temperature, high-pressure wells. *Journal of Petroleum Exploration and Production Technology*, *10*(3), 1081–1095. https://doi.org/10.1007/s13202-019-00802-6

Albukhari, T. M., Beshish, G. K., Abouzbeda, M. M., Madi, A., & others. (2018). Geomechanical Wellbore Stability Analysis for the Reservoir Section in JNC186 Oil Field. *1st International Conference on Advances in Rock Mechanics-TuniRock 2018*.

Aljubran, M. J., Aramco, S., Arabia, S., Hussain,), Albahrani, I., Ramasamy, J., & Magana-Mora, A. (2022). *Drilling Fluid Properties Prediction: A Machine Learning Approach to Automate Laboratory Experiments*. 0–20.

Allawi, R. H. (2023). Chemical and mechanical model to analysis wellbore stability. *Petroleum Science and Technology*, 1–23.

Allawi, R. H., & Al-Jawad, M. S. (2021). Wellbore instability management using geomechanical modeling and wellbore stability analysis for Zubair shale formation in Southern Iraq.

Journal of Petroleum Exploration and Production Technology, *11*(11), 4047–4062. https://doi.org/10.1007/s13202-021-01279-y

Ayoub, D., Masoud, C. S., & Anthony, W. D. (2019). Wellbore stability analysis to determine the safe mud weight window for sandstone layers. *Petroleum Exploration and Development*, *46*(5), 1031–1038. https://doi.org/10.1016/S1876-3804(19)60260-0

Beheshtian, S., Rajabi, M., Davoodi, S., Wood, D. A., Ghorbani, H., Mohamadian, N., Alvar, M. A., & Band, S. S. (2022). Robust computational approach to determine the safe mud weight window using well-log data from a large gas reservoir. *Marine and Petroleum Geology*, *142*(May), 105772. https://doi.org/10.1016/j.marpetgeo.2022.105772

Chen, L., Fissha, Y., Hasanipanah, M., Ghodhbani, R., Dehghani, H., & Khatti, J. (2025). Accurate Prediction of Blast-Induced Ground Vibration Intensity Using Optimized Machine Learning Models. Defence Technology.

Caenn, R., Darley, H. C. H., & Gray, G. R. (2011). *Composition and properties of drilling and completion fluids*. Gulf professional publishing.

Deka, B. (2023). Chapter-9 drilling fluids'functions. *Theory of drilling fluids*, 23.

Dorigo, M., & Blum, C. (2005). Ant colony optimization theory: A survey. Theoretical Computer Science, 344(2–3), 243–278. https://doi.org/10.1016/j.tcs.2005.05.020

DRILLING FLUID. (n.d.). Retrieved December 17, 2023, from viking-intl.com/Viking-intl/index.php/drilling-fluid/

Ding, X., Hasanipanah, M., & Rezaei, M. (2025). Assessment of mechanical properties of rock using deep learning approaches. Measurement, 250, 117180.

Ding, X., Hasanipanah, M., Rouhani, M. M., & Nguyen, T. (2025). Hybrid catboost models optimized with metaheuristics for predicting shear strength in rock joints. Bulletin of Engineering Geology and the Environment, 84(3), 150.

Ding, Xiaohua, Maryam Amiri, and Mahdi Hasanipanah. "Enhancing shear strength predictions of rocks using a hierarchical ensemble model." Scientific Reports 14, no. 1 (2024): 20268.

Ebadati, N., & Najari, M. (2016). Calculating the drilling mud weight window and geo mechanical properties of Darian limestone formation in Reshadat oil field. *Journal of Geotechnical Geology*, *12*(1), 39.

Epelle, E. I., & Gerogiorgis, D. I. (2020). A review of technological advances and open challenges for oil and gas drilling systems engineering. AIChE Journal, 66(4), e16842.

Freij-Ayoub, R., Tan, C. P., Choi, S. K., & others. (2003). SPE/IADC 85344 Simulation of Time-Dependent Wellbore Stability in Shales Using A Coupled Mechanical-Thermal-Physico-Chemical Model. *SPE/IADC Middle East Drilling Technology Conference and Exhibition*.

Gholami, R., Raza, A., Rabiei, M., Fakhari, N., Balasubramaniam, P., Rasouli, V., & Nagarajan, R. (2021). An approach to improve wellbore stability in active shale formations using nanomaterials. *Petroleum*, *7*(1), 24–32. https://doi.org/10.1016/j.petlm.2020.01.001

Gowida, A., Ibrahim, A. F., & Elkatatny, S. (2022). A hybrid data-driven solution to facilitate safe mud window prediction. *Scientific Reports*, *12*(1), 1–14. https://doi.org/10.1038/s41598-022-20195-7

Hasanipanah, M., & Amnieh, H. B. (2025). Enhancing Ground Vibration Prediction in Mine Blasting: A Committee Machine Intelligent System Optimized with Metaheuristic Algorithms: Hasanipanah and Amnieh. Natural Resources Research, 1-27.

Hasanipanah, M., Jamei, M., Mohammed, A. S., Amar, M. N., Hocine, O., & Khedher, K. M. (2022). Intelligent prediction of rock mass deformation modulus through three optimized cascaded forward neural network models. Earth Science Informatics, 15(3), 1659-1669.

Hasanipanah, M., Monjezi, M., Shahnazar, A., Armaghani, D. J., & Farazmand, A. (2015). Feasibility of indirect determination of blast induced ground vibration based on support vector machine. Measurement, 75, 289-297.

Harifi, S., Khalilian, M., Mohammadzadeh, J., & Ebrahimnejad, S. (2019). Emperor Penguins Colony: a new metaheuristic algorithm for optimization. Evolutionary Intelligence, 12(2), 211–226. https://doi.org/10.1007/s12065-019-00212-x

Karaboga, D. (2005). An idea based on honey bee swarm for numerical optimization (Vol. 200). Technical report-tr06, Erciyes University, Computer Engineering Department.

Karaboga, D., & Basturk, B. (2008). On the performance of artificial bee colony (ABC) algorithm. Applied soft computing, 8 (1), 687–697. https://doi.org/10.1016/j.asoc.2007.05.007

Mozie, K. N. (n.d.). *Characterization of Ultrasonic Waves in Various Drilling Fluids*.

Nunez, Y. J., Sameer, M., Ruiz, F., Al Mutawa, A. A., Al Shamisi, E. D., Hamdy, I., Al Hendi, M., Al Dhaheri, K. H., & Torres, J. (2021). Deviated Drilling Through Salt Dome and Horizontalization Across Extremely Heterogeneous Formations: A Case Study in North Abu Dhabi. In *SPE/IADC Middle East Drilling Technology Conference and Exhibition*. https://doi.org/10.2118/202149-MS

Olson, J. E., Srinivasan, S., Zhang, J., & Chenevert, M. E. (2005). The impact of shale properties on wellbore stability. *Faculty of the Graduate School*, *Doctor of*.

Pao, W., Faris, M., Ali, B., & Pao, W. K. (2016). *Mud Weight Prediction for Offshore Drilling*. *December*.

Phan, D. T., Liu, C., AlTammar, M. J., Han, Y., & Abousleiman, Y. N. (2022). Application of Artificial Intelligence To Predict Time-Dependent Mud-Weight Windows in Real Time. *SPE Journal*, *27*(1), 39–59. https://doi.org/10.2118/206748-PA

Reuters. (2013). *Iran says oil well blowout controlled, no injuries*. https://www.reuters.com/article/uk-iran-blowout-idUKBRE93G09S20130417/

Sabah, M., Mehrad, M., Ashrafi, S. B., Wood, D. A., & Fathi, S. (2021). Hybrid machine learning algorithms to enhance lost-circulation prediction and management in the Marun oil field. *Journal of Petroleum Science and Engineering*, *198*, 108125.

Soroush, Dr. H. (2020). *Field Development Geomechanics* [Video recording]. *Technology Roundtable: Drilling Fluids*. (2017, October).

Tohidi, A., Fahimifar, A., & Rasouli, V. (n.d.). *The effect of Non-Darcy Flow on Induced Stresses Around a Wellbore in an anisotropic in-situ stress field*.

Tohidi, A., Fahimifar, A., & Rasouli, V. (2017). Analytical Solution to Study Depletion/Injection Rate on Induced Wellbore Stresses in an Anisotropic Stress Field. *Geotechnical and Geological Engineering*. https://doi.org/10.1007/s10706-017-0429-z

Tatar, A., Naseri, S., Bahadori, M., Rozyn, J., Lee, M., Kashiwao, T., & Bahadori, A. (2015). Evaluation of different artificial intelligent models to predict reservoir formation water density. Petroleum Science and Technology, 33(20), 1749-1756.

Zahiri, J., Abdideh, M., & Golab, E. G. (2018). Determination of safe mud weight window based on well logging data using Determination of safe mud weight window based on well logging data using artificial intelligence Javad Zahiri, Mohammad Abdideh & Elias Ghaleh Golab. *Geosystem Engineering*, *00*(00), 1–13. https://doi.org/10.1080/12269328.2018.1504697

SAŽETAK

Predviđanje težine i vrste isplake metodom strojnoga učenja

Odabir optimalnoga fluida za bušenje, definiranoga njegovom težinom i kemijskom vrstom, ključan je za sprječavanje nestabilnosti kanala bušotine i skupih katastrofalnih nesreća. Tradicionalne metode često se oslanjaju na metodu pokušaja i pogreške, prošla iskustva ili pojednostavnjene modele koji ne uspijevaju opisati složene interakcije stijena i fluida. Iako obrada velikoga broja podataka nudi obećavajuću alternativu, nedostaju istraživanja o istodobnome predviđanju težine i vrste isplake. Ovim istraživanjem predstavlja se novi okvir temeljem na strojnome učenju koji istovremeno predviđa ove važne faktore. Koristeći se sveobuhvatnim skupom podataka dobivenim iz 50 godina dnevnih izvješća o bušenju na 20 naftnih bušotina, napravljena su i uspoređena tri algoritma inspirirana prirodom: optimizacija *Ant Colony* (ACO), *Bee Colony* (BCO) i *Emperor Penguins Colony* (EPC). Rezultati pokazuju visoku prediktivnu točnost svih modela, pri čemu se algoritam optimizacije *Bee Colony* (BCO) pokazao kao najprecizinji, dajući koeficijent korelacije (R2) od 0,9841 i srednju kvadratnu pogrešku (engl. *root-mean-square error*, RMSE) od 0,0245. Nadalje, analiza osjetljivosti pokazala je da je na svojstva isplake mehanička brzina bušenja (ROP) najutjecajniji parametar, nadmašujući ostale varijable bušenja. Ključni je rezultat istraživanja dosljedno podudaranje modela sa 79–87 % pouzdanosti, da je isplaka na bazi morske vode s dodatkom polimera i *soltex* aditivima (SW-PO-SX) idealan bušaći fluid za pročavano polje. Ovo istraživanje pruža robusno rješenje temeljeno na podatcima koje omogućuje sustavan i proaktivan pristup odabiru bušaćega fluida znatno povećavajući sigurnost i učinkovitost rada.

Ključne riječi:
grupiranje podataka, proaktivni model, težina isplake, vrsta isplake, stabilnost kanala bušotine

Author's contribution

Amin Tohidi (Assistance Professor): conceptualization, investigation, original draft and writing. **Alireza Afradi** (PhD): software and Data Analysises, review & editing.
All authors have read and agreed to the published version of the manuscript.

RGNZ/MGPB

Rudarsko-geološko-naftni zbornik
(The Mining-Geology-Petroleum Engineering Bulletin)
DOI: 10.17794/rgn.2026.3.2

Original scientific paper

Integrated Mathematical and Physical Modelling of Salt Ions Leaching from Coal-Mining Waste: Implications for Ecological Safety and Civil Protection

Vasyl Karabyn[1]*, Iryna Kochmar[2], Oksana Karabyn[3], Clint Sutherland[4], Valentyna Loboichenko[5,6], Andrii Khorolskyi[7]

[1] *Department of Civil Protection, Lviv State University of Life Safety, Lviv, Ukraine.*
[2] *Department of Environmental Safety, Lviv State University of Life Safety, Lviv, Ukraine.*
[3] *Department of Applied Mathematics and Mechanics, Lviv State University of Life Safety, Lviv, Ukraine.*
[4] *Project Management and Civil Infrastructure Systems, The University of Trinidad and Tobago, Trinidad.*
[5] *Departamento de Ingeniería Energética, Escuela Técnica Superior de Ingeniería, Universidad de Sevilla, Camino de los Descubrimientos s/n., Sevilla, Spain.*
[6] *Department of Civil Security, Lutsk National Technical University, Lvivska St., 75, Lutsk, Ukraine.*
[7] *Laboratory of Mining Problems, Branch for Physics of Mining Processes of the National Academy of Sciences of Ukraine, Dnipro, Ukraine.*

Abstract

Coal-mining waste heaps represent a significant source of dissolved salts that can be mobilised by precipitation, posing risks to ecological safety and civil protection. This study focuses on the Chervonohrad Central Concentration Plant spoil heap in western Ukraine, where both thermally altered and unaltered argillite were tested. Laboratory column experiments were performed on 100 g samples flushed with deionised water to simulate leaching under controlled conditions. The cumulative leachate volumes reached approximately 432 L, allowing quantification of total dissolved solids and ion-specific contributions. We flushed 100 g columns for 24 h at 300 mL·min^{-1} (8.5 L recirculated; ≈ 432 L passed), which yielded final filtrate total dissolved solids of 462 vs. 185 mg·L^{-1} for burnt and unburnt argillite and cumulative leached masses of 3.93 vs. 1.57 g (≈ 2.5× higher for burnt). Early-time contrast was also strong: after 2 h (≈ 0.7 L), burnt reached 183 mg·L^{-1} vs. 50 mg·L^{-1} (≈3.7×). Physical observations were combined with a mathematical modelling approach to establish a precipitation-response relationship linking annual rainfall to total dissolved solids release. The results indicate a strong linear increase of annual salt release with precipitation, with burnt materials exhibiting markedly higher fluxes. This integrated framework demonstrates how laboratory data and simple models can be applied to anticipate pollutant releases, supporting ecological safety and informing civil protection measures in coal-mining regions prone to hydrological extremes.

Keywords:
civil protection, ecological safety, emergency warning, geochemistry, predictive modelling

1. Introduction

Coal-fired power generation reached a new high of 10.7 TW h in 2024, primarily driven by electricity demand, which consumes roughly two-thirds of global coal and supplies about 35% of the world's electricity. In Ukraine, coal reserves exceed 117 Gt, representing over 90% of the country's fossil fuel resources, thus critically underpinning the national energy infrastructure (**International Energy Agency, 2025**). Expansive coal waste piles throughout Europe, including those in Ukraine, represent significant environmental challenges resulting from decades of coal mining and beneficiation activities. These wastes contain a heterogeneous mixture of minerals, including sulphide phases such as pyrite (FeS_2) and chalcopyrite ($FeCuS_2$), together with carbonates, silicates and halite-type salts. As water and oxygen infiltrate the waste material, these minerals undergo oxidation and dissolution, releasing a wide range of major ions, such as SO_4^{2-}, HCO_3^-, Cl^-, Na^+, K^+, Ca^{2+}, and Mg^{2+}, into surrounding waters. For example, pyrite oxidation generates sulphate and acidity, which in turn enhance the release of major cations and trace metals. This acidification promotes the mobility of toxic elements including Zn, Pb, Mn, Cu, and Fe, thereby increasing the risk of groundwater and surface water contamination (**Kochmar and Karabyn, 2023; Rouhani et al., 2023; Rouhani et al., 2024**). Microbial redox transformations are a primary control on leachate chemistry in mine-waste settings. Experiments with *Desulfuromonas* sp. have shown that bacteria can reduce sulfate/sulfur and alter

* Corresponding author: Vasyl Karabyn
e-mail address: vasyl.karabyn@gmail.com
Received: 6 September 2025. Accepted: 14 November 2025.
Available online: 14 May 2026

oxidized nitrogen species under iron-mediated conditions - processes mechanistically aligned with redox pathways expected in spoil-leachate systems (**Moroz et al., 2020**). Studies highlight that biosorption techniques (**Sutherland et al., 2023**) and biomodification of waste rock with sulfate-reducing bacteria are promising methods for the treatment of mine wastewater from sulfur and heavy metals (**Xu et al., 2025**). Studies highlight that biosorption techniques are promising for the remediation of heavy metals in such systems; however, their large-scale implementation remains technically challenging (**Sutherland et al., 2023**). Future investigations may also benefit from incorporating machine learning models to improve spatial prediction accuracy for heavy metal distributions in mining-affected soils (**Proshad et al., 2025**).

The environmental and human health impacts of elevated concentrations of major anions such as SO_4^{2-}, Cl^-, and HCO_3^- are profound. These impacts include increased risks of groundwater contamination, degradation of water bodies, and associated public health hazards, notably heavy metal exposure and fluorosis (**Loboichenko and Leonova, 2021; Xu et al., 2024; Tkachenko et al., 2021**). Uncontrolled disposal of waste rock by introducing it into the soil, including for agricultural purposes, changes its pH and negatively affects the qualitative and quantitative composition of the microbiome. Accordingly, this may have consequences for the food security of the state (**Garbacz at al., 2025**). Moreover, coal waste sites significantly heighten the risk of environmental emergencies such as spontaneous combustion, landslides, and acute contamination events (**Hoxha et al., 2025; Petlovanyi et al., 2023; Monteiro et al., 2025**). However, even after the closure of coal mines and the implementation of reclamation measures, excess polutant are observed in water bodies located downstream of these mines. (**Cooke et al., 2025**). Due to the seepage of sediments, leaching of pollutants occurs along with further entry into natural ecosystems. Negative cumulative effects may occur due to the additional impact of mine waters, in the presence of several mining centers (**Tyndyk et al., 2024**).

These environmental emergencies pose severe challenges to civil protection systems, particularly in Ukraine. The State Emergency Service must coordinate responses across mining regions whereas managing limited resources during wartime conditions. Recent technological advancements, such as ground robot technologies, provide new avenues for monitoring and mitigating these risks, especially under hazardous conditions typical of post-mining landscapes (**Gromek and Lowe, 2025**). Given these risks, it is crucial to quantify the leaching of major ions under realistic precipitation conditions, as their concentrations, especially sulphates, chlorides, and bicarbonates, directly affect pH and metal transport. This study combines column experiments with a linear model to quantify total dissolved solids (TDS) leaching from the waste dump of a coal enrichment plant. Current precipitation-driven TDS models lack integration with civil protection frameworks, limiting their utility for emergency preparedness and community risk assessment in coal mining regions. While many studies characterise TDS leaching and management, comparatively few develop precipitation-driven annual-load models for coal-mine spoils; recent syntheses and related leaching work underscore this gap (**Welch et al., 2021; Daniels et al., 2016b; Castillo-Meza et al., 2020; Gao et al., 2025**). The predictive models developed estimate annual sulfur mobilisation, particularly emphasising climatic factors like precipitation. Comparative analyses illustrate how climate and geology modulate acid mine drainage (AMD) severity, as humid climates sustain continuous leaching, whereas arid regions experience episodic pulses (**Alvarenga et al., 2021; Rouhani et al., 2024**).

This research addresses a crucial gap by modelling the mobilisation of major ions from coal waste materials at the Chervonohrad Central Concentration Plant (CCCP) waste pile, emphasising the ecological impacts of sulphide mineral oxidation and the consequent potential for environmental emergencies. The integrated methodological approach informs risk assessment and environmental management tailored to Ukraine's temperate climatic conditions, while also providing a transferable framework for other mining regions and supporting the development of integrated environmental - civil protection response systems. Understanding the leaching behaviour of sulphate-rich mine wastes is essential not only for hydrogeochemical modelling but also for assessing risks to civil protection and emergency response planning in mining regions. Embedding such predictive frameworks within broader strategic environmental assessment instruments would further enhance their utility for civil protection and sustainable resource management (**Karabyn et al., 2022**). The study area and the laboratory methods underpin the model calibration and scaling.

2. Materials and methods

2.1. Study Area

The CCCP, operational since 1979 in Ukraine's Lviv-Volyn coal basin, has served as a key facility for processing low-grade coal from surrounding mines. The substantial waste pile at CCCP covers approximately 0.8638 km² and rises to 68 m, encompassing about 48.89 Mm³ of waste at an average density of 2680 kg·m^{-3} (**Bosak et al., 2020**). The accumulated waste poses environmental risks because of its large volume and the possibility of pollutant leaching. The study area is in Western Polissya, a humid continental (Dfb) climate zone with cold winters and warm summers. Meteorological data from the Volodymyr weather station indicate significant an-

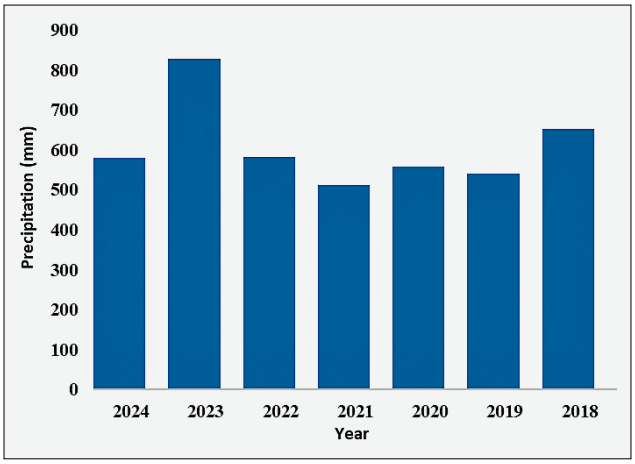


Figure 1. Total annual rainfall observed at Volodymyr station (Ukraine) during 2018-2024 (**URL 1**).

nual precipitation variability of 511 - 829 mm (see **Figure 1**), which provides the range used later for precipitation-based projections.

The CCCP waste primarily consists of argillite, siltstone, sandstone, and coal-associated sediments. The predominant minerals-siderite ($FeCO_3$), pyrite (FeS_2), and chalcopyrite ($FeCuS_2$) - undergo oxidation, significantly contributing to environmental contamination through iron and sulphur mobilisation (**Kochmar et al., 2024**). As a consequence, these mineralogical processes promote the leaching of major ions and trace metals into surrounding hydrological systems (**Karabyn and Kochmar, 2025**). Leachate from the site may reach nearby surface waters such as the Western Bug River, which flows into the Vistula. As Vistula runs mostly through Poland, this transboundary connection requires coordinated monitoring and management.

Documented landslides, groundwater contamination, and episodes of spontaneous combustion in waste piles underscore the need for robust hazard-mitigation measures to protect regional ecosystems and communities (**Kochmar et al., 2022; Petlovanyi et al., 2023**). Understanding precipitation-driven leaching processes is essential for designing targeted environmental protection measures, improving waste management practices in Ukraine's coal basin.

2.2. Research methods

Column experiments and processing of results. To simulate the leaching dynamics of TDS from spoil rock, a laboratory-scale column experiment was conducted using an apparatus assembled at the Environmental Safety Laboratory, Lviv State University of Life Safety (**Kochmar et al., 2024; Stepova et al., 2023**). The test material was argillite collected from the CCCP spoil heap. Ten grab samples from different sectors of the heap were composited to improve spatial coverage, then air-dried at 20-25°C to constant mass over 30 d, gently comminuted in an agate mortar, and dry-sieved through a 1.25 mm stainless-steel mesh. The < 1.25 mm fraction was used in subsequent leaching tests, with no secondary fractionation. Sampling targeted 0.2-0.3 m to capture the biologically active and hydrologically responsive near-surface layer of the spoil, where infiltration, oxygen exchange, and temperature fluctuations are most pronounced, promoting sulphide oxidation, dissolution of readily soluble salts, and mobilisation of sulphate and chloride ions. A similar focus on near-surface layers has been used for coal-waste piles undergoing self-heating, where the upper horizons control infiltration and thereby increase the leaching of major ions and potentially toxic elements (**Espinha Marques et al., 2024, Anghelescu and Diaconu, 2024**).

For the tests, two material conditions were used: unburned argillite; and thermally altered argillite obtained by laboratory firing of the composite material in a muffle furnace for 4 h at temperatures up to 600°C. In this study, "thermally altered (burnt) argillite" refers to argillite that has undergone oxidation and partial mineralogical transformation through laboratory firing at 600°C, producing a reddish-brown material. The term "unaltered (unburnt) argillite" denotes material that has not experienced thermal alteration and retains the original grey, compact lithology typical of the parent rock. Each experiment used a 100 g subsample packed into a vertical column 10 cm high and 36 mm in diameter (cross-sectional area 0.001018 m^2; packed volume ≈101.8 cm^3) (see **Figure 2**). To ensure reliability, each treatment was run in triplicate: three identical columns were packed in parallel with the same mass of material (burnt or unburnt) and operated under identical flow and temperature conditions. Leachate was collected from each column at corresponding time intervals and analysed separately for TDS; reported values are means across the three parallel runs, which were used for the precipitation-response modelling. The corresponding standard deviations did not exceed the instrument's measurement accuracy.

The concentrations of major ions in the filtrate were determined using standard chemical analysis methods at the Environmental Safety Laboratory at Lviv State University of Life Safety (certificate of attestation No. RL 091/21, dated 11/30/2021). In particular, acid titration to the appropriate end-point pH following Standard Methods was used (HCO_3^-); argentometric titration with silver nitrate and potassium chromate as indicator, according to the Mohr method, was applied (Cl^-). EDTA complexometric titration with murexide and Eriochrome Black T was performed (Ca^{2+} and Mg^{2+}), with magnesium calculated by difference. Gravimetric determination as barium sulphate after precipitation with Ba^{2+} and subsequent ignition and drying of the $BaSO_4$ precipitate was used (SO_4^{2-}). Sodium and potassium (Na^+, K^+) were estimated by the ionic charge balance method, based on equivalents of the directly determined major ions (**APHA, 2017**).

The leaching system comprised a vertical filtration column and a circulation pump that continuously drove



Figure 2. Laboratory setup showing the column apparatus used for TDS leaching experiments.

deionized water through the packed bed. Deionized water (8.5 L) was recirculated at 300 mL·min⁻¹ for 24 h, yielding a cumulative passed volume of ≈432 L (≈50 flushing cycles). Aliquots of the filtrate were collected at fixed intervals (every 4 h over 24 h), with additional early-time sampling during the first 2 h of circulation (**Kochmar et al., 2024**).

Filtrate samples were collected at multiple time intervals and analysed for TDS (mg·L⁻¹), which were derived from measurements of electrical conductivity (EC). EC was measured with a bench-top EC 215 (Hanna Instruments), which automatically converts EC to TDS using a built-in conversion factor. The meter was two-point calibrated daily with standards bracketing the sample range and verified against a mid-range check, with recalibration performed if drift exceeded ±2%. The manufacturer-stated accuracy is ±1% of full scale. TDS values were calculated from temperature-corrected EC at 25°C according to the relationship TDS = $f \times EC_{25}$, with $f = 0.50$ appropriate for sulphate-rich matrices. The method detection limit was 1.5 mg·L⁻¹ (based on 3σ of low-level EC checks at 25°C, converted to TDS). Quality control included reagent blanks, duplicate aliquots (~10%), and periodic check-standards (every 2 h), all within predefined acceptance limits.

Concentrations were multiplied by the cumulative filtrate volume to calculate cumulative mass (M) at each sampling stage; dividing M by the passed volume V yielded the mean leachate concentration (mg·L⁻¹). The results were used to model both the cumulative leaching behaviour and the incremental leachate concentration per unit water volume. The latter was obtained by calculating the change in TDS-derived mass over the change in water volume between successive sampling points, providing a dynamic view of concentration evolution throughout the experiment. Based on the observed ***M-V*** relationship, a linear regression model was fitted to describe salt removal as a function of water input. The model estimated $M = a_v \cdot V + b_v$, where M is cumulative leached mass and V is passed water volume. The regression coefficients a_v (mg·L⁻¹) and b_v (mg) were derived from experimental data and subsequently used to parameterise the site-scale precipitation model.

A two-stage approach was applied to process the column data. The primary experimental values were the TDS (mg·L⁻¹) in the leachate measured at specific time intervals. At the first stage, these values were converted into the cumulative mass of leached salts M (mg) by volume-weighting across successive sampling intervals:

$$M_i = \Delta V_i \sum_j TDS_j \quad (1)$$

where ΔV_i is the incremental water volume between samplings.

At the second stage, the **incremental leachate concentration** between successive points was computed as:

$$\left(\frac{dM}{dV}\right)_i \approx \frac{M_i - M_{i-1}}{V_i - V_{i-1}}, \text{(mg·L}^{-1}\text{)} \quad (2)$$

Calibration of column-derived regression coefficients for model parametrisation. Column data were used **solely to calibrate** the linear mass-volume relation $M=a_vV+b_v$ for each material (burnt vs unburnt), yielding a_v (mg·L⁻¹) and b_v (mg). These **dimensional** coefficients are then **transferred to the site scale** in the mathematical model, where the real spoil area S_{site}, spoil mass $m_{ore,site}$, hydrologic partitioning ($V_{p,site}$, $V_{f,site}$) and annual duration T=1 yr govern the predicted mass export as a function of precipitation. To avoid ambiguity with the **dimensionless** formulation used later, we denote the column-regression coefficients by a_v, b_v here; when introduced into the site-scale dimensionless expression, they appear through **dimensionless combinations** denoted as a, b.

Column data were used **solely to calibrate** the linear mass-volume relation $M=aV+b$ for each material (burnt vs unburnt), yielding the regression coefficients a_v (mg·L⁻¹) and b_v (mg). These coefficients are then **transferred to the site scale** in the mathematical model, where the **real spoil area** S_{site}, **spoil mass** $m_{ore,\,site}$ **hydrologic partitioning** ($V_{p,\,site,}$ $V_{f,\,site}$) and **annual duration** T=1 yr govern the predicted mass export as a function of precipitation. Thus, while the column analysis is expressed in terms of cumulative water throughput (M, V), the **field application** uses the calibrated (a, b) with **site-specific geometry and hydroclimate**.

Statistical processing of column data. For each treatment (unburnt and burnt), the cumulative mass–volume relation was fitted by ordinary least squares (OLS) as $M = a_vV + b_v$. We report the slope a_v, intercept b_v, their standard errors (SE_a, SE_b), the coefficient of determina-

tion (R^2) and the sample size (n). Two-sided 95% confidence intervals (CI) for the slope were computed as $a_v \pm t_{0.975,n-2}\, SE_a$, where $t_{0.975,n-2}$ is the Student's t-critical value for $n-2$ degrees of freedom. Units are expressed in SI; since $1\,\mathrm{mg\,L^{-1}} \equiv 1\,\mathrm{t\,Mm^{-3}}$, the coefficient a_v in mg·L⁻¹ is numerically identical to a per-volume sensitivity in t·Mm⁻³. Residual plots were inspected to check for obvious non-linearity or heteroscedasticity. The calibrated coefficients and their uncertainties are then propagated to per-100 mm sensitivities and site-wide annual increments using scalar error propagation (delta method), i.e. $SE(K_{100}) = V_{100}\, SE_a$ and $CI_{95\%}(K_{100}) = K_{100} \pm t_{0.975,n-2}\, SE(K_{100})$, where V_{100} is the effective infiltration volume associated with +100 mm precipitation. These procedures follow standard treatments of simple linear regression and interval estimation (**Montgomery et. al., 2021**).

Mathematical Model Formulation. Building on column-leaching formulations and hydroclimatic transport-reaction metrics from prior work (**Long et al., 2020; Kumar et al., 2020**), together with similarity π-theorem scaling and leaching time-scale criteria (**Vladyko et al., 2022; Crundwell, 2005**), we formulate a dimensional-analysis framework for cumulative TDS leaching from coal spoil. We first outline the controlling processes and variables retained in the analysis, before assembling them into a compact set of dimensionless groups that couple precipitation forcing and infiltration with pore-scale retention/adsorption and heap geometry, thereby enabling scalable links from column conditions to field-scale predictions (**Long et al., 2020; Kumar et al., 2020; Crundwell, 2005; Vladyko et al., 2022**).

Leaching of SO_4^{2-}, Cl^- and HCO_3^- from coal waste is controlled by meteoric infiltration, mineral structure, and oxidation at the surface. To generalise these effects, we applied dimensional analysis and similarity theory, producing a predictive model of cumulative ion release.

Under the working assumption that the cumulative mass of leached TDS scales with the infiltrated water volume and is modulated by physical characteristics of the spoil heap, we construct a system of dimensionless groups governing the leaching process. These comprise: (i) terms characterising the dependence of TDS mass on precipitation intensity and cumulative volume; (ii) groups combining hydraulic conductivity, leaching duration, porosity, density and water-solid interaction time; and (iii) geometrical and structural descriptors of the spoil that influence transport pathways and retention capacity.

The general non-dimensional form of the model is given by:

$$M_{TDS} = f\left(V_p, V_f, T, S, P_p, m_{ore}, \varepsilon, \rho, k_{ads}\right) \quad (3)$$

Where:

M_{TDS} – total mass of leached TDS over the integration period T within the chosen control volume (column or spoil block) (kg),

V_p – cumulative precipitation volume that falls onto the active infiltration area (S) during (T) (m³),

V_f – effective infiltration volume that actually reaches the reactive pore space (after run-off/evaporation losses) (m³),

T – leaching duration (integration time) (h or d),

S – infiltration area, i.e. the active surface of the spoil (or cross-section in a column set-up) through which water enters the system (m²),

P_p – precipitation intensity, (mm·h⁻¹),

m_{ore} – mass of solid spoil within the control volume that participates in leaching over (T) (kg),

ε – effective (mobile) porosity, the fraction of pore space available to flow, dimensionless (0-1),

ρ – bulk density of the spoil mass, (kg·m⁻³),

k_{ads} – effective adsorption/distribution coefficient (m³·kg⁻¹).

The cumulative precipitation volume is defined as:

$$V_p = S \int_0^T P(t)dt \quad (4)$$

where $P(t)$ is the precipitation intensity (m·h⁻¹), S is the active infiltration area (m²), and T is the integration period (h or d).

For periods with approximately constant mean precipitation intensity P_p, this integral can be approximated as:

$$V_p \approx T \cdot S \cdot P_p \quad (5)$$

The effective infiltration volume is then defined as $V_f = \eta \cdot V_p$, where $0 \le \eta \le 1$ is the infiltration coefficient accounting for runoff and evaporation losses:

$$V_f = \eta \cdot V_p \quad (6)$$

Assuming separable contributions from water flux and solid-phase reactivity, the normalised expression is:

$$\frac{M_{TDS}}{m_{ore}} = f\left(\frac{T \cdot S \cdot P_p \cdot m_{ore}}{V_p \cdot V_f \cdot \rho \cdot \varepsilon}\right) + \varphi\left(\frac{T \cdot S \cdot P_p \cdot m_f}{V_p \cdot V_f \cdot \rho \cdot \varepsilon}\right) \quad (7)$$

Where:

m_f – mass of the sorbing (fine) fraction (kg).

The non-linear function $\varphi(\cdot)$, associated with sorption and secondary mechanisms, can be expanded as:

$$\varphi(\cdot) = c \cdot \frac{T \cdot S \cdot P_p \cdot m_f \cdot k_{ads}}{V_p \cdot V_f \cdot \rho \cdot \varepsilon} + d \cdot \frac{T \cdot S \cdot P_p}{V_p \cdot V_f} + e \cdot k_{ads} \quad (8)$$

Under the assumption that $f\left(\frac{T \cdot S \cdot P_p \cdot m_{ore}}{V_p \cdot V_f \cdot \rho \cdot \varepsilon}\right)$ is *approximately* linear in its argument, the linear component of the model (the first term of **Equation 6**) is:

$$a \cdot \frac{T \cdot S \cdot P_p \cdot m_{ore}}{V_p \cdot V_f \cdot \rho \cdot \varepsilon} \quad (9)$$

where *a, b, c, d*, e are empirical coefficients obtained from laboratory column leaching experiments.

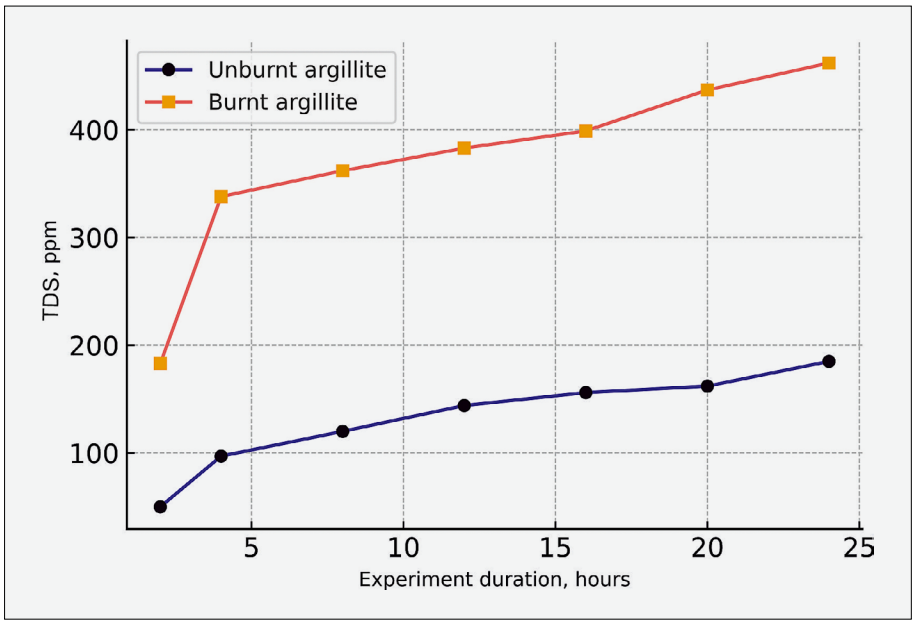


Figure 3. Temporal leaching behaviour of TDS from argillite in a laboratory column test.

The function $\varphi(\cdot)$ is infinitesimal compared with the function f and may therefore be neglected. Therefore, the model can be simplified to the linear approximation:

$$\frac{M_{TDS}}{m_{ore}} \approx a \cdot \frac{T \cdot S \cdot P_p \cdot m_{ore}}{V_p \cdot V_f \cdot \rho \cdot \varepsilon} + b \qquad (10)$$

Whereas this formulation was validated primarily for TDS *in our column experiments*, the same framework is directly transferable to other major ions, provided their leaching behaviour is similarly governed by water input and physical retention. The resulting model enables estimation of contaminant fluxes (expressed, for instance, in kg·Mm^{-3}, equivalent to 10^{-9} kg·m^{-3}) based on precipitation regime, heap structure, and material characteristics, supporting applications in mine site risk assessment and remediation planning. These column-scale metrics provide the empirical basis for the precipitation-based scaling $M_{TDS} = k \cdot P$, which is calibrated and applied to site-wide predictions.

3. Results

3.1. General Leaching Patterns of Major Ions

This section reports laboratory outcomes and translates them into precipitation-scaled predictions for site-wide loads. A comparison of the concentrations of dissolved solids in the leachates from thermally altered (burnt) and unaltered samples shows a much higher concentration of TDS in the burnt material: after 24 h of leaching (8.5 L of deionised water), the TDS content reached 462 mg·L^{-1} in the burnt sample, compared to 185 mg·L^{-1} in the unburnt one (see **Figure 3**). In both materials, a pronounced early-time spike in TDS is observed at ~2 h, after which concentrations decline towards quasi-steady values over the remainder of the 24 h run.

This corresponds to more than double the cumulative mass of dissolved salts - approximately 3.93 g versus 1.57 g. These masses follow directly from the closed recirculating setup: $M=\sum C_j \Delta V_j$ over the 24-h run (see **Equation 1**), which is numerically identical to $C_{final}\times 8.5$ L because the entire dissolved load resides in the tank at the end; equivalently, $M=(M/V)_{avg}\times 432$ L (see **Table 1**).

Differences in leaching behaviour are evident even at the early stages of the experiment. For instance, after only 2 h (≈0.7 L of water), the TDS in the burnt sample reached 183 mg·L^{-1}, which is 3.7 times higher than in the unburnt counterpart (50 mg·L^{-1}).

Analysis of individual ions in the final filtrates confirms this trend (see **Figure 4**). Sulphate (SO_4^{2-}) concentrations in the burnt sample reached 318 mg·L^{-1}, more than double the value observed in the unburnt sample (141.5 mg·L^{-1}). Similar increases were observed for bicarbonates, Ca^{2+}, Mg^{2+}, K^+, and Cl^-.

Conventions. Sulphate (SO_4^{2-}) concentrations are shown **rescaled by ×0.1** to maintain all ions on a common y-axis scale. This rescaling was applied solely for graphical clarity and does not affect the relative trends or ratios among ions.

3.2. Experimental Leaching as a Basis for Model Calibration

The laboratory column leaching test provided the empirical foundation for calibrating the mathematical model that describes TDS release from coal spoil material under rainfall conditions. Specifically, the experimental setup enabled computation of the average leaching of salt ions concentration per unit water volume (M/V, mg·L^{-1}) for unburnt and burnt argillite, as well as the cumulative leached mass. During the 24-hour experiment, 8.5 L of deionised water was passed through each

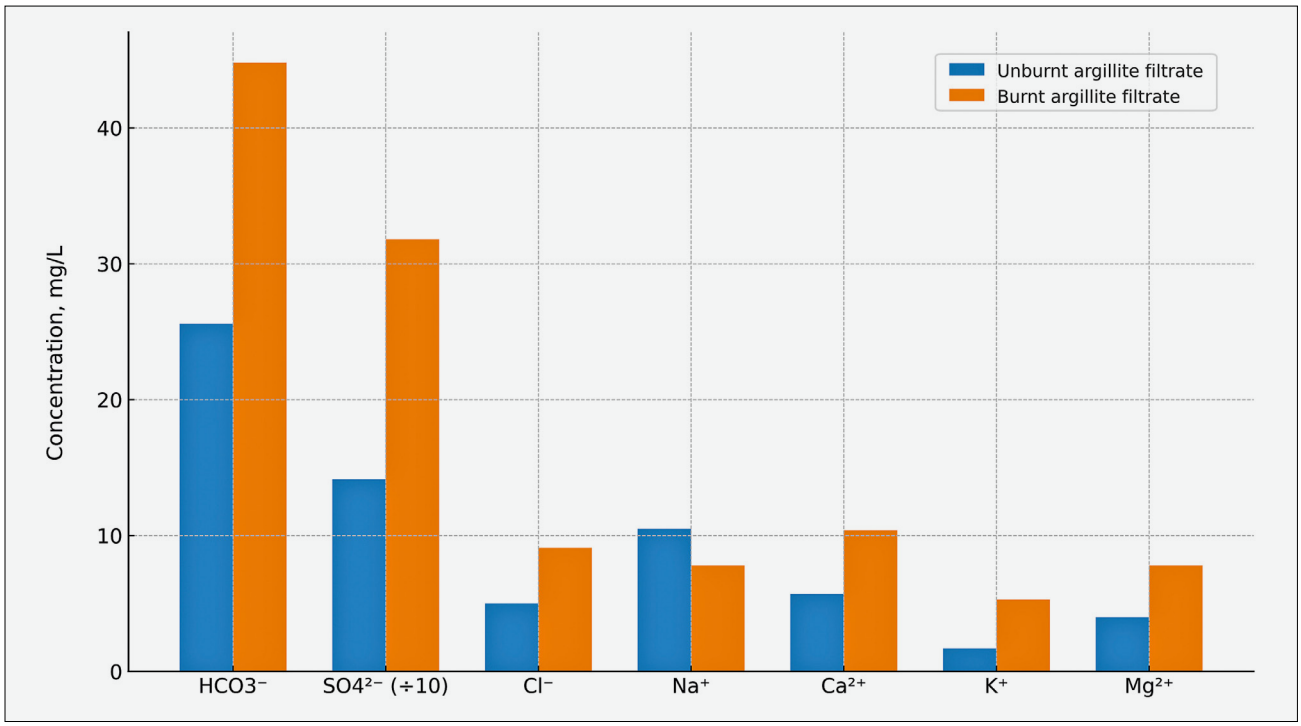


Figure 4. Distribution of water-soluble ions in filtrates of thermally altered and unaltered argillite samples (sulphate bars scaled by ×0.1).

100 g sample under a controlled flow rate of 300 mL·min⁻¹. At the end of the flushing cycle, the cumulative TDS concentration in the filtrate reached 185 mg·L⁻¹ for the unburnt sample and 462 mg·L⁻¹ for the thermally altered (burnt) one. These values correspond to cumulative leached masses of approximately 1.57 g and 3.93 g per sample, respectively.

Table 1. Column leaching results for unburnt and burnt argillite samples (24 h circulation; 8.5 L deionised water; 100 g material).

Parameter	Unburnt Argillite	Burnt Argillite
Mass of sample (g)	100	100
Volume of leachant (L)	8.5	8.5
Total filtrate passed (L)	432	432
Total TDS leached (mg)	1572.5	3927.0
Average *M/V* over total passed volume, (mg·L⁻¹)	3.64	9.09
Final TDS in filtrate (mg·L⁻¹)	185	462

Conventions. Average *M/V* is computed as total leached mass divided by the total passed volume (V_{total} = 432 L). Final TDS in filtrate refers to the concentration measured in the last collected solution portion.

Assuming a linear relationship between water volume and salt release over the tested range, the average TDS per unit water volume was computed as *M/V* (units: mg·L⁻¹); detailed values are reported in **Table 1**. Given the geometric characteristics of the test columns (cross-sectional area ≈ 0.001 m²), the corresponding **column-scale areal fluxes** were approximately J_{24h}≈1570 g m⁻² day⁻¹ (unburnt) and J_{24h}≈3930 g m⁻² day⁻¹ (burnt), computed as J_{24h}=*M*/(*A*·24 h) using the column cross-section.

These experimentally derived column metrics (*M, V,* and *M/V*) informed the calibration of the precipitation-based model, which was then used to simulate TDS leaching as a function of annual precipitation. **Table 1** summarises the primary data and calculations used for model calibration. This ensured consistency between laboratory observations and the field-scale predictive framework.

Table 2. Linear regression diagnostics for *M–V* calibration (column experiments)

Treatment	a_v (slope, mg·L⁻¹ = t·Mm⁻³)	SE_a (mg·L⁻¹)	95% CI for a_v (mg·L⁻¹)	b_v (intercept, mg)	SE_b (mg)	R^2
Unburn	190.94	9.81	[165.70, 216.18]	−156.38	50.26	0.987
Burnt	474.40	18.79	[426.07, 522.73]	−274.74	96.30	0.992

Conventions. (i) Units: a_v in mg·L⁻¹ are numerically equivalent to t·Mm⁻³ (since 1 mg L⁻¹ = 1 t Mm⁻³). (ii) 95% CI computed as $a_v \pm t_{0.975,n-2}\, SE_a$ (here $t_{0.975,5} = 2.571$). (iii) Intercepts reflect linear extrapolation towards $V \to 0$ and are not used for site-scale projections.

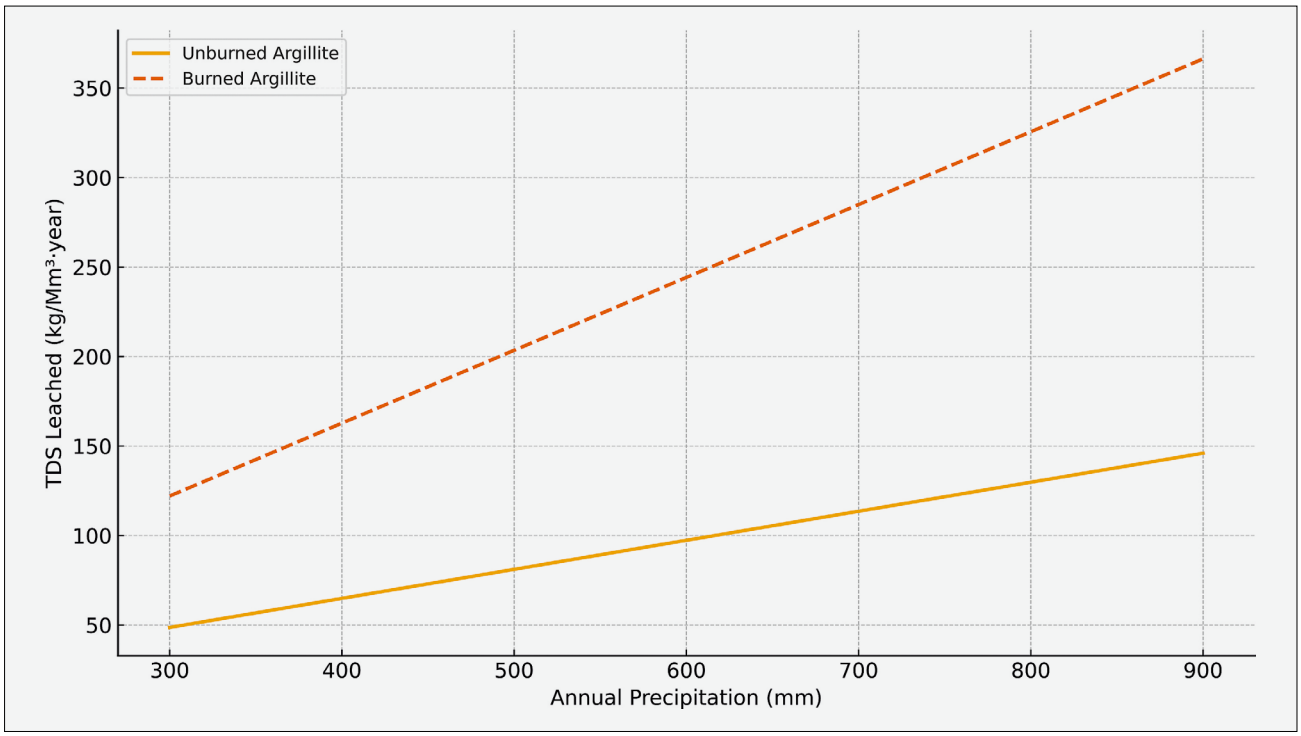


Figure 5. Sensitivity of per-volume TDS release to precipitation: comparison of unburnt vs. burnt argillite.

To quantify linearity and propagate uncertainty into the site-scale model, the cumulative mass-volume relation was fitted as $M = a_v V + b_v$ for each treatment. The regression diagnostics-slope (a_v), standard error of the slope (SE_a), 95% confidence interval, intercept (b_v), its standard error, the coefficient of determination (R^2) and sample size (n) – are compiled in **Table 2**.

3.3. *Precipitation-TDS response and sensitivity (per-volume and site-scale)*

As a result of the mathematical modelling, we quantified the relationship between annual precipitation P (mm·yr^{-1}) and the annual TDS release per unit spoil volume M_{TDS} (t·Mm^{-3}·yr^{-1}) for unburnt and burnt argillite (see **Figure 5**).

For clarity, the relations used in **Figure 5** are written explicitly as:

$$M_{TDS\ unburnt} = 3.31 \times 10^{-3} \cdot P \quad (11)$$

$$M_{TDS\ burnt} = 8.78 \times 10^{-3} \cdot P \quad (12)$$

with slope parameters $k_{unburnt}$=3.31×10^{-3} and k_{burnt}= 8.78×10^{-3}. Across the tested precipitation range, the model yielded approximately 1.0-3.0 t·Mm^{-3}·yr^{-1} for unburnt and approximately 2.6-7.9 t·Mm^{-3}·yr^{-1} for burnt argillite, confirming a monotonic response and consistently higher release for thermally altered material.

In this precipitation-based representation (per-volume release vs. annual P), the burnt/unburnt slope ratio equals $k_{burnt}/k_{unburnt}$=2.653. At the column scale, however, the corresponding ratios obtained from independent metrics are close to ≈2.50: final filtrate concentrations were 462 vs. 185 mg·L^{-1} (ratio 2.497), and cumulative leached masses were 3.93 vs. 1.57 g (ratio 2.503). Using a constant column cross-section of 0.001018 m², these masses imply areal fluxes of ≈ 3930 vs. ≈ 1570 g·m^{-2} per 24 h (ratio 2.497). Taken together, the burnt/unburnt ratio is **metric-dependent** (concentration, mass, areal flux, or precipitation-based per-volume release) and should therefore be interpreted strictly within the normalisation used in each plot.

Model-based scaling using calibrated coefficients; areal annual fluxes Jyear are reported in the text for each scenario.

Site-wide scaling. Using the column-calibrated coefficients *a, b* and the site parameters (S_{site}, $m_{ore,site}$,, ρ, ε), the annual mass export of dissolved solids is estimated from precipitation as:

$$V_{p,site} = S_{site} P_{tot} \quad (13)$$

$$V_{f,site} = \eta V_{p,site} \quad (14)$$

where P_{tot} is the annual precipitation depth (m·yr^{-1}) and $0 < \eta < 1$ is the effective infiltration coefficient.

Results are expressed as mass load per year (e.g., t·yr^{-1}) and, where required, as areal annual flux:

$$J_{year} = \frac{M_{\mathrm{TDS},site}}{S_{site}\, T} \quad (15)$$

(e.g. kg·m^{-2}·yr^{-1}), enabling comparison across spoil heaps of different size and morphology. Formally, the **areal annual flux** is:

Table 3. Scenario TDS loads vs. annual precipitation (CCCP heap)

Scenario	P (mm·yr⁻¹)	Unburnt M_{TDS} (t·Mm⁻³·yr⁻¹)	Burnt M_{TDS} (t·Mm⁻³·yr⁻¹)	Unburnt site-wide (t·yr⁻¹)	Burnt site-wide (t·yr⁻¹)	Δ vs. 670 mm (Unburnt, t·yr⁻¹)	Δ vs. 670 mm (Burnt, t·yr⁻¹)
Dry	511	1.69	4.49	82.69	219.35	-25.73	-68.25
Average	670	2.22	5.88	108.42	287.60	+0.00	+0.00
Wet	829	2.74	7.28	134.15	355.85	+25.73	+68.25

Conventions. (i) Units: per-volume values in t·Mm⁻³·yr⁻¹; site-wide totals assume V = 48.89 Mm³. (ii) Relations: M_{TDS}, unburnt = 3.31×10⁻³·P, M_{TDS}, burnt = 8.78×10⁻³·P; P in mm·yr⁻¹.

Table 4. Fixed marginal sensitivity (linear model)

Metric	Unburnt	Burnt
Per-volume increment per +100 mm (t·Mm⁻³·yr⁻¹)	0.33	0.88
Site-wide increment per +100 mm (t·yr⁻¹)	16.18	42.93

$$J_{year} = \frac{M_{TDS,site}}{S_{site} \cdot 1_{yr}} \quad (\mathrm{kg \cdot m^{-2} yr^{-1}}) \qquad (16)$$

For S_{site} = 0.8638 km², the scenario values are: **Dry (511 mm)** – J_{year} ≈ 0.096 (unburnt) and 0.254 (burnt); **Average (670 mm)** – 0.1260 (unburnt) and 0.333 (burnt); **Wet (829 mm)** – 0.155 (unburnt) and 0.412 (burnt) kg·m⁻²·yr⁻¹.

For each additional 100 mm of annual precipitation, the predicted release increases by 0.331 t·Mm⁻³·yr⁻¹ for unburnt and 0.878 t·Mm⁻³·yr⁻¹ for burnt argillite. When scaled by the CCCP spoil volume V=48.89 Mm³, these per-100 mm sensitivities correspond to **+16.18 t·yr⁻¹** (unburnt) and **+42.93 t·yr⁻¹** (burnt) in site-wide annual loads. These sensitivities are constant within the applicability domain of the adopted linear approximation; slope values and their ratio will differ if a different metric or normalisation is used, which is why the specific definition is provided alongside each figure.

To operationalise the linear precipitation – TDS relations reported above, **Table 3** summarises per-volume responses and the corresponding site-wide annual loads for three precipitation scenarios spanning the CCCP site range, while **Table 4** lists the fixed marginal sensitivities per +100 mm of precipitation.

Table 3 summarises the per-volume model M_{TDS} = k·P and the corresponding site-wide annual loads for three representative precipitation scenarios – Dry (511 mm), Average (670 mm) and Wet (829 mm). These values confirm a monotonic increase with P and consistently higher magnitudes for burnt argillite. Relative to the Average scenario (670 mm), the Dry scenario reduces the site-wide load by − 25.73 t·yr⁻¹ (unburnt) and – 68.25 t·yr⁻¹ (burnt), whereas the Wet scenario increases it by +25.73 t·yr⁻¹ and +68.25 t·yr⁻¹, respectively. Across the full span from 511 to 829 mm, the site-wide TDS load rises by 51.46 t·yr⁻¹ (unburnt) and 136.50 t·yr⁻¹ (burnt).

*According to **Table 4**, the constant increments implied by the linear model per +100 mm of annual precipitation are summarised.* This tabular presentation facilitates straightforward application of the model to varying climatic scenarios without the need for recalculation. These increments are invariant within the calibration domain and can be used to interpolate between scenarios or to adjust loads for intermediate P. They also facilitate quick updates using observed or forecast precipitation without re-fitting the model. For instance, +200-300 mm above mean annual precipitation would increase site-wide TDS export by ≈32-64 t·yr⁻¹ for unburnt-dominant scenarios and ≈ 86-129 t·yr⁻¹ where burnt materials prevail.

Building directly on the per-volume precipitation - TDS relations (**Equations 11-12; Figure 5**), our results show a robust, approximately linear increase of annual salt release with increasing annual precipitation for both lithological states of argillite, with consistently higher magnitudes for thermally altered (burnt) material. The slope parameters $k_{unburnt}$ = 3.31×10⁻³ and k_{burnt} = 8.78×10⁻³ (t·Mm⁻³·mm⁻¹) quantify this contrast and, together with the site-scale volume of the CCCP spoil heap, allow direct translation from climatic variability to annual salt loads. This contrast between burnt and unburnt rock is consistent with the results of our earlier studies (**Kochmar and Karabyn, 2023**).

3.4. Ion-specific response of leaching to precipitation

Building on the linear precipitation-TDS relations described in Section 3.3, we apportioned the precipitation-driven release to individual dissolved species using the final filtrate composition from the column experiments (see **Table 5**). **For each material regime** m **(unburnt or burnt), we treat the leachate composition as quasi-stationary, i.e.** $c_i(t) \approx \alpha_{i,m}\, c_{TDS}(t)$. **We compute** $\alpha_{i,m}$ **from the final tank composition as** $\alpha_{i,m} = C_{i,final} / \sum_{j \in J} C_{j,final}$ **over the major ions listed in Table 5, so that** $\sum_i \alpha_{i,m} = 1$. **Integrating the mass balance** $M_i = \int c_i\, dV$ **gives** $M_i = \alpha_{i,m} M_{TDS}$**; together with** $M_{TDS} = k_{TDS,m} P$ **and** $M_i = k_{i,m} P$**, this yields** $k_{i,m} = \alpha_{i,m} k_{TDS,m}$**. For transparency, we also report** $\sum_i \alpha_{i,m}$ **and the variability of** C_i/C_{TDS} **across samples (median and coefficient of variation) to document the quasi-stationarity assumption.** Here, $\alpha_{i,m}$

denotes the mass fraction of ion i among the major ions in the filtrate of material m (HCO_3^-, SO_4^{2-}, Cl^-, Na^+, K^+, Mg^{2+}, Ca^{2+}), and $k_{TDS,m}$ is the precipitation-based slope ($k_{unburnt} = 3.31 \times 10^{-3}$; $k_{burnt} = 8.78 \times 10^{-3}$ t·Mm^{-3}·mm^{-1}). The fractions are normalised to sum to unity, ensuring that $\Sigma_i k_{i,m} = k_{TDS,m}$. The resulting composition weights are: burnt argillite dominated by sulphate (≈79%) with bicarbonate ≈11%; unburnt argillite ≈72% sulphate and ≈13% bicarbonate; alkali and alkaline-earth cations (Na^+, K^+, Mg^{2+}, Ca^{2+}) contribute only a few per cent each.

Table 5. Major-ion shares in the filtrate, used for partitioning the TDS slope

Ion	Unburnt (%)	Burnt (%)
HCO_3^-	13.0	11.1
SO_4^{2-}	71.7	78.6
Cl^-	2.5	2.2
Na^+	5.3	1.9
K^+	0.9	1.3
Mg^{2+}	2.0	1.9
Ca^{2+}	2.9	2.6

Conventions. (i) Fractions ($\alpha_{i,m}$, %) are calculated from the major-ion concentrations and normalised within the major-ion set. (ii) For unburnt material, Cl^- is treated as 5.0 mg·L^{-1} (upper bound).

To complement the composition weights in **Table 5**, **Table 6** presents the marginal sensitivities per +100 mm of precipitation for individual ions, reported both as per-volume and site-wide values.

Building on these marginal sensitivities, **Table 7** presents the predicted annual releases of major ions at a representative precipitation level of 670 mm·yr^{-1}, expressed both per-volume and as site-wide loads.

Sulphate dominates the precipitation-driven response in both materials, contributing ≈72% (unburnt) and ≈79% (burnt) of the bulk TDS slope. The bicarbonate fraction is 11-13%, consistent with carbonate buffering and dissolution. Among cations, Ca^{2+} and Mg^{2+} increments are modest but non-negligible. Since the model is linear, the difference in ion release between dry years (511 mm) and wet years (829 mm) can be obtained directly by multiplying the +100 mm sensitivities from **Table 6** by the corresponding precipitation difference. As a reference point, **Table 7** summarises the predicted annual releases of major ions at 670 mm·yr^{-1} (the average precipitation scenario), showing that sulphate overwhelmingly dominates the total loads, followed by bicarbonate, with other cations contributing only marginally. This linearity assumption simplifies projections but may under-represent potential nonlinear responses during extreme hydrological events.

Table 6. Marginal increase in annual load per +100 mm of precipitation (ΔP = 100 mm).

Ion	Unburnt (per-volume, t·Mm^{-3}·yr^{-1} per +100 mm)	Burnt (per-volume, t·Mm^{-3}·yr^{-1} per +100 mm)	Unburnt (site-wide, t·yr^{-1} per +100 mm)	Burnt (site-wide, t·yr^{-1} per +100 mm)
HCO_3^-	0.043	0.097	2.10	4.75
SO_4^{2-}	0.237	0.690	11.61	33.74
Cl^-	0.008	0.020	0.41	0.97
Na^+	0.018	0.017	0.86	0.83
K^+	0.003	0.012	0.14	0.56
Mg^{2+}	0.007	0.017	0.33	0.83
Ca^{2+}	0.010	0.023	0.47	1.10

Conventions.Values are reported both as per-volume (t·Mm^{-3}·yr^{-1} per +100 mm) and as site-wide increments (t·yr^{-1} per +100 mm), assuming a spoil volume of V = 48.89 Mm³.

Table 7. Predicted major-ion releases at P = 670 mm·yr^{-1}

Ion	Unburnt (t·Mm^{-3}·yr^{-1}; t·yr^{-1})	Burnt (t·Mm^{-3}·yr^{-1}; t·yr^{-1})
HCO_3^-	0.288 (14.07)	0.651 (31.84)
SO_4^{2-}	1.590 (77.76)	4.623 (226.04)
Cl^-	0.056 (2.75)	0.132 (6.45)
Na^+	0.118 (5.77)	0.113 (5.54)
K^+	0.019 (0.94)	0.077 (3.76)
Mg^{2+}	0.045 (2.19)	0.113 (5.53)
Ca^{2+}	0.064 (3.13)	0.151 (7.39)

Conventions. Values are reported as per-volume rates $\Delta M_i/V$ (t·Mm^{-3}·yr^{-1}) and as site-wide loads ΔM_i (t·yr^{-1}, in parentheses), computed for a spoil volume of V = 48.89 Mm³.

This equal-rate assumption follows the linear relationship $M_{TDS} = kTDS, m{\cdot}P$. These methodological choices do not affect additivity or the dominant sulphate signal, but they should be reconsidered if time-resolved compositions become available. The results have direct implications for anticipating water-quality impacts under extreme precipitation scenarios, which may escalate into local emergency situations requiring civil protection measures. Furthermore, the ion-resolved relationships established here underpin the scenario analysis linking climatic variability to composition-specific load changes. These quantified responses and sensitivities are inter-

preted in the context of mechanisms, published ranges, and implications for civil protection. These quantified responses and sensitivities are interpreted below in the context of mechanisms, published ranges, and implications for civil protection.

4. Discussion

4.1.-Leaching mechanisms

The approximately linear precipitation-TDS relation indicates that annual salt export is primarily water-flux-limited, whereas thermally altered argillite exhibits higher reactivity across scales. Two features are salient: (i) fixed marginal sensitivities enable scenario-based extrapolation across climatic regimes; and (ii) the magnitude of the burnt-unburnt contrast is contingent on the normalisation of the response metric (per spoil volume, per water volume, or per exposed area).

Thermal alteration augments salt release by breaking mineral lattices and exposing fresh reactive surfaces, by oxidising sulphides (e.g. pyrite) and promoting formation of readily soluble sulphate-bearing secondary phases (e.g. gypsum, anhydrite), and by altering pore architecture toward higher connectivity for percolating water (**Castillo-Meza et al., 2020; Gao et al., 2025**). Coal-spoil studies show higher SC/TDS ratios and sulphate-chloride fluxes from thermally altered (self-heated) materials in both column and field settings (**Daniels et al., 2016b; Orndorff et al., 2015; Clark et al., 2017**).

These pathways are consistent with the elevated sulphate and chloride measured in burnt filtrates and with widely observed increases in ionic strength from thermally affected mine wastes (**Daniels et al., 2016a; Clark et al., 2017; Welch et al., 2021**). In our columns, burnt material exhibits larger initial concentrations and cumulative masses than unburnt material under the same water input, supporting the interpretation that a thermally produced pool of labile salts is efficiently mobilised during wetting cycles. The persistence of a steeper precipitation-response slope in the annual model suggests that, beyond this transient pool, thermally altered rock maintains higher long-term reactivity. At other regional landfills, such as the Nadiya mine spoil tip, concentrations of major ions are also elevated, indicating that coal industry waste is a regional source of pollution throughout the Lviv-Volyn coal basin (**Skrobala et al., 2022**).

A sharp TDS peak around 2 hours (see **Figure 3**) reflects the rapid dissolution and wash-off of soluble secondary salts accumulated on reactive near-surface materials. The concentration then reduces as these salts are depleted and flow stabilises. Field and analogue studies of mine pools associate this 'first flush' to dissolution of efflorescent sulphate salts formed during oxidation. These salts produce highly mineralised waters at the onset of flushing, followed by a gradual reduction in concentrations (**Mugova et al., 2024**). Column tests on empty rock also show an 'early weathering' stage, characterised by high specific conductivity and peak ion concentrations, indicating rapid mobilisation of soluble salts prior to slower, reaction-limited release from less reactive phases (**Martin & Langman, 2024**). This interpretation aligns with the observed post-peak decline in our columns and supports treating early-time pulses as transient contributions superimposed on the longer-term, precipitation-modulated leaching captured by the linear model (**Merritt & Power, 2022**).

These findings align with laboratory and field evidence from other coal basins. Column studies on Appalachian spoils show high early-time TDS and specific conductance that decline toward quasi-steady levels after multiple pore-volume flushes, with higher values for unweathered, sulphide-rich mudstones and black shales (**Orndorff et al., 2015; Daniels et al., 2016b**). Work on closure salinity risk likewise documents rapid declines in Na-Cl where halite is initially present, followed by longer-term sulphate-dominated leaching (**Park et al., 2013**). Weathering-cycle simulations demonstrate that fine-grained fractions can produce extremely high initial TDS pulses that collapse after repeated wetting-drying cycles (**Dang et al., 2019**). At field scale, lysimeter and catchment monitoring confirm the same direction of change but over years to decades, with typical SC declining from >1000 - 3000 $\mu S \cdot cm^{-1}$ to 300 - 700 $\mu S \cdot cm^{-1}$, depending on lithology and management (**EPA, 2011; Daniels et al., 2016a; Welch et al., 2021**). Against this backdrop, our burnt/unburnt contrasts (≈2.5 at column scale; 2.653 at precipitation-based per-volume scale) fall within reported ranges.

4.2. Model adequacy and emergency risks

The linear precipitation-response model adopted in Section 3.3 aligns with established hydrological theory. In chemostatic catchments, solute concentrations vary only weakly with discharge, so annual loads scale approximately linearly with water flux; this behaviour is well documented and has been reaffirmed in recent reassessments (**Godsey et al., 2009**). At broader hydroclimatic scales, export vulnerability is governed by transport-reaction time-scale ratios (a Damköhler-type control), which implies stronger mass mobilisation with greater water inputs across realistic precipitation ranges (**Kumar et al., 2020**). These lines of evidence provide a physically consistent basis for a linear precipitation-mass relation and justify its application to the tested materials and site-relevant precipitation regime (**Godsey et al., 2009, Knapp et al., 2024; Kumar et al., 2020**).

From a civil protection perspective, the constant marginal sensitivities imply that wet-year anomalies translate linearly into elevated TDS loads, with a stronger effect for burnt zones. Wet-year anomalies will proportionally increase site-wide loads, with stronger effects where burnt materials prevail. For instance, +200-300 mm above mean annual precipitation would increase

site-wide TDS export by ≈32-64 t·yr^{-1} for unburnt-dominant scenarios and ≈ 86-129 t·yr^{-1} where burnt materials prevail. Since sulphate and chloride remain mobile under neutral to mildly alkaline conditions, such increases can influence ionic strength, cation exchange, metal speciation, and downstream aquatic ecology (**Daniels et al., 2016a; EPA, 2011; Welch et al., 2021**). These risks may escalate into local environmental emergencies, underscoring the need for preventive measures such as stabilisation of burnt sectors, interception of first-flush leachates, selective covers where f_b is high, and monitoring of SC and sulphate with thresholds informed by per-100 mm sensitivities.

4.3. Model limitations and future directions

The discussion reconciles column-scale evidence and a parsimonious precipitation-response model into a coherent picture of salt leaching from coal-derived argillites. Thermal alteration emerges as the principal intensifier, with effects that are visible across metrics and preserved after scale-up to annual, per-volume predictions. The linear form captures first-order climatic control while remaining transparent enough to support decision-making: every +100 mm of precipitation implies a fixed, material-specific increase in annual TDS export per-volume of spoil and, by extension, a predictable increment in site-wide load at the heap scale.

Methodologically, the approach integrates controlled column leaching (100 g samples, 24 h, 300 mL·min^{-1} flow rate, ≈ 432 L cumulative throughput) with dimensional analysis and simple scaling to the spoil-heap volume (48.89 Mm³). The model thus links micro-scale leaching processes with meso- and macroscale hydrological forcing, allowing the evaluation of salinity export in a form directly applicable to early-warning and planning frameworks of civil protection.

The framework developed here is not limited to the Chervonohrad district. Its formulation is transferable to other spoil piles and mining waste facilities across Ukraine, particularly in eastern regions where spontaneous combustion, shelling, and extreme precipitation combine to create conditions of heightened risk. In such settings, thermal alteration and hydrologic forcing interact to intensify contaminant release, underscoring the importance of a predictive tool that can quantify expected load increments under different climatic scenarios. Extending application to eastern Ukraine provides an opportunity to support civil protection planning under conditions of ongoing military threat. The ability to forecast ion-specific releases strengthens preparedness for potential emergency situations, where contaminated runoff or groundwater could directly impact local communities and ecosystems.

Several limitations should be noted. First, depth coverage was restricted to **0.2 - 0.3 m,** which targets the **near-surface leaching** zone rather than the full vertical variability of **element mobility** within the heap. This upper horizon is hydrologically responsive and biologically active - where infiltration, oxygen exchange and temperature fluctuations enhance sulphide oxidation, dissolution of readily soluble salts, and mobilisation of major ions (notably SO_4^{2-}, Cl^-, HCO_3^-) into percolating waters - yet it does not resolve potential deeper pathways of mobilisation governed by compaction, moisture storage and redox stratification. Accordingly, the reported leachate chemistry should be interpreted as **characteristic of the active near-surface source zone** for first-flush export, with recognition that metre-scale subsurface processes - including low-temperature oxidation and self-heating fronts - may develop below the surface and alter migration pathways and fluxes at depth (**Espinha Marques et al., 2024; Anghelescu & Diaconu, 2024**).

The relationship between the sediment and the mass applied in this study represents a linear approximation of a more general model, in which non-linear sorption and secondary processes are grouped into a term $\varphi(\cdot)$. In this analysis $\varphi(\cdot)$ is set to zero, giving the simplified form used in further modelling. The approach was validated mainly for total dissolved solids using recirculating column experiments, and ion-specific loads were estimated by applying quasi-stationary composition weights. Additional uncertainty arises at field scale from **hydrological** representation and scale transition: runoff generation, preferential flow and seasonal storage can decouple precipitation from effective infiltration; stratification and patchiness within spoil heaps may bias scaling; and column geometries differ from field conditions. Accordingly, confidence intervals should be propagated when translating **per-volume** sensitivities into **site-wide** annual loads for risk management. Finally, the fixed **per-100 mm** sensitivities should be applied as constants only within the stated applicability and calibration domain of the linear model.

In summary, the synthesis highlights both the mechanistic insight and the applied relevance of the model. It provides a robust, adaptable framework for environmental management in mining regions and a practical foundation for integrated civil protection strategies across Ukraine and beyond.

Future work should aim to extend the modelling framework beyond the CCCP heap, applying it to other spoil piles and concentration plant dumps across Ukraine, particularly in the eastern regions that are subject to shelling and therefore present higher risks than the Chervonohrad district. Further developments should also integrate a dynamic water balance module that translates precipitation into effective infiltration as a function of cover, slope, and season. In order to implement such approaches under real constraints, optimisation based on dynamic programming is an effective method for selecting and sequencing technological actions (**Lousada et al., 2024**). In addition, model calibration should be extended not only to total TDS, but also separately to sulphates, bicarbonates and chlorides. Such

improvements will enhance the accuracy and reliability of the model and will be useful in planning civil protection measures for mining regions.

4.4.-Recommendations

Given the calibrated linear precipitation–TDS response ($k_{unburnt}$ = 3.31 × 10^{-3} and k_{burnt} = 8.78 × 10^{-3} t·Mm^{-3}·mm^{-1}) and the fixed marginal sensitivities per +100 mm of annual precipitation (+0.331 and +0.878 t·Mm^{-3}·yr^{-1}; site-wide +16.18 and +42.93 t·yr^{-1} for unburnt and burnt material, respectively), management should prioritise (i) stabilisation and hydrologic control of thermally altered (burnt) sectors, where per-volume slopes and loads are consistently higher; (ii) interception of first-flush leachates during heavy rainfall and snowmelt, as early-time pulses dominate short-term export; (iii) routine monitoring of specific conductance and sulphate as pragmatic early-warning indicators, with action thresholds derived directly from the +100 mm sensitivities in **Table 4** and the precipitation scenarios in **Table 3**; (iv) selective covers and drainage measures in areas with high effective infiltration (η), to reduce *Vf* and thus annual loads; and (v) contingency planning for wet-year anomalies (+200 – 300 mm), which, under linear scaling, translate into predictable tens-of-tonnes increases in site-wide TDS export. These measures follow directly from the observed burnt/unburnt contrasts, the linear precipitation dependence over the site-relevant range, and the ion partitioning that highlights sulphate as the dominant contributor to annual loads.

5. Conclusions

This study developed and applied an integrated mathematical and physical modelling framework to quantify the leaching dynamics of salt ions from coal-mining waste, with particular emphasis on the contrasting behaviours of thermally altered (burnt) and unaltered (unburnt) argillite. By linking controlled column experiments with a precipitation-response model scaled to the CCCP spoil heap, we demonstrated that annual releases of TDS increase linearly with precipitation input, and that burnt materials consistently exhibit higher fluxes across multiple metrics. This outcome reflects both the mobilisation of labile salts and the sustained reactivity of sulphide-bearing phases subjected to thermal alteration.

The analysis of ion-specific contributions revealed that sulphate overwhelmingly dominates the precipitation-driven signal (≈ 72 - 79%), with bicarbonate providing secondary buffering and other cations contributing marginally. This composition indicates that environmental risks from coal-mining waste leachates are not uniformly distributed among ions but are heavily shaped by sulphate oxidation processes, which directly threaten ecological safety through elevated ionic strength, potential metal mobilisation, and downstream impacts on aquatic systems.

From a methodological standpoint, the use of linear precipitation-response functions provides a parsimonious yet robust predictor of annual TDS loads, facilitating the translation of climatic variability into site-wide estimates of pollutant release. Such predictive capacity is essential for integrating hydrogeochemical insights into risk assessments and early-warning systems for civil protection. Collected sensitivity data (+0.331 and +0.878 t Mm^{-3} yr^{-1} per +100 mm for unburnt and burnt argillite, respectively) provide practical thresholds for scenario planning across dry, average, and wet-year conditions.

Coal-mining waste heaps are not only local sources of salinity but can also trigger environmental emergencies during extreme hydrological events. Linear upscaling indicates that wet-year anomalies (+200–300 mm) may increase site-wide TDS exports by tens of tonnes per year – a load high enough to stress receiving waters. These results suggest that spoil-heap leaching should be included in regional strategies for emergency readiness and civil protection.

For civil protection and ecological safety planning in Ukraine and other coal mining regions, particularly those exposed to armed conflict and the associated risks of spontaneous combustion, the findings underscore several priorities. First, stabilisation and hydrological control of thermally altered sectors are essential to minimise salt ions leaching. Second, interception of first-flush leachates during heavy rainfall and snowmelt can substantially reduce the load of dissolved salts reaching receiving waters. Third, continuous monitoring of sulphate and electrical conductivity should be implemented as early-warning indicators, ensuring timely detection of elevated releases. These measures are critical to reducing vulnerability to environmental emergencies and strengthening adaptive capacity.

Overall, the modelling framework presented here is transferable beyond the Chervonohrad region. It provides a generic yet adaptable tool for anticipating the mobilisation of dissolved loads from coal-derived wastes under variable climatic forcing. The study not only advances hydrogeochemical science but also directly supports the development of integrated environmental-civil protection systems, thereby bridging ecological research with applied disaster risk reduction in mining-affected landscapes.

6. References

Alvarenga, P., Guerreiro, N., Simões, I., Imaginário, M. J. and Palma, P. (2021). Assessment of the environmental impact of acid mine drainage on surface water, stream sediments, and macrophytes using a battery of chemical and ecotoxicological indicators. Water, 13(10), 1436. https://doi.org/10.3390/w13101436

American Public Health Association (APHA), American Water Works Association (AWWA), & Water Environment Federation (WEF). (2017). Standard Methods for the Ex-

amination of Water and Wastewater (23rd ed.). Washington, DC: APHA-AWWA-WEF.

Anghelescu, L., and Diaconu, B. M. (2024). Advances in detection and monitoring of coal spontaneous combustion: Techniques, challenges, and future directions. Fire, *7*(10), 354. https://doi.org/10.3390/fire7100354

Bosak, P., Popovych, V., Stepova, K. and Dudyn, R. (2020). Environmental impact and toxicological properties of mine dumps of the Lviv-Volyn coal basin. News of the National Academy of Sciences of the Republic of Kazakhstan, Series of Geology and Technical Sciences, 2(440), 48-54. https://doi.org/10.32014/2020.2518-170X.30

Castillo-Meza, A.J., Daniels, W.L., Zipper, C.E. and Orndorff, Z.W. (2020). Estimating total dissolved solids release from coal mine spoils using laboratory leaching procedures. International Journal of Coal Geology, 218, 103353. https://doi.org/10.1016/j.coal.2019.103353

Clark, G. M., Daniels, W. L., Orndorff, Z.W. and Zipper, C.E. (2017). Thermal alteration and leaching dynamics in Appalachian coal spoil piles. Applied Geochemistry, 82, 125-138. https://doi.org/10.1016/j.apgeochem.2017.05.012

Cooke, C. A., Emmerton, C. A., Donahue, W. F., & Kerr, J. G. (2025). Downstream water quality impacts persist despite mountaintop coal mine reclamation in the Canadian Rocky Mountains. *Environmental Pollution*, *383*, 126841. https://doi.org/10.1016/j.envpol.2025.126841

Crundwell, F.K. (2005). The leaching number: its definition and use in determining the performance of leaching reactors and autoclaves. Minerals Engineering, 18(13-14), 1315-1324. https://doi.org/10.1016/j.mineng.2005.06.014

Dang, Z., Li, P., Edraki, M. and Huang, L. (2019). The effect of weathering on salt release from coal mine spoils. Minerals, 9(12), 760. https://doi.org/10.3390/min9120760

Daniels, W.L., Orndorff, Z.W., Zipper, C.E. and Beck, M.A. (2016a). Column and field-scale leaching of treated and untreated coal spoils: sulphate mobilisation post-heating. Journal of Environmental Quality, 45(3), 743-753. https://doi.org/10.2134/jeq2015.06.0313

Daniels, W.L., Zipper, C.E., Orndorff, Z.W., Skousen, J., Barton, C.D., McDonald, L.M. and Beck, M.A. (2016b). Predicting total dissolved solids release from central Appalachian coal mine spoils. Environmental Pollution, 216, 371-379. https://doi.org/10.1016/j.envpol.2016.05.044

EPA. (2011). A field-based study of TDS impacts on benthic macroinvertebrate communities in central Appalachian streams. EPA/600/R-09/138F. https://www.epa.gov/sites/default/files/2015-03/documents/final_tds_report_1333.pdf

Espinha Marques, J., Narayan, A., Santos, P., Ribeiro, J., Antunes, S. C., Melo, A., Rocha, F., Flores, D., and Mansilha, C. (2024). Hydropedological characterization of a coal mining waste deposition area affected by self-burning. Hydrology, 11(5), 62. https://doi.org/10.3390/hydrology11050062

Gao, S., Li, J.S., Zhang, S. and Poon, C.S. (2025). A state-of-the-art review of solid waste leaching mechanisms and evaluation methodologies. Waste Management, 204, 114941. https://doi.org/10.1016/j.wasman.2024.114941

Garbacz, A., Nowak, A., Marzec-Grządziel, A., Przybyś, M., Gałązka, A., Jaroszuk-Ściseł, J., and Grzywaczewski, G. (2025). Impact of Coal Waste Rock on Biological and Physicochemical Properties of Soils with Different Agricultural Uses. *Sustainability*, *17*(6), 2603. https://doi.org/10.3390/su17062603

Godsey, S.E., Kirchner, J.W. and Clow, D.W. (2009). Concentration-discharge relationships reflect chemostatic characteristics of US catchments. Hydrological Processes, 23(13), 1844-1864. https://doi.org/10.1002/hyp.7315

Gromek, P. and Lowe, T. (2025). Ground robot technologies in wildfire risk reduction: the viewpoint of the fire service. Progress in Disaster Science, 20, 100435. https://doi.org/10.1016/j.pdisas.2025.100435

Hoxha, E., Symochko, L. and Pinheiro, M. N. C. (2025). The environmental impact of mining activities in Europe: a comprehensive analysis. EQA-International Journal of Environmental Quality, 66, 30-42.

International Energy Agency. (2025). Global Energy Review 2025. IEA. https://www.iea.org/reports/global-energy-review-2025

Karabyn, V. and Kochmar, I. (2025). Distribution of different forms of manganese in coal mining waste: A case study of the Vizeyska mine, Ukraine. IOP Conference Series: Earth and Environmental Science, 1499, 012045. https://doi.org/10.1088/1755-1315/1499/1/012045

Karabyn, V., Shuryhin, V., Shutiak, S., Chmiel, M. and Kulhanek, R. (2022). Strategic environmental assessment - underestimated tool for sustainable subsoil use. Environmental Problems, 7(3), 140-146. https://doi.org/10.23939/ep2022.03.140

Knapp, J.L. A., Li, L. and Musolff, A. (2024). Concentration-discharge relationships revisited: Overused but underutilised? Hydrological Processes. Advance online publication. https://doi.org/10.1002/hyp.15328

Kochmar, I. and Karabyn, V. (2023). Water extracts from waste rocks of the coal industry of Chervonohrad mining area (Ukraine): problems of environmental safety and civil protection. Ecological Engineering & Environmental Technology, 24(1), 247-255. https://doi.org/10.12912/27197050/156939

Kochmar, I., Karabyn, V. and Karabyn, O. (2022). Lead Speciation in the Technogenesis Zone of Coal Mining Sites (Case of Vizeyska Mine of Chervonohrad Mining Area, Lviv Region, Ukraine). Petroleum and Coal, 64(2): 445-454

Kochmar, I., Karabyn, V. and Kordan, V. (2024). Ecological and geochemical aspects of thermal effects on argillites of the Lviv-Volyn coal basin spoil tips. Scientific Bulletin of the National Mining University, 3, 100-107.

Kumar, R., Heße, F., Rao, P.S.C., Musolff, A. and Jawitz, J.W. (2020). Strong hydroclimatic controls on vulnerability to subsurface nitrate contamination across Europe. Nature Communications, 11, 6302. https://doi.org/10.1038/s41467-020-19955-8

Loboichenko, V. and Leonova, N. (2021). Assessment of the impact of natural and anthropogenic factors on the state of water objects in urbanized and non-urbanized areas in Lozova district (Ukraine). Ecological Engineering and Environmental Technology, 22(2), 69-76. https://doi.org/10.12912/27197050/135188

Long, P., Wang, G.-S., Zhang, S., Hu, S.-L. and Huang, Y. (2020). A mathematical model for column leaching of ion adsorption-type rare earth ores. International Journal of Minerals, Metallurgy and Materials, 27(4), 463-471. https://doi.org/10.1007/s12613-019-1883-9

Lousada, S., Delehan, S. and Khorolskyi, A. (2024). Application of dynamic programming models for improvement of technological approaches to combat negative water leakage in the underground space. Water, 16(14), 1952. https://doi.org/10.3390/w16141952

Martin, J., & Langman, J. B. (2024). Leachate experiments to evaluate weathering of waste rock for backfill aquifers in restored coal mine pits, Powder River Basin, USA. *Geosciences, 14*(1), 4. https://doi.org/10.3390/geosciences14010004

Merritt, P., & Power, C. (2022). Assessing the long-term evolution of mine water quality in abandoned underground mine workings using first-flush based models. *Science of the Total Environment, 846*, 157390. https://doi.org/10.1016/j.scitotenv.2022.157390

Monteiro, M., Santos, P., Espinha Marques, J., Flores, D., Azenha, M., & Ribeiro, J. A. (2025). Assessment of Potential Environmental Risks Posed by Soils of a Deactivated Coal Mining Area in Northern Portugal–Impact of Arsenic and Antimony. Pollutants, *5*(2), 15. https://doi.org/10.3390/pollutants5020015

Montgomery, D. C., Peck, E. A., & Vining, G. G. (2021). *Introduction to linear regression analysis* (6th ed.). Hoboken, NJ: Wiley.

Moroz, O.M., Hnatush, S.O. and Maslovska, O.D. (2020). Reduction of sulfur and oxidized forms of nitrogen by bacteria of Desulfuromonas sp., isolated from Yavorivske Lake, under the influence of ferrum citrate. Biosystems Diversity, 28(1), 78-85. https://doi.org/10.15421/012011

Mugova, E., Molaba, L., & Wolkersdorfer, C. (2024). Understanding the mechanisms and implications of the first flush in mine pools: Insights from field studies in Europe's deepest metal mine and analogue modelling. *Mine Water and the Environment, 43*, 73–86. https://link.springer.com/article/10.1007/s10230-024-00969-3

Orndorff, Z.W., Daniels, W.L., Zipper, C.E., Eick, M. and Beck, M. (2015). A column evaluation of Appalachian coal mine spoils' temporal leaching behaviour. Environmental Pollution, 204, 39-47. https://doi.org/10.1016/j.envpol.2015.03.049

Park, J.H., Li, X., Edraki, M., Baumgartl, T. and Kirsch, B. (2013). Geochemical assessments and classification of coal mine spoils for better understanding of potential salinity issues at closure. Environmental Science: Processes & Impacts, 15(6), 1235-1244. https://doi.org/10.1039/c3em30672k

Petlovanyi, M., Sai, K., Malashkevych, D., Popovych, V. and Khorolskyi, A. (2023). Influence of waste rock dump placement on the geomechanical state of underground mine workings. IOP Conference Series: Earth and Environmental Science, 1156, 012007. https://doi.org/10.1088/1755-1315/1156/1/012007

Proshad, R., Chandra, K., Islam, M., Khurram, D., Rahim, M.A., Asif, M.R. and Idris, A.M. (2025). Evaluation of machine learning models for accurate prediction of heavy metals in coal mining region soils in Bangladesh. Environmental Geochemistry and Health, 47(5), 1-25. https://doi.org/10.1007/s10653-024-01782-3

Rouhani, A., Newton, R.A., Al Souki, K.S., Quattrini, G. and Gusiatin, M.Z. (2024). A 6-year review status on soil pollution in coal mining areas from Europe. Environmental Geochemistry and Health, 46(10), 392. https://doi.org/10.1007/s10653-023-01666-7

Rouhani, A., Skousen, J. and Tack, F.M.G. (2023). An overview of soil pollution and remediation strategies in coal mining regions. Minerals, 13(8), 1064. https://doi.org/10.3390/min13081064

Skrobala, V., Popovych, V., Tyndyk, O. and Voloshchyshyn, A. (2022). Chemical pollution peculiarities of the Nadiya mine rock dumps in the Chervonohrad Mining District, Ukraine. Mining of Mineral Deposits, 16(4), 71-79. https://doi.org/10.33271/mining16.04.071

Stepova, K., Fediv, I., Mažeikiene, A., Šarko, J. and Mažeika, J. (2023). Adsorption of ammonium ions and phosphates on natural and modified clinoptilolite: Isotherm and breakthrough curve measurements. Water, 15, 1933. https://doi.org/10.3390/w15101933

Sutherland, C., Chittoo, B.S. and Samlal, A. (2023). The status of scientific development on the application of biosorption of heavy metals at laboratory and pilot-scale: A review. Desalination and Water Treatment, 299, 13-49. https://doi.org/10.5004/dwt.2023.29729

Tkachenko, H., Kurhaluk, N., Skaletska, N., Maksin, V. and Osadowski, Z. (2021). Elemental status and lipid peroxidation in the blood of children with endemic fluorosis. Biological Trace Element Research, 199(4), 1237-1245. https://doi.org/10.1007/s12011-020-02193-y

Tyndyk, O., Popovych, V., Sai, K., and Petlovanyi, M. (2024). Natural phytomelioration of the coastal water zone of man-made reservoirs in mining areas. E3S Web of Conferences, 526, 01005. https://doi.org/10.1051/e3sconf/202452601005

URL 1. https://meteopost.com. (accessed 1st August 2025).

Vladyko, O., Maltsev, D., Sala, D., Cichoń, D. and Buketov, V. (2022). Simulation of leaching processes of polymetallic ores using the similarity theorem. Rudarsko-Geološko-Naftni Zbornik, 37(5), 169-180.

Welch, C., Barbour, S. L. and Hendry, M. J. (2021). The geochemistry and hydrology of coal waste rock dumps: A systematic global review. Science of the Total Environment, 795, 148798.

Xu, K., Zhong, W., Qian, L., Xia, F., Han, X., Yu, X., & Zhu, X. (2025). Harnessing bio-modified coal gangue for mine wastewater remediation: a sustainable approach. Environmental Geochemistry and Health, 47(9). https://doi.org/10.1007/s10653-025-02698-0

Xu, W., Jin, Y., & Zeng, G. (2024). Introduction of heavy metals contamination in the water and soil: a review on source, toxicity and remediation methods. Green Chemistry Letters and Reviews, *17*(1). https://doi.org/10.1080/17518253.2024.2404235

SAŽETAK

Integrirano matematičko i fizičko modeliranje izluživanja ionskih soli iz rudarskoga otpada ugljena: implikacije za ekološku sigurnost i civilnu zaštitu

Odlagališta rudarskoga otpada iz eksploatacije ugljena predstavljaju znatan izvor otopljenih soli koje se mogu mobilizirati pod utjecajem oborina, što stvara rizike za ekološku sigurnost i sustave civilne zaštite. Ovo istraživanje usmjereno je na odlagalište jalovine Centralne flotacije Červonohrad u zapadnoj Ukrajini, gdje su ispitivani i termalno izmijenjeni i neizmijenjeni argiliti. Laboratorijska istraživanja izluživanja provedena su na uzorcima mase 100 g, koji su izluženi deioniziranom vodom radi simulacije procesa izluživanja pod kontroliranim uvjetima. Kumulativni volumeni procijeđene otopine iznosili su približno 432 L, što je omogućilo kvantifikaciju ukupnih otopljenih tvari te pojedinačnih ionskih doprinosa. Tijekom 24 sata provedeno je izluživanje kroz stupce brzinom od 300 mL·min^{-1} (ukupno 8,5 L recirkulirano, ≈ 432 L prošlo kroz uzorak), pri čemu je izmjerena konačna koncentracija ukupnih otopljenih tvari od 462 mg·L^{-1} za izgorjeli argilit i 185 mg·L^{-1} za neizgorjeli, dok su kumulativne mase izluženih soli iznosile 3,93 g odnosno 1,57 g (≈ 2,5 puta više za izgorjeli uzorak). Razlika u početnoj fazi izluživanja bila je još izraženija: nakon 2 sata (≈ 0,7 L) koncentracija je kod izgorjeloga uzorka iznosila 183 mg·L^{-1}, a kod neizgorjeloga 50 mg·L^{-1} (≈ 3,7 puta više). Fizička opažanja povezana su s matematičkim modeliranjem radi uspostave odnosa između količine oborina i oslobađanja ukupnih otopljenih tvari. Rezultati upućuju na izraženu linearnu povezanost između godišnje količine oborina i oslobađanja soli iz procesa izluživanja, pri čemu termalno izmijenjeni materijali pokazuju znatno veće tokove iona. Ovaj integrirani modelni pristup pokazuje kako se laboratorijski podatci i jednostavni modeli mogu koristiti za predviđanje izluživanja onečišćujućih tvari, čime se pridonosi ekološkoj sigurnosti i planiranju mjera civilne zaštite u rudarskim područjima sklonim hidrološkim ekstremima.

Ključne riječi:
civilna zaštita, ekološka sigurnost, sustavi ranoga upozorenja, geokemija, prediktivno modeliranje, izluživanje

Author's contribution

Vasyl Karabyn (Dr Eng; Professor of Civil Protection): conceptualisation, methodology, supervision, writing - original draft, project administration. **Iryna Kochmar** (Lecturer): selected representative spoil materials, prepared the samples and carried out column experiments; she curated laboratory data and contributed to manuscript revision, mathematical modelling, writing - original draft. **Oksana Karabyn** (PhD; Associate Professor of Mathematics): formulation of the mathematical model, formal analysis; modelling, writing - original draft & editing. **Clint Sutherland** (Dr Eng; Associate Professor of Civil Engineering): methodology; supervision; writing - original draft & editing. **Valentyna Loboichenko** (Dr Eng; Professor of Civil Protection): methodology; supervision; writing - original draft & editing. **Andrii Khorolskyi** (PhD; Head of Laboratory): methodology; formal analysis; visualisation; writing - review & editing.
All authors have read and agreed to the published version of the manuscript.

RGNZ/MGPB

Data-driven and knowledge-driven MARCOS method to Cu porphyry prospectivity modelling, a case study, Shahr-e-Babak area, southeastern Iran

Rudarsko-geološko-naftni zbornik
(The Mining-Geology-Petroleum Engineering Bulletin)
DOI: 10.17794/rgn.2026.3.3

Original scientific paper

Moslem Jahantigh[1] ✉, **Hamidreza Ramazi**[1] ✉
[1] *Faculty of Mining engineering, Amirkabir University of Technology, Hafiz Street, Tehran, Iran.*

Abstract
The present study aims to compare the performance of data-driven and knowledge-driven Multi-Criteria Decision-Making (MCDM) in producing a mineral potential model in the Shahr-e-Babak study area in south-eastern Iran. To achieve this goal, eight evidential layers, including geological, Cu signature, principal component analysis, argillaceous alteration, phyllic alteration, iron oxide alteration (Gossan), airborne geophysics layers, and linear structures, were pre-processed and produced. To produce the optimal model, first, all layers were scaled and shifted to the zero to one interval. To create the mineral potential model in the area, the Measurement Alternatives and Ranking according to Compromise Solution (MARCOS) method was introduced. For the exploration control layer weighting, two methods were used: the area prediction rate (P-A) method and the Analytic Hierarchy Process (AHP) method. Then, the results were compared with the Multi-Objective Optimization by Ratio Analysis (MOORA) method, which is a proven method in mineral potential assessment. To compare these methods, two methods – area prediction rate and the area under the curve (AUC) – were used. The findings show that the data-driven MARCOS approach provides the best performance and displays the best mineral potential model. The normalized density for the data-driven MARCOS, data-driven MOORA, knowledge-driven MARCOS, and knowledge-driven MOORA methods is equal to 3.00, 2.84, 2.7, and 2.57, respectively. The AUC for the data-driven MARCOS, data-driven MOORA, knowledge-driven MARCOS, and knowledge-driven MOORA methods is equal to 0.939, 0.938, 0.933, and 0.932, respectively.

Keywords:
Porphyry, MARCOS, MOORA, Shahr-e-Babak, Data-driven

1. Introduction

The primary step in the exploration of economic mineral resources is the identification of areas with high potential. Identifying and exploring minerals is inherently time-consuming and costly (**Feizi et al., 2021; Karbalaeiramezanali et al., 2025; Riahi et al., 2023; Tešić et al., 2023**). Therefore, it is necessary and mandatory to limit the areas to be explored. Mineral Potential Modelling (MPM) is a fundamental and key method in integrating geoscience data sets (geophysics, geochemistry, geology, remote sensing, etc.). The primary objective of MPM is to identify potential mineral areas within the study areas. The primary function of MPM is to increase the profitability of mining projects and reduce the risk related to cost and time. There are three basic steps in MPM: the first step is to identify and collect information related to the study area and the studied deposit. The second step is to weigh the exploration witness maps related to the target deposit. The third and final step is to integrate the exploration witness maps and determine the potential and mineral potential areas. Data integration is done through various operators and complex mathematical functions. This integration is done to determine target areas and potential areas of mineral potential (**Mami Khalifani et al., 2025**).

In the last decade, Geographic Information System (GIS) software has become an important tool to prioritize potential areas for minerals by integrating spatial science data. Various methods have been proposed to produce MPM based on GIS software. These methods are categorized into two categories: data-driven and knowledge-driven. In data-driven methods, known mineralization points are used to train and generate mineral models (**Tshanga et al., 2024**). Also, by relying on these points, the degree of relationship between exploration witness layers and the type of target deposit can be examined. Some data-driven methods include Support Vector Machine (SVM), Random Forest Algorithm (RF), Adaptive Neuro-Fuzzy Inference System (ANFIS), and Convolutional Neural Network (CNN). MCDM methods have been used in the past mainly in a knowledge-based manner, and expert knowledge has been used to weight the exploratory evidence layers.

* Corresponding author: Hamidreza Ramazi
e-mail address: ramazi@aut.ac.ir
Received: 11 June 2025. Accepted: 1 November 2025.
Available online: 14 May 2026

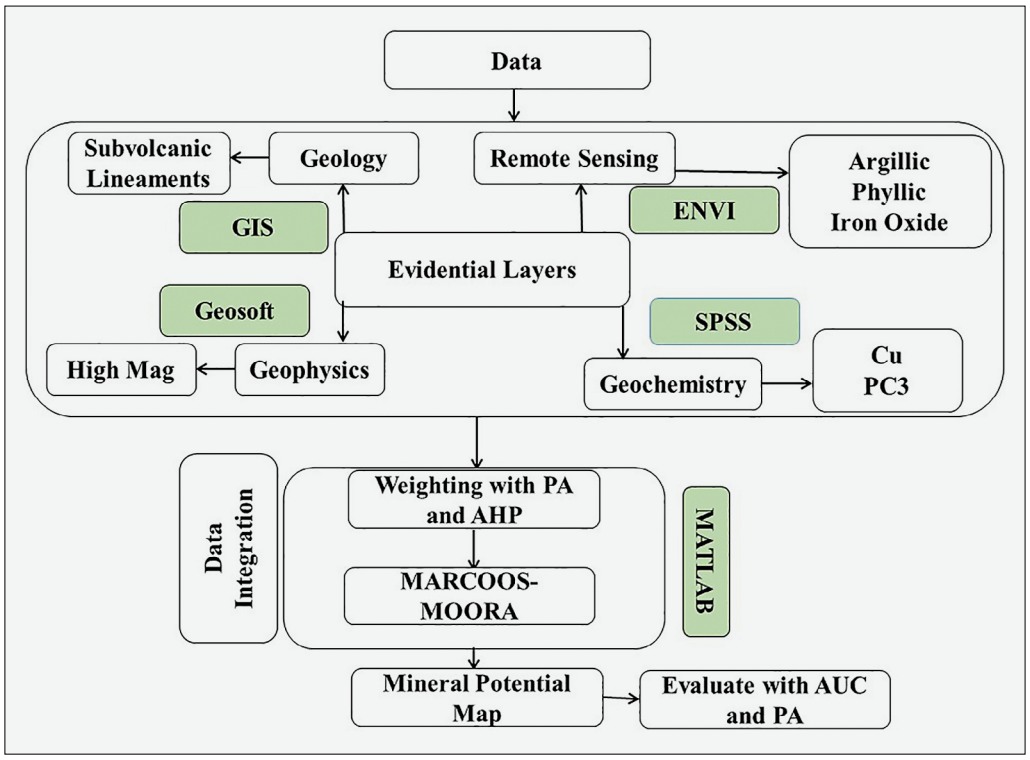


Figure 1. Flowchart of recent research on porphyry prospectivity modelling.

Knowledge-based methods are suitable for areas that have not been explored or where few mineralization points of the target deposit type have been identified. Knowledge-based methods are based on the experience of geoscientists. These methods use the knowledge of geoscientists to weigh the layers of exploratory evidence. They contain such methods of index overlay (**Bonham-Carter et al., 1989, Carranza et al., 1999, Mirzaei et al., 2014**), fuzzy logic (**An et al., 1991, Brown et al., 2000, Porwal et al., 2003, Nykänen et al., 2008, Parsa et al., 2016**), Boolean logic. (**Bonham-Carter et al. 1989**), the outranking method (**Abedi et al., 2012**), wildcat mapping (**Carranza, 2010**), Dempster-Shafer belief theory (**Moon, 1990**), and multi-criteria decision-making approaches (**Pazand et al., 2015; Yousefi & Carranza, 2015**). Over the past decade, new methods have become popular, often used in combination. In these methods, the mineralization points in the area are used to select and weight the exploration witness layers. In many studies, a combination of two or more MCDM methods has been used to make better decisions and solve the MPM problem. In fact, to successfully solve an MPM problem, it is necessary to select appropriate exploration witness layers and then generate an MPM map. From this perspective, MPM is considered an MCDM method. In fact, the application of MCDM methods in a data-driven manner enables geoscientists to reduce uncertainties for the MPM problem and eliminate inconsistencies between criteria.

In the present study, knowledge-based and data-based methods have been used to weight the exploration witness layers. Then, the obtained weights have been applied to the exploration witness layers. The weighted layers have been merged using the MOORA method, a proven approach for producing a mineral potential model. Additionally, this paper introduces the MARCOS method as a novel approach for creating a mineral potential model. The results obtained using the Marcus method have been compared with those obtained using the Mora method.

The flowchart of recent research is shown in **Figure 1.**

2. Geology and Cu Mineralization in the study area

2.1. Geology

The study area is located in the areas with the following coordinates: 55° 6.5′ to 55° 20′ east longitude and 30° 20′ to 30° 27′ north latitude (see **Figure 2a** and **b**). In this area, several Mio-Pliocene dacite-andesite volcanic masses have erupted into the rocks of the Urmia-Dokhtar magmatic belt in the form of domes or small volcanic cones that are located in the south and northeast of the Masahim Volcano. The age of these masses is reported to be Mio-Pliocene based on the Shahr-e-Babak geological map (**Safari et al., 2018**). The volcanic rocks related to the Eocene are older, and the dacite-andesite masses have intruded them and are younger, containing older fragments. The high altitude compared to the adjacent Eocene volcanic rocks and the light colour of the dacite rocks distinguish these masses from other rocks in

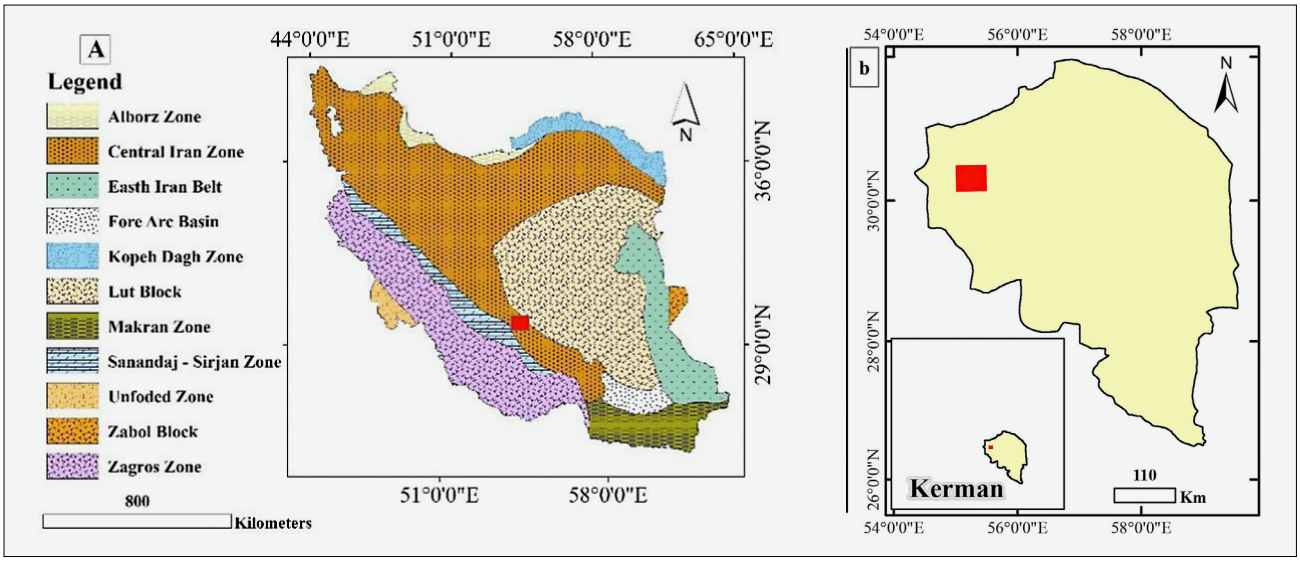


Figure 2. Location of Shahr-e-Babak in Iran structural zones map. b Location of Shahr-e-Babak in Kerman Province.

the region. In the study area, the andesitic units of the region have been investigated and studied. The andesites of the region are seen in the desert in the form of lava flows and dykes (see **Figure 3**). Andesitic dykes are younger than the lavas (**Jahantigh & Ramazi, 2024; Jahantigh & Ramazi, 2025**). In terms of petrological characteristics, most of the andesites have a porphyry texture in which plagioclase, amphibole, and pyroxene crystals are noticeable.

2.2. Cu mineralization (Cu indices) in the study area

Several porphyry copper deposits have been identified in the Shahr-e-Babak area. Some of these deposits, such as the Miduk, Sara, Dareh-Hezar, and Abdar deposits, are involved in the world-class porphyry copper deposits. Exploration drilling operations have been carried out in some active porphyry mines of the study area, including Miduk, Sara Dareh Hezar, and Abadar, and the reserves of these mines have been estimated, such as 0.224 Mt and a grade of 2.147% in Miduk and 1.825 Mt and a grade of 1.06% in Abadar (**Taghipour et al., 2008**). The porphyry copper indices and mines of the study area are presented in **Table 1** and **Figure 4.**

3. Conceptual model for Porphyry Cu-Au Deposits

Porphyry copper deposits in Iran are consistent with Tertiary volcano-plutonic belts and are located within the Tethys belt (**Waterman & Hamilton, 1975**). In Iran, calk-alkaline volcano-plutonic rocks in the Urmia-Dokhtar magmatic arc have a high potential for exploration of Cu±Mo±Au deposits, so many of the most important porphyry copper deposits in Iran are located from the northwest to the southeast of Urmia-Dokhtar (**Shahabpour, 1999**). In terms of tectonic setting, a significant part of porphyry copper deposits are formed at the margins of convergent plates (active continental margins and arc islands). Porphyry copper systems are prominently distributed in subduction zones associated with continents and island arcs. Subduction is a characteristic feature of these regions; however, other metallogenic factors also control the formation of these deposits (**Sillitoe, 1994**). It has been shown that the formation of porphyry copper deposits is not only controlled by hydrothermal and magmatic processes, but also by regional tectonics at the time of the formation of these deposits (**Sillitoe, 1994; Richards et al., 2001**).

Exploration of porphyry deposits is mainly possible with the help of geological, geochemical, geophysical, and remote sensing studies, and their detailed study will significantly contribute to the exploration of porphyry copper deposits.

Geochemical studies, particularly the geochemistry of stream sediments, play a significant role in identifying hidden reserves. It is primarily a good guide in determining the location of porphyry systems. Additionally, multivariate methods, such as principal component analysis, can be employed to more effectively identify the impact of porphyry systems (**Nathan et al., 2021**).

Geophysical methods help to explore and characterize porphyry copper deposits at all scales. At the regional scale, the airborne magnetometer method provides insights into the large-scale crustal structure and magmatic setting of mineralizing zones. Fault zones, sedimentary basins, and masses can be mapped and characterized using airborne magnetic data.

Remote sensing is another important tool for regional-scale exploration of porphyry copper deposits. Argillaceous, phyllic, and iron oxide alteration have distinct spectral absorption features that can be mapped using multispectral and hyperspectral remote sensing data (**Mars, 2006**).

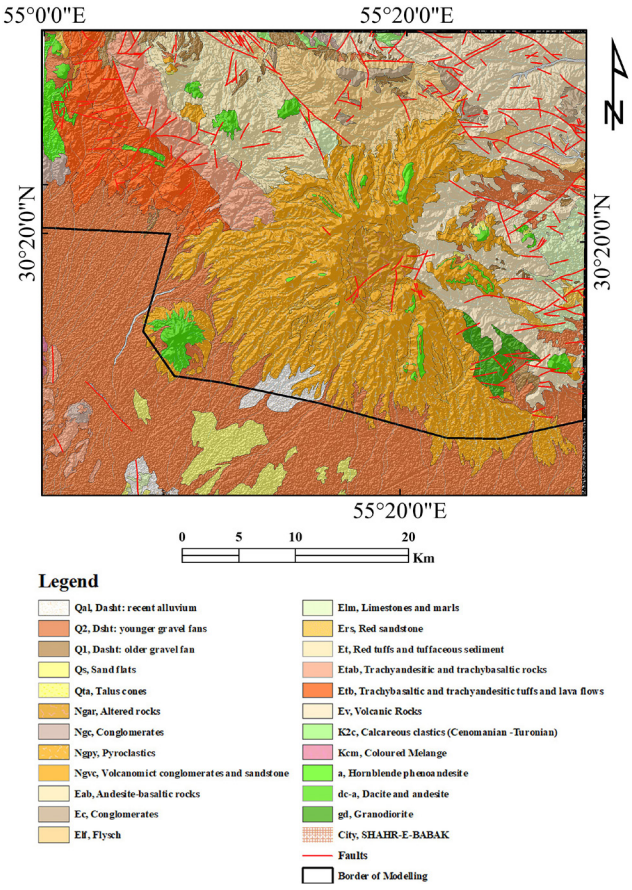


Figure 3. Geology map of the Shahr-e-Babak study area.

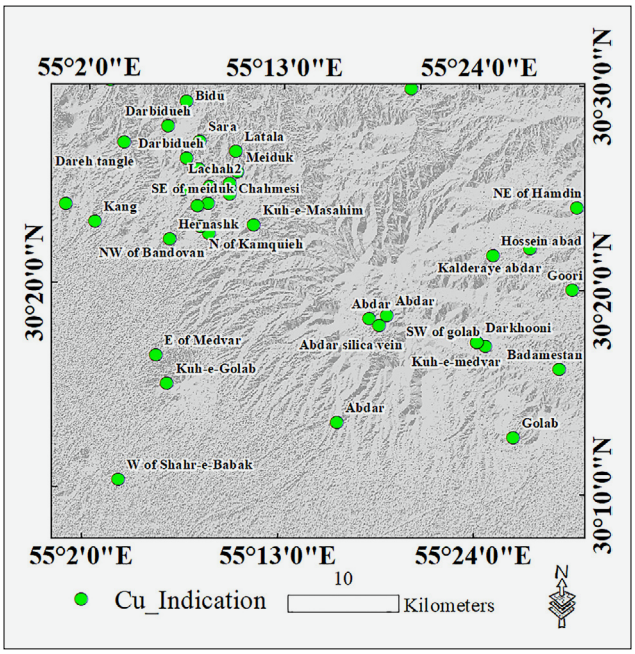


Figure 4. Location of Cu indication on digital elevation model of the Shahr-e-Babak study area.

Fractures and vein systems, as well as shear, are inevitable consequences of porphyry magmatism. Trans-compressive tectonics are characterized by strike-slip faults with significant reverse motion in highly compressive environments. Stress relief is accompanied by the

Table 1. Important Cu indication in the Shahr-e-Babak study area

Name	X	Y	Name	X	Y
Bidu	55.125	30.483	South of Miduk	55.137	30.398
Kuh-e-Masahim	55.190	30.383	Hossein abad	55.415	30.361
Miduk	55.174	30.426	SW of golab	55.409	30.287
Sara	55.138	30.451	Darkhooni	55.401	30.290
E of Medvar	55.100	30.276	Golab	55.436	30.213
Kahatookara	55.013	30.398	Kuh-e-medvar	55.401	30.290
W of Shahr-e-Babak	55.067	30.174	NE of Hamdin	55.493	30.401
Kang	55.041	30.384	Goori	55.490	30.334
Dareh tangle	55.067	30.449	Badamestan	55.479	30.269
S of Miduk silica vein	55.167	30.413	Abdar	55.300	30.308
Kuh-e-Golab	55.111	30.253	Chahmesi	55.167	30.408
Hernashk	55.111	30.371	Abdar	55.271	30.223
Darbidueh	55.126	30.437	Lachah2	55.167	30.417
Darbidueh	55.108	30.463	Kalderaye abdar	55.450	30.367
E of Miduk station	55.123	30.411	NW of Miduk	55.138	30.428
W of Miduk station	55.148	30.414	Godkalgovari	55.053	30.500
NW of Bandovan	55.148	30.376	Reshkan	55.336	30.496
N of Kamquieh	55.140	30.381	Abdar silica vein	55.309	30.303
SE of Miduk	55.147	30.400	Abdar	55.316	30.311
			Latala	55.172	30.443

emplacement of mineralized porphyry intrusions (**Richards et al., 2001**). The injection of these intrusive masses is accompanied by the injection of mechanical energy and steam from the magma, which leads to fractures that are characteristic of porphyry deposits.

Porphyry copper deposits are mainly formed in the upper crust of the Earth (depth less than 5 to 10 km), on the margins of active convergent, and usually in high-altitude areas or areas that are subject to high rates of uplift.

Building a conceptual model for regional exploration is a key point in quantitative mineral resource prediction. A conceptual model refers to a written representation of a mineral resource model that is used in various methods of mineral potential modelling, and, along with various features of the deposit controller, the effects and integration of data (including assumptions and genesis), deposit models, regional exploration models, and local exploration models are used as a guide for predicting mineral resources. In this study, a conceptual model of porphyry copper has been used for mineral resource exploration.

4. Methods

4.1. MCDM method for mineral potential modelling

4.1.1. MARCOS method

The MARCOS method consists of 7 steps, which were first introduced by **Stević et al. (2020)**. The steps of the Markov method are as follows:

Step 1: Create an initial decision matrix. This decision matrix includes n criteria and m alternatives.

Step 2: Create an initial matrix based on an extended initial matrix. In this step, for creating a decision matrix, the ideal (AI) and anti-ideal (AAI) solution will be defined.

The anti-ideal solution (AAI) is the worst alternative, while the ideal solution (AI) is an alternative with the best characteristic. Depending on the nature of the criteria, AAI and AI are defined by applying **Equations 1** and **2**:

$$AAI = minx_{ij} \quad if\ j\varepsilon\ B\ and \quad maxx_{ij} \quad if \quad j\varepsilon\ C \quad (1)$$

$$AI = maxx_{ij} \quad if\ j\varepsilon\ B\ and \quad minx_{ij} \quad if \quad j\varepsilon C \quad (2)$$

Where B is the utility group of criteria, while C represents a group of cost criteria

Step 3: in the third step the extended initial matrix should be normalized.

Step 4: in this step, the weight matrix should be determined.

Step 5: in this step, the utility degree of the alternative k_i should be calculated. By multiplying the following equation, the utility degree of an alternative related to ideal and anti-ideal is calculated. The s_{aai} and s_{ai} are the elements of the decision matrix.

$$\boldsymbol{k_i^-} = \frac{\boldsymbol{s_i}}{\boldsymbol{s_{aai}}} \quad (3)$$

$$\boldsymbol{k_i^+} = \frac{\boldsymbol{s_i}}{\boldsymbol{s_{ai}}} \quad (4)$$

$\boldsymbol{s_i}$ is the summation of all elements of weighted matrix V, as shown in the following equation:

$$\boldsymbol{s_i} = \sum_{i=1}^{n} \boldsymbol{v_{ij}} \quad (5)$$

Step 6: in this step determination of the utility function of alternative $\boldsymbol{f(k_i)}$ should be calculated. The utility function is the compromise of the observed alternative about the ideal and anti-ideal solution. The utility function of alternatives can be calculated from the following equation:

$$f(k_i) = \frac{k_i^+ + k_i^-}{1 + \frac{1 - f(k_i^+)}{f(k_i^+)} + \frac{1 - f(k_i^-)}{f(k_i^-)}} \quad (6)$$

Where $\boldsymbol{f(k_i^-)}$ is the beneficial function related to the anti-ideal solution and $\boldsymbol{f(k_i^+)}$ is the beneficial function related to the ideal solution.

Beneficial functions related to the ideal and anti-ideal solutions can be calculated from the following equation:

$$\boldsymbol{f(k_i^-)} = \frac{\boldsymbol{k_i^+}}{\boldsymbol{k_i^+ + k_i^-}} \quad (7)$$

$$\boldsymbol{f(k_i^+)} = \frac{\boldsymbol{k_i^-}}{\boldsymbol{k_i^+ + k_i^-}} \quad (8)$$

Step 7: in the final step the ranking of alternatives is distinguished. Ranking of alternatives is based on beneficial function.

After calculating the seven steps that were mentioned the MARCOS model was generated.

4.1.2. MOORA

The MOORA method is widely regarded as valuable for improving the best alternatives and determining the most viable substitute among a set of options in multi-criteria decision-making (**Brauers & Zavadskas, 2006; Jahantigh & Ramazi, 2024**).

To achieve this objective, the subsequent measures need to be implemented:

- Step 1: The process includes developing and producing a decision matrix
- Step 2: The process includes normalizing the decision matrix.
- Step 3: Determination of the vector of weights for criteria with the AHP method.
- Step 3: The process involves enhancing various qualities by incorporating standardized achieve-

ment when maximizing (positive qualities) and subtracting when minimizing (negative qualities).

- Step 4: To predict a specific event accurately, it is important to consider that certain attributes hold more significance.

4.2. Prediction-Area (P-A) plot (Data-driven method)

Using the P-A model and determining the prediction rate according to the intersection point can determine the order and relative importance of the evidence maps as criteria related to the type of mineralization under investigation. Furthermore, using values on both the right and left axes of this graph can be used to weight the evidence layers as a data-driven method. Since the main objective of the present study is to obtain a potential map for identifying porphyry copper mineralization, obtaining quantitative weights for each layer is required. We can obtain a normalized density quantity by calculating the ratio of the prediction rate to the corresponding occupied area. The following equations explain the use of the P-A model (**Yousefi & Carranza, 2015**):

$$N_d = \frac{P_r}{Q_a} \tag{9}$$

The N_d normalized density, P_r is the predicted rate and Q_a is the area occupied by mineralization, which is extracted from the intersection point of the P-A model. Normal density is used to calculate the weight of each map according to the following formula:

$$W_E = \ln N_d \tag{10}$$

W_E is the final weight of each exploratory evidential layer calculated using the P-A model and the intersection point of its graph.

Data-driven models are based on the spatial relationship between the exploration witness layers and the mineralization points. The factors affecting mineralization are very complex and may be outside the view and knowledge of geoscientists, causing errors in the production of the mineral potential model. Data-driven methods address this deficiency and improve the mineral potential model produced.

4.3. Analytic Hierarchy Process (AHP) (knowledge driven method)

Saaty (1977) first introduced the analytical hierarchy process (AHP), widely recognized as one of the most popular MCDM techniques. Among the advantages of this method are: measuring the consistency of decision-makers' judgments, creating pairwise comparisons in choosing the optimal solution and option, being able to consider criteria and sub-criteria in evaluating options, and creating the ability to achieve the best option through pairwise comparisons. The Analytic Hierarchy Process is a method that aids in decision-making. It emphasizes the importance of a decision-maker's intuitive judgments as well as the consistency of comparing alternative options in the decision-making process. Since a decision-maker bases his judgments on knowledge and experience, and therefore makes decisions based on them, the AHP approach is consistent with the behaviour of a decision-maker. The strength of this approach is that it systematically organizes tangible and intangible factors and provides a structured but relatively simple solution to decision-making problems.

Furthermore, by breaking down a significant logical problem and then descending in gradual steps to smaller and smaller ones, one can connect the small to the significant through simple pairwise comparison judgments. Rosaria and **Camanho (2015)** believe that AHP is a measurement tool through pairwise comparisons. This method relies on expert judgments to derive priority scales. The hierarchical decision tree of Shahr-e-Babak is shown in **Figure 5**, where the main tree creations are considered, including geochemistry signature, airborne magnetic anomaly, geology, and remote sensing. These sub-criteria consist of Cu, principal component analysis (PC3), reduction to pole (RTP), intrusive rocks, faults, argillaceous alteration, phyllic alteration, and iron oxide alteration. These criteria were used to make ready evidential layers related to Cu porphyry mineralization.

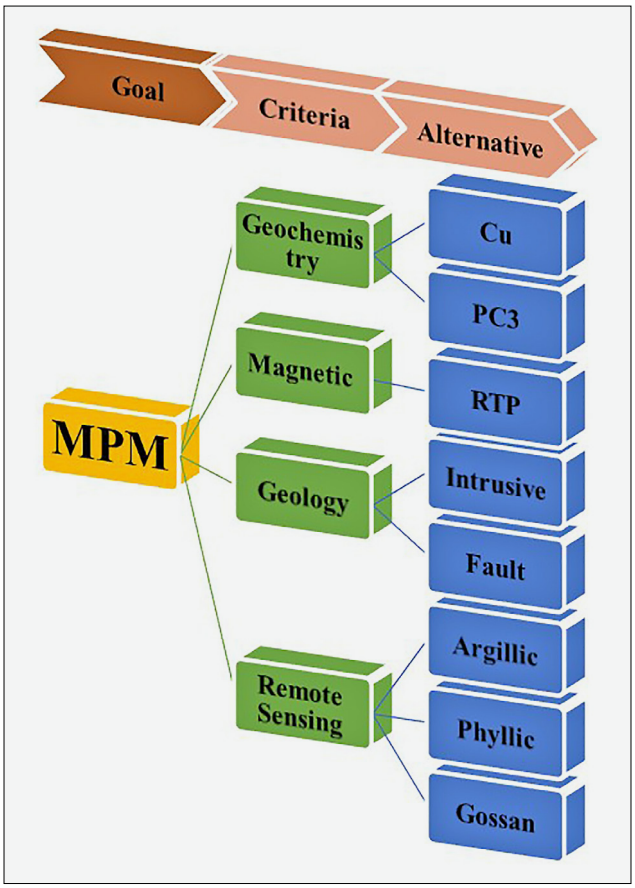


Figure 5. Hierarchy is applied for prospective modelling and weighting exploratory evidential layers

4.4. Preparing exploratory evidential layers

In modelling the mineral potential for a type of prospecting deposit, all the characteristics of the mineral type being explored are first identified and collected. At this stage, a regional conceptual model can be derived based on general studies of mineral-type reserves that exist around the world, because a good conceptual model is the best tool for identifying exploration criteria and extracting predictive patterns for the mineral of interest. To model the mineral potential of a given type of prospecting deposit in a specific region, the exploration dataset used is based on the conceptual model of that type of deposit. Then, based on the data, witness maps are generated and weighted, and finally combined to identify target areas.

To build a conceptual regional model of porphyry copper deposits in the Shahr-e-Babak, geological, geochemical, and remote sensing exploration criteria were used. Five exploration witness maps (layers), including host rock, fault density, geochemical trace, iron oxide alteration, and argillaceous, phyllic, and propylitic alteration, were generated to search for copper mineralization in the region using the continuous fuzzy method. Since these values are derived from different spatial data sets, their minimum and maximum values differ, and their spatial extents are also distinct. In this study, the values of different exploratory evidence datasets are transformed into a similar space by using the following logistic function as a nonlinear transformation (**Yousefi et al., 2021**):

$$F_E = \frac{1}{1 + e^{-s(x-i)}} \tag{11}$$

Where x is the actual value of the exploratory evidential layers and F_E is the value of the evidential layers after the logistical transformation. The s and i are the slope and inflection points of this transformation. The exploratory evidential layers are shown in **Figure 5** and the fuzzy exploratory evidential layers are shown in **Figure 7**.

Porphyry copper deposits in the Urmia-Dokhtar belt are genetically and spatially related to subvolcanic units. This relationship is because the margins of the subvolcanic units are fractured and crushed, which allows for the circulation and movement of hydrothermal fluids and, consequently, heat exchange. For this reason, the probability of porphyry copper deposits forming in areas close to and adjacent to the subvolcanic units is higher.

To produce exploratory evidential layers of the subvolcanic units in the study area, the Euclidean distance of the subvolcanic units was utilized (see **Figure 6a**). Then, to create exploratory evidential layers, **Equation 9** was employed to transform the evidential layer into the logistic space (weight space) (**Figure 7a**).

Structural studies show the important role of rock permeability in the formation of mineral deposits. In this regard, the presence of structural faulting is also generally considered an important criterion for the presence of some deposits. Faults facilitate the passage of magma and the circulation of hydrothermal fluids, and it is generally accepted that faults and fractured areas act as the primary channels for the passage of hydrothermal fluids. Faults and fractures play a role in the formation of many mineral deposits. Therefore, the presence of such geological features indicates an increase in the structural permeability of rocks in the subsurface. Therefore, areas with high fault density and fractures can transport and circulate mineralized solutions. In this paper, fault density has been used as a structural control layer for the formation of porphyry copper deposits in the study area. To produce the fault density map, the total length of the faults in each pixel of the study area, i.e. the fault density, was calculated (see **Figure 6b**). Then, since the fault density values do not have a specific range and are outside the logistic space, **Equation 9** was applied to the fault density dataset (see **Figure 7b**).

In geology and mineral exploration, airborne geophysical data are used as one of the most important sources of information to study geological features and subsurface structures, such as faults, intrusive masses, and hidden plutonic masses. The use of airborne magnetic data in obtaining magnetic information layers, structures, and edges is considered a guide for porphyry copper mineralization (**Holden et al., 2008**). The airborne magnetic data acquired by the Atomic Energy Organization of Iran (AEOI) during 1977 and 1978 were used to prepare the total magnetic intensity map of the study area. These data were obtained with a flight line spacing of about 1000 m and an altitude of about 120 m. The International Geomagnetic Reference Field (IGRF) filter was used to remove regional anomalies from the aeromagnetic map. Then, the RTP filter was performed on the total magnetic intensity map, and the anomalies were extracted from the resulting map. The fractal method was used to extract high magnetic anomalies. Then the Euclidean distance was calculated for high magnetic anomalies (see **Figure 6c**). Also, lineament structures were extracted with the tilt angle method (**Salem et al., 2007**). Magnetic lineaments were combined with geological faults, and the density map resulting from this combination was calculated. The Euclidean distance of high magnetic anomalies was transformed to the logistic space with **Equation 9** (see **Figure 7c**).

Geochemical surveys can be used at various stages of mineral resource exploration, from regional to local. The basis of geochemical exploration is the search and detection of areas where the concentration of one or more specific elements is higher than usual. In other words, with the help of geochemical exploration, areas with such anomalies are identified. The main problem in identifying anomalies in geochemical surveys of mineral exploration is the determination and inference of multi-element traces indicative of the mineralization sought. In

Table 2. Principal component analysis for multi-element geochemical data, where component 3 corresponds to Cu mineralization.

	Component		
	1	2	3
Ni	.883	-.047	.136
Ba	-.016	.818	-.056
Pb	.153	.468	.695
B	.714	-.080	.258
Co	.842	-.065	-.080
Sb	-.110	.685	.098
Cr	.615	.557	.157
Cu	.521	.295	.515
Zn	.059	-.150	.808

Table 3: Total Variance Explained

Component	Total % of Variance	Cumulative
1	27.061	27.061
2	20.258	47.319
3	17.837	65.156

this regard, principal component analysis, as one of the multivariate analysis methods, has been widely used to interpret geochemical data of stream sediments. Principal component analysis can reveal multi-element compositions from the data set that can be used as geochemical traces indicative of the mineralization type sought. Cu geochemical signature (stream sediment) has been used as an exploratory evidential layer to create a porphyry prospectivity model (see **Figure 7d**).

Also, Principal Component Analysis (PCA) method has been used for multivariate analysis and dimensionality reduction of geochemical data.. **Table 2** shows the PCA of stream sediment geochemistry data for the study area. PC3, which shows higher values of Cu, Pb, and Zn, was determined to be associated with porphyry mineralization. A geochemical map with PCA scores (PC3) was also created as another control layer. The multivariate geochemical map (PC3) is shown in **Figure 6e**. **Table 3** shows the PCs variances and Total variances from the principal component analysis of the geochemical data.

Geochemical signature layers, including the Cu signature map and geochemical map with PCA scores (PC3), were transformed to the logistic space with **Equation 9** (see **Figure 6d** and **Figure 7e**).

One of the key ideas of remote sensing techniques in exploration geology is to display rocks, minerals, and structures associated with a specific mineral type, for which several logical reasons have been presented. Therefore, given that minerals do not always emerge at the Earth's surface and due to the slight expansion of the mineralization area, remote sensing can be helpful in most cases in the search for and exploration of mineral deposits, as well as in reducing the study area. Identification and detection of alterations by remote sensing are also efficient tools in the exploration of mineral resources, and their application in deposits with broad and prominent halos has been efficient. One of the important characteristics of hydrothermal deposits is the formation of alteration halos. Iron oxide (gossan) is evidence that reinforces the possibility of the presence of porphyry copper deposits, which may extend several kilometers from the center of mineralization.

A band ratio of 3:1 was applied to detect the iron oxide alteration zone in the study area. Band ratios 7/6 and (5+7)/6 were applied for extracting argillaceous and phyllic alteration zones, respectively. The Euclidean distance maps from argillaceous, phyllic, and iron oxide alteration were created (see **Figure 6f, 6g, 6h**). The Euclidean distance maps of alteration exploratory evidential layers have been transformed to the logistic space with **Equation 9** (see **Figure 7f, Figure 7g,** and **Figure 7h**).

5. Results and Discussion

One of the basic steps in regional exploration and mineral potential assessment is to identify the exploratory evidential layers to limit the exploration area and determine the regional anomaly. Next, the effective weight of each layer is determined, and then these weights are applied to the relevant layers. Selecting appropriate weights is done in two ways. In the first method, which is the knowledge-based method, the weights of the layers are determined based on expert opinion. The second method, which is the data-driven method, selects weights based on the mineralization points in the area. In this way, the relationship between exploration layers and mineralization points is determined based on data-driven methods. Finally, the weights obtained from these methods are applied to the relevant exploratory evidential layers. In this article, the AHP, MOORA, and MARCOS methods have been used to determine mineral potential using a knowledge-based method. The relevant weights have been determined based on the AHP method. Accordingly, the pairwise comparison is shown in **Table 4**, and the weights assigned to the exploratory control layers using the AHP method are shown in **Table 5**. According to **Table 5**, the most effective layers are the univariate geochemical layer, the multivariate geochemical layer, and the subvolcanic units. The weight of all these layers is 0.211. The following effective layers are phyllic, argillaceous, and iron oxide alterations. The weights of these layers are 0.128, 0.078, and 0.078, respectively. Argillaceous and iron oxide alteration have the same weights.

The fault and geophysical layers are the least influential layers with weights of 0.049 and 0.033.

In the data-driven method, the mineralization points in the area are used to obtain the weight of the layers. Thus, by drawing a curve, the relationship between the evidential layers and the mineralization points is expressed quantitatively, and this value is considered as the

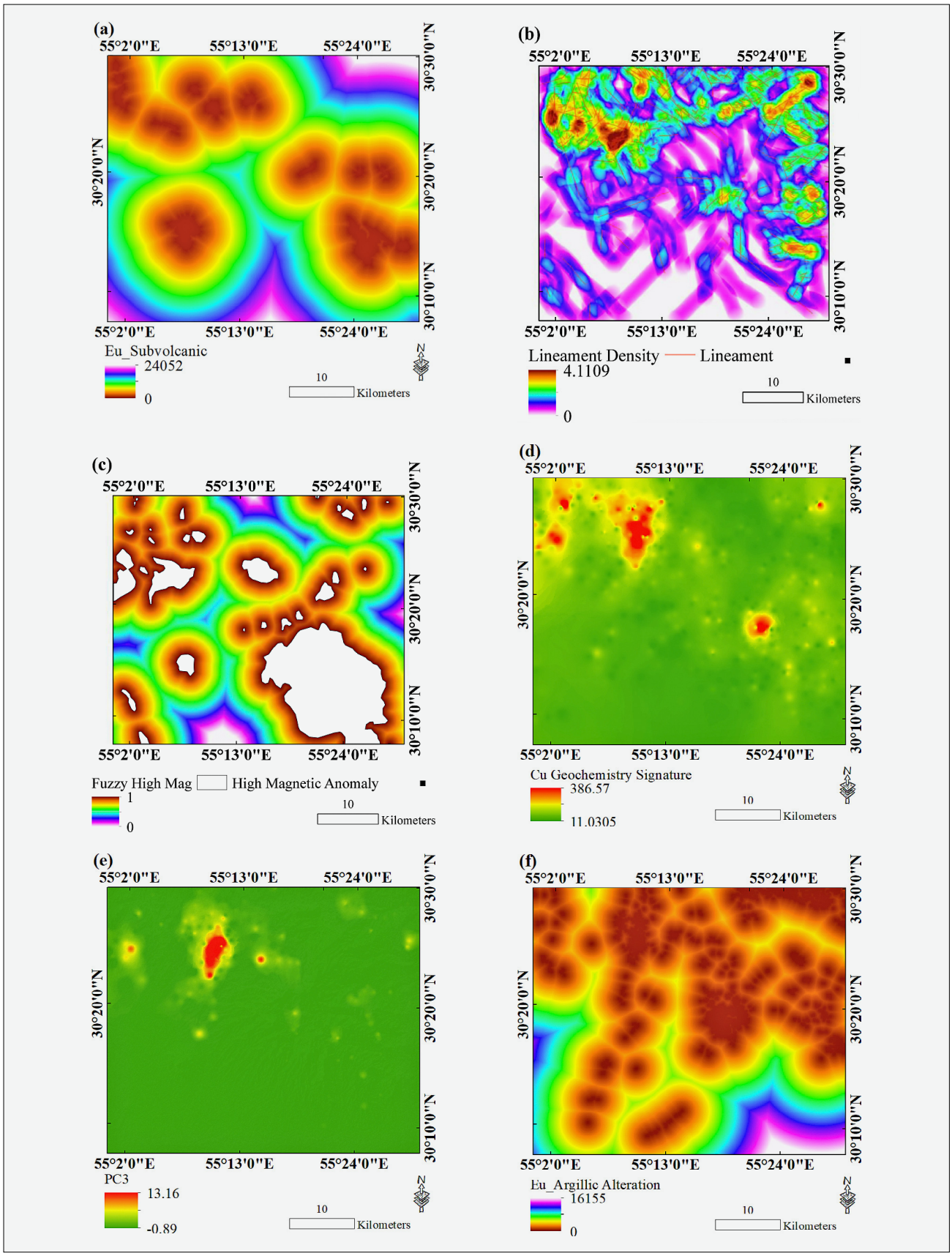


Figure 6. Evidential layer input for MPM model: (a) Euclidean distance from subvolcanic units (b) Lineament density (c) Euclidean distance from aeromagnetic anomalies (d) Cu signature (e) Multivariate geochemistry signature (PC_3) (f) Euclidean distance from argillic alteration (g) Euclidean distance from iron oxide alteration (h) Euclidean distance from phyllic alteration.

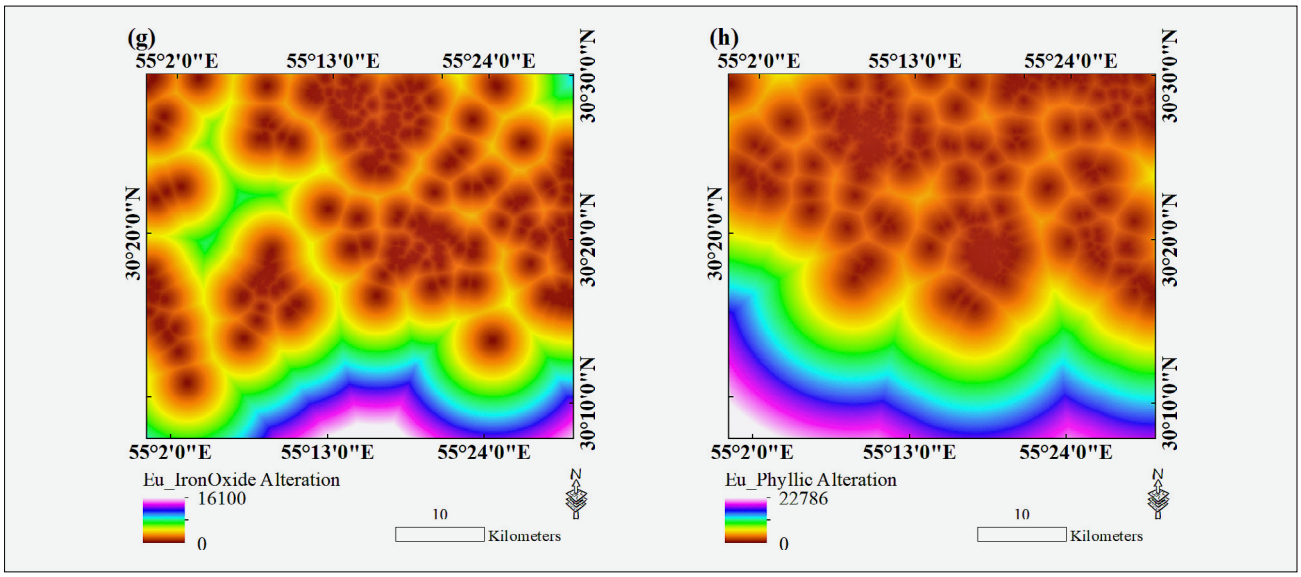


Figure 6. Continued

Table 4. Pairwise comparison matrix for exploratory control layers using the AHP method

Cu	PC3	Lithology	Phyllic	Iron Oxide	Argillic	Fault	Geophysics
1	1	1	2	3	3	4	5
1	1	1	2	3	3	4	5
1	1	1	2	3	3	4	5
0.5	0.5	0.5	1	2	2	3	4
0.33	0.33	0.33	0.5	1	1	2	3
0.33	0.33	0.33	0.5	1	1	2	3
0.25	0.25	0.25	0.33	0.5	0.5	1	2
0.2	0.2	0.2	0.25	0.33	0.33	0.5	1

Table 5. Weights calculated for exploratory evidential layers using the AHP method

Criteria	Cu	PC3	Lithology	Phyllic	Iron Oxide	Argillic	Fault	Geophysics	Weights
Cu	0.217	0.217	0.217	0.233	0.217	0.217	0.195	0.179	0.211
PC3	0.217	0.217	0.217	0.233	0.217	0.217	0.195	0.179	0.211
Intrusive	0.217	0.217	0.217	0.233	0.217	0.217	0.195	0.179	0.211
Phyllic	0.108	0.108	0.108	0.117	0.145	0.145	0.146	0.143	0.128
Iron Oxide	0.072	0.072	0.072	0.058	0.072	0.072	0.098	0.107	0.078
Argillic	0.072	0.072	0.072	0.058	0.072	0.072	0.098	0.107	0.078
Fault	0.054	0.054	0.054	0.038	0.036	0.036	0.049	0.071	0.049
Geophysics	0.043	0.043	0.043	0.029	0.024	0.024	0.024	0.036	0.033

effective weight of the evidential layer. The P-A plot method was used to draw a curve and quantify the relationship between the exploratory evidential layers and mineralization points. Based on this, the P-A plot has been drawn for eight layers of exploratory evidence (see **Figure 8**), and the normalized density (Nd) was presented for the evidential layers in **Table 6**. According to the P-A plot method, the most effective layers are the subvolcanic unit, the univariate geochemical layer, the phyllic alteration layer, the faults, and the PC3 layer, respectively. The weights of these layers are 0.84, 0.75, 0.7, 0.53, and 0.44. The least influential layers are the argillaceous alteration, iron oxide alteration, and the aeromagnetic layer. The weights of these layers are calculated to be 0.4, 0.35, and 0.23, respectively.

According to **Figure 1**, mineral potential modelling using the two methods, FAHP MOORA and FAHP MARCOS, includes four steps: (1) Selection of criteria, (2) Fuzzification of exploratory evidential layers, (3) assigning weights obtained from the AHP method on exploratory evidential layers, and (4) Use of the MOORA and MARCOS methods to combine layers and generate

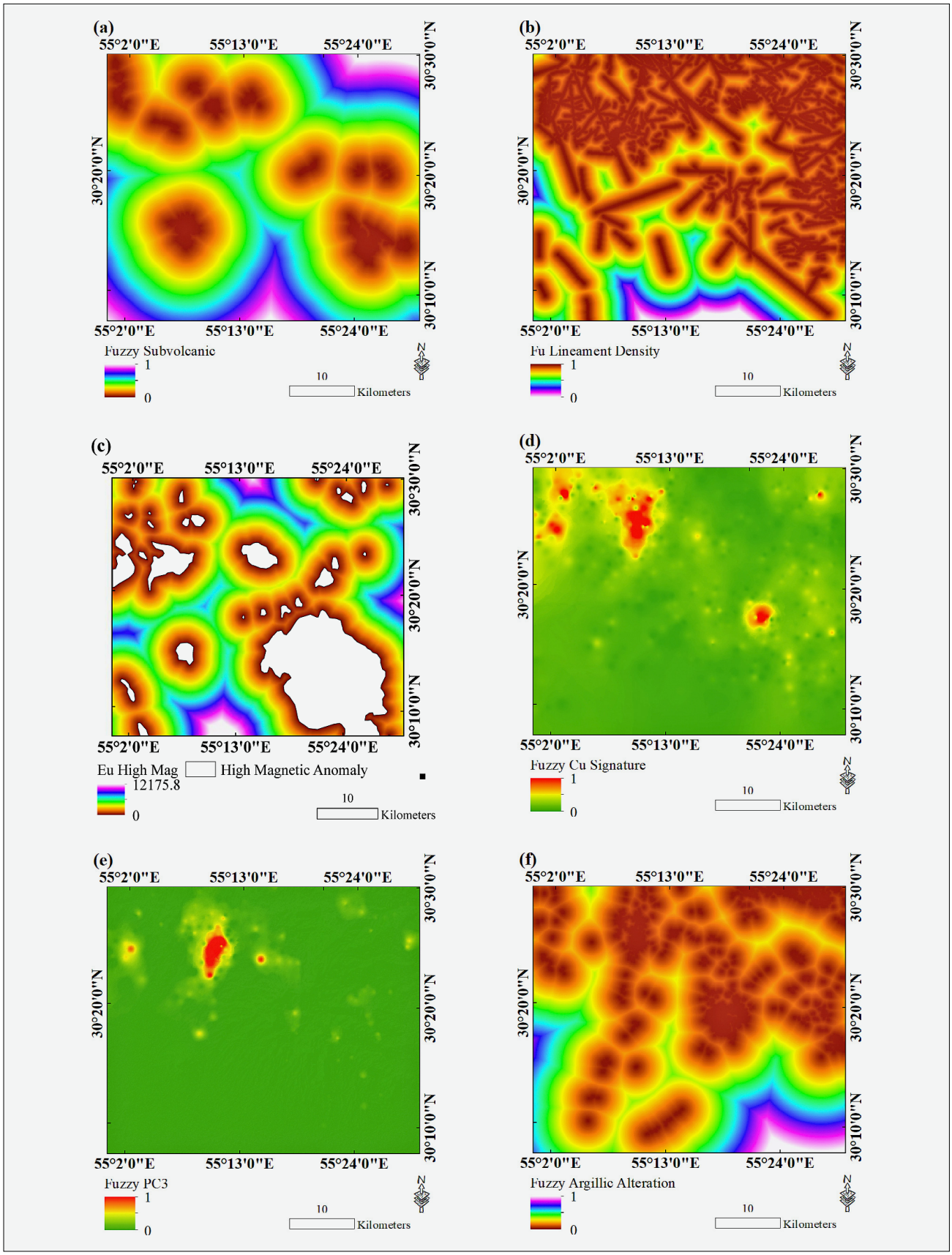


Figure 7. Fuzzified of evidential layer input for MPM model: (a) Euclidean distance of subvolcanic units (b) Lineament density (c) Euclidean distance of aeromagnetic anomalies (d) Cu signature (e) Multivariate geochemistry signature (f) Euclidean distance from argillic alteration (g) Euclidean distance from iron oxide alteration (h) Euclidean distance from phyllic alteration.

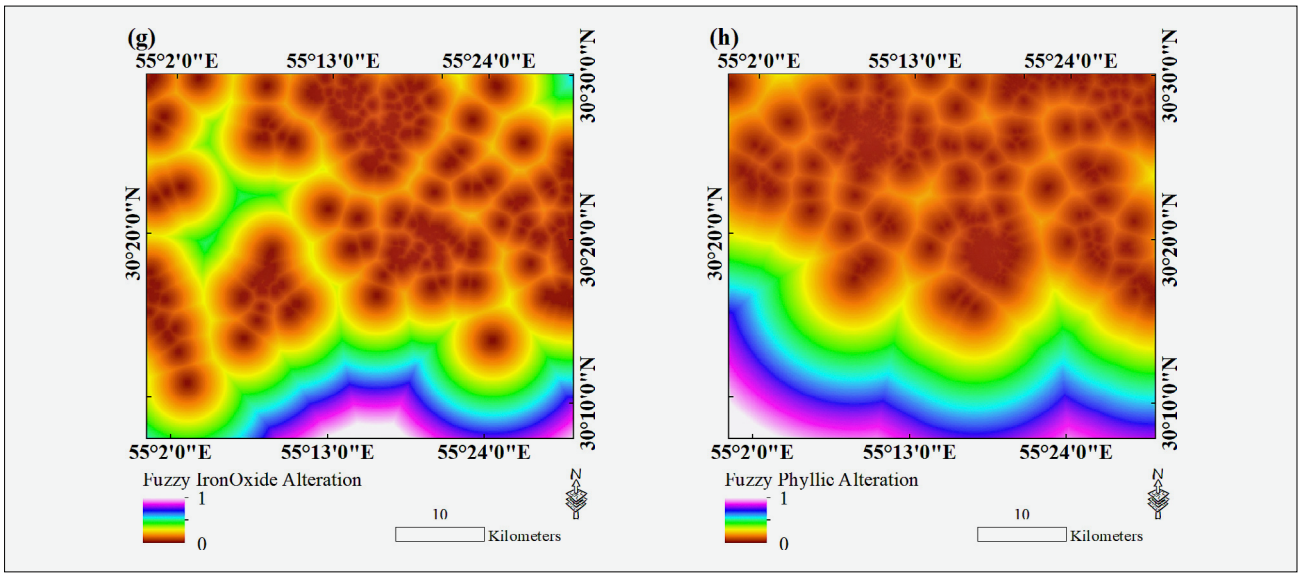


Figure 7. Continued

a mineral potential model. For the aforementioned functions, after selecting the layers, fuzzification, and assigning the weights obtained using the AHP method (see **Table 2**), a decision matrix with eight layers of exploratory evidence and 196,320 pixels is constructed. MATLAB software was used to write the code for the MOORA and MARCOS methods, and four porphyry copper mineral potential models were generated (see **Figure 9**).

In this study, two mineral potential models were generated using the MOORA and MARCOS methods. To generate the mineral potential model using data-driven methods, the weight of the exploratory evidential layers is first calculated using the porphyry copper mineralization indices. For this purpose, the P-A diagram was first drawn for eight exploratory evidential layers, using the Nd weights initially. Then, the normalized weights were calculated based on the normalized density. A decision matrix was formed for the above calculated weights. The columns of this matrix are the exploratory evidential layers derived from geological, geochemical, remote sensing, and airborne geophysical data. The rows of this matrix represent the pixels that comprise the raster maps. Finally, programming in the MATLAB environment was used to generate a porphyry copper mineral potential model using the above matrix and based on the data-driven methods of MOORA and MARCOS (see **Figure 9**).

The data-driven P-A plot method was used to evaluate and compare models produced by data-driven and knowledge-driven methods. For this purpose, 37 copper mineralization points in the area have been used. Jenks' method was used to discretize mineral potential maps. With the application of this method, the exploratory evidential layers were divided into ten parts. Based on this, the P-A plot diagrams for mineral potential models were drawn. Prediction-Area plots for the four mineral potential models are shown in **Figure 10**. In these plots, the intersection points of the prediction-area plots are specified. The intersection points for the knowledge-based MOORA, data-based MOORA, knowledge-based MARCOS, and data-based MARCOS models are 72%, 74%, 73%, and 75%, respectively. Accordingly, the normalized density values for the aforementioned models are 2.57, 2.84, 2.7, and 3, respectively. Also, the objective weights of these models are 0.94, 1.04, 0.99, and 1.09, respectively (see **Table 7**). Accordingly, the high-potential areas identified in the four models can be applied in future exploration programs, given that they have a normalized density of approximately one or greater than one.

The main characteristic curve was used to evaluate the performance of the four models. The curve obtained from the four methods shows the high accuracy of the MARCOS and MOORA methods in modelling the potential of porphyry copper in the study area. The areas under the curves of the four models, including AHP-MOORA, data-driven MOORA, AHP MARCOS, and data-driven MARCOS, are 0.932, 0.938, 0.933, and 0.939, respectively (see **Figure 11**). These values show the high accuracy of these four methods in modelling. Given that the area under the curve in the Data-Driven MARCOS method is higher than the other three methods, it indicates that the Data-Driven method has produced the potential of porphyry copper in the study area with more accuracy.

As explained in the previous section, the mineral potential model was generated using four methods: MOORA knowledge-based, MOORA data-based, MARCOS knowledge-based, and MARCOS data-based. In knowledge-based modelling methods, the AHP method was implemented to weight the layers. The pairwise comparison matrix and the calculated weights are shown in **Tables 1** and **2**, respectively. In the AHP method, the highest weights are attributed to the univariate and mul-

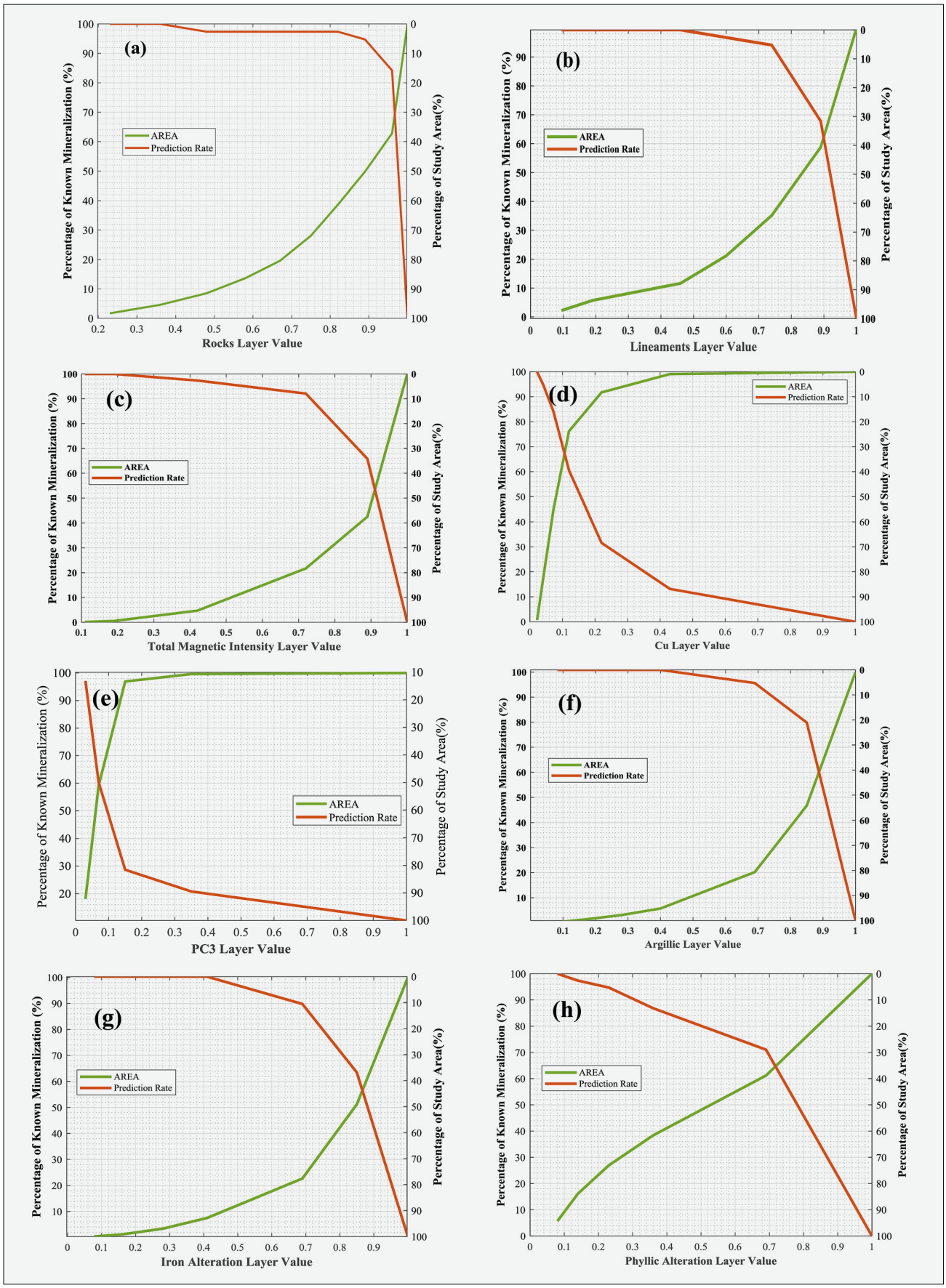


Figure 8. Prediction- area plot (P-A) for (a) subvolcanic units (b) Lineament density (c) aeromagnetic anomalies (d) Cu signature (e) Multivariate geochemistry signature (f) argillic alteration (g) iron oxide alteration (h) phyllic alteration.

Table 6. Calculated weights using P-A plots

Map	Prediction rate (P_r)%	Occupied area (O_a)%	Normalized Density (N_d)	Weight (W_e)
Lithology	70	30	2.33	0.84
Lineaments	63	37	1.7	0.53
Geophysics	56	44	1.27	0.23
Cu Signature	68	32	2.12	0.75
PC3	61	39	1.56	0.44
Argillic alteration	60	40	1.5	0.4
Iron-oxide alteration	59	41	1.43	0.35
Phyllic alteration	67	33	2.03	0.7

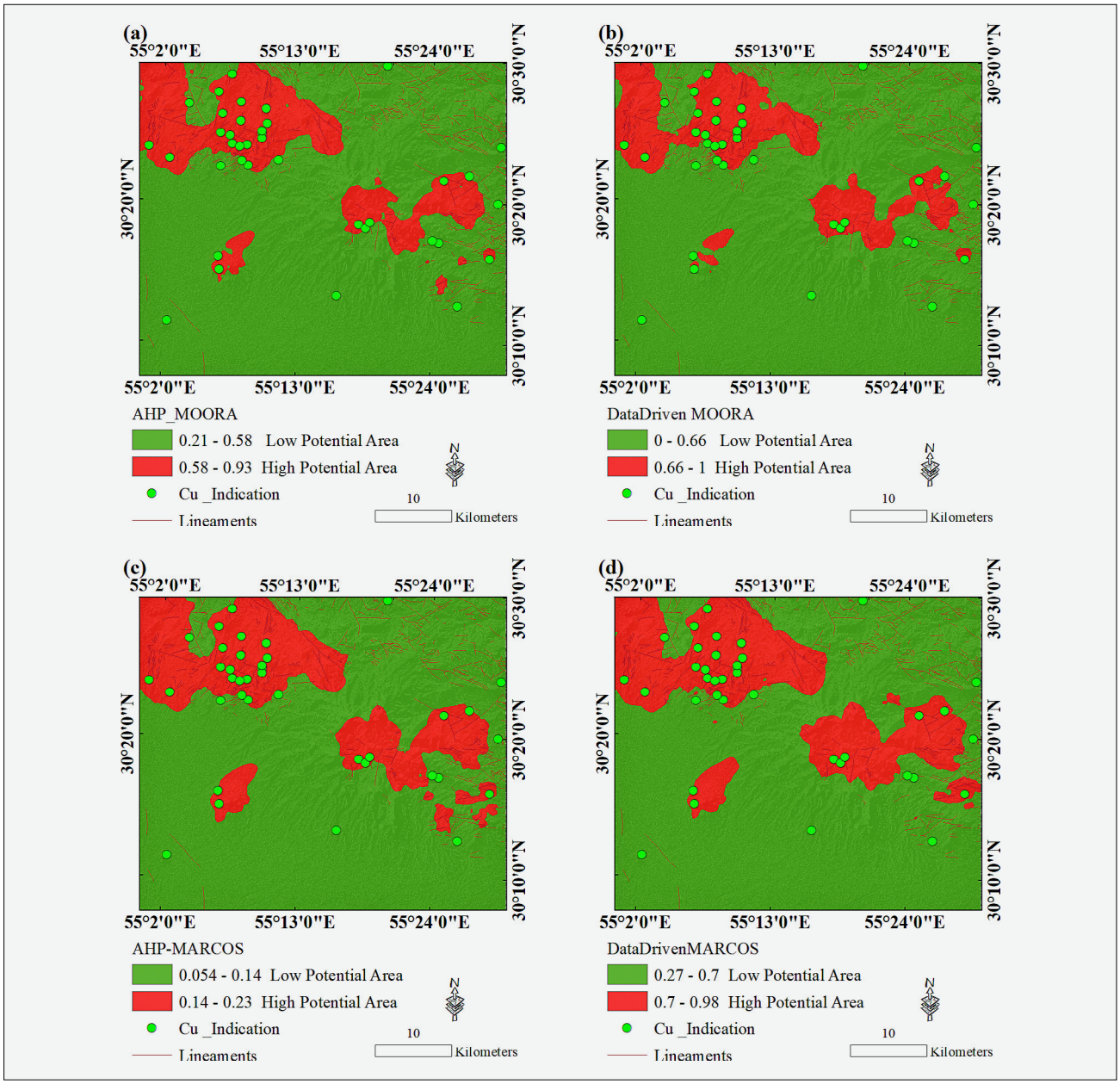


Figure 9. Mineral prospectivity model (a) MARCOS method (b) MOORA method (c) AHP MARCOS (d) Data-Driven MARCOS.

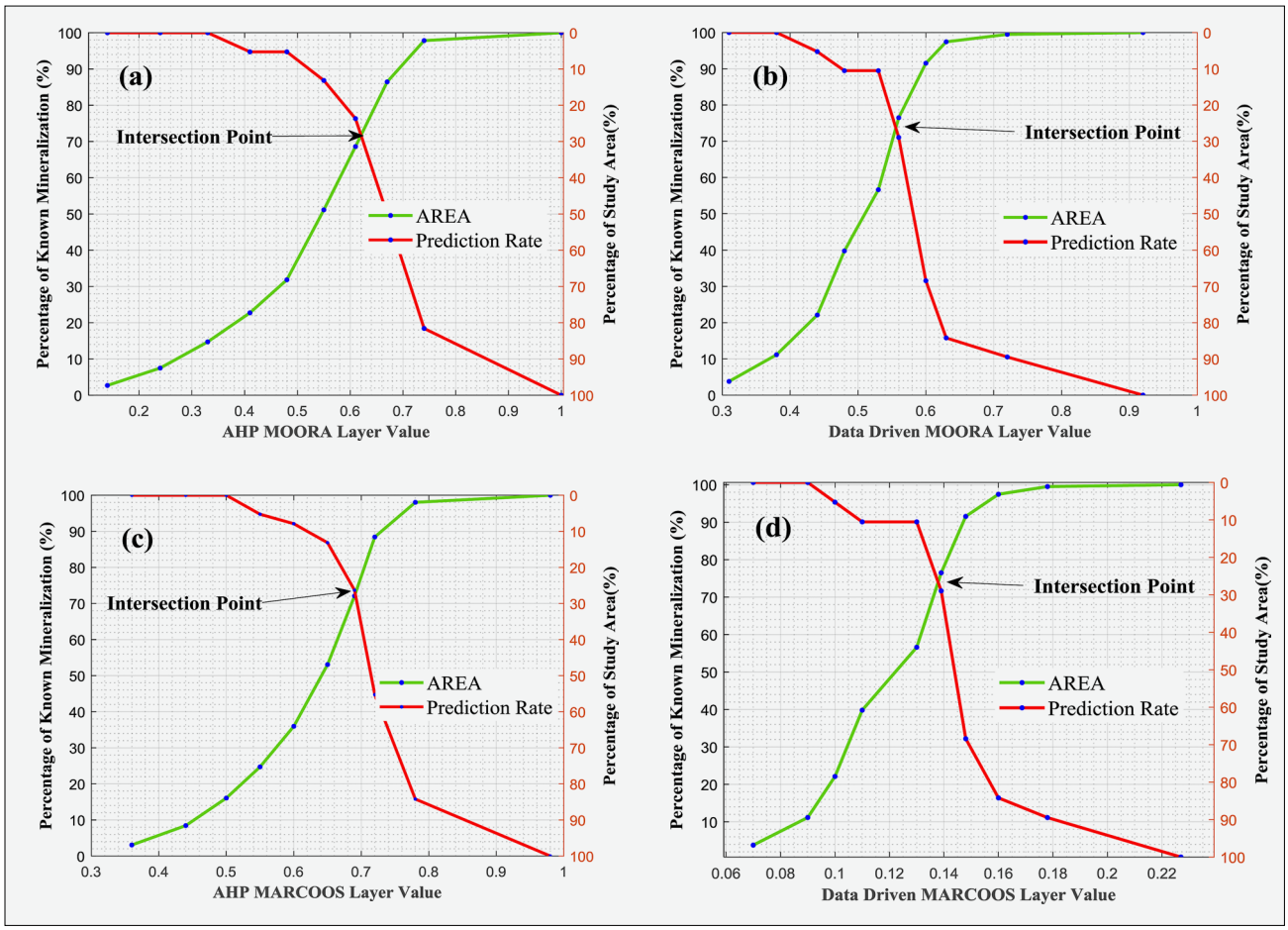


Figure 10. Prediction- area plot (P-A) for evaluating mineral prospectivity models: (a) AHP MOORA (b) Data driven MOORA (c) AHP MARCOS (d) Data driven MARCOS.

Table 7. Calculated weights using P-A plots

Map	Prediction rate (P_r)%	Occupied area (O_a)%	Normalized Density (N_d)	Weight (W_c)
AHP MOORA	72	28	2.57	0.94
Data Driven MOORA	74	26	2.84	1.04
AHP MARCOS	73	27	2.70	0.99
Data Driven MARCOS	75	25	3.00	1.09

tivariate geochemical layers, as well as the subvolcanic intrusive body layer. Visually, acquired models obtained using knowledge-based methods (see **Figure 9**) show a good agreement between the existence of porphyry copper mineralization indices in the area and the areas with high potential (see **Figure 8a** and **c**).

Unlike knowledge-driven methods, data-driven methods apply existing exploratory evidential layers and Cu indices for weighting. The basis of weighting in the data-driven method is the use of P-A plots. The weights obtained from the P-A plot method show that the highest weight is related to the subvolcanic layer. After that, the highest weight is related to the univariate geochemical layer of the copper element. The phyllic alteration, fault layer, multivariate geochemical layer, argillic alteration, iron oxide alteration, and airborne geophysical layer are in the following ranks, respectively (see **Table 3**). The weights obtained from the P-A plot method for the lithology layer, univariate geochemistry, phyllic alteration, fault layer, multivariate geochemistry layer, argillic alteration layer, and airborne geophysics layer are 0.84, 0.75, 0.7, 0.53, 0.44, 0.4, 0.35, and 0.23, respectively (Jenks' discretization method was applied to draw the P-A plot diagram). Then, with the assignment of these weights on the exploratory evidential layers, the MOORA and MARCOS. methods were implemented to generate a mineral potential model (see **Figure 8b** and **d**). By comparing the models obtained from knowledge-based and data-based methods, the highest probability of mineralization potential is in the northwestern part of the study area. Also, a high potential area is observed in the eastern part of the area.

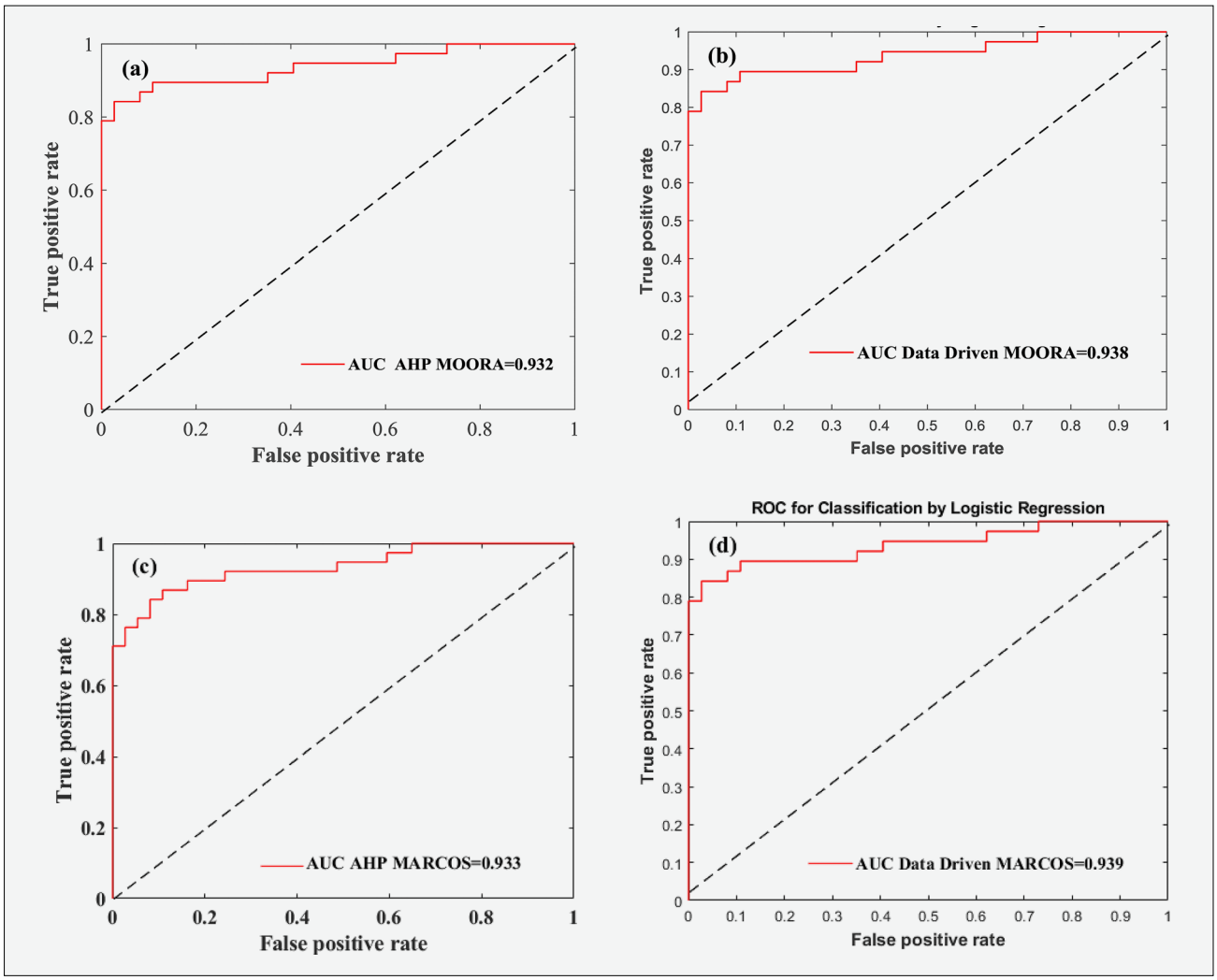


Figure 11. The area under the curve for evaluating mineral prospectivity models
(a) AHP MOORA model (b) Data-driven MOORA (c) AHP MARCOOS (d) Data-Driven MARCOS model.

Unlike knowledge-driven methods, data-driven methods apply existing exploratory evidential layers and Cu indices for weighting. The basis of weighting in the data-driven method is the use of P-A plots. The weights obtained from the P-A plot method show that the highest weight is related to the subvolcanic layer. After that, the highest weight is related to the univariate geochemical layer of the copper element. The phyllic alteration, fault layer, multivariate geochemical layer, argillic alteration, iron oxide alteration, and airborne geophysical layer are in the following ranks, respectively (see **Table 3**). The weights obtained from the P-A plot method for the lithology layer, univariate geochemistry, phyllic alteration, fault layer, multivariate geochemistry layer, argillic alteration layer, and airborne geophysics layer are 0.84, 0.75, 0.7, 0.53, 0.44, 0.4, 0.35, and 0.23, respectively (Jenks' discretization method was applied to draw the P-A plot diagram). Then, with the assignment of these weights on the exploratory evidential layers, the MOORA and MARCOS methods were implemented to generate a mineral potential model (see **Figure 8b** and **d**). By comparing the models obtained from knowledge-based and data-based methods, the highest probability of mineralization potential is in the northwestern part of the study area. Also, a high potential area is observed in the eastern part of the area.

By comparing the models produced using data-driven and knowledge-driven methods, it becomes clear that the models produced by data-driven methods have a stronger correlation with Cu porphyry indices. Also, the data-driven MARCOS method has a greater ability than the other three models in producing a mineral potential model. In the data-driven MARCOS method, 75% of the Cu indices are located in the potential areas while, this value is 74% for the data-driven MOORA method. The prediction rates for the knowledge-driven MOORA and MARCOS methods are 73% and 72%, respectively.

A quantitative comparison between the models generated using the ROC method is performed. Based on the results of this method, it is clear that the performance of the four modelling methods is very similar to each other. However, the model generated by the data-driven MAR-

COS method shows a slightly better performance than the other three methods.

This research, like other research, faces limitations. For example, the preparation of data by the relevant organizations. The reason for this limitation is its high cost. Another limitation is the lack of gold analysis. The presence of gold analysis could lead to better results in generating a mineral potential model.

6. Conclusions

The present study introduces the MARCOS method as a multivariate decision-making approach for producing mineral potential models. Also, in this study, a comparison has been made between models produced using knowledge-based and data-based methods. Another goal of this study is to reduce the uncertainty caused by expert opinions by relying on data-based methods. A quantitative comparison has been made between different models produced using the P-A plot and the ROC methods. Based on this comparison, data-based methods have produced models with higher accuracy, and the MARCOS data-based method has also produced a better model than the other three methods. The prediction rate for the data-driven MARCOS method is 75%, which is the highest prediction rate among the produced models.

7. References

Abedi, M., Norouzi, G.-H., & Bahroudi, A. (2012). Support vector machine for multi-classification of mineral prospectivity areas. Computers & Geosciences, 46, 272–283. https://doi.org/10.1016/j.cageo.2011.12.014

Moon, W. M. (1990). An evidential reasoning structure for integrating geophysical, geological and remote sensing data. Proceedings of IGARSS '93 - IEEE International Geoscience and Remote Sensing Symposium, 1359–1361. https://doi.org/10.1109/IGARSS.1993.322084

Bonham-carter, G. F., & Agterberg, F. P. (1999). Arc-WofE : a GIS tool for statistical integration of mineral exploration datasets. Bulletin of the International Statistical Institute, 52.

Brown, W. M., Gedeon, T. D., Groves, D. I., & Barnes, R. G. (2000). Artificial neural networks: A new method for mineral prospectivity mapping. Australian Journal of Earth Sciences, 47(4), 757–770. https://doi.org/10.1046/j.1440-0952.2000.00807.x

Carranza, E. J. M. (2010). Improved Wildcat Modelling of Mineral Prospectivity. Resource Geology, 60(2), 129–149. https://doi.org/10.1111/j.1751-3928.2010.00121.x

Carranza, E. J. M., & Hale, M. (1997). A catchment basin approach to the analysis of reconnaissance geochemical-geological data from Albay Province, Philippines. Journal of Geochemical Exploration, 60(2), 157–171. https://doi.org/10.1016/S0375-6742(97)00032-0

Feizi, F., Karbalaei-Ramezanali, A. A., & Farhadi, S. (2021). FUCOM-MOORA and FUCOM-MOOSRA: new MCDM-based knowledge-driven procedures for mineral potential mapping in greenfields. SN Applied Sciences, 3(3), 358. https://doi.org/10.1007/s42452-021-04342-9

Jahantigh, M., & Ramazi. H. (2025-a). Knowledge Driven methods for Cu-Au Porphyry Potential Modelling; a case study of the Mokhtaran area, Eastern Iran. Journal of Mining and Environment.

Jahantigh, M., & Ramazi. H. (2025-b). Mineral Prospectivity Modeling with Airborne Geophysics and Geochemistry Data: a Case Study of Shahr-e-Babak Studied Area, Southern Iran. Journal of Mining and Environment.

Jahantigh, M., & Ramazi. H. (2024). Integration of Airborne Geophysics Data with Fuzzy c-means Unsupervised Machine Learning Method to Predict Geological Map, Shahr-e-Babak Study Area, Southern Iran. Journal of Mining and Environments, 273–287.

Karbalaeiramezanali, A., Parsa, M., Lentz, D. R., & Thorne, K. G. (2025). Prospectivity Modeling of Devonian Intrusion-Related W–Mo–Sb–Au Deposits in the Pokiok Plutonic Suite, West-Central New Brunswick, Canada, Using a Monte Carlo-Based Framework. Natural Resources Research, 34(2), 669–702. https://doi.org/10.1007/s11053-024-10437-y

Mami Khalifani, F., Lentz, D., Walker, J., & Khammar, F. (2025). Applying Mineral System Criteria to Develop a Predictive Modelling for Epithermal Gold Mineralization in Northern New Brunswick: Using Knowledge-Driven and Data-Driven Methods. Minerals, 15(4), 345. https://doi.org/10.3390/min15040345

Mars, J. (2006). Radiometer (ASTER) data and logical operator algorithms arc, Iran, using Advanced Spaceborne Thermal Emission and Reflection Regional mapping of phyllic- and argillic-altered rocks in the Zagros magmatic. Geosphere, 2(3), 161. https://doi.org/10.1130/GES00044.1

Mirzaei Misagh, A. P. A. A. K. M. Z. Z. A. (2014). Prospection of Iron and Manganese Using Index Overlay and Fuzzy Logic Methods in Balvard 1:100,000 Sheet, SE Iran. Iranian Journal of Earth Sciences, 6(1), 1–11.

Nykänen, V., Groves, D. I., Ojala, V. J., Eilu, P., & Gardoll, S. J. (2008). Reconnaissance-scale conceptual fuzzy-logic prospectivity modelling for iron oxide copper – gold deposits in the northern Fennoscandian Shield, Finland. Australian Journal of Earth Sciences, 55(1), 25–38. https://doi.org/10.1080/08120090701581372

Parsa, M., Maghsoudi, A., Yousefi, M., & Sadeghi, M. (2016). Recognition of significant multi-element geochemical signatures of porphyry Cu deposits in Noghdouz area, NW Iran. Journal of Geochemical Exploration, 165, 111–124. https://doi.org/10.1016/j.gexplo.2016.03.009

Pazand, K., Hezarkhani, A., & Ataei, M. (2015). Using TOPSIS approaches for predictive porphyry Cu potential mapping: A case study in Ahar-Arasbaran area (NW, Iran). Computers & Geosciences, 49, 62–71. https://doi.org/10.1016/j.cageo.2012.05.024

Porwal, A., Carranza, E. J. M., & Hale, M. (2003). Artificial Neural Networks for Mineral-Potential Mapping: A Case Study from Aravalli Province, Western India. Natural Resources Research, 12(3), 155–171. https://doi.org/10.1023/A:1025171803637

Riahi, S., Bahroudi, A., Abedi, M., Lentz, D. R., & Aslani, S. (2023). Application of data-driven multi-index overlay

and BWM-MOORA MCDM methods in mineral prospectivity mapping of porphyry Cu mineralization. Journal of Applied Geophysics, 213, 105025. https://doi.org/10.1016/j.jappgeo.2023.105025

Richards, J. P., Boyce, A. J., & Pringle, M. S. (2001). Geologic Evolution of the Escondida Area, Northern Chile: A Model for Spatial and Temporal Localization of Porphyry Cu Mineralization. Economic Geology, 96(2), 271–305. https://doi.org/10.2113/gsecongeo.96.2.271

Safari, M., Maghsoudi, A., & Pour, A. B. (2018). Application of Landsat-8 and ASTER satellite remote sensing data for porphyry copper exploration: a case study from Shahr-e-Babak, Kerman, south of Iran. Geocarto International, 33(11), 1186–1201. https://doi.org/10.1080/10106049.2017.1334834

Shahabpour, J. (1999). The role of deep structures in the distribution of some major ore deposits in Iran, ne of the Zagros thrust zone. Journal of Geodynamics, 28(2–3), 237–250. https://doi.org/10.1016/S0264-3707(98)00040-4

Sillitoe, R. H. (1994). Erosion and collapse of volcanoes: Causes of telescoping in intrusion-centered ore deposits. Geology, 22(10), 945. https://doi.org/10.1130/0091-7613(1994)022<0945:EACOVC>2.3.CO;2

Stević, Ž., Pamučar, D., Puška, A., & Chatterjee, P. (2020). Sustainable supplier selection in healthcare industries using a new MCDM method: Measurement of alternatives and ranking according to COmpromise solution (MARCOS). Computers & Industrial Engineering, 140, 106231. https://doi.org/10.1016/j.cie.2019.106231

Taghipour, N., Aftabi, A., & Ramezani, M. R. (2009). Investigation on the Alteration-Mineralization Haloes and Distribution Patterns of Cu, Au, Ag and Mo in the Miduk Porphyry Copper Deposit, Shahr-Babak, Kerman. Scientific Quarterly Journal of Geosciences, 18(72), 45–54. https://doi.org/10.22071/gsj.2010.57137

Tešić, D., Božanić, D., Puška, A., Milić, A., & Marinković, D. (2023). Development of the MCDM fuzzy LMAW-grey MARCOS model for selection of a dump truck. Reports in Mechanical Engineering, 4(1), 1–17. https://doi.org/10.31181/rme20008012023t

Tshanga M, M., Ncube, L., & van Niekerk, E. (2024). Remote sensing insights into subsurface-surface relationships: Land Cover Analysis and Copper Deposits Exploration. Earth Science Informatics, 17(5), 3979–4000. https://doi.org/10.1007/s12145-024-01423-2

Waterman, G. C., & Hamilton, R. L. (1975). The Sar Cheshmeh porphyry copper deposit. Economic Geology, 70(3), 568–576. https://doi.org/10.2113/gsecongeo.70.3.568

Yousefi, M., & Carranza, E. J. M. (2015). Geometric average of spatial evidence data layers: A GIS-based multi-criteria decision-making approach to mineral prospectivity mapping. Computers & Geosciences, 83, 72–79. https://doi.org/10.1016/j.cageo.2015.07.006

Yousefi, M., Carranza, E. J. M., Kreuzer, O. P., Nykänen, V., Hronsky, J. M. A., & Mihalasky, M. J. (2021). Data analysis methods for prospectivity modelling as applied to mineral exploration targeting: State-of-the-art and outlook. Journal of Geochemical Exploration, 229, 106839. https://doi.org/10.1016/j.gexplo.2021.106839

SAŽETAK

Modeliranje potencijala Cu porfirita korištenjem MARCOS metode vođene podatcima i znanjem, studija slučaja, područje Shahr-e-Babak, jugoistočni Iran

Cilj je ove studije usporediti učinkovitost višekriterijskoga odlučivanja (MCDM) vođenoga podatcima i znanjem u izradi modela mineralnoga potencijala u području istraživanja Shahr-e-Babak u jugoistočnome Iranu. Kako bi se postigao taj cilj, obrađeno je i izrađeno osam slojeva, uključujući geološku podlogu, sadržaj bakra, analizu glavnih komponenti, argilične alteracije, hidrotermalne alteracije, alteracije željezovih oksida (Gossan), geofizičke podatke i linearne strukture. Za izradu optimalnoga modela prvo su svi slojevi skalirani i pomaknuti na interval od nule do jedan. Za izradu modela mineralnoga potencijala u istraživanome području uvedena je MARCOS metoda (alternativna mjerenja i rangiranje prema kompromisnome rješenju). Za ponderiranje kontrolnoga sloja korištene su dvije metode: metoda stope predviđanja površine (P-A) i metoda analitičkoga hijerarhijskog procesa (AHP). Zatim su rezultati uspoređeni s metodom višekriterijske optimizacije analizom omjera (MOORA) koja je dokazanu u procjeni mineralnoga potencijala. Za usporedbu ovih metoda korištene su dvije metode – stopa predviđanja površine i površina ispod krivulje (AUC). Rezultati su pokazali da MARCOS pristup vođen podatcima pruža najbolje performanse i prikazuje najbolji model mineralnoga potencijala. Normalizirana gustoća za MARCOS metodu vođenu podatcima, MOORA metodu vođenu podatcima, MARCOS metodu vođenu znanjem te MOORA metodu vođenu znanjem jednaka je 3,00, 2,84, 2,7 i 2,57, dok su AUC vrijednosti iznosile 0,939, 0,938, 0,933 i 0,932.

Ključne riječi:
porfirit, MARCOS, MOORA, područje Shahr-e-Babak, vođeno podatcima

Author's contribution

Moslem Jahantigh (Dr): data curation, formal analysis and software. **Hamidreza Ramazi** (Dr): supervision and validation.
All authors have read and agreed to the published version of the manuscript.

RGNZ/MGPB

Experimental Investigation of the Effects of Temperature and Oil Composition on CO_2-Crude Oil Swelling, Extraction Mechanisms, and Displacement Performance

Rudarsko-geološko-naftni zbornik
(The Mining-Geology-Petroleum Engineering Bulletin)
DOI: 10.17794/rgn.2026.3.4

Original scientific paper

Kartika Hartono[1]*, Asep K. Permadi[2], Ucok W. R. Siagia[2], Andri L. Hakim[2], Sumadi Paryoto[3], Ahlul H. Resha[4], Syaeful A. Satya[4], Reno Pratiwi[1], Maman Djumantara[1], Dina A. Chusniah[1]

[1] *Petroleum Engineering Department, Faculty of Earth Technology and Energy, Universitas Trisakti, West Jakarta 11440, Indonesia.*

[2] *Petroleum Engineering Department, Faculty of Mining and Petroleum Engineering (FTTM), Institut Teknologi Bandung, Bandung, West Java 40132, Indonesia.*

[3] *Upstream Research and Technology Innovation (URTI), PT. Pertamina, South Jakarta 12920, Indonesia.*

[4] *Laboratory Enhanced Oil Recovery, Research and Technology Innovation (RTI), PT. Pertamina, East Jakarta 13920, Indonesia.*

Abstract

CO_2 flooding has several advantages for enhancing oil recovery, including a reduction in crude oil viscosity, a decrease in interfacial tension, and an increase in oil volume through swelling. Although the mechanisms of oil swelling and extraction in CO_2–crude oil systems have been widely studied, the combined effects of temperature and oil composition on these mechanisms – and their influence on CO_2 displacement efficiency in porous media – remain insufficiently understood, especially under high reservoir temperatures. Therefore, this study investigates how temperature and crude oil composition affect swelling-extraction behaviour and CO_2 displacement efficiency. High-pressure and high-temperature (HPHT) PVT tests were conducted to evaluate swelling and extraction phenomena, while slim tube experiments were used to assess oil recovery performance. Tests were carried out at 70°C and 90°C using two light dead oils from an Indonesian field under varying injection pressures. Compositional analysis of produced oils was performed using Gas Chromatography (GC) and further interpreted through SARA fractions (saturates, aromatics, resins, and asphaltenes). Results show that lower temperatures enhance CO_2 extraction efficiency due to higher CO_2 density, leading to more pronounced swelling and miscibility effects. The miscibility was observed within the extraction region, emphasizing the role of hydrocarbon extraction in the miscibility mechanism. Higher temperatures were found to improve oil recovery, primarily due to viscosity reduction. Additionally, increasing CO_2 injection pressure reduced resin and asphaltene content, with evidence of asphaltene precipitation in the porous medium – particularly at lower temperatures. These findings provide valuable insight into how temperature and oil composition influence CO_2–oil interactions and support more effective implementation of CO_2 flooding at elevated reservoir temperatures.

Keywords:
CO_2 flooding, Swelling-extraction mechanisms, Miscibility, Asphaltene precipitation, Oil Recovery, SARA fractions

1. Introduction

CO_2 flooding is a promising Enhanced Oil Recovery (EOR) method that has successfully increased oil production (**Ghorbani et al., 2014; Hartono et al., 2021; Zhang et al., 2019**). The fundamental mechanism between CO_2 and crude oil interactions is shown in CO_2 solubility (**Rezk & Foroozesh, 2019**). During the interaction of CO_2 in hydrocarbon oils, the CO_2 will diffuse into these oils and cause the oils to swell (**Holm & Josendal, 1974; Wei et al., 2017; Yang & Gu, 2006**). The swelling phenomenon will help crude oil obtain several advantageous characteristics in oil recovery, such as lower viscosity, interfacial tension (IFT) reduction, and a larger volume. Furthermore, CO_2 has the ability to extract or vaporize light to intermediate hydrocarbons from crude oil. The extraction mechanism of CO_2-hydrocarbon becomes the principle in developing multicontact miscibility (**Permadi et al., 2021; Siagian & Grigg, 1998; Yellig, 1982**). Therefore, the swelling and extraction phenomena in the CO_2 and crude oil interactions are the fundamental mechanisms for oil recovery. An increase in CO_2 injection pressure enhances both its solubility in oil and the oil swelling effect. Conversely, raising the temperature reduces CO_2 solubility, as CO_2 molecules become more active at elevated temperatures, which diminishes their interaction with crude oil (**Fakher & Imqam, 2020; Svrcek et al., 1982**). **Fakher & Imqam (2020)** concluded that oil swelling strongly

* Corresponding author: Kartika Hartono
e-mail address: kartika@trisakti.ac.id
Received: 12 August 2025. Accepted: 1 November 2025.
Available online: 14 May 2026

depends on CO_2 injection pressures and reservoir temperatures. Many studies investigated the oil swelling and extraction mechanisms in the interactions of CO_2 and crude oil systems. Also, the swelling and extraction mechanisms have received attention from several researchers to determine the miscibility pressure of CO_2 and crude oil. However, most previous studies and experiments were conducted at relatively low temperatures. Only a few have focused on its application at high reservoir temperatures and the effects of oil composition on swelling extraction mechanisms and CO_2 displacement performance. Investigating the swelling and extraction mechanisms in high-temperatures environments is important for applying CO_2 flooding at high reservoir temperatures. For example, most of Indonesia's oil fields have reservoir temperatures above 90°C. **Fakher & Imqam (2020)**, based on their data analysis, showed that most swelling tests were conducted at the temperature range of 20 – 50°C. The interpretation of the swelling test data at 20 - 50°C might differ with the higher temperature. Therefore, more swelling test data for high reservoir temperatures is needed to understand the swelling and extraction mechanisms for applying CO_2 flooding in high reservoir temperatures.

Moreover, the extraction of hydrocarbons by dense CO_2 is also strongly influenced by crude oil compositions (**Orr & Silva, 1987; Silva et al., 1987**). As the principle of multi-contact miscibility in the interaction of CO_2 and crude oil system, the extraction mechanism will significantly affect CO_2 displacement performance, such as oil recovery. As previously mentioned, only a few studies have investigated the effects of temperatures and oil composition on swelling extraction mechanisms and CO_2 displacement performance. Therefore, the comprehensive study investigated the effect of temperature and crude oil compositions on swelling–extraction mechanisms and the impact on CO_2 displacement performance, particularly in high reservoir temperatures, are limited. Understanding the effect of temperatures and oil compositions on CO_2 EOR fundamental mechanisms such as swelling-extraction and CO_2 flow mechanisms in porous media is vital to optimizing CO_2 flooding process implementation. **Siagian & Grigg (1998)** studied the capacity of CO_2 in extracting hydrocarbons from crude oil as a function of pressure at relatively low temperatures of 35°C and 59°C and compared the results with the slim tube experiments. The findings showed that the CO_2 extraction capacity increased with increasing pressure and formed a sharp transition pressure range which corresponded effectively with the slim tube breakpoint or Minimum Miscibility Pressure (MMP). They considered that the sharp transition pressure range could be used to estimate the MMP reasonably. However, their study did not investigate the effect of change in crude oil composition due to the extraction of light–intermediate hydrocarbon on CO_2 displacement performance. **Tsau et al. (2010)** investigated the effect of temperature on swelling and extraction at 37°C – 52°C with a small sample size of 3-14 cc. They showed that at a given pressure, the swelling factor of oil decreases with an increase in temperature. The results also showed that the pressure at which extraction starts by CO_2 depends on the initial volume of oil and temperatures. They concluded that the intersection of significant extraction lines could determine the miscibility at these temperature conditions. Abdurrahman et al., investigated the swelling phenomena at 60°C and 66°C using light crude oil samples (**Abdurrahman et al., 2015 & 2019**). They proposed three stages in swelling factor versus pressure plot: condensation stage, condensation and extraction stage, and extraction stage. They also estimated the MMP using the slim tube but did not investigate the effect of oil composition on the CO_2 displacement performance.

As discussed earlier, the extraction mechanism is a key principles of CO_2 - enhanced oil recovery and will impact displacement performance in porous media. This study aims to provide a comprehensive assessment of the effects of temperature and crude oil composition on swelling–extraction mechanisms and their subsequent impact on displacement performance efficiency. To achieve this, a series of high-pressure, high temperature (HPHT) visual PVT experiments were performed using light oil crude from an Indonesian oil field to obtain swelling data. The observation of CO_2 displacement performance was performed using a slim tube apparatus. The experiments were conducted at 90°C, representing the reservoir temperature. Then, it was re-conducted at 70°C, approximately the average of wellbore temperature condition. This study is expected to provide more data on the swelling and extraction mechanisms for implementing CO_2 flooding at high reservoir temperatures. Moreover, this study is also expected to provide insight into understanding the effect of different parameters such as, temperatures and oil compositions, on CO_2 flow mechanisms in porous media and optimizing CO_2 flooding process implementation.

2. Materials and Experimental Methods

The materials or crude samples in this study were taken from Indonesian oilfield. This experimental was conducted at different crude samples, pressures, and temperatures.

Table 1. Properties of Dead Oil Samples

Properties	JTB	RDG
API Gravity (°API)	36.4	42.6
Oil density (kg/m³)	837	787
Oil viscosity (cp)	0.195	0.17
Molecular weight (g/mol)	187.7	174.8
Reservoir temperature (°C)	90	90
Average porosity (%)	16-33	15-23
Average permeability (mD)	22	37

Table 2. Compositions of Dead Oil Samples

JTB Oil				RDG Oil			
Component	**%Mole fraction**	**Component**	**%Mole Fraction**	**Component**	**%Mole fraction**	**Component**	**%Mole fraction**
nC_6	0.00	nC_{24}	3.42	nC_6	0.00	nC_{24}	2.43
nC_7	2.26	nC_{25}	3.24	nC_7	3.10	nC_{25}	2.13
nC_8	3.85	nC_{26}	2.77	nC_8	3.21	nC_{26}	1.72
nC_9	7.28	nC_{27}	2.63	nC_9	5.06	nC_{27}	1.57
nC_{10}	9.13	nC_{28}	1.87	nC_{10}	6.53	nC_{28}	1.11
nC_{11}	6.58	nC_{29}	1.69	nC_{11}	5.25	nC_{29}	1.00
nC_{12}	5.30	nC_{30}	1.02	nC_{12}	5.65	nC_{30}	0.63
nC_{13}	4.75	nC_{31}	0.90	nC_{13}	6.09	nC_{31}	0.52
nC_{14}	4.62	nC_{32}	0.50	nC_{14}	7.45	nC_{32}	0.31
nC_{15}	4.57	nC_{33}	0.42	nC_{15}	8.42	nC_{33}	0.26
nC_{16}	4.10	nC_{34}	0.16	nC_{16}	8.15	nC_{34}	0.10
nC_{17}	3.97	nC_{35}	0.11	nC_{17}	6.67	nC_{35}	0.07
nC_{18}	3.95	nC_{36}	0.00	nC_{18}	5.45	nC_{36}	0.00
nC_{19}	4.23	nC_{37}	0.00	nC_{19}	4.23	nC_{37}	0.00
nC_{20}	4.04	nC_{38}	0.00	nC_{20}	3.42	nC_{38}	0.00
nC_{21}	4.25	nC_{39}	0.00	nC_{21}	3.34	nC_{39}	0.00
nC_{22}	4.31	nC_{40}	0.00	nC_{22}	3.20	nC_{40}	0.00
nC_{23}	4.10	Total	100.00	nC_{23}	2.94	Total	100.00

Table 3. The Composition of SARA Components

SARA Contents	JTB Crude Oil	RDG Crude Oil
Saturates	61.6%	58.2%
Aromatics	26.4%	36.1%
Resins	6.9%	3.9%
Asphaltenes	5.1%	1.8%

2.1. Materials

Crude oil samples used in this study were dead crude oil with 42°API and 36°API obtained from the RDG and JTB Indonesian oilfield, respectively. The fluid reservoir properties and compositions of the crude oil samples are shown in **Table 1** and **Table 2**, respectively. Meanwhile, **Table 3** shows the composition of the crude oil measured based on the fractions of saturates, aromatics, resins, and asphaltenes (SARA). Moreover, the CO_2 used for gas injection was ultra-high pure (99.9%). The field's average reservoir temperature was found to be 90°C which was set as a temperature condition during experiments. The experiment was repeated at 70°C, which approximates the average of wellbore temperature condition, to observe the influence of temperature on oil swelling, extraction behaviour, and the effectiveness of CO_2 displacement.

2.2. Experimental Apparatus

The experiments were carried out using two main high-pressure and high-temperature (HPHT) systems. The PVT apparatus was utilized to analyze the swelling and extraction behaviour, while the slim tube apparatus was employed to evaluate oil recovery and CO_2 displacement efficiency. Additionally, fluid composition analysis was performed using the Agilent 7890B Gas Chromatography (GC) system.

2.2.1. PVT Set-up

A visual PVT cell was employed to examine CO_2–crude oil interactions under varying conditions. The cell, equipped with a sight glass and magnetic stirrer, allows real-time observation and mixing of fluids. A rotating mechanism was incorporated to accelerate phase equilibrium, while pressure control was achieved through an internal moving piston. Temperature was maintained using a thermostatically controlled oven with a circulating bath. The gas–oil interface was monitored using a high-resolution camera, and key parameters – pressure, temperature, volume, and visual data – were recorded via an integrated data acquisition system. The simplified diagram of visual PVT system is presented in **Figure 1**.

2.2.2. Slim tube Apparatus

The slim tube apparatus system used in this study was STS 700 with the specifications of high pressure and high temperature measurement. The detail specifications of the slim tube are as stated in **Table 4**. In general, the slim tube consist of a coil tube with sand pack and includes several components: high-pressure floating pis-

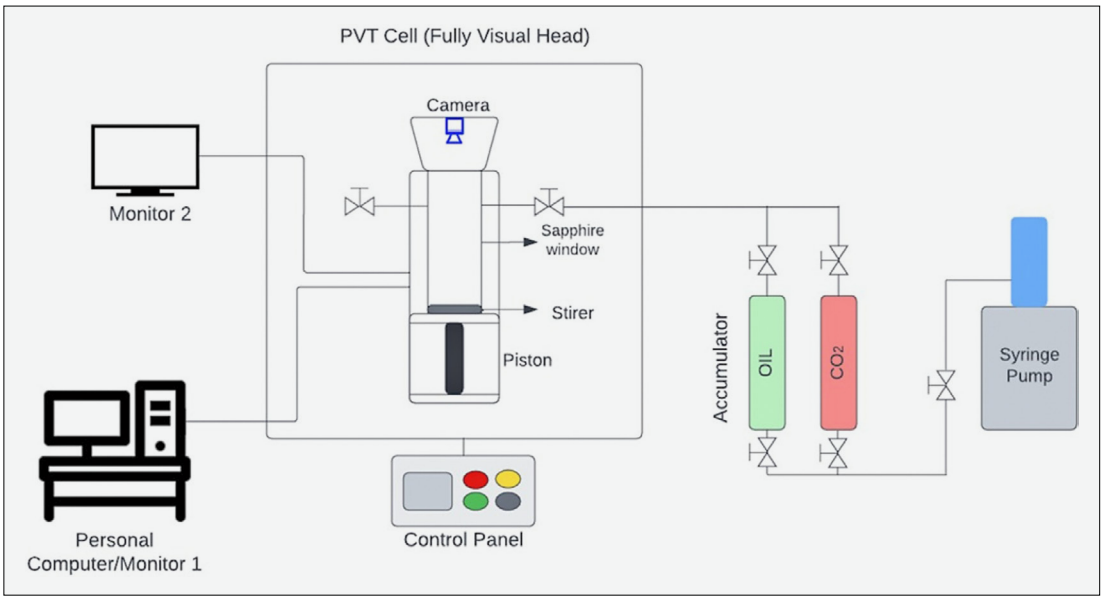


Figure 1. Schematic Diagram of Visual Fluid Eval PVT System

Table 4. The Specifications of Slim Tube Apparatus

Specification	Parameters (Units)	Values
Overall System	Maximum Pressure (Psi)	10000
	Temperature Range (°C)	Room temperature to 150°C
	Multiple Fluids	Up to 3 different fluids
	Wetted Material	Hastelloy
Injection pump	Flow Range (mL/min)	0.01 to 100 mL/min
	Delivery Mode	Constant-Flow or Constant-Pressure
	Wetted Material	Stainless Steel 316
	Dimension	25 cm x 41 cm x 97 cm
Slim tube	Length (m)	24
	Inner Diameter (mm)	4
	Porous media (µm)	Calibrated 230 – 310 µm Silica
	Average Porosity (%)	35
	Pore volume (mL)	120
Visual Cell	Material	Titanium
	Sapphire Inside Diameter (mm)	1.5
	Sapphire Outside Diameter (mm)	20
	Sapphire Length (cm)	7

ton accumulators for oil, gas, and solvent; oven with a temperature-controller; a back-pressure pump; a gasometer; a remote-control panel; and visual cell. Additionally, a densitometer is installed to monitor the density of fluids exiting the slim tube. The system is illustrated in **Figure 2**.

2.3. Experimental Procedures

The experiments were categorized into three main parts, which include (1) swelling/extraction using Visual Fluid Eval PVT; (2) the CO_2 displacement process using a slim tube apparatus system; and (3) compositional analysis of the effluent oils in the CO_2 flooding process which was analyzed by Gas Chromatography. Subsequently, the residual oil samples were examined to determine their SARA (Saturates, Aromatics, Resins, and Asphaltenes) fractions, following the ASTM D6560 standard method (**Ashoori et al., 2017; Santos et al., 2019**).

2.3.1. Swelling and Extraction Experimental Procedures

The swelling and extraction experiments were performed in a visual PVT cell, which was tested for any leakage using nitrogen, cleaned, vacuumed, and made ready to be filled. The cell was initially charged with a crude oil sample at atmospheric pressure, corresponding to 10% of the total cell volume, in accordance with the suggestion of **Hand & Pinczewski (1990)** recommendation that the maximum initial oil volume for swelling and shrinkage curve should not exceed 30% of the total cell capacity. The cell temperature was then elevated to the experimental reservoir condition of 90°C. Once the PVT cell reached the desired temperature stability, this was followed by an increase in the pressure in discrete steps by injecting CO_2 into the cell until it reached 4000 Psi. The cell was sealed, stirred by a magnetic stirrer, and rotated to accelerate the CO_2 and oil sample dissolution. After the oil became fully saturated with CO_2, the oil and gas volume were determined through visual digital imaging, with measurements recorded using an integrated computer system. The Swelling Factor (SF) was calculated as the ratio between the oil volume fully satu-

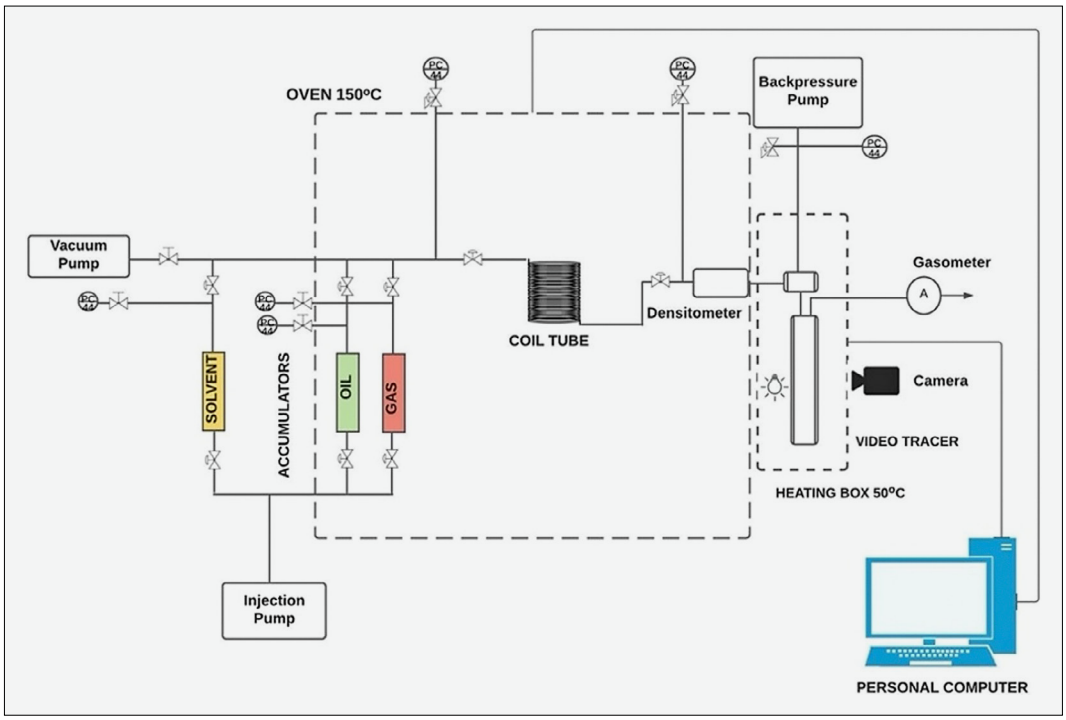


Figure 2. Schematic Diagram of Slim Tube System

rated with CO_2 at the test pressure and temperature, and the initial oil volume at atmospheric pressure under the same temperature (**Welker, 1963; Simon & Graue, 1964**). These swelling/extraction experimental procedures were repeated at the temperature of 70°C to investigate the influence of decreasing temperature on swelling and extraction mechanism.

2.3.2. Slim tube Experiment

The slim tube experiment procedure in this study was adopted from the previous work of **Hartono et al. (2024)**. Generally, the experiment was carried out into three main steps: preparation, cleaning, and coil tube saturated by the oil until reaching 1.5 pore volumes (PV), then continued with CO_2 injection. The pressure is maintained to be constant by back-pressure regulator. Subsequently, CO_2 was injected into the slim tube at a rate of 0.06 mL/min, and the effluent fluids were monitored visually through a separator equipped with a visual cell. The recovery factor of oil for each pressure condition was calculated and plotted to determine the MMP. The MMP was identified from the inflection point of the recovery curve at 1.2 PV of injected gas (**Glaso, 1990; Hudgins et al., 1990**). These experimental steps were also repeated under reservoir conditions of 70°C. In addition, the composition of the effluent oil was evaluated by gas chromatography to examine the extraction of hydrocarbon components at various pressures.

3. Results and Discussions

The discussion begins by examining how temperature and oil composition influence the swelling and extraction mechanisms. This is followed by an analysis of how these same factors affect CO_2 flow behaviour and displacement efficiency within porous media. Additionally, changes in oil composition, specifically the SARA (Saturates, Aromatics, Resins, and Asphaltenes) fractions, resulting from CO_2 injection are also evaluated to understand their impact on the overall displacement performance.

3.1. Effect of Temperature on Swelling – Extraction Mechanisms

The swelling and extraction phenomena of CO_2 and crude oil were observed at different pressures and temperatures. The results of swelling factor versus pressure at temperatures of 70°C and 90°C for JTB and RDG crude samples are shown in **Figures 3** and **4**, respectively. The swelling curves are divided into three stages, as suggested by **Abdurrahman et al. (2015) and Siagian & Grigg (1998)**. The first stage, known as the condensation region, is characterized by an increase in the swelling factor as pressure rises. The second stage represents the condensation and extraction region, where the oil phase volume drops sharply. The third stage, the extraction region, shows a more gradual decrease in oil phase volume with increasing pressure. The data indicate that the rate of oil swelling declines as temperature increases. **Figure 3** for JTB oil shows that the peak of the swelling factor at 90°C is slightly higher than 70°C. Then, the oil volume starts to decrease rapidly at 2500 Psi, indicating that some hydrocarbon components are extracted by dense CO_2. The condensation and extraction regions also show that the oil phase volume of JTB at 70°C decreases sharper than at 90°C. It indicates that CO_2 has a higher capacity to extract hydrocarbon com-

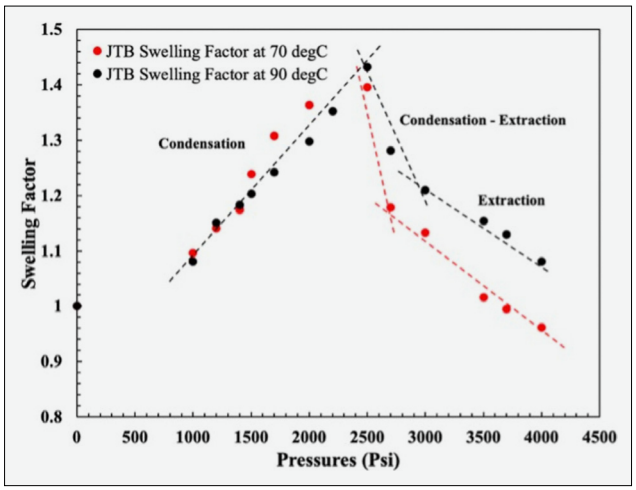


Figure 3. Swelling Factor curves of CO_2 – JTB oil sample at 70°C and 90°C with various pressures

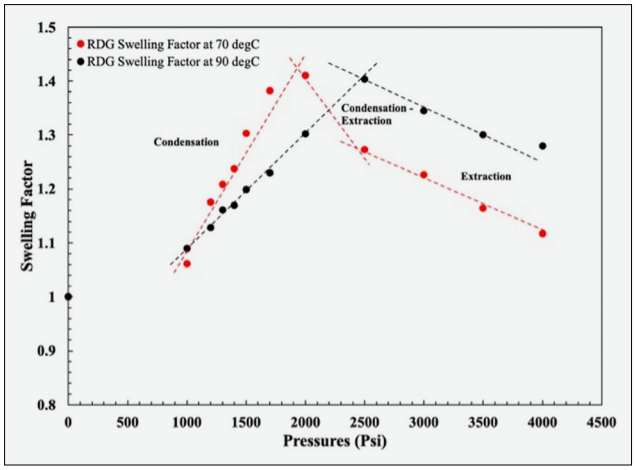


Figure 4. Swelling Factor curves of CO_2 – RDG oil sample at 70°C and 90°C with various pressures

ponents at lower temperatures than at higher temperatures at the given pressures.

Figure 4 presents the swelling factor as a function of pressure for RDG crude oil. Similar to the trend observed in JTB oil, the swelling rate at 70°C is greater than at 90°C. For the RDG sample, the maximum swollen oil volume reached almost one and half times the initial volume at both 70°C and 90°C. It was found from the figures that the rate of oil swelling decreased as the temperature increased for both samples and a similar trend was observed to have been reported by **Hand & Pinczewski (1990) and Rezk & Foroozesh (2019)**. The influence of crude oil composition on the CO_2 flooding flow mechanisms within porous media will be explained detail in the subsequent chapter.

3.2. Effect of Oil Composition on Swelling – Extraction Mechanisms

The influence of oil composition on swelling and extraction mechanisms is shown by comparing the swelling and extraction curves of JTB and RDG crude oil samples, as presented in **Figures 3** and **4**, respectively. Even though JTB oil has a higher Molecular Weight (MW) than RDG oil, the pressure required to achieve maximum swell is similar at 90°C. However, at a temperature of 70°C, the pressure required to achieve maximum swell for RDG crude samples was lower than that for JTB oil. Interestingly, JTB oil has a more significant decrease in the condensation-extraction region than RDG oil, although JTB has a higher molecular weight or is heavier than RDG oil. It should be noted that the extraction of hydrocarbon components from oil increases as the gas density increases with the pressure (**Dindoruk et al, 2020**). However, the amount of extraction also depends on the composition of the oil, particularly the fraction of the oil that includes components that are soluble in dense CO_2. Hence, it requires to be observed the compositions of oil samples.

The extraction phenomena occurred in JTB and RDG oil samples can be seen from the changes of hydrocarbon compositional of the original oil sample and the characterization of the residue oil with various CO_2 injection pressures at a temperature of 90°C, as shown in **Figures 5** and **6**, respectively. **Figures 5** and **6** show that the mole percentage of intermediate components (C_6-C_9) reduces with increasing CO_2 injection pressures. On the other hand, the heavier components (C_{23}-C_{30}) showed a relatively higher mole percentage with increasing CO_2 injection pressures. The depletion of light - intermediate hydrocarbon fractions results in an increase in the bulk fluid density. This compositional shift can also enhance asphaltene solubility, as the removal of volatile components alters the thermodynamic equilibrium and promotes the incorporation of higher-molecular-weight asphaltenes into the crude oil phase (**Kokal & Sayegh, 1995; Rezk & Foroozesh, 2019**). During CO_2 flooding, the properties of both produced and residual oils can be altered through mutual interaction between CO_2 and crude oil. A reduction in the mole fraction of light to intermediate components – primarily within the saturates fraction – can compromise crude oil stability, leading to the precipitation of heavier hydrocarbon constituents such as asphaltenes (**Wang et al., 2016**).

Hagedorn & Orr (1994) reported that ring structures of components generally reduce solubility, especially for multi-ring aromatics. As indicated by the SARA analysis in **Table 3**, the RDG crude oil sample contains a higher fraction of aromatics compared to JTB oil. Aromatics are hydrocarbon components that are generally nonpolar, distinguished by their unsaturated ring structures containing multiple carbon–carbon double bonds (**Fakher et al., 2020**).

3.3. Effect of Temperature on CO_2 Displacement Performance

The performance of CO_2 displacement was examined using a slim tube through seven experimental runs con-

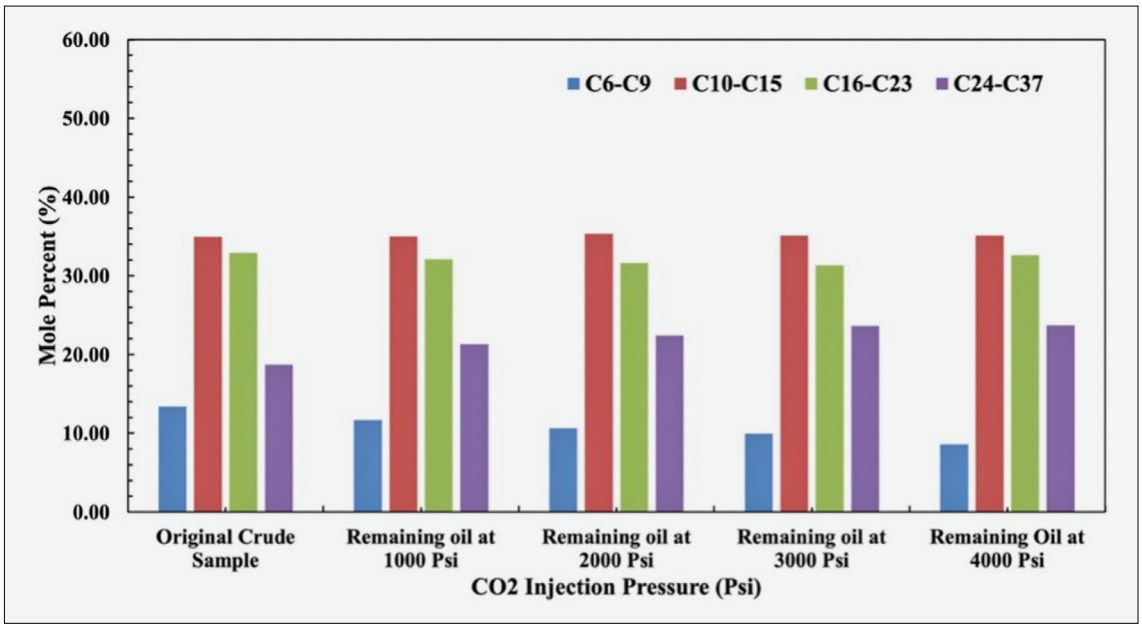


Figure 5. Hydrocarbon compositions of the original JTB sample and the residual oil after the swelling test at 90°C

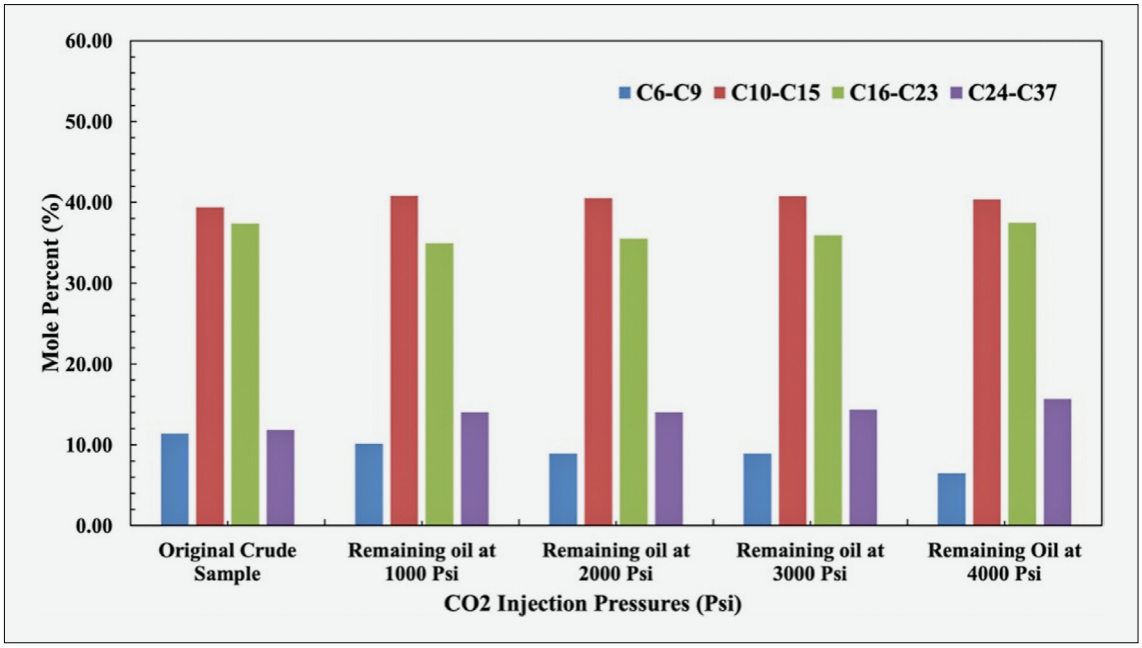


Figure 6. Hydrocarbon compositions of the original RDG sample and the residual oil after the swelling test at 90°C

ducted at varying pressures and temperatures. The experiments were carried out at high pressures of 1000 to 5000 Psi and the oil recovery outcomes from the CO_2 flooding process are shown in **Table 5**. Each displacement test was initially conducted at 90°C, representing the average reservoir temperature, and then repeated at 70°C, which reflects the wellbore temperature condition. As shown in **Table 5**, oil recovery at 70°C is lower compared to 90°C for both RDG and JTB crude oil samples. Specifically, the maximum recovery at 70°C reached 85.7% for RDG and 89% for JTB, while at 90°C, the recoveries increased to 93.5% and 94.5%, respectively. These results suggest that higher temperatures enhance oil recovery, which is likely due to the reduction in oil viscosity with increasing temperature (**Maqbool et al., 2011**). Therefore, the oil recovery results from the CO_2 displacement tests are crucial for determining the MMP.

MMP values for JTB and RDG samples are presented in **Figure 7** and **8**, respectively. The MMP was determined by plotting recovery factor (%) values against the corresponding injection pressures, as described by **Glaso (1990)** and **Hudgins et al. (1990)**. **Figure 7** shows that the MMP for JTB oil is higher at a higher temperature. Additionally, the figure suggests that miscibility

Table 5. Recovery Factor (%) obtained from slim tube experiments at 70°C and 90°C

Injection Pressure (Psi)	RF (%) RDG 70°C	RF (%) RDG 90°C	RF (%) JTB 70°C	RF (%) JTB 90°C
1000	51	51.6	47.5	46
2000	61.7	79	64.2	64
2500	-	-	-	76.3
3000	78.5	93.5	86.5	90.6
3500	85.7	-	88	-
4000	84.6	93.5	89	93.5
5000	83	93.5	82	94.5

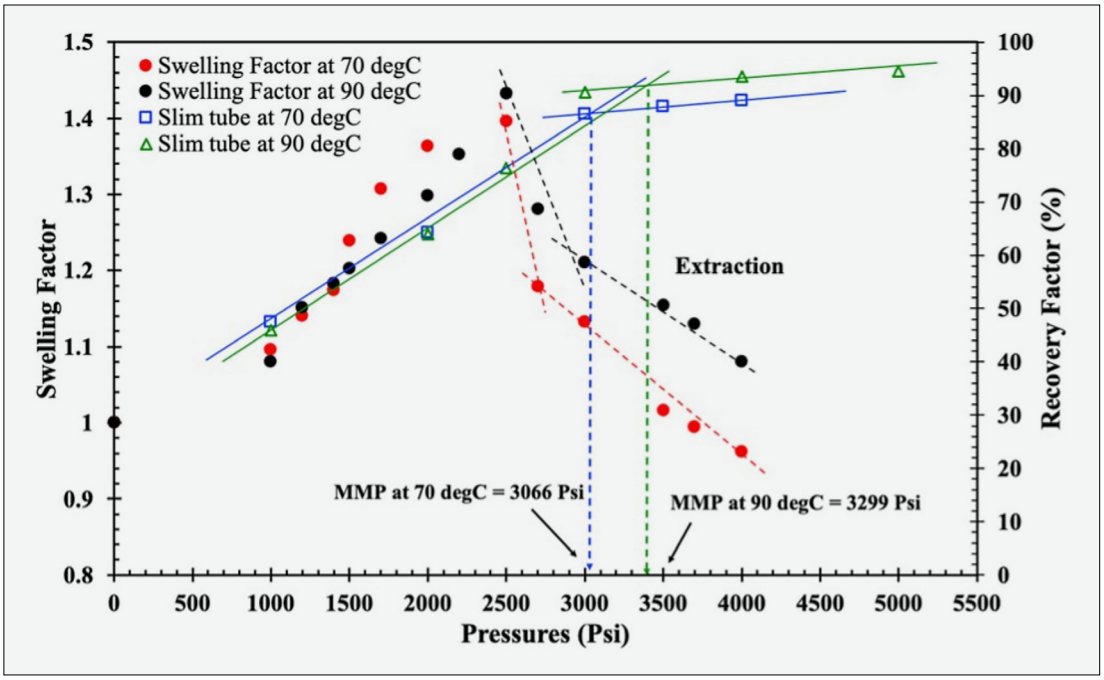


Figure 7. MMP Estimation from slim tube and Swelling Factor JTB oil at 70°C and 90°C

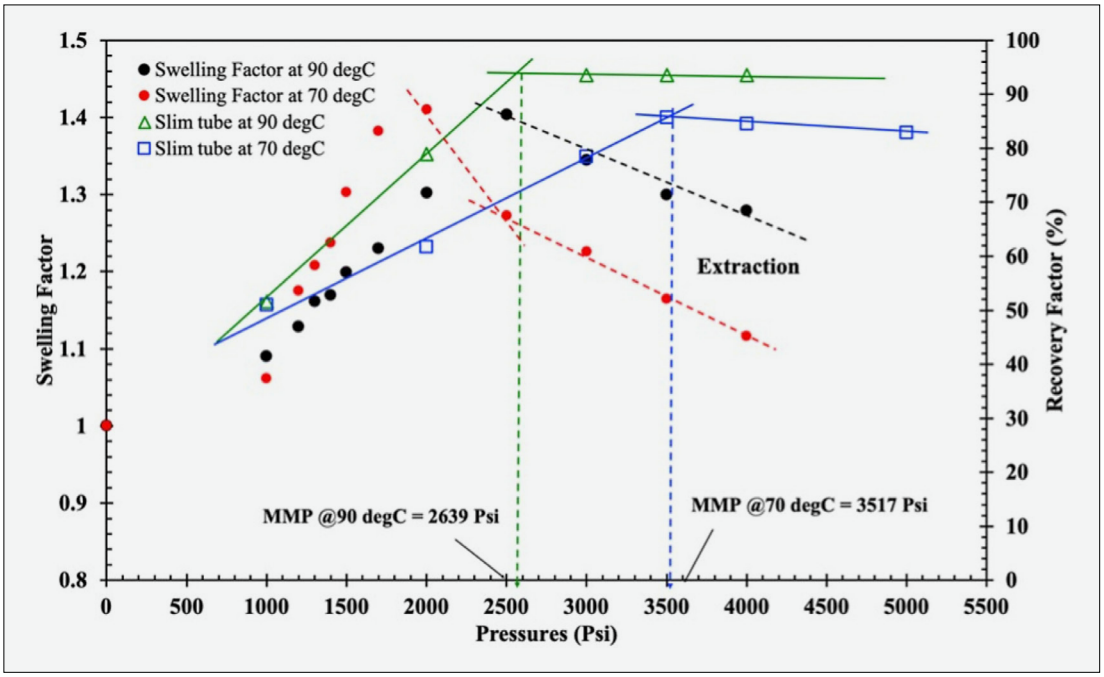


Figure 8. MMP Estimation from slim tube and Swelling Factor RDG oil at 70°C and 90°C

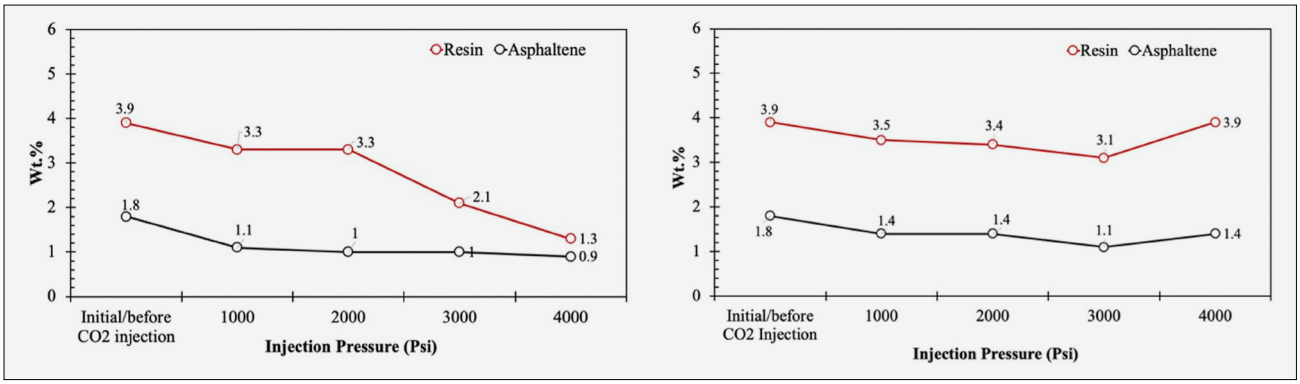


Figure 9. Resin and Asphaltene Fraction (wt.%) of RDG sample at (a) 70°C and (b) 90°C in varying injection pressures

between CO_2 and the crude oil occurs within the extraction region, indicating that the extraction of hydrocarbon components by CO_2 plays a significant role in achieving miscibility. On the other hand, for the RDG crude oil, **Figure 8** demonstrates that the MMP at 70°C is notably higher compared to that at 90°C. This phenomenon shows that the extraction of hydrocarbon components by CO_2 is one of the mechanisms of miscibility. In contrast to the MMP of the JTB oil sample, the RDG oil shows that the MMP at 70°C is much higher than at 90°C, as shown in **Figure 8**. According to **Lashkarbolooki & Ayatollahi (2018)** and **Yellig & Metcalfe (1980)**, an increase in temperature typically leads to a rise in MMP. However, some of the MMP data summarized from the literature showed that some oil fields with lower reservoir temperatures have higher MMP than those with higher reservoir temperatures, as shown in **Figure 11**. Therefore, the experimental results on the effect of temperature on displacement performance require further analysis to investigate the effect of oil compositions on the CO_2 displacement process in porous media. The effect of oil composition on displacement performance will be discussed in the subsequent section.

3.4. Effect of Oil Composition on CO_2 Displacement Performance

As previously discussed, **Figure 8** shows that the MMP for the RDG sample at a temperature of 70°C is much higher than at 90°C, which contrasts with the JTB oil sample. Therefore, further investigation into the influence of oil composition on CO_2 displacement is important. In this study, the impact of oil composition was examined by analyzing changes in crude oil resulting from CO_2–oil interactions. This was achieved through SARA fraction analysis of produced oil obtained from slim tube experiments at each injection pressure. **Figures 9** and **10** present the changes in the wt.% of resins and asphaltene fractions from the produced oil of RDG and JTB samples, respectively. Notably, JTB crude oil is classified as heavier than the RDG and initially contains a higher concentration of asphaltenes. Interestingly, the MMP for RDG at 70°C is considerably higher than at 90°C. The data in both tables reveal a general trend of decreasing resin and asphaltene content with increasing CO_2 injection pressure. Although JTB oil exhibits a higher initial asphaltene content than RDG, it also possesses a higher resin fraction.

Asphaltenes are among the most complex constituents of crude oil, characterized by their insolubility in normal alkanes and composed of highly polar, structurally intricate molecules (**Fakher et al., 2020; Soleymanzadeh et al., 2019**). In contrast, resins contribute significantly to the stability of crude oil by exhibiting both polar and non-polar properties, enabling them to function as peptizing and bridging agents that connect polar asphaltenes with non-polar hydrocarbon components (**Miadonye & Evans, 2010**). The observed decline in asphaltene content with increasing injection pressure indicates potential asphaltene deposition within the porous media. This phenomenon is likely driven by a concurrent reduction in resin concentration, which weakens the peptizing effect necessary to maintain asphaltene dispersion. As reported by **Deo & Parra (2012)**, repeated between CO_2 - crude oil interactions can result in asphaltene precipitation within the reservoir. Such deposition may adversely affect both the efficiency of oil recovery and the MMP.

Figure 9 shows that the resin and asphaltene content of RDG oil at 70°C (see **Figure 9a**) decrease more significantly than at 90°C (see **Figure 9b**). The decreasing of resin and asphaltene also indicates that temperatures also affect the change of SARA composition during the CO_2 flooding process, which can cause the possibility of the asphaltene precipitation phenomenon in porous media. It can be seen that at 70°C, the resin reduces from 3.9 wt.% at initial composition (before CO_2 was injected) to 1.3 wt.% at a CO_2 injection pressure of 4000 Psi. The asphaltene fraction also reduces from 1.8 wt.% to 0.9 wt. % at 4000 Psi. The reduction in resin and asphaltene content at 70°C is more pronounced compared to 90°C, resulting in lower oil recovery at the lower temperature. A similar finding was also reported by **Hagedorn & Orr (1994)** that crude oils containing substantial amounts of multi-ring aromatic compounds face challenges in achieving miscibility with CO_2. These aro-

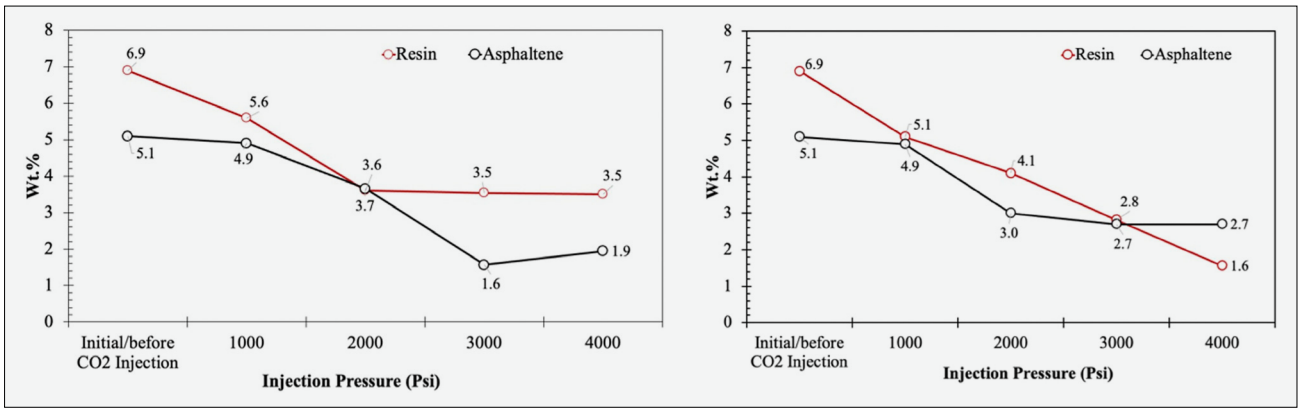


Figure 10. Resin and Asphaltene Fraction (wt.%) of RDG Sample at (a) 70°C and (b) 90°C in Varying Injection Pressures

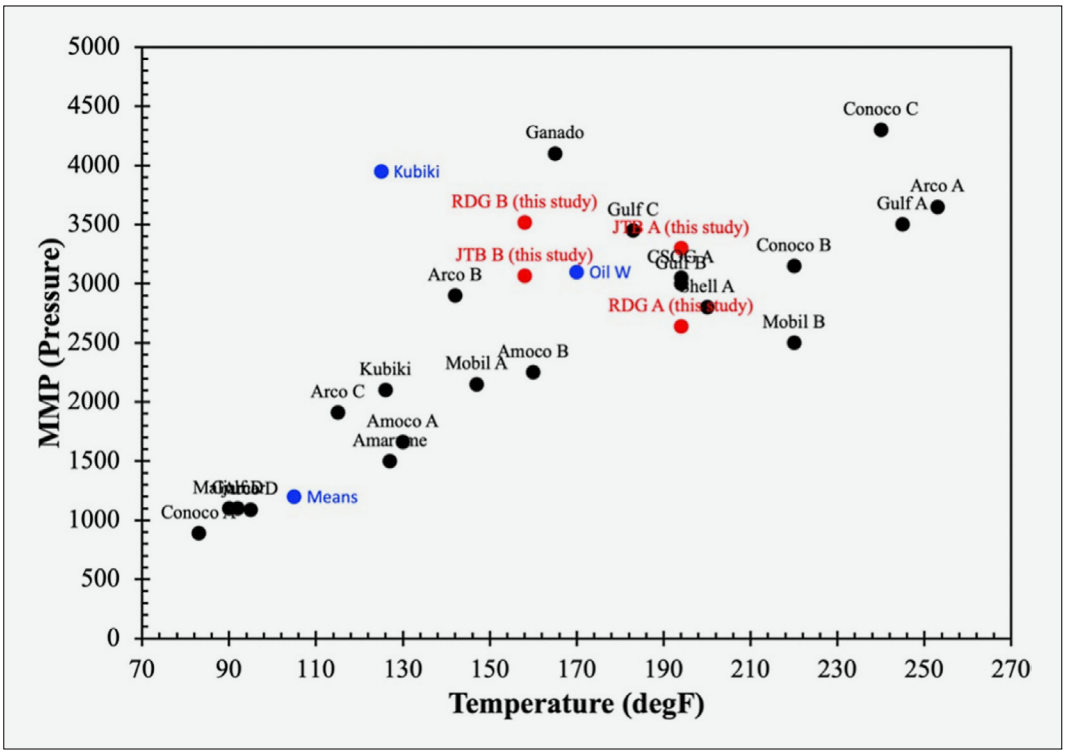


Figure 11. Minimum Miscibility Pressure (MMP) oil fields data vs. Reservoir Temperatures (summarized from **Hagedorn & Orr, 1994 and Orr & Silva, 1987**)

matic compounds are not easily extracted by dense CO_2, leading to decreased oil recovery in slim tube tests at a given pressure and consequently requiring a higher MMP. As shown in **Table 3**, RDG sample contains a higher proportion of aromatic components compared to JTB crude oil.

Figure 10 also presents the resin and asphaltene content of JTB oil at 70°C (see **Figure 10a**) and 90°C (see **Figure 10b**) under varying pressures. Although the initial asphaltene fraction in JTB is higher than in RDG, the resin content in JTB is also significantly greater. In contrast, the initial aromatic fraction in JTB oil is lower than in RDG oil. As previously discussed, dense CO_2 has limited ability to extract multi-ring aromatic compounds. Due to its high resin and lower aromatic content, JTB crude exhibits greater stability compared to RDG. Consequently, asphaltene precipitation is more likely to occur in RDG oil upon CO_2 injection, despite RDG having a higher API gravity. This difference results in lower oil recovery from CO_2 flooding process in the RDG crude than in the JTB crude.

The findings indicate that variations in pressure, temperature, and crude oil composition resulting from CO_2 injection significantly influence the efficiency of CO_2 displacement. These factors, in turn, affect both oil recovery and the determination of the MMP. The performance of the displacement process is closely linked to the collective behaviour and proportion of all crude oil components – saturates, aromatics, resins, and asphaltenes – as shown in **Table 3**, rather than being at-

tributed to a single component alone. The findings are also aligned with the work by **Fan et al. (2024)** that investigated the effect of some complex components in the interaction of the CO_2 and crude oil by the insight of convolutional neural networks.

4. Conclusions

This study investigated the effect of temperature and oil compositions on swelling-extraction behaviour and CO_2 displacement mechanisms. Understanding the influence of temperatures and oil compositions on CO_2 EOR fundamental mechanisms such as swelling-extraction and CO_2 flow mechanisms in porous media is vital to optimizing CO_2 flooding process implementation. This study is expected to provide more data on the swelling and extraction mechanisms for implementing CO_2 flooding at high reservoir temperatures. Moreover, this study is also expected to provide insight into understanding the effect of different parameters such as, temperatures and oil compositions, on CO_2 flow mechanisms in porous media and optimizing CO_2 flooding process implementation. The main conclusions from the research that has been carried out are shown below.

1. An increase in temperature led to a reduction in the oil swelling rate. This effect is attributed to the decreased solubility of CO_2 at elevated temperatures, resulting from the increased kinetic energy of CO_2 molecules, which weakens the attractive interactions between the gas and crude oil molecules.
2. The pressure point at which the oil starts to shrink significantly is strongly affected by both the temperature and composition of the oil. At 70°C, the swelling factor indicates a more pronounced oil shrinkage compared to that at 90°C. This suggests that CO_2 exhibits greater efficiency in extracting hydrocarbon components at lower temperatures under the same pressure conditions. Generally, hydrocarbon extraction by CO_2 improves with increasing CO_2 density and pressure. Since lower temperatures typically result in higher CO_2 density, the extraction rate tends to increase more rapidly with pressure at cooler conditions. JTB oil has a more significant decrease in the condensation-extraction region than RDG oil, although JTB has a higher molecular weight or is heavier than RDG oil. It shows that the amount of extraction also depends on the composition of the oil, particularly the fraction of the oil that includes components that are soluble in dense CO_2.
3. The RDG crude oil contains a greater proportion of aromatic compounds compared to the JTB sample. Aromatics are typically nonpolar hydrocarbons characterized by ring structures with multiple carbon double bonds. These molecular features tend to reduce the solubility of CO_2 in crude oil.
4. Higher temperatures led to an improvement in oil recovery, primarily because increasing temperature causes a reduction in crude oil viscosity, thereby enhancing fluid mobility.
5. Alterations in crude oil composition resulting from interactions with CO_2 significantly influence displacement efficiency. As CO_2 injection pressure increases, the contents (wt.%) of resins and asphaltenes in the crude oil tend to decline. The observed reduction in asphaltene content with rising pressure suggests that asphaltene precipitation occurs within the porous medium. This precipitation is further linked to the decrease in resin content, which normally functions as a peptizing agent that maintains asphaltene stability in crude oil.

Acknowledgement

This work was funded by the Research and Community Service Institute (LPPM), Universitas Trisakti. All experimental work was carried out at the Enhanced Oil Recovery (EOR) Laboratory of Pertamina Research and Technology Innovation (RTI), PT. Pertamina (Persero), Indonesia.

5. References

Abdurrahman, M., Bae, W., & Permadi, A. K. (2019). Determination and evaluation of minimum miscibility pressure using various methods: Experimental, visual observation, and simulation. *Oil and Gas Science and Technology*, 74. https://doi.org/10.2516/ogst/2019028

Abdurrahman, M., Permadi, A. K., & Bae, W. S. (2015). An improved method for estimating minimum miscibility pressure through condensation-extraction process under swelling tests. *Journal of Petroleum Science and Engineering*, 131, 165–171. https://doi.org/10.1016/j.petrol.2015.04.033

Ashoori, S., Sharifi, M., Masoumi, M., & Mohammad Salehi, M. (2017). The relationship between SARA fractions and crude oil stability. *Egyptian Journal of Petroleum*, 26 (1), 209–213. https://doi.org/10.1016/j.ejpe.2016.04.002

Deo, M., Parra, M. (2012). Characterization of carbon-dioxide-induced asphaltene precipitation. *Energy and Fuels*, 26 (5), 2672–2679. https://doi.org/10.1021/ef201402v

Dindoruk, B., Johns, R., & Orr, F. M. (2020). Measurement of Minimum Miscibility Pressure: A State of the Art Review. *SPE Improved Oil Recovery Conference*. SPE-200462-MS. https://doi.org/10.2118/200462-MS

Fakher, S., Ahdaya, M., Elturki, & M., Imqam, A. (2020). Critical review of asphaltene properties and factors impacting its stability in crude oil. *Journal of Petroleum Exploration and Production Technology*. Vol. 10, Issue 3, pp. 1183–1200. Springer. https://doi.org/10.1007/s13202-019-00811-5

Fakher, S. and Imqam, A. (2020). A data analysis of immiscible carbon dioxide injection applications for enhanced oil recovery based on an updated database. *SN Applied Sciences*, 2 (3). https://doi.org/10.1007/s42452-020-2242-1

Fan, J., Yao, M., Fan, Z., Chen, P., He, K., & Wang, D. (2024). Unveiling the Effect of Complex Components on CO_2 –

Oil Minimum Misciblity Pressure: Insight from Deep Convolutional Neural Networks. *Energy & Fuels*, 38, 6116 – 6126. ACS Publications. https://doi.org/10.1021/acs.energyfuels.3c04709

Ghorbani, M., Momeni, A., Safavi, S., & Gandomkar, A. (2014). Modified vanishing interfacial tension (VIT) test for CO_2 - oil minimum miscibility pressure (MMP) measurement. *Journal of Natural Gas Science and Engineering*, 20, 92–98. https://doi.org/10.1016/j.jngse.2014.06.006

Glaso, O. (1990). Miscible Displacement: Recovery Tests With Nitrogen. *SPE Reservoir Engineering,* 5 (01), 61-68. SPE-17378-PA. https://doi.org/10.2118/17378-PA

Hagedorn, K. D. and Orr, F. M. (1994). Component Partitioning III CO_2 / Crude Oil Systems: Effects of Oil Composition on CO_2 Displacement Performance. *SPE Advanced Technology,* 2 (02), 177 – 184. SPE-25169-PA. https://doi.org/10.2118/25169-PA

Hand, J. L. and Pinczewski, W. V. (1990). Interpretation of Swelling / Extraction Tests. *SPE Reservoir Engineering*, 5 (04), 595-600. SPE-19471-PA. https://doi.org/10.2118/19471-PA

Hartono, K. F., Permadi, A. K., & Prakoso, S. (2021). The Prospect of CO_2 Flooding and Its Potential Application to Indonesian Mature Fields. *AIP Conference Proceeding* 2363, 020008. https://doi.org/10.1063/5.0061058

Hartono, K. F., Permadi, A. K., Siagian, U. W. R., Hakim, A. L. L., Paryoto, S., Resha, A. H., Adinugraha, Y., & Pratama, E. A. (2024). The Impacts of CO_2 Flooding on Crude Oil Stability and Recovery Performance. *Journal of Petroleum Exploration and Production Technology*, 14, 107 – 123. https://doi.org/10.1007/s13202-023-01699-y

Holm, L. W. and Josendal, V. A. (1974). Mechanisms of Oil Displacement by Carbon Dioxide. *Journal of Petroleum Technology,* 26 (12), 1427-1438. SPE-4736-PA. https://doi.org/10.2118/4736-PA

Hudgins, D. A., Uave, F. M., & Chung, F. T. H. (1990). Nitrogen Miscible Displacement of Light Crude Oil: A Laboratory Study. *SPE Reservoir Engineering,* 5 (01), 100-106. SPE-17372-PA. https://doi.org/10.2118/17372-PA

Kokal, S. L. and Sayegh, S. G. (1995). Asphaltenes: The Cholesterol of Petroleum. SPE-29787-MS. https://doi.org/10.2118/29787-MS

Lashkarbolooki, M. and Ayatollahi, S. (2018). Experimental investigation on CO_2 - light crude oil interfacial and swelling behavior. *Chinese Journal of Chemical Engineering*, 26 (2), 373–379. https://doi.org/10.1016/j.cjche.2017.07.010

Maqbool, T., Srikiratiwong, P., & Fogler, H. S. (2011). Effect of temperature on the precipitation kinetics of asphaltenes. *Energy & Fuels*, 25 (2), 694–700. https://doi.org/10.1021/ef101112r

Miadonye, A. and Evans, L. (2010). The solubility of asphaltenes in different hydrocarbon liquids. *Petroleum Science and Technology*, 28 (14), 1407–1414. https://doi.org/10.1080/10916460902936960

Orr, F. M. and Silva, M. K. (1987). Effect of Oil Composition on Minimum Miscibility Pressure-Part 2: Correlation. *SPE Reservoir Engineering,* 2 (04), 479-491. SPE-14150-PA. https://doi.org/10.2118/14150-PA

Permadi, A. K., Pratama, E. A., Hakim, A. L. L., Widi, A. K., & Abdassah, D. (2021). The effect of carbonyl and hydroxyl compounds addition on CO_2 injection through hydrocarbon extraction processes. *Applied Sciences (Switzerland)*, 11(1), 1–11. https://doi.org/10.3390/app11010159

Rezk, M. G. and Foroozesh, J. (2019). Phase behavior and fluid interactions of a CO_2 - Light oil system at high pressures and temperatures. *Heliyon*, 5 (April), e02057. https://doi.org/10.1016/j.heliyon.2019.e02057

Santos, D., Amaral, M., Filho, E. B. M., Dourado, R. S., Coutinho, J. A. P., Borges, G. R., Franceschi, E., & Dariva, C. (2019). Revisiting the methodology for asphaltenes precipitation. *Journal of Petroleum Science and Engineering*, 178, 778–786. https://doi.org/10.1016/j.petrol.2019.03.074

Siagian, U. W. R. and Grigg, R. B. (1998). The Extraction of Hydrocarbons from Crude Oil by High Pressure CO_2. *SPE/DOE Improved Oil Recovery Symposium*. SPE-39684-MS. https://doi.org/10.2118/39684-MS

Silva, M. K. and Orr Jr, F.M. (1987). Effect of Oil Composition on Minimum Miscibility Pressure-Part 1: Solubility of Hydrocarbons in Dense CO_2. *SPE Reservoir Engineering,* 2 (04), 468-478. SPE-14149-PA. https://doi.org/10.2118/14149-PA

Simon R. and Graue, D. J. (1965). Generalized Correlations for Predicting Solubility, Swelling, and Viscosity Behavior of CO_2 - Crude Oil Systems. *Journal of Petroleum Technology*, 17 (01), 102-106. SPE-917-PA. https://doi.org/10.2118/917-PA

Soleymanzadeh, A., Yousefi, M., Kord, S., & Mohammadzadeh, O. (2019). A review on methods of determining onset of asphaltene precipitation. *Journal of Petroleum Exploration and Production Technology*, Vol. 9, Issue 2, pp. 1375–1396. Springer Verlag. https://doi.org/10.1007/s13202-018-0533-5

Svrcek, W. Y. and Mehrotra, A. K. (1982). Gas Solubility, Viscosity, and Density Measurements for Athabasca Bitumen. *Journal of Canadian Petroleum Technology*, 21 (04), PETSOC-82-04-02. https://doi.org/10.2118/82-04-02

Tsau, J. S., Bui, L. H., & Willhite, G. P. (2010). Swelling / Extraction Test of a Small Sample Size for Phase Behavior Study. *SPE Improved Oil Recovery Symposium*. SPE 129728-MS. https://doi.org/10.2118/129728-MS

Wang, S., Chen, S., & Li, Z. (2016). Characterization of Produced and Residual Oils in the CO_2 Flooding Process. *Energy & Fuels*, 30 (1), 54–62. https://doi.org/10.1021/acs.energyfuels.5b01828

Wei, B., Gao, H., Pu, W., Zhao, F., Li, Y., Jin, F., Sun, L., & Li, K. (2017). Interactions and phase behavior between oleic phase and CO_2 from swelling to miscibility in CO_2 - based enhanced oil recovery (EOR) process: A comprehensive visualization study. *Journal of Molecular Liquids*, 232, 277–284. https://doi.org/10.1016/j.molliq.2017.02.090

Welker, J.R. (1963). Physical Properties of Carbonated oils. *Journal of Petroleum Technology,* 15 (08), 873-876. SPE-567-PA. https://doi.org/10.2118/567-PA

Yang, C. and Gu, Y. (2006). Diffusion coefficients and oil swelling factors of carbon dioxide, methane, ethane, propane, and their mixtures in heavy oil. *Fluid Phase Equilib-*

ria, 243(1–2), 64–73. https://doi.org/10.1016/j.fluid.2006.02.020

Yellig, W. F. (1982). Carbon Dioxide Displacement of a West Texas Reservoir Oil. *SPE Journal,* 22 (06), 805-815. SPE-9785-PA. https://doi.org/10.2118/9785-PA

Yellig, W. F. and Metcalfe, R. S. (1980). Determination and Prediction of CO_2 Minimum Miscibility Pressures. *Journal of Petroleum Technol*ogy, 32 (01): 160-168. SPE-7477-PA. https://doi.org/10.2118/7477-PA

Zhang, K., Jia, N., Zeng, F., Li, S., & Liu, L. (2019). A review of experimental methods for determining the Oil–Gas minimum miscibility pressures. *Journal of Petroleum Science and Engineering*, 183 (July), 106366. https://doi.org/10.1016/j.petrol.2019.106366

SAŽETAK

Eksperimentalno ispitivanje utjecaja temperature i sastava nafte na bubrenje nafte izazvano istiskivanjem s CO_2, mehanizme ekstrakcije i karakteristike istiskivanja

Povećanje iscrpka nafte utiskvanjem CO_2 ima nekoliko prednosti, uključujući smanjenje viskoznosti sirove nafte, smanjenje međufazne napetosti i povećanje volumena nafte bubrenjem. Iako su mehanizmi bubrenja i istiskivanja nafte u sustavima CO_2-sirova nafta puno proučavani, kombinirani učinci temperature i sastava nafte na te mehanizme – i njihov utjecaj na učinkovitost istiskivanja CO_2 u poroznim medijima – još uvijek nisu dovoljno poznati, posebice pri visokim temperaturama ležišta. Stoga se u ovome radu istražuje kako temperatura i sastav sirove nafte utječu na ponašanje bubrenja i istiskivanje te učinkovitost istiskivanja s CO_2. Za procjenu fenomena bubrenja i istiskivanja provedeni su PVT testovi u uvjetima visokoga tlaka i visoke temperature (HPHT), dok je procjena iscrpka nafte napravljena ispitivanjem metodom istiskivanja nafte iz cijevi maloga promjera (engl. *slim tube experiments*). Ispitivanja su provedena na dvije lake otplinjene nafte s indonezijskoga polja pri temperaturi od 70 °C i 90 °C i različitim tlakovima utiskivanja. Analiza sastava proizvedenih nafti napravljena je plinskom kromatografijom (engl. *Gas Chromatography*, GC), a rezultati su interpretirani prema SARA klasifikaciji (zasićeni ugljikovodici, aromati, smole, asfalteni). Rezultati pokazuju da niže temperature povećavaju učinkovitost istiskivanja s CO_2 zbog veće gustoće CO_2, što dovodi do izraženijega efekta bubrenja i mješljivosti. Mješljivost je uočena unutar područja istiskivanja, što naglašava ulogu istiskivanja ugljikovodika u mehanizmu mješljivosti. Utvrđeno je da više temperature povećavaju iscrpak nafte, primarno zbog smanjenja viskoznosti. Osim toga, povećanje tlaka utiskivanja CO_2 smanjilo je sadržaj smole i asfaltena u proizvedenoj nafti, uz utvrđeno taloženje asfaltena u poroznome mediju, posebice na nižim temperaturama. Ovi rezultati daju vrijedan uvid u to kako temperatura i sastav nafte utječu na interakcije CO_2 i nafte te omogućuju učinkovitiju primjenu povećanja iscrpka nafte utiskivanjem CO_2 pri povišenim temperaturama ležišta.

Ključne riječi:
povećanje iscrpka nafte utiskivanjem CO_2, mehanizam bubrenja – istiskivanja, mješljivost, taloženje asfaltena, iscrpak nafte, SARA frakcije

Author's contribution

Kartika F. Hartono (Dr.): conceptualization, methodology, validation, formal analysis, investigation, writing – original draft, and visualization. **Asep K. Permadi (Prof.)**: conceptualization, formal analysis, writing – review & editing, and supervision. **Utjok. W. R. Siagian (Dr.)**: conceptualization, formal analysis. **Andri, L. L. Hakim (Dr.)**: conceptualization, formal analysis, writing – review & editing. **Sumadi Paryoto**: resources, methodology, project administration. **Ahlul H. Resha:** resources, methodology, and project administration. **Syaeful A. Satya**: methodology, and project administration. **Reno Pratiwi (Dr.), Maman Djumantara, Dina A. Chusniah:** writing – review & editing.
All authors have read and agreed to the published version of the manuscript.

RGNZ/MGPB

Seismogenic Analysis of the 2023 Mw6.9 Murghob Earthquake, Tajikistan, based on Multi-Track InSAR and Modelling

Rudarsko-geološko-naftni zbornik
(The Mining-Geology-Petroleum Engineering Bulletin)
DOI: 10.17794/rgn.2026.3.5

Original scientific paper

Rana Jaladara[1], Naufal Setiawan[1]*, Erlan Sumanjaya[2]

[1] *Geomatic Engineering, Faculty of Mineral Technology and Energy, Universitas Pembangunan Nasional "Veteran" Yogyakarta, Sleman 55283, Indonesia.*

[2] *Department of Geodesy and Geomatics Engineering, Faculty of Engineering, University of Lampung, Bandar Lampung 35141, Indonesia.*

Abstract

This study investigates the 2023 Murghob Earthquake in Tajikistan (Mw 6.9) using modelling and multi-track InSAR techniques to analyze the surface deformation and fault dynamics. The modelling approach using Pyrocko produced observation, model, and residual images, each revealing aspects of the fault geometry and rupture characteristics. Our study identified a dominant right-lateral strike-slip event, with a calculated fault strike of 128°, dip of 67°, and rake of 177°, differing slightly from previous studies. Furthermore, the modelling also suggested mixed-slip faulting, incorporating normal faulting components along the Sarez-Karakul Fault system and the Sarez-Murghab Thrust system. These findings indicate a more complex rupture process than previously emphasised in other models. Multi-track InSAR analysis supported these findings by providing high-resolution measurements of horizontal (dH) and vertical (dV) displacements. The horizontal displacements revealed significant strike-slip movements (-0.53 to 0.12 meters) along the Aksu Murghab Fault system. Meanwhile, the vertical displacements indicated substantial uplift (-0.13 and 0.32 meters), likely due to normal and thrust faulting interactions. The results highlight the complexity of the region's tectonic setting, which is influenced by multiple fault systems, including the Sarez-Karakul and Aksu Murghab faults. The study underscores the importance of integrating various geophysical methods to understand earthquake mechanisms better and improve seismic hazard assessments in tectonically active regions like Tajikistan.

Keywords:
InSAR, Multi-track InSAR, earthquake modelling, 2023 Murghob Earthquake

1. Introduction

Tajikistan is situated at the collision spot of the Indian Plate and the Eurasian Plate, moving at a speed of 20-30 mm/year (**Avouac & Tapponnier, 1993; Zhou et al., 2016**). This ongoing plate collision has formed mountainous terrain, such as the Himalayan Mountains and the Tibetan (**Tapponnier et al., 2001**). Due to frequent earthquakes stemming from this collision, Tajikistan is considered one of the seismically dangerous regions (**Singh & Ghosh, 2019**). The Pamir Mountains region, commonly called the 'Pamir Fault,' stands out as one of Tajikistan's most significant seismic zones (**Avouac & Tapponnier, 1993; Singh & Ghosh, 2019; Tapponnier et al., 2001**).

On February 23, 2023, a 6.9 in magnitude earthquake struck Murghob, Gorno-Badakhshan, Tajikistan, occurring at 00:37:38 UTC. According to information provided by the United States Geological Survey (USGS), the earthquake's epicentre was located in a seismic zone at coordinates 38.055° N, 73.229° E, at a depth of 9 km. In contrast, the Global Centroid Moment Tensor Project (GCMT) reported the recent earthquake's epicentre at 38.16° N, 73.32° E, with a depth of 14.5 km. This earthquake was notably intense, registering a value of 9 on the intensity scale and 7 on the shaking intensity scale (**USGS Earthquake Hazard Program, 2024**).

From the beginning of 2023 until March 3, 2023, the USGS recorded approximately 33 earthquakes in the area, ranging in magnitudes from 4 to 5. This region has a history of significant earthquakes, such as the one on December 7, 2015, measuring 7.2 in magnitude, and another on February 18, 1911, with a magnitude of 7.3 (USGS, 2023). The Sarez-Karakul Fault and the Aksu Murghab Fault are among the fault systems responsible for the seismic activity in the region. The Sarez-Karakul Fault currently remains active as a sinistral fault system occupying the meridian axis of the Pamir. On the other hand, the Aksu-Murghab Fault system constitutes a dextral active fault zone located southeast of the Pamir. Additionally, the Tanymas Thrust system and the Sarez-Murghab Thrust system exists (see **Figure 1**) (**Avouac & Tapponnier, 1993**).

* Corresponding author: Naufal Setiawan
e-mail address: naufal.setiawan@upnyk.ac.id
Received: 15 April 2025. Accepted: 3 November 2025.
Available online: 14 May 2026

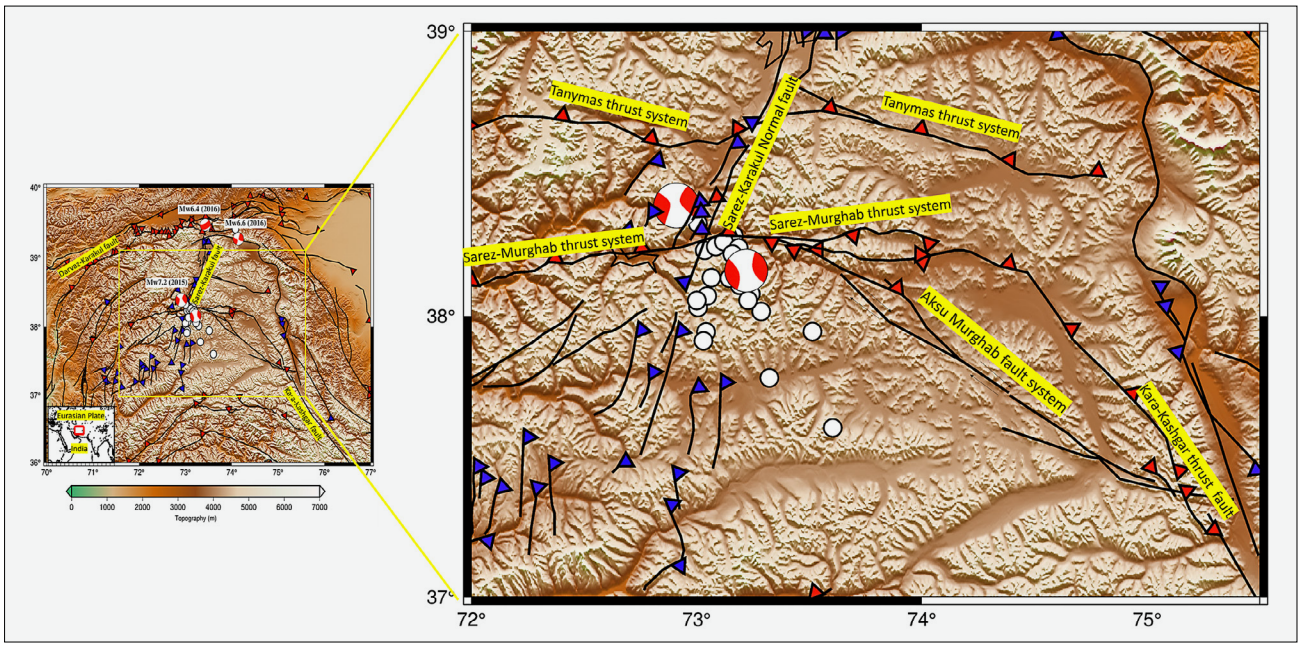


Figure 1. Tectonic setting around the 2023 Murghob earthquake. The white circles indicate aftershock events over a week. The two beach balls represent the epicentres of the 2015 Mw 7.2 and 2023 Mw 6.9 earthquakes. The lines with red triangles represent thrust faults, while the lines with blue triangles represent normal faults. The yellow box highlights the area of interest.

In geodesy, various methods are commonly employed to observe surface deformation, including the Global Navigation Satellite System (GNSS) method (**Abidin et al., 2009**) and the Interferometric Synthetic Aperture Radar (InSAR) method (**Massonnet & Feigl, 1998**). InSAR is more suitable for earthquake areas because the affected areas are often large, making GNSS less efficient (**He et al., 2023**). Moreover, GNSS observations are limited to specific receiver station locations.

Interferometric Synthetic Aperture Radar (InSAR) is a technique used to depict surface topography and surface displacement by using the phase values from two or more Synthetic Aperture Radar (SAR) images (**Furuya, 2011**). Radar waves can penetrate clouds and are effective in various weather conditions, including nighttime. The precision of InSAR can reach the centimetre level or better. InSAR works by utilizing two SAR images of the same Area of Interest (AOI) taken at different times, which are then processed to obtain range values based on phase differences. These elevation differences determine whether an area has experienced upward or downward movement.

The detection of changes on the Earth's surface using InSAR (Interferometric Synthetic Aperture Radar) has been rapidly advancing since the early 1990s. The InSAR technique calculates the interferometric phase differences between two Synthetic Aperture Radar (SAR) images, revealing changes in the terrain between the ground and the SAR instrument (**Massonnet & Feigl, 1998**). One of the pioneering studies using the InSAR method to detect changes on the Earth's surface caused by an earthquake in Landers, California. The study utilized the European Remote-Sensing Satellite-1 (ERS-1) and provided valuable insight into the potential of InSAR for earthquake monitoring and surface deformation analysis (**Massonnet et al., 1993**). Their findings significantly contributed to developing the InSAR technique as a powerful tool for studying seismic events and their impacts on the Earth's surface. Furthermore, earthquakes with a magnitude greater than 5.5 Mw and a shallow depth of less than 10 km tend to be detectable through InSAR processing techniques (**Funning & Garcia, 2019**).

Previous research on the 2023 6.9 Mw Murghob earthquake using Sentinel-1 data has yielded varied insight. The first study (**Shi, et al., 2023**) determined the total moment and identifying a 28.1° strike value based on modelling from Sentinel-1 InSAR. Furthermore, they deduced that the 7.2 Mw Sarez earthquake in 2015 initiated the 6.9 Mw Murghob earthquake. Meanwhile, (**Chen et al., 2024**) reported a dextral strike-slip fault mechanism with a maximum displacement of 0.7 meters, determined through InSAR inversion.

In this study, we investigate the 6.9 Mw Murghob earthquake using different approaches. First, we processed ascending and descending InSAR pairs utilizing Sentinel Application Platform (SNAP), followed by Forward Modelling with Pyrocko (**Heimann et al., 2017**) using the Bayesian Bootstrap Optimization (BABO) algorithm. Another notable difference is the Digital Elevation Model (DEM) used for geocoding. While the previous study (**Shi et al., 2023**) employed the Shuttle Radar Topography Mission (SRTM) DEM with a 90-meter resolution, our study implements the SRTM DEM with a

resolution of 30 meters. The accuracy of terrain correction during the InSAR processing step heavily depends on the spatial resolution of the DEM. Consequently, our results are anticipated to be more accurate, given our enhanced capability to mitigate topographic phase components. Therefore, our modelling approach supposedly has greater accuracy. Furthermore, we implement multi-track InSAR to the 6.9 Mw Murghob earthquake. Multi-Track InSAR demonstrates notable efficiency in thoroughly measuring complex displacements by decomposing surface motion into horizontal (dH) and vertical (dV) components. This methodology has been effectively utilized in examining three-dimensional displacement fields, as demonstrated in the study of the Turkey Earthquake 2023 (**Liu et al., 2024**). Previous studies have typically relied on a single InSAR pair to derive earthquake parameters, which limits the ability to resolve three-dimensional displacement fields. In this study, we address this gap by employing a multi-track InSAR methodology to enhance the analysis of surface deformation associated with the Murghob earthquake. This approach is expected to enable a more comprehensive understanding of fault dynamics by systematically decomposing line-of-sight (LOS) displacements into their horizontal and vertical components.

2. Methods

This research primarily utilizes secondary data sourced from the official website of the European Space Agency (ESA). Specifically, it employs satellite imagery from Sentinel-1A Single Look Complex (SLC) data for descending and ascending orbits. These images were accessed via the Copernicus Open Access Hub (https://scihub.copernicus.eu/dhus/#/home). Detailed information regarding the Interferometric Synthetic Aperture Radar (InSAR) data used for ascending and descending scenes in this study is provided in **Table 1**. The flowchart illustrates our research's main steps: InSAR processing, earthquake modelling, and multi-track InSAR processing (see **Figure 2**).

2.1. InSAR Processing

We utilised Sentinel Application Platform (SNAP), an open-source tool to process Sentinel-1 images, downloadable from the European Space Agency's (ESA) official website. One of SNAP's key advantages is its user-friendly graphical user interface (GUI), simplifying image processing. The processing stages include co-registration, interferogram formation, phase unwrapping, and terrain correction. Co-registration is a crucial step that aligns images by utilizing statistical values to achieve sub-pixel accuracy in spatial matching between them. This process consists of two main steps: the Apply Orbit Information step, which employs precise orbit files, and the Back Geocoding step, which uses the Shuttle Radar Topography Mission (SRTM) Digital Elevation Model (DEM) with a 1 arc-second resolution.

Table 1. Scene used for InSAR processing

Scene	Date Acquisition	Heading	Path and Frame
Ascending reference	February 3, 2023	346.6836°	Path 100, Frame 122
Ascending secondary	March 23, 2023	346.6830°	Path 100, Frame 122
Descending reference	February 21, 2023	193.2598°	Path 5, Frame 466
Descending secondary	March 5, 2023	193.2598°	Path 5, Frame 466

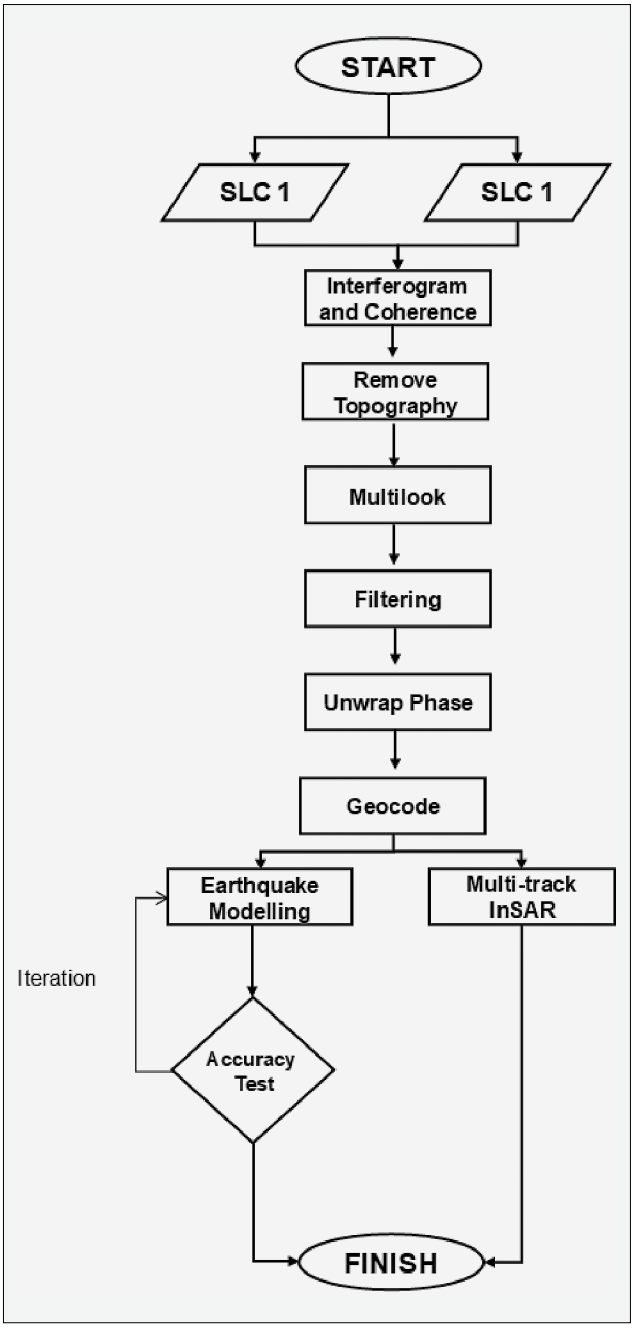


Figure 2. Research flowchart

An interferogram is generated by multiplying the reference image with the complex conjugate of the secondary image, where the amplitudes of both images are combined, and the resulting phase reflects the phase difference between the two images. The interferometric phase at each pixel of the SAR image is determined by the difference in the travel paths of the radar signals between the two SAR acquisitions to the resolution cell under consideration. The calculated interferogram exhibits phase variations (ΔØinsar) due to several contributing factors, including flat Earth phase (ΔØorb), topographic phase (ΔØtopo), atmospheric phase (ΔØatm), phase noise (ΔØnoise), and surface deformation (ΔØdefo). These components are represented mathematically, as shown in **Equation 1**.

$$\Delta\emptyset insar = \Delta\emptyset orb + \Delta\emptyset topo + \\ + \Delta\emptyset atm + \Delta\emptyset noise + \Delta\emptyset\, defo \quad (1)$$

Factors other than surface deformation (ΔØdefo) are eliminated to extract the displacement or vertical change value. The process begins with subtracting the Flat Earth Phase, which is calculated using orbit metadata and removed from the interferometric phase. Subsequently, the Topographic Phase is eliminated by differencing the interferogram data with the Digital Elevation Model (DEM). The atmospheric phase, comprising tropospheric and ionospheric components (**Furuya, et al., 2017; Setiawan & Furuya, 2021; Setiawan & Furuya, 2024**), is considered. However, for certain cases, such as large earthquakes, the phase changes due to atmospheric effects are significantly smaller than the deformation signal **(He et al., 2023**). To further reduce noise, multilooking and filtering are applied. Goldstein Phase Filtering (**Goldstein & Werner, 1998**) filters the data. Since the phase in interferometry is inherently ambiguous and confined to the range of 2π, a phase unwrapping process is necessary to connect the interferometric phase with the actual topographic height. Additionally, a multilooking process is performed after interferogram formation to optimise phase unwrapping. The multi-looking parameters used are 6 for range and 2 for azimuth. The Statistical-Cost, Network-Flow Algorithm for Phase Unwrapping (SNAPHU) (**Chen & Zebker, 2001**) is utilised for phase unwrapping. After the unwrapping process, Phase-to-Displacement Conversion and terrain correction are performed. The Phase-to-Displacement Conversion transforms the image data, measured initially in radians, into metric units (**Equation 2**). Meanwhile, the Terrain Correction process involves geocoding the image by correcting geometric distortions using the Digital Elevation Model (DEM), resulting in a georeferenced product.

$$d = -\frac{\lambda \Delta\emptyset_d}{4} \quad (2)$$

Where d is the surface displacement, λ is the wavelength, υ is Poisson's ratio, $\emptyset_d$ is the phase different.

2.2. Earthquake Modelling

Earthquake modelling in this study is conducted using Pyrocko (https://git.pyrocko.org/pyrocko), an open-source software designed for applications in seismology and geophysics. Built on the Uniplexed Information Computing System (UNIX), Pyrocko offers diverse toolboxes for analyzing and processing seismic and geophysical data. It is particularly suited for studying Earth's movements, earthquakes, and geodynamics (**Heimann et al., 2017**).

Kite, one of the toolboxes available in Pyrocko, can be used to process data from the Sentinel Application Platform (SNAP). Specifically, Kite is designed to process and analyze surface displacement data derived from InSAR (**Isken et al., 2017**). Within Kite, a data downsampling process is performed to facilitate modelling. The quadtree sampling methodology efficiently manages high-resolution Interferometric Synthetic Aperture Radar (InSAR) data. This approach subdivides the dataset into a hierarchical arrangement of tiles based on spatial variability, as illustrated in **Figure 3**. The epsilon parameter modulates the sensitivity of tile refinement, thereby ensuring that regions exhibiting significant variability are sampled at elevated resolutions, while uniform areas are represented by a smaller number of larger tiles. Parameters such as minimum tile size and maximum tile size establish the constraints for tile dimensions, thereby achieving a balance between resolution and computational efficiency. This adaptive technique facilitates effective data processing while maintaining critical spatial details, particularly in regions characterized by complex surface displacement patterns.

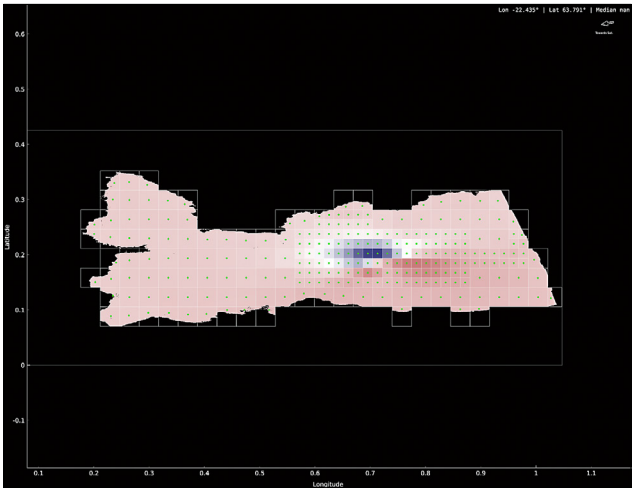


Figure 3. Downsampling of InSAR data using the Kite module. The figure illustrates how interferogram data points are reduced to representative subsets, allowing efficient modelling while preserving the main deformation signal.

Earthquake modelling in this study is performed using the Grond (**Heimann et al., 2018**) toolbox, with data imported from the Kite toolbox. To conduct modelling utilizing Pyrocko, it is essential to acquire two distinct

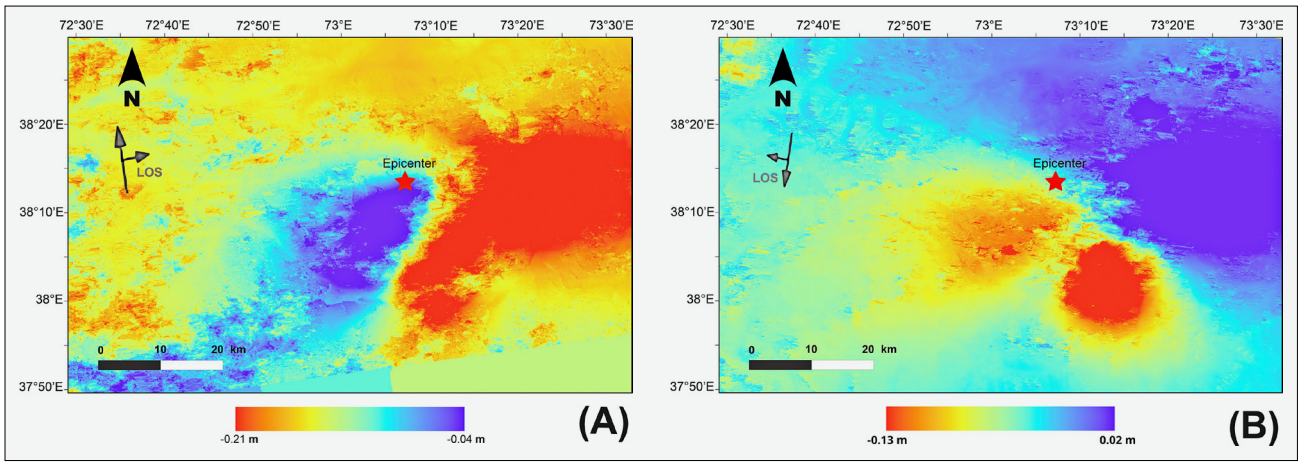


Figure 4. Unwrapped interferograms reveal coseismic deformation from the Murghob earthquake: (a) ascending and (b) descending Sentinel-1 tracks. Changes in colour gradients point to displacements in the line of sight, predominantly with maximum alterations occurring near the epicentral region. Negative measurements reveal ground displacement moving away from the satellite (subsidence), while positive measurements reflect an upward shift (uplift).

scenes, specifically those characterized by ascending and descending trajectories within the earthquake-affected region. The modelling employs a rectangular finite fault model, requiring the input of various parameters. Eight iterations are conducted, progressively increasing: 250, 500, 750, 1000, 3125, 6250, 12500, and 25000 iterations. The primary input parameters for the model include depth values, east_shift, north_shift, length, width, strike, dip, and rake. Calculations are performed using the Bayesian Bootstrap Optimization (BABO) statistical approach. BABO is a global optimization algorithm designed for multi-objective functions through directed searches. It enables the formation of a set of objective function, identifying multiple minima, irregularly shaped minima, and evaluating parameter trade-offs and uncertainties in terms of probability.

2.3. Multi-Track InSAR Processing

The multi-track InSAR approach combined multiple Sentinel-1 tracks to differentiate surface displacement's horizontal (dH) and vertical (dV) components. The dH and dV maps were derived from ascending and descending track data and thoroughly processed to ensure precise deformation characterizations. This approach facilitates enhanced discernment of horizontal and vertical movements that might remain obscured in the Line-of-Sight (LOS) data alone.

It is important to note that the multi-track technique implemented in this analysis explicitly maps the vertical (dV) and horizontal (dH) displacement dimensions. However, most SAR observation (including Sentinel-1) has a near-polar orbit, so the North-South displacement cannot be observed and produces a negligible phase change (**Equation 3**) (**Fuhrmann & Garthwaite, 2019; Fujiwara et al., 2000**). Nonetheless, complete 3D displacement from InSAR observation may be obtained if right-looking and left-looking images are available (**Wright et al., 2004**), or by combining with Global Navigation Satellite System (GNSS) observation.

$$\begin{pmatrix} v_{asc} \\ v_{des} \end{pmatrix} = \begin{pmatrix} -sin\ \theta_{asc}\, cos\ \alpha_{asc} & cos\ \theta_{asc} \\ -sin\ \theta_{des}\, cos\ \alpha_{des} & cos\ \theta_{des} \end{pmatrix} \begin{pmatrix} v_E \\ v_U \end{pmatrix} \quad (3)$$

3. Results

3.1. InSAR Result

The interferometric process using Synthetic Aperture Radar (SAR) images produces a spectral pattern known as fringes, where each concentric circle represents half the wavelength of the radar signal. These fringes were converted into unwrapped phase imagery using the SNAPHU algorithm and subsequently transformed into displacement measurements in meters. This process provides a detailed depiction of surface deformation within the research area.

Analysis of the ascending track data (see **Figure 4a**) reveals displacement values ranging from -0.21 to -0.04 meters. Similarly, the descending track data (see **Figure 4b**) indicates displacement values ranging from -0.13 to 0.02 meters. Particularly, the area surrounding the earthquake's epicenter exhibits a distinct pattern, with some regions showing significant subsidence while others experience uplift. This phenomenon is attributed to active fault movement in the region, particularly during the Murghob earthquake, highlighting the dynamic tectonic activity shaping the Earth's surface in this area.

3.2. Earthquake Modelling Result

We used the standard epsilon value of 0.04 m in the quadtree meshing method. This value was chosen to preserve minor deformation signals while preventing excessive patch subdivision from noise. A lower epsilon value would increase the number of quadtree patches,

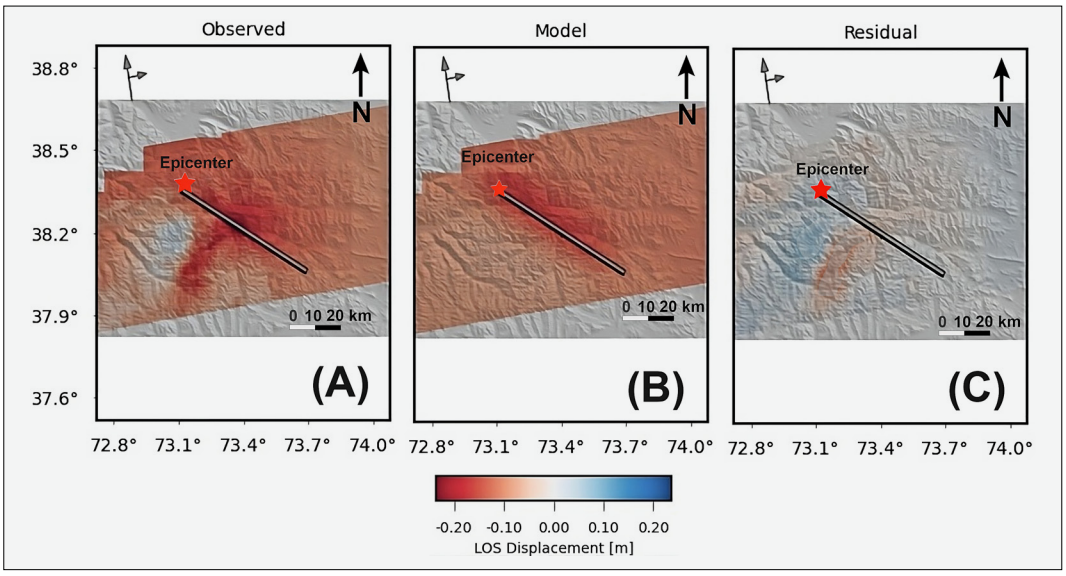


Figure 5. Modelling results for the ascending track: (A) observed displacement from InSAR, (B) best-fit synthetic model, and (C) residuals (observed–modelled). The residuals are significantly reduced, indicating the model adequately reproduces the observed deformation.

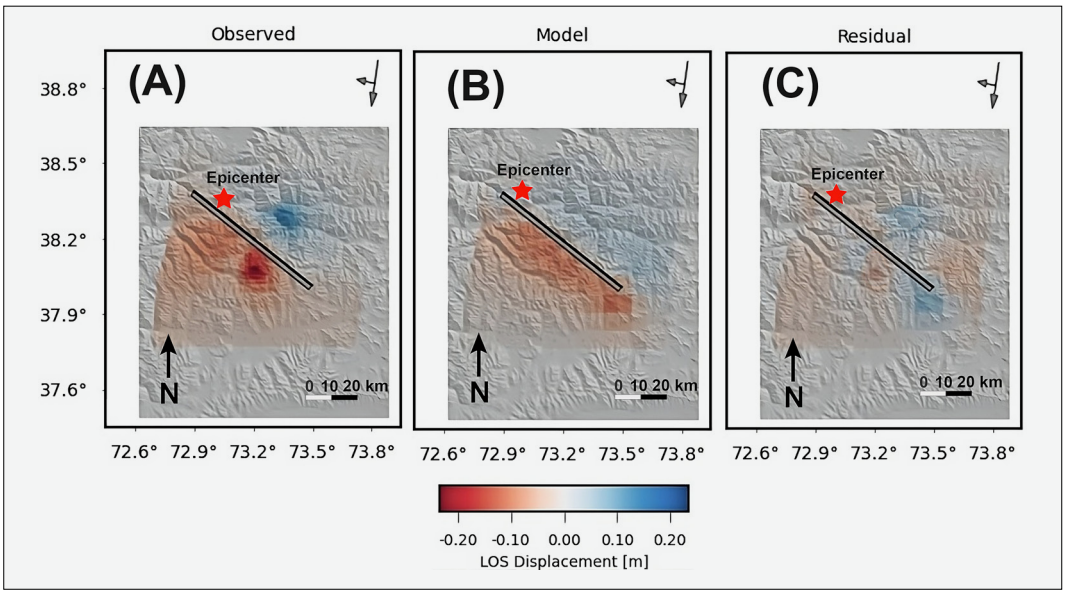


Figure 6. Modelling results for the descending track: (A) observed displacement from InSAR, (B) best fit synthetic model, and (C) residuals (observed–modelled). The residuals indicate a strong correlation between observations and model prediction, akin to the ascending track.

potentially introducing noise, whereas a higher value could smooth deformation features excessively, reducing spatial resolution.

We adjusted the prior distributions for source parameters (strike, dip, rake, depth, and slip) from their default settings for the Bayesian inversion process. These adjustments were informed by data from the USGS and GCMT assessments of the 2023 Mw 6.9 Murghob earthquake and relevant regional tectonic factors. This use of informative priors ensured that the search space accurately represented credible fault geometries for the research area. Although we did not perform a sensitivity analysis, the posterior results matched catalog solutions, suggesting that the selected priors and the standard epsilon value did not significantly bias the inversion results.

The modelling stage using Grond produces a series of images (see **Figure 5** and **Figure 6**) critical to the research analysis. These include the observed, modelled, and residual images, each serving a specific purpose in understanding the fault dynamics. The observed image represents the raw data, visualizing all available information without modifications or processing. This image serves as a baseline, capturing the unaltered characteristics of the earthquake's surface deformation. The modelled image depicts the data after being processed through the modelling software. It provides a refined

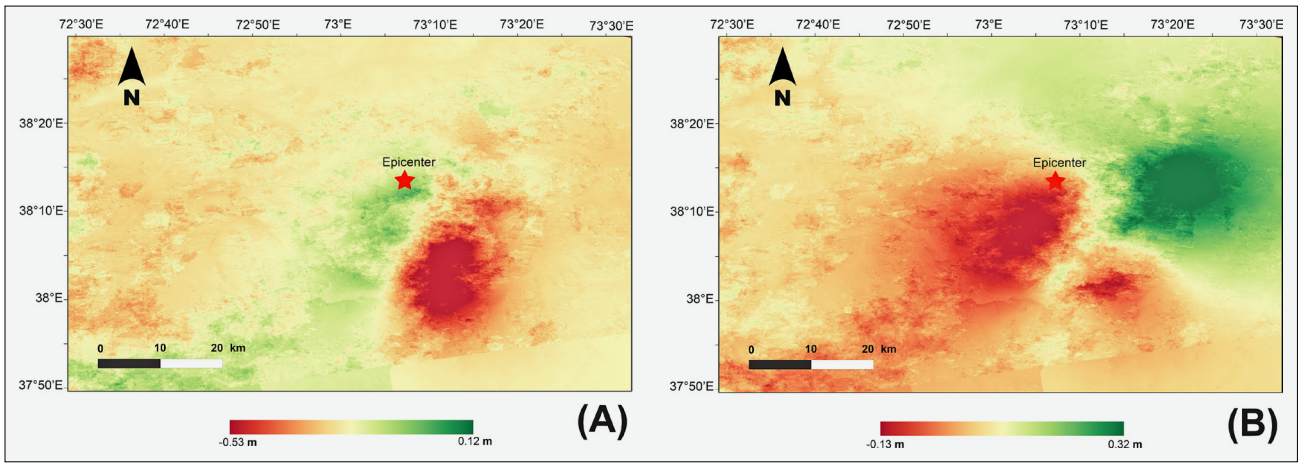


Figure 7. Studying the multi-track InSAR results uncovers (A) east to west horizontal movement and (B) vertical changes in position. The horizontal dimension points to substantial east–west ground activity in the fault sector, whereas the vertical dimension stresses uplift and subsidence dynamics near the epicenter. The data corresponds with strike-slip faulting tied to the seismic phenomenon.

representation of the fault system by incorporating the modelled parameters, offering insight into the earthquake's underlying mechanisms. Lastly, the residual image highlights the discrepancies between the observed and modelled data. It represents the portions of the observed data that the model could not fully explain, pointing to areas where additional complexities or variations remain unaccounted for in the current modelling framework.

The iterative process is critical in producing an effective model. We performed the iteration process eight times, adjusting the iteration count parameter at each step. This iterative approach is vital because it allows the model to be refined through repetition, improving the accuracy of the model's representation of the observed phenomenon. We decided to halt the iterations after reaching 25,000 iterations, as the modelling results at that point were deemed sufficient and aligned with our research objectives. In addition to generating the images, the modelling process yields the best-fit parameters. Our result displayed a calculated fault strike of 128°, with a dip of 67° and a rake of 177°.

3.3. Multi-Track InSAR Result

Figure 7a and **Figure 7b** represent the horizontal (dH) and vertical (dV) displacements, respectively, derived from multi-track InSAR analysis of the 2023 Murghob earthquake in Tajikistan, offering invaluable insight into the surface deformation caused by this significant seismic event. **Figure 7** shows horizontal displacement (dH), with values ranging from -0.53 to 0.12 meters, while Figure 7 depicts vertical displacement (dV) with values between -0.13 and 0.32 meters. Both displacement fields were generated by combining multiple Sentinel-1 radar tracks, allowing for precise separation of horizontal and vertical movement components that would otherwise be hidden in line-of-sight (LOS) data alone. The ability to isolate these movements is crucial for understanding the full extent of tectonic shifts during the earthquake.

4. Discussion

4.1. The essential of Digital Elevation Model (DEM) selection in InSAR processing

Utilizing an external DEM to correct topographic phase is crucial in InSAR processing (**Hanssen, 2002; Furuya, 2011**). A higher spatial resolution DEM can be beneficial in rugged terrain (such as in our study area), since DEM height errors cause residual fringes in the interferogram (**Lazecký et al., 2015**). The high variable topography may be smoothed out in a coarse DEM, which later can cause unwrapping error. However, in relatively flat areas, the difference between using 30 m or 90 m DEM in InSAR processing could be minimal, since the elevation-induced phase is small (**Du et al., 2017**).

4.2. Fault Parameters and Tectonic Complexity of the 2023 Murghob Earthquake

The fault parameters obtained in our study show some differences compared to the results of **Chen et al. (2024); Shi et al. (2023)**, although all studies agree on the dominant right-lateral strike-slip event of the earthquake. In our study, the calculated fault strike was 128°, with a dip of 67° and a rake of 177°, reflecting a high dip, almost vertical fault geometry. On the other hand, **Chen et al. (2024)** observed a strike of 124°, a dip of 86°, and a rake of -147.35°, while **Shi et al. (2023)** reported a strike of 28.08°, a dip of 72.89°, and a rake of -1.85° (see **Table 2**). These variations in fault parameters may arise due to differences in the data sources, modelling techniques, and assumptions used by each study.

Table 2. Parameters comparison with our study

Source	Epicenter		Depth (km)	Fault Plane		
	Longtitude (°)	Latitude (°)		Strike (°)	Dip (°)	Rake (°)
USGS	73.23	38.06	13.5	203	57	-21
gCMT	73.22	38.15	16.9	210	88	1
GFZ	73.29	38.06	10.0	122	73	-156
IPGP	73.208	38.073	8.0	27	73	-20
CENC	73.29	37.98	12.0	313	52	-131
Shi et al., 2023	73.206	38.153	3.67	28.08	72.89	-1.85
Chen et al., 2024	73.2	38.16	16.96	122	86	-147.35
Our study	73.16	38.16	8.51	128	67	177

While our approach integrates 30 m resolution Digital Elevation Models (DEM) and both ascending and descending track InSAR data to achieve detailed spatial resolution of surface deformation, we do not aim to claim methodological superiority over prior studies by institutions such as GFZ (Germany), IPGP (France), USGS, or the Global CMT (gCMT) project. Instead, our study offers a complementary perspective – focusing on the near-surface deformation field and possible complex rupture behaviour. InSAR-based modelling is particularly sensitive to surface displacements and provides a fine-scale view of fault slip distribution, while seismic-based methods such as waveform or moment tensor inversion (e.g. USGS, gCMT) are more effective in characterizing source parameters at depth. Thus, both approaches offer valuable and complementary insight into the rupture process.

In terms of fault geometry, our results align more closely with the models proposed by **Chen et al. (2024)** and GFZ, especially regarding strike and dip values. This alignment may be attributed to the shared reliance on geodetic data and similar inversion methodologies. In contrast, the USGS and gCMT models suggest different orientations and rake angles, possibly generalizing the event as a pure strike-slip rupture. These differences highlight how methodological approaches – InSAR versus seismic inversion – can influence fault parameter interpretations across studies.

The differences in fault geometry and slip characteristics further underline the complexity of the earthquake's seismogenic structure. While prior studies (**Chen et al., 2024; Shi et al., 2023**) focus on the dominant strike-slip component with minor variations in dip and rake angles, our model reveals additional complexity by identifying normal faulting contributions in the northern rupture zone, particularly along the Sarez-Karakul Fault system and the Sarez-Murghab Thrust system. This mixed-slip behaviour, which is less emphasized in other studies, may reflect a more intricate rupture process. Analogous patterns of mixed-mode rupture have been documented in other tectonically complex settings, such as the 2008 Wenchuan (**Lei & Zhao, 2009**) and 2011 Tohoku earthquakes (**Yagi & Fukahata, 2011**), where rupture propagation involved multiple fault systems and mechanisms.

The use of InSAR in our study allows direct measurement of surface deformation at high spatial resolution, making it well suited to identify distributed deformation and possible secondary faulting. However, we recognize the importance of combining this geodetic information with seismic data to better capture the full rupture process from surface to depth.

All three studies – our own, **Chen et al. (2024)**, and **Shi et al. (2023)** – recognize the involvement of multiple fault zones in the rupture. Prior studies. emphasize the Sarez-Karakul and Aksu Murghab fault systems as major contributors **(Chen et al., 2024)**, while **Shi et al. (2023)** focus more heavily on the Sarez-Karakul zone. Our findings are consistent with these, but introduce added complexity by suggesting the involvement of a blind right-lateral strike-slip fault along the eastern segment of the Aksu Murghab Fault system. Additionally, we observe indications of normal and minor left-lateral strike-slip components in the northern rupture area, which were not as clearly detected in other models. These differences further emphasize the tectonic intricacy of the Central Asia collision zone, where oblique convergence between the Indian and Eurasian plates leads to varied faulting styles (**Avouac & Tapponnier, 1993; Singh & Ghosh, 2019; Styron et al., 2011; Tapponnier et al., 2001; Tapponnier, et al., 1981**).

Previous seismic events may also help explain the rupture behaviour of the 2023 earthquake. The 2015 Mw7.2 Murghab earthquake occurred near the epicentral area and involved left-lateral strike-slip and normal faulting in the northern segment (**Sangha et al., 2017**). It likely altered the local stress field, with Coulomb stress transfer potentially promoting failure along the Sarez-Karakul Fault system and other regional structures in 2023 (**Li et al., 2021; Li, et al., 2020; Wang et al., 2017**). Similar triggering effects have been observed in other large strike-slip earthquakes, such as the 1999 Izmit (**Reilinger et al., 2000**) and 1992 Landers events (**Massonnet et al., 1993**).

In conclusion, all major studies agree that the 2023 Tajikistan earthquake was predominantly a right-lateral strike-slip event. However, there are essential differences in fault parameters, geometries, and inferred fault sys-

tem contributions. Our model, which incorporates additional normal faulting and thrust components, adds new dimensions to understanding this rupture. These differences reflect the complexity of the regional tectonics and the complementary nature of diverse modelling techniques. These differences reflect not only the complexity of the regional tectonics but also the complementary nature of diverse modelling techniques. We emphasize that our results are not meant to supersede existing models, but rather to enhance the seismogenic interpretation of this event. We advocate for the continued integration of high-resolution InSAR, seismic data, and tectonic history to develop more complete and accurate assessments of earthquake behaviour in tectonically complex regions like the Pamir and Hindu Kush **(Ischuk et al., 2013; Schurr et al., 2014; Sippl et al., 2013)**.

4.3. Insights into Fault Dynamics and Tectonic Complexity from Multi-Track InSAR Displacements

Vertical displacement can be derived from a single pair of InSAR based on Line of Sight (LoS) and satellite incidence angles (**Cigna & Tapete, 2022**). Nonetheless, the conversion must be carefully taken and assume the movement is only in the vertical direction. Thus, any movement in the horizontal component can have huge inaccuracies (**Fuhrmann & Garthwaite, 2019**). In the region with two SAR tracks (ascending and descending) available, pseudo 3D (2.5 D) can be used (**Fujiwara et al., 2000**).

The vertical displacement (dV) image from multi-track InSAR highlights a predominant upward movement in certain areas, with the positive displacement (green) being more dominant than the negative displacement (red) (see **Figure 7**). This vertical movement suggests the occurrence of uplift, which is consistent with normal faulting or thrust faulting processes that often accompany lateral fault movement in compressional settings. The Sarez-Karakul normal fault and other thrust and strike-slip fault components in the region likely contributed to these vertical shifts.

On the other hand, the horizontal displacement (dH) image reveals significant westward and eastward motions, with red zones indicating negative displacements (westward movement) and green zones showing positive displacements (eastward movement) (see **Figure 7**). This pattern suggests that the earthquake involved lateral fault movements, typical of strike-slip faulting, where two blocks of the Earth's crust move horizontally past each other. The distribution of displacements in these directions aligns with the region's fault system, specifically the Aksu Murghab Fault system, known for its strike-slip characteristics.

The tectonic complexity of the Tajikistan region is further underscored by the various fault systems that interact in the area. Studies such as those by **Chen et al. (2024; Shi et al. (2023)** have highlighted the importance of the Sarez-Karakul Fault system and the Aksu Murghab Fault system as primary contributors to the 2023 earthquake. However, our study adds further detail by suggesting that the rupture also likely involved a blind right-lateral strike-slip fault, primarily driven by the Aksu Murghab Fault system in the east. Additionally, we observe influences of normal faulting and left-lateral strike-slip faulting in the northern part of the region, which were less emphasized in previous studies.

The region's tectonic setting is further complicated by its position within the broader Central Asia collision zone, where the Indian and Eurasian plates interact. Various faulting styles characterize this collision zone, including oblique collision, strike-slip faulting, and thrust faulting. The role of these different fault types in shaping the region's tectonic landscape has been well-documented in numerous studies (**Avouac & Tapponnier, 1993; Singh & Ghosh, 2019**). The interactions between these fault systems contribute to the complex seismic activity observed in Tajikistan and surrounding regions. Understanding the contributions of various fault zones to earthquake rupture is essential for improving seismic hazard assessments and developing more effective disaster mitigation strategies in the region.

Additionally, the analysis of horizontal and vertical displacements through multi-track InSAR provides a detailed understanding of the seismic deformations caused by the 2023 Murghob earthquake. The horizontal displacements reveal significant strike-slip faulting, while the vertical displacements suggest a complex combination of uplift and normal faulting. These findings underscore the importance of further research into the fault systems in Tajikistan to better understand the tectonic forces shaping the region and to improve earthquake preparedness and risk assessment.

5. Conclusions

The 2023 Murghob earthquake in Tajikistan, examined through the integration of multi-track InSAR observations and detailed geodetic modelling, reveals a complex rupture process involving multiple fault systems within a tectonically intricate region. The inversion results confirm that the earthquake was predominantly governed by a right-lateral strike-slip mechanism, characterized by a fault strike of 128°, a dip of 67°, and a rake of 177°. Beyond this dominant slip behaviour, the analysis also identifies significant contributions from normal and thrust faulting, particularly concentrated in the northern rupture segment. These findings suggest that the event exhibited a mixed-mode rupture, reflecting the structural complexity of the Pamir tectonic regime. Compared with previously published models (**Chen et al., 2024; Shi et al., 2023**), the fault parameters derived in this study exhibit notable differences. Such discrepancies are likely attributable to variations in

input data, inversion methodologies, and modelling assumptions. Our approach, which combines 30 m Digital Elevation Models (DEMs) with ascending and descending track InSAR datasets, enables improved spatial resolution of surface deformation and fault slip distribution. This methodological framework enhances the capacity to resolve fine-scale features of the rupture, including distributed deformation and secondary fault activation. While our results are broadly consistent with those of **Chen et al. (2024)** and the GFZ model in terms of strike and dip values, the present study contributes several novel insights. These include the potential involvement of a blind right-lateral strike-slip fault along the eastern segment of the Aksu Murghab Fault system, as well as the identification of minor left-lateral and normal faulting components in the northern rupture area – features that have not been prominently reported in prior seismic-only analyses. Such observations highlight the complex nature of fault interactions in this region and underscore the utility of InSAR in capturing near-surface deformation patterns that are not always discernible through seismic data alone. The findings presented here affirm the value of integrating geodetic and seismic data to comprehensively understand earthquake rupture dynamics, from the surface to seismogenic depths. Rather than replacing existing models, this study provides a complementary interpretation that refines the broader seismotectonic characterization of the 2023 event. Further investigations should be planned to enhance the robustness of these interpretations. These include joint inversions incorporating InSAR and seismic waveform data, field-based validation of surface rupture features, and Coulomb stress transfer modelling to assess fault interaction and potential triggering effects. Additionally, time-series InSAR analyses will be employed to monitor postseismic deformation. These future efforts aim to improve regional seismic hazard assessments and support more effective earthquake preparedness and risk mitigation strategies in the broader Pamir and Hindu Kush regions.

Acknowledgement

The authors are grateful for the insightful feedback from the anonymous reviewers. We also thank the European Space Agency (ESA) for granting free access to Sentinel-1 data.

6. References

Abidin, H. Z., Andreas, H., Meilano, I., Gamal, M., Gumilar, I., & Abdullah, C. I. (2009). Deformasi Koseismik dan Pascaseismik Gempa Yogyakarta 2006 dari Hasil Survei GPS. *Indonesian Journal on Geoscience*, *4*(4). https://doi.org/10.17014/ijog.v4i4.87

Avouac, J.-P., & Tapponnier, P. (1993). *Kinematic Model of Active Deformation in Central Asia* (Vol. 20).

Chen, C., & Zebker, H. (2001). Two-dimensional phase unwrapping with use of statistical models for cost functions in nonlinear optimization. *Journal of the Optical Society of America. A, Optics, Image Science, and Vision*, *18*, 338–351. https://doi.org/10.1364/JOSAA.18.000338

Chen, R., Li, J., Liu, D., Yushan, A., Li, R., & Kong, X. (2024). InSAR coseismic deformation and seismogenic structure of the 2023 MW6.9 Tajikistan earthquake. *Geodesy and Geodynamics*. https://doi.org/10.1016/j.geog.2023.12.004

Cigna, F., & Tapete, D. (2022). Land Subsidence and Aquifer-System Storage Loss in Central Mexico: A Quasi-Continental Investigation With Sentinel-1 InSAR. *Geophysical Research Letters*, *49*(15). https://doi.org/10.1029/2022GL098923

Du, Y., Feng, G., Li, Z., Peng, X., Zhu, J., & Ren, Z. (2017). Effects of external digital elevation model inaccuracy on StaMPS-PS processing: A case study in Shenzhen, China. *Remote Sensing*, *9*(11). https://doi.org/10.3390/rs9111115

Fuhrmann, T., & Garthwaite, M. C. (2019). Resolving three-dimensional surface motion with InSAR: Constraints from multi-geometry data fusion. *Remote Sensing*, *11*(3). https://doi.org/10.3390/rs11030241

Fujiwara, S., Nishimura, T., Murakami, M., Nakagawa, H., Tobita, M., & Rosen, P. A. (2000). 2.5-D surface deformation of M6.1 earthquake near Mt Iwate detected by SAR interferometry. *Geophysical Research Letters*, *27*(14), 2049–2052. https://doi.org/10.1029/1999GL011291

Funning, G. J., & Garcia, A. (2019). A systematic study of earthquake detectability using Sentinel-1 InterferometricWide-Swath data. *Geophysical Journal International*, *216*(1), 332–349. https://doi.org/10.1093/gji/ggy426

Furuya, M. (2011). SAR Interferometry. In H. K. Gupta (Ed.), *Encyclopedia of Solid Earth Geophysics* (pp. 1041–1049). Dordrecht: Springer Netherlands. https://doi.org/10.1007/978-90-481-8702-7_97

Furuya, M., Suzuki, T., Maeda, J., & Heki, K. (2017). Midlatitude sporadic-E episodes viewed by L-band split-spectrum InSAR. *Earth, Planets and Space*, *69*(1). https://doi.org/10.1186/s40623-017-0764-6

Goldstein, R. M., & Werner, C. L. (1998). Radar interferogram filtering for geophysical applications. *Geophysical Research Letters*, *25*(21), 4035–4038. https://doi.org/10.1029/1998GL900033

Hanssen, R. F. (2002). *Radar Interferometry, Data Interpretation and Error Analysis*.

He, L., Feng, G., Xu, W., Wang, Y., Xiong, Z., Gao, H., & Liu, X. (2023). Coseismic Kinematics of the 2023 Kahramanmaras, Turkey Earthquake Sequence From InSAR and Optical Data. *Geophysical Research Letters*, *50*(17). https://doi.org/10.1029/2023GL104693

Heimann, S., Isken, M., Kühn, D., Sudhaus, H., Steinberg, A., Vasyura-Bathke, H., … Dahm, T. (2018). *Grond - A probabilistic earthquake source inversion framework*. https://doi.org/10.5880/GFZ.2.1.2018.003

Heimann, S., Kriegerowski, M., Isken, M. P., Cesca, S., Daout, S., Grigoli, F., … Dahm, T. (2017). *Pyrocko - An open-source seismology toolbox and library*. Retrieved from https://api.semanticscholar.org/CorpusID:217360137

Ischuk, A., Bendick, R., Rybin, A., Molnar, P., Khan, S. F., Kuzikov, S., … Zubovich, A. V. (2013). Kinematics of the pamir and hindu kush regions from gps geodesy. *Journal of Geophysical Research: Solid Earth*, *118*(5), 2408–2416. https://doi.org/10.1002/jgrb.50185

Isken, M. P., Sudhaus, H., Heimann, S., Steinberg, A., Daout, S., & Vasyura-Bathke, H. (2017). *Kite - Software for Rapid Earthquake Source Optimisation from InSAR Surface Displacement*. Retrieved from https://api.semanticscholar.org/CorpusID:217349180

Lazecký, M., Bakon, M., & Hlavácová, I. (2015). Effect of DEM inaccuracy on precision of satellite inSAR results. *Lecture Notes in Geoinformation and Cartography*, *211*, 165–171. Kluwer Academic Publishers. https://doi.org/10.1007/978-3-319-18407-4_14

Lei, J., & Zhao, D. (2009). Structural heterogeneity of the Longmenshan fault zone and the mechanism of the 2008 Wenchuan earthquake (Ms 8.0). *Geochemistry, Geophysics, Geosystems*, *10*(10). https://doi.org/10.1029/2009GC002590

Li, Y., Huang, L., Ding, R., Yang, S., Liu, L., Zhang, S., & Liu, H. (2021). Coulomb stress changes associated with the M7.3 Maduo earthquake and implications for seismic hazards. *Natural Hazards Research*, *1*(2), 95–101. https://doi.org/10.1016/j.nhres.2021.06.003

Li, Y., Shao, Z., Shi, F., & Chen, L. (2020). Stress evolution on active faults in the southwestern Yunnan region, southeastern Tibetan Plateau, and implications for seismic hazard. *Journal of Asian Earth Sciences*, *200*. https://doi.org/10.1016/j.jseaes.2020.104470

Liu, Y., Wu, S., Zhang, B., Xiong, S., & Wang, C. (2024). Accurate Deformation Retrieval of the 2023 Turkey–Syria Earthquakes Using Multi-Track InSAR Data and a Spatio-Temporal Correlation Analysis with the ICA Method. *Remote Sensing*, *16*(17), 3139. https://doi.org/10.3390/rs16173139

Massonnet, D., & Feigl, K. L. (1998). Radar interferometry and its application to changes in the earth's surface. *Reviews of Geophysics*, *36*(4), 441–500. https://doi.org/10.1029/97RG03139

Massonnet, D., Rossi, M., Cesar, C., Adragna, F., Peltzer, G., Feigl, K., & Rabaute, T. (1993). The Displacement Field of The Landers Earthquake Mapped by Radar Interferometry. *Nature*, *364*, 138–142.

R. E. Reilinger, S. Ergintav, R. Burgmann, S. McClusky, O. Lenk, A. Barka, … M. N. Toksoz. (2000). *Coseismic and Poseismic Fault Slip for the 17 August 1999 M=7.5, Izmit, Turkey Earthquake*. https://doi.org/DOI:10.1126/science.289.5484.1519

Sangha, S., Peltzer, G., Zhang, A., Meng, L., Liang, C., Lundgren, P., & Fielding, E. (2017). Fault geometry of 2015, Mw7.2 Murghab, Tajikistan earthquake controls rupture propagation: Insights from InSAR and seismological data. *Earth and Planetary Science Letters*, *462*, 132–141. https://doi.org/10.1016/j.epsl.2017.01.018

Schurr, B., Ratschbacher, L., Sippl, C., Gloaguen, R., Yuan, X., & Mechie, J. (2014). Seismotectonics of the Pamir. *Tectonics*, *33*(8), 1501–1518. https://doi.org/10.1002/2014TC003576

Setiawan, N., & Furuya, M. (2021). Tropospheric dispersive phase anomalies during heavy rain detected by L-band InSAR and their interpretation. *Earth, Planets and Space*, *73*(1). https://doi.org/10.1186/s40623-021-01470-9

Setiawan, Naufal, & Furuya, M. (2024). Heavy Rain Episodes Identified by L-band InSAR and Limitations of Split-Spectrum Method in Indonesia. *Geosfera Indonesia*, *9*(1), 1. https://doi.org/10.19184/geosi.v9i1.38154

Shi, Y., Wang, Y., & Bian, Y. (2023). Coseismic Source Model of the February 2023 Mw 6.8 Tajikistan Earthquake from Sentinel-1A InSAR Observations and Its Associated Earthquake Hazard. *Remote Sensing*, *15*(12). https://doi.org/10.3390/rs15123010

Singh, S., & Ghosh, A. (2019). Surface Motions and Continental Deformation in the Indian Plate and the India-Eurasia Collision Zone. *Journal of Geophysical Research: Solid Earth*, *124*(11), 12141–12170. https://doi.org/10.1029/2018JB017289

Sippl, C., Schurr, B., Yuan, X., Mechie, J., Schneider, F. M., Gadoev, M., … Radjabov, N. (2013). Geometry of the Pamir-Hindu Kush intermediate-depth earthquake zone from local seismic data. *Journal of Geophysical Research: Solid Earth*, *118*(4), 1438–1457. https://doi.org/10.1002/jgrb.50128

Styron, R. H., Taylor, M. H., & Murphy, M. A. (2011). Oblique convergence, arc-parallel extension, and the role of strike-slip faulting in the High Himalaya. *Geosphere*, *7*(2), 582–596. https://doi.org/10.1130/GES00606.1

Tapponnier, P., Zhiqin, X., Roger, F., Meyer, B., Arnaud, N., Wittlinger, G., & Jingsui, Y. (2001, November 23). Oblique stepwise rise and growth of the tibet plateau. *Science*, Vol. 294, pp. 1671–1677. https://doi.org/10.1126/science.105978

Tapponnier, Paul, Mattauer, M., Proust, F., & Cassaigneau, C. (1981). Mesozoic ophiolites, sutures, and large-scale tectonic movements in Afghanistan. In *Earth and Planetary Science Letters* (Vol. 52).

USGS Earthquake Hazard Program. (n.d.). Retrieved from https://earthquake.usgs.gov/earthquakes/eventpage/us6000jqxc/executive

Wang, J., Xu, C., Freymueller, J. T., & Li, Z. (2017). Probing Coulomb stress triggering effects for a Mw > 6.0 earthquake sequence from 1997 to 2014 along the periphery of the Bayan Har block on the Tibetan Plateau. *Tectonophysics*, *694*, 249–267. https://doi.org/10.1016/j.tecto.2016.11.009

Wright, T. J., Parsons, B. E., & Lu, Z. (2004). Toward mapping surface deformation in three dimensions using InSAR. *Geophysical Research Letters*, *31*(1). https://doi.org/10.1029/2003GL018827

Yagi, Y., & Fukahata, Y. (2011). Rupture process of the 2011 Tohoku-oki earthquake and absolute elastic strain release. *Geophysical Research Letters*, *38*(19). https://doi.org/10.1029/2011GL048701

Zhou, Y., He, J., Oimahmadov, I., Gadoev, M., Pan, Z., Wang, W., … Rajabov, N. (2016). Present-day crustal motion around the Pamir Plateau from GPS measurements. *Gondwana Research*, *35*, 144–154. https://doi.org/10.1016/j.gr.2016.03.011

SAŽETAK

Seizmogena analiza potresa magnitude 6,9 u Murghobu 2023. godine, Tadžikistan, temeljena na Multi-Track InSAR tehnici i modeliranju

Ova studija istražuje potres u Murghobu u Tadžikistanu 2023. godine (Mw 6,9) korištenjem modeliranja i Multi-Track InSAR tehnike s ciljem definiranja deformacija površine i dinamike rasjeda. Pyrocko pristup modeliranju rezultirao je stvaranjem opažačkih, modeliranih i rezidualnih slika, od kojih svaka otkriva određene aspekte geometrije rasjeda i karakteristika loma. Naša studija identificirala je dominantni događaj desnoga lateralnog pomaka po pružanju, s izračunanim pravcem pružanja rasjeda od 128–308°, smjerom nagiba 218°, kutom nagiba od 67° i smjerom pomaka krovine prema azimutu 177°. Nadalje, modeliranje je također uputilo na postojanje dijagonalnoga pomaka po rasjedu, uključujući komponente normalnoga rasjedanja duž rasjednoga sustava Sarez-Karakul i navlačnoga sustava Sarez-Murghab. Ta saznanja upućuju na složeniji proces rasjedanja nego što je prethodno naglašavano u drugim modelima. Multi-Track InSAR analiza podržala je ove rezultate mjerenjima visoke rezolucije horizontalnih (dH) i vertikalnih (dV) pomaka. Horizontalni pomaci otkrili su znatne pomake po pružanju (–0,53 do 0,12 metara) duž rasjednoga sustava Aksu Murghab. U međuvremenu vertikalni pomaci uputili su na znatno izdizanje (–0,13 i 0,32 metra), vjerojatno zbog interakcije između normalnih rasjeda i navlaka. Rezultati ističu postojanje složenoga tektonskog okruženja u regiji, na koje utječu višestruki rasjedni sustavi, uključujući rasjede Sarez-Karakul i Aksu Murghab. Rezultati istraživanja naglašavaju važnost integriranja različitih geofizičkih metoda kako bi se bolje razumjeli mehanizmi potresa i poboljšale procjene seizmičke opasnosti u tektonski aktivnim regijama poput Tadžikistana.

Ključne riječi:
InSAR, Multi-Track InSAR, modeliranje potresa, potres u Murghobu 2023. godine

Author's contribution

Rana Jaladara: conceptualization, processing data, writing – original draft and editing, visualization, validation, data curation, and formal analysis. **Naufal Setiawan**: conceptualization, methodology, writing – original draft and editing, validation, investigation, and formal analysis. **Erlan Sumanjaya**: methodology, writing – original draft and editing, validation, investigation, and formal analysis.
All authors have read and agreed to the published version of the manuscript.

RGNZ/MGPB

Rudarsko-geološko-naftni zbornik
(The Mining-Geology-Petroleum Engineering Bulletin)
DOI: 10.17794/rgn.2026.3.6

Original scientific paper

Geographic Information System Application for Prospecting the Sandstone-type Uranium Deposit in the Melawi Region, West Kalimantan, Indonesia

Tyto Baskara Adimedha[1]*, Roni Cahya Ciputra[1], Frederikus Dian Indrastomo[1], I Gde Sukadana[1], Heri Syaeful[1], Yoshi Rachael[1]

[1]*Research Center for Nuclear Material and Radioactive Waste Technology, Research Organization for Nuclear Energy, National Research and Innovation Agency (BRIN), South Tangerang 15314, Indonesia.*

Abstract

The Melawi region in Indonesia has been identified as a metamorphic-hosted uranium deposit. The occurrence of sedimentary formations in the downstream area suggests the potential for sandstone-type uranium deposits. Previous studies have concentrated on metamorphic-hosted mineralization, resulting in limited exploration of the sedimentary rocks. Geographic Information System (GIS) technology offers valuable support for mineral prospectivity analysis, including uranium exploration. Among various techniques, fuzzy logic has been demonstrated to be effective in generating prospectivity maps to guide uranium resource development. This research aims to develop a prospectivity map for a sandstone-type uranium deposit in the Melawi region. A GIS-based analysis is performed using available spatial datasets, including geological maps, digital elevation models, and uranium occurrences in Melawi. These datasets served as input for constructing a fuzzy logic model based on the genetic model of sandstone-type uranium deposits. The datasets were reclassified, assigned suitability scores, and operated within a fuzzy logic framework to generate a prospectivity map. The results indicate that 36.64% of the Melawi area is high prospectivity zones, 25.34% is medium prospectivity zones, and 38.02% is the low prospectivity zones. The northern part of Melawi exhibits the most favourability for sandstone-hosted uranium mineralization. This study demonstrates fuzzy logic as a practical tool to delineate the favourable area of a sandstone-type uranium deposit in Melawi. Nevertheless, incorporating more diverse spatial datasets and implementing systematic field validation is necessary to locate uranium deposits accurately.

Keywords:
Melawi, GIS, fuzzy logic, mineral prospectivity, sandstone-type uranium

1. Introduction

As the global demand for clean and sustainable energy rises, nuclear power is increasingly seen as a reliable low-carbon solution (**Karakosta et al., 2013; Yue et al., 2022**). Indonesia has included nuclear energy in its national energy strategy, with plans to develop nuclear power plants (NPP) in the coming decades to ensure long-term energy security and reduce dependence on fossil fuels (**Permana et al., 2022**). This policy direction highlights the importance of identifying domestic uranium resources to support future nuclear fuel needs. Indonesia hosts several types of uranium deposits, including metamorphic-type in West Kalimantan (**Adimedha et al., 2024; Ciputra et al., 2022; Ngadenin et al., 2017**), alkaline volcanic-related-type in West Sulawesi (**Rosianna et al., 2020, 2023; Said et al., 2017; Sukadana et al., 2016**), placer-type in Bangka Belitung (**Ngadenin et al., 2014; Syaeful et al., 2021**), and sandstone-type in North Sumatra (**Ciputra et al., 2019a; Subandrio et al., 2010; Sukadana & Syaeful, 2016**). Despite this geological potential, uranium deposits remain difficult to locate due to economic, environmental, and geological challenges. Therefore, a method capable of integrating and analysing diverse geoscientific data is essential to improve the effectiveness and efficiency of uranium exploration in Indonesia.

In recent years, Geographic Information Systems (GIS) have emerged as powerful tools for mineral exploration, offering spatial analysis capabilities that allow integration of multiple geoscientific datasets (**Carranza, 2008; Porwal & Kreuzer, 2010; Yousefi et al., 2019**). When combined with fuzzy logic modelling, GIS enables the quantification of expert geological knowledge and the handling of uncertainty in data, which is particularly relevant in early-stage uranium exploration. Although recent advancements in machine learning and deep learning have shown promise in mineral prospectivity modelling (**Brandmeier et al., 2020; Kong et al.,**

* Corresponding author: Tyto Baskara Adimedha
e-mail address: tyto001@brin.go.id
Received: 11 August 2025. Accepted: 2 December 2025.
Available online: 14 May 2026

2024; Li et al., 2024; Senanayake et al., 2023; Sun et al., 2024), these data-driven methods typically require a large number of known mineral occurrences and high-quality, high-density datasets to establish reliable statistical relationships. In contrast, the fuzzy logic approach is knowledge-driven and therefore well-suited to data-sparse environments. Fuzzy logic also allows expert judgment and qualitative geological reasoning to be formally expressed in a quantitative framework. This characteristic provides a key advantage over purely statistical or training-based algorithms, which may fail to capture subtle geological reasoning when a sample size is small or uncertain (**Bierlein & Bruce, 2018**). GIS-fuzzy logic approaches have proven to be effective in reducing exploration risks and improving targeting efficiency by producing spatially explicit prospectivity maps (**Carranza, 2008**). Fuzzy logic models allow qualitative geological concepts, such as favourability based on lithology, topography, or hydrogeological conditions, to be translated into quantitative inputs (**Berthold, 1999**). This method is particularly suitable for sandstone-type uranium deposits, which require the presence and interplay of three primary geological components: (1) a uranium source, commonly felsic igneous or metamorphic rocks enriched in uranium; (2) transport pathways, typically through permeable sandstones and aided by groundwater circulation; and (3) trap environments, such as reducing facies within sandstones, often interbedded with carbonaceous or pyritic material, that allow uranium precipitation and accumulation (**Bruneton & Cuney, 2016**). The use of GIS-fuzzy logic for uranium exploration has already demonstrated encouraging results (**Bierlein & Bruce, 2018; Kreuzer et al., 2010**). In North Sumatra, Indonesia, prospectivity maps developed using fuzzy logic successfully delineated areas with high favourability that were later confirmed by the presence of uranium mineralization (**Ciputra et al., 2019b**). However, as with any predictive model, the outputs must be validated through field investigations and supporting geophysical and geochemical techniques to ensure accuracy and reliability.

Despite Indonesia's favourable geological setting and the documented presence of various uranium deposit types, systematic exploration remains at a relatively early stage. One of the major challenges is the absence of integrated, data-driven approaches that can effectively address the inherent geological complexity and data uncertainty characteristic of Indonesia. The Melawi region in West Kalimantan represents a geologically promising but largely underexplored area for uranium mineralization. The regional geology is characterized by Pre-Tertiary granitoid intrusions, metamorphic basement rocks, and extensive Tertiary sedimentary sequences, including sandstone formations (**Amiruddin & Trail, 1993**). Granitoids and metamorphic rocks in the southern part of Melawi could represent viable uranium sources **(Syaeful et al., 2021**). Moreover, metamorphic rocks in the southern part of Melawi have been extensively explored for uranium mineralization (**Ciputra et al., 2020, 2022; Farrenzo et al., 2023; Muhammad et al., 2019; Sukadana et al., 2024; Syaeful et al., 2021**). This fact is supported by the potential uranium traps of sandstone in the northern part of Melawi, particularly due to the presence of thin coal seams and mudstones that could serve as reductive agents (**Cakrabuana et al., 2021a; Indrastomo et al., 2024**). Despite these favourable geological conditions, exploration focusing on sandstone-type uranium deposits in this area remains limited to date. The lack of quantitative spatial assessment integrating these components (source, transport, and trap) has hindered the ability to delineate prospective zones and prioritize exploration targets.

To address these limitations, this study applies a GIS-based fuzzy logic approach to develop a prospectivity map for sandstone-type uranium deposits in the Melawi region. This research provides spatially integrated assessment of sandstone-type uranium potential in West Kalimantan, integrating key geological parameters related to uranium source, transport pathways, and trap mechanisms within mineralization framework. This research demonstrates how integrated spatial analysis can enhance exploration target delineation in data-sparse regions. The proposed methodology provides a replicable framework that can be adapted to other sedimentary basins across Indonesia and Southeast Asia. The resulting prospectivity map is expected to serve as a strategic guide for further exploration activities and contribute to a broader understanding of Indonesia's uranium resource potential.

1.1. Geological Background

1.1.1. Sandstone-type Uranium Deposit

Sandstone-type uranium deposits were formed in diagenetic–epigenetic and low-temperature origin (**Bruneton & Cuney, 2016; IAEA, 2009**). An essential element that controls the formation of sandstone-type uranium deposits consists of source rock, permeability, groundwater chemistry, depositional environment, the presence of adsorptive/reducing agents, and an arid to semi-arid climate (**Bruneton & Cuney, 2016; IAEA, 2009**). Lithologies that are considered to be potential uranium source rocks are felsic volcanic, crystalline terrains, or other lithologies with sufficient amounts of uranium content. The favourable area for a uranium source is exposed granitoid rocks, as it is more likely to release uranium during weathering (**Dahlkamp, 2009**). The oxygenated surface and groundwaters could act as leaching and transporting agents for uranium. The uranium transport is also controlled by topographic relief and the permeability of rocks. Then uranium would be trapped in medium to coarse-grained sandstone with the presence of reducing agents such as carbonaceous materials, sulphides, or ferromagnesian minerals. The depositional environments of

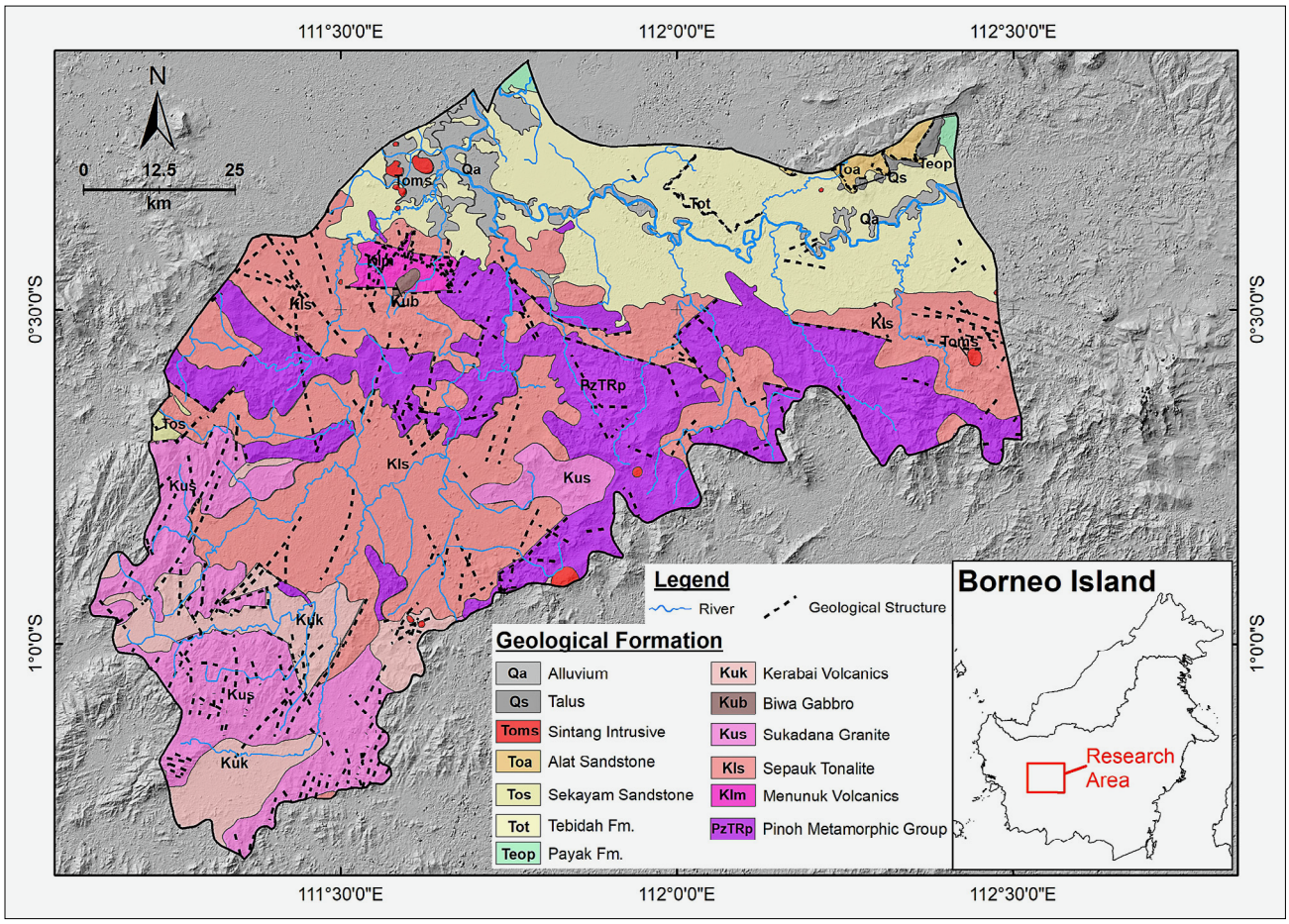


Figure 1. Geological map of Melawi, West Kalimantan, Indonesia (modified from Amiruddin & Trail (1993)).

sandstone-type uranium deposits are fluvial to lacustrine in intracratonic to epicratonic sedimentary basins (**Bruneton & Cuney, 2016; IAEA, 2009**).

1.1.2. Geology of the Melawi Region

The Melawi region lies within the Melawi basin (**Sutjipto, 1991**) and is part of the Northern Zone of Schwaner Mountains (**Breitfeld et al., 2020; Hennig et al., 2017**), where the basement of the Melawi basin is exposed. The Melawi basin, a Paleogene-aged sedimentary basin located in western Kalimantan, is bounded by the Semitau Plateau to the north and the Schwaner Mountains to the south (**Sutjipto, 1991**). The basement rocks of this basin consist of Early Cretaceous Pinoh Metamorphics, composed of quartz-muscovite schist, phyllite, hornfels, tuff, and quartzite (**Amiruddin & Trail, 1993**). These metamorphic rocks were later intruded by several Upper Cretaceous plutonic bodies, including Sukadana Granite, Sepauk Tonalite, and Biwa Gabbro (**Breitfeld et al., 2020; Davies et al., 2014; Hennig et al., 2017**).

The Sepauk tonalite comprises tonalite and light gray hornblende-biotite granodiorite, with occurrences of diorite, granite, monzodiorite, and quartz diorite. The Sukadana Granite is predominantly composed of alkaline feldspar granite and monzogranite, while the Biwa Gabbro consists mainly of Olivine Gabbro. The Pinoh Metamorphic is overlaid by Upper Cretaceous Menunuk Volcanics (tuff, siltstone, and mudstone) and the Kerabai Volcanic (andesite, basalt, and dacite). The sedimentary sequence of the Melawi region begins with the Late Eocene – Early Oligocene Payak Formation, consisting of tuffaceous quartz wacke interbedded with grey mudstone and siltstone, which are notably rich in fossils (**Badaruddin et al., 2018; Sutjipto, 1991**). This formation is overlaid by the Early Oligocene Tebidah Formation is composed of lithic arenite interbedded with mudstone and thin coal seams (**Badaruddin et al., 2018; Sutjipto, 1991**). Above this lies the Early Oligocene Sekayam Sandstone, comprising massive to thick-bedded sandstone with mudstone interbeds (**Badaruddin et al., 2018; Sutjipto, 1991**), followed by the Alat Sandstone, which includes thick-bedded sandstones and conglomerates (**Amiruddin & Trail, 1993**). These sedimentary formations were later intruded by the Upper Oligocene–Lower Miocene Sintang Intrusive Suite, consisting of andesite, dacite, rhyolite, quartz diorite, and granodiorite. Quaternary deposits of talus and alluvium are the youngest geological units in the region (**Amiruddin & Trail, 1993**). The geological framework of the Melawi region is illustrated in **Figure 1.**

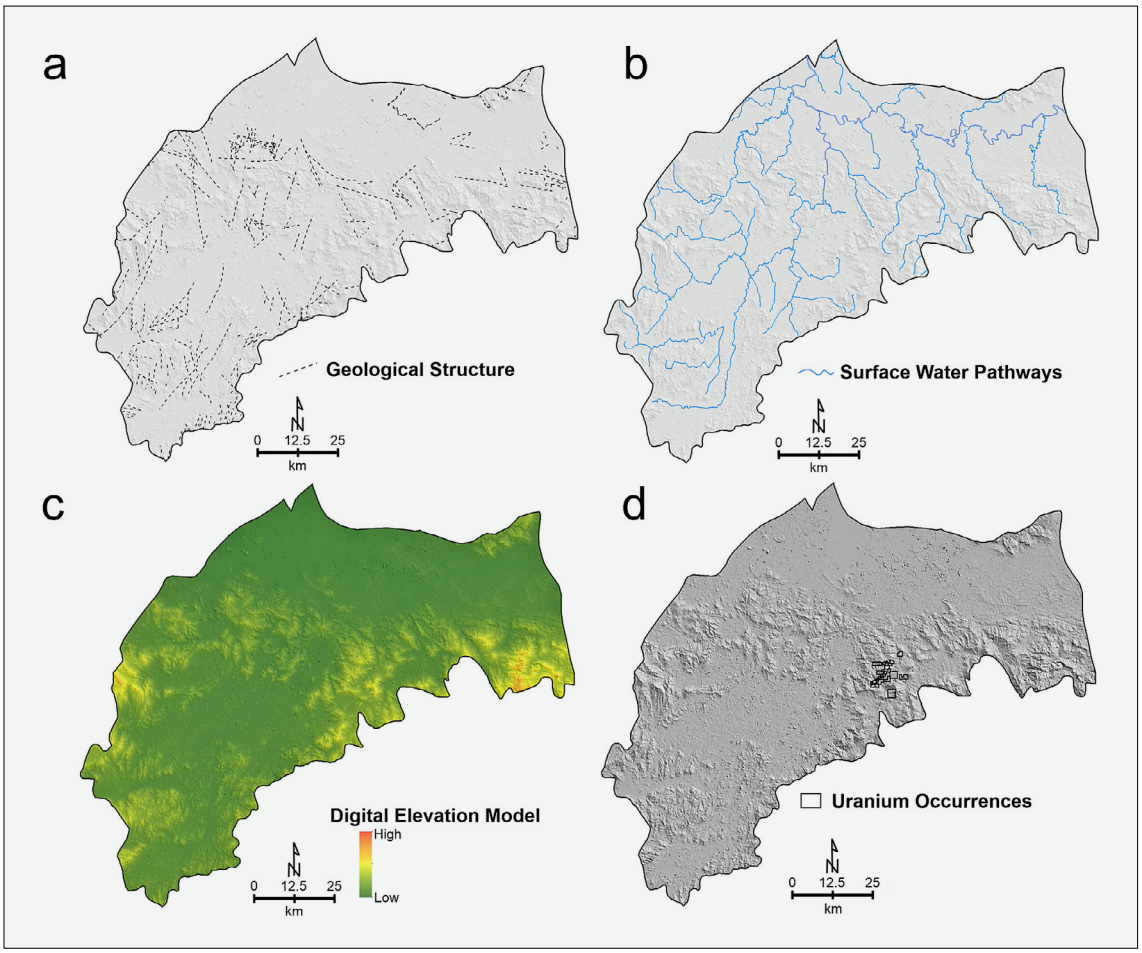


Figure 2. Illustration of spatial datasets used as input in fuzzy logic (a) geological structure (after Amiruddin & Trail (1993)), (b) surface water pathways (after Badan Informasi Geopasial (2017)), (c) digital elevation model (after United States Geological Survey), (d) uranium mineralization occurences (after Ciputra et al. (2022)).

Uranium mineralization within the Melawi region has been documented in the Kalan area, located upstream of the Kalan River and situated within the Pinoh Metamorphic Complex. The metamorphic rock has been intruded by granitoid bodies, particularly the Sepauk Tonalite and Sukadana Granite (**Ciputra et al., 2022; Tjokrokardono et al., 2004**). Uranium occurs in low-grade metamorphic rocks, especially metasiltstones and metapelites, which are characterized by clay-rich mineral assemblages (**Farrenzo et al., 2023; Syaeful et al., 2021**). The inferred uranium resource in the Kalan area is estimated at approximately 2470 tonnes of uranium (tU) (**Syaeful et al., 2021**). The uranium mineralization is associated with a diverse suite of uranium-bearing minerals, including uraninite, brannerite, davidite, gummite, and high-uranium monazite (**Adimedha et al., 2024; Syaeful et al., 2021; Tjokrokardono et al., 2004**). Faults, structural openings, and tectonic breccias control the mineralization. Additionally, uranium enrichment is locally concentrated along schistosity planes within the host rocks, reflecting the structural and lithological control on mineral distribution (**Tjokrokardono et al., 2004**).

Table 1. Spatial datasets used in GIS-based prospectivity mapping for a sandstone-type uranium deposit.

Spatial Datasets	Criteria
Regional Geology (**Amiruddin & Trail, 1993**)	Lithology reclassification as a uranium source
	Geological structure as fluid media
	Sandstone as a uranium trap
	Permeability reclassification as fluid transport media
Surface water pathways (**Badan Informasi Geopasial, 2017**)	Surface water pathways as transport media
Digital Elevation Model (ASTER GTM2) **(United States Geological Survey, n.d.)**	Local lows generation
Uranium Occurrences (**Ciputra et al., 2022**)	Uranium potential areas in the Melawi region

2. Methods

Studies in fuzzy logic methods for mineral prospectivity mapping have been conducted not only for uranium, but other mineral deposits, for example, iron-copper-gold (**Nykänen et al., 2008**), polymetallic mineralization (**Arjmand Lary et al., 2024**), and a hydrothermal gold deposit (**Abdelkareem & Al-Arifi, 2021**). These studies commonly integrate multiple spatial datasets such as regional geology, geochemistry, and satellite imagery. The selection of parameters and analytical techniques for uranium prospectivity mapping using GIS generally follows established frameworks (**Bierlein & Bruce, 2018; Ciputra et al., 2019b**). which outline typical data sources and suitable spatial analysis methods.

In this research, the approach was adapted to align with the geological characteristics of the Melawi region and the sandstone-type uranium model, with parameter selection reflecting the datasets available at the regional scale. Accordingly, the analysis emphasizes geological, geomorphological, and structural information relevant to the mineralization framework. The datasets incorporated into this study are described in detail below.

2.1. Spatial Data

The spatial datasets utilized in this research are selected based on key geological and environmental components relevant to the formation of sandstone-type uranium deposits. The spatial datasets are sourced from publicly available online data or digitized from existing regional maps. The spatial datasets include a 1:250,000 scale regional geological map, incorporating regional geology (see **Figure 1**) and geological structure (see **Figure 2a**), a surface water drainage map (see **Figure 2b**), a digital elevation model (DEM) (see **Figure 2c**), and a map of known uranium occurrence within the Melawi region (see **Figure 2d**). Each dataset plays a specific role in supporting the modelling and analysis of sandstone-type uranium prospectivity, which is described in **Table 1**.

2.2. Predictor Map Generation

Using the collected spatial data, a series of predictor maps is developed, each representing a key component of the genetic model for uranium mineralization. These maps are generated using GIS software, employing the UTM zone 49S coordinate system and WGS 1984 datum. The predictor maps are generated by reclassifying and processing spatial criteria derived from the datasets, which correspond to geological and environmental factors with sandstone-type uranium deposits. The resulting predictor maps include the following:

2.2.1. 'Source' map

The uranium source predictor map ('Source') was generated using surface geological data from the Melawi region. Rock units are reclassified into favourable uranium sources (granitoid igneous rocks) and less favourable sources (sedimentary, volcanic, and alluvial rocks). Furthermore, granitoid rocks are categorized based on their age, with older intrusions considered more favorable for uranium generation than the younger ones due to their longer exposure to weathering. A special case for the Melawi region is the Pinoh Metamorphic Complex, which hosts known uranium occurrences, particularly in the Kalan area (**Ngadenin et al., 2017**). The metamorphic rocks in this area are scored slightly lower with granitoid sources.

The genetic model of sandstone-type uranium mineralization states that potential sources of uranium are areas close to granitoid rocks because they are more likely to release uranium during the weathering process. The further from the granitoid source, the less favorable it becomes. Therefore, a five-level distance buffer ranging from 100 m to 5 km that accommodates potential uranium sources is applied around granitoid and metamorphic rocks (see **Figure 3a-c**). These buffer distances are considered reasonable, rational, and realistic given the scale of the research area, though they can be modified based on future adjustments in mapping resolution.

In addition to crystalline sources, sedimentary rocks themselves may also serve as minor uranium sources, as they can contribute to uranium enrichment within the sandstone host, albeit to a lesser extent. Therefore, lithological classification maps are also integrated into the model to accommodate the potential uranium ontribution from sedimentary or other rock types (see **Figure 3d**).

2.2.2. 'Transport' map

The critical factor influencing the mobility and transport of uranium in sandstone-type deposits is groundwater flow through porous and permeable media. These media are typically associated with specific geological structures and lithological units, which provide pathways for fluid migration. Surface water patterns are also an important component in uranium transport. In addition to subsurface flow, surface water systems, such as rivers and drainage networks, also play a significant role in uranium mobilization, particularly in facilitating the redistribution of dissolved uranium. Although the river networks reflect the current hydrological condition, it is reasonable to assume that the uranium mineralization in the Melawi region formed under a relatively undeformed paleogeographic setting. In addition, the paleochannels are expected to be present in the vicinity of the current river channel or within adjacent valley systems. Therefore, surface water features remain relevant indicators for interpreting historical fluid migration pathways.

A five-level buffer was applied to the river flow datasets and geological structure, ranging from 500 m to 2 km, to simulate zones of potential fluid migration and uranium transport along surface water pathways, faults, and fractures (see **Figure 4a-b**). The presence of porous

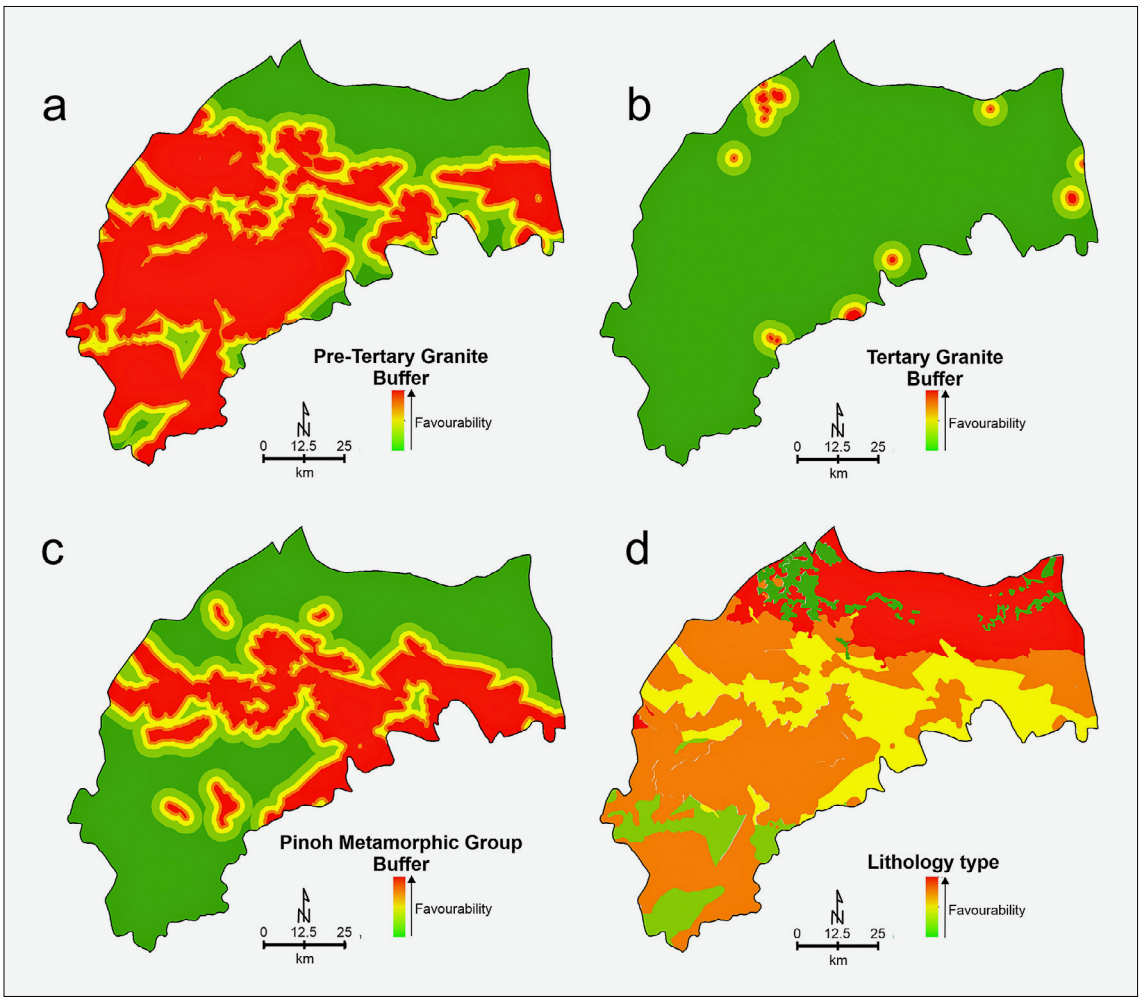


Figure 3. Predictor maps to generate the 'Source' map. (a) pre-tertiary granite, (b) tertiary granite, (c) Pinoh Metamorphic Group, and (d) lithology type.

and permeable media is another essential factor in facilitating uranium migration. These properties are typically reflected in sedimentary, volcanic, and alluvial lithologies in the Melawi region. The rock permeability map is classified into two categories: permeable and non-permeable rocks (see **Figure 4c**). Permeability values were assigned based on typical hydraulic conductivity ranges for unfractured rocks. Sandstones and pyroclastic rocks exhibit relatively high hydraulic conductivity, generally ranging from 10^{-10} to 10^{-4} m/s, with pyroclastic units reaching up to 10^{-6} m/s (**Zhang, 2013**). These lithologies were therefore classified as permeable. In contrast, granites and metamorphic rocks typically have much lower hydraulic conductivity values, ranging from 10^{-14} to 10^{-9} m/s (**Zhang, 2013**) and were accordingly classified as non-permeable. Although hydraulic conductivity can also be significantly influenced by fracturing, this effect is captured separately through the geological structure predictor map, which enhances favourability in areas where fracturing increases localized permeability.

To enhance the interpretation of surface water pathways and support paleochannel identification, a local topographic depression (local low) map is also generated (see **Figure 4d**). These depressions serve as natural catchments for surface runoff and are likely to align with former or existing flow paths. The local lows data were extracted from a digital elevation model (DEM) using 'Focal Statistics' tool within ArcGIS software. The resulting favourability classification for this map is binary (i.e. favourable or not favourable).

2.2.3. 'Trap' map

The potential of sandstone-type uranium deposits is interpreted based on the distribution of sandstone formation within the research area (see **Figure 5**). To assess this potential, sandstone formations are identified and grouped to delineate areas that provide a favorable geological environment for uranium accumulation. Based on regional geological maps, the sandstone formations contain significant amounts of organic material that could act as potential uranium traps. These formations include the Tebidah Formation, Payak Formation, Sekayam Sandstone, and Alat Sandstone. These formations serve as the primary host rocks in the genetic model of sandstone-type uranium deposits. The favourability of

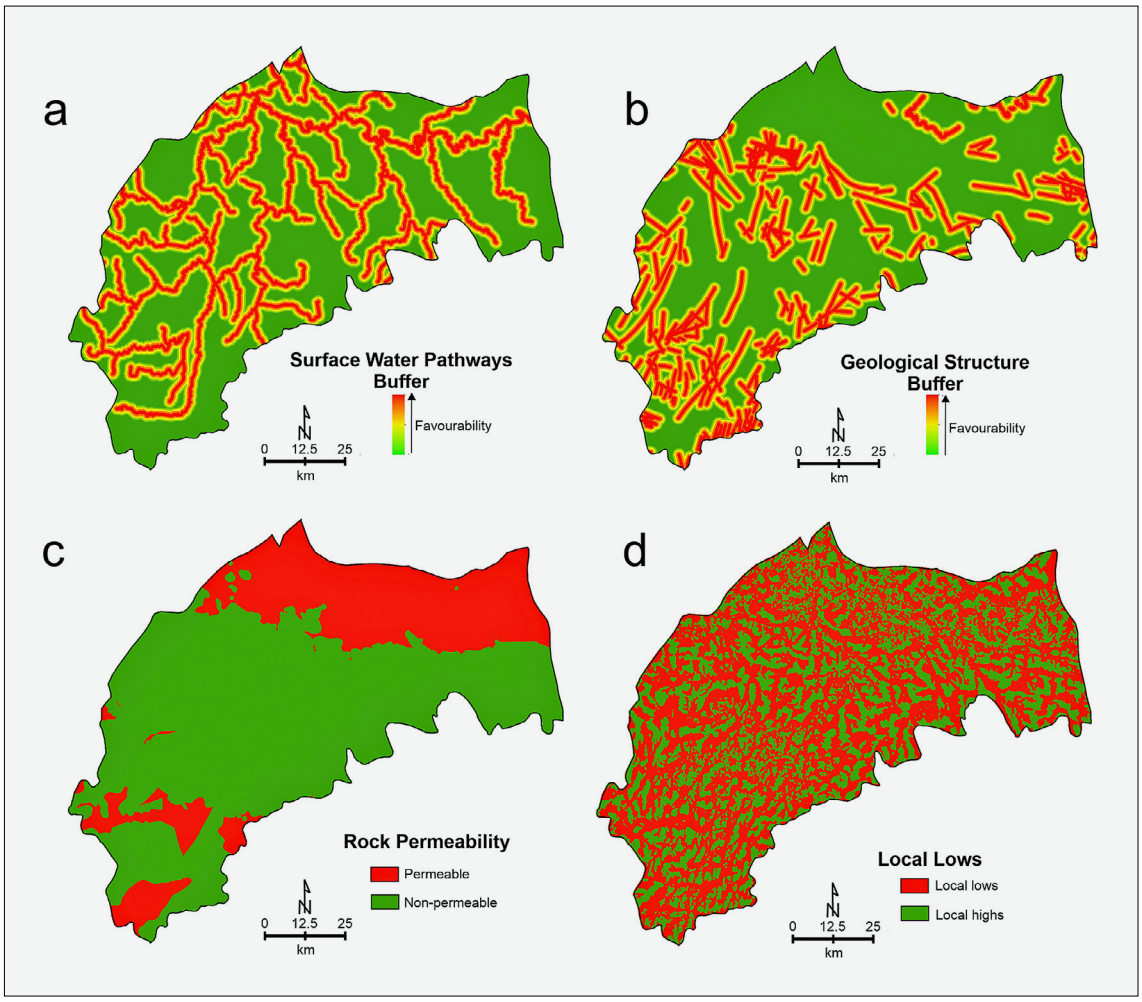


Figure 4. Predictor maps to generate the 'Transport' map. (a) surface water pathways, (b) geological structure, (c) rock permeability, and (d) local lows.

each unit was classified using a binary system ('yes' or 'no'), indicating whether the lithological conditions are conducive to uranium deposition. In addition, geomorphological features associated with groundwater and surface water movement are also considered in the analysis. Surface water pathways and topographic depressions (local lows) are integrated as potential trap components in the model. These features are critical for uranium deposition, as they influence fluid flow and create redox boundaries necessary for uranium precipitation. By incorporating these elements, the resulting prospectivity map provides a more comprehensive representation of the spatial conditions that control uranium accumulation in a sandstone-type system.

2.3. Fuzzy Value Scoring and Weighting

After compiling all predictor maps, a scoring and weighting procedure was applied to quantify the relative importance of each factor in the context of uranium mineralization model. Class scores were assigned on a 1–10 scale based on their geological favourability for uranium mineralization and each predictor map was then assigned a map weight, reflecting how strongly that parameter influences uranium sourcing, transport, or trap-

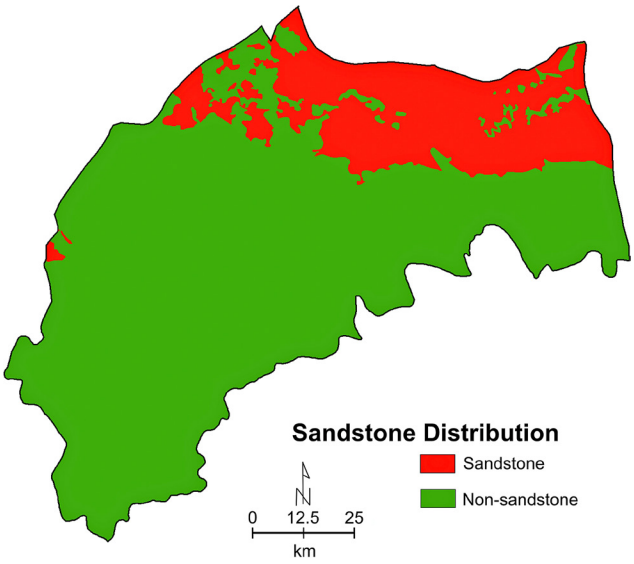


Figure 5. Sandstone distribution acts as a trap in fuzzy logic modelling.

Table 2. Justification of favourability for each parameter in fuzzy logic.

Maps			Favourability	Comment
'Source'	Granitoid Sources	Pre-tertiary granitoids	High	Older granitoids are more favorable due to prolonged weathering exposure. The older the rocks, the higher the favourability. The distance to the source also affect the favourability. The closer to the source, the higher the favorability
		Tertiary granitoids	Moderate - High	
	Metamorphic Sources		Moderate	Metamorphic rocks are generally unfavorable, but the Pinoh Metamorphic is an exception due to known uranium occurrences in the Kalan area. the closer to the source, the higher the favorability
	Lithology type		Moderate	All lithologies are considered to have a slight uranium potential.
'Transport'	Surface Water pathways		High	Plays a significant role in uranium mobilization. The closer to the water pathways, the higher the favourability.
	Geological structure		Low-Moderate	Creates subsurface flow and acts as a permeable medium. The closer to the structure, the higher the favourability.
	Local lows		Moderate	Serves as a natural catchment for surface runoff. Only local lows act as natural catchment.
	Rock permeability		Moderate - High	Functions as a permeable pathway for uranium transport. The more permeable the rocks, the more favourable as 'Transport' factor.
'Trap'	Surface Water pathways		Moderate - High	Reflects a paleochannel with potential as a uranium trap. The closer to the water pathways, the higher the favourability.
	Local lows		Moderate	Acts as a potential trap for uranium deposition
	Sandstone		High	Represents a major trap in sandstone-type uranium deposits

Table 3. Weighting of fuzzy values for each class in the generation of the 'Source' map.

Maps			Class	Class Score	Map Weight	Class Weight	Fuzzy Value
'Source'	Granitoid sources	Pre-tertiary granitoids	0.1 km	10	9	90	0.9
			1 km	9	9	81	0.81
			2.5 km	7	9	63	0.63
			5 km	5	9	45	0.45
			> 5 km	3	9	27	0.27
		Tertiary granitoids	0.1 km	10	7	70	0.7
			1 km	9	7	63	0.63
			2.5 km	7	7	49	0.49
			5 km	5	7	35	0.35
			> 5 km	3	7	21	0.21
	Metamorphic sources	Pinoh Metamorphic	0.1 km	10	5	50	0.5
			1 km	9	5	45	0.45
			2.5 km	7	5	35	0.35
			5 km	5	5	25	0.25
			> 5 km	3	5	15	0.15
	Lithology type		Intrusive	7	5	35	0.35
			Metamorphic	5	5	25	0.25
			Sedimentary	9	5	45	0.45
			Volcanic	3	5	15	0.15
			Alluvial	1	5	5	0.05

ping in the Melawi region, with the justification for each parameter and map weight summarized in **Table 2**.

To convert these inputs into fuzzy membership values, the scoring followed a two-step process. First, the class score was multiplied by the map weight to produce a class weight (class weight = class score × map weight). This value incorporates both the intrinsic favourability of each class and the relative significance of the parameter. Second, the class weight was divided by 100 to obtain the fuzzy membership value, resulting in standardized values between 0 and 1 that can be integrated within the fuzzy logic model.

Table 4. Weighting of fuzzy values for each class in the generation of the 'Transport' map.

Maps		Class	Class Score	Map Weight	Class Weight	Fuzzy Value
'Transport'	Surface water pathways	0,5 km	9	8	72	0.72
		1 km	7	8	56	0.56
		1.5 km	5	8	40	0.4
		2 km	3	8	24	0.24
		> 2 km	1	8	8	0.08
	Geological structure	0,5 km	9	4	36	0.36
		1 km	7	4	28	0.28
		1.5 km	5	4	20	0.2
		2 km	3	4	12	0.12
		> 2 km	1	4	4	0.04
	Local Lows	Local Low	9	5	45	0.45
		Local High	0	5	0	0.001
	Rock permeability	Permeable	9	7	63	0.63
		Non-Permeable	2	7	14	0.14

Table 5. Weighting of fuzzy values for each class in the generation of the 'Trap' map.

Maps		Class	Class Score	Map Weight	Class Weight	Fuzzy Value
'Trap'	Surface water pathways	0.5 km	9	7	63	0.63
		1 km	7	7	49	0.49
		1.5 km	5	7	35	0.35
		2 km	3	7	21	0.21
		> 2 km	1	7	7	0.07
	Local Lows	Local Low	9	5	45	0.45
		Local High	0	5	0	0.001
	Sandstone	Yes	9	9	81	0.81
		No	0	9	0	0.001

The assignment of class score and map weights was guided by three considerations: (1) the genetic model of sandstone-type uranium deposits, (2) geological evidence from Melawi, and (3) weighting references from **Bierlein & Bruce (2018**). For example, pre-Tertiary granitoids received the highest weights in the 'Source' map because they are the most plausible uranium sources, while lithology types received lower weights due to their more indirect role. In the 'Transport' component, surface water pathways and rock permeability were weighted more heavily because they exert strong control on uranium mobility, whereas structures and local lows were weighted moderately. In the 'Trap' component, sandstone units received the highest weights as the main host for uranium precipitation, while local lows and surface water pathways were assigned moderate weights as secondary trapping indicators. The final class scores, map weights, class weights, and corresponding fuzzy membership values are presented in **Table 3 to Table 5**.

2.4. Prospectivity Map Generation

The predictor maps are integrated using fuzzy operators to generate the 'Source', 'Transport', and 'Trap' components, based on the process applied by **Bierlein & Bruce (2018) and Ciputra et al. (2019)**. This process culminates in the final prospectivity map for sandstone-type uranium deposits in the Melawi region, as illustrated in **Figure 6**. The fuzzy logic approach enables the combination of multiple spatial datasets with varying degrees of uncertainty and influence. In this analysis, the fuzzy operators employed include 'OR', 'SUM', and 'GAMMA', each selected based on its ability to represent specific relationships among the predictor variables. These operators facilitate the aggregation of input maps by capturing the cumulative favorability of multiple factors, thereby producing a continuous surface that reflects the spatial potential for uranium mineralization.

In constructing the 'Source' predictor map, proximity to uranium-bearing source rocks is the primary consideration. Buffer zones and weighting are applied to quantify the spatial influence of granitoid, metamorphic, and sedimentary units known or inferred to contain uranium. The overlay between multiple source types does not increase the favourability of the area to be a 'Source'. Therefore, the fuzzy 'OR' operator is employed to analyse the fuzzy values, as it selects the highest favourabil-

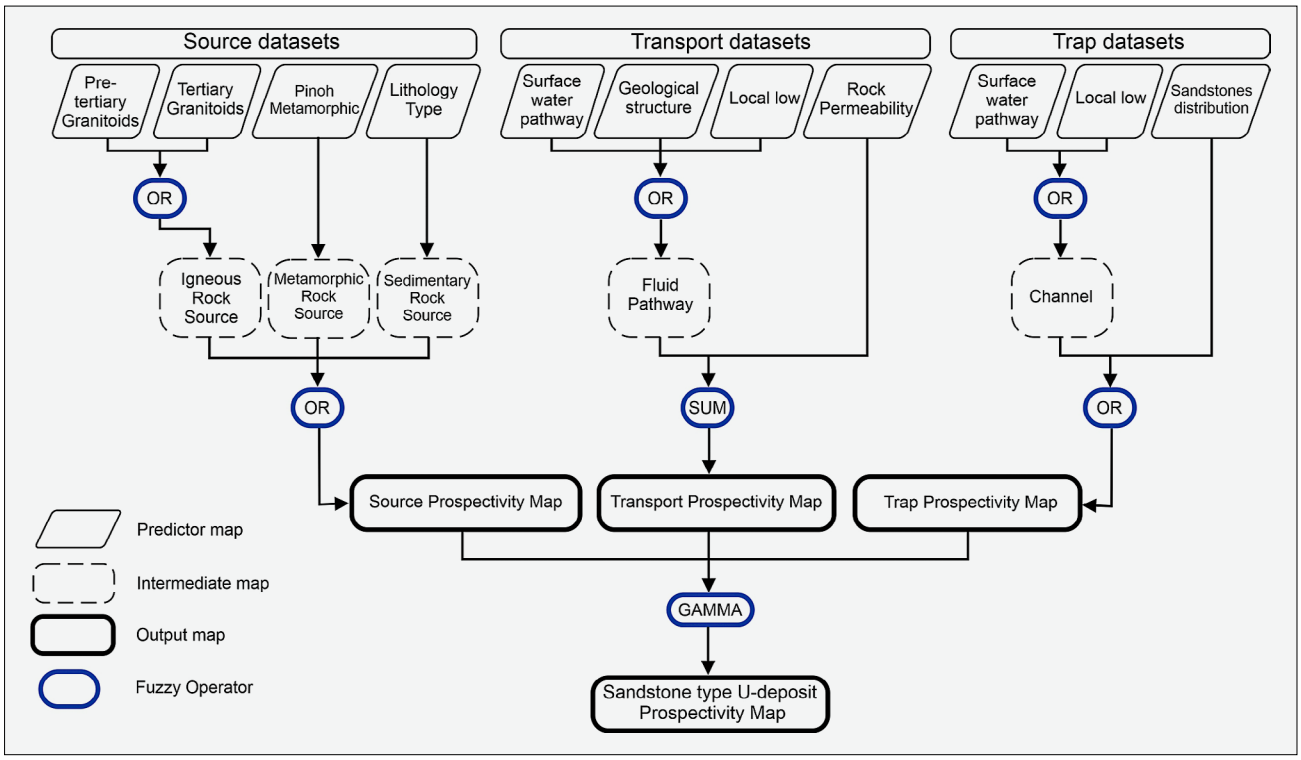


Figure 6. The fuzzy logic flowchart for generating a sandstone-type uranium deposit prospectivity map.

ity among overlapping layers. As a result, the final 'Source' map reflects the maximum favourability value from each of the contributing predictor maps, granitoid, metamorphic, and sedimentary rock units, rather than summing their individual effects.

For the 'Transport' map, a two-step fuzzy logic integration is applied. First, structural features, stream networks, and local lows are combined using the fuzzy 'OR' operator to create a composite 'Fluid Path' map, representing potential conduits for fluid movement. This layer is then merged with the rock permeability map using the fuzzy 'SUM' operator. The 'SUM' operator is chosen because both permeability and fluid pathways are mutually reinforcing factors in facilitating uranium transport. Their combined effect increases the overall favorability of the transport system.

The 'Trap' map is developed by identifying areas of potential uranium accumulation, primarily within sandstone-rich formations and channel-like features derived from surface hydrology and local lows. These predictor maps are integrated using the fuzzy 'OR' operator, as the presence of any one trapping mechanism is sufficient to suggest potential for uranium deposition.

In the final stage of analysis, the 'Source', 'Transport', and 'Trap' maps are integrated to generate the overall prospectivity map using the 'GAMMA' operator. This operator represents a compromise between the 'SUM' and 'PRODUCT' functions and requires the specification of gamma values. A low gamma input will produce an effect closer to 'PRODUCT' than 'SUM' and vice versa. In this study, a relatively low gamma value (gamma = 0.3) is applied to emphasize locations where all three components ('Source', 'Transport', and 'Trap') show high favourability. This approach ensures that areas with consistently high values across all three components are highlighted, while regions with lower favourability in one or more components still retain moderate potential depending on their composite fuzzy scores.

3. Results

The 'Source' favourability map for sandstone-type uranium mineralization (see **Figure 7a**) illustrates the potential of various lithological units to act as primary uranium sources. Zones of highest favourability, depicted in red, are prominently concentrated in the central and southern regions, spatially associated with the Menunuk Volcanic and the Sepauk Tonalite. These pre-Tertiary granitoid complexes are theoretically capable of contributing significant amounts of uranium to the mineralizing system. A secondary zone of moderately high favourability (shown in orange) is located in the western region, corresponding to the Sintang Intrusion, a Tertiary granitoid body also recognized for its uranium-bearing potential. Conversely, the northern segment of the area is characterized by low favourability (green), correlating with widespread sedimentary and metamorphic units of the Melawi region. These formations are generally considered to be geochemically depleted in uranium and thus less suitable as source rocks.

The 'Transport' favourability map (see **Figure 7b**) delineates zones that facilitate uranium mobilization

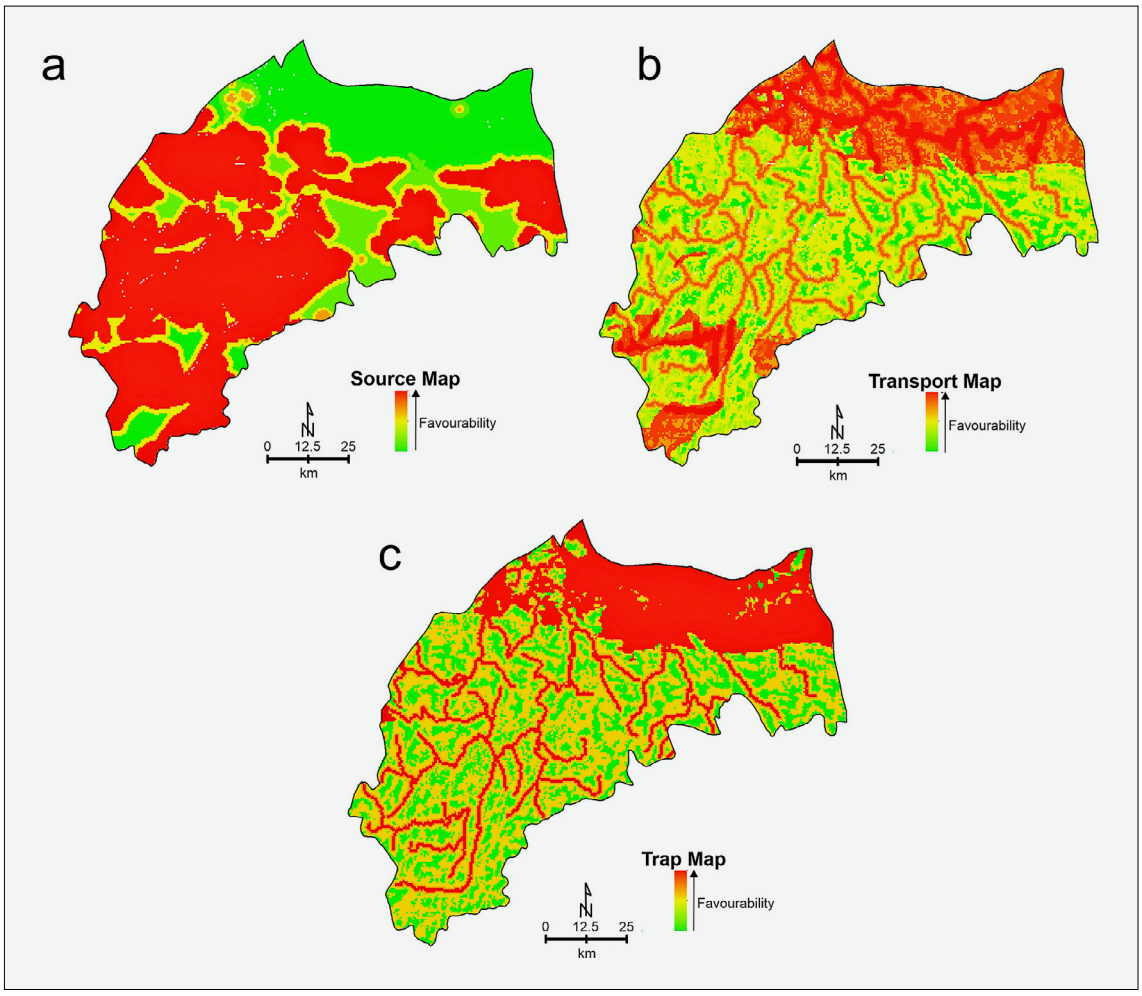


Figure 7. Favourability maps of (a) Source, (b) Transport, and (c) Trap for sandstone-type uranium deposit in Melawi.

through groundwater flow. Zones of high transport favourability are predominantly located in the northern and southwestern parts of the region, where steeper topographic gradients and dense drainage networks enhance subsurface fluid movement. These areas are underlain by permeable lithologies, including sandstones and pyroclastic volcanic deposits, which promote efficient uranium migration. Moderate favourability zones are dispersed across the central region, reflecting areas of partial hydrological connectivity and intermediate topographic slope. In contrast, low favourability zones are found in hydrologically isolated and topographically elevated areas, particularly in the southern part of Melawi, where limited permeability restricts fluid migration..

The 'Trap' favourability map (see **Figure 7c**) highlights zones with favorable conditions for the physical and geochemical retention of mobilized uranium. High trap favourability zones are concentrated in the northern region, corresponding to the Tebidah and Payak formations. These sedimentary units comprise interbedded sandstones with mudstones, siltstones, and subordinate coal seams, offering a combination of porosity, permeability, and redox interfaces ideal for uranium deposition. Additional high favourability zones are aligned with major surface water pathways, where topographic depressions and drainage convergence zones create localized trap environments. In contrast, the central and southern parts of the region exhibit low to moderate trap favourability. These regions are generally characterized by impermeable lithologies or elevated terrain, limiting their capacity to act as effective uranium traps.

The integrated prospectivity map for sandstone-hosted uranium deposits in the Melawi region, as illustrated in **Figure 8**, synthesizes the three critical components of the mineralizing system: source, transport, and trap. The highest prospectivity is concentrated in the northern part of the area, particularly where the Sepauk Tonalite is in direct contact with the Tebidah Formation, a geologically favorable interface for uranium mineralization. This area benefits from proximal source rocks, well-developed fluid transport pathways, and adequate sedimentary traps, representing approximately 36.64% of the total study area. Areas of moderate prospectivity, covering about 25.34%, are distributed along the regional drainage network and in topographic depressions, both of which act as potential zones for uranium pre-

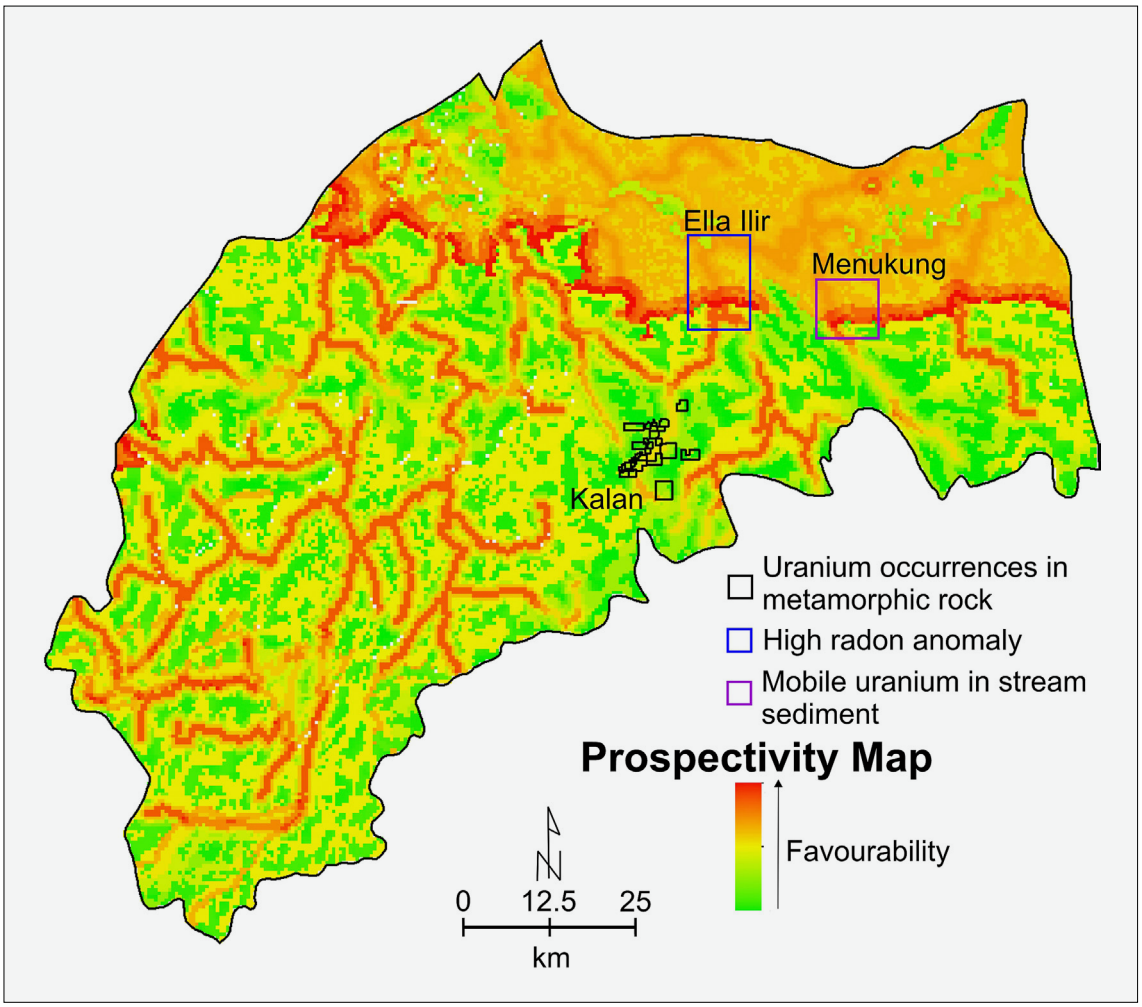


Figure 8. Prospectivity Map of sandstone-type uranium deposit in Melawi, West Kalimantan, Indonesia.

cipitation and concentration. In contrast, low prospectivity zones account for 38.02% of the area and correspond to areas lacking in one or more essential system components, typically those with inadequate source potential, limited permeability, or absence of trap mechanisms.

4. Discussion

The implementation of the source–transport–trap framework within a GIS-based fuzzy logic model provides a systematic and reproducible approach to assess uranium prospectivity in the Melawi region. By integrating geological, hydrological, and geomorphological data, the model enables spatially explicit assessments of favorability across diverse terrain. This discussion critically examines the extent to which the model outputs correspond with known regional geological features like lithological distributions, structural trends, and sedimentary environments. Additionally, the discussion identifies areas where the model may benefit from refinement, particularly in regions with limited data resolution, complex structural histories, or ambiguous geochemical signatures. These insights provide a foundation for improving predictive accuracy and guiding future field investigations.

4.1. Evaluation and validation of Prospectivity Mapping in the Melawi Region

The favourability of uranium source rocks in the Melawi region is closely associated with the occurrence of Pre-Tertiary granitoids, particularly the Sepauk Tonalite and Menunuk Volcanics. These felsic magmatic bodies are characteristically enriched in uranium and other incompatible elements (**Cuney, 2014**), suggesting that they represent the primary contributors to uranium supply in the regional system. The central and southern parts of the study area, where these granitoids are exposed, correspond to high favourability zones in the 'Source' fuzzy layer of the model. Geochemical analyses of granitoid rocks in West Kalimantan reveal variable uranium concentrations: 1.0–3.0 ppm U in Sepauk Tonalite, 0.3–3.7 ppm U in Menunuk Volcanics, and 4.0–7.48 ppm U in Sukadana Granite (**Breitfeld et al., 2020; Hennig et al., 2017**). In addition, metamorphic rocks in the Melawi region exhibit similar uranium con-

centrations, ranging from 0.3 to 3.8 ppm U (**Breitfeld et al., 2020**), could play a subsidiary role in sustaining long-term leaching and uranium release through weathering and fluid–rock interactions. Uranium concentrations in the Kalan area, specifically in the host rocks and associated weathered soils, range from 38.7 to 392.0 ppm U. While uranium concentration in the ore bodies has been reported to contain up to 2.8 wt.% U (**Adimedha et al., 2024**). These data suggest that both granitoid and metamorphic units in the region represent viable uranium sources, contributing to the overall mineralization system.

The configuration of slope gradients, drainage convergence, and permeable lithologies in the central-to-northern corridors of Melawi defines a coherent uranium transport pathway. This spatial pattern is consistent with the classical sandstone-type uranium system, in which oxidizing fluids leach uranium from felsic sources and migrate through porous host formations (**Bierlein & Bruce, 2018; IAEA, 2009**). The distribution of sandstones and fine-grained volcaniclastic rocks favours fluid infiltration and the maintenance of an oxidizing geochemical environment required for uranium transport. The topographic depressions and zones of drainage convergence identified in the fuzzy logic model coincide with possible uranium accumulation sites, consistent with known depositional settings where fluid velocity decreases and reductive conditions may dominate.

The Tebidah and Payak formations in the northern part of the Melawi region provide a particularly plausible trap environment. These formations exhibit favourable porosity and permeability conditions and contain interbedded mudstone and thin coal seams that serve as natural reductants (**Badaruddin et al., 2019**). The alternation between permeable and impermeable strata allows redox interfaces to develop within confined aquifer systems, analogous to those observed in well-documented sandstone-type uranium provinces such as the Wyoming basin and Ordos basin (**Hall et al., 2017; Jin et al., 2019**). The spatial proximity between the Tebidah–Payak sedimentary sequences and the granitoid bodies in the south further reinforces the geological plausibility of an integrated source–transport–trap mineralization system (**Cuney et al., 2022; Dahlkamp, 2009**).

The strong anomalous radon concentrations detected in the Ella Ilir area and the elevated mobile uranium in the Menukung stream sediments are consistent with this model, indicating active uranium mobility within the basin (**Cakrabuana et al., 2021b; Indrastomo et al., 2024**). Such patterns are typically associated with uranium-bearing fluids migrating from granitoid sources into reductive sandstone traps. The spatial alignment between these geochemical indicators and the modelled high-prospectivity zones suggests that the northern Melawi corridor may represent a dynamic interface between oxidizing and reducing regimes, where uranium could precipitate and accumulate. Overall, the geological configuration of the Melawi basin exhibits strong internal coherence with the source–transport–trap model, implying high geological plausibility for the occurrence of sandstone-type uranium mineralization.

4.2. Limitations and Improvements for Prospectivity Mapping in the Melawi Region

The prospectivity map generated for sandstone-type uranium mineralization in the Melawi region demonstrates the utility and flexibility of GIS-based fuzzy logic modeling. However, it also reveals certain limitations and assumptions that affect the precision and reliability of the analysis. A key issue lies in the input data quality and the assumptions embedded within the source–transport–trap model used in this study. In constructing the 'Source' favourability map, granitoid rocks were uniformly assumed to be uranium-bearing. While this generalization is useful for regional-scale mapping, it oversimplifies the geochemical variability inherent in granitic bodies. Not all granitoid rocks possess elevated uranium content; compositional differences linked to petrogenesis, tectonic setting, and magmatic evolution critically influence uranium enrichment potential. Incorporating the SIAM classification proposed by **Winter (2001)** and radiometric datasets (**Cakrabuana et al., 2021a; Sukadana et al., 2021**) would significantly improve model validity and discriminative capacity.

Similarly, the geological structure dataset used to represent the 'Transport' factor was derived from regional geological maps, which often include lineaments of ambiguous kinematic and temporal significance. In this study, all mapped structures were assumed to be open and capable of facilitating fluid migration. However, fluid pathways are governed by fracture aperture, connectivity, and orientation relative to stress fields (**Boadu, 2000**). Integrating high-resolution structural interpretations, fault kinematics, and fracture density from field-based or remote sensing analyses (e.g. InSAR, LiDAR) could significantly refine this model. The substitution of hydrogeological data with lithology-derived permeability assumptions is another simplification that affects the accuracy of the 'Transport' model. Actual groundwater flow conditions, governed by porosity, water table gradient, and recharge/discharge dynamics, are more complex and can significantly influence uranium mobility and localization. The inclusion of groundwater data, such as hydraulic conductivity and potentiometric surfaces, would offer a more realistic representation of the uranium migration pathway (**Bierlein & Bruce, 2018; Kreuzer et al., 2010**). Furthermore, the use of current surface water networks as proxies for paleochannels, although practical, introduces uncertainty. Paleochannels, which are often deeply buried, are key conduits and traps for uranium-bearing fluids in sandstone-type deposits (**IAEA, 2009**). Geophysical methods, along with sedimentological reconstructions, can help identify paleochannel features more accurately. Regarding the

'Trap' factor, the model correctly emphasizes the presence of Tebidah and Payak formations, both dominated by sandstones interbedded with mudstones and coal seams, as favourable lithologies for uranium precipitation. These units provide the reductive environment essential for sandstone-type uranium mineralization. However, incorporating redox interface mapping and detailed stratigraphic profiles would further constrain the trap potential of these units.

Despite these limitations, the fuzzy logic approach has shown strong potential in delineating prospective zones. Its ability to incorporate expert-driven weights and handle fuzzy boundaries between favourability classes is beneficial in areas with limited data resolution. The success of this approach in Melawi echoes its application in North Sumatra (**Ciputra et al., 2019b**), where high-favourability zones identified through fuzzy logic were validated through occurrences of uranium mineralization. Nevertheless, the outcomes of this study must be viewed as preliminary. To transition from broad regional modelling to exploration-ready targets, field validation is essential. High-resolution ground radiometric surveys, radon gas measurements, and stratigraphic test drilling should be prioritized in high-favourability zones to verify subsurface uranium concentrations and depth profiles. Subsequent petrographic and mineralogical analyses of core samples will provide valuable insight into uranium-hosting phases and alteration processes. Furthermore, continued integration of remote sensing, geophysics, and detailed geological mapping will enhance the predictive power of the model. Overall, the application of GIS-based fuzzy logic has proven effective in identifying sandstone-type uranium prospectivity in the Melawi region, but further refinement through advanced datasets and field-based confirmation will be crucial to advancing uranium exploration in this geologically promising area.

5. Conclusions

This study provides the first systematic regional-scale assessment of sandstone-type uranium prospectivity in the Melawi region, West Kalimantan, using an integrated GIS-based fuzzy logic approach. The results demonstrate that approximately 36.64% of the area exhibits high prospectivity, concentrated in the northern sector where the granitoid rocks are in direct contact with the sandstone formation, creating an interface that fulfills the essential 'source–transport–trap' criteria for uranium mineralization. These outcomes demonstrate the effectiveness of fuzzy logic in addressing geological uncertainty and limited dataset conditions that commonly challenge early-stage exploration in Indonesia. This finding also offers new insight into the spatial correlation between granitoid-derived uranium sources and sedimentary trap environments in Indonesia, highlighting Melawi as a geologically coherent and underexplored uranium deposit.

The prospectivity map produced in this study provides a prioritized uranium exploration area in Melawi region, West Kalimantan. This work advances uranium exploration research in Indonesia by establishing a replicable and transparent methodology that can be applied to other sedimentary basins across Indonesia. While the model successfully delineates key target zones, further refinement will require additional datasets and multidisciplinary validation. Integrating airborne radiometric surveys, hydrogeochemical sampling, fracture-density modelling, and paleochannel reconstruction would significantly enhance predictive confidence. Overall, this study establishes a new benchmark for regional uranium prospectivity modelling in Indonesia, providing both scientific insight and practical guidance to support the development of domestic uranium resources for sustainable energy security.

Acknowledgement

The authors would like to express gratitude to the Research Center for Nuclear Material and Radioactive Waste Technology, National Research and Innovation Agency (BRIN), for providing the facilities and support for the completion of this research.

6. References

Abdelkareem, M., & Al-Arifi, N. (2021). Synergy of remote sensing data for exploring hydrothermal mineral resources using gis-based fuzzy logic approach. *Remote Sensing*, *13*(22). https://doi.org/10.3390/rs13224492

Adimedha, T. B., Farrenzo, R. A., Sukadana, I. G., & Nugraheni, R. D. (2024). Distribution and Characteristics of Rare Earth Elements in Uranium-Ore Deposits from Rirang Area , West Kalimantan Province , Indonesia. *Eksplorium*, *45*(1), 1–16. https://doi.org/10.55981/eksplorium.2024.7058

Amiruddin, & Trail, D. S. (1993). *Geological Map of The Nangapinoh Sheet, Kalimantan, Scale 1:250000*.

Arjmand Lary, Z., Honarmand, M., Shahriari, H., & Hosseinjani Zadeh, M. (2024). Data Integration by Fuzzy Logic for Mineral Prospectivity Mapping in Ferdows–Gonabad–Bajestan Belt, Khorasan Razavi Province, Iran. *Journal of the Indian Society of Remote Sensing*, *52*(6), 1223–1243. https://doi.org/10.1007/s12524-024-01873-7

Badan Informasi Geopasial. (2017). *Ina-Geoportal*.

Badaruddin, D. F., Hidayat, Adlan, R., Ramli, T., & Nurhidayat, M. (2019). Sintang Intrusive Delineation and Focus Area for Hydrocarbon Exploration in Melawi Basin, West Kalimantan. *Proceedings Indonesian Petroleum Association 43th Annual Convention & Exhibition*, *November 2020*. https://doi.org/10.29118/ipa19.g.172

Badaruddin, D. F., Suyono, Nurhidayat, M., Baharuddin, Asmoro, P., & Saragih, R. Y. (2018). Post-Mortem Analysis of Drilling Failure of Kayan-1 and Kedukul-1 Wells in Melawi Basin, West Kalimantan. *Indonesia Petroleum Association*, *August 2023*.

Berthold, M. (1999). *Fuzzy Logic BT - Intelligent Data Analysis: An Introduction* (M. Berthold & D. J. Hand (eds.); pp. 269–298). Springer Berlin Heidelberg. https://doi.org/10.1007/978-3-662-03969-4_8

Bierlein, F. P., & Bruce, M. P. (2018). A Continent-Scale GIS-Based Assessment of the Distribution and Potential for Sandstone-Hosted Uranium Deposits. In *Quantitative and Spatial Evaluation of Undiscovered Uranium Resources* (pp. 133–168). International Atomic Energy Agency.

Boadu, F. K. (2000). Hydraulic Conductivity of Soils from Grain-Size Distribution: New Models. *Journal of Geotechnical and Geoenvironmental Engineering*, *126*(8), 739–746. https://doi.org/10.1061/(ASCE)1090-0241(2000)126:8(739)

Brandmeier, M., Cabrera Zamora, I. G., Nykänen, V., & Middleton, M. (2020). Boosting for Mineral Prospectivity Modeling: A New GIS Toolbox. *Natural Resources Research*, *29*(1), 71–88. https://doi.org/10.1007/s11053-019-09483-8

Breitfeld, H. T., Davies, L., Hall, R., Armstrong, R., Forster, M., Lister, G., Thirlwall, M., Grassineau, N., Hennig-Breitfeld, J., & van Hattum, M. W. A. (2020). Mesozoic Paleo-Pacific Subduction Beneath SW Borneo: U-Pb Geochronology of the Schwaner Granitoids and the Pinoh Metamorphic Group. *Frontiers in Earth Science*, *8*(December). https://doi.org/10.3389/feart.2020.568715

Bruneton, P., & Cuney, M. (2016). Geology of uranium deposits. In *Uranium for Nuclear Power: Resources, Mining and Transformation to Fuel* (Issue 1956). Elsevier Ltd. https://doi.org/10.1016/B978-0-08-100307-7.00002-8

Cakrabuana, W., Argianto, E. N. S., Ciputra, R. C., & Kamajati, D. (2021a). Geological, Geochemical, and Radiometric Study of Sandstone-Type Uranium Deposit Exploration in Menukung Area, West Borneo. *Indonesian Association of Geologists Journal*, *1*(1), 1–12. https://doi.org/10.51835/iagij.2021.1.1.15

Cakrabuana, W., Ciputra, R. C., & Syaeful, H. (2021b). Assessing the undiscovered resources of uranium and thorium in Mamuju, West Sulawesi. *IOP Conference Series: Earth and Environmental Science*, *851*(1). https://doi.org/10.1088/1755-1315/851/1/012041

Carranza, E. J. M. (2008). *Geochemical Anomaly and Mineral Prospectivity Mapping in GiS. In: Handbook of Exploration and Environmental Geochemistry, volume 11*. Elsevier.

Ciputra, R. C., Muhammad, A. G., Adimedha, T. B., Syaeful, H., & Sukadana, I. G. (2019a). Estimasi Sumber Daya Uranium Tipe Batupasir di Sektor Aloban, Sibolga, Tapanuli Tengah (Uranium Resources Estimation of Sandstone-Type Deposit in Aloban Sector, Sibolga, Tapanuli Tengah). *Eksplorium*, *40*(1), 1-10. (in Indonesian-English abstract available). https://doi.org/10.17146/eksplorium.2019.40.1.5360

Ciputra, R. C., Adimedha, T. B., & Syaeful, H. (2019b). Fuzzy Logic Application for Sandstone-Hosted Uranium Deposit Prospectivity Mapping of Sibolga Area, North Sumatera. *The 11th MGEI Annual Convention, "Unlocking Concealed and Complex Deposits,"* 89–98.

Ciputra, R. C., Suharji, Kamajati, D., & Syaeful, H. (2020). Application of geostatistics to complete uranium resources estimation of Rabau Hulu Sector, Kalan, West Kalimantan. *E3S Web of Conferences*, *200*. https://doi.org/10.1051/e3sconf/202020006001

Ciputra, R. C., Heriawan, M. N., Syaeful, H., Kamajati, D., & Rahmawati, P. (2022). Geostatistical Ore Body Modeling on Uranium Mineralization in Remaja Sector, Kalan Area, West Kalimantan. *Eksplorium*, *43*(1), 41. https://doi.org/10.17146/eksplorium.2022.43.1.6622

Cuney, M. (2014). Felsic magmatism and uranium deposits. *Bulletin de La Societe Geologique de France*, *185*(2), 75–92. https://doi.org/10.2113/gssgfbull.185.2.75

Cuney, M., Mercadier, J., & Bonnetti, C. (2022). Classification of Sandstone-Related Uranium Deposits. *Journal of Earth Science*, *33*(2), 236–256. https://doi.org/10.1007/s12583-021-1532-x

Dahlkamp, F. J. (2009). *Uranium Deposits of the World: Asia*. Springer-Verlag.

Davies, L., Hall, R., & Armstrong, R. (2014). Cretaceous Crust in South West Borneo: Petrological, Geochemical, and Geochronological Constraints from the Schwaner Mountains. *Proceedings Indonesian Petroleum Association 38th Annual Convention & Exhibition*. https://doi.org/10.1017/CBO9781107415324.004

Farrenzo, R. A., Nugraheni, R. D., Sukadana, I. G., Indrastomo, F. D., & Adimedha, T. B. (2023). Characterization of Metapelite and Metasiltstone as Uranium-REE hosted rocks in Rirang Area, West Kalimantan. *IOP Conference Series: Earth and Environmental Science*, *1233*(1), 012027. https://doi.org/10.1088/1755-1315/1233/1/012027

Hall, S. M., Mihalasky, M. J., Tureck, K. R., Hammarstrom, J. M., & Hannon, M. T. (2017). Genetic and grade and tonnage models for sandstone-hosted roll-type uranium deposits, Texas Coastal Plain, USA. *Ore Geology Reviews*, *80*, 716–753. https://doi.org/10.1016/j.oregeorev.2016.06.013

Hennig, J., Breitfeld, H. T., Hall, R., & Nugraha, A. M. S. (2017). The Mesozoic tectono-magmatic evolution at the Paleo-Pacific subduction zone in West Borneo. *Gondwana Research*, *48*, 292–310. https://doi.org/10.1016/j.gr.2017.05.001

IAEA. (2009). *World Distribution of Uranium Deposits (UDEPO) with Uranium Deposit Classification, 2009 Edition, IAEA-TECDOC-1629*. IAEA. https://doi.org/ISBN 978-92-0-1-110509-7 NV - 1629

Indrastomo, F. D., Sukadana, I. G., Adimedha, T. B., Cakrabuana, W., Fauzi, R., Syaeful, H., Ciputra, R. C., & Rachael, Y. (2024). Uranium Deposit Reflection from Radon-Thoron in Melawi Basin, West Kalimantan. *AIP Conference Proceedings*, *2967*(1). https://doi.org/10.1063/5.0192880

Jin, R., Teng, X., Li, X., Si, Q., & Wang, W. (2019). Genesis of sandstone-type uranium deposits along the northern margin of the Ordos Basin, China. *Geoscience Frontiers*, *March*. https://doi.org/10.1016/j.gsf.2019.07.005

Karakosta, C., Pappas, C., Marinakis, V., & Psarras, J. (2013). Renewable energy and nuclear power towards sustainable development: Characteristics and prospects. *Renewable and Sustainable Energy Reviews*, *22*, 187–197. https://doi.org/10.1016/j.rser.2013.01.035

Kong, W., Chen, J., & Zhu, P. (2024). Machine Learning-Based Uranium Prospectivity Mapping and Model Explainability Research. *Minerals*, *14*(2), 1–20. https://doi.org/10.3390/min14020128

Kreuzer, O. P., Markwitz, V., Porwal, A. K., & McCuaig, T. C. (2010). A continent-wide study of Australia's uranium potential. Part I: GIS-assisted manual prospectivity analysis. *Ore Geology Reviews*, *38*(4), 334–366. https://doi.org/10.1016/j.oregeorev.2010.08.003

Li, Q., Chen, G., & Wang, D. (2024). Mineral Prospectivity Mapping Using Semi-supervised Machine Learning. *Mathematical Geosciences*. https://doi.org/10.1007/s11004-024-10161-6

Muhammad, A. G., Saputra, R. C., & Syaeful, H. (2019). Fracture Analysis of Uranium-Bearing Rock in Eko-Remaja Exploration Tunnel at Depth 50-200 Meters, Kalan, West Kalimantan. *Journal of Physics: Conference Series*, *1363*(1). https://doi.org/10.1088/1742-6596/1363/1/012013

Ngadenin, Sumaryanto, A., Syaeful, H., & Sukadana, I. G. (2017). Geologi dan Mineralisasi Uranium di Daerah Kalan, Kabupaten Melawi, Kalimantan Barat (Geology and Uranium Mineralization in Kalan Area, Melawi Regency, West Kalimantan). *Seminar Nasional Kebumian XII*, 108-114. (in Indonesian).

Ngadenin, Syaeful, H., Widana, K. S., & Nurdin, M. (2014). Potensi Thorium dan Uranium di Kabupaten Bangka Barat (Potency of Thorium and Uranium in West Bangka Region). *Eksplorium*, *35*(2), 69-84.(in Indonesian-English abstract available). https://doi.org/https://doi.org/10.17146/eksplorium.2014.35.2.2754

Nykänen, V., Groves, D. I., Ojala, V. J., Eilu, P., & Gardoll, S. J. (2008). Reconnaissance-scale conceptual fuzzy-logic prospectivity modelling for iron oxide copper - Gold deposits in the northern Fennoscandian shield, Finland. *Australian Journal of Earth Sciences*, *55*(1), 25–38. https://doi.org/10.1080/08120090701581372

Permana, S., Trianti, N., & Rahmansyah, A. (2022). Nuclear Energy Contribution for Net Zero Emission and National Energy Mix 2060 in Indonesia. *Journal of Physics: Conference Series*, *2243*(1). https://doi.org/10.1088/1742-6596/2243/1/012066

Porwal, A. K., & Kreuzer, O. P. (2010). Introduction to the Special Issue: Mineral prospectivity analysis and quantitative resource estimation. *Ore Geology Reviews*, *38*, 121–127.

Rosianna, I., Nugraha, E. D., Syaeful, H., Putra, S., Hosoda, M., Akata, N., & Tokonami, S. (2020). Natural radioactivity of laterite and volcanic rock sample for radioactive mineral exploration in Mamuju, Indonesia. *Geosciences (Switzerland)*, *10*(9), 1–13. https://doi.org/10.3390/geosciences10090376

Rosianna, I., Nugraha, E. D., Tazoe, H., Syaeful, H., Muhammad, A. G., Sukadana, I. G., Indrastomo, F. D., Ngadenin, Pratiwi, F., Sumaryanto, A., Sucipta, Pratama, H. A., Mustika, D., Nirwani, L., Nurokhim, Omori, Y., Hosoda, M., Akata, N., & Tokonami, S. (2023). Uranium Isotope Characterization in Volcanic Deposits in a High Natural Background Radiation Area, Mamuju, Indonesia. *Geosciences*, *13*(12), 388. https://doi.org/10.3390/geosciences13120388

Said, M. I. N., Anggraini, M., Mubarok, M. Z., & Widana, K. S. (2017). Studi Ekstraksi Bijih Thorit dengan Metode Digesti Asam dan Pemisahan Thorium dari Logam Tanah Jarang dengan Metode Oksidasi-Presipitasi Selektif. *Eksplorium*, *38*(2), 109. https://doi.org/10.17146/eksplorium.2017.38.2.3930

Senanayake, I. P., Kiem, A. S., Hancock, G. R., Metelka, V., Folkes, C. B., Blevin, P. L., & Budd, A. R. (2023). A Spatial Data-Driven Approach for Mineral Prospectivity Mapping. *Remote Sensing*, *15*(16). https://doi.org/10.3390/rs15164074

Subandrio, A. S., Sudradjat, A., Rosana, M. F., & Syafri, I. (2010). Uranium Mineralisation Hosted By Albite-Rich Granitoid Rocks of Sibolga – North Sumatra . *The 39th IAGI Annual Convention and Exhibition*.

Sukadana, I. G., Burhannudinnur, M., Rachael, Y., Indrastomo, F. D., Sendjadja, P., Sutarto, S., & Ciputra, R. C. (2024). Rare Earth Elements and Uranium Prospect on Weathered Granitic Rocks in Tanah Merah, West Kalimantan. *AIP Conference Proceedings*, *2967*(1). https://doi.org/10.1063/5.0193064

Sukadana, I. G., & Syaeful, H. (2016). Evaluasi Sistem Pengendapan Uranium Pada Batuan Sedimen Formasi Sibolga, Tapanuli Tengah (Evaluation of Uranium Depositional System in Sedimentary Rocks of Sibolga Formation, Tapanuli Tengah). *Eksplorium*, *37*(2), 125-138.(in Indonesian-English abstract available). https://doi.org/https://doi.org/10.17146/eksplorium.2016.37.2.3112

Sukadana, I. G., Syaeful, H., Indrastomo, F. D., Widana, K. S., & Rakhma, E. (2016). Identification of Mineralization Type and Specific Radioactive Minerals in Mamuju, West Sulawesi. *Journal of East China University of Technology*, *39*(December), 39–48.

Sukadana, I. G., Warmada, I. W., Harijoko, A., Indrastomo, F. D., & Syaeful, H. (2021). The Application of Geostatistical Analysis on Radiometric Mapping Data to Recognized the Uranium and Thorium Anomaly in West Sulawesi, Indonesia. *IOP Conference Series: Earth and Environmental Science*, *819*(1). https://doi.org/10.1088/1755-1315/819/1/012030

Sun, K., Chen, Y., Geng, G., Lu, Z., Zhang, W., Song, Z., Guan, J., Zhao, Y., & Zhang, Z. (2024). A Review of Mineral Prospectivity Mapping Using Deep Learning. *Minerals*, *14*(10). https://doi.org/10.3390/min14101021

Sutjipto, R. H. (1991). *Sedimentology of the Melawi and Ketungau Basins, West Kalimantan, Indonesia* [Doctor of Philosophy Thesis, Department of Geology, University of Wollongong]. https://ro.uow.edu.au/

Syaeful, H., Sukadana, I. G., Susilo, Y. S. B., Indrastomo, F. D., Muhammad, A. G., & Ngadenin. (2021). Uranium exploration, deposit and resources: The key of nuclear power plant development program in Indonesia. *Journal of Physics: Conference Series*, *2048*(1). https://doi.org/10.1088/1742-6596/2048/1/012003

Tjokrokardono, S., Soetarno, D., Sapardi, Lilik, S., & Witjahyati, R. (2004). Studi Geologi Regional dan Mineralisasi Uranium di Pegunungan Schwaner Kalimantan Barat dan Tengah (Study on Regional Geology and Uranium Mineralization of Schwaner Mountains West and Central Kalim-

antan). *Seminar Geologi Nuklir Dan Sumberdaya Tambang*, 64-84. (in Indonesian-English abstract available). http://www.iaea.org/inis/collection/NCLCollectionStore/_Public/39/123/39123070.pdf

United States Geological Survey. (n.d.). *Earth Explorer*. 2019. https://earthexplorer.usgs.gov/

Winter J.D. (2001). *An Introduction to Igneous and Metamorphic Petrology*. Prentice Hall Inc.

Yousefi, M., Kreuzer, O. P., Nykänen, V., & Hronsky, J. M. A. (2019). Exploration information systems – A proposal for the future use of GIS in mineral exploration targeting. *Ore Geology Reviews*, *111*(February). https://doi.org/10.1016/j.oregeorev.2019.103005

Yue, X., Peng, M. Y. P., Anser, M. K., Nassani, A. A., Haffar, M., & Zaman, K. (2022). The role of carbon taxes, clean fuels, and renewable energy in promoting sustainable development: How green is nuclear energy? *Renewable Energy*, *193*, 167–178. https://doi.org/10.1016/j.renene.2022.05.017

Zhang, L. (2013). Aspects of rock permeability. *Frontiers of Structural and Civil Engineering*, *7*(2), 102–116. https://doi.org/10.1007/s11709-013-0201-2

SAŽETAK

Primjena geografskoga informacijskog sustava za istraživanje ležišta uranija pješčenjačkoga tipa u regiji Melawi, Zapadni Kalimantan, Indonezija

Regija Melawi u Indoneziji identificirana je kao metamorfno ležište uranija. Pojava sedimentnih formacija u nizvodnome području upućuje na potencijal za ležišta uranija pješčenjačkoga tipa. Prethodne studije usredotočile su se na metamorfnu mineralizaciju, što je rezultiralo ograničenim istraživanjem sedimentnih stijena. Tehnologija geografskoga informacijskog sustava (GIS) nudi vrijednu podršku za analizu mineralne perspektive, uključujući istraživanje uranija. Među raznim tehnikama pokazalo se da je *fuzzy* logika učinkovita u generiranju karata perspektivnosti za usmjeravanje razvoja resursa uranija. Cilj je ovoga istraživanja razvoj karte perspektivnosti za ležište uranija pješčenjačkoga tipa u regiji Melawi. Analiza temeljena na GIS-u provedena je korištenjem dostupnih prostornih skupova podataka, uključujući geološke karte, digitalne modele reljefa i pojave uranija u Melawiju. Ovi skupovi podataka poslužili su kao ulaz za izradu *fuzzy* logičkoga modela temeljenoga na genetskome modelu ležišta uranija pješčenjačkoga tipa. Skupovi podataka reklasificirani su, dodijeljeni su im bodovi prikladnosti i obrađeni su unutar okvira *fuzzy* logike za generiranje karte perspektivnosti. Rezultati pokazuju da je 36,64 % područja Melawi zona visoke perspektivnosti, 25,34 % zona srednje perspektivnosti, a 38,02 % zona niske perspektivnosti. Sjeverni dio Melawija pokazuje najpovoljnije uvjete za mineralizaciju uranija u pješčenjaku. Ova studija demonstrira *fuzzy* logiku kao praktičan alat za određivanje povoljnoga područja ležišta uranija pješčenjačkoga tipa u Melawiju. Ipak, za točno lociranje ležišta uranija potrebno je uključivanje raznolikijih prostornih skupova podataka i provedba sustavne terenske validacije.

Ključne riječi:
Melawi, GIS, *fuzzy* logika, mineralna perspektiva, uran pješčenjačkoga tipa

Author's contribution

Tyto Baskara Adimedha (Researcher, Geology): conceptualization, methodology, formal analysis, writing-original draft, and visualization. **Roni Cahya Ciputra** (Researcher, Geology): methodology, formal analysis, writing-original draft, and visualization. **Frederikus Dian Indrastomo** (Researcher, Geology): resources, validation, writing – review and editing. **I Gde Sukadana** (Doctor, Geology): methodology, resources, validation, writing – review and editing. **Heri Syaeful** (Doctor, Geology): conceptualization, methodology, supervision, writing – review and editing. **Yoshi Rachael** (Researcher, Geology): formal analysis, writing – review and editing.
All authors have read and agreed to the published version of the manuscript.

RGNZ/MGPB

Stress Transfer and Seismicity Along the Southern Great Sumatran Fault: Insights from the 1994 Liwa Earthquake

Rudarsko-geološko-naftni zbornik
(The Mining-Geology-Petroleum Engineering Bulletin)
DOI: 10.17794/rgn.2026.3.7

Original scientific paper

Andri Kurniawan[1]*, Nicolas Silaen[2], Khalil Ibrahim[2], Arsy Nurrochman[1], Ridho Destawan[1], Nanda Hanyfa Maulida[1], Irfan Prasetyo[2], Ahmad Zaenudin[1], Adhi Wibowo[3]

[1] *Department of Geophysical Engineering, Faculty of Engineering, Universitas Lampung, Lampung, Indonesia.*
[2] *Geophysical Engineering, Faculty of Mining and Petroleum Engineering, Institut Teknologi Bandung, West Java 40132, Indonesia.*
[3] *Agency for Meteorology, Climatology, and Geophysics, Indonesia.*

Abstract

The February 15, 1994 Mw 6.8 Liwa earthquake ruptured the southern Great Sumatran Fault (GSF), yet its static stress legacy and relation to subsequent seismicity remain weakly quantified. We integrate high-precision double-difference relocation with Coulomb failure stress (ΔCFS) modelling to evaluate post-1994 stress transfer along the Semangko sector. Using ~16,000 P/S picks and identical inversion settings, we test two 1-D velocity models; CRUST1.0 yields near-zero, narrow differential-time residuals (± 0.3–0.4 s) compared with broader heavy tails for AK135 (± 0.7–0.8 s) and are adopted for the final catalogue. Since phase archives are sparse before 2010, events from 1994 – 2009 are treated as background, whereas 2010–2024 earthquakes are relocated; quality control retains 416 events. Relocation suppresses the artificial ~10 km depth band and collapses epicenters into coherent clusters that delineate the West/East Semangko Faults and Semangko Bay. ΔCFS was computed for depths of 5–20 km and μ′ = 0.2–0.8. All scenarios produce the expected four-lobed right-lateral pattern with maxima >0.10 MPa around WSF-B, ESF-A, and the Kumering Fault. Relocated events preferentially occupy positively loaded regions: ~74% fall at ΔCFS > 0 and ~73% at ΔCFS ≥ 0.01 MPa (10 kPa), robust to μ′ and depth. The results indicate unresolved post-1994 loading on multiple Semangko branches and adjacent segments, highlighting the potential for cross-segment triggering. We advocate expanding seismic and geodetic monitoring and targeted paleoseismic surveys in the Semangko–Kumering corridor to refine recurrence estimates and update physics-based hazard models for southern Sumatra.

Keywords:
Coulomb stress transfer, earthquake relocation, Great Sumatran Fault, Semangko segment, seismic hazard

1. Introduction

On February 15, 1994, at 17:08 UTC, a Mw 6.8 earthquake struck west of Lampung in southern Sumatra, Indonesia (see the yellow star in **Figure 1**). This destructive mainshock occurred on the southern segment of the Great Sumatran Fault (GSF) near the city of Liwa, in the Semangko Fault. Around 207 people died, over 2,000 were injured, and 75,000 were displaced; most of the damage and fatalities occurred in the Liwa area. The earthquake damaged over 6,000 homes, shops, and government buildings (**Widiwijayanti et al., 1996**). Since the early 20th century, at least three significant earthquakes (M ≥ 6.0) have occurred around Liwa (red star in **Figure 1**): (1) the 1908 event on the western Semangko segment of the GSF; (2) the 1933 event on the Kumering segment, Ms 7.5 (**Natawidjaja & Triyoso, 2007**); and (3) the 1994 Liwa earthquake on the Semangko segment, Mw 6.8 (**Soehaimi et al., 2002**).

According to **Bellier et al. (1997)**, **Natawidjaja et al. (2017)**, and **Wang et al. (2023)**, the GSF is about 1,900 km long and an important part of the strike-slip fault system that allows the Indo-Australian–Eurasian plate to move at an angle. Regional convergence rates are ~44 mm/yr in the Andamans, ~60 mm/yr in southern Sumatra, and ~68 mm/yr in southern Java (**DeMets et al., 2010**). Based on these rates, the GSF can handle several millimeters of trench-parallel motion per year. Interseismic geodetic modelling puts the system-wide slip at about 15 mm/yr. The slip rates in the southern GSF are about 18 mm/yr on the Manna segment and about 12 mm/yr on Kumering. Musi is less well known, with locking depths of about 1–20 km (**Lubis et al., 2024**). The Semangko section divides into the West and East Semangko Faults close to Liwa, moving at rates of 16.5 ± 2 and 12.5 ± 2 mm/yr, respectively (**Alif et al., 2020**).

* Corresponding author: Andri Kurniawan
e-mail address: andrikurniawan@eng.unila.ac.id
Received: 20 September 2025. Accepted: 2 December 2025.
Available online: 14 May 2026

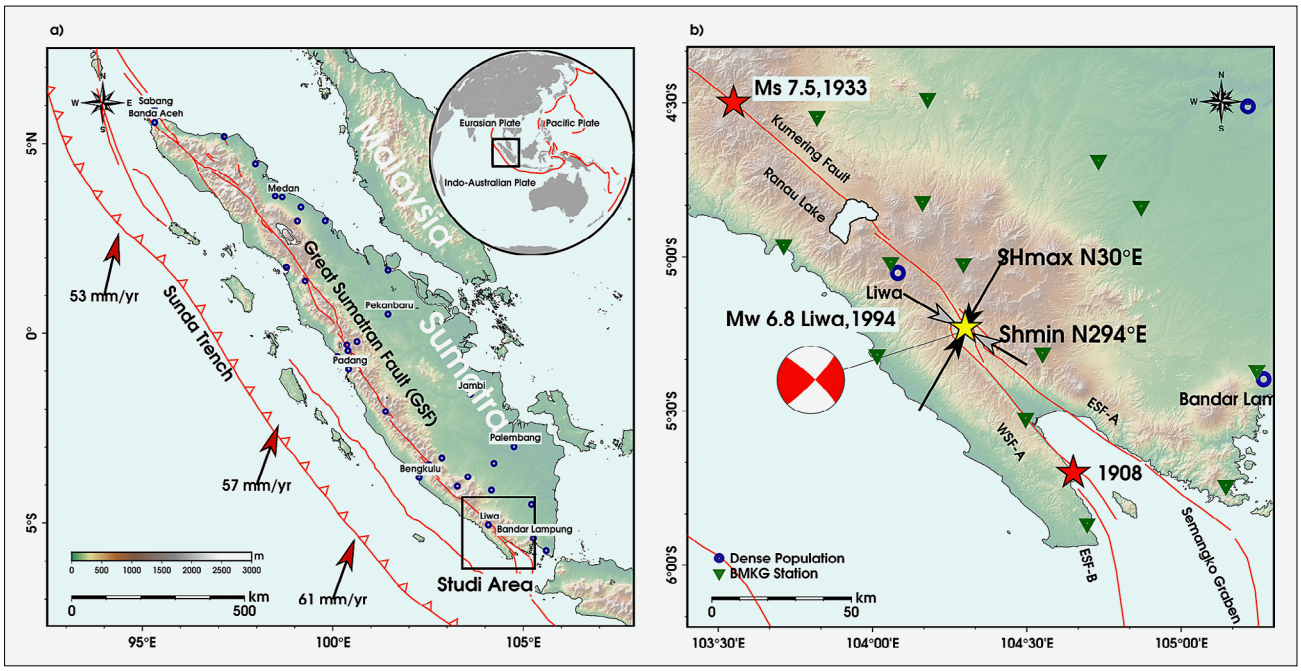


Figure 1. (a) Sumatra in the Sunda subduction system. The red triangles represent the Sunda Trench, and the arrows show the trench-normal convergence rates, which are about 53–61 mm yr^{-1}. The Barisan Mountains extend from Banda Aceh to the Sunda Strait via the Great Sumatran Fault (GSF; red lines). The blue circles show where most people live, and the green triangles show where BMKG stations are located. The study area is shown by the black rectangle, and the inner rectangle shows the borders of the Indo-Australian, Eurasian, and Pacific plates. (b) Zoom in on the area of study. The GSF separates into the Kumering Fault and the West and East Semangko Faults (WSF and ESF). The yellow star shows the Mw 6.8 Liwa mainshock on February 15, 1994, with a focal mechanism. The red stars show the 1933 Ms 7.5 Kumering and 1908 occurrences on WSF. The main stress frame is shown with SHmax ~ N30°E and Shmin ~ N294°E, aligning with initial motion and regional stress parameters (e.g. **Widiwijayanti et al., 1996; Heidbach et al., 2018**).

Even though these rates are significant, no Mw ≥ 6.0 earthquake has occurred on the southern GSF since the 1994 Liwa event, indicating continuous stress accumulation and unresolved seismic potential (**Salman et al., 2020; Hutchings & Mooney, 2021; Triyoso & Suwondo, 2023; Kurniawan et al., 2024**).

Coulomb Failure Stress (ΔCFS) modelling has been widely applied to quantify stress changes caused by earthquakes and ongoing loading, and is effective for identifying regions with increased failure potential. Numerous studies have demonstrated that static stress changes on the order of 0.01–0.1 MPa can promote or inhibit fault slip, depending on fault orientation and pre-existing conditions (**King & Devès, 2015; Pope & Mooney, 2020; Segou & Parsons, 2020; Mildon et al., 2022**). ΔCFS modelling is now used in many different types of tectonic settings, including strike-slip systems in California (**Pope & Mooney, 2020**), thrust faulting in the Himalayas, India (**Parija et al., 2021**), and normal-fault systems in the Central Apennines, Italy (**Valentini et al., 2024**). In Indonesia, ΔCFS evaluations have addressed segments of the GSF following megathrust earthquakes along the Sunda subduction zone (**Rafie et al., 2023; Sukrungsri et al., 2024**) and several onshore sequences, such as the Pasaman, West Sumatra sequence (**Supendi et al., 2023; Wulandari et al., 2023**) and the Angkola segment, North Sumatra (**Sahara et al., 2018**). However, applications of ΔCFS are rare in southern Sumatra. To close this gap, we need to do a thorough job of characterizing ΔCFS patterns. This will help us better assess seismic hazards, find areas where seismic energy is more likely to be released, prioritize mitigation efforts, and set requirements for infrastructure resilience.

Triyoso and Suwondo (2023) recently found high compression around Liwa along the Kumering–Semangko section of the GSF. They also found high slip rates and a high correlation dimension, all of which are signs of high stress. Since Liwa is close to the GSF and could make it stronger, we need an integrated risk framework that clearly limits the crustal GSF source along with megathrust and intermediate-depth sources. We use the double-difference method to relocate earthquakes more accurately and combine these results with static ΔCFS modelling to (i) figure out how much stress the 1994 mainshock changed things; (ii) see how well the relocated clusters match up with the ΔCFS lobes; and (iii) see what this means for future rupture potential and seismic risk along the southern GSF. This analysis will help discriminate whether the 1994 rupture involved a previously unmapped GSF segment or a distinct, as-yet unidentified fault, thereby tightening physics-based constraints for regional hazard models.

Table 1. The source parameters of the Liwa earthquake by **Widiwijayanti et al. (1996)** and **Soehaimi et al. (2002)**. The length and the width were estimated based on the empirical relations of **Wells & Coppersmith (1994)**.

Date	Lat (°S)	Long (°E)	Depth (km)	M_w	Strike	Dip	Rake	Length (km)	Width (km)	Right lateral slip (m)	Dip slip (m)
15 Feb 1994	5.24	104.30	12.5	6.8	44 313	83 82	8 173	45.47	14.40	0.89	0.07

Southern Sumatra remains under-documented despite pronounced tectonic complexity; pre-2010 phase picks are not publicly available and station coverage is heterogeneous, which constrains relocation fidelity before 2010. Our hypoDD workflow therefore uses 1-D velocity models and differential times to reduce model dependence, and the ΔCFS analysis adopts static Okada solutions in a homogeneous, isotropic half-space (**Okada, 1992**). These assumptions provide a first-order, physics-based baseline for the southern GSF but do not capture viscoelastic relaxation or afterslip. This gap motivates targeted acquisition (denser seismic arrays), integration of GNSS/InSAR and 3-D tomography, and focused paleoseismic work on ESF-A/WSF-B to refine fault geometry, locking depth, and recurrence in future studies.

2. Seismotectonics of the Great Sumatran Fault (GSF)

Sumatra Island is located on the southern edge of the Sunda Plate, which engages morphologically with the subducting Indo-Australian Plate beneath it. The convergence component of about 50–70 mm/year has been divided up: the part that runs parallel to the trench is mostly taken up by the right-lateral strike-slip fault system of the GSF, and the part that runs perpendicular to the trench is taken up by the Sunda megathrust (**Sieh & Natawidjaja, 2000**). The GSF extends from Banda Aceh in the north, across the Barisan Mountains, and ends at the Sunda Strait (**Figure 1a; Natawidjaja, 2018**). It is one of the most active fault systems in Indonesia. The GSF was first divided into 19 segments with various characteristics (**Sieh & Natawidjaja, 2000**). Later, PUSGEN (Pusat Studi Gempa Nasional) improved the map by adding about 40 additional segments (**Irsyam et al., 2017**).

A series of large megathrust earthquakes off the coast of Sumatra have raised the seismic risk along the GSF. These earthquakes have transferred static stress and are likely to put more strain on the GSF (**Rafie et al., 2023**). The Mw 9.2 Sumatra-Andaman earthquake on December 26, 2004, the Mw 8.6 Nias-Simeulue earthquake on March 28, 2005, and the Mw 8.4 Bengkulu earthquake on September 12, 2007, all came first in this sequence. Because of these major events, stress accumulation along the GSF is believed to have increased, thereby elevating the likelihood of subsequent earthquakes along this fault system. **Rafie et al. (2023)** emphasize the importance of continuous seismic monitoring and preparedness in the region, as static stress transfer can potentially trigger new seismic activity with significant impacts on communities and infrastructure throughout Sumatra.

This effect is reflected in the growing frequency of moderate (M~6) earthquakes along the GSF after these large megathrust events. Consistently, a series of moderate earthquakes have repeatedly occurred along the fault, including two Mw 6.4 and 6.3 events near Lake Singkarak in 2007 (**Daryono et al., 2012**), the Mw 6.0 Toru earthquake in 2008 that ruptured the Toru segment, the Mw 6.6 Dikit seismic gap earthquake in 2009 (**Hurukawa et al., 2014**), the Mw 6.1 creeping segment earthquake in Aceh in January 2013 (**Ito et al., 2016**), and the Mw 6.1 Pasaman earthquake in February 2022 involving the Angkola, Sumpur, Sianok, and Barumun segments (**Supendi et al., 2023; Wulandari et al., 2023**). This sequence underscores the dual influence of both the megathrust and the GSF fault systems in shaping seismic hazard patterns across Sumatra.

In the southern sector, the Semangko segment forms a branching fault system, the West Semangko Fault (WSF), East Semangko Fault A (ESF-A) and East Semangko Fault B (ESF-B), which are separated by a step-over structure in the Ranau Caldera region. This geometry causes the deformation regime to transition from predominantly strike-slip to transtensional within the pull-apart basin. The presence of Quaternary volcanic-sedimentary infill overlying the Barisan Mountains arc basement produces a stiffness contrast and weak zones, focusing strain along the basin margins and minor splays. Regionally, the obliquity of the Sunda subduction arranges a transpressional regime characterized by right-lateral strike-slip accumulation along the GSF. However, at the Ranau step-over, stress field rotation introduces an oblique-normal faulting component on secondary faults, consistent with shallow crustal seismicity clusters near Liwa (**Heidbach et al., 2018; Triyoso & Suwondo, 2023**). P-wave first-motion mechanism inversion reveals a strike-slip regime with a maximum horizontal stress axis of approximately N30°E and a minimum of about N294°E (e.g. **Widiwijayanti et al., 1996; Heidbach et al., 2018**). Concurrently, heterogeneity in slip rates between branches and variations in locking depth generate a differential stress gradient that increases the likelihood of cross-segment triggering (**Alif et al., 2020; Lubis et al., 2024**). Post seismic static stress transfer following the 1994 Liwa earthquake (ΔCFS) is also thought to have reinforced local loading

on splays and the caldera margins. The combination of step-over fault geometry, weaker basin materials, and interconnected fault sources makes the southern Semangko–Ranau zone a critical focus for seismic hazard assessment.

3. Data and Methods

The earthquake dataset covers a span of 30 years from February 1994 to January 2024 (following the 1994 Mw 6.8 Liwa earthquake) and is sourced from BMKG's permanent seismic network in Lampung. Within this timeframe, we compiled 498 events (Mw 0.9–5.0) monitored by 209 BMKG stations in the southern Sumatra and western Java regions (see **Figure 1**). For the period 1994–2009, only catalog data are available because of limitations in station density and phase archives. From 2010 to 2024, P- and S-wave arrival times are available, enabling double-difference relocation. Operationally, the initial hypocenters were determined through linear inversion in SeisComP3 (**Supendi et al., 2022**). This initial solution is sufficient for monitoring, but accuracy may suffer due to the subsurface velocity model's simplification and the uneven distribution of propagation paths, particularly in complex tectonic regions. Active faults around the Liwa earthquake source were compiled from PUSGEN (**Irsyam et al., 2017**). The direction of the fault plane and the type of displacement (focal mechanism) of the 1994 Mw 6.8 main earthquake are based on the research based on **Soehaimi et al. (2002)**. The aftershock distribution was taken from the seismic observations of **Widiwijayanti et al. (1996)** and digitized to get the event coordinates, limit the shape of the rupture, and make sure the static stress change modelling was correct. The source dimensions and slip magnitude were estimated using the well-established empirical relationship developed by **Wells & Coppersmith (1994)**, known for its accuracy in seismic source parameter estimation, and are detailed in **Table 1**.

We relocated hypocenters using the hypoDD double-difference algorithm (**Waldhauser & Ellsworth, 2000; Waldhauser, 2001**), which reduces the difference in travel time between two nearby events as much as possible. The main idea is that when the distance between events is much smaller than the distance between sources and stations, the paths of the rays are almost the same, and they sample similar velocity structures. This means that differential times can be used to get very accurate relative locations. We did two separate inversions with the same parameters to see how the 1-D velocity model affected the accuracy of the relocation (see **Figure 2**): CRUST1.0 (**Laske et al., 2013**) and AK135 (**Kennett et al., 1995; Hu et al., 2023; Pranata et al., 2023**). The quality of the move was judged by looking at the distribution of differential-time residuals, which were shown as histograms with the same number of bins and axes for both cases. The reference model was selected based on a stronger concentration of residuals near 0 s (a sharper peak), indicating a better overall data–model fit.

We limited the distance between events to 100 km, let up to 30 nearest neighbors per event, and needed at least 10 differential-time links to ensure the network was connected. To keep differential-time quality, we also limited the distance between the station and the cluster centroid to 300 km. These constraints were applied uniformly to both velocity-model tests to enable a fair comparison. We chose the parameters by running repeated sensitivity tests until we found a stable configuration that moved things consistently across a range of possible inputs. This workflow mitigates bias from unmodelled lateral velocity heterogeneity and enhances the spatial coherence of seismic clusters, thereby improving the interpretability of subsequent static stress modelling in structurally complex fault systems (e.g. **Muttaqy et al., 2023; Supendi et al., 2023**).

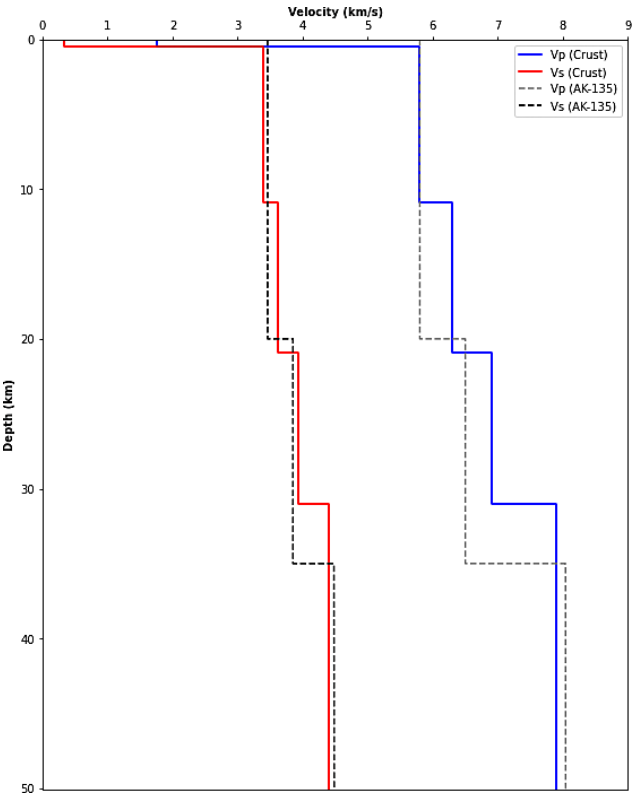


Figure 2. One-dimensional (1D) velocity models tested in the relocation experiments. Solid lines show the CRUST1.0 model and dashed lines the AK135 model; blue curves denote P-wave velocity (Vp) and red curves S-wave velocity (Vs). Depth is in kilometers, positive downward.

We looked at how stress changed after the earthquake using static ΔCFS modelling with Coulomb 3.3 (**Toda et al., 2011**), which was based on the work of **King et al. (1994)**. We define

$$\Delta CFS = \Delta\tau - \mu' \Delta\sigma_n \quad (1)$$

Where $\Delta\tau$ is the change in shear stress, $\Delta\sigma_n$ is the change in normal stress (positive for unclamping), and μ' is the

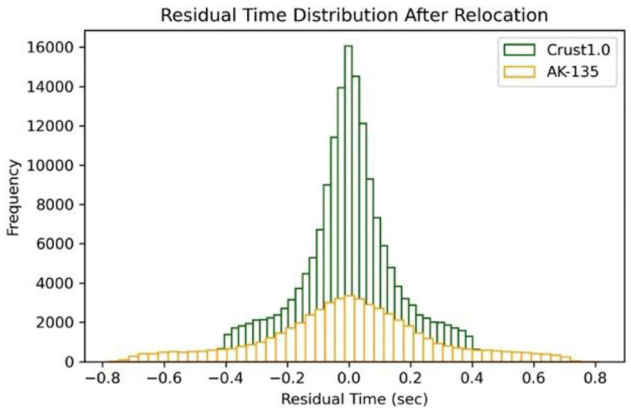


Figure 3. Post-relocation differential travel-time residuals from hypoDD for two 1-D velocity models. Histograms use identical axes and binning. CRUST1.0 (green) exhibits sharp, near-zero peaks with a narrow spread (≈±0.3–0.4 s), whereas AK135 (orange) is broader with heavier tails (±0.7–0.8 s) and a slight negative bias. The tighter, near-zero-centered distribution indicates a superior data–model fit; accordingly, CRUST1.0 is adopted for the final relocations and subsequent analyses.

effective coefficient of friction. We calculated stress changes on two types of receiver faults: (i) planes that were perfectly aligned with the Semangko Fault's local strike at depths of 5, 10, 15, and 20 km (these were the seismogenic layers); and (ii) mapped active faults around the mainshock that were used as receiver faults and had their own strike–dip–rake. These faults came from the national active-fault database (**Irsyam et al., 2017**). Receiver faults are potential slip surfaces (either hypothetical, optimally oriented planes or mapped structures) on which we evaluate whether stress changes would promote ($\Delta CFS > 0$) or inhibit ($\Delta CFS < 0$) failure. The mainshock was shown as a flat displacement whose size, shape, rake, strike, and dip were limited by the focal-mechanism solution and the geometry of the aftershock. **Wells and Coppersmith's (1994)** empirical relations were used to estimate the fault parameters. We assumed a homogeneous, isotropic elastic half-space with Poisson's ratio = 0.25 (**Xu et al., 2016**). To bracket frictional uncertainty, simulations were run for $\mu' = 0.2$, 0.4, 0.6, and 0.8 (**Wulandari et al., 2023**). To make sure the numbers were correct, CFS values were taken at the hypocenters and at random locations inside the convex hull of events that were widened by 0.2°. Interpolation was linear (nearest neighbor checked for robustness). We report the fractions of $\Delta CFS > 0$ and $\Delta CFS > 0.01$ MPa, median values, and results of a one-sided Kolmogorov–Smirnov test comparing the two populations.

We measured the correlation between ΔCFS and relocated seismicity, in addition to spatial coincidence. For each hypocenter, ΔCFS was collected using depth-specific grids (5-20 km) estimated for the 1994 Liwa source and an effective friction range ($\mu' = 0.2$-0.8). For a fair baseline, N=5000 random sites were chosen inside the convex hull of the event distribution extended by a 0.2° buffer, and ΔCFS was derived by linear interpolation (nearest checked for robustness). We quantified the association using the fraction of events with $\Delta CFS > 0$ and $\Delta CFS \geq 0.01$ MPa (10 kPa), median contrasts, and a one-sided Kolmogorov–Smirnov test (H_1: events exhibit higher ΔCFS than random points). Fraction-above-threshold metrics are commonly used because the random domain is largely dominated by $\Delta CFS = 0$ outside stress-change zones (e.g. **King et al., 1994; Toda et al., 2005**), thereby complementing whole-distribution tests. For the Liwa mainshock, Coulomb stress modelling was performed under the assumption of a static, elastic, homogeneous half-space based on the Okada dislocation formulation (**Okada, 1992**), with the rupture represented as a planar fault geometry. The receiver faults were defined by mapped strands of the ESF and WSF. Sensitivity analyses were conducted to evaluate the influence of effective friction (μ'), source depth, interpolation scheme, and the extent of the random-domain buffer.

4. Results

4.1. Seismicity Relocation Quality

Using identical inversion parameters, we evaluated 16,000 combined P- and S-wave arrivals. The post-relocation residual distributions show a clear contrast between the two 1-D velocity models (see **Figure 3**). CRUST1.0 yields a tight, nearly symmetric distribution centered at 0 s, with most residuals within ± 0.3–0.4 s. By contrast, AK135 produces a broader, heavy-tailed distribution extending to ± 0.7–0.8 s and a slight negative bias, implying an underestimation of crustal velocities along local paths. The sharper near-zero peak and reduced spread achieved with CRUST1.0 indicate a superior data–model fit and a more realistic representation of shallow crustal heterogeneity in the study area. We therefore adopted CRUST1.0 for the final relocated catalog and all subsequent analyses. Since station coverage and phase archives are limited before 2010, events from 1994–2009 are treated as background, whereas 2010–2024 earthquakes with phase picks were relocated. **Figure 4** contrasts the pre-relocation catalogue with the double-difference solution. The operational locations exhibit diffuse epicenters and a pronounced fixed-depth band near at ~10 km in the A–B section, typical of 1-D linearized inversions with uneven path coverage. The hypoDD relocation markedly reduces depth scatter and collapses epicenters into coherent clusters that delineate the Semangko Fault system, with prominent concentrations beneath Liwa and Semangko Bay. The improved geometry provides a more reliable basis for subsequent ΔCFS analysis.

4.2. Coulomb Failure Stress Distribution

ΔCFS was modelled using focal mechanism parameters (strike, dip, rake) and source dimensions estimated

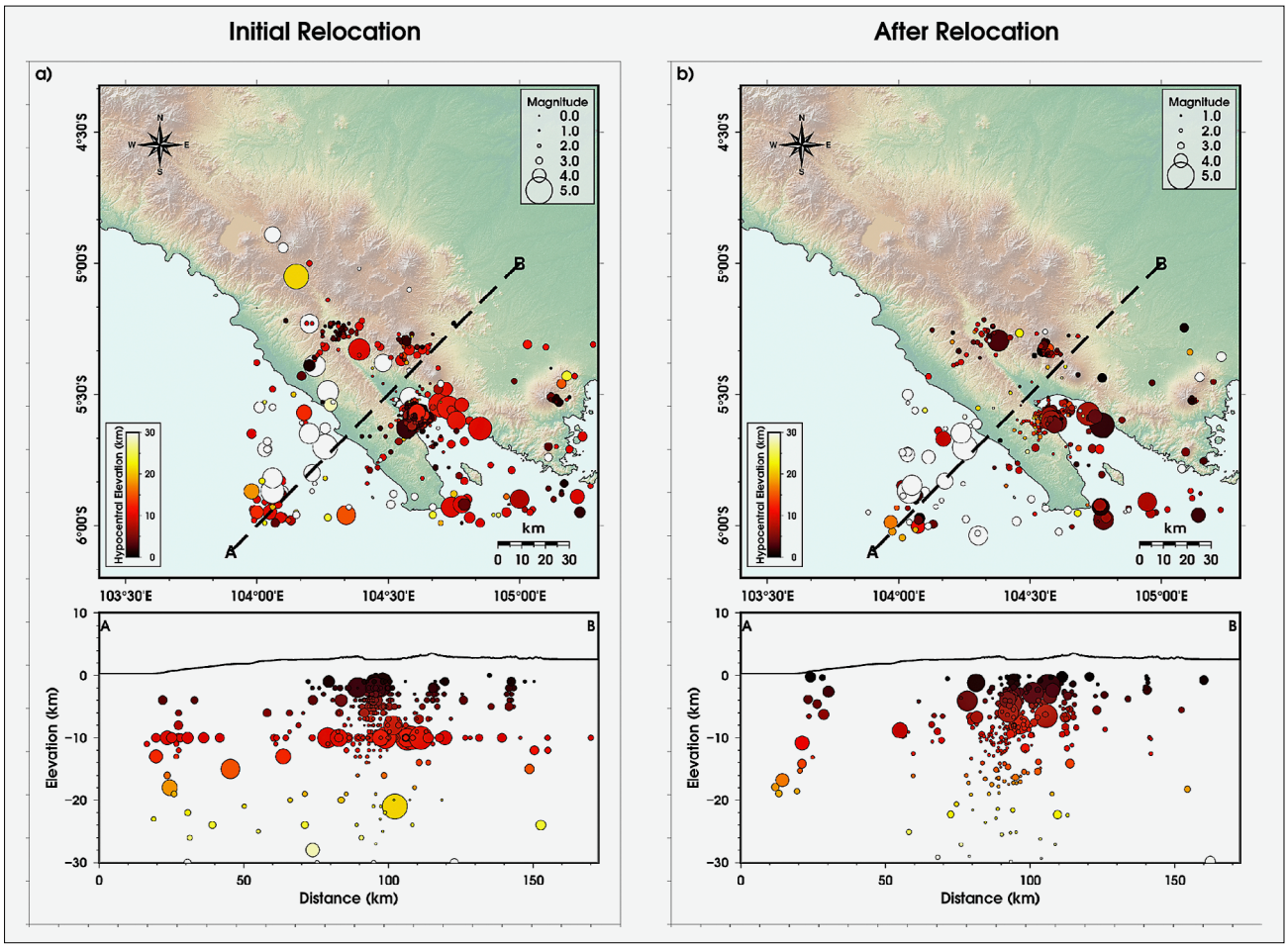


Figure 4. (a) Operational catalogue locations for events used in this study; (b) relocations obtained with hypoDD. Symbol size scales with magnitude; colour indicates hypocentral elevation (km). The dashed A–B line marks the profile trace; lower panels show A–B cross-sections with surface topography (**Tozer et al., 2019; Wessel et al., 2019**). Of the 498 events with usable picks, 416 were retained after relocation; removed events failed the graph-connectivity/quality criteria (≥10 differential links, ≤100 km inter-event distance, ≤300 km station-cluster offset). Relocation suppresses the artificial fixed-depth band near ~10 km and tightens spatial clustering near Liwa, Semangko Bay, and along the Semangko Fault system

from the empirical scaling relations of Wells and Coppersmith (1994). A receiver fault was defined with strike = 313°, dip = 82°, and rake = 173°, matching the geometry of the 1994 Liwa mainshock. ΔCFS was calculated on a spatial grid of 0.05° at various depths of 5 km, 10 km, 15 km, and 20 km. A range of effective friction coefficients (μ′ = 0.2, 0.4, 0.6, and 0.8) was tested to assess model sensitivity and reduce uncertainty (**Wulandari et al., 2023**). **Figure 5** illustrates the ΔCFS distributions under the four friction scenarios. All scenarios exhibit the characteristic four-lobed stress pattern typical of strike-slip ruptures, with zones of positive ΔCFS (red) and negative ΔCFS (blue) radiating from the rupture plane. The lobes extend toward the northeast, southwest, northwest, and southeast, mirroring the Liwa rupture orientation. The spatial structure of stress changes remains consistent across μ′ values, although the amplitude of stress perturbation varies slightly. Seismicity clusters were observed along major mapped fault traces, including WSF-B and ESF-A, and within areas that coincide with positive ΔCFS lobes in all μ′ scenarios. Additional clusters occurred in zones lacking mapped fault traces. These clusters are in proximity to the mainshock rupture and appear across multiple ΔCFS scenarios shown in **Figure 5**.

4.3. Statistical Validation of ΔCFS and Seismicity

To examine the relationship between stress perturbations and relocated seismicity, we performed a straightforward statistical assessment. Each relocated event from 2010 to 2024 was assigned a ΔCFS value at its hypocentral location using the static Coulomb stress-change model. The dataset was then divided into two categories: positive ΔCFS (>0.0 MPa) and negative ΔCFS (<0.0 MPa). The results indicate that approximately 72% of relocated earthquakes (n = 345 of 480) occurred within regions of positive ΔCFS, whereas about 28% (n ≈ 135) were in negative stress-change domains.

This asymmetric distribution supports the hypothesis that static stress redistribution from the 1994 Liwa earthquake promoted subsequent seismicity on adjacent fault

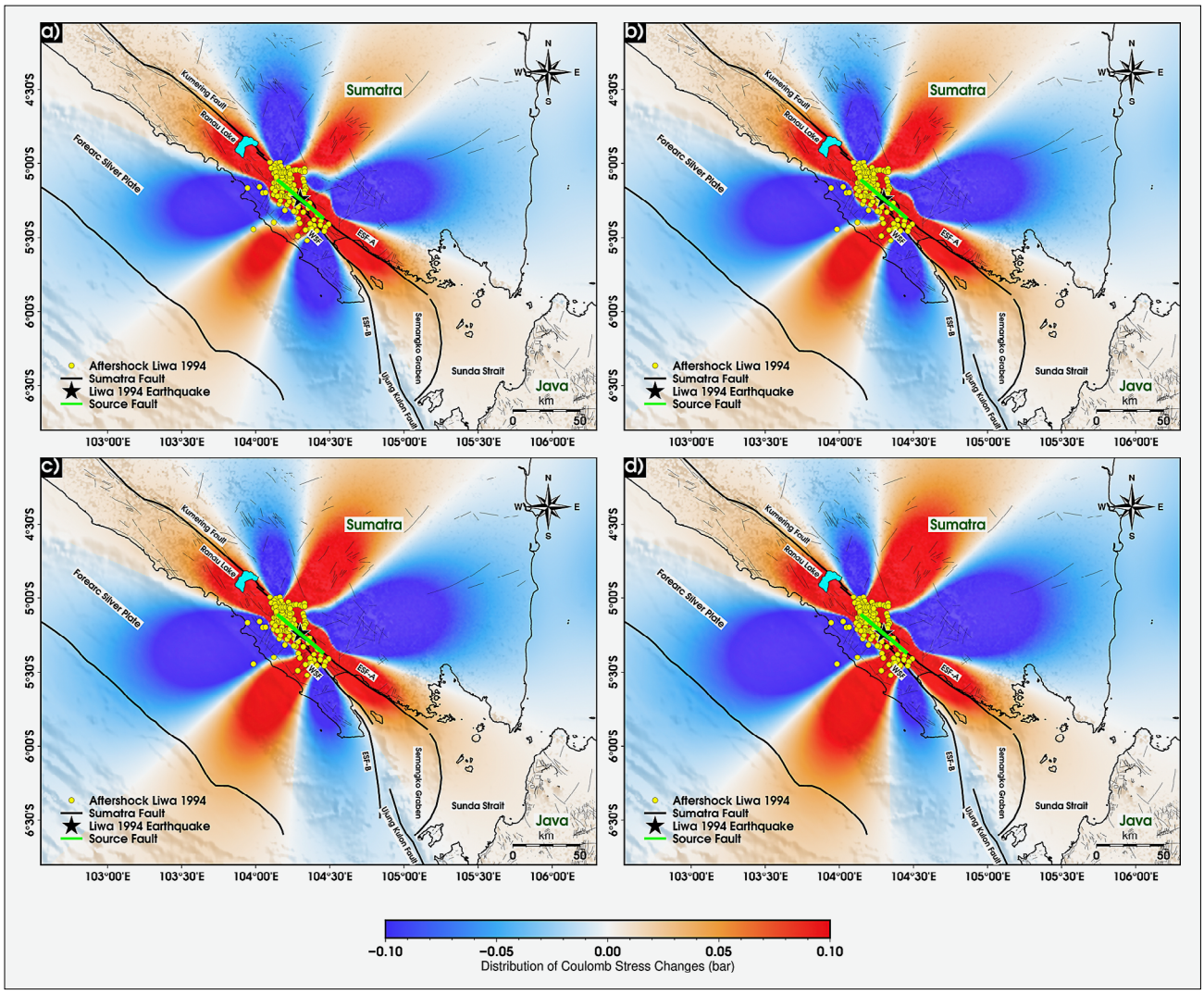


Figure 5. Spatial distribution of static ΔCFS changes at 10 km depth following the 1994 Mw 6.8 Liwa earthquake. Panels (a)–(d) show ΔCFS for μ′ = 0.2, 0.4, 0.6, and 0.8, respectively. Red and blue lobes indicate regions of positive and negative ΔCFS, respectively, with values ranging from −0.10 to +0.10 MPa. Aftershock locations (yellow–green circles) and mapped faults are overlaid for reference.

segments. A Kolmogorov–Smirnov (K–S) test further confirms that the observed seismicity distribution is statistically distinct ($p < 0.05$) from a uniform random distribution with respect to ΔCFS. This strengthens the interpretation of the positive lobes of the Coulomb stress transfer function as preferential sites for earthquake triggering.

According to ECDF and histogram analyses, relocated events exhibit higher ΔCFS values than randomly sampled sites within the convex-hull-plus-buffer domain. Seventy-four percent of the events occurred at locations with ΔCFS > 0, while 73% exceeded the commonly applied promotion threshold of 10 kPa (0.01 MPa). The median ΔCFS at event sites (0.108 MPa) is substantially greater than the random-site median (0.002 MPa). A one-sided Kolmogorov–Smirnov test yielded $D = 0.051$ and $p = 0.128$, indicating a rightward shift in the event distribution but reduced statistical power due to the clustering of random samples near ΔCFS ≈ 0. Taken together, these observations highlight a pronounced preference for positively loaded lobes in post-1994 seismicity.

5. Discussion

5.1. Earthquake Relocation

Before relocation, the hypocenter distribution appeared more scattered and unstructured, with numerous events concentrated at fixed depths. This pattern reflects the limitations of conventional initial location methods. After relocation (right panel), the hypocenter distribution became significantly more focused, forming geologically plausible clusters, particularly around Semangko Bay and the WSF and ESF-A segments. These results indicate that the double difference method effectively mitigates the influence of local velocity heterogeneities and systematic inter-station errors, consistent with findings by **Waldhauser (2001)** and **Supendi et**

al. (2023). Post-relocation results reveal a pronounced linear alignment of seismic events, highlighting a clear spatial coherence between the relocated hypocenters and known surface fault traces. Notably, the WSF and ESF-A segments exhibit intensified clustering of seismicity that follows the orientation of the mapped fault lines, reinforcing their seismotectonic significance. In addition, a substantial increase in seismic event density is observed within the central portion of the study area. This heightened concentration may indicate zones of elevated stress accumulation or the activity of previously unrecognized secondary structures. The spatial distribution of these events suggests the potential involvement of complex fault geometries, including antithetic fault systems, graben structures, or fault bifurcations, in accommodating crustal deformation. These observations are consistent with previous studies in tectonically active volcanic regions, where intricate subsurface fault networks often govern the pattern and intensity of seismicity (**Supendi et al., 2022**). The improved resolution achieved through the double difference relocation method thus offers valuable insight into the underlying fault architecture and may aid in the identification of seismogenic structures that remain undetected through surface mapping alone.

The depth cross-section reveals a significant contrast in hypocenter distribution before and after relocation. Prior to relocation, many events were artificially constrained at a uniform depth near 10 km, which likely reflects the limitations of conventional location algorithms rather than the actual seismogenic structure. Such vertical clustering can obscure interpretations of fault geometry and crustal deformation processes. After applying the double difference relocation, the events display a more geologically plausible vertical spread, ranging from 5 to 20 km in depth. This broader distribution delineates an active seismogenic zone and agrees with regional tomographic results and crustal velocity models reported by **Hu et al. (2023)**. Most of the seismicity concentrates between 8 and 15 km depth, coinciding with the transitional zone from brittle to ductile deformation regimes. This observation supports the hypothesis that mid-crustal earthquakes in the GSF region are associated with thermal and rheological gradients, consistent with the findings of **Pranata et al. (2023)**. Overall, the relocated seismicity provides improved constraints on the depth extent of faulting and enhances our understanding of the mechanical layering within the crust.

Several earthquake clusters are observed outside the main fault traces, particularly in the southwestern sector of the study area. These clusters are not spatially aligned with any documented surface faults, suggesting the possible existence of buttress structures, blind faults, or antithetic faulting. Similar patterns have been noted by **Supendi et al. (2023)**, who associated certain clusters in the Semangko region with unmapped minor fault segments not reflected in current regional geological maps.

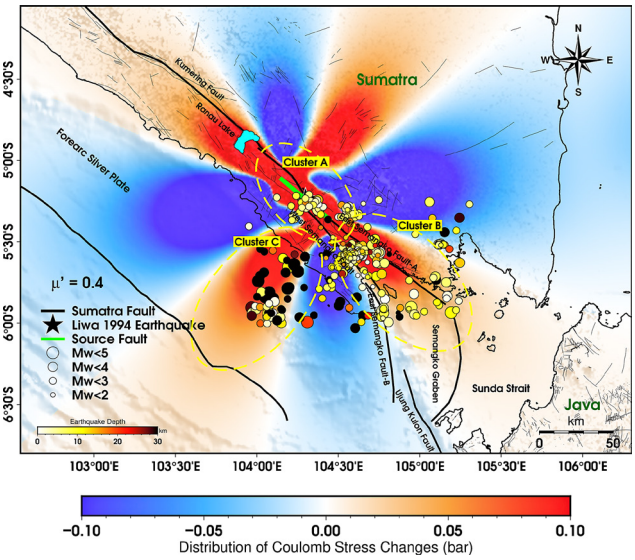


Figure 6. Spatial distribution of Coulomb Failure Stress (ΔCFS) changes induced by the 1994 Mw 6.8 Liwa earthquake, calculated at 10 km depth with an effective friction coefficient (μ′) of 0.4. The four-lobed stress pattern is characteristic of strike-slip fault rupture, showing areas of stress increase (red) and decrease (blue). Relocated seismicity from 2010–2024 is overlaid, with symbol sizes indicating event magnitude and colours representing focal depths. Three primary seismic clusters (A, B, and C) are delineated by dashed yellow ellipses.

5.2. *Coulomb Failure Stress Distribution and Seismotectonic Implications*

The ΔCFS distribution model presented in this study exhibits a consistent pattern of positive stress changes along segments of the Semangko Fault near the source area of the 1994 Liwa earthquake. The presence of elongated positive stress lobes (in red), aligned parallel to the fault and asymmetrically distributed on both sides of the rupture, indicates the occurrence of static stress transfer to adjacent fault segments with spatial and structural proximity (see **Figure 6**). Theoretically, this pattern supports the potential for future triggered seismicity, as originally proposed by **King et al. (1994)** and further substantiated by subsequent studies (**Toda et al., 2005; Pope and Mooney, 2020**).

Validation of the ΔCFS model against the historical seismicity distribution reveals a strong spatial correlation, particularly within clusters A, B, and C, which exhibit increased post-1994 earthquake activity (see **Figure 6**). These clusters coincide with areas of modelled stress increase exceeding 0.05 bar, supporting the interpretation that static stress redistribution enhanced the likelihood of subsequent seismicity in these zones. Similar findings have been reported by **Xiong et al. (2017)** and **Mildon et al. (2018)**, who demonstrated that seismicity concentrations often align with positive ΔCFS anomalies in transfer zones and fault segment intersections.

The ΔCFS model is consistent with the findings of **Supendi et al. (2022)**, who identified the presence of a gra-

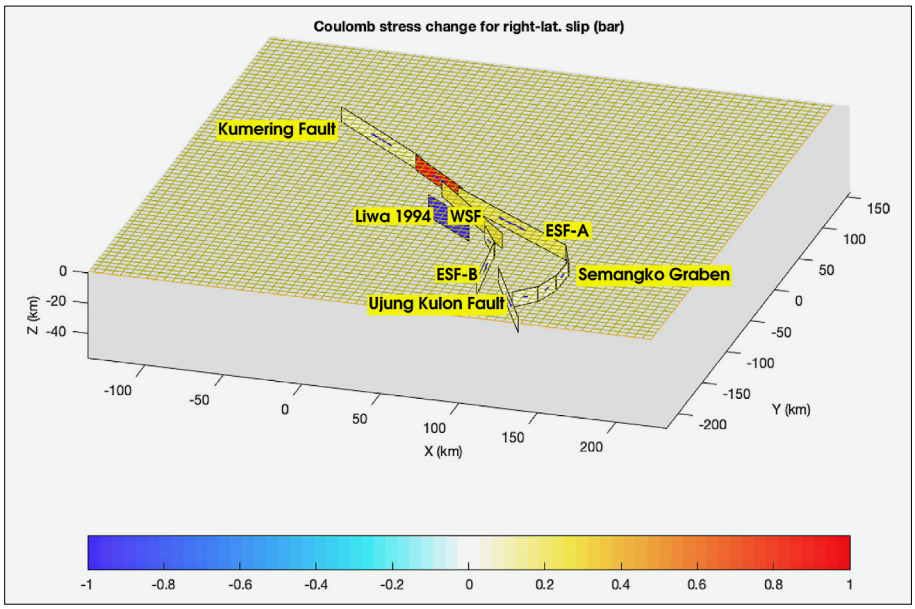


Figure 7. Three-dimensional visualization of ΔCFS distribution for right-lateral slip across segmented faults in the southern Sumatra region. Blue is the rupture plane of the Liwa earthquake. The model simulates stress changes following the 1994 Liwa earthquake, highlighting key fault segments including the Kumering Fault, West and East Semangko Faults (A and B), Ujung Kulon Fault, and Semangko Graben.

ben system and antithetic faults beneath Semangko Bay features that contribute to the complex seismic response observed in the area. Activation of antithetic faults may locally amplify ΔCFS through mechanical interactions and the internal structural geometry of the graben. This highlights the importance of incorporating minor fault elements in static stress transfer modelling to adequately capture the complexity of stress redistribution. At the regional scale, these results also align with the findings of **Sahara et al. (2018)**, which demonstrated that stress heterogeneity within bifurcation zones of the GSF such as the Barumun, Angkola, Toru segment can lead to the concentration of moderate-to-large magnitude earthquakes. Bifurcation and step-over zones along the GSF, as previously characterized in paleoseismic studies (**Bellier et al., 1997**), suggest that fault geometry complexity significantly enhances local stress accumulation and contributes to the occurrence of seismic clusters. In this case, fraction-based diagnostics (ΔCFS > 0 and ΔCFS ≥ 10 kPa) provide stronger evidence for static triggering than whole-distribution tests, with ~74% of events located in positively stressed regions. This proportion is consistent with previously reported ranges (≈60–80%) for other strike-slip fault systems.

5.3. *Three-Dimensional Stress Transfer and Fault Interaction in Southern Sumatra*

The model indicates that several fault segments, including ESF-A, WSF, and the Kumering Fault, experienced an increase in ΔCFS following the 1994 mainshock (see **Figure 7**). Areas of positive ΔCFS are represented by red shading on the grid surface, theoretically corresponding to zones brought closer to failure and thus exhibiting an elevated potential for triggered seismicity. In contrast, regions of negative ΔCFS (blue) are predominantly observed along the rupture segment of the 1994 Liwa earthquake, suggesting a stress decrease in those areas.

The elevated ΔCFS observed on the ESF-A and ESF-B segments corresponds with their fault geometry being aligned or subparallel to the rupture plane of the 1994 mainshock (see **Figure 7**). This observation is consistent with findings by **Parija et al. (2021)** and **Supendi et al. (2022)**, which suggest that fault segments with orientations optimally aligned with the regional stress field tend to receive greater static stress transfer, thereby increasing their susceptibility to secondary seismic energy release.

Furthermore, the existence of minor structures and fault geometry complexity, such as the East Semangko Fault A/B, Ujung Kulon Fault, and Semangko Graben, emphasizes the significant role of local structural features in static stress redistribution. The 3D ΔCFS model (see **Figure 7**) supports **Bellier et al. (2006)**'s findings and **Sahara et al. (2018)**'s en-echelon fault patterns inside the GSF bifurcation zone, revealing positive stress concentrations that propagate southward and eastward by minor faults. These results show that minor faults cannot be ignored in tectonically complex systems such as southern Sumatra. Integrating ΔCFS modelling with high-resolution hypocenter relocation improves the understanding of stress evolution in fault networks, as seen in other complex locations including California, the Himalayas and Taiwan (**Pope & Mooney, 2020; Parija et al., 2021; Ishimaru et al., 2025).**

The spatial distribution of ΔCFS across depths of 5–20 km (see **Figure 8**) reveals patterns that reflect mechanical heterogeneity within the crust. At shallower depths (5–10 km), stress changes are more laterally dispersed, whereas at intermediate depths (15–20 km), ΔCFS becomes more concentrated along the trace of the main fault. The plots indicate that relocated events preferentially occur in ΔCFS-positive regions. This depth-

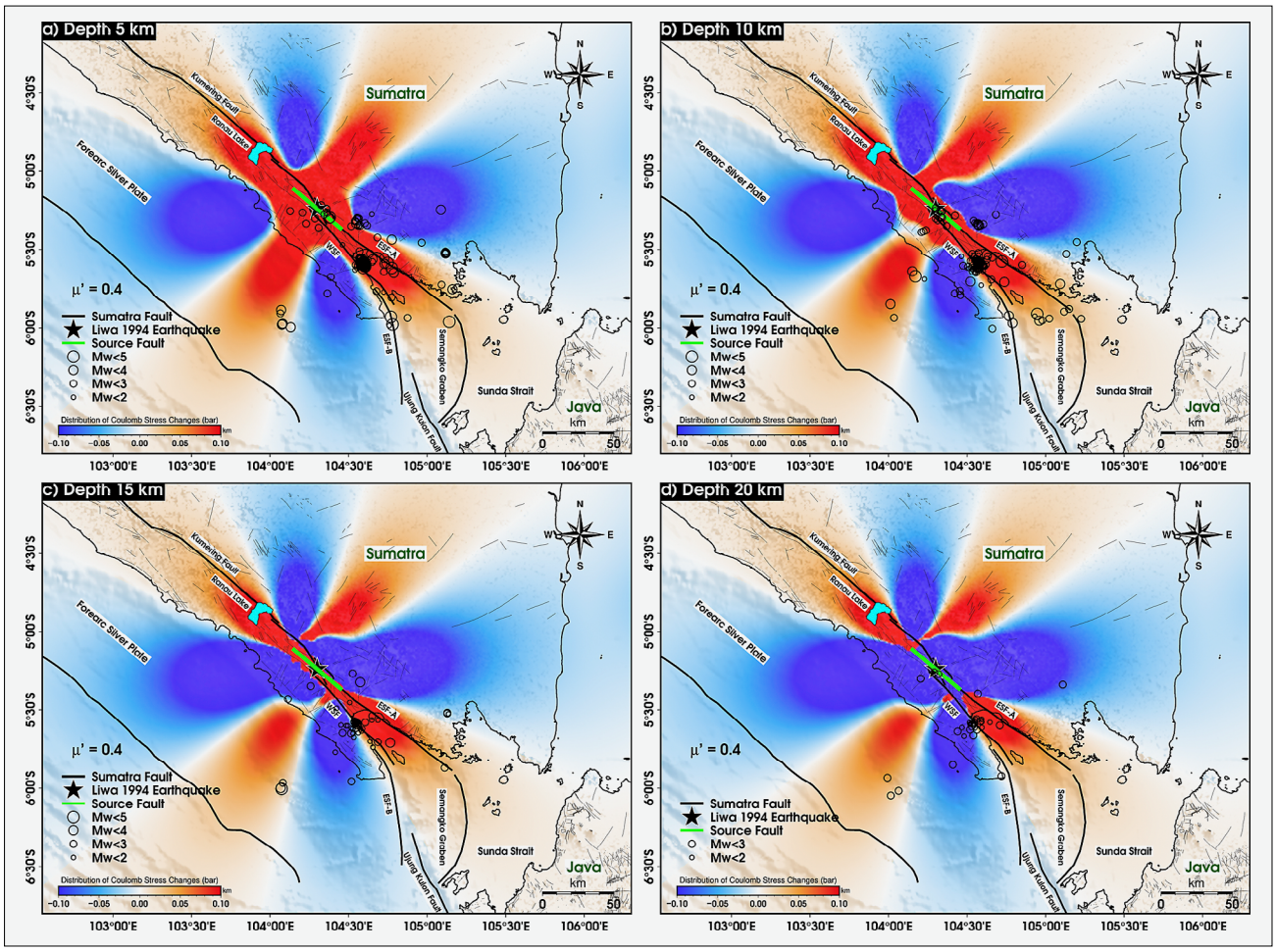


Figure 8. Coulomb failure stress changes induced by the 1994 Mw 6.8 Liwa earthquake, modelled at four different depths: (a) 5 km, (b) 10 km, (c) 15 km, and (d) 20 km. The stress lobes show systematic propagation along and across the mapped fault segments, with notable positive ΔCFS regions coinciding with the WSF-B, ESF-A, and Kumering Fault.

dependent variation is most likely caused by variations in effective friction and rheological characteristics with increasing depth (**Cattin et al., 2009**), as well as the distribution from previous slip events, for instance, the 1933 and 1994 earthquakes.

The ΔCFS results presented here exhibit features comparable to global case studies, such as those in the California region (**Pope & Mooney, 2020**) and the Western Himalayas (**Parija et al., 2021**), particularly in the asymmetric distribution of stress lobes and the potential for post-seismic seismicity clustering. However, Sumatra's tectonic setting is distinct, primarily governed by forearc sliver motion, which plays a critical role in accelerating stress accumulation along the GSF (**Natawidjaja & Triyoso, 2007; Rafie et al., 2021**). This tectonic control is further emphasized by **Hutchings and Mooney (2021)**, who reported that the rate of stress accumulation in Sumatra is among the highest observed in subduction zones worldwide.

The model results, particularly for the Semangko segment, support concerns regarding the accumulation of unreleased stress since the last major earthquake in 1994. The western section of this segment displays positive ΔCFS values exceeding 0.1 bar across all modelled depths. According to the time-evolution ΔCFS model by **Rafie et al. (2023)**, a fault segment with a stress accumulation rate of 17 kPa/year would require approximately 100–150 years to reach a critical seismic threshold. This suggests that the Semangko and Kumering segments would be ideal candidates for a future large-magnitude event if stress is not released by seismic creep or small earthquakes.

The presence of elevated ΔCFS values in this model further indicates that the Semangko Fault system is currently in a critical stress state, particularly in the southwestern section, which has not experienced significant stress release since the 1933 earthquake. This observation is broadly consistent with the concept of "stress recovery time" along the GSF, which is estimated to range between 100 and 200 years for stress levels to return to failure thresholds following a major rupture. These findings carry important implications for seismic hazard modelling in southern Sumatra. In particular, the potential for stress concentration within transition zones between fault segments (e.g. between the Semangko and Ujung Kulon faults) should be considered in future haz-

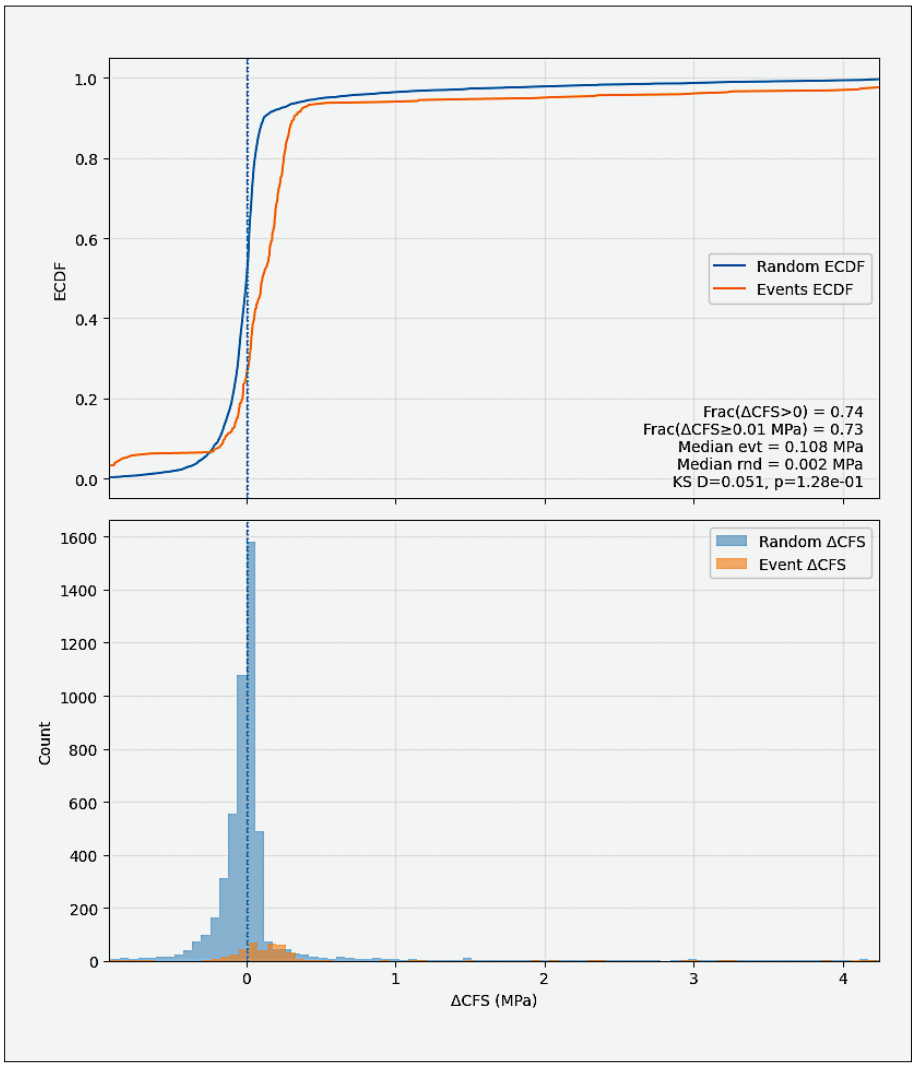


Figure 9. Joint diagnostics of ΔCFS at relocated earthquake hypocenters (orange) versus random samples (blue) drawn from within the convex-hull-plus-buffer domain. (Top) Empirical cumulative distribution functions (ECDFs) with vertical reference lines at ΔCFS = 0 and ΔCFS = 0.01 MPa (10 kPa). (Bottom) Histograms constructed using a Freedman–Diaconis bin width. Annotated statistics include Frac (ΔCFS > 0) = 0.74, Frac (ΔCFS ≥ 0.01 MPa) = 0.73, median(event) = 0.108 MPa, median(random) = 0.002 MPa, KS D = 0.051, and p = 0.128. Collectively, the plots indicate that relocated events preferentially occur in ΔCFS-positive regions relative to random expectation.

ard zoning updates (**Irsyam et al., 2017**). Moreover, this study highlights the need for continuous monitoring of microseismicity and ΔCFS modelling, especially in regions exhibiting high static stress but limited recorded seismic activity.

5.4. Policy and mitigation implications

The ΔCFS maps and relocated clusters provide operational inputs for hazard management: (1) incorporate ΔCFS-positive lobes as spatial priors in source weighting for PSHA and as tiers for microzonation; (2) require site-specific geotechnical/ground-motion studies (Vs30/HVSR) and targeted retrofits for hospitals, schools, bridges, and lifelines within the ESF-A, WSF-B, Semangko Bay, and Kumering corridors; (3) expand seismic and geodetic monitoring in these corridors to enable performance-based updates of hazard models; (4) apply fault-setback buffers and crossings-design guidelines where lifelines intersect mapped strands; and (5) prioritize paleoseismic trenching on ΔCFS-elevated segments to refine recurrence and inform building-code enforcement and land-use planning. These measures translate our physics-based results into actionable risk-reduction steps for southern Sumatra.

Several limitations should be acknowledged in this study. These include the spatial extent of hypocenter relocation, which remains constrained to regions with dense seismic station coverage, as well as the simplified assumptions in the ΔCFS modelling, which employs a homogeneous receiver fault. As show by **Mildon et al. (2018)**, local fault-geometry variations strongly modulate stress change, integrating GNSS, interseismic coupling/slip rates (**Wulandari et al., 2023**), seismic tomography, 3-D velocity and depth structure (**Hu et al., 2023**), and 3-D dynamic modelling (rupture/interaction scenarios) reduces epistemic uncertainty in receiver-fault geometry, locking depth, and ΔCFS sign/amplitude, thereby strengthening the robustness of physics-based seismic-hazard assessments.

Future research is encouraged to incorporate regional GNSS observations and interferometric geodetic data (InSAR) to better characterize cumulative strain patterns. New paleoseismic investigations in areas exhibiting elevated ΔCFS values are also critical for refining slip rate estimates and earthquake recurrence intervals. Further-

more, detailed mapping of antithetic faults and blind structures within the Semangko Bay region should be prioritized, utilizing shallow geophysical techniques or active seismic imaging to improve structural resolution.

The statistical analysis indicates that nearly three-quarters of the relocated seismicity occurred in regions of positive ΔCFS (see **Figure 9**). This result is consistent with global case studies where 60–80% of earthquakes following large events are observed within positive stress-change zones (e.g. **King et al., 1994; Toda et al., 2005; Pope & Mooney, 2020**). This finding reinforces the utility of ΔCFS as a first-order predictor of post-mainshock clustering and motivates its incorporation as a spatial prior and time-dependent constraint in physics-based seismic-hazard models (e.g. weighting PSHA sources, conditioning ETAS/Coulomb forecasts, and prioritizing scenario ruptures in the southern GSF).

6. Conclusions

This study quantifies the ΔCFS induced by the Mw 6.8 Liwa mainshock in 1994 and evaluates their correlation with the relocated seismicity along the southern segment of the Semangko Fault. By integrating high-resolution hypocenter relocation and ΔCFS modelling across multiple depths and fault geometries, several key findings have emerged:

1. The static ΔCFS distribution exhibits a characteristic four-lobe pattern associated with a right-lateral source, with maxima >0.10 MPa around WSF-B, ESF-A, and the Kumering Fault; conjugate negative lobes (ΔCFS < 0) delineate potential stress-shadow domains where failure likelihood may be temporarily reduced. These zones are interpreted as having elevated seismic potential due to stress transfer from the mainshock.
2. The relocated seismicity reveals spatial clustering that aligns with areas of positive ΔCFS, particularly within the 5–15 km depth range. This spatial correspondence strongly suggests that static stress redistribution following the mainshock likely triggered subsequent seismic activity on adjacent fault segments.
3. The presence of secondary or antithetic fault structures that are not yet mapped but may have seen notable stress increases is suggested by the occurrence of seismic events off the main fault trace, especially within the Semangko Graben and the transitional zone between the ESF and WSF. These results suggest that seismic risk is not just found in major fault segments but can also involve sophisticated and poorly understood structural features.

The integration of earthquake relocation and ΔCFS modelling is effective for identifying zones where seismic hazard is modulated by static stress transfer, elevated within positive-ΔCFS lobes and potentially reduced within stress-shadow regions (ΔCFS < 0). We note that postseismic creep/viscoelastic relaxation may further decrease stresses with time; our static ΔCFS results represent the instantaneous post-mainshock state. These results highlight the critical importance of sustained seismotectonic monitoring in southern Sumatra, including the expansion of seismic station networks, integration with geodetic observations (e.g. GPS and InSAR), and the implementation of paleoseismic studies to reconstruct the region's earthquake history.

Acknowledgement

The authors would like to express their sincere gratitude to the Department of Geophysical Engineering for their assistance and support in facilitating the administrative processes required for this research. We also thank the Indonesian Agency for Meteorology, Climatology, and Geophysics (BMKG) for providing the seismic data used in this study. Their contributions were essential to the successful completion of this work.

7. References

Alif, S. M., Fattah, E. I., & Kholil, M. (2020). Geodetic slip rate and locking depth of East Semangko Fault derived from GPS measurement. Geodesy and Geodynamics, 11(3), 222–228. https://doi.org/10.1016/j.geog.2020.04.002

Bellier, O., Sébrier, M., Pramumijoyo, S., Beaudouin, T., Harjono, H., Bahar, I., & Forni, O. (1997). Paleoseismicity and seismic hazard along the Great Sumatran Fault (Indonesia). Journal of Geodynamics, 24(1–4), 169–183. https://doi.org/10.1016/S0264-3707(96)00051-8

Cattin, R., Chamot-Rooke, N., Pubellier, M., Rabaute, A., Delescluse, M., Vigny, C., Fleitout, L., & Dubernet, P. (2009). Stress change and effective friction coefficient along the Sumatra–Andaman–Sagaing fault system after the 26 December 2004 (Mw 9.2) and the 28 March 2005 (Mw 8.7) earthquakes. Geochemistry, Geophysics, Geosystems, 10(3). https://doi.org/10.1029/2008GC002167

Daryono, M. R., Natawidjaja, D. H., & Sieh, K. (2012). Twin-surface ruptures of the March 2007 M > 6 earthquake doublet on the Sumatran Fault. Bulletin of the Seismological Society of America, 102(6), 2356–2367. https://doi.org/10.1785/0120110220

DeMets, C., Gordon, R. G., & Argus, D. F. (2010). Geologically current plate motions. Geophysical Journal International, 181(1), 1–80. https://doi.org/10.1111/j.1365-246X.2009.04491.x

Heidbach, O., Rajabi, M., Cui, X., Fuchs, K., Müller, B., Reinecker, J., Reiter, K., Tingay, M., Wenzel, F., Xie, F., Ziegler, M., Zoback, M.-L., & Zoback, M. (2018). The World Stress Map database release 2016: Crustal stress pattern across scales. Tectonophysics, 744, 484–498. https://doi.org/10.1016/j.tecto.2018.07.007

Hu, H., Zhao, D., Lin, J., & Pilia, S. (2023). A slab window beneath North Sumatra revealed by P-wave mantle tomography. Journal of Geophysical Research: Solid Earth, 128(6). https://doi.org/10.1029/2022JB025976

Hurukawa, N., Wulandari, B. R., & Kasahara, M. (2014). Earthquake history of the Sumatran Fault, Indonesia, since 1892, derived from relocation of large earthquakes. Bulletin of the Seismological Society of America, 104(4), 1750–1762. https://doi.org/10.1785/0120130201

Hutchings, S. J., & Mooney, W. D. (2021). The seismicity of Indonesia and tectonic implications. Geochemistry, Geophysics, Geosystems, 22(9). https://doi.org/10.1029/2021GC009812

Ishimaru, Y., Takada, Y., Ching, K. E., & Chang, W. L. (2025). Strong fault interaction in double-vergence structure: Lessons from the 2022 Yuli and 2022 Chihshang earthquakes, eastern Taiwan. Journal of Geophysical Research: Solid Earth, 130(7). https://doi.org/10.1029/2025JB031225

Irsyam, M., Sengara, I. W., Aldiamar, F., Widiyantoro, S., Triyoso, W., Natawidjaja, D. H., Kertapati, E., Meilano, I., Suhardjono, Suharyadi, R., & Ridwan, M. (2017). Peta Sumber dan Bahaya Gempa Indonesia Tahun 2017. PUSGEN, Kementerian PUPR, Jakarta.

Ito, T., Gunawan, E., Kimata, F., Tabei, T., Meilano, I., Agustan, …, & Sugiyanto, D. (2016). Co-seismic offsets due to two earthquakes (Mw 6.1) along the Sumatran Fault system derived from GNSS measurements. Earth, Planets and Space, 68(1), 57.

Kennett, B. L. N., Engdahl, E. R., & Buland, R. (1995). Constraints on seismic velocities in the Earth from travel times. Geophysical Journal International, 122(1), 108–124. https://doi.org/10.1111/j.1365-246X.1995.tb03540.x

King, G. C. P., & Devès, M. H. (2015). Fault interaction, earthquake stress changes, and the evolution of seismicity. In Treatise on Geophysics (2nd ed., Vol. 4, pp. 243–271). Elsevier. https://doi.org/10.1016/B978-0-444-53802-4.00077-4

King, G. C., Stein, R. S., & Lin, J. (1994). Static stress changes and triggering earthquakes. Bulletin of the Seismological Society of America, 84(3), 935–953.

Kurniawan, A., Wibowo, R. C., Nurrochman, A., Zaenudin, A., Wibowo, A., Destawan, R., & Hanif, I. (2024). Analisis seismisitas dan mekanisme fokus Sesar Sumatera: Studi kasus segmen Semangko dan Selat Sunda. Jurnal Teknologi dan Inovasi Industri (JTII), 5(2). https://doi.org/10.23960/jtii.v5i2.98

Laske, G., Masters, G., Ma, Z., & Pasyanos, M. (2013, April). Update on CRUST1.0 – A 1-degree global model of Earth's crust. Geophysical Research Abstracts, 15, 2658.

Lubis, A. M., Salman, R., Hermawan, I., Bradley, K., Feng, L., Qiu, Q., Sahputra, R., Natawidjaja, D. H., Sieh, K., & Hill, E. M. (2024). Slip rates and locking depths of the southern Sumatran Fault Zone revealed by new campaign GPS observations. Geophysical Journal International, 239(1), 248–257. https://doi.org/10.1093/gji/ggae257

Lubis, R. F., Bradley, K. E., Natawidjaja, D. H., & Bellier, O. (2024). Coseismic and postseismic deformation along the southern Great Sumatran Fault derived from InSAR analysis. Journal of Geophysical Research: Solid Earth, 129(2), e2023JB027432. https://doi.org/10.1029/2023JB027432

Mildon, Z., Toda, S., Walker, J., & Roberts, G. (2018). Evaluating models of Coulomb stress transfer: Is variable fault geometry important? Geophysical Research Letters, 43(24), 1–8. https://doi.org/10.31223/OSF.IO/7XU2B

Muttaqy, F., Nugraha, A. D., Puspito, N. T., Sahara, D. P., Zulfakriza, Z., Rohadi, S., & Supendi, P. (2023). Double-difference earthquake relocation using waveform cross-correlation in Central and East Java, Indonesia. Geoscience Letters, 10(1). https://doi.org/10.1186/s40562-022-00259-2

Natawidjaja, D. H. (2018). Updating active fault maps and slip rates along the Sumatran Fault Zone, Indonesia. IOP Conference Series: Earth and Environmental Science, 118, 012001. https://doi.org/10.1088/1755-1315/118/1/012001

Natawidjaja, D. H., & Triyoso, W. (2007). The Sumatran fault zone – from source to hazard. Journal of Earthquake and Tsunami, 1(1). https://doi.org/10.1142/S1793431107000031

Okada, Y. (1992). Internal deformation due to shear and tensile faults in a half-space. Bulletin of the Seismological Society of America, 82(2), 1018–1040. https://doi.org/10.1785/BSSA0820021018

Parija, M. P., Kumar, S., Tiwari, V. M., Biswal, S., Biswas, A., & Velliyidathu, A. (2021). Coulomb stress modeling and seismicity in the western Himalaya, India, since 1905: Implications for the incomplete ruptures of the Main Himalayan Thrust. Tectonics, 40(9), 1–16. https://doi.org/10.1029/2020TC006204

Pope, N., & Mooney, W. D. (2020). Coulomb stress models for the 2019 Ridgecrest, California earthquake sequence. Tectonophysics, 791, 228555. https://doi.org/10.1016/j.tecto.2020.228555

Pranata, B., Ramdhan, M., Hanif, M., Sulaiman, M. I., Maulana, M. P., Wandono, Widiyantoro, S., Suhardja, S. K., Hidayat, E., Supendi, P., Kusnandar, R., & Setyonegoro, W. (2023). Seismic imaging beneath Sumatra Island and its surroundings from local–regional P-wave tomography. Rudarsko-Geološko-Naftni Zbornik, 38(3), 119–132. https://doi.org/10.17794/rgn.2023.3.10

Rafie, M. T., Cummins, P. R., Sahara, D. P., Widiyantoro, S., Triyoso, W., & Nugraha, A. D. (2021). Variations in forearc stress and changes in principal stress orientations caused by the 2004–2005 megathrust earthquakes in Sumatra, Indonesia. Frontiers in Earth Science, 9, 712144. https://doi.org/10.3389/feart.2021.712144

Rafie, M. T., Sahara, D. P., Cummins, P. R., Triyoso, W., & Widiyantoro, S. (2023). Stress accumulation and earthquake activity on the Great Sumatran Fault, Indonesia. Natural Hazards, 116(3), 3401–3425. https://doi.org/10.1007/s11069-023-05816-2

Sahara, D. P., Widiyantoro, S., & Irsyam, M. (2018). Stress heterogeneity and its impact on seismicity pattern along the equatorial bifurcation zone of the Great Sumatran Fault, Indonesia. Journal of Asian Earth Sciences, 164, 1–8. https://doi.org/10.1016/j.jseaes.2018.06.002

Salman, R., Lindsey, E. O., Feng, L., Bradley, K., Wei, S., Wang, T., Daryono, M. R., & Hill, E. M. (2020). Structural controls on rupture extent of recent Sumatran Fault Zone earthquakes, Indonesia. Journal of Geophysical Research: Solid Earth, 125(2), e2019JB018101. https://doi.org/10.1029/2019JB018101

Segou, M., & Parsons, T. (2020). A new technique to calculate earthquake stress transfer and to probe the physics of aftershocks. Bulletin of the Seismological Society of America, 110(2), 863–873. https://doi.org/10.1785/0120190033

Sieh, K., & Natawidjaja, D. (2000). Neotectonics of the Sumatran Fault, Indonesia. Journal of Geophysical Research: Solid Earth, 105(B12), 28295–28326. https://doi.org/10.1029/2000JB900120

Soehaimi, A., Widarto, D. S., Matsuryono, & Effendi, I. (2002). The seismotectonic database as main parameter for prediction of the tectonic earthquake hazard level at Liwa, West Lampung District. In Proceedings of the 31st Annual Convention of the Indonesian Association of Geologists.

Sukrungsri, S., Khamsiri, S., & Pailoplee, S. (2024). Investigation of co-seismic stress and aftershock distribution along the Sumatra–Andaman subduction zone. Geoscience Letters, 11(1), 1–15. https://doi.org/10.1186/s40562-024-00366-2

Supendi, P., Rawlinson, N., Prayitno, B. S., Sianipar, D., Simanjuntak, A., Widiyantoro, S., Palgunadi, K. H., Kurniawan, A., Shiddiqi, H. A., Nugraha, A. D., Sahara, D. P., Daryono, D., Triyono, R., Adi, S. P., Karnawati, D., Daniarsyad, G., Ahadi, S., Fatchurochman, I., Anugrah, S. D., Heryandoko, N., Sudrajat, A. (2022). A previously unidentified fault revealed by the February 25, 2022 (Mw 6.1) Pasaman Earthquake, West Sumatra, Indonesia. Physics of the Earth and Planetary Interiors, 334, 106973. https://doi.org/10.1016/j.pepi.2022.106973

Supendi, P., Widiyantoro, S., Rawlinson, N., Wibowo, A., Priyobudi, P., Palgunadi, K. H., Nugraha, A. D., Imran, I., Marliyani, G. I., Daryono, D., Prayitno, B. S., Sadly, M., Karnawati, D., Sari, N., & Sugiharto, A. (2022). Analysis of the 2021 Semangko Bay earthquake sequence in southern Sumatra, Indonesia, using broadband seismic network data. Seismological Research Letters, 93(3), 1373–1381. https://doi.org/10.1785/0220210304

Tozer, B., Sandwell, D. T., Smith, W. H. F., Olson, C., Beale, J. R., & Wessel, P. (2019). Global bathymetry and topography at 15 arc sec: SRTM15+. Earth and Space Science, 6(10), 1847–1864. https://doi.org/10.1029/2019EA000658

Toda, S., Stein, R. S., Richards-Dinger, K., & Bozkurt, S. B. (2005). Forecasting the evolution of seismicity in southern California: Animations built on earthquake stress transfer. Journal of Geophysical Research: Solid Earth, 110(B5). https://doi.org/10.1029/2004JB003415

Toda, S., Stein, R. S., Sevilgen, V., & Lin, J. (2011). Coulomb 3.3 – Graphic-rich deformation and stress-change software for earthquake, tectonic, and volcano research and teaching (User Guide). USGS Open-File Report 2011-1060.

Valentini, G., Volatili, T., Galli, P., & Tondi, E. (2024). Investigating the last millennium Coulomb stress transfer in the Central Apennine Fault System (CAFS). Tectonics, 43(10), e2024TC008328. https://doi.org/10.1029/2024TC008328

Waldhauser, F. (2001). hypoDD – A program to compute double-difference hypocenter locations (version 1.0-03/2001). USGS Open-File Report 01-113. https://doi.org/10.3133/ofr01113

Waldhauser, F., & Ellsworth, W. L. (2000). A double-difference earthquake location algorithm: Method and application to the Northern Hayward Fault, California. Bulletin of the Seismological Society of America, 90(6), 1353–1368. https://doi.org/10.1785/0120000006

Wang, Y., Gao, Y., Morley, C. K., Seagren, E. G., Qian, X., Rimando, J. M., et al. (2023). Pleistocene accelerated exhumation within the Sumatran Fault: Implications for late Cenozoic evolution of Sumatra (Indonesia). Geophysical Research Letters, 50, e2022GL100028. https://doi.org/10.1029/2022GL100028

Wells, D. L., & Coppersmith, K. J. (1994). New empirical relationships among magnitude, rupture length, rupture width, rupture area, and surface displacement. Bulletin of the Seismological Society of America, 84(4), 974–1002. https://doi.org/10.1785/BSSA0840040974

Wessel, P., Luis, J. F., Uieda, L., Scharroo, R., Wobbe, F., Smith, W. H. F., & Tian, D. (2019). The Generic Mapping Tools version 6. Geochemistry, Geophysics, Geosystems, 20(11), 5556–5564. https://doi.org/10.1029/2019GC008515

Widiwijayanti, C., Déverchère, J., Louat, R., Sébrier, M., Harjono, H., Diament, M., & Hidayat, D. (1996). Aftershock sequence of the 1994 Mw 6.8 Liwa earthquake (Indonesia): Seismic rupture process in a volcanic arc. Geophysical Research Letters, 23(21), 3051–3054. https://doi.org/10.1029/96GL02048

Wulandari, A., Supendi, P., & Natawidjaja, D. H. (2023). Kinematic behavior of the Angkola–Sianok fault system based on the 2022 Pasaman earthquake sequence. Journal of Asian Earth Sciences, 254, 105153. https://doi.org/10.1016/j.jseaes.2023.105153

Wulandari, R., Chan, C. H., & Wibowo, A. (2023). The 2022 Mw 6.2 Pasaman, Indonesia, earthquake sequence and its implication for seismic hazard in central-west Sumatra. Geoscience Letters, 10(1). https://doi.org/10.1186/s40562-023-00279-6

Xiong, X., Shan, B., Zhou, Y. M., Wei, S. J., Li, Y. D., Wang, R. J., & Zheng, Y. (2017). Coulomb stress transfer and accumulation on the Sagaing Fault, Myanmar, over the past 110 years and its implications for seismic hazard. Geophysical Research Letters, 44(10), 4781–4789. https://doi.org/10.1002/2017GL072770

SAŽETAK

Prijenos naprezanja i seizmičnost duž južnoga Velikog sumatranskog rasjeda: uvidi iz potresa u Liwi 1994.

Potres u Liwi magnitude 6,8 koji se dogodio 15. veljače 1994. godine prekinuo je južni Veliki sumatranski rasjed (GSF), no statička naprezanja zaostala nakon potresa i njihova povezanost s naknadnom seizmičnošću ostaju slabo kvantificirani. U ovome istraživanju integrira se visoko precizna dvostruko razlikovna realokacija s modeliranjem Coulombova naprezanja (ΔCFS) kako bi se procijenio prijenos naprezanja nakon 1994. godine duž sektora Semangko. Koristeći ~16,000 P/S odabira i ista prilagođavanja inverzije, testiraju se dva 1-D modela brzine; CRUST1.0 daje gotovo nulte, uske diferencijalne vremenske reziduale (± 0.3 – 0.4 s) u usporedbi sa širim raspodjelama s izraženim „repovima" za AK135 (± 0.7 – 0.8 s) te se usvaja za konačni katalog. Budući da su arhive faza oskudne prije 2010. godine, događaji od 1994. do 2009. tretiraju se kao pozadinski, dok se potresi od 2010. do 2024. realociraju; kontrola kvalitete zadržava 416 događaja. Realokacija suprimira umjetnu dubinsku traku od ~10 km i grupira epicentre u koherentne skupine koje ocrtavaju zapadne/istočne rasjede Semangko i zaljev Semangko. ΔCFS je izračunan za dubine od 5 do 20 km i $\mu' = 0{,}2 – 0{,}8$. Svi scenariji proizvode očekivani četverorežanjski desni lateralni uzorak s maksimumima >0,10 MPa oko WSF-B, ESF-A i rasjeda Kumering. Realocirani događaji preferencijalno zauzimaju pozitivno opterećena područja: ~74 % pada na ΔCFS > 0 i ~73 % na ΔCFS ≥ 0,01 MPa (10 kPa), robusno prema μ' i dubini. Rezultati upućuju na neriješeno opterećenje nakon 1994. na više grana Semangka i susjednim segmentima ističući potencijal za aktiviranje između segmenata. Predlaže se proširenje seizmičkoga ili geodetskoga nadzora i ciljanih paleoseizmičkih istraživanja u koridoru Semangko–Kumering kako bi se precizirale procjene ponavljanja i ažurirali fizički modeli opasnosti za južnu Sumatru.

Ključne riječi:
Coulombov prijenos naprezanja, realokacija potresa, Veliki sumatranski rasjed, segment Semangko, seizmički hazard

Author's contribution

Andri Kurniawan conceived and designed the study, performed Coulomb stress modelling, interpreted results, and drafted the original manuscript. **Nicolas Silaen** contributed to data curated and processed seismic data (phase picks, double-difference relocation), relocation processing, and figure preparation, and assisted with writing. **Khalil Ibrahim** contributed to seismotectonic interpretation and manuscript editing. **Arsy Nurrochman** contributed to data processing, visualization, and figure preparation. **Ridho Destawan** contributed to seismic-catalogue preparation, quality control, and manuscript review. **Nanda Hanyfa Maulida** compiled datasets, performed preliminary statistical analyses, and assisted with manuscript preparation. **Irfan Prasetyo** contributed to parts of the modelling workflow and manuscript review. **Ahmad Zaenudin** verified the catalogue, contributed to data cleaning and validation, and reviewed the manuscript. **Adhi Wibowo** (BMKG) provided BMKG catalogue and station metadata, contributed to results validation, and reviewed the final manuscript.
All authors have read and agreed to the published version of the manuscript.

RGNZ/MGPB

Enhanced desorption of Cobalt from contaminated sandy silty-clay soils

Rudarsko-geološko-naftni zbornik
(The Mining-Geology-Petroleum Engineering Bulletin)
DOI: 10.17794/rgn.2026.3.8

Original scientific paper

Tamás Bacsó[1,2]*, Márton Tóth[1]
[1] *Institute of Water Resources and Environmental Management, University of Miskolc, H-3515 Miskolc, Egyetem str. 1.*
[2] *Adept Enviro Ltd., H-1111 Budapest, Lágymányosi str. 12.*

Abstract
In the present study, we investigated the potential for enhancing the desorption of cobalt contamination in a sandy silty-clay soil contaminated with Cobalt(II)-chloride-hexahydrate. In soils containing silt–clay fractions, effective remediation is primarily prevented by strong surface binding and adsorption processes. Overcoming these limitations requires the establishment of favourable conditions for desorption. In contrast to industrial practices, the potential for desorption was investigated under gradually alkalinizing and reducing conditions. Based on the results, the decrease in the ORP of the saturated system, together with the increase in pH, initiated cobalt desorption. Consequently, within the range above a redox potential from 0 mV to -80 mV and above pH 7.8, the $[Co(H_2O)_6]^{2+}$ cobalt-complex initially formed. Further alkalinization and decreasing redox potential led to the precipitation of the remaining contaminant as $Co(OH)_2$ cobalt hydroxide. As a result of treatment, an average of 7.33 mg of cobalt was desorbed from the silty-clay surface within 29 days from the initiation of the desorption treatment, corresponding to about 12% of the contaminant present in the system. Furthermore, a lognormal distribution-based prediction function series (average R^2 = 0.941) was fitted to the obtained concentration data. The results indicate, that the applied procedure is capable of desorbing approximately 15% of cobalt contaminant, which presumably indicates the desorption capacity of the system. The applied method is widely accessible, cost-effective, and environmentally friendly which qualities that are essential for industrial application. The proposed novel approach represents an efficient and effective complementary technique for the future remediation of certain heavy metal compounds.

Keywords:
remediation, adsorption, desorption, sandy silty-clay soils, cobalt

1. Introduction

Due to intensive industrial activities over the past decades, substantial amounts of toxic heavy metal derivatives have accumulated in subsurface environments. Remediation of these contaminants – particularly in soils with high silt and clay content – remains a major challenge, as it is a costly and complex process for which no widely accepted and effective treatment method currently exists. One of the primary obstacles to successful remediation is the strong adsorption of contaminants onto soil surfaces, which continuously replenishes groundwater pollution through back-diffusion processes. The present study aims to explore strategies for mobilizing cobalt adsorbed onto soil surfaces and to identify conditions that can enhance the extent of its desorption.

The present research focuses on cobalt, an inorganic heavy metal component that, owing to its unique properties, has become an indispensable element in certain modern industrial applications. However, when released into the environment at high concentrations, cobalt is highly toxic to aquatic organisms and poses a significant risk to human health. This study presents the results of a novel remediation approach aimed at enhancing cobalt desorption in soil with high clay mineral content, in sandy silty-clay soil. Our hypothesis is that the combined effect of the alkalinizing compounds added to the assembled column system and the reductive shift of the medium facilitates the transformation of adsorbed cobalt. Initially, this leads to the formation of complex species, which ultimately precipitate from the system. Finally, this section provides an overview of the major soil components, highlighting their key sorption characteristics, and outlines the principal physicochemical properties of cobalt that are relevant to its environmental behaviour.

1.1. Soil properties significant in term of adsorption

The key properties influencing the interactions between soil and any contaminant include soil pH, the nature and quantity of soil colloids, organic matter content,

* Corresponding author: Tamás Bacsó
e-mail address: tamas.bacso@outlook.com
Received: 9 September 2025. Accepted: 4 December 2025.
Available online: 14 May 2026

as well as soil structure and permeability (**Filep et al., 2002**). Additional studies have identified several other critical parameters, such as cation exchange capacity (CEC), redox potential, moisture content, and specific surface area of the soil, all of which collectively affect the potential for removing adsorbed contaminants.

Adsorption, as the phenomenon responsible for contaminant retention, primarily occurs on the surfaces of clay minerals and at the edges of their crystal structures, the latter of which are referred to as active sites. In addition to mineral components, soil constituents within the colloidal size range, such as the humus fraction, Fe–Al–Mn (oxy)hydroxides, and silicate clay minerals, play a particularly important role in determining the soil surface characteristics. Most clay minerals and oxides are present in the colloidal fraction of the soil, which strongly influences its physical and chemical properties. They are critically involved in ion adsorption and ion exchange processes, as well as in the adsorption of organic matter. The environmental significance of the soil organic components of the soil manifests in their sorption capacity and, in the case of heavy metals, their chelation ability (**Ertli, 2005**).

Soil colloids represent the most active and reactive components of the soil, typically falling within the particle size range below 0.002 mm. Colloidal mineral particles, including oxides and clay minerals, together with the humic substances adsorbed onto their surfaces, form the so-called clay–humus complex. Soil colloids possess a high specific surface area and are key determinants of interfacial sorption phenomena. Mineral colloids include clay minerals, iron–manganese and aluminum hydroxides and oxyhydroxides, as well as colloidal-sized mineral fragments (**Schaetzl et al., 2015**).

1.2. Characteristics of Cobalt

Cobalt is chemically less reactive, yet it exhibits moderate solubility in both acidic and alkaline media, typically forming various complex compounds in which it can occur in multiple oxidation states.

Cobalt is widely utilized in industrial applications due to its unique properties. The element plays a critical role in the production of specialized metal alloys, which exhibit exceptional heat resistance and wear resistance. These cobalt-based alloys are highly resistant to elevated temperatures and corrosion, making them ideal for industrial applications under extreme conditions. In recent years, the demand for cobalt has significantly increased, primarily driven by its use in battery manufacturing, particularly as a cathode material in lithium-ion batteries. In aqueous media, cobalt compounds often display a reddish colouration and are commonly employed in inks, paints, and varnishes. Biologically, cobalt is an essential trace element that cannot be synthesized by the human body. However, high concentrations of dissolved cobalt are toxic to aquatic organisms, and certain cobalt compounds are classified as carcinogenic, potentially causing skin cancer and cardiovascular issues in humans. Environmental contamination by cobalt is largely a consequence of mining and industrial usage, posing risks to ecosystems, wildlife, and human health (**URL 1**).

2. Methods

The soil sample used in this study was collected from Aszód, Pest County, Hungary. To assess the desorption potential, it was considered essential to perform a detailed geotechnical characterization of the silty-clay soil. The qualitative analysis of the soil sample was refined through sieving and hydrometer methods, determination of consistency limits, and laser particle size analysis.

Prior to the experiments, the soil sample was appropriately prepared: it was dried in an oven at 105°C until constant mass, then crushed in a hammer mill to a particle size of 2 mm, followed by sieving to obtain a uniform fraction (**Szász and Tóth, 2024**).

Since the soil sample is dominated by silt- and clay-sized particles, a hydrometer analysis was also performed to accurately determine the particle size distribution of the finer fractions (**Lopez et al., 2021**). In addition, soil mechanical analyses and laser (HORIBA LA-950) particle size distribution measurements were also performed. Based on the combined evaluation of these analyses was classified as a clayey-silt soil and some of its key properties are presented in **Table 1**. This sample was homogenized with quartz-sand in order to obtain a deposit with more favourable vertical permeability for the experiments, thereby cutting the sampling time. The applied medium-grained quartz-sand mixed into the clay–silt sample was not examined separately, as due to its physical properties, it participates in the adsorption process only to a negligible extent compared to the silty-clay fraction. However, it should be noted that the soil sample used is very close to the clay-silt or silt-clay boundary.

Table 1. Soil mechanical qualification of sample

Sample ID	Ip (%)	Wp (%)	Qualification
Asz	25.53	17.32	silty-clay

Subsequently, the organic matter content as well as the quantity and type of clay minerals were determined, as these properties play a crucial role in adsorption processes. The mineralogical composition of the soil was determined by X-ray diffraction-XRD analysis (see **Table 2**) which provides a detailed and accurate evaluation of the soil's mineral constituents (**Adams, 2005; Zhou et al., 2018**). The chemical constituents of Asz soil-sample can be found in **Table 3** and **Table 4** (LOI index) by XRF analysis.

5 g portion of the finely ground sample was dried in an oven at 120°C for 2 hours to remove all free water

Table 2. Primary mineralogical constituents of soil-sample

Mineralogical composition (wt%)										
Sample ID	**Quartz**	**Calcite**	**Illite**	**Muscovite**	**Albite**	**Smectite**	**Kaolinite**	**Dolomite**	**Orthoclase**	**Chlorite (II)**
Asz (silty-clay)	43.9	21.4	8.3	7.3	6.0	3.9	3.7	1.8	2.4	1.3

Table 3. Chemical constituents of soil-sample

Sample ID	**SiO_2**	**Al_2O_3**	**MgO**	**CaO**	**Na_2O**	**K_2O**	**Fe_2O_3**
Asz (silty-clay)	46.2	10.1	2.3	18.7	0.4	1.8	3.7
Sample ID	**MnO**	**TiO_2**	**P_2O_5**	**S**	**F**	**LOI**	***TOTAL***
Asz (silty-clay)	0.1	0.6	0.1	0.1	<0.3	15.9	*99.9*

Table 4. LOI (Loss on Ignition) value of Asz soil-sample

Parameter	**Measured value**
LOI (m/m%)	**15.9**
a) Hygroscopic and interlayer water (%)	7
b) Total organic content (%)	3
c) Carbonate decomposition - CO_2 (%)	5.9

present in the soil sample. Elemental calibration was performed under a vacuum of 1.2–1.5 Pa using a RIGAKU Supermini 200 WDXRF spectrometer, equipped with LiF200, PET, and XR25 analyzer crystals. From the dried sample, 1.6–1.8 g was placed into a pre-heated and pre-weighed porcelain boat. The prepared specimen was then heated to 1050°C at a controlled rate of 10°C per minute and maintained at this temperature for 15 minutes.

2.1. Parameters affecting adsorption

Adsorption is influenced by a range of physicochemical and environmental parameters. Redox potential exerts a pronounced effect on pollutant behaviour. Under strongly reducing conditions (Eh<-100 mV), the mobility of specific cations may be substantially constrained, thereby influencing their availability and transport. Time constitutes an additional factor, as extended contact periods typically enhance the extent of adsorption, reflecting the progressive nature of sorption equilibria.

Soil pH is equally critical in regulating adsorption processes. Under acidic conditions, the affinity of soils for cations declines, which can result in increased concentrations of toxic heavy metals and organic hydrocarbon contaminants in the pore moisture. Other soil properties, such as cation exchange capacity (CEC) and soil organic matter (SOM), further modulate sorption behaviour. Although these factors are recognized as influential, their roles are not addressed in detail within the scope of this study.

2.2. Sorption tests

In this study, a hypothetical contamination event was modelled, simulating the infiltration of cobalt pollution into the subsurface through column experiments. The tests were conducted in triplicate, with the inclusion of a control column. The sample holders were cylindrical, made of clear, transparent glass, with identical dimensions and geometry (24/20 mm diameter, 400 mm height). Each column was equipped with a filter stone at the bottom, and sampling was facilitated via a teflon-lined tap.

Following the assembly of the column system, a contaminant stock solution was prepared by dissolving 2.8 g of Cobalt-chloride-hexahydrate ($CoCl_2 \cdot 6H_2O$) in 1000 ml of distilled water. The initial pH of the solution was adjusted to 7.7 at a temperature of 29°C. After assembling the column systems, each sample holder was filled with a thoroughly homogenized mixture of 35 g of silty-clay and 35 g of medium-grained quartz sand. From the prepared contaminant solution, 20 ml was applied to each of the three column samples and saturated using a vacuum pump operating at 0.9 bar. The system was then allowed to stand until adsorption equilibrium was established. In total, approximately 56 mg of dissolved cobalt contaminant was introduced into each column. After every sampling event, 20 ml of distilled water was pumped through the system to flush out any residual, non-adsorbed contaminants within the columns. This procedure ensured that subsequent desorption enhancement was solely attributed to the applied reagents. During the first five days of the experiment, three sampling events confirmed the establishment of adsorption equilibrium. The cobalt concentration in the effluent solution was determined to be 0.0 mg/l for all columns, indicating that the introduced contaminant had been completely retained within the system. Adsorption occurred predominantly on the silty-clay particles, as the relatively large particle size of the quartz sand (0.3–0.63 mm) did not facilitate significant adsorption.

Once the adsorption equilibrium was established, a desorption-enhancing treatment was initiated using a mixture of 30% sodium-bicarbonate, 10% monocalcium-phosphate, and 25% sodium aluminum-sulfate, with the remaining volume comprised of cornstarch-equivalent to household baking powder. The treatment solution was prepared by mixing 2 g of the additive blend with 60

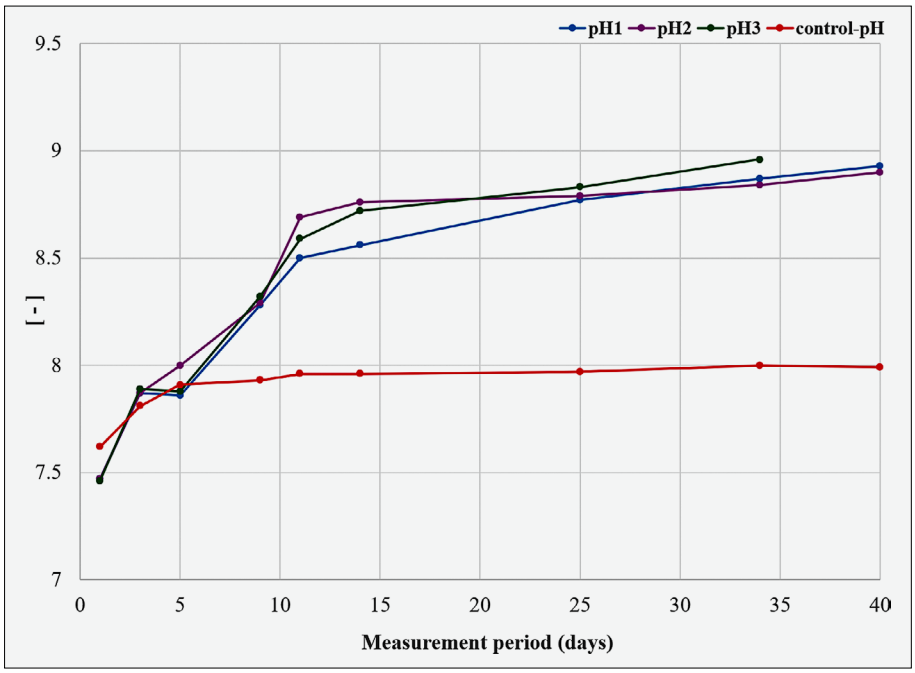


Figure 1. pH-value changes during the whole measurement period

ml of distilled water, which was then applied in equal one-third portions to the three treated columns. The same treatment was administered three times throughout the entire experimental period (on days 5, 8, and 11). In total, 6 g of the dissolved mixture was introduced into the system to enhance cobalt desorption. The initial pH of the treatment solution was pH 8,44. The control column received no treatment, serving as a baseline for the untreated condition. Throughout the experiment, pH, oxidation-reduction potential (ORP), and temperature were continuously monitored to assess temporal changes in the system.

3. Results

To enhance desorption, it was considered essential to shift the established sorption equilibrium toward desorption, which requires modifying the system conditions. It is important to note that, alongside the triplicate column tests, a control column was also included. This control column contained the same amount of soil and cobalt contaminant concentration as the treated columns, labelled Co1–Co3. Thus, the control column appropriately represented the scenario in which the system is left undisturbed, without any external intervention.

Following the initiation of the experimental series, adsorption equilibrium was confirmed in each column by three consecutive measurements over approximately five days. During sampling, the cobalt concentration in the effluent, as well as the pH, oxidation-reduction potential (ORP), and temperature, were continuously recorded as a function of time. The results are illustrated in the series of figures presented below (see **Figures 1–4**).

In **Figure 4**, the cobalt desorption curve is presented as a function of time. Following the complete adsorption of the total cobalt introduced into the system, the desorption-inducing treatment solution was applied, which was added on the 5th day. Based on the measurement results, approximately six days were required for desorption to commence due to the combined effect of the additives and the alkalinization of the medium. Consequently, a gradual increase in cobalt concentration was observed in the effluent samples.

During the desorption phase, an average cobalt concentration of approximately 413 mg/L was determined. It should be noted that, from the onset of desorption, only four sampling events could be performed, as clogging within the columns-caused by the geometry of the applied cylinders-prevented further sampling. As long as effluent samples from the parallel control column consistently exhibited a cobalt concentration of 0.0 mg/L throughout the measurement series following adsorption.

In order to determine the amount of desorbed cobalt contaminant, the obtained concentrations were plotted as a function of the sampling volume, as presented in **Figure 5**.

The amount of desorbed contaminant at the desorption phase points shown in **Figure 5** was determined using the trapezoidal method. The area under the desorption curve was treated as a surface integral, allowing the desorption period to be divided into four segments. The mass of the contaminant within each interval was then calculated according to the following relationship. Assuming f(x) as a continuous function over the interval [a,b], the definite surface integral can be approximated as follows (**Equation 1**):

$$\int_a^b f(x)dx = \frac{a+b}{2}\, dV \qquad (1)$$

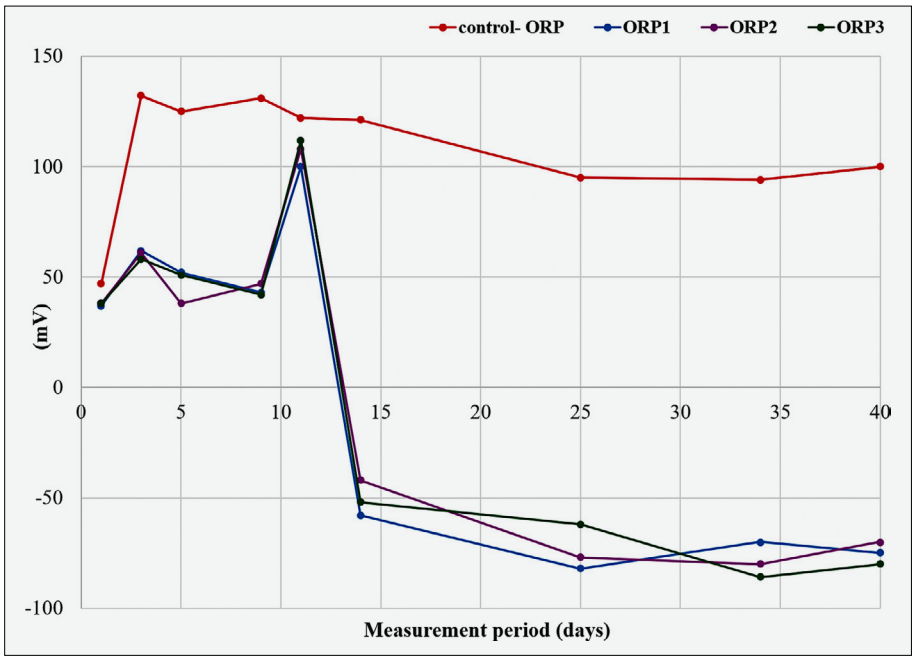


Figure 2. ORP-value changes during the whole measurement period

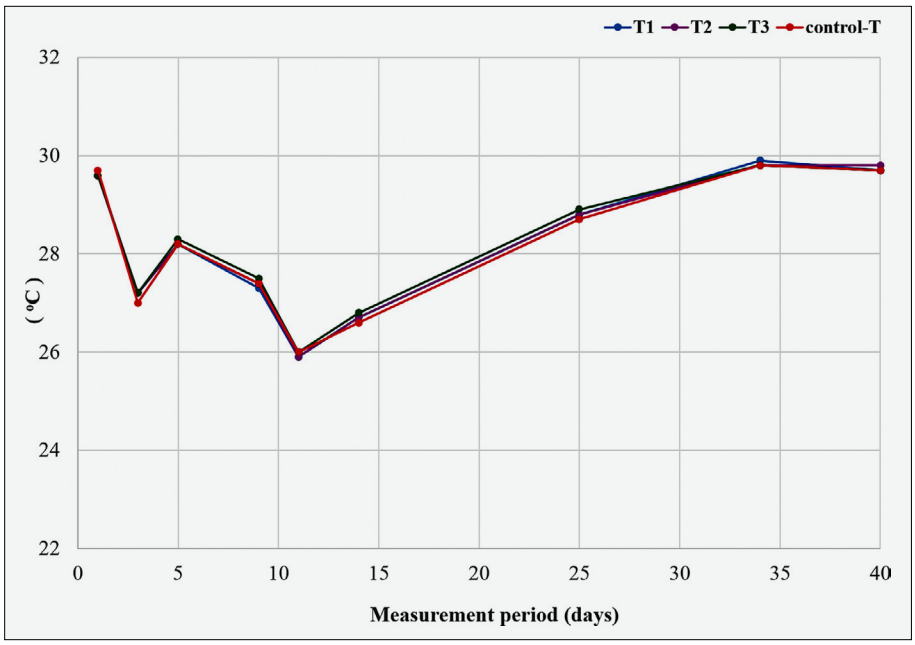


Figure 3. Temperature changes during the whole measurement period

Where:

a – Cobalt concentration of sample-a (mg/dm^3),

b – Cobalt concentration of sample-b (mg/dm^3),

dV – Amount of sampling (cm^3).

In summary, the average concentrations determined during successive sampling periods were multiplied by the corresponding sampling volume, and the resulting values were summed to obtain the area under the curve for the desorption phase, which corresponds to the total mass of cobalt contaminant desorbed from the system. The amount of cobalt released from the system is presented in **Figure 6** and **Table 5**. It must be emphasized, however, that due to colmatation in the sample holders, calculations regarding the initial amount of desorbed contaminant could only be performed based on the first four points of the desorption curve.

The determined cobalt mass at the points of the desorption phase is shown cumulatively in **Table 5**.

4. Discussion

The evaluation of the experimental series begins with the presentation of the measured pH and ORP values, as well as the temperature changes.

The redox potential measured in the treated columns was initially balanced, but during days 11–14 it dropped sharply into the negative range, followed by a further slow yet gradual decline. This trend reflects ongoing bi-

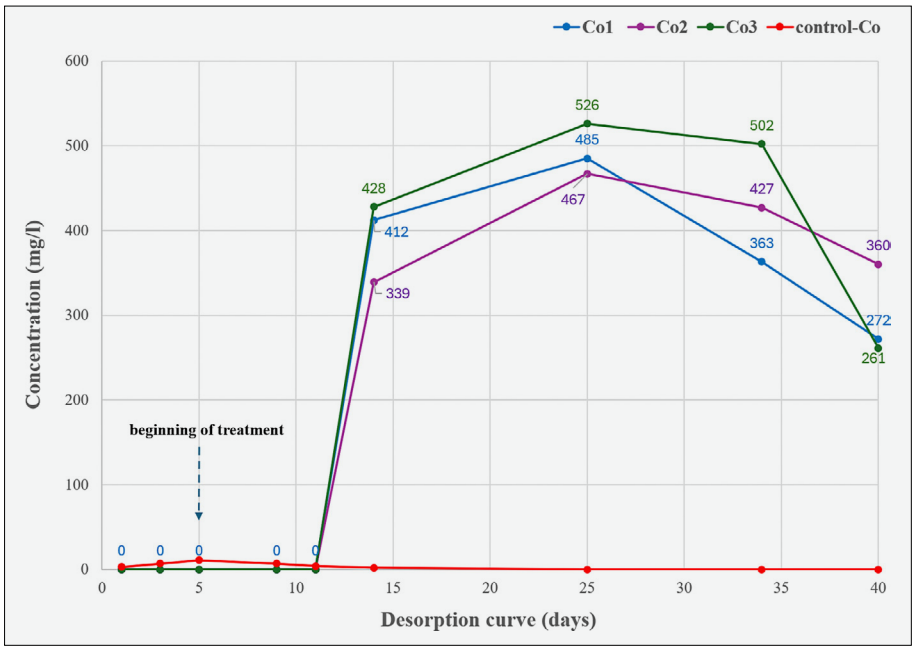


Figure 4. Desorption curve – concentration changes as a result of treatment

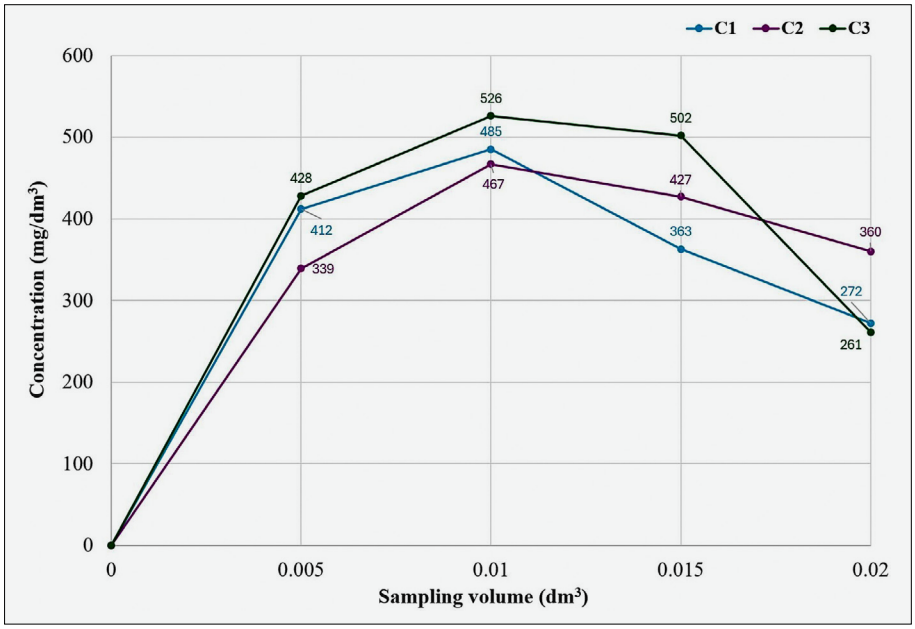


Figure 5. Desorption curve – concentration changes as a function of sampling volume

ological activity within the system, during which bacteria consume dissolved oxygen while degrading the organic matter of the silt–clay matrix. This process led to a decrease in dissolved oxygen concentration, consequently resulting in a reduction of the system's ORP. We have to mention that the addition of phosphate salts can create a reductive environment, leading to anaerobic conditions and a gradual decrease in ORP values. The sodium bicarbonate ($NaHCO_3$) caused a continuous increase in the pH value of water, as higher pH levels render the system less oxidative due to the lower concentration of protons, which contributes to a decrease in redox potential. Finally, the cornstarch present in the treatment solution - which is a simple polysaccharide - has no direct effect on either pH or ORP and is neutral, exhibiting neither acidic or basic properties. However, its potential indirect effect is that soil microorganisms may degrade the starch, resulting in oxidation, which could slightly further decrease the system's ORP.

Furthermore, cobalt compounds exhibit strong affinity for the hydroxyl groups (–OH) present on the surfaces of iron and manganese oxides involving the soil particles. Under the induced reductive conditions, the dissolution of these oxides (Fe^{3+} à Fe^{2+}, Mn^{4+} à Mn^{2+}) releases the cobalt species previously adsorbed or bound to them, thereby enhancing cobalt desorption (**Anthony et al., 2010; Yan et al., 2011; Nicholas, 2013; Clare et al., 1995**).

Moreover, the applied silty–clay soil contains approximately 3% organic matter and under increasingly re-

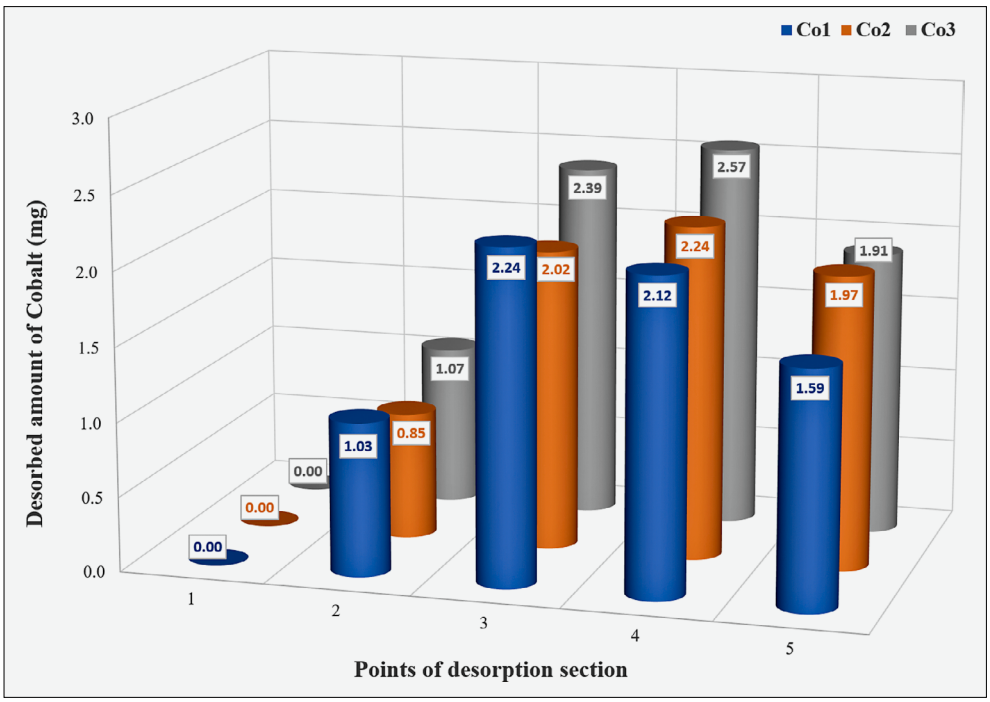


Figure 6. Desorbed amount of cobalt (mg) at desorption section

ductive conditions, the organic colloids lose part of their surface negative charge, which likewise promotes the desorption of bound cobalt.

Continuing with the evaluation of the cobalt concentration curve, it can be observed that following the establishment of sorption equilibrium (effluent cobalt concentration: 0.0 mg/L), we initiated the enhancement of desorption. After treatment of the Co1-Co2-Co3 columns, six days were required for the induced redox potential to start the cobalt desorption process.

We examined the chemical forms of cobalt compounds under the induced pH and redox potential conditions, as illustrated by the Pourbaix diagram. This diagram is one of the most important tools for understanding adsorption and metal ion speciation in water-saturated systems. The combined effect of pH and redox potential determines the redox state of the chemical environment, indicating the types of electron transfer processes occurring within the system. An aqueous solution of Cobalt(II)-chloride-hexahydrate formed the $[Co(H_2O)6]^{2+}$ water complex (Equation 2) under modified medium parameters (decreasing ORP, higher pH) as described by the following interpretation:

$$CoCl_2\ 6H_2O \rightarrow [Co(H_2O)_6]^{2+} + 2Cl^- \qquad (2)$$

The resulting species remains as a dissolved complex ion within this pH range (until 7,5) and ORP: -300 mV. The effluent solution appeared slightly pink and was clear and transparent. As the medium became increasingly alkaline and reductive, and the pH exceeded a value of 7.8, hydroxide ions (OH^-) became available, leading to the precipitation of the remaining undesorbed

Table 5. Desorbed cumulative amount of cobalt (mg)

Sorption tests (mg)		
Co1	**Co2**	**Co3**
6.98	7.07	7.93

Co^{2+} ions as cobalt(II)- hydroxide, according to the following reaction (**Equation 3**):

$$[Co(H_2O)_6]^{2+} + 2OH^- \rightarrow Co(OH)_2 + 6H_2O \qquad (3)$$

The initially precipitated cobalt contaminant exhibited a dark purple tone, which gradually oxidized in the presence of oxygen from the ambient air, turning dark brown as $Co(OH)_3$ formed. Notably, from the second sampling point of the desorption phase (t=25 days) onwards, the effluent appeared turbid with slight sedimentation, further confirming the precipitation process. Thus, cobalt ions remaining in the system above pH 7.8 did not remain in solution but precipitated. This observation is further supported by the fact that the measured cobalt concentrations began to decrease. Although the observed colour change and the decline in cobalt concentrations do not constitute direct evidence of precipitation, but they strongly suggest that such a process has occurred (**Jing et al., 2009; Yanglong et al., 2005; Yang et al., 2011**). Moreover, the ions from dissolved salts alter the structure of water molecules and the hydration case of the dissolved cobalt ions, restricting their mobility. Consequently, sulfate and phosphate ions draw water away from the hydration case of the dissolved species, enhancing electrostatic interactions and reducing solubility. The solubility product of cobalt hydroxide is ex-

tremely low (5.92×10^{-15}), which further supports its precipitation.

The results indicate that under moderately alkaline conditions (pH>7.8), precipitation occurred which is more likely than the previously assumed cation exchange. Cation exchange would require surface-adsorbed Co^{2+} to be replaced by another cation (e.g. Ca^{2+}, Na^{+}), but in alkaline conditions, the concentration of H^{+} is too low to displace Co^{2+} from the soil surface. In summary, the speciation of the cobalt is governed by its dependence on ORP and pH, as characterized using the cobalt Pourbaix diagram (**Ersin et al., 2016; Kamal et al., 2014; Rou-Chen et al., 2020; Chivot et al., 2008**). This diagram illustrates the chemical forms in which cobalt is stable under varying redox potentials and pH conditions in an aqueous environment. Since the pH of the assembled system continuously increased due to the repeated addition of carbonates, the chemical state of cobalt also evolved in response to the rising pH. Initially, shifting toward desorption equilibrium, cobalt remained in a dissolved state, but subsequently precipitated from the system. Moreover, the applied silty-clay exhibits a strongly negative surface charge under alkaline conditions, making it less capable of retaining Co^{2+}. This demonstrates that heavy metal remediation can be effective not only in so in suitably alkaline environments. While metal precipitation has been studied for pharmaceutical industrial wastewater, its application for environmental remediation has not yet been explored.

The addition of carbonates generated OH^{-} ions in the saturated medium, thereby increasing its alkalinity. Heterotrophic catabolic processes produced CO_2 within the system, which induced the formation of carbonic acid. It dissolved the high calcite content of the soil sample, resulting in the release of additional carbonate ions. The combined effect of these processes led to a gradual increase in pH. Due to the intensified treatment, the proportion of carbonate ions in the system shifted, leaving progressively less carbonic acid within the column. Consequently, the escape of CO_2 reduced the amount of carbonic acid formed, shifting the carbonate equilibrium toward CO_3^{2-}, thereby increasing the pH of the soil solution (**Choi et al., 1998**). The following reaction (**Equation 4**) occurs as a result of CO_2 release:

$$2HCO_3^- \rightleftharpoons CO_3^{2-} + CO_2 + H_2O \quad (4)$$

Furthermore, at the beginning of the measurement series, the acidic functional groups of the soil suppressed the increase in soil-solution pH. As the treatment solution was repeatedly added, the soil's buffering capacity eventually became exhausted, allowing the pH of the soil solution to gradually rise, approaching the initial pH of the treatment solution. In other words, the applied alkaline treatment solution displaced the "acidic" cations, leading to the neutralization of protons on the soil particles, which in turn resulted in an increase in the pH of the effluent. To verify the progressively increasing pH values, we performed a calculation to determine the alkalinity of the system, which is presented below.

The molar mass of the applied $NaHCO_3$ is 84.01 g/mol (**URL 2**). In the treatment solution, a total of 0.6 g $NaHCO_3$ was dissolved in 60 mL of distilled water, which was added to the columns in three portions. Consequently, each column received 0.2 g $NaHCO_3$, corresponding to 0.00238 mol. Since the treatment was applied three times, approximately 7.14 mmol $NaHCO_3$ was introduced into each soil sample during the measurement series. The HCO_3^- component can act as an acid (pK_2) by donating a proton or as a base (pK_1) by accepting a proton. The dissociation equilibria of the carbonate ion can be expressed in two steps under standard conditions (**Lewis et al., 1999**) at 25°C, as shown below (**Equation 5):**

$$H_2CO_3 \rightleftharpoons H^+ + HCO_3^- \ (\mathrm{pK_1})$$
$$HCO_3 \rightleftharpoons H^+ + CO_3^{2-} \ (\mathrm{pK_2}) \quad (5)$$

The dissociation constants of the carbonate system (i.e. the acid–base equilibrium constants of carbonic acid) express the extent to which carbonic acid (H_2CO_3) dissociates by proton donation into bicarbonate and carbonate ions in aqueous solution. The first and second dissociation constants are as follows (**Equation 6**):

$$pK_1 = -log_{10} K_1 =$$
$$= 6.35 \rightarrow \mathrm{K_1} = 4{,}3\times10^{-7}\ (\mathrm{mol/dm^3})$$

$$pK_2 = -log_{10} K_2 =$$
$$= 10{,}33 \rightarrow \mathrm{K_2} = 4{,}8\times10^{-11}\ (\mathrm{mol/dm^3}) \quad (6)$$

We investigated the relationship between the system's alkalinity and pH. Alkalinity represents the solution's capacity to neutralize acidic conditions, that is, its basic potential, and is composed of the following ions (**Equation 7**):

$$\text{Alkalinity} = [HCO_3^-] + 2[CO_3^{2-}] + [OH^-] - [H^+] \quad (7)$$

which represent the equilibrium (**Equation 8**) concentrations of the carbonates in the system as a function of pH:

$$[HCO_3^-] = \frac{K_1[CO_2]}{[H^+]} \text{ and } [CO_3^{2-}] = \frac{K_1K_2[CO_2]}{[H^+]^2} \quad (8)$$

By solving the above equations, we obtain that $[H^+] = 1.6\times10^{-9}$ M, which corresponds to a solution pH = $-\log_{10}[H^+] = 8.8$, in agreement with the soil-solution pH values measured during the final stage of the experimental series. Finally, we verified by calculation whether the specified initial pH of the applied treatment solution (pH= 8.44) indeed corresponds to the equilibrium pH of the system. The amount of $NaHCO_3$ in a single application was 0.00238 mol, which considering the total added amount, corresponds to a concentration of 0.119 M,

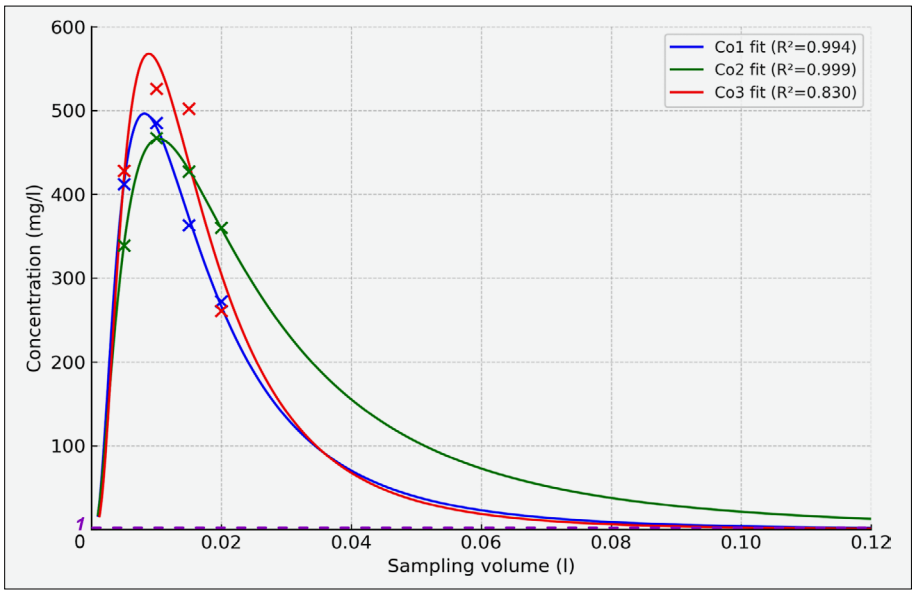


Figure 7. Log-normal fitted function indicating the expected completion of desorption

yielding a calculated pH of 8.34. The discrepancy between the measured and calculated values arises from environmental parameters and the difference of 0.1 is considered as negligible.

During the desorption process, only four samples could be collected, due to column geometry and the resulting colmatation, which prevented further sampling. Based on these data points, we attempted to predict the likely endpoint of desorption by fitting a log-normal function to the desorption curve.

The log-normal distribution is appropriate for modelling the desorption process because it is influenced by multiple factors - binding forces, pore structure, diffusion, pH, ORP - whose combined effect is multiplicative, naturally leading to log-normal behaviour. The binding energy on the soil particle surface is heterogeneous, allowing some contaminant molecules to desorb more readily, while regions with higher binding energy release molecules more slowly. This heterogeneity results in the asymmetric, elongated shape of the desorption curve. Additionally, the desorption rate is not constant; it is initially rapid and gradually slows over time. Consequently, the temporal distribution does not follow a normal distribution but is better described as log-normal.

Thus, the desorption process can be accurately modelled using a log-normal distribution, as illustrated by the predictive curve in **Figure 6**. The log-normal fitting equation (**Equation 9**) was determined according to the method described by **Limpert et al. (2001)**.

The measured cobalt concentration initially increases slowly, followed by a sharp rise corresponding to the desorption peak concentration, and is subsequently followed by a longer declining phase. The temporal variation of the desorption concentration can be described by the following mathematical relationship, as the process involves the gradual release of the total contaminant load:

$$C(v) = \frac{1}{V\,\sigma\sqrt{2\pi}}\,\exp\left(-\frac{(\ln(V)-\mu)^2}{2\sigma^2}\right) \text{ if V>0;} \quad (9)$$

Where:

- $C(v)$ – concentration as a function of volume (mg/dm^3),
- V – sampling volume (dm^3),
- σ – he standard deviation on the logarithmic time scale (indicates the curve's width),
- μ – the logarithmic mean, which defines the location of the peak of the curve on the log-time scale.

For the modelling of the desorption process, the application of a lognormal function fitting was found to provide an excellent approximation. By solving the mathematical formulation, the efficiency of the desorption process, as well as its potential completion, could be predicted. In **Figure 7**, only the concentration values of the Co1–Co2–Co3 columns were considered to which the lognormal fitting was applied. In accordance with the typical behaviour of a desorption curve, an asymmetric pattern was obtained. The measurement points were initiated from a concentration of 0.0 mg/L, followed by a steeply increasing section where the maximum concentration was reached. This was succeeded by the peak phase, during which the desorption rate attained its maximum, and subsequently by a prolonged, gradually declining section, within which the desorbed cobalt precipitated. A purple dashed-line corresponding to 1.0 mg/L was also indicated on the curve, representing a remediation threshold concentration calculated from an assumed risk assessment.

Based on the lognormal prediction, it was observed that in all three modelled cases the fitted curves showed strong agreement with the measured data. The fitted curves were found to closely follow the experimental values, as demonstrated by R^2 values exceeding 0.99 for

the Co1 and Co2 series and greater than 0.83 for the Co3 series. These results are considered to indicate a very good fit, thereby supporting the applicability of the proposed mathematical model.

With respect to the calculated desorbed mass, it was determined that the amount of cobalt desorbed per column averaged 7.33 mg, which corresponded to approximately 12% of the introduced amount within 29 days. According to the predictive fitting, an additional sampling volume of approximately 0.13 L was required for the Co1 curve, and about 0.1 L for the Co2 and Co3 curves, in order to reach the desorption capacity of the system, i.e. the maximum desorbable amount of contaminant. In summary, when related to the adsorbed cobalt quantity across the Co1, Co2, and Co3 curves, the combined effect of the applied additives was capable of desorbing, on average, a maximum of approximately 15%.

5. Conclusions

To enhance desorption, it is essential to shift the established sorption equilibrium toward desorption by altering environmental conditions and applying newly introduced compounds. The ions of the added salts modified the hydration shell of the dissolved cobalt ions and restricted their mobility, thereby strengthening electrostatic interactions and significantly reducing the water solubility of cobalt. By continuously alkalinizing the column system, desorption was promoted under conditions that have not previously been applied in environmental remediation. Furthermore, cobalt compounds exhibit a strong affinity for the hydroxyl groups located on the surfaces of iron and manganese oxides coating soil particles. Under the induced reductive conditions, the dissolution of these oxides releases the cobalt species previously adsorbed or bound to them, thereby enhancing cobalt desorption. Moreover, as the reducing conditions intensify, organic colloids lose part of their surface negative charge, which likewise promotes the desorption of bound cobalt. In this scenario, the desorbed cobalt contaminant was initially released as a complex species (up to pH 7.8), and with further pH increase (>7.8), it precipitated assumably as cobalt hydroxide.

The predictive analysis of the desorption dataset demonstrated that cobalt desorption was enhanced by the applied novel method, suggesting its applicability as an effective supplementary approach in future remediation technologies. Based on the mass balance calculations of the desorbed contaminant, it was determined that nearly 15% of the introduced cobalt could be removed through this procedure. The additives employed were found to be available in industrial quantities, relatively cheap and effective in the examined soil medium. On the basis of these findings, it can be concluded that the combined application of the precipitation method and the alteration or shift of environmental conditions, such as increasing pH and decreasing ORP, may effectively support future remediation technologies in the case of heavy metals.

Acknowledgement

We would like to express our sincere gratitude to Imre Czinkota, PhD retired Associate Professor at the Institute of Environmental Sciences, Hungarian University of Agriculture and Life Sciences, Gödöllő, for his invaluable professional guidance in the field of chemical sciences, without which this manuscript would not have been possible.

We also extend our thanks to Ádám Bosznai, PhD retired Associate Professor and expert in mathematical modelling at MOHU, for his invaluable professional guidance in the mathematical evaluation of the measurement data series.

6. References

Adams, F. (2005). X-ray absorption and diffraction - Overview. Encyclopedia of Analytical Science, 365–377. https://doi.org/10.1016/b0-12-369397-7/00668-3

Anthony S., William D., Hao Z., John H-T. (2010). The Association of Cobalt with Iron and Manganese (Oxyhydr)oxides in Marine Sediment, Aquatic Geochemistry 16(4):575-585, https://DOI.org/10.1007/s10498-010-9092-1

Chivot, L. Mendoza, C. Mansour, T. Pauporté, M. Cassir (2008). New insight in the behaviour of Co–H2O system at 25–150 °C, based on revised Pourbaix diagrams, Corrosion Science, Volume 50, Issue 1, January 2008, Pages 62-69, https://doi.org/10.1016/j.corsci.2007.07.002

Clare A. B., Ronald G., Andrew W., Roger S. (1995). Kinetics of cadmium and cobalt desorption from iron and manganese oxides; Lincoln University (Pennsylvania), Commonwealth Scientific and Industrial Research Organisation; Soil Science Society of America Journal (Soil Science Society of America)

Lewis, E., Feely, R. A., Millero, F. J. (1999). The optimal carbonate dissociation constants for determining surface water pCO2 from alkalinity and total inorganic carbon, M. Chemistry, Volume 65, Issues 3–4, June 1999, Pages 291-30, https://doi.org/10.1016/S0304-4203(99)00021-3

Ersin,Y., Pelin,A., Oktay,C., Haci,D (2016). Recovery of Cobalt from Sulphate Solutions by Precipitation via Persulphate Oxidation, Conference: 15th International Mineral Processing Symposium (IMPS 2016), Istanbul, Turkey

Ertli, T. (2005). Gyomirtószerek szorpciójának tanulmányozása különböző talaj-oldat rendszerekben. Doktori (PhD) értekezés.

Filep Gy., Kovács B., Lakatos J., Madarász T., Szabó I. (2002). Szennyezett területek kármentesítése, Miskolci Egyetem

Choi, J., Hulseapple, S.M, Conklin, M.H, Harvey, J.W (1998). Modeling CO2 degassing and pH in a stream–aquifer system, Volume 209, Issues 1–4, August 1998, Pages

297-310, Journal of Hydrology, https://doi.org/10.1016/S0022-1694(98)00093-6

Jing Y., Hongwei L., Wayde M., Ray L. F. (2009). Synthesis and Characterization of Cobalt Hydroxide, Cobalt Oxyhydroxide, and Cobalt Oxide Nanodiscs, The Journal of Physical Chemistry.

Kamal R., Célia L., Frédéric G., Myriam D., Chantal G., Jean-Marie H. (2014). Degradation of a cobalt(II)–EDTA complex by photocatalysis and H2O2/UV-C. Application to nuclear wastes containing 60Co, Journal of Radioanalytical and Nuclear Chemistry 303(1):131-137, https://doi.org/10.1007/s10967-014-3311-y

Limpert, E., Stahel, W. A., & Abbt, M. (2001). Log-normal Distributions across the Sciences: Keys and Clues. BioScience, 51(5), 341–352.

Lopez, A., Gustavsson, H., Korkiala-Tanttu, L. (2021). Comparison between hydrometer and laser diffraction methods in the determination of clay content in fine-grained soils, IOP Conf. Series: Earth and Environmental Science 710 (2021) 012012, p.3., https://doi.org/10.1088/1755-1315/710/1/012012

Nicholas C. U. (2013). Cobalt and Manganese, In book., Heavy Metals in Soils (pp.335-366)

Ruo-Chen, X., C. Batchelor-McAuley, E. Rauwel, P. Rauwel, Richard G. (2020). Electrochemical Characterisation of Co@Co(OH)2 Core-Shell Nanoparticles and their Aggregation in Solution, ChemElectroChem. https://doi/10.1002/celc.202001199

Schaetzl, R. J., Thompson, M. L. (2015). "Soils: Genesis and Geomorphology." Cambridge University Press.

Szász N., Tóth A (2025). "Analysis of Atterberg limits of clayey soils exposed to pollutants" Rudarsko-geološko-naftni zbornik, (The Mining-Geology-Petroleum Engineering Bulletin), UDC: 624, https://doi.org/10.17794/rgn.2025.1.8

Zhou, X., Liu, D., Bu, H., Deng, L., Liu, H., Yuan, P., Song, H. (2018). XRD-based quantitative analysis of clay minerals using reference intensity ratios, mineral intensity factors, Rietveld, and full pattern summation methods: A critical review. Solid Earth Sciences, 3(1), 16–29. https://doi: 10.1016/j.sesci.2017.12.002

Yan W., Ren X., Jiu L. (2011): Effect of Fe/Al oxides on desorption of Cd2+ from soils and minerals as related to diffuse layer overlapping Available to Purchase, Research Article, Soil Res (2011) 49 (3): 231–237., https://doi.org/10.1071/SR10148

Yang, J.,Cheng, Hongfei,Frost, Ray L. (2011) Synthesis and characterisation of cobalt hydroxy carbonate $Co_2CO_3(OH)_2$ Nanomaterials. Spectrochimica Acta Part A: Molecular and Biomolecular Spectroscopy, 78(1), pp. 420-428.

Yanglong H., Hiroshi K., Masatsugu S., Toshihiro K., Toshiaki O. (2005). High-Yield Preparation of Uniform Cobalt Hydroxide and Oxide Nanoplatelets and Their Characterization, The Journal of Physical Chemistry B, Vol 109.

URL 1. https://www.ncbi.nlm.nih.gov/books/NBK587403/

URL 2. https://www.chemos.de/import/data/msds/GB_en/144-55-8-A0015267-GB-en.pdf

SAŽETAK

Poboljšana desorpcija kobalta iz onečišćenih pjeskovitih muljevito-glinovitih tala

U ovoj studiji istražena je mogućnost poboljšanja desorpcije kobaltnoga onečišćenja u pjeskovitome, muljevito-glinovitom tlu onečišćenom kobalt(II)-klorid-heksahidratom. U tlima koja sadržavaju frakcije praha i gline učinkovitu sanaciju ponajprije otežavaju jaki procesi površinskoga vezanja i adsorpcije. Prevladavanje tih ograničenja zahtijeva uspostavljanje povoljnih uvjeta za desorpciju. Za razliku od uobičajenih industrijskih praksi, potencijal za desorpciju istražen je pod postupno alkalizirajućim i redukcijskim uvjetima. Na temelju dobivenih rezultata, smanjenje ORP-a zasićenog sustava zajedno s porastom pH potaknulo je desorpciju kobalta. Posljedično, unutar raspona iznad redoks potencijala od 0 mV do –80 mV i iznad pH 7,8, u početku se formirao kobaltov kompleks $[Co(H_2O)_6]^{2+}$. Daljnja alkalizacija i smanjenje redoks potencijala doveli su do taloženja preostale onečišćujuće tvari kao $Co(OH)_2$ kobaltova hidroksida. Kao rezultat tretmana prosječno 7,33 mg kobalta desorbirano je s površine muljevite gline unutar 29 dana od početka tretmana desorpcije, što odgovara oko 12 % onečišćujuće tvari prisutne u sustavu. Nadalje, na temelju dobivenih podataka o koncentraciji prilagođen je niz prediktivnih funkcija temeljen na lognormalnoj raspodjeli (prosječni R^2 = 0,941). Rezultati pokazuju da je primijenjeni postupak sposoban desorbirati približno 15 % kobaltnoga onečišćenja, što vjerojatno upućuje na desorpcijski kapacitet sustava. Primijenjena metoda široko je dostupna, isplativa i ekološki prihvatljiva, što su kvalitete ključne za industrijsku primjenu. Predloženi pristup predstavlja učinkovitu i djelotvornu komplementarnu tehniku za buduću sanaciju određenih spojeva teških metala.

Ključne riječi:
remedijacija, adsorpcija, desorpcija, pjeskovita muljevito-glinovita tla, kobalt

Author's contribution

Tamás Bacsó (PhD student) provided the raw materials preparation, performed the laboratory work and the presentation of the results. **Márton Tóth** (Associate professor) provided the evaluation of the experimental results and the presentation of the results.
All authors have read and agreed to the published version of the manuscript.

RGNZ/MGPB

Geochemistry and genesis of the manganese ores in the Nawagai ophiolitic melange, Mohmand District, Khyber Pakhtunkhwa, Pakistan

Rudarsko-geološko-naftni zbornik
(The Mining-Geology-Petroleum Engineering Bulletin)
DOI: 10.17794/rgn.2026.3.9

Original scientific paper

Irfan Ullah[1], Aamir Khan[2,3,1*], Mohammad Tahir Shah[1], Liaqat Ali[1*], Asad Khan[4,5], Muhammad Mustafa[6]

[1] *National Center of Excellence in Geology, University of Peshawar, Peshawar 25130, Pakistan.*
[2] *State Key Laboratory for Critical Mineral Research and Exploration, Institute of Geochemistry, Chinese Academy of Sciences, Guiyang 550081, China.*
[3] *University of Chinese Academy of Sciences, Beijing, 100049, China.*
[4] *Department of Earth Sciences, FATA University, FR Kohat 26100, Pakistan.*
[5] *State Key Laboratory of Critical Mineral Research and Exploration, School of Geosciences and Info-Physics, Central South University, Changsha 410083, China.*
[6] *College of Geosciences, China University of Petroleum (Beijing), Beijing 102249, China.*

Abstract

The Nawagai ophiolitic melange is present in the western part of the Main Mantle Thrust /Indus Suture Zone (MMT/ISZ) in northern Pakistan and is considered as a part of the fold belt that contains ophiolitic sequences. The studied manganese ore bodies are present in the Nawagai ophiolitic melange in the Mohmand District of Khyber Pakhtunkhwa, Pakistan. These ores are dislocated lenticular bodies of various size and are generally associated with the cryptocrystalline meta-chert. Both Mn-ores and the host meta-cherts are highly tectonized and are, therefore, subjected to metamorphism/deformation. Mineralogically, the studied Mn-ores are dominantly composed of braunite with a lesser amount of pyrolusite and piemontite as Mn-bearing phases while the gangue minerals are mainly cryptocrystalline quartz with a lesser amount of calcite. The Mn-phases are interlocked within the cryptocrystalline quartz; however, the cross cutting micro-veins of quartz and calcite are also noticed. At places the pyrolusite and piemontite are replacing braunite. Geochemically, the studied Mn-ores are highly variable in their grade. These are generally high-grade to low-grade but as a whole, from an economic perspective, these ores can be considered as low-grade ores on the basis of MnO, Fe_2O_3 and SiO_2 contents. No correlation among the major elements has been found, however, significant positive correlation between SiO_2 and MnO has been noted. The fractionation behaviour of Mn and Fe and the concentration of various major and trace elements suggest that the studied Mohmand area Mn-ores have been formed from the hydrothermal fluid distal to the source (vent) with the input from the pelagic sediments along the mid-ocean ridges within the Neo-Tethys Ocean. These have been obducted, as exotic bodies within ophiolitic sequences, on the Indian Plate due to the subduction of Indian Plate underneath the Kohistan Island Arc along the MMT/ISZ. These Mn-ores and the meta-cherts have attained severe metamorphism and deformation during and after the emplacement of the ophiolitic bodies in the existing position.

Keywords:
manganese, petrography, mineralogy, geochemistry, ore genesis

1. Introduction

Manganese is a key element of the ferroalloy metals which is mainly used in steel making, and other metallurgical, battery and chemical industries. It is mostly used in the form of ferromanganese (FeMn) and silicomanganese (SiMn) and various compounds such as $MnSO_4$, $MnCl_2$, KMn, etc. in various industries. In the steel industry, it is used for the removal of oxygen and sulfur, which imparts hardness, malleability, and tenacity to steel. Steel made of ferromanganese and silicomanganese is used in construction and transportation machinery (**Siddiquie et al. 2015; Rehman et al. 2020**). The chemical grade of Mn is used in the production of chemicals, batteries, glass, plant food, paints, and pigments, as well as in the textile industry. It is also used as a water purifier, catalyst and as a carrier of oxygen for chemical looping combustion (CLC) (**Mehdilo and Irannajad 2014; Haider et al. 2016**). Globally, most of the Mn (90-95%) produced annually (with Mn content greater than 40 %) is used in the steel industry as a deoxidizer and desulfurizer. The remaining (5-10%) is

* Corresponding author: Aamir Khan
e-mail address: aamir-khan@mail.gyig.ac.cn
Received: 14 August 2025. Accepted: 2 December 2025.
Available online: 14 May 2026

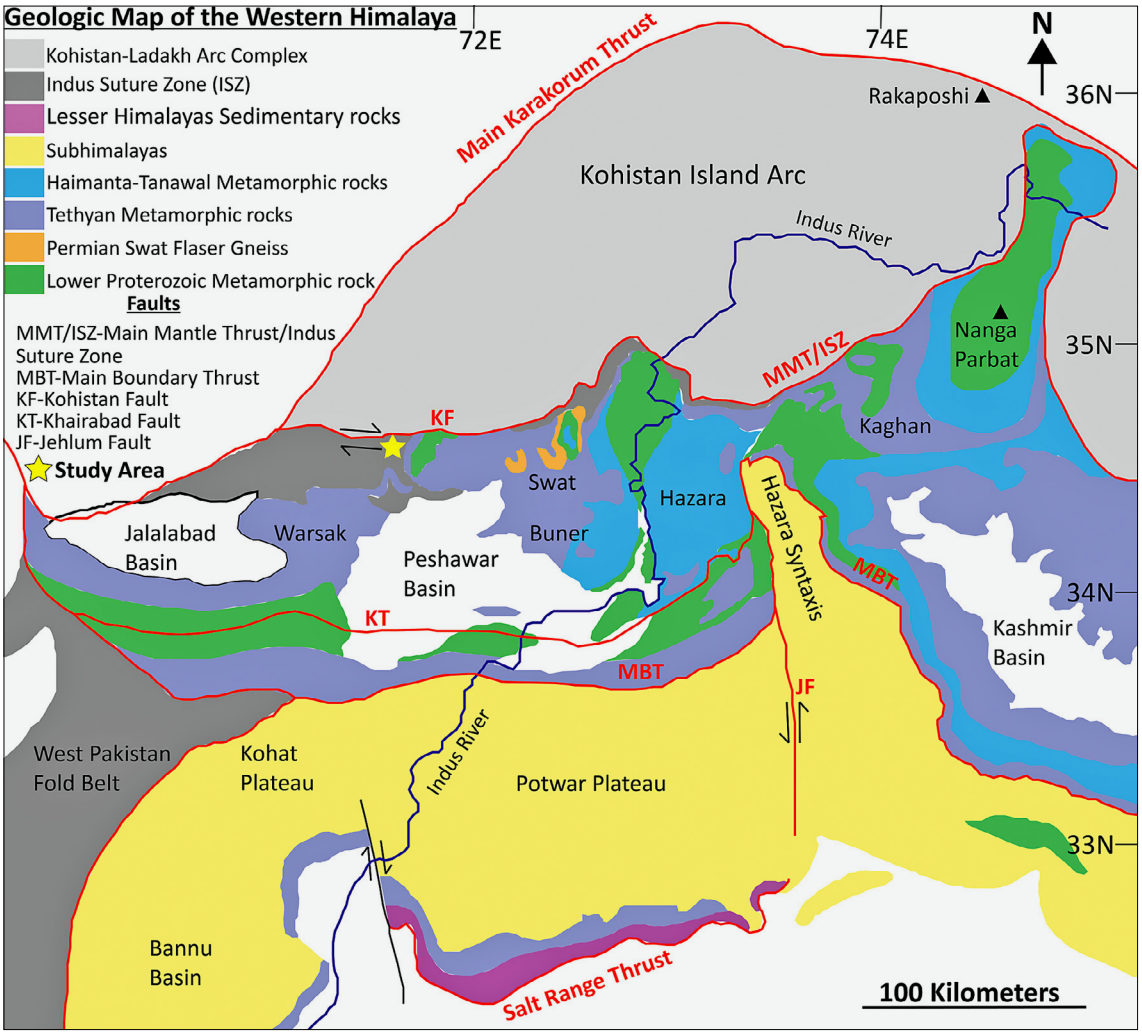


Figure 1. Geotectonic map of northern Pakistan showing the location of the study area (after **DiPietro and Pogue 2004**)

consumed by other sectors, such as the chemical, paint, fertilizer, batteries and glass industries (**Lasheen et al. 2009**).

World over, Mn-deposits have been formed in various tectonic settings which include continental sedimentary sequences, as well as ophiolites. These deposits can be divided into three broad categories (1) hydrothermal (2) hydrogenous and (3) digenetic/biogenetic-bacterial deposits (**Polgári et al. 2012; Öksüz 2011**). Hydrothermal deposits form through direct precipitation from hydrothermal solutions at low temperatures (**Hein et al. 1997; Ingram et al. 1990**). These deposits are typically strata bound and laminated or can exist as irregular bodies and epithermal veins. They are discovered in both present-day and past marine environments, located near spreading centers or intraplate seamounts, as well as in island arc settings associated with subduction (**Polgári et al. 2012; Baba et al. 2003; Öksüz and Okuyucu 2014**). Hydrogenous deposits are composed of ferromanganese crusts, which are rich in amorphous iron compounds and usually depleted in Mn minerals. It slowly precipitates from seawater from microbial activity at rates of 2 to 10 mm per Ma on the seafloor (**Öksüz 2011; Jach and Dudek 2005; Toth 1980**). Hydrogenous deposits are characterized by high trace element concentrations, particularly Ni and Cu and a low Mn/Fe ratio (~1) (**Hein et al. 1997, 1996; Usui and Someya 1997; Usui and Nishimura 1992; Ingram et al. 1990; Toth 1980**). Diagenetic/biogenetic-bacterial manganese deposits are formed in nodules and precipitate with the effect of hydrothermal solutions in the form of Mn-carbonate mineralization due to oxidation of organic matter (**Polgári 1991; Polgári et al. 2012; Öksüz 2011**). Although the hydrothermal and diagenetic deposits are characterized by high Mn/Fe ratios and low trace metal contents (**Hein et al. 1996, 2013**) but these can be distinguished on the basis of their morphology, tectonic setting and growth rates (**Kuhn et al. 1998**; **Choukrad et al. 2022**).

In Pakistan, low to medium-grade Mn-deposits, associated with a continental sedimentary sequence, are reported in Chura Gali, Galdanian and Kakul from the Hazara region of Khyber Pakhtunkhwa Province, (**Shah and Moon 2004, 2007**). Similarly, Mn deposits that are associated with ophiolitic rocks are reported from North

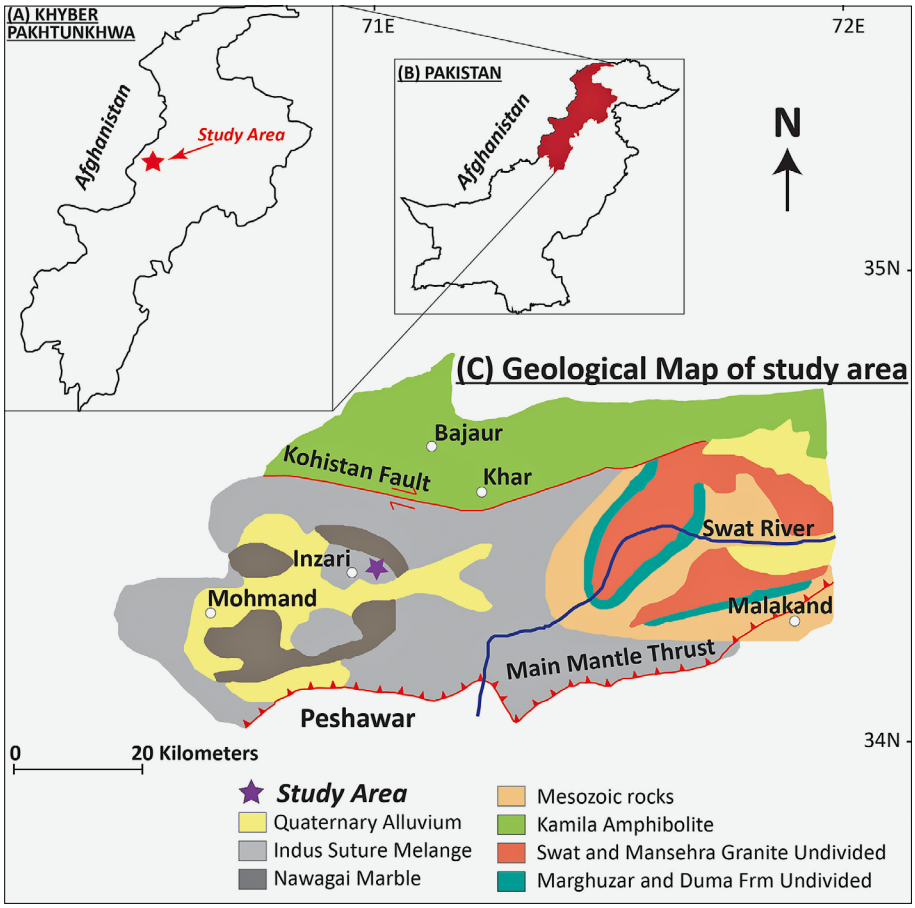


Figure 2. Geological map of the Mohmand District taken and modified from **Aslam et al. (2006)**, showing the location of the study area.

Waziristan (**Shah and Khan 1999; Shah and Moon 2007**), Lasbela-Khuzdar, Zhob (**Naseem et al. 1997; Khan et al. 2020**) and the Bela area (**Narijo et al. 2019**).

2. Regional Geology

Northern Pakistan has two major regional-scale tectonic faults, namely the Main Mantle Thrust (MMT) / Indus Suture Zone (ISZ) in the south and the Main Karakorum Thrust (MKT) in the north (see **Figure 1**). These two thrust faults have geologically divided northern Pakistan into three separate tectonic domains from north to south, i.e. Karakoram block (KB), the Kohistan Island Arc (KIA) and the Indian Plate (IP) (see **Figure 1**) (**Tahirkheli 1979; Bard 1983; Treloar 1989; Khan et al. 1993; Burg 1996; Kazmi and Jan 1997; Searle et al. 1999**). The MMT/ISZ defines the tectonic boundary between the KIA and the IP in the south. During the Paleogene, it developed as a result of the closing of the Neo-Tethys Ocean and eventual collision of the northern Indian Plate edge with the Kohistan and Ladakh Arc (**Molnar and Tapponnier 1975; Tahirkheli 1979; Klootwijk et al. 1992**). The MMT/ISZ is not a single fault but a sequence of faults with varying ages and tectonic histories (**Searle et al. 1999; DiPietro et al. 2000**). A thick zone of sheared ophiolitic melanges appears along the MMT/ISZ (see **Figure 1**). From east to west along the MMT/ISZ, these are the Mingora, Charbagh and Shangla ophiolitic melange zone, Malakand and Dargai ophiolitic melanges and the Nawagai ophiolitic melange (**Kazmi et al. 1984; DiPietro et al. 1991; 2008**). These ophilitic melanges are characterized by a variety of highly deformed ophiolitic rocks that have undergone varying degrees of metamorphism (**Kazmi and Jan 1997; Ahmad and Jehan 2006**). Serpentinite, dunite, lherzolite, gabbro, basalt, and sedimentary rocks like limestone and chert (pelagic sediments) are the predominant rocks of these melange zones. These rocks have undergone varying degrees of mixing and metamorphism as a result of the numerous tectonic processes that occurred during the development of the suture zone (**Robertson 2000**). These melanges also contain a range of valuable metallic and non-metallic mineralization including chromite, manganese, platinum group elements (PGEs), nickel, emerald and nephrite, etc. (**Ahmad and Jehan 2006**).

2.1. Geology of Study Area

The study area lies in the Toposheet No. 38N/06 of the Geologic Survey of Pakistan. It is located in the vicinity of Inzari Village in the Mohmand District which is easily accessible from Peshawar, the capital city and a district of Khyber Pakhtunkhwa (KP) Province (see **Figure 2**). The Mohmand District shares its borders with the Bajaur District in the north, the Khyber District in the

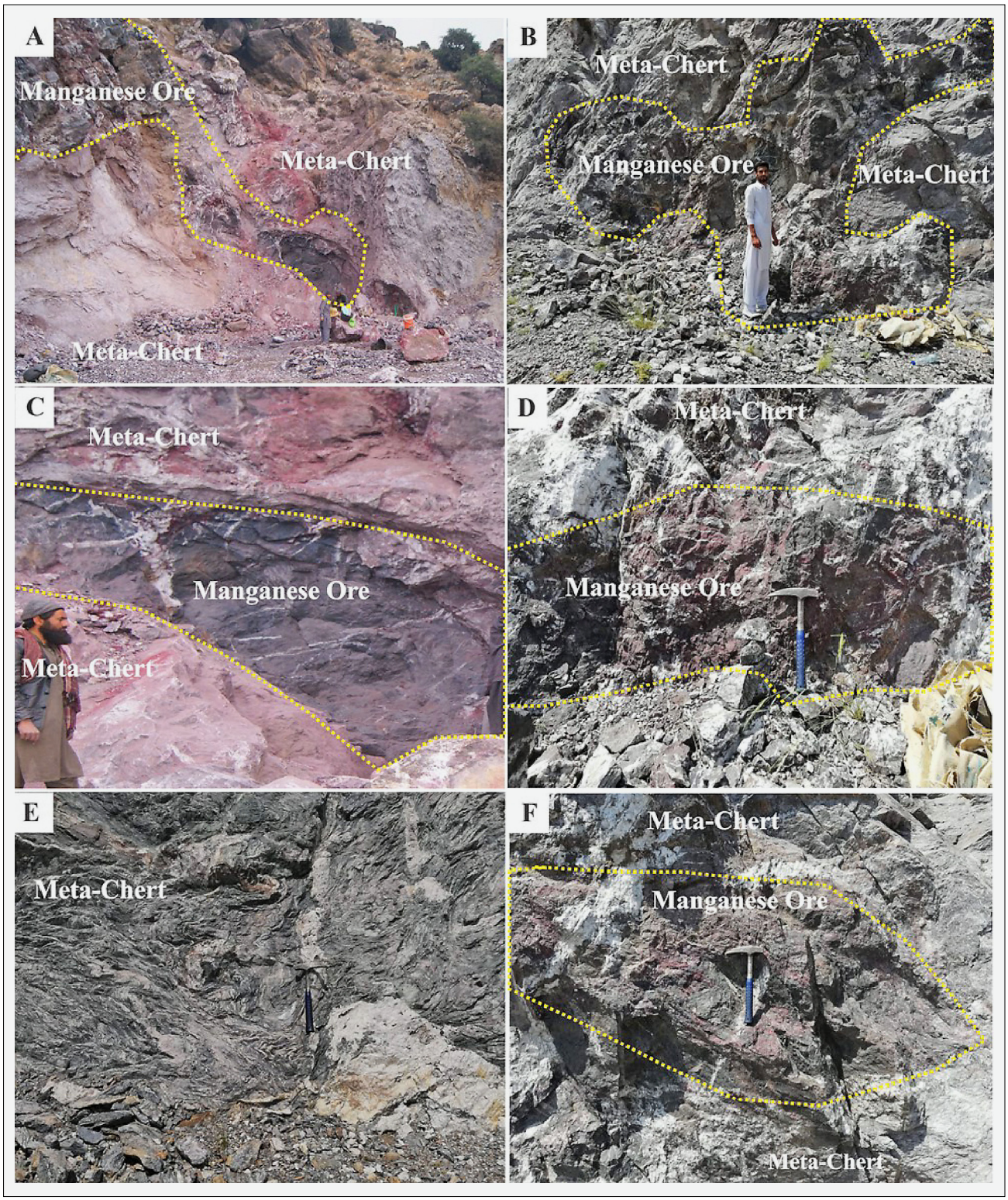


Figure 3. Field photographs of manganese ores: (A & B) tectonized bodies of manganese enclosed in the host rock (meta-chert), (C) Manganese ores are cross-cut by quartz and calcite veins, (D) Hand specimen showing pull apart texture where fractures are filled with quartz and carbonates, (E) Intense shearing and foliation in shear zones, (F) Lensed shaped manganese ore enveloped by host rock.

south, Malakand and Charsadda districts in the east and the Peshawar District in the southeast. Geologically, the study area is located in the Nawagai ophiolitic melange (**DiPietro et al. 1991; 2008**), which is a part of the Indus suture melange and is lying in the western most part of the MMT/ISZ (**DiPietro and Pogue 2004**). The dominant lithologies of the Nawagai ophiolitic melange are marble, dunite, serpentinite, greenstone, grey to black

and green phyllites while talc-carbonate schist occurs as a subordinate lithology (**Aslam et al. 2006**). Cryptocrystalline meta-chert showing grey to reddish-brown colouration, along with clay minerals and at places marble is hosting the Mn mineralization in the Mohmand area (see **Figure 3**). The manganese ores are identified by their black colour and silvery luster in the field. These ore bodies are scattered in the form of irregular massive lenticular bodies with varying dimensions (see **Figure 3**). At places, the ores and host rocks (meta-cherts) contain cross-cutting fractures filled veins of quartz and carbonates. These ores and their host rocks are fragmented, folded, faulted and sheared suggesting that the metamorphism/deformation has occurred after the formation of these ores.

3. Methods

Detailed field work was carried out in the study area to collect representative samples from the Mn-ores and the host rocks, and also to identify the various field features, as shown in **Figure 3**. During fieldwork, 15 fresh looking samples of Mn-ores and 7 samples of host rocks (meta-chert) were collected for the experimental work in the Geochemistry Laboratory of the National Centre of Excellence in Geology (NCEG), University of Peshawar, Pakistan. These samples were crushed and pulverized to -200 mesh size, using a tungsten carbide cup mill (FRITSCH PULVERISETTE 9). The open-acid digestion technique after **Jeffery and Hutchison (1986)** using PTFE Teflon beakers was adopted whereby known weights of Mn-ores powdered samples were treated with HCL (10ml) and HF (5ml) for the complete digestion and known weights of host rock powdered samples were treated with HF: HNO3:HClO4 in the ratio of 7:3:1 for their complete digestion**.** The digested sample solutions of both ores and host rocks were analyzed for major oxides (i.e. MnO, Fe_2O_3, CaO, MgO, Na_2O and K_2O) and trace elements (i.e. Co, Cr, Cu, Cd, Pb, Ag and Ni) using Atomic Absorption Spectrometer (AAS) (**Perkin Elmer 7000**, equipped with graphite furnace) under the standard calibrated conditions. The analysis of SiO_2, TiO_2, P_2O_5, and Al_2O_3 was carried out using a Pye Unicam UV/visible spectrophotometer as described by **Jeffery and Hutchison (1986)**. The loss on ignition (LOI) was determined gravimetrically by heating the known weight of powdered samples of both ores and host rocks in a muffle furnace at 1200°C for four hours.

Petrographically, the Mn-ores and host rock samples were studied using polished thin sections under polarized and reflected light microscopy. For the identification of different Mn-bearing phases and gangue minerals X-ray diffraction (XRD: JEOL-JDX-3532) and scanning electron microscopic (SEM: JEOL-JSM-IT-100) techniques were carried out at the Centralized Resource Laboratory (CRL), and NCEG, University of Peshawar, respectively.

4. Results and Discussion

4.1. Petrography and Mineralogy

The XRD analysis of selected samples of the manganese ores revealed that two types of Mn-ore minerals, such as Mn silicate-oxide (braunite) and Mn-oxide (pyrolusite), are present in these ores along with quartz, calcite and hematite as accessory minerals (see **Figure 4**). Braunite, being the principal Mn-bearing phase, is in various shapes which range from microcrystalline to subhedral to euhedral coarse-grained. Microcrystalline braunite is intermixed with cryptocrystalline quartz, while the coarse-grained are interlocked having planar to sutured contacts, and the ore minerals are cross-cut by the quartz and calcite veinlets (see **Figure 5a**). Anhedral to subhedral, spindle and fibrous shaped pyrolusite grains are present in association with braunite and cryptocrystalline quartz (see **Figure 5b**). Pyrolusite also occurs as fractures filled phase (see **Figure 5a** and **e**). Cryptocrystalline quartz, a major accessory mineral, is generally enclosing the braunite, pyrolusite and piemontite (see **Figure 5b, f** and **d**). Piemontite and pyrolusite are replacing braunite at places (see **Figure 5e** and **g**). Fine-grained hematite is found in dissemination (see **Figure 5h**). In general, the coarse-grained quartz is found in the form of veins while the cryptocrystalline quartz is either enclosing or enclosed in the braunite (see **Figure 5h** and **i**). The petrographic features suggest that there could be two stages of formation of ore phases within the studied Mn-ores. The early stage is represented by massive braunite and minor pyrolusite minerals, while the late stage is characterized by replacement phases such as pyrolusite, piemontite and hematite. Braunite may have been altered to pyrolusite and hematite through chemical weathering and leaching due to silica removal and re-oxidation of Mn in low-grade surface environments (**Shaif et al. 2020; Safarov et al. 2024**) while the piemontite may have been formed by the alteration of braunite during medium to high-grade metamorphism (**Sinisi et al. 2018; Marescotti and Frezzotti 2000**).

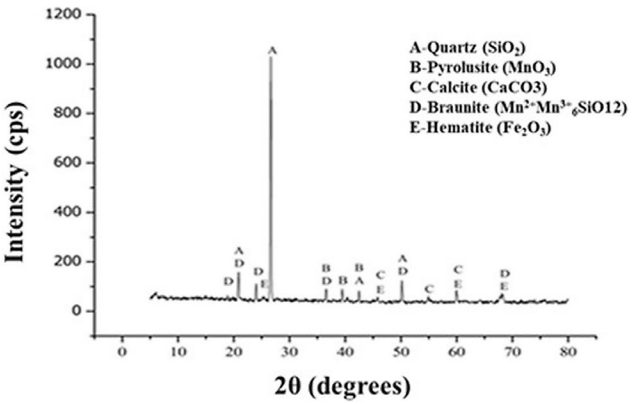


Figure 4. XRD graph showing the 2θ position of braunite, pyrolusite, hematite, quartz and calcite in the Mn-ores of the study area.

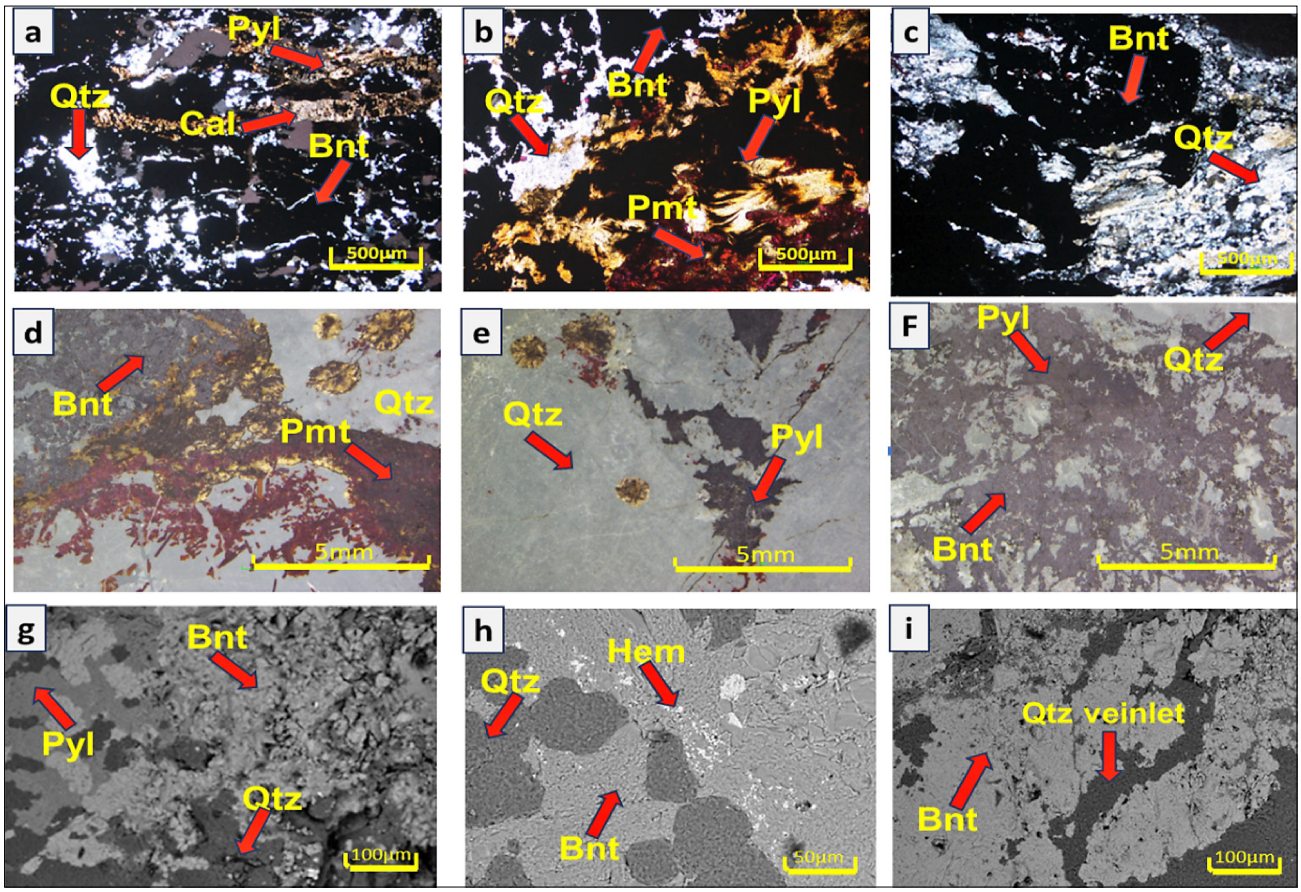


Figure 5. Photomicrographs (plane polarized: a-c; reflected light: d-f and SEM images: g-i) showing (a) veinlets of quartz and calcite cross-cutting the braunite grains while pyrolusite is present as fracture filled phase, (b) coarse-grained pyrolusite and piemontite are replacing braunite while spindle and fibrous shape pyrolusite is also visible (c) coarse-grained braunite is enclosed in cryptocrystalline quartz, (d) piemontite and braunite are enclosed in cryptocrystalline quartz, (e) pyrolusite occurs as fractured filled phase within cryptocrystalline quartz, (f) intermixing of braunite, pyrolusite and cryptocrystalline quartz, (g) pyrolusite is replacing braunite while quartz is also enclosed in braunite, (h) fine-grained hematite and quartz grains are present within braunite, (i) cryptocrystalline quartz veinlets are cross-cutting the Mn-minerals.
Abbreviation: Bnt: braunite; Pyl: Pyrolusite; Qtz: Quartz; Hem: Hematite; Pmt: Piemontite; Cal: Calcite.

The meta-cherts, generally hosting the Mn-ores, are mainly composed of microcrystalline to cryptocrystalline quartz / chalcedony and a lesser amount of hematite. The pseudomorphs of radiolarian chert, occasionally replaced by microcrystalline quartz, hematite, carbonates and clay minerals, are also noticed.

4.2. Geochemistry

The representative samples of the studied Mn-ores and host rocks (i.e. meta-chert) have been analyzed for major and trace elements and the results are presented in the **Tables 1** and **2**, respectively. According to the classification of **Dorokhin et al. (1969)**, the studied Mn-ores, as of having 19.08 wt% to 45.21 wt% MnO, can be considered as low-grade (<35 wt% MnO), medium-grade (35-40 wt% MnO) and high grade (>40 wt% MnO) manganese ores. Economically, the studied Mn-ores, having 31.93 wt% MnO on average, can be termed as low-grade ores as a whole (see **Table 1**). The Mn-ores of the study area have SiO_2 contents ranging from 30.14 to 62.23 wt% (average: 48.41 wt%), TiO_2 from 0.03 to 0.46 wt% (average: 0.15 wt%), Al_2O_3 from 1.86 to 3.87 wt% (average: 2.68 wt%), Fe_2O_3 from 1.42 to 5.30 wt% (average: 3.26 wt%), MnO from 19.08 to 45.21 wt% (average: 31.93 wt%), MgO from 0.11 to 2.13 wt% (average: 0.91 wt%), CaO from 3.95 to 7.96 wt% (average: 5.85 wt%), Na_2O from 0.93 to 1.60 wt% (average: 1.22 wt%), K_2O from 0.02 to 1.30 wt% (average: 0.73 wt%) and P_2O_5 from 0.02 to 0.21 wt% (average: 0.08 wt%). Among the trace elements, Co is in the range of 2-48 ppm (average: 12 ppm), Cr: 1-56 ppm (average: 19 ppm), Cu: 8-402 ppm (average: 190), Cd: 1-5 ppm (average: 3 ppm), Pb: 10-131 ppm (average: 39 ppm), Ag: 1-17 ppm (average: 9 ppm) and Ni: 1-150 ppm (average: 65 ppm). All the trace elements are highly variable in the studied Mn-ores. The Mn/Fe and Fe/Mn ratios are also having greater variation and are ranging from 7.67 to 19.39 and 0.05 to 0.13 with the average values of 10.85 and 0.09, respectively. The major oxides have been correlated with the MnO in **Figure 6**. It has been found that all the major oxides, except SiO_2, exhibit no any correla-

Table 1. Geochemical analysis (major oxides in wt % and trace elements in ppm) in the Mn-ores of the Mohmand area.

Sample	IMS-1	IMS-2	IMS-3	IMS-4	IMS-5	IMS-6	IMS-7	IMS-8	IMS-9	IMS-10	IMS-11	IMS-12	IMS-13	IMS-14	IMS-15	MIN	MAX	AVG
SiO_2	48.61	42.53	38.21	41.45	30.14	36.15	38.25	57.21	62.23	55.61	52.45	56.01	55.28	54.02	57.96	30.14	62.23	48.41
TiO_2	0.03	0.08	0.24	0.03	0.11	0.16	0.08	0.34	0.09	0.20	0.05	0.09	0.06	0.46	0.23	0.03	0.46	0.15
Al_2O_3	2.65	2.22	2.06	2.14	3.02	1.86	3.87	2.18	3.06	3.23	2.98	3.23	3.23	2.55	1.99	1.86	3.87	2.68
Fe_2O_3	3.18	3.64	4.74	2.56	5.30	4.91	3.65	2.11	2.35	2.38	3.08	1.42	3.23	3.20	3.15	1.42	5.30	3.26
MnO	35.80	38.01	44.37	39.75	45.21	43.54	40.37	28.22	19.08	26.05	23.69	24.86	22.36	24.92	22.65	19.08	45.21	31.93
MgO	1.23	2.13	0.95	0.96	1.65	0.64	1.58	0.67	0.23	0.19	1.77	0.97	0.24	0.11	0.34	0.11	2.13	0.91
CaO	3.95	6.23	4.56	5.56	7.01	5.63	6.56	4.56	4.97	5.03	7.96	5.15	7.35	6.93	6.32	3.95	7.96	5.85
Na2O	0.93	1.00	1.16	1.38	1.07	1.60	1.09	1.60	1.31	1.11	1.17	1.30	1.24	1.10	1.23	0.93	1.60	1.22
K2O	0.80	1.10	0.71	0.06	0.24	1.10	1.30	0.02	1.23	0.03	1.14	0.98	0.88	0.44	0.85	0.02	1.30	0.73
P_2O_5	0.02	0.04	0.15	0.12	0.05	0.11	0.03	0.11	0.21	0.09	0.05	0.06	0.02	0.10	0.07	0.02	0.21	0.08
L.O.I	2.54	3.05	2.75	5.98	6.20	4.23	3.25	3.15	5.23	6.12	5.41	5.93	6.04	6.36	4.98	2.54	6.36	4.75
Total	99.73	100.10	99.89	99.87	100.20	99.93	100.00	100.10	99.99	99.98	99.75	100.01	99.92	100.19	99.78			99.96
Trace Elements																		
Co	10	48	28	25	22	10	4	2	3	2	2	3	3	7	5	2	48	12
Cr	17	56	33	23	25	9	17	4	1	7	5	12	7	14	52	1	56	19
Cu	210	229	402	74	325	345	185	97	8	168	209	189	153	129	122	8	402	190
Cd	3	2	5	1	3	2	2	3	3	3	2	2	4	3	2	1	5	3
Pb	19	131	95	20	75	21	28	19	34	10	21	38	26	23	31	10	131	39
Ag	1	4	1	4	11	8	12	12	12	11	17	10	12	12	9	1	17	9
Ni	26	35	123	98	125	98	52	1	18	34	19	50	19	150	131	1	150	65
Zn	30	25	20	50	10	121	60	14	18	40	35	42	29	65	35	10	121	39.6
Mn/Fe	12.47	11.56	10.37	17.19	9.45	9.82	12.25	14.81	8.99	12.12	8.52	19.39	7.67	8.62	7.96	7.67	19.39	10.84
Fe/Mn	0.08	0.09	0.10	0.06	0.11	0.10	0.08	0.07	0.11	0.08	0.12	0.05	0.13	0.12	0.13	0.05	0.13	0.09

MIN: Minimum; MAX: Maximum; AVG: Aver

Table 2. Geochemical analysis (major oxides in wt % and trace elements in ppm) of the host rocks (meta-cherts) of the Mohmand area.

Sample	HRS-1	HRS-2	HRS-3	HRS-4	HRS-5	HRS-6	HRS-7	MIN	MAX	AVG
SiO_2	80.13	81.25	81.11	79.56	82.65	78.23	79.56	78.23	82.65	80.36
TiO_2	0.03	0.15	0.041	0.056	0.011	0.21	0.096	0.01	0.21	0.08
Al_2O_3	4.52	6.25	4.69	7.54	4.95	8.41	5.11	4.52	8.41	5.92
Fe_2O_3	4.5	1.35	3.56	4.02	2.97	1.86	2.14	1.35	4.50	2.91
MnO	0.45	0.38	0.24	0.453	0.63	0.432	0.34	0.24	0.63	0.42
MgO	2.12	1.26	0.15	0.1	1.08	1.54	3.25	0.10	3.25	1.36
CaO	3.13	2.46	3.18	2.77	2.84	3.24	4.17	2.46	4.17	3.11
Na_2O	1.06	1.63	0.84	0.96	0.35	1.05	1.08	0.35	1.63	1.00
K_2O	0.76	0.98	0.85	0.65	0.92	1.63	1.14	0.65	1.63	0.99
P_2O_5	0.042	0.13	0.011	0.025	0.41	0.31	0.035	0.01	0.41	0.14
L.O.I	3.68	4.05	4.25	3.35	2.65	3.12	3.68	2.65	4.25	3.54
Total	100.42	99.88	98.92	99.48	99.46	100.03	100.60	98.92	100.60	99.83
Trace elements										
Co	7	8	7	11	5	12	8	5	12	8
Cr	8	6	3	114	13	8	11	3	114	23
Cu	26	103	49	53	5	44	71	5	103	50
Cd	3	4	3	4	3	3	2	2	4	3
Pb	17	15	10	7	16	12	9	7	17	12
Ag	7	7	4	6	1	6	7	1	7	5
Ni	17	70	9	28	10	52	49	9	70	33
Zn	56	60	49	66	80	41	47	41	80	57

tion with MnO. However, SiO_2 has well-defined positive correlation with MnO (see **Figure 6a**). This can be attributed to the formation of higher amount of braunite in the studied Mn-ores.

The studied meta-cherts are mainly composed of SiO_2 in the range of 78.23 to 82.65 wt%, Al_2O_3: 4.52 to 8.41 wt%, Fe_2O_3: 1.35 to 4.50 wt%, MgO: 0.10 to 3.25 wt% and CaO: 2.64 to 4.17 wt% while rest of the major oxides are in very low concentrations (see **Table 2**). The average concentration of trace elements such as Co, Cr, Cd, Pb, Ag and Ni in the studied mata-cherts are 8 ppm, 23 ppm, 50 ppm, 3 ppm, 12 ppm, 5 ppm and 33 ppm, respectively.

It is now well established that the geochemical characteristics of various types of manganese deposits have played a major role in characterizing the ancient analogues of hydrothermal and hydrogenous manganese deposits that are formed on the modern ocean floor (**Crerar et al. 1982**). During the precipitation of hydrothermal solution along the mid ocean ridges, the fractionation of Mn and Fe is resulted in the low and high Mn/Fe or Fe/Mn ratios in exhalative sediments (**Bonatti 1972; Bonatti et al. 1972, 1976; Shah and Khan 1999; Shah and Moon 2007; Khan et al. 2020**). The ratios of Mn/Fe are ranging from 7.67 to 19.39 and Fe/Mn from 0.05 to 0.13 in the studied Mn-ores. These ratios are consistent with that of the hydrothermal exhalative Mn-deposits formed in ophiolitic sequences and along the mid-ocean ridges (**Bonatti et al. 1972, 1976; Jach and Dudek 2005; Shah and Moon 2007; Jiancheng et al. 2013; Sasmaz et al. 2014**). Various researchers have used major and trace elements to distinguish manganese ores of hydrothermal and hydrogenous origin (**i.e. Bonatti et al. 1972; Toth 1980; Crerar et al. 1982; Adachi et al. 1986; Peters 1988; Choi and Hariya 1992; Nicholson 1992**). The geochemical data of the studied Mn-ores have been plotted in the discrimination diagrams, as shown in **Figure 7**. Almost all the samples fall within or close to the field of hydrothermal Mn-deposits in Co/Zn vs Co+Ni+Zn diagram (see **Figure 7a**) of **Toth (1980)**, Si vs Al diagram (see **Figure 7b**) of **Crerar eta al (1982)**, Zn-Ni-Co diagram (see **Figure 7c**) of **Choi and Harira (1992)** while in the Mn-Fe-(Ni+Co+Cu)*10 diagram (see **Figure 7d**) of **Bonatti (1972) and Crerar et al. (1982)**, the data fall in the overlapping fields of hydrothermal and diagenetic Mn-deposits.

The very low Fe/Mn ratio due to very low amount of Fe in the studied Mn-ores suggest that fractionation of Fe has occurred well before the formation of these ores (**Roy 1992; Frakes and Bolton 1992; Shah and Khan 1999; Shah and Moon 2007**). It is reported that the concentrations of trace elements (i.e. Cu, Zn, Ni and Co) in the modern submarine manganese deposits of East Pacific Rise and the Galapagos areas are higher than the pelagic sediments, but are much lower in the hydrother-

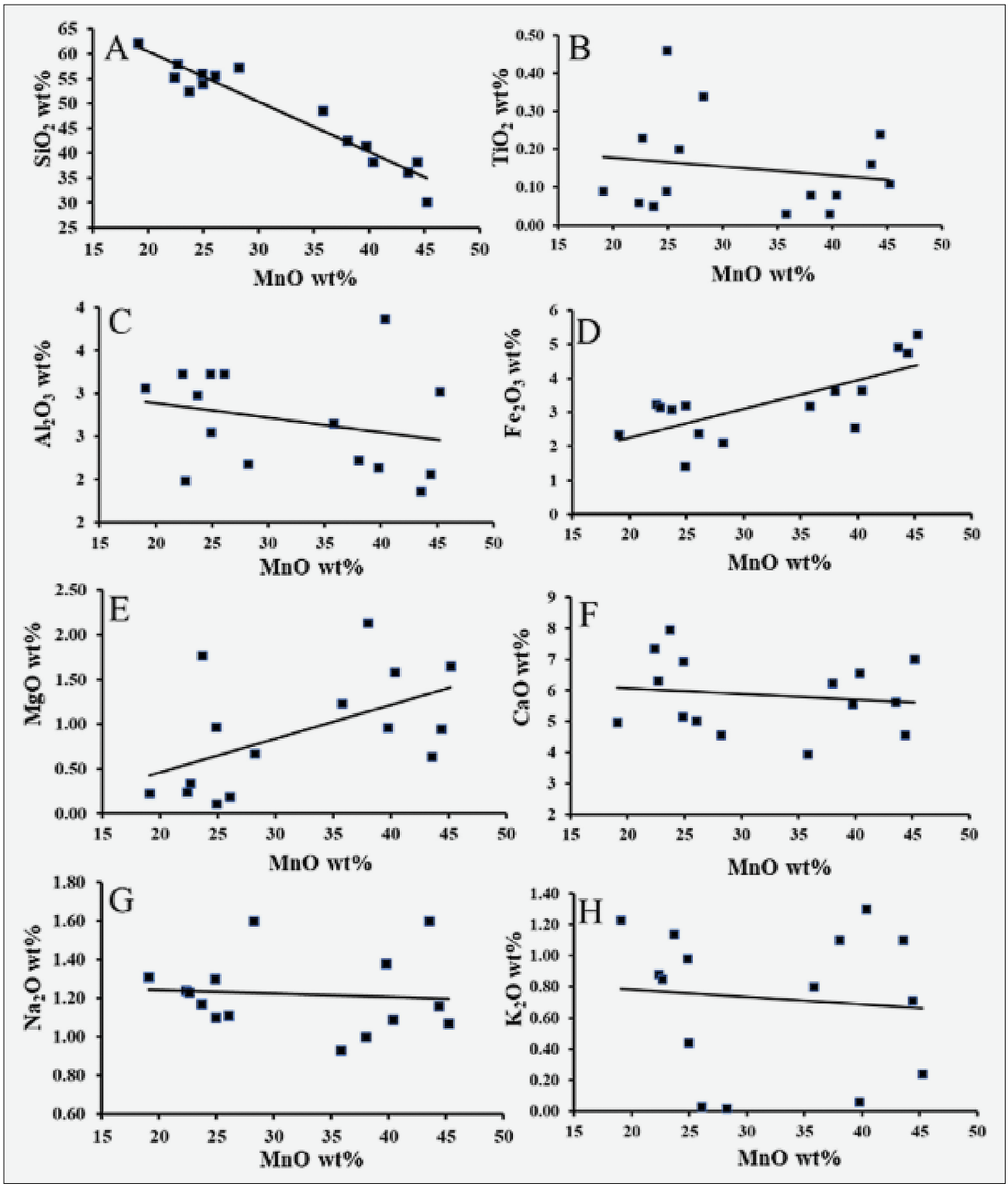


Figure 6. Major oxides versus MnO variation diagram of the studied Mn-ores.

mal Mn-deposits relative to the hydrogenous Mn-deposits (**Cronan 1980**). This is also confirmed in the case of the studied Mn-ores (see **Figure 7**). The plotting of the samples of studied Mn-ores along the Ni-Zn join line in **Figure 7c** also confirms the relationship of the studied Mn-ores with the modern submarine hydrothermal Mn-deposits. It is now well understood that the Fe compounds are less stable than the Mn compounds, whereby the Eh and/or pH is playing an important role, therefore, the precipitation of Fe has been reported proximal and Mn distal to the vent along the sea floor spreading centers (**Panagos and Varaavas 1984; Roy 1992; Frakes and Bolton 1992; Shah and Khan 1999; Shah and Moon 2004, 2007; Khan et al. 2010**).

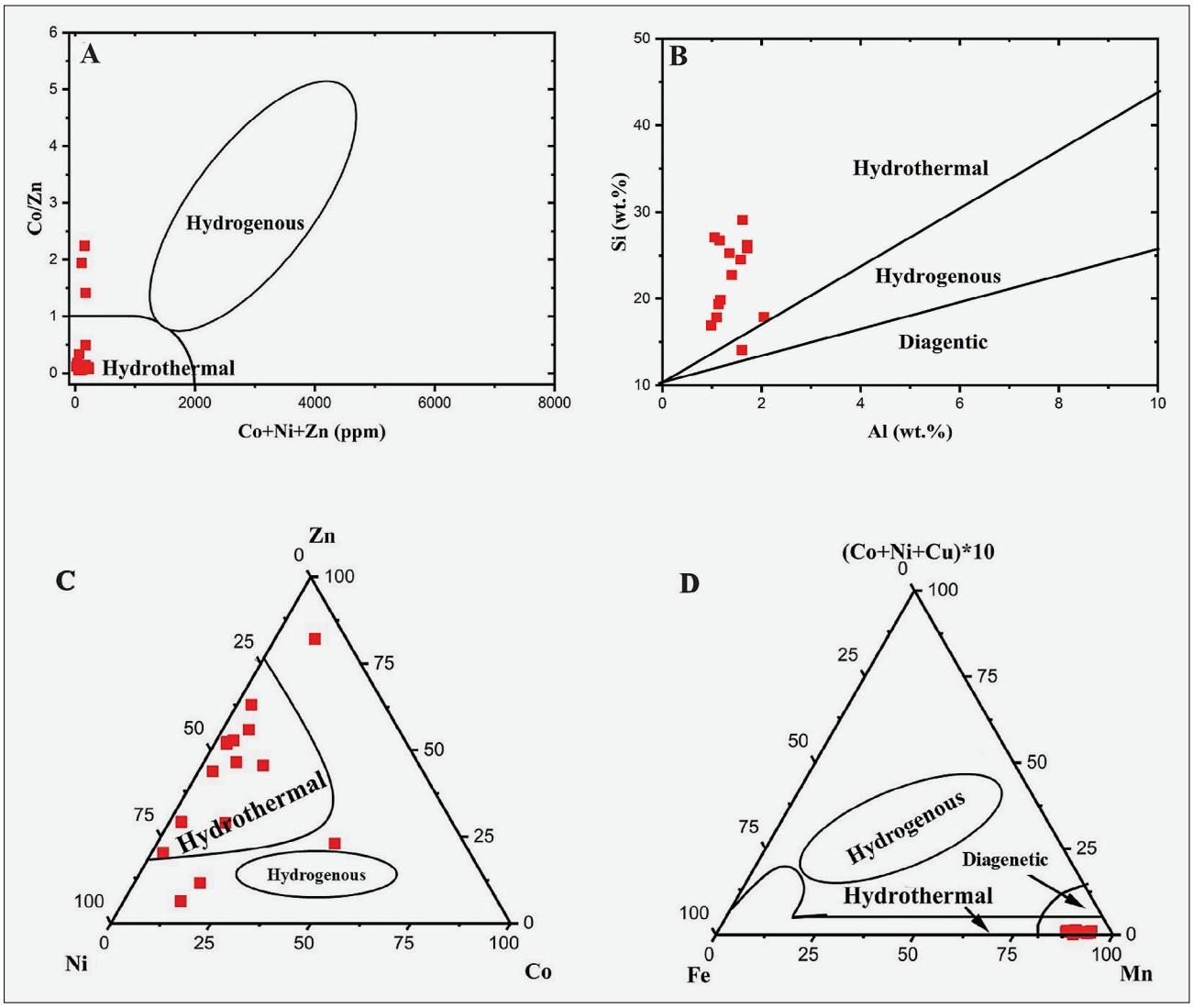


Figure 7. Plotting of the geochemical data of the studied Mn-ores from Mohmand area in the various discrimination diagrams: a) Co/Zn vs Co+Ni+Zn diagram of **Toth (1980)**; b) Al vs Si diagram of **Choi and Hariya (1992)**; c) Zn-Co-Ni diagram of **Choi and Hariya (1992)**; d) Mn-Fe-(Ni+Co+Cu) diagram of **Bonatti et al. (1972)** and **Crerar et al. (1982)**.

4.3. Genetic Model

The Nawagai ophiolitic melange in the Mohmand District, like the other ophiolitic melanges along MMT/ISZ, are the remnants of the Neo-Tethys oceanic crust which were formed during the opening and closing of the Neo-Tethys with the later supra-subduction stage. These are later on obducted on to the Indian Plate during collision of the KIA with the Indian Plate in Late Cretaceous. The KIA was formed during the intra-oceanic subduction of the Neo-Tethys oceanic lithosphere and latter on merging with the Karakoram Plate to form an Andean type margin and finally collided with the Indian Plate (**Molnar and Tapponier 1975; Tahirkheli 1979; Klootwijk et al. 1992; Arif and Jan 2006; Ullah et al. 2025**).

By considering the models of **Bonatti et al. (1976), Canon and Force (1983), Buehn et al. (1992), Shah and Khan (1999), Khan et al. (2020), Ullah et al. (2025)**, a very simple genetic model can be proposed for the formation of the Mn-ores of the Mohmand area from the hydrothermal solution along the mid-ocean ridges in the Neo-Tethys and later on obduction of these ores within the Nawagai ophiolitic melange along MKT/ISZ (see **Figure 8**). According to this model, during the early stage (Late Jurassic) of Neo-Tethys Ocean, a mid-oceanic ridge setting was present where the sea water was percolating through the hot oceanic basaltic crust and resulted in the formation of hydrothermal solutions. During this process, the hydrothermal solutions started leaching out the Mn, Fe, Cu, Pb, Zn, Co, and other metals from the basaltic crust. These metals enriched hydrothermal solutions started discharging and precipitating on to the sea floor. Due to change in temperature and pressure and an increase in Eh and/or pH, the various metal sulfides started precipitating along or closer to the discharge vents, while the Fe and Mn fractionation in the form of ferromanganese and manganese ores took place

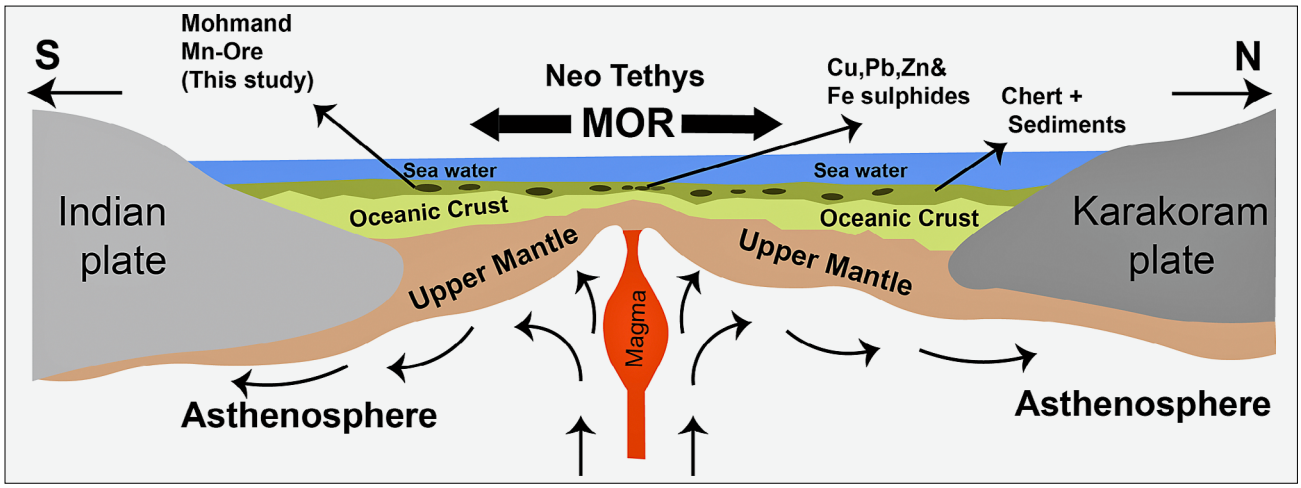


Figure 8. Hypothetical model showing the geological environment for the formation of Mohmand Mn-ores in the Neo-Tethys (modified after **Ullah et al. 2025**)

proximal and distal to the vent, respectively (**Bonatti et al. 1976; Crerar et al. 1982; Thornton and Seyfried 1985; Sawkins,1984; Roy 1992; Shanks et al. 1995; Shah and Khan 1999, Shah and Moon 2007; Khan et al. 2020**).

Considering the lower amount of Fe, higher amount of Si and higher Mn/Fe ratio in the Mn-deposits of the Mohmand area, these ores may have been formed distal to the discharge vent on the sea floor due to the early precipitation of ferromanganese ores near the source of hydrothermal solution and manganese ores distal to the source with input from the pelagic sediments within the mid-oceanic spreading center. This can be correlated with the present-day hydrothermal system within the mid-oceanic spreading centers (**Roy 1992; Shah and Khan 1999; Shah and Moon 2007; Narejo et al. 2019; Khan et al. 2020**). The development of mid-ocean ridges environment in the Neo-Tethys Ocean during Late Jurassic was followed by the origination of KIA by the northward double subduction during Early to Late Cretaceous. Afterwards, the closure of the Neo-Tethys Ocean and finally collision of KIA with the Indian Plate resulted in the formation of supra-subduction zone ophiolites, including the Nawagai ophiolitic melange, in northern Pakistan (**Ullah et al. 2025**).

The studied Mn-ores of the Mohmand area after their formation along the spreading centers were later on obducted on to the Indian Plate along the MMT/ISZ as part of the Nawagai ophiolitic melange during the subduction and later on collision of the Indian Plate with the Kohistan Island Arc. The field features such as the massive lenticular shape tectonized bodies with folding, faulting and shearing suggest that these ores and the host rocks may have undergone severe metamorphism and deformation during and after emplacement of the ophiolitic bodies in the existing position. This may have caused the recrystallization of manganese oxides and hydroxides into braunite by incorporating silica from the associated quartz (chert) during metamorphism. However, the essential geochemical characteristics of the deposits remained intact (see also **Bonatti et al. 1976; Shah and Khan 1999; Khan et al. 2020**). The geochemical characteristics of the studied Mn-ore bodies of the Mohmand area occurring in the Nawagai ophiolitic melange have been compared with the hydrothermal manganese deposits of other ophiolitic sequences elsewhere in the world in **Table 3**, for example, the Bela ophiolitic complex, Pakistan (**Narejo et al. 2019**); the Zhob ophiolites, Pakistan (**Khan et al. 2020**), the Waziristan ophiolite complex, Pakistan (**Shah and Khan 1999; Shah and Moon 2007**), Dehoo, ophiolitic unit, Iran (**Lotfi et al. 2017**), Cayirli, Ankara ophiolitic melange, Turkey (**Zarasvandi et al. 2013**) and Wakasas, Tokoro Belt, Hokkaido, Japan (**Öksüz 2011**). The studied Mn-ores of Mohmand area are very well correlated with the hydrothermal manganese deposits associated with ophiolitic sequences elsewhere in the world by having a higher Mn/Fe ratio, lower Fe/Mn ratio and lesser amount of trace elements (**Table 3**) as compared to hydogenous manganese deposits (**Nicholson et al, 1997; Jach and Dudek 2005**).

5. Conclusions

Manganese ores of the district Mohmand occur in the form of lenticular and irregular bodies of varying dimensions with cross-cutting quartz veins associated with cryptocrystalline meta-chert in the Nawagi ophiolitic melange zone. The ore bodies are highly sheared and fractured and these fractures are filled in by quartz and carbonates in the form of veins. Braunite is the dominant Mn-bearing phase with a lesser amount of pyrolusite and piemontite. Microcrystalline quartz, calcite and hematite occur as gangue minerals. Geochemical data suggest that the major and trace elements are highly variable in these ores and on the basis of the presence of Mn and Fe contents, these ores can be classified as high to low-grade but economically, as a whole, these ores can be

considered as low-grade. The geochemical data further suggest that these ores have been formed due to the precipitation of hydrothermal solution distal to the discharge source (vent) with some input from the pelagic sediments on the sea floor within the spreading centers in the Neo-Tethys Ocean during Late Jurassic. These ores are then obducted on to the Indian Plate as part of the Nawagai ophiolitic melange due to the subduction and later on collision of Indian Plate with the KIA along the MMT/ISZ during Late Cretaceous.

Acknowledgement

We are very thankful to the Director, National Centre of Excellence in Geology, University of Peshawar for providing financial support for field work and laboratory work to the first author for his MS research. The Director Centralized Resource Laboratory, University of Peshawar is thanked for the X-ray Diffraction analysis. Mr. Muhammad Tariq, Lab Technician, and Mr. Uzair Ahmad, Lab Technician, are also thanked for their assistance during the geochemical and SEM analyses, respectively.

6. References

Adachi M, Yamamoto K, Sugisaki R (1986). Hydrothermal chert and associated siliceous rocks from the modern Pacific: their geologic significance as indication of ocean ridge activity. Sedimentary Geology, 47: 125±148.

Ahmad I, Jehan N (2006). Occurrence of a melange along the Malakand pass north of Dargai, northern Pakistan. *Journal of Himalayan Earth Science,* 39: 55-59.

Arif M, Jan MQ (2006). Petrotectonic significance of the chemistry of chromite in the ultramafic-mafic complexes of Pakistan. *Journal of Asian Earth Sciences,* 27: 628–646. https://doi.org/10.1016/j.jseaes.2005.06.004.

Aslam, M., Hussain, A., Ashraf, M., Afridi, A.G.K., 2006. Geological Map of North West Frontier Province Pakistan, first ed. Directorate of publication geological survey of Pakistan Quetta: Quetta.

Baba AA, Ibrahim L, Adekola FA, Bale RB, Ghosh MK, Sheik AR, Pradhan, BS, Treloar P (2003) Northward subduction of the Indian Plate beneath the Kohistan island arc, Pakistan Himalaya: new evidence from isotopic data. *Jornal of Geological Society* 160(3): 377-384.

Bard JP (1983). Metamorphism of an obducted island arc: Example of the Kohistan sequence (Pakistan)in the Himalayan Collided range. *Earth and Planetary Science Letters,* 65: 133-144.

Bonatti E, Kraemer T, Rdell H (1972). Classification and genesis of submarine iron-manganese deposits. In: Horn D (ed) Ferro-manganese deposits on the ocean: International Decadron Ocean Exploration Washington DC Nation Sci Found 149±166.

Bonatti E, Zerbi M, Kay R, Rydell H (1976). Metalliferous deposits from the Apennine ophiolites: Mesozoic equivalents of modern deposits from oceanic spreading centers. *Geological Society of American Bulletin,* 87:83±94.

Bonatti E (1972). Classification and genesis of submarine iron-manganese deposits.

Buehn B, Stanistreet IG, Okrusch M (1992). Late Proterozoic outer shelf manganese and iron deposits at Otjosondu (Namibia) related to the Damaran oceanic opening. *Economic Geology,* 87: 1393±144.

Burg JP, Chaudhry MN, Ghazanfer M, Anczkiewicz R, Spencer D (1996). Structural evidence of back sliding of Kohistan arc in the collision system of the northwest Pakistan. *Geology,* 24: 739-742.

Cannon WF, Force ER (1983). Potential for high-grade shallow-marine manganese deposits in North America. In: Shanks WCIII (ed) Cameron volume on unconventional mineral deposits. New York Society Mining Engineers/ American Institute of Mining, *Metallurgy and Petroleum Engineers,* 177±190.

Choi JH, Hariya Y (1992). Geochemistry and depositional environment of Mn oxide deposits in the Tokoro Belt, northeastern Hokkaido, Japan. *Economic Geology*, 87(5): 1265-1274.

Choukrad J, Ouahzizi Y, Ali AA, Charroud M (2022). Geology, mineralogy, geochemistry and deposit model of iron and manganese in Bouarfa mine, Eastern High Atlas Morocco. *Scientific African,*18:e01401. https://doi.org/10.1016/j.sciaf.2022.e01401

Chyi MS, Crerar DA, Carlson RW, Stallard RF (1984). Hydrothermal Mn-deposits of the Francisean assemblage, II. Isotope and trace element geochemistry, and implication for hydrothermal convection at spreading centres. *Earth and Planetary Science Letters,* 71: 31±45

Crerar DA, Namson J, Chyi MS, Williams L, Feigenson MD (1982). Manganiferous cherts of the Franciscan assemblage; I, General geology, ancient and modern analogues, and implications for hydrothermal convection at oceanic spreading centers. *Economic Geology*, 77(3): 519-540.

Cronan DS (1980) Underwater minerals: Academic Press, Lond, 362p

DiPietro JA, Ahmad I, Hussain A (2008). Cenozoic kinematic history of the Kohistan fault in the Pakistan Himalaya. *Geological Society of American Bulletin,* 120(11-12): 1428-1440.

DiPietro JA, Hussain A, Ahmad I, Khan MA (2000). The Main Mantle Thrust in Pakistan: its character and extent. *Geological Society of London Special Publication,* 170(1): 375-393.

DiPietro JA, Pogue R (2004). Tectonostratigraphic subdivisions of the Himalaya: A view from the west. *Tectonics*, 23(5), 1-20. TC5001, doi:10.1029/2003TC001554.

DiPietro, J. A. (1991), Metamorphic pressure-temperature conditions of Indian plate rocks south of the Main Mantle Thrust, Lower Swat, Pakistan, Tectonics, 10, 742–757

Dorokhin IV, Bogachero EN, Druzhiniv AV, SobolevskiVI, Gorbunov EV (1969). Economic mineral deposits. *Higher School, Moscow*, 368.

Fleet A, Robertson AHF (1980). Ocean-ridge metalliferous and pelagic sediments of the Semail Nappe, Oman. *Journal of the Geological Society of London* 137: 403±422

Frakes L, Bolton BR (1992). Effects of Ocean Chemistry, Sea Level, and Climate on the Formation of Primary Sedimentary Manganese *Ore Deposits. Economic Geology*, 87(5): 1207–1217. https://doi.org/10.2113/gsecongeo.87.5.1207

Haider SK, Azimi G, Duan L, Anthony EJ, Patchigolla K, Oakey JE, Leion H, Mattisson T, Lyngfelt A (2016). Enhancing properties of iron and manganese ores as oxygen carriers for chemical looping processes by dry impregnation. *Applied Energy,* 163: 41-50.

Hein JR, Gibbs AE, Clague DA, (1996). Hydrothermal mineralization thermal convection at spreading centres. *Earth and Planetary Science Letters,*71: 31±45

Hein JR, Koschinsky A, Halbach P (1997). Iron and Manganese Oxide Mineralization in the Pacific. In: Nicholson K, Hein JR, Buhn B (eds) Manganese Mineralization: Geochemistry and Mineralogy of Terrestrial and Marine Deposits. *Geological Society Special Publication,* 123–138.

Hein JR, Mizell K, Koschinsky A, Conrad TA (2013). Deep-ocean mineral deposits as a source of critical metals for high- and greentechnology applications: comparison with land-based resources. *Ore Geology Reviews,* 51:1–14. https://doi.org/10.1016/j.oregeorev.2012. 12.001

Ingram BL, Hein JR, Farmer GL (1990). Age Determinations and Growth Rates of Pacific Ferromanganese Deposits Using Strontium Isotopes. *Geochimica et Cosmochimica Acta,* 54(6): 1709–1721. https://doi.org/10.1016/0016-7037(90)90402-7

Jach R, Dudek T (2005). Origin of a Toarcian manganese carbonate/silicate deposit from the Krížna unit, Tatra Mountains, Poland. *Chemical Geology*,224(1-3): 136-152.

Jeffery PG, Hutchison D (1986). Chemical methods of rock analysis. *Prgamon Press, New York*, 370p.

Jiancheng X, Weidong S, Jianguo D (2013) Geochemical studies on Permian manganese deposits in Guichi, eastern China. Implications for their origin and formative environments, *Journal of Asian Earth Sciences,* 74: 155–166.

Karakuş A, Yavuz B, Koç S (2010). Mineralogy and Major-Trace Element Geochemistry of the Haymana Manganese Mineralizations, Ankara, Turkey. *Geochemistry International*, 48(10): 1014–1027. https://doi.org/10.1134/s00167 0291010006x.

Kazmi, A. H., R. D. Lawrence, H. Dawood, L. W. Snee, and S. Hussain (1984), Geology of the Indus suture zone in the Mingora-Shangla area of Swat, N. Pakistan, Geological Bulliten University of Peshawar,, 17, 127–144

Kazmi A, Jan M (1997). Geology and Tectonics of Pakistan Graphic Publishers.

Khan MA (ed), Aslam M, Hussain A, Ashraf M, Afridi AGK (Authors) (2006). Geological map of North West Frontier Province, Pakistan (Colored, Scale 1:1,000,000). *Geological Survey of Pakistan* (Map Series).

Khan MA, Jan MQ, Weaver BL (1993). Evolution of the lower arc crust in Kohistan, N. Pakistan: temporal arc magmatism through early, mature and intra-arc rift stage. In: Treloar PJ and Searl MP (eds) Himalayan Tectonics. *Geological Society of London Special Publications,* 74: 123-138.

Khan MA, Kakar MI, Ulrich T, Ali L, Kerr AC, Mehmood K, Siddiqui RH (2020). Genesis of Manganese Deposits in the Ali Khanzai Block of the Zhob Ophiolite, Pakistan: Inferences from Geochemistry and Mineralogy. *Journal of Earth Sciences* 31(5) 884–895.

Klootwijk CT, Gee JS, Peirce JW, Smith GM, McFadden PL (1992). An early India- Asia contact: paleomagnetic constraints from Ninety east ridge, ODP Leg 121. *Geology* 20(5): 395-398.

Kuhn T., Bau M, Blum, N, Halbach P (1998). Origin of Negative Ce Anomalies in Mixed Hydrothermal-Hydrogenetic Fe-Mn Crusts from the CentralIndian Ridge. 163(1/2/3/4): 207–220. https://doi.org/10.1016/s0012-821x(98)00188-5.

Lasheen TA, El-Hazek MN, Helal AS El-Nagar W (2009). Recovery of Manganese Using Molasses as Reductant in Nitric Acid Solution. *International Journal of Mineral Processing*, 92: 109-114. https://doi.org/10.1016/j.minpro.2009.03.001

Lee JS (1982). Manganese deposits and plate tectonics, Olympic Peninsula, Washington. Abstr I.A.G.O.D. 6th, *Symposium of Tbilisi*, 6±12, 295±296.

Lotfi M, Kahrazehi M, Ghaderi M (2017). Geochemistry and Origin of Dehoo Manganese Deposit, South Zahedan, Southeastern Iran. *Arabian Journal of Geosciences*, 10(6): 142. https://doi.org/10.1007/s12517-017-2865-8.

Marescotti P, Frezzotti M (2000). Alteration of braunite ores from Eastern Liguria (Italy) during syntectonic veining processes: Mineralogy and fluid inclusions. *European Journal of Mineralogy,* 12(2):341-356.

Mehdilo A, Irannajad M (2014). Evaluation of pyrolusite flotation behavior using a cationic collector. *Journal of Mining Science,* 50(5): 982-993.

Molnar P, Tapponnier P, (1975). Cenozoic tectonics of Asia: effects of a continental collision. *Science* 189: 419-426

Narejo AA, Shar AM, Fatima N, Sohail K (2019). Geochemistry and origin of Mn deposits in the Bela ophiolite complex, Balochistan, Pakistan. *Journal of Petroleum Exploration and Production Technology,* 9:2543–2554

Naseem S, Sheikh SA, Mallick KA (1997) Lithiophorite and associated manganese mineralization in Lasbela area, Balochistan, Pakistan. *Geosciences Journal* 1(1): 10-15.

Nicholson K (1992). Contrasting mineralogical-geochemical signatures of manganese oxides; guides to metallogenesis. *Economic Geology* 87(5): 1253-1264.

Nicholson K, Nayak VK., Nanda JK (1997). Manganese Ores of the Ghoriajhor-Monmunda Area, Sundergarh District, Orissa, India: Geochemical Evidence for a Mixed Mn Source. *Geological Society* of *London Special Publication,* 119(1): 117–121. https://doi.org/10.1144/gsl.sp.1997. 119.01.08.

Öksüz N (2011). Geochemical characteristics of the Eymir (Sorgun-Yozgat) manganese deposit, Turkey. *Journal of Rare Earths,* 29(3): 287–296

Öksüz N, Okuyucu N (2014). Mineralogy, geochemistry, and origin of Buyukmahal manganese mineralization in the Artova ophiolitic complex, Yozgat, Turkey. *Journal of Chemistry,* 2014:837972. https ://doi.org/10.1155/2014/ 83797 2

Panagos AG Varanavas SP (1984). On the genesis of some manganese deposits from eastern Greece, Syngenesis and Epigenesis in the Formation of Mineral Deposits 553–561.

Polgári PMO (1991). Stable Isotope Evidence for the Origin of the Urkut Manganese Ore Deposit, Hungary. *J Sed Res* 61(3): 384–393. https://doi.org/10.1306/d426771c-2b26-11d7-8648000102c1865d

Polgári M, Hein J, Vigh T, Szabó-Drubina M, Fórizs I, Bíró L, Müller A, Tóth A (2012). Microbial processes and the origin of the Úrkút manganese deposit, Hungary. *Ore Geology Reviews* 47: 87-109.

Rehman WU, Rehman AU, Khan F, Muhammad A, Younas M (2020). Studies on beneficiation of manganese ore through high intensity magnetic separator. *Advanced Science and Engineering*,12(1): 21-27.

Robertson A (2000). Formation of melanges in the Indus suture zone, Ladakh Himalaya by successive subduction-related, collisional and post-collisional processes during late Mesozoic-late Tertiary time. *Geological Society of London Special Publications,* 170(1): 333-374.

Roy S (1992). Environments and processes of manganese deposition. *Economic Geology* 87(5) 1218–1236.

Safarov RZ, Kargin JB, Zhandildenova AK, Aibuldinov YK, Vatin NI, Seo J, Barnes CHW, Valladares LDLS (2024) Oxide Metamorphic Manganese Ores: An Experimental Results of Heat Treatment. *Preprints.org.* 1-15.

Sasmaz A, Turkyilmaz B, Ozturk N (2014). Geology and geochemistry of middle Eocene madden complex ferromanganese deposits from Elazı˘g-Malatya Region, Eastern, Turkey. *Ore Geology Reveiws* 56: 352–372.

Sawkins FJ (1984). Metal deposits in relation to plate tectonics. 2nd Ed. *Springer-Vereng, Berlin*.

Searle M, Khan MA, Fraser J, Gough S, Jan MQ (1999). The tectonic evolution of the Kohistan- Karakoram collision belt along the Karakoram Highway transect, north Pakistan. *Tectonics* 18(6): 929-949.

Shah MT, Moon CJ (2004). Mineralogy, geochemistry and genesis of the ferromanganese ores from Hazara area, NW Himalayas, northern Pakistan. *Journal Asian Earth Sciences,* 23(1): 1-15.

Shah M, Khan A, (1999). Geochemistry and origin of Mn-deposits in the Waziristan ophiolite complex, north Waziristan, Pakistan. *Mineralium Deposita,* 34(7): 697-704.

Shah MT, Moon CJ, (2007). Manganese and ferromanganese ores from different tectonic settings in the NW Himalayas, Pakistan. *Journal Asian Earth Sciences* 29, 455-465.

Shaif M, Siddiquie FN, Ahmad M (2020). Mineralogical Studies of the Manganese Ores in Banswara Manganese Belt, Banswara District, Rajasthan Available to Purchase *Journal of Geological Society of India,* 96 (2): 189–198.

Shanks WC, Bohlke JK, Seal RR (1995). Stable isotopes in mid-ocean ridge hydrothermal system: implications between fluid, mineral and organism. *Geophysical Monograph Ser,*194-221.

Siddiquie F, Burhamuddin K, Shaif, M, Alam S (2015). Manganese ore minerals assemblages and mineral paragenesis with the help of ore petrography and XRD studies of Balaghat District,(MP) India. *Global Journal of Science Frontier Research: Environment & Earth Science,* 15(3): 21-34.

Sinisi R, Mongelli G, Peri F, Rizzo G (2018). The braunite (3Mn2O3·MnSiO3)-rich mineralization in the metasedimentary succession from southern Apennines (Italy): Genesis constraints. *Ore Geology Reveiws*, 94(169), 1-11. https://doi.org/10.1016/j.oregeorev.2018.01.014

Tahirkheli RK (1979). Geology of Kohistan and adjoining Eurasian and Indo-Pakistan continents, Pakistan. *Geological Bulliten University of Peshawar*, 11(1): 1-30.

Tahirkheli RK (1979). The India-Eurasia suture zone in northern Pakistan: Synthesis and interpretation of recent data at plate scale. *Geodynamics of Pakistan* 125-130.

Thornton EC, Seyfried Jr WE (1985). Sediment–sea water interaction at 200_and 300 C, 500 bars pressure: the role of sediment composition in diagenesis and lowgrade metamorphism of marine clay. *Geological Society of America Bulletin*, 96: 1287–1295.

Toth JR (1980). Deposition of submarine crusts rich in manganese and iron. *Geol Soc Amer Bull* 91(1): 44-54.

Treloar PJ (1989). Imbrication and unroofing of the Himalayan Thrust stack of the north Indian plate, north Pakistan. *Geological Bulletin University of Peshawar* 22: 25-44.

Ullah Z, Khan A, Li H, Zafat T, Ali A, Farhan M, Hussain Z, Khan A, Idress M, Ibrar M (2025). Petrogenesis and tectonic implications of peridotites of the Shangla Complex Ophiolite along Main Mantle Thrust, Northern Pakistan. Geoscience Frontiers. Published online 2025:102070.

Usui A, Nishimura A (1992). Submersible Observations of Hydrothermal Manganese Deposits on the Kaikata Seamount, Izu-Ogasawara (Bonin) Arc. *Marine Geology*, 106(3/4): 203–216. https://doi.org/10.1016/0025-3227(92)90130-a

Usui A, Someya M (1997). Distribution and Composition of Marine Hydrogenetic and Hydrothermal Manganese Deposits in the Northwest Pacific. *Geological Society London Special Publication* 119(1): 177–198. https://doi.org/10.1144/gsl.sp.1997.119.01.12

SAŽETAK

Geokemija i geneza manganovih ruda u ofiolitnome melanžu Nawagai, okrug Mohmand, Khyber Pakhtunkhwa, Pakistan

Ofiolitni melanž Nawagai nalazi se u zapadnome dijelu glavne navlake plašta Indske suturne zone (MMT/ISZ) u sjevernome Pakistanu i smatra se dijelom naboranoga pojasa koji sadržava ofiolitne sekvencije. Istraživana tijela manganove rude prisutna su u ofiolitnome melanžu Nawagai u okrugu Mohmand u Khyber Pakhtunkhwi u Pakistanu. Ove rude dislocirana su lećasta tijela različitih veličina i općenito su povezana s kriptokristalastim metarožnjakom. Manganove rude i metarožnjaci jako su tektonizirani te su podložni metamorfizmu/deformaciji. Mineraloški, istraživane manganove rude dominantno se sastoje od braunita s manjom količinom piroluzita i piemontita kao faza koje sadržavaju Mn, dok se minerali jalovine uglavnom odnose na kriptokristalasti kvarc s manjom količinom kalcita. Manganove faze ispreplетene su unutar kriptokristalastoga kvarca; međutim uočavaju se i poprečne mikrožile kvarca i kalcita. Na pojedinim mjestima piroluzit i piemontit zamjenjuju braunit. Geokemijski istraživane manganove rude vrlo su varijabilne po svojemu sadržaju. Općenito su od visokoga do niskoga sadržaja, no u cijelosti, s ekonomskog gledišta mogu se smatrati rudama niskoga obogaćenja gledajući sadržaj MnO, Fe_2O_3 i SiO_2. Nije pronađena korelacija među glavnim elementima, međutim uočena je znatna pozitivna korelacija između SiO_2 i MnO. Frakcioniranje Mn i Fe te koncentracije različitih glavnih i elemenata u tragovima upućuju na to da su proučavane manganove rude područja Mohmand nastale iz hidrotermalnoga fluida distalno od izvora (hidrotermalnoga izvora) uz doprinos iz pelagičnih sedimenata duž srednjooceanskih grebena unutar Neotetisa. One su prenesene kao egzotična tijela unutar ofiolitskih sekvencija na Indijsku ploču uslijed subdukcije Indijske ploče ispod otočnoga luka Kohistan duž MMT/ISZ. Ove manganove rude i metarožnjaci pretrpjeli su jak metamorfizam i deformaciju tijekom i nakon postavljanja ofiolitskih tijela u postojeći položaj.

Ključne riječi:
mangan, petrografija, mineralogija, geokemija, geneza rude

Author's contribution

Irfan Ullah (MS Scholar): conceptualization, methodology, field investigation, data curation, and draft writing **Aamir Khan** (PhD Scholar): contributed to data curation, conceptualization, reviewing, editing, and writing the original draft. **Muhammad Tahir Shah** (PhD, Professor) contributed to conceptualization, complilation, reviewing and editing. **Liaqat Ali** (PhD, Professor): supervision, data curation, reviewing and editing and funding acquisition. **Asad Khan** (PhD, lecturer) contributed to laboratory work, and data support.
All authors have read and agreed to the published version of the manuscript.

RGNZ/MGPB

Rudarsko-geološko-naftni zbornik
(The Mining-Geology-Petroleum Engineering Bulletin)
DOI: 10.17794/rgn.2026.3.10

Original scientific paper

Enhancing Hypocenter Relocation for Seismic Hazard Evaluation in Central Java and Yogyakarta Indonesia: Findings from the BMKG Earthquake Catalog of August-October 2024

Wahyu Hidayat[1]*, Nanda Agustina[1], Ekalia Ardenti[2], Suharsono[1], Ardian Novianto[1], Uli Ulfa[1], Maman Rohaman[1], Herry Riswandi[3]

[1] *Geophysical Engineering Department, Faculty on Mineral Technology and Energy, Universitas Pembangunan Nasional "Veteran" Yogyakarta, Jl Pajajaran 104, Condongcatur Depok, Sleman Yogyakarta, 55283, Indonesia.*

[2] *Agency for Meteorology, Climatology, and Geophysics (BMKG), Jl. Raya Banjarmangu No.KM. 12, Kalilunjar, Central Java, 53454 Indonesia.*

[3] *Geological Engineering Department, Faculty on Mineral Technology and Energy, Universitas Pembangunan Nasional "Veteran" Yogyakarta, Jl Pajajaran 104, Condongcatur Depok, Sleman Yogyakarta, 55283, Indonesia.*

Abstract

We present a hypocenter relocation analysis to examine the distribution of seismicity in the Central Java and Yogyakarta regions in Indonesia. The data were obtained from the BMKG earthquake database for the period August–October 2024, covering the area between 6.0°–11.0° S and 108.5°–111.6° E. The dataset was divided into three monthly groups to observe the spatial and temporal patterns of earthquake sources in the study area. The analysis was carried out by overlaying the relocated hypocenters onto active fault maps and the subduction pattern of southern Java, allowing for a clearer characterization of the earthquake sources. Data from August - October 2024, comprising 393, 424, and 276 earthquake events respectively, were analyzed using the Double - Difference relocation method based on 26,610 - 19,429 P-wave pairs and 21,447 - 15,933 S-wave pairs recorded by 28 seismic stations. The findings reveal significant activity along the Baribis - Kendeng Fault, Kebumen - Meratus Trend, and Progo - Muria Lineament, exhibiting diverse fault mechanisms and hypocenter depths from shallow to intermediate. Clustering near the Opak Fault Zone and associated structures indicates complex fault interactions with potential intersegment stress transfer, while offshore seismicity shows a steeply dipping subduction slab with intermediate- to deep-focus events (50-250 km). The combined occurrence of shallow crustal, intermediate, and deep intraslab earthquakes expands the regional hazard spectrum, highlighting risks of strong ground shaking, site amplification, and localized tsunamis. The findings highlight the importance of integrating multisource and multimechanism earthquake characteristics into probabilistic hazard models to improve spatial planning, infrastructure resilience, and community preparedness.

Keywords:
Seismic hazard, Hypocenter relocation, Double – difference, Active fault

1. Introduction

Java Island is one of the regions in Indonesia with a high seismic hazard level due to its position within an active seismotectonic arc system extending from Sumatra to East Java (**Aribowo et al., 2022; Muttaqy et al., 2023; Raharja et al., 2024; Soehaimi, 2008**). This seismic zone is influenced by the complex interaction between the Indo Australian and Eurasian tectonic plates, with the active subduction zone south of Java serving as the primary principal of seismic activity (**Gunawan and Widiyantoro, 2019; Koulali et al., 2017**). Java's catastrophe index and seismic risk level are influenced by various factors, including earthquake magnitude and proximity to the seismic source, population density, local geological characteristics, and the resilience of infrastructure (**Liu et al., 2024; Soehaimi, 2008**). Central Java and Yogyakarta are particularly known for their relatively high levels of seismic activity, both offshore and onshore (**Muttaqy et al., 2023; Ramdhan et al., 2020**). Most earthquakes in this region occur in the offshore area south of Java, near the active subduction zone, indicating that tectonic plate subduction is the dominant mechanism. Conversely, shallow inland earthquakes are generally associated with the activity of local active faults. This situation highlights the importance of seismicity analysis to better understand subsurface structures, tectonic configurations, and earthquake hazard assessments.

The coexistence of subduction driven offshore earthquakes, active fault systems, and complex backarc structures creates a multihazard environment where the po-

* Corresponding author: Wahyu Hidayat
e-mail address: wahyu.hidayat@upnyk.ac.id
Received: 15 August 2025. Accepted: 18 November 2025.
Available online: 14 May 2026

tential impacts extend beyond strong ground shaking to include secondary hazards such as tsunamis, liquefaction, and landslides (**Aribowo et al., 2022**). Thick volcanic deposits in the area can amplify seismic waves, further exacerbating structural damage in densely populated zones. These factors highlight the importance of integrating seismotectonic analysis into disaster risk reduction frameworks, ensuring that urban planning, infrastructure design, and community preparedness measures are aligned with the region's multisource and multimechanism earthquake characteristics (**Soehaimi, 2008**). A comprehensive understanding of these hazards is essential for reducing potential casualties, safeguarding critical infrastructure, and enhancing the resilience of communities in Central Java and Yogyakarta. Due to the complicated interactions between tectonic processes in Yogyakarta and Central Java, thorough seismic characterization is an essential part of hazard assessment. High precision earthquake source parameters and a comprehensive seismotectonic framework are both necessary to comprehend the temporal and spatial patterns of earthquake activity. Refinement of earthquake locations by hypocenter relocation is an initial stage in this process, allowing the identification of active fault segments, elucidating subsurface structural configurations, and ultimately improving the accuracy of seismic hazard models for the area (**Hidayat et al., 2024**).

Accurate hypocenter location data is essential for such analyses (**Hidayat et al., 2024; Muttaqy et al., 2023; Syahbana et al., 2021; Zulfakriza et al., 2024**). One technique to improve the precision of earthquake localization is hypocenter relocation, which involves recalculating earthquake positions based on seismic wave travel time data, thereby reducing errors related to the velocity model used (**Garini et al., 2014**). Accurate hypocenter relocation enables better visualization of earthquake distributions, which can reflect underlying geological structures and provide deeper insight into regional seismotectonic environments (**Waldhauser and Ellsworth, 2000**). Hypocenter relocation is a technique for recalculating or correcting the position of hypocenter using seismic data to achieve a more precise location (**Garini et al., 2014**). Since it enables the viewing of hypocenter continuity that reflects subsurface structures, precise hypocenter relocation is essential for increasing earthquake localization precision (**Waldhauser, 2001**). Additionally, it makes it possible to identify seismotectonic settings by looking at the spatial distribution of earthquakes. The Double-Difference (DD) method is one of the most used approaches for hypocenter displacement. The relative locations of hypocenters are ascertained using the DD approach (**Hidayat et al., 2022, 2024; Waldhauser, 2001**). It is based on the variations in travel times between earthquake pairs that were recorded at the same seismic station. The principle states that if the distance between two paired earthquakes is relatively modest in comparison to their distances from the seismic station, their ray trajectories and waveforms can be deemed substantially equal. This assumption minimizes mistakes caused by the velocity model by allowing the travel time difference between the two earthquakes recorded at the same station to be interpreted as a function of the distance between their hypocenters (**Waldhauser dan Ellsworth, 2000**).

Central Java and Yogyakarta have been identified as the most densely inhabited regions in Indonesia, with over 73 million inhabitants residing in this highly seismic zone (**Muttaqy et al., 2023**). Given the significant seismic risk, the examination of earthquake clusters in this area is crucial to enhance and highlight the Indonesian seismic hazard map (**Muttaqy et al., 2023**). We performed hypocenter relocation using the 1-D AK135 velocity model, following the methodology previously applied in studies focusing on the Central Java and Yogyakarta regions (**Ramdhan et al., 2020; Saputra et al., 2021; Wagner et al., 2007**). The primary dataset for this relocation process was the earthquake event catalog data from August to October 2024, which we obtained from the BMKG Banjarnegara Station and processed using SeisComp4. This research aims to analyze the seismicity of Central Java and Yogyakarta in both spatial and temporal dimensions, with particular emphasis on the subduction zone and its associated structural features. In this research, we considered the existence of active earthquake sources in the Yogyakarta and Central Java regions that have not been fully identified by the National Center for Earthquake Studies (PUSGEN). By considering this, it is expected that this research can produce new findings related to the distribution of local earthquake activity and indications of active fault structures that have not been documented before, thereby contributing to updating disaster information in the region. The results are expected to provide a foundational reference for future, more comprehensive studies and to serve as an initial step toward effective earthquake disaster mitigation in the region.

Refining earthquake hypocenter locations is not just a methodological improvement; it is a basic need to make seismic source characterization less uncertain. Accurate relocation helps to map out active fault segments, make the geometry of subduction-related seismicity clearer, and find hidden seismotectonic structures that normal catalog data can't show. These improvements directly help make seismic hazard models more accurate in places like Central Java and Yogyakarta, which are very densely populated and culturally important. This makes mitigation strategies stronger, helps with urban planning, and makes communities more resilient to future earthquakes.

2. Geodinamics of Central Java and Yogyakarta

The geodynamics of Central Java and Yogyakarta are influenced by the interplay of subduction processes to

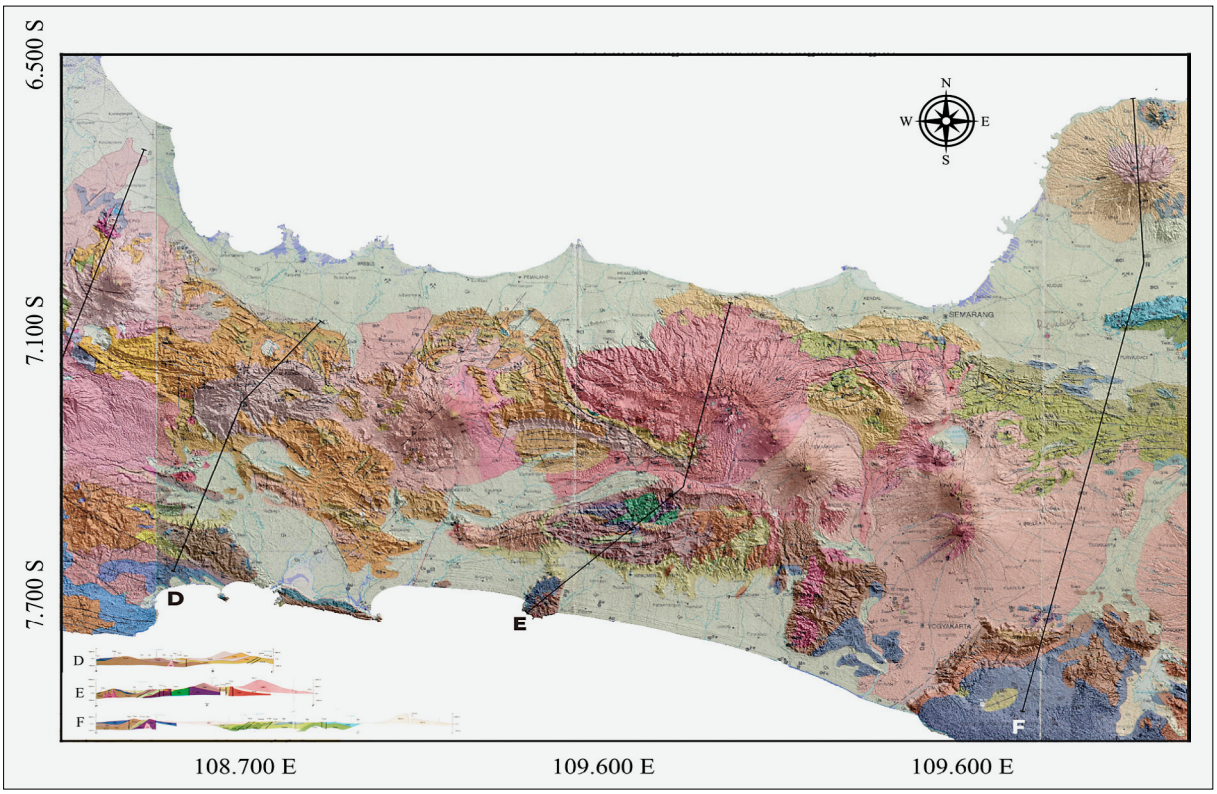


Figure 1. Geological map of the Central Java sheet at a scale of 1:500.000 (modified from **Amin et al., (1999)**)

the south of Java, active volcanism to the north, and fault systems that extend E – W and SW – NE (see **Figure 1**). Because of how the tectonic plates are arranged, the area is more likely to have earthquakes, both shallow and intermediate, that can do a lot of damage in locations with a lot of people. The presence of unconsolidated volcanic material, basin sedimentary deposits, and steep terrain further exacerbates the seismic hazard, raising ground shaking amplification and increasing the possibility for liquefaction in specific zones. These conditions illustrate that regional geodynamics not only modify the terrain and geological history, but they also make earthquakes more likely, which can have a huge influence on infrastructure and society in this area.

The Indo-Australian oceanic plate is moving south of Java and sliding beneath the Eurasian continental plate. This is causing the area around Central Java and Yogyakarta to change over time. This ongoing subduction has created the Central Java Quaternary Volcanic Arc, which is located to several active volcanoes, such as Merapi, Merbabu, Sindoro, Sumbing, and Slamet. These volcanoes are still showing signs of magmatic activity. The Southern Mountains, made up of mostly Tertiary carbonate rocks, are the most prominent feature in the southern part of the region. They make up the famous Gunung Sewu karst system, which has many caves and rivers that run underground. The Kendeng Zone to the north is made up of sedimentary rocks from the Miocene to the Plio-Pleistocene that have been bent into complicated folds and faults. The Opak Fault and other active fault systems show that tectonic processes are just as important as volcanism in shaping the landscape and hazards in the area. All of these things together make Central Java and Yogyakarta two of the most seismically active places in Indonesia. The area has tectonic and volcanic earthquakes that happen over and over again. One of the most damaging was the 2006 Yogyakarta earthquake. Unconsolidated volcanic deposits and sedimentary basins make the area even more dangerous because they tend to make the ground shake more and cause secondary hazards like liquefaction and slope failures.

2. Methods

We used the Double Difference (DD) method for this study. The DD approach is highly effective in areas with numerous closely situated local earthquake events clusters, resulting in a more concentrated distribution that aligns with the geological structure (**Muttaqy et al., 2023; Zhang, 2003; Zhang and Thurber, 2006**). The DD method relies on the assumption that when the distance between two earthquake sources is considerably smaller than their distances to a recording station, and the velocity heterogeneity along their respective ray paths is roughly equivalent, the wave rays from both sources can be regarded as nearly indistinguishable (**Waldhauser and Ellsworth, 2000**). The precision of hypocenter determination is affected by various parameters, such as the configuration of the seismic station

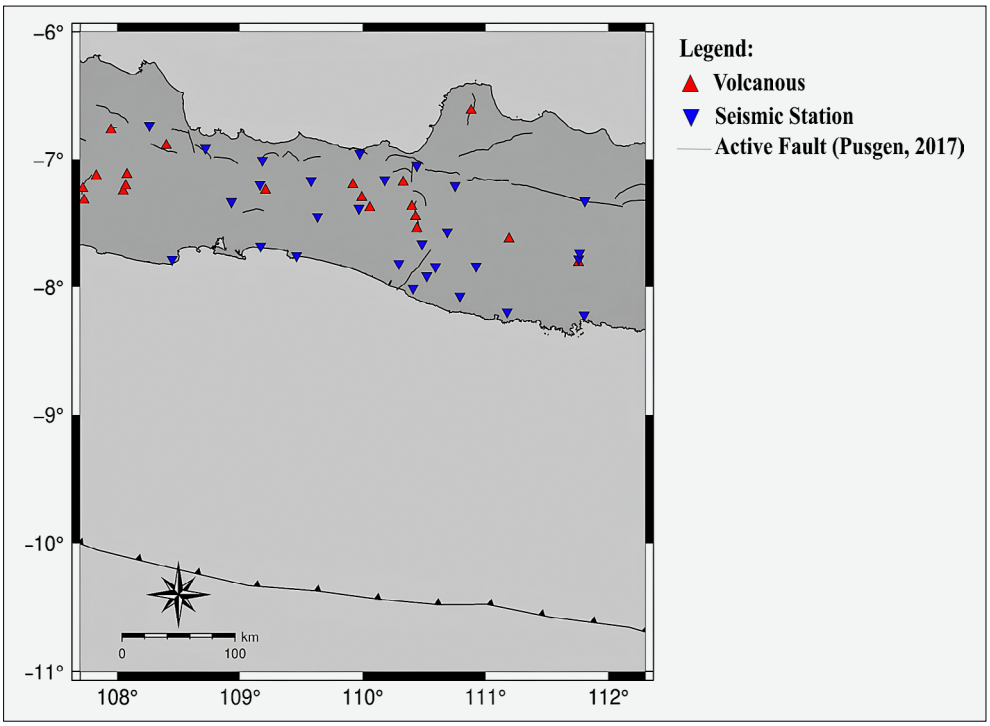


Figure 2. The distribution of the seismic network in Central Java and Yogyakarta is represented by blue triangle symbols, while the red triangles indicate volcanoes located within the study area. All elements are overlaid with the active fault map in the region

network, the quality and quantity of seismic phases, and the accuracy of the recorded arrival timings. The DD technique posits that when the interhypocentral distance of two earthquakes is minimal compared to their distance from the station, their wave raypaths reaching the station are substantially identical. Consequently, the disparity in transit time between the two events, measured at a shared station, can be understood as a function of the relative distance between their hypocenters (**Hidayat et al., 2022**). This method enables the minimization of velocity model error without requiring station corrections (**Waldhauser and Ellsworth, 2000**). The DD method has certain limitations, particularly when earthquake distributions are sparse or do not form clusters, making the principle of comparing nearby earthquake pairs less effective. Moreover, DD relocation requires handling a large number of earthquake pairs, which results in higher computational demands, especially for large datasets (**Hidayat et al., 2024**).

The travel time of seismic waves from an earthquake source iii to a seismic station kkk can be expressed using ray theory (**Um & Thurber, 1987**):

$$T_k^i = \tau^i + \int_i^k u\, ds \tag{1}$$

where τ^i represents the origin time of the earthquake, i, u is the slowness vector, and ds denotes the partition of the ray path. The relationship between arrival time and source location is highly non-linear; therefore, linearization is applied by calculating the misfit between observed and predicted travel times, given by:

$$r_k^i = \sum_{l=1}^{3} \frac{\partial T_k^i}{\partial x_l^i} \Delta x_l^i + \Delta\tau^i + \int_i^k \delta u\, ds \tag{2}$$

By substituting the arrival times of another earthquake source j recorded at the same station j, the expression becomes:

$$r_k^i - r_k^j = \sum_{l=1}^{3} \frac{\partial T_k^i}{\partial x_l^i} \Delta x_l^i + \Delta\tau^i +$$

$$+ \int_i^k \delta u\, ds - \sum_{l=1}^{3} \frac{\partial T_k^j}{\partial x_l^j} \Delta x_l^j - \Delta\tau^j - \int_i^j \delta u\, ds \tag{3}$$

$$r_k^i - r_k^j = \sum_{l=1}^{3} \frac{\partial T_k^i}{\partial x_l^i} \Delta x_l^i + \Delta\tau^i - \sum_{l=1}^{3} \frac{\partial T_k^j}{\partial x_l^j} \Delta x_l^j - \Delta\tau^j \tag{4}$$

By assuming that the two sources are located very close to each other, the ray paths become nearly identical and cancel out, reducing **Equation 3** to **Equation 4**, where $r_k^i - r_k^j$ represents the Double-Difference (**Waldhauser and Ellsworth, 2000**). The Double-Difference method refers to the difference in travel times between observed data and calculated data for two nearby earthquake sources, which can be expressed as:

$$r_k^i - r_k^j = (T_k^i - T_k^j)^{obs} - (T_k^i - T_k^j)^{cal} \tag{5}$$

To further investigate the spatial orientation of these relocated hypocenters, it is necessary to compute the azimuth and relative distance between earthquake pairs.

This is achieved using the Haversine formula, which provides an accurate estimation of great-circle distances on a spherical Earth:

$$d = 2R\ arcsin\left(\sqrt{sin^2\left(\frac{\Delta\varphi}{2}\right) + cos(\varphi_1)\ cos(\varphi_2)\ sin^2\left(\frac{\Delta\lambda}{2}\right)}\right) \quad (6)$$

where R is the Earth's radius, $\Delta\varphi = \varphi_2 - \varphi_1$ is the difference in latitude, and $\Delta\varphi = \lambda_2 - \lambda_1$ is the difference in longitude between two hypocenters. The calculated azimuthal orientations are then represented using a rose diagram, which provides a statistical visualization of dominant structural trends, seismic alignments, and fault orientations. In this study, the integration of double-difference relocation with Haversine based azimuth analysis allows for a more robust characterization of seismicity patterns in Central Java and Yogyakarta.

The data used for this research came from a catalog of earthquakes in Central Java and Yogyakarta from August to October 2024 and from stations in Banjarnegara using Seiscomp-4 with a geographic range of 6.0˚-11.0˚ and 108.5˚-111.6˚ (see **Figure 2**). The data catalog comprises information about the earthquake occurrence, date, time, location, depth, agency, mode, status, RMS residual, azimuthal gap, magnitude, phase, and the station that recorded the earthquake.

The hypocenter relocated in this research through two programs, ph2dt and hypoDD. As required by the relocation software, the first step was to convert the original BMKG earthquake catalog data from.txt format to.pha format. The (*.pha) catalog file is the primary input for the ph2dt program. Important details about the event, including the earthquake's date and time, hypocenter coordinates (latitude and longitude), depth, magnitude, RMS error, seismic station, seismic wave arrival times, quality indicators, and wave phases, are provided by the (*.pha) catalog. We calculate the difference in travel times between earthquake pairs using this precise event information. The hypocenter is then moved using the hypoDD algorithm. The hypoDD program's Double-Difference (DD) method for moving things around entails putting similar earthquake occurrences into clusters based on a set distance threshold. The MINLNK parameter can be used to find the best arrangement of these clusters by setting the least number of observations needed to form a cluster equal to the minimum number of observations needed for events that are nearest through. The initial development of clusters is additionally affected by the maximum inter-event distance within a cluster, denoted by the WDCT parameter. To ensure dependable outcomes, the WDCT value must be equal to or less than the MAXSEP parameter, which delineates the maximum permissible spacing between event pairings. A further crucial factor is the implementation of a suitable one-dimensional (1D) velocity model. This investigation utilized the AK135 velocity model, characterized by a Vp/Vs ratio of 1.74, as illustrated in **Figure 2**. This model establishes the foundation for computing travel durations and is essential for the precision of relocations. Furthermore, an essential parameter that requires meticulous assessment is the Condition Number (CND), which indicates the quality of the inversion process. For dependable relocation outcomes, CND values must reside between 40 and 80. A low CND value may signify overdamping, wherein excessive regularization causes few or no alterations in event locations throughout the inversion process, leading to trivial decreases in travel-time residuals. A high CND number may indicate underdamping, where insufficient regularization leads to unstable and excessive shifts in event positions, thereby jeopardizing the accuracy of the relocation results.

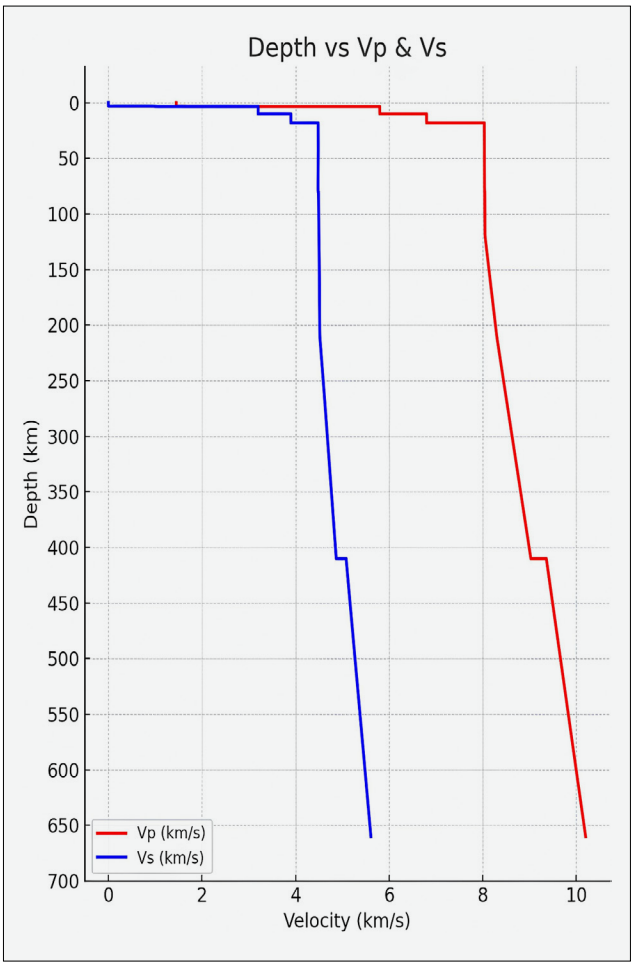


Figure 3. Velocity profiles of P-waves (Vp) and S-waves (Vs) based on the AK135 velocity model down to a depth of 700 km. The blue line represents S-wave velocities, whereas the red line represents P-wave velocities

The dataset used in this study consists of earthquake catalog data from BMKG Banjarnegara, covering the Central Java and Yogyakarta regions for the period of August to October 2024. A total of 393 earthquake events were recorded in August 2024, 424 events in September 2024, and 276 events in October 2024, resulting in a total of 1,093 events recorded by 29 seismic stations. The recorded earthquake magnitudes ranged from 1.0 to 5.8 Mw, with focal depths ranging from 5 to 256

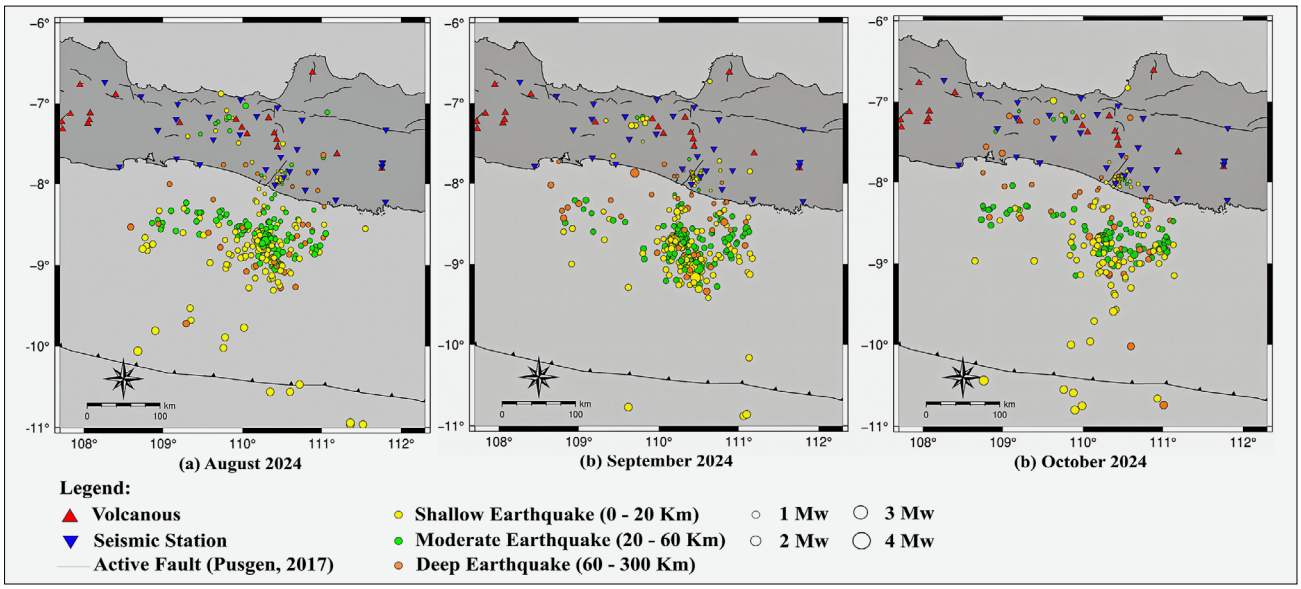


Figure 4. Spatial distribution of earthquake events during (a) August 2024, (b) September 2024, and (c) October 2024. Earthquake depth is colour-coded: yellow for shallow, green for moderate, and orange for deep events. The blue triangles indicate the locations of seismic stations, and the red triangles represent volcanoes.

km. The earthquake data were initially processed using SeisComP4 and then relocated using the Double-Difference (DD) method. The relocation process involved two main steps: using the ph2dt program followed by the hypoDD program.

Relocation process involved two main steps: first, applying the ph2dt program to calculate differential travel times, and then using the hypoDD program to relocate the earthquake hypocenters. The number of earthquake events before and after relocation differed because not all events satisfied the selection criteria required for processing in ph2dt. Specifically, events were excluded if they had an insufficient number of associated phase readings, poor azimuthal station coverage, or large residuals in the travel-time data. These conditions are necessary to ensure that the double-difference algorithm can accurately minimize relative location errors between nearby event pairs. In addition, some relocated events exhibited so-called "airquake" effects, in which the hypocenter positions were incorrectly shifted to locations above the Earth's surface. Such artifacts typically occur when the available phase data are too sparse or unevenly distributed, leading to unstable inversion results in hypoDD. Therefore, only events that fulfilled the minimum criteria of station coverage, phase quality, and residual thresholds were retained for the final relocated catalog.

Hypocenter relocation in this study was carried out using HypoDD. The parameters applied in the hypocenter relocation process for August, September, and October 2024 included MAXNGH, MINWGHT, MINLNK, MINOBS, and MAXOBS. The MAXNGH parameter was consistently set to 16 for each month. The maximum distance between events and stations (MAXDIST) was set at 600 km, while MAXSEP, which represents the maximum separation between event pairs, was fixed at 100 km throughout the three-month observation period. The selection of these parameters was meant to make sure that the inversion process was stable and that the relocated hypocenters were reliable. We chose a MAXNGH value of 16 to keep enough neighbouring events in each cluster without putting too much strain on the computer. The relatively large MAXDIST (600 km) made it possible to include stations that were far away and gave more phase data, which improved azimuthal coverage and made it less likely that the location was wrong. The MAXSEP of 100 km made sure that event pairs were still related in space, but it also let bigger clusters form in areas with few earthquakes. Similarly, thresholds for MINWGHT, MINLNK, MINOBS, and MAXOBS were applied to guarantee that only events with adequate observational constraints and reasonable travel-time residuals were included in the relocation process. These settings reflect a balance between data quality control and the need to retain a sufficient number of events for meaningful seismicity analysis. The ph2dt program provides output in the form of dt.ct data containing the travel time differences of the selected event pairs, event.sel containing information on the events selected as pairs, and ph2dt.log containing information on the results of the ph2dt process. The output of the ph2dt program is used for the relocation process in the hypoDD program. There are important things in the ph2dt program, namely outliers and weakly linked events. The program will reduce events that are considered outliers, the smaller the percentage of outliers, the better the data. Furthermore, only events that have a strong link will be used in the relocation process, so the smaller the percentage of weakly linked events, the fewer weakly linked event pairs there will be.

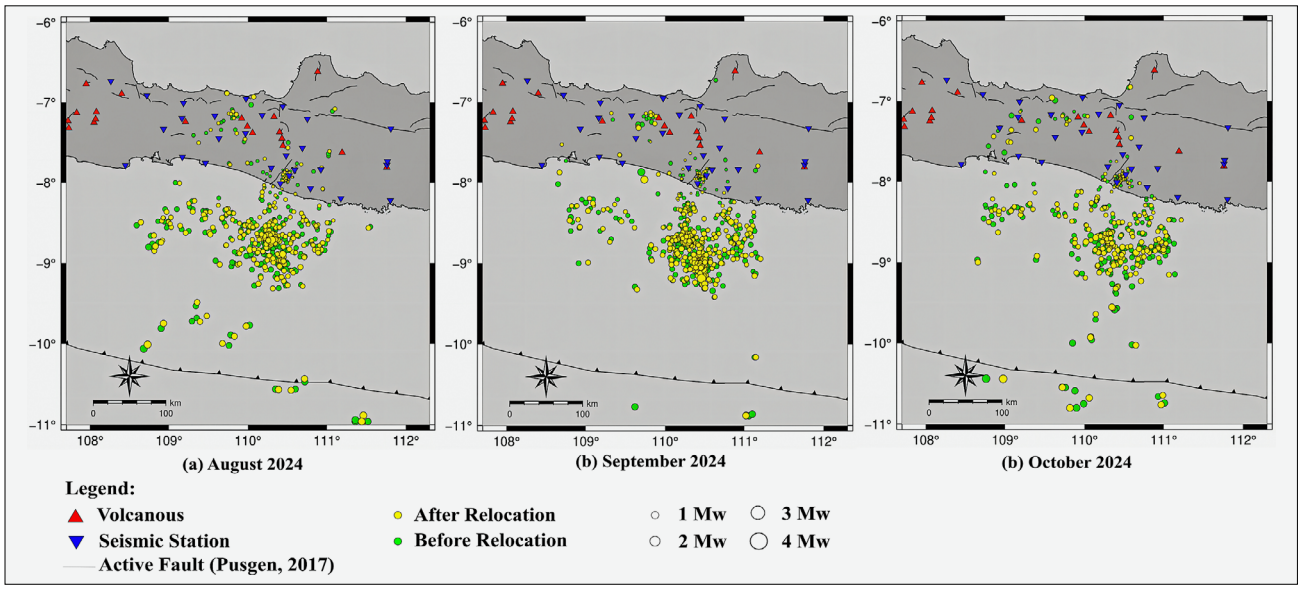


Figure 5. Spatial distribution map of hypocenters before (green circles) and after (yellow circles) relocation. The size of each circle is proportional to the moment magnitude of the event.

The proportion of data classified as outliers was relatively low, accounting for 1% in August (756 pairs) and September (843 pairs), and 0% in October (266 pairs). After filtering, the number of P-wave phase pairs used for relocation was 13,801 (54%) in August, 15,100 (54%) in September, and 9,968 (55%) in October. Likewise, the number of S-wave phase pairs used was 12,301 (56%), 11,230 (54%), and 8,835 (57%), respectively. Regarding the connectivity between events, a number of earthquakes were found to be weakly connected, with 33 events (8%) in August, 21 events (4%) in September, and 17 events (6%) in October. The total number of earthquake pairs formed was 4,114 (August), 4,497 (September), and 2,938 (October), with an average number of phase records per pair being 6, 5, and 6, respectively.

Figure 4 depicts the distribution of earthquake hypocenter positions in August 2024, September 2024, and October 2024. The green circles on the maps reflect the hypocenter positions before and after relocation, whereas the yellow circles represent the hypocenter positions following relocation. Each circle's size corresponds to the magnitude of the earthquake. Magnitudes range from 1 Mw to ≥ 4 Mw, as represented by varying circle sizes. Volcanic locations are indicated by red triangles, whereas seismic stations are represented by blue triangles. **Figure 4a** illustrates the distribution of seismic events in August 2024, **Figure 4b** depicts the distribution for September 2024, and **Figure 4c** represents the distribution for October 2024. In August 2024, 393 earthquake events were initially recorded. After processing with ph2dt, the dataset was reduced to 392 events, and after relocation with hypoDD, 354 events remained. In September 2024, 424 events were initially recorded, which became 421 after ph2dt processing and 391 after hypoDD relocation. In October 2024, the original 276 events were reduced to 275 after ph2dt and finally to 257 events after relocation using hypoDD.

3. Results and Discussion

3.1. Distribution of Hypocenter Locations Before and After Relocation

The distribution of hypocenters during the observation period is shown in the Comparison Maps of Hypocenter Positions Before and After Relocation for August, September, and October 2024 (see **Figure 5**). In these maps, the green circles illustrate the hypocenter locations before relocation, whereas the yellow circles denote the positions following the relocation process. The diameter of each circle reflects the magnitude of the earthquake, with larger circles indicating magnitudes of 1 Mw, 2 Mw, 3 Mw, and ≥ 4 Mw, respectively. In the study area, the red triangular symbols mark the active volcanoes, whereas the blue triangles represent the seismic stations utilized for data collection. This visualization effectively showcases the spatial distribution and magnitude of seismic events, while also delivering crucial insight for analyzing earthquake occurrence patterns and their connection to geological structures. Additionally, it highlights the distribution of seismic stations, which plays a vital role in enhancing the accuracy of hypocenter determination. The map illustrates the hypocenter's position before and after the relocation, suggesting that the hypocenter seems more concentrated and centralized. A rose diagram, as seen in **Figure 6**, is constructed to determine the direction of the shift in hypocenter relocation.

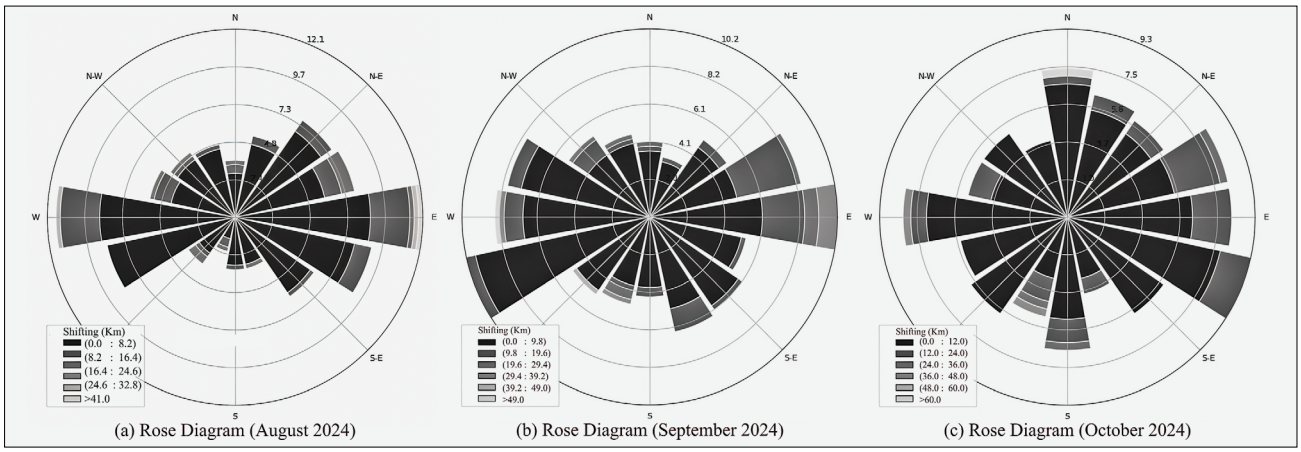


Figure 6. Rose diagrams of hypocenter location shifting after relocation, with colour indicating the displacement distance: (a) August 2024, (b) September 2024, and (c) October 2024.

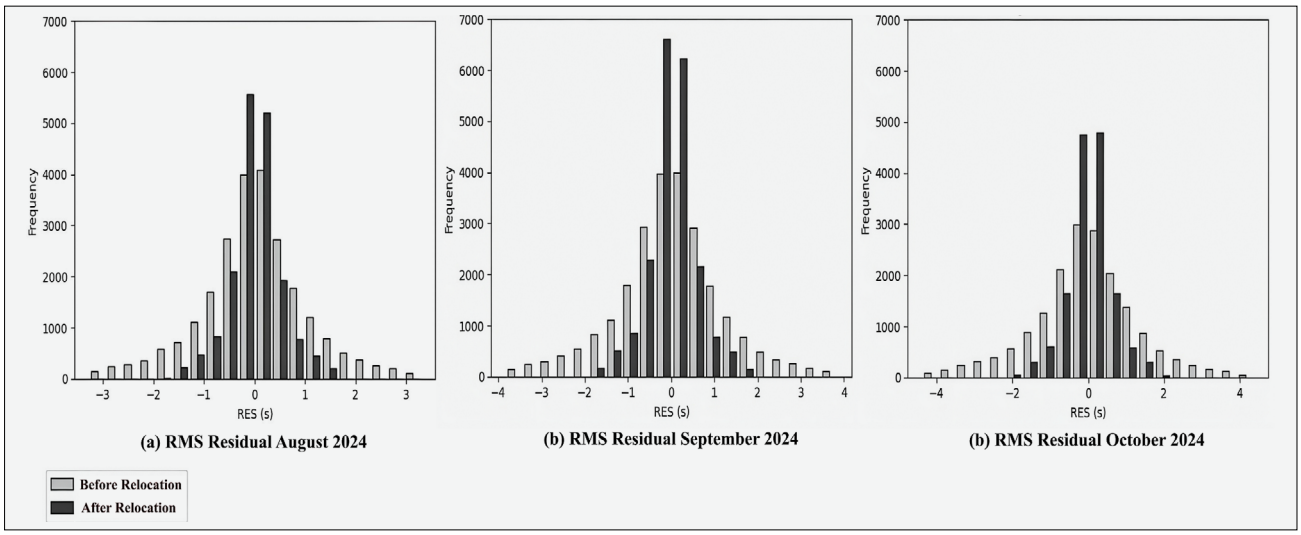


Figure 7. Histogram Comparison of Travel Time Residuals Before and After Relocation: (a) RMS August 2024, (b) RMS September 2024, and (C) RMS October 2024. Greyscale bars represent the travel time residuals before relocation, while black bars indicate the travel time residuals after relocation.

The depiction of the shift pattern of the earthquake hypocenter position after being relocated by the DD method can be seen in **Figure 6**. The data used in making this rose diagram are latitude and longitude data before relocation with latitude and longitude data after relocation. The distance and azimuth shift values can be calculated using the Haversine formula. **Figure 6** shows the shift in hypocenter position after relocation in August 2024, September 2024, and October 2024. Green to yellow colours indicate the distance of the hypocenter position shift after relocation, from 0 km to > 60 km. The diameter of the circle indicates the frequency of the data in its azimuthal direction (N, N-E, E, S-E, S, S-W, W, and N-W). **Figure 6** shows the rose diagram of the shift of the hypocenter position after relocation. The rose diagram shows that the position of the hypocenter has shifted in all directions. In August 2024, the hypocenter position shift tends to azimuth between 85˚ - 95˚ to the east and azimuth between 265˚ - 275˚ to the west with a shift distance of 0 to > 41 km. In September 2024, the hypocenter position shift tends to azimuth between 50˚ - 104˚ to the east and azimuth between 240˚ - 280˚ to the west with a shift distance of 0 to > 49 km. In October 2024, the hypocenter position shift tends to azimuth between 50˚ - 110˚ to the east and azimuth between 265˚ - 275˚ to the west with a shift distance of 0 to > 60 km. So that the tendency of shifting the position of the hypocenter for the period August-October 2024 tends to shift to the E- W direction

Figure 6 illustrates a comparative analysis of travel time residuals before and after the relocation process. The construction of the residual histogram aims to evaluate the accuracy of the relocation results. A residual value that approaches zero indicates that the calculated travel time is close to the actual travel time, which in turn suggests that the relocated hypocenter is closer to its true position. Greyscale bars represent the residuals before relocation, while black bars indicate the residuals

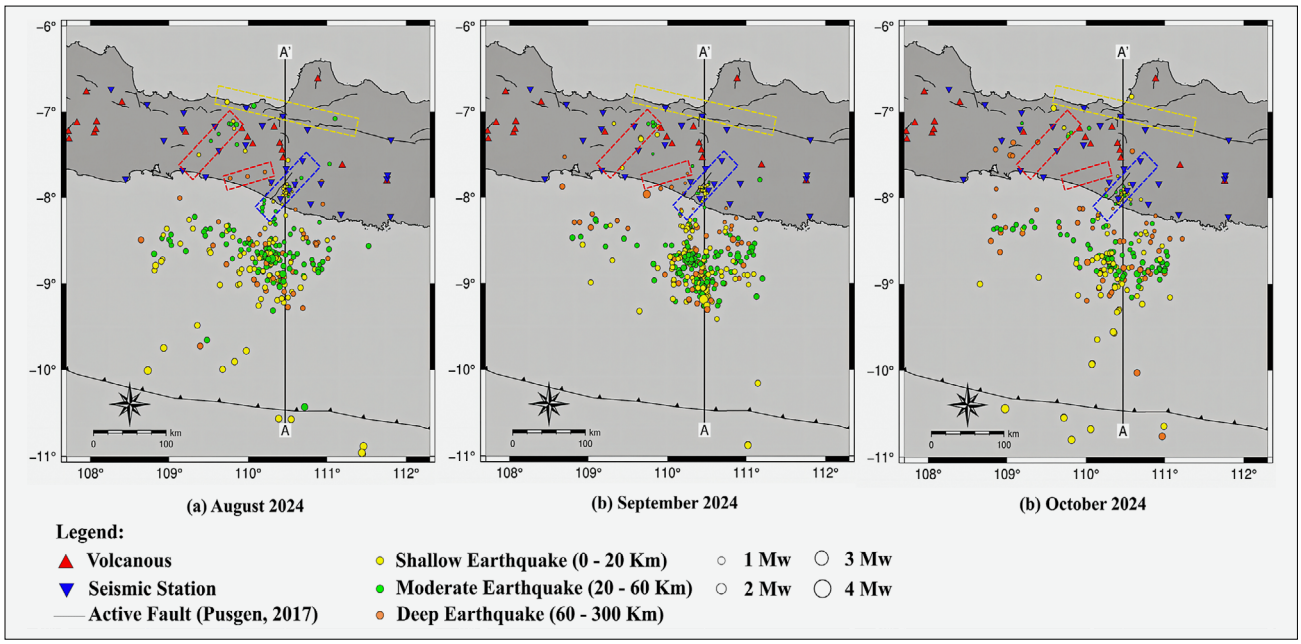


Figure 8. Seismicity maps based on relocated hypocenters in the Central Java and Yogyakarta regions are presented as follows: a) seismicity in August, b) seismicity in September, and c) seismicity in October 2024. The seismicity maps are overlaid with a cross-section A-A'. Yellow dots represent shallow earthquakes, green indicates moderate depth events, and orange corresponds to deep earthquakes. Blue triangles denote the distribution of seismic stations, while red triangles indicate the locations of volcanoes.

after relocation. Each month exhibits different residual frequency distributions, reflecting variations in data quality and event characteristics over time. The data used in generating these histograms consist of travel time residuals both before and after the relocation process. **Figure 7a** presents the travel-time residuals of the hypocenter before and after relocation for August 2024. The histogram shows that the residual values prior to relocation ranged from -3 s to 3 s. The frequency of residuals between -1 s and 1 s was approximately 18,000, while the frequency of residuals less than -1 s and greater than 1 s was around 3,800. After relocation, the residual values ranged from -1.7 s to 1.7 s. The frequency of residuals between -1s and 1s was approximately 16,000, whereas those beyond this range totaled around 1,900. **Figure 7b** shows the travel-time residuals of earthquakes before and after relocation for September 2024. The histogram indicates that the residuals before relocation ranged from -4 s to 4 s. The frequency of residuals within -1 s to 1 s was about 18,000, while those outside this range were approximately 3,800. After relocation, the residual values were within -1.9 s to 1.9 s, with around 18,000 residuals falling within -1 s to 1 s and only about 900 beyond that range. **Figure 7c** illustrates the travel-time residuals before and after relocation for October 2024. Before relocation, the residuals ranged from -4 s to 4 s. The number of residuals between -1 s and 1 s was approximately 13,000, while those outside this range numbered around 3,800. After relocation, the residual range narrowed to -2 s to 2 s, with around 16,000 residuals between -1 s and 1 s and about 2,500 outside that range. The results after relocation show better accuracy for the earthquake hypocenter, as the data shows that the residuals are more closely grouped around zero in every month. This implies that the positions of the earthquake hypocenters are getting closer to their actual locations (**Hidayat et al., 2021**).

3.3. Seismicity Characteristics of the Central Java and Yogyakarta Region

Figure 8 displays the relocated hypocenter locations. The size of the circular symbols represents the earthquake magnitude, while the colour indicates the depth. From the smallest to the largest, the circles correspond to magnitudes of 1 Mw, 2 Mw, 3 Mw, and ≥ 4 Mw, respectively. Yellow indicates shallow earthquakes (0-20 km), green represents moderate depth earthquakes (20-60 km), and orange indicates deep earthquakes (> 60 km). The red triangles mark the locations of volcanoes, while the blue triangles represent the positions of seismic stations. We observed fluctuations in the number of earthquake events over the course of three months in the Central Java and Yogyakarta regions. In August, a total of 354 earthquake events were recorded, consisting of 121 shallow earthquakes, 189 moderate depth earthquakes, and 44 deep earthquakes. In September, there was an increase in the number of events, particularly in shallow earthquakes, which rose from 121 in August to 161 events. In contrast, the number of moderate depth earthquakes decreased from 189 to 175 events, while deep earthquakes increased from 44 to 55 events. The

total number of earthquake events in September reached 391. In October, a significant decrease in the number of events was observed, especially in shallow and moderate depth events. A total of 257 earthquakes were recorded during this month, comprising 101 shallow events, 103 moderate depth events, and 53 deep events. The spatial distribution of earthquakes is primarily concentrated in the Central Java and Yogyakarta regions, especially along the Baribis - Kendeng Fault (yellow box) and the Opak Fault Zone (blue box), according to active fault data from the National Center for Earthquake Studies (**Damanik et al., 2021; Gunawan and Widiyantoro, 2019; Novianto et al., 2021; Pratama et al., 2021; Saputra et al., 2021; Tsuji et al., 2009**). Furthermore, there are clusters of seismic occurrences that have not been correlated with any recognized active fault, indicated by the red boxes (see **Figure 8**).

Seismic activity is prominently detected in the Baribis - Kendeng Fault zone. The existence of an active Baribis Fault extending eastward from the Sunda Strait together with a Kendeng Fault traversing from West Java to the east (**Damanik et al., 2021; Gunawan and Widiyantoro, 2019**). This fault extends from East Java to West Java, the Kendeng Fault segment dominates in the eastern and central parts, while the Baribis Fault is in the western part. The Kendeng-Baribis Fault is part of a back-arc thrust system in northern Java formed by the collision of the Indo-Australian Plate with the Eurasian Plate (**Koulali et al., 2017; Raharja et al., 2024**). The results of a recent study conducted by **Damanik et al., (2021)**, mainly using a network of borehole seismometers deployed around the Baribis segment from 2019 to 2021, have identified a number of small earthquake events with magnitudes of 2 - 4 Mw that are closely located, showing an earthquake event on December 10, 2019, with a magnitude moment of 3.0 Mw and on March 29, 2020, of 3.2 Mw. An earthquake occurred on August 3, 2024, with a moment magnitude of 2.3 Mw, situated north of the Baribis - Kendeng Fault (see **Figure 8a** and **Figure 8c**). Subsequently, a comparable event transpired south of the same fault zone on October 20, 2024, registering a moment magnitude of 2.6 Mw. These results indicate persistent tectonic activity along the Baribis - Kendeng Fault. Despite the relatively small magnitude, the event's location and mechanism furnish direct evidence of the seismotectonic activity of the Baribis - Kendeng Fault segment.

The upcoming seismic cluster is located in the Central Java and Yogyakarta regions, with a SW-NE orientation. Administratively, it covers Kebumen Central Java and Kulon Progo Yogyakarta. Based on the direction and distribution pattern of earthquake occurrences, we assume that the cluster in the Kebumen area is associated with the Meratus Pattern, also known as the Kebumen - Meratus Trend (**Satyana, 2008**), which extends as far as Kalimantan. Other researchers have referred to this fault as the Central Java Fault (CJF) (**Hall et al., 2007; Hoffmann-Rothe et al., 2001**). Seismic activity in this area is relatively intense, with earthquakes occurring at shallow to moderate depths. **Satyana (2008)** identified the Muria-Kebumen Fault in Central Java as one of the main Paleogene structures that has a SW-NE orientation and left-lateral strike-slip characteristics. This structure is also referred to as the Meratus Trend due to its alignment and possible tectonic linkage with the structural line of the Meratus Mountains in Kalimantan. From a seismological perspective, this SW-NE orientation has the potential to play a role in controlling the direction of propagation and segmentation of earthquake sources in the southern region of Central Java. The tectonic linkage between the Meratus Trend indicates a structural continuity formed since the Paleogene, which then experienced reactivation due to Quaternary tectonic forces. Seismic activity was recorded in August 2024 and continued to decline until October 2024, with a moment magnitude > 3 Mw with shallow to moderate depth. The results of research from **Novianto et al. (2025)** showed a low Bouguer anomaly value in the direction of the Kebumen - Meratus Trend. The evidence of this earthquake cluster reinforces that this zone is likely to contain active faults that have not been mapped by the National Earthquake Study Center.

Moving eastward, specifically in the Kulon Progo region of Yogyakarta, there is a noticeable concentration of earthquake events with a dominant SW - NE orientation. These events were particularly active during August and September 2025. Unlike the cluster located further west, this cluster consists predominantly of deep focus earthquakes. Previous studies have identified this cluster as part of the Progo - Muria Lineament adapted from (**Hall et al., 2007; Novianto et al., 2025**), a tectonic lineament that extends from south to north and continues toward the Muria Mountains. This lineament is referred to as the inferred Progo - Muria Lineament or the strikeslip Central Java Fault. The frequency of seismic occurrences in the Kulon Progo area of Yogyakarta signifies a busy tectonic zone characterized by intricate geodynamics. Deep earthquakes dominate this cluster, contrasting with shallow seismicity in the surrounding area, and indicate the involvement of subcrustal processes that may relate to the geometry of the subduction slab beneath southern Central Java. The temporal clustering of seismic events in August and September 2025 confirms the potential for episodic stress release patterns, which may be influenced by regional plate convergence and local fault kinematics.

From a hazard perspective, the Progo - Muria Lineament has the potential to generate medium to large magnitude earthquakes with a significant horizontal movement component, which can create building damage. Although deep-focused earthquakes generally produce lower shaking intensity at the surface than shallow earthquakes, their proximity to densely populated areas increases the potential for cumulative hazards, especially

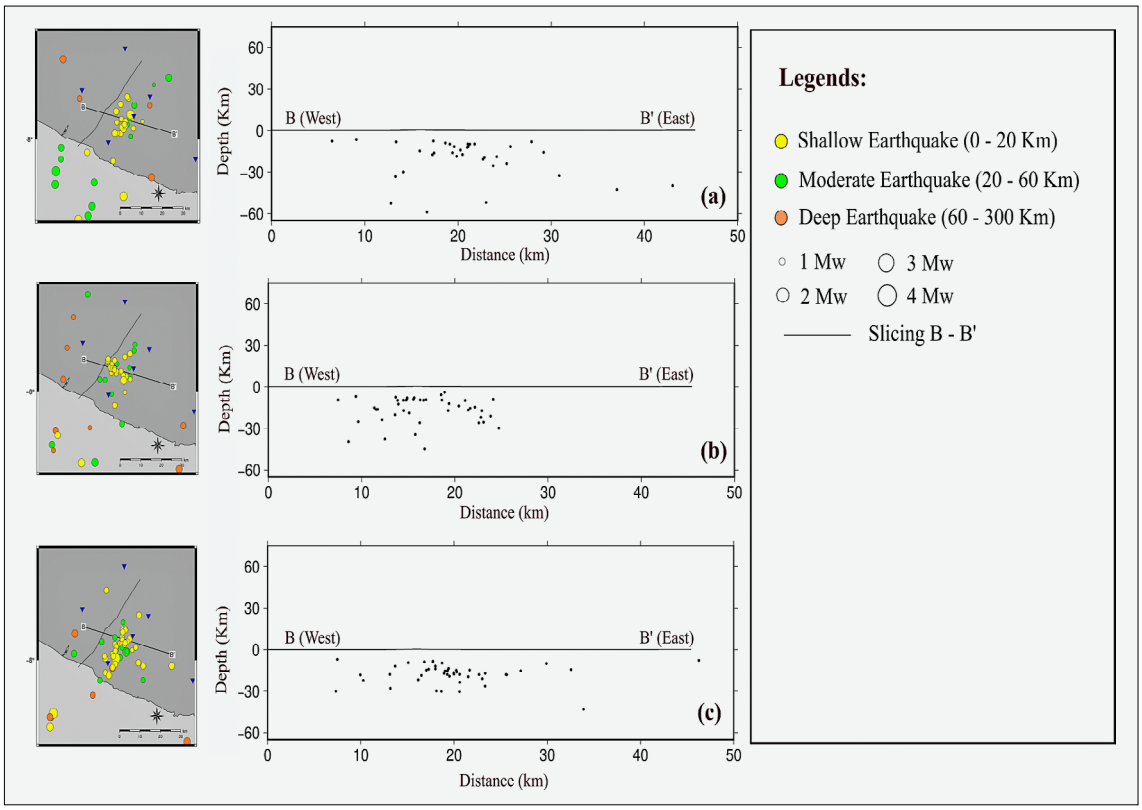


Figure 9. Vertical cross-section along profile B-B' depicting seismicity distribution for (a) August 2024, (b) September 2024, and (c) October 2024 inside the Opak Fault Zone section and surrounding areas.

if accompanied by possible triggering of shallow seismicity. The SW-NE orientation of this seismic cluster corresponds with the structural directions of several active faults in Central Java, enhancing concerns regarding the potential for fault to fault rupture propagation during significant events. Due to its tectonic significance and recurrent seismic activity, the Progo - Muria Linement line should be considered one of the main sources of seismic hazards in regional disaster risk assessments. This requires continuous seismic monitoring to identify changes in activity rate or hypocenter depth distribution, detailed fault mapping and paleoseismological studies to estimate its return interval and shear rate, and integration of this fault line into a probabilistic seismic hazard model for Central Java.

The persistent seismic pattern east of the Opak Fault Zone, characterized by earthquake events distributed approximately 5-10 km from its primary trace and aligned SW-NE, demonstrates the intricate nature of fault interactions in this area. While **Ramdhan et al. (2020)** noted that the Opak Fault Zone inclines to the east, cross-sectional analysis indicates that the recorded seismicity does not exhibit a distinct cluster directly on the fault plane. Instead, the eastward distribution of hypocenters points to the possible involvement of secondary fault segments or other structures in the vicinity, such as the Oyo Fault or Ngalang Fault (see **Figure 9**). From a hazard perspective, the proximity of these seismic sources to the Opak Fault Zone indicates the possibility of an interconnected fault network with the potential to produce damaging earthquakes. Multiple fault interactions, including stress transfer from one segment to another, may increase the probability of complex rifting scenarios extending beyond the main line of the Opak Fault Zone. The circumstances could contribute to increased fault lengths, higher magnitudes, and extended areas of strong shaking, particularly if the displacement crosses the fault border.

The location of seismic events in areas with high population density has direct implications for increasing seismic risk levels. Residential areas located along the Opak Fault Zone covering the Bantul, Sleman, and Gunungkidul regencies have a significant level of vulnerability. The presence of thick volcanic deposits around Yogyakarta has the potential to cause seismic wave amplification, which in turn can magnify the intensity of shaking and exacerbate infrastructure damage. Analysis of the events following the 2006 Yogyakarta earthquake shows that fatalities were generally caused by building collapses rather than by the earthquake shaking itself. Meanwhile, most of the injuries occurred as a result of mass panic and lack of preparedness. This confirms that structural and non-structural vulnerability factors play a major role in determining the level of damage and the number of casualties. Within the framework of disaster risk management, adequate investment is needed in Dis-

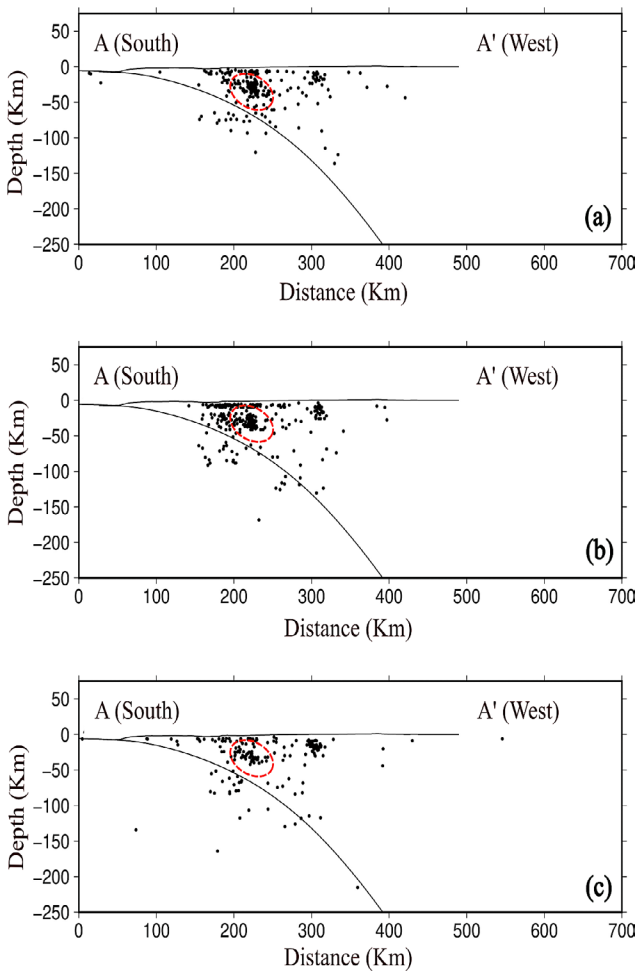


Figure 10. Vertical cross-sections along profile A-A' depicting the seismicity distribution for (a) August 2024, (b) September 2024, and (c) October 2024, overlay on the Slab 1.0 model (**Hayes et al., 2012**).

aster Risk Reduction (DRR) programs that include improving the quality of earthquake-resistant buildings, hazard-based spatial planning, and community education. In areas that have been affected by disasters, the application of the build back better and safer principle is very important in the rehabilitation and reconstruction phases to ensure that the rebuilt infrastructure is more resilient to future seismic events.

The A-A' cross-sectional profiles for August, September, and October 2024 are presented in **Figure 7**. These profiles are correlated with the Slab 1.0 model (**Hayes et al., 2012**). **Figure 8** shows a vertical cross-section along A-A', cutting through the subduction zone from south to north and intersecting the Opak Fault Zone. The results reveal a distribution of hypocenters that follows a sharply dipping subducting slab. This steep slab geometry is likely associated with the relatively old age of the oceanic plate (**Pesicek et al., 2008**). In September, a concentration of seismic events is observed at a depth of approximately 50 km, indicated by red circles. This pattern corresponds to increased seismicity in the offshore region south of Java during that month, as shown in **Figure 10**. The concentration of seismicity at depths of roughly 50 km, which coincides with increased activity off the southern coast of Java, indicating a risk from intermediate crustal earthquakes. Earthquakes at this depths can generate significant shaking in coastal areas, including the potential for seabed deformation and local tsunamis, especially if the process involves upward fault movement in accretionary prisms (**Aribowo et al., 2022; Xu et al., 2015**). The identification of shallow earthquake clusters associated with backthrust structures also adds to the complexity of the hazard source. Although generally relatively small in size, backthrust earthquakes occurring near the surface can cause high shaking intensity in the coastal zone and southern mainland of Yogyakarta, given their proximity to the population. In the Java subduction zone, the main thrust dips northward, consistent with the dominant tectonic stress orientation across the island. Between depths of 50 and 250 km, a cluster of earthquakes is distributed along the slab interface. These are intraslab earthquakes, occurring within the subducting oceanic plate along the Java Benioff Zone. Their distribution forms an inclined pattern that aligns with the subduction dip. Such seismicity is generally attributed to slab-pull forces acting within the descending plate (**Lallemand et al., 2005**).

According to the discussion, it can be concluded that the Central Java and Yogyakarta regions are located in a complex tectonic environment, influenced by the interaction of multiple earthquake sources ranging from the main subduction zone, shallow crustal faults such as Baribis - Kendeng and Progo - Muria Lineament, to local faults around Opak Fault Zone. According to our analysis of the Progo - Muria lineament, seismic activity in August and September belonged to the category of deep earthquakes, which is different from the pattern on the Kebumen-Meratus Trend that is dominated by shallow to medium earthquakes. We identified that the earthquake events in that period were more caused by subduction/deep earthquake activity, and not from the Progo - Muria lineament. Hence, a seismic data sequence with a longer recording period is needed to confirm whether the earthquakes actually originated from the Progo - Muria lineament. The presence of shallow earthquakes on accretionary prisms, intermediate crustal earthquakes at depths of around 50 km, and intraslab earthquakes at depths >50 km creates a diverse spectrum of threats, both in terms of shaking intensity, potential infrastructure damage, and tsunami risk. Seismicity patterns distributed according to regional structural orientation show the existence of linkages between earthquake sources that have the potential to trigger compound fault scenarios. This condition requires the integration of the latest seismotectonic data, modelling of multisource shaking scenarios, and detailed mapping of active fault lines in the preparation of seismic hazard maps. In addition, disaster mitigation should focus on improving building resilience, strengthening hazard-based spatial

planning, and educating the public to minimize the risk of casualties and material losses when large earthquakes occur in the future.

Subduction zone earthquakes have a significant potential to trigger liquefaction, particularly in coastal and lowland areas characterized by loose sediments, water saturated sands, and alluvial deposits. Liquefaction occurs when pore water pressure increases due to dynamic earthquake loading, causing the soil to lose its shear strength and behave like a fluid The 2018 Palu earthquake serves as a notable example in Indonesia, where widespread liquefaction induced massive lateral ground displacements and extensive infrastructure damage (**Cilia et al., 2021; Susanta et al., 2019; Upomo et al., 2023**). Similarly, research in Bengkulu has shown that the 2007 subduction earthquake had the potential to trigger shallow liquefaction in coastal zones (**Mase et al., 2024; Mase et al., 2025**). As shown by research in Mae Lao and Bengkulu, soil conditions with low shear wave velocities (Vs) have been shown to increase seismic wave amplification and liquefaction potential in shallow water-saturated sand layers (**Mase et al., 2020; Mase et al., 2024**). Similar phenomena are particularly relevant in Yogyakarta, which is composed of young volcanic deposits and unconsolidated alluvium, making it vulnerable to ground deformation during large earthquakes. Therefore, seismic hazard mitigation in this region needs to be conducted comprehensively, including microtremor measurements, horizontal to vertical spectral ratio (HVSR) analysis, shear wave velocity inversion, as well as microzonation mapping to determine liquefaction-prone and amplification zones. From a hydrogeological perspective, Yogyakarta is underlain by shallow aquifers with relatively high groundwater tables, as well as unconsolidated volcanic sand deposits derived from Mount Merapi eruptions. These conditions significantly increase susceptibility to pore water pressure buildup during strong ground shaking, thereby amplifying the likelihood of liquefaction.

In addition to strong ground shaking, earthquakes originating from the Opak Fault and other active fault systems in Central Java and Yogyakarta can trigger secondary geotechnical hazards such as liquefaction, especially in areas composed of unconsolidated alluvial and volcanic deposits (**Mase et al., 2024; Mase et al., 2025**). The 2006 Yogyakarta earthquake, for example, caused several liquefaction and lateral displacement events in the Bantul area and surrounding low-lying areas, indicating that the soil characteristics in this region are highly susceptible to increased pore pressure during seismic shaking. Recent studies have also emphasized that zones composed of young volcanic sediments and water-saturated sand layers common in the Yogyakarta Basin are highly susceptible to such failure mechanisms. Yogyakarta and Central Java, as well as other cities such as Bengkulu, Palu, which have been studied previously, exhibit high earthquake hazard potential due to active seismotectonic conditions, soft soil characteristics, and the presence of local faults such as the Opak Fault (**Mase et al., 2024; Mase et al., 2025**). The results of this study, which refine the spatial distribution of local seismicity and map active fault segments, are critical for identifying high-risk zones for liquefaction. The integration of these seismotectonic insights into liquefaction hazard modelling will improve the precision of the microzonation maps and provide a stronger basis for the design of earthquake-resistant structures, infrastructure planning, as well as community-based mitigation strategies aimed at reducing the cascading impacts of future seismic events in the Central Java and Yogyakarta regions. Collectively, these findings underscore that the interplay between subduction driven earthquakes, hydrogeological conditions, and local volcanic sediments plays a critical role in shaping liquefaction hazards. Therefore, integrated analyses combining seismotectonic data, groundwater conditions, and local geological characteristics are essential to improve the accuracy of hazard mapping and to strengthen disaster mitigation strategies in Indonesia's subduction prone regions.

5. Conclusions

Significant activity is identified on the Baribis-Kendeng Fault, Kebumen-Meratus Trend (Central Java Fault), and Progo-Muria Lineament, each of which exhibits different fault mechanism characteristics and hypocenter depths varying from shallow, medium to deep. In addition, the distribution of seismicity around the Opak Fault Zone and associated structures (Oyo Fault, Ngalang Fault) confirms the existence of a complex fault network with potential inter-segment interaction and stress transfer, which has implications for multisegment earthquake scenarios. In the southern subduction zone of Java, the distribution of hypocenters shows a steep slab geometry, with a concentration of intermediate crustal earthquakes around 50 km deep and a cluster of intraslab earthquakes at 50–250 km depth. This activity is related to slab-pull forces and tectonic mechanisms in accretionary prisms and backthrust structures. The combination of nearshore shallow earthquakes, intermediate crustal earthquakes, and intraslab earthquakes broadens the hazard spectrum, including the potential for strong shaking, amplification of seismic waves due to thick volcanic deposits, local tsunamis in the event of seafloor deformation, and secondary hazards such as liquefaction in areas underlain by young alluvial deposits, volcanic sediments, and shallow aquifers. Moreover, several active faults that have not yet been officially mapped in the Indonesian Earthquake Source and Hazard Map (PUSGEN) may also pose a serious threat to the Central Java and Yogyakarta regions. Therefore, urgent attention and policy support from the government are required to update fault inventories, strengthen seismic hazard assessments, and integrate these findings into national disaster mitigation

strategies. The findings confirm that seismic hazard modelling in Central Java and Yogyakarta should consider the multisource and multimechanism nature of earthquakes, with data integration into probabilistic models, detailed mapping of active earthquake sources, and simulation of shaking, liquefaction, and tsunami scenarios. This approach is needed to update risk maps, support hazard-based spatial planning, and improve infrastructure resilience and community preparedness.

Acknowledgement

The authors would like to thank the Meteorology, Climatology, and Geophysics Agency (BMKG) Banjarnegara for supplying the seismic data utilized in this work. Their assistance and data submission were critical to the accomplishment of this research. This paper represents one of the outcomes of the research collaboration agreement between BMKG and UPN "Veteran" Yogyakarta.

Funding

This research was supported by funding from the Institute for Research and Community Service (LPPM), UPN "Veteran" Yogyakarta, under Grant No. 422/UN 62.21/PG.00.00/2025, awarded to Wahyu Hidayat.

6. References

Amin, T., N. Ratman, & S. Gafoer. (1999). *Geological Map of Middle Part of Java* [Map]. Geological Research and Department Centre.

Aribowo, S., Husson, L., Natawidjaja, D. H., Authemayou, C., Daryono, M. R., Puji, A. R., Valla, P. G., Pamumpuni, A., Wardhana, D. D., De Gelder, G., Djarwadi, D., & Lorcery, M. (2022). Active Back-Arc Thrust in North West Java, Indonesia. *Tectonics*, *41*(7), e2021TC007120. https://doi.org/10.1029/2021TC007120

Cilia, M. G., Mooney, W. D., & Nugroho, C. (2021). Field Insights and Analysis of the 2018 Mw 7.5 Palu, Indonesia Earthquake, Tsunami and Landslides. *Pure and Applied Geophysics*, *178*(12), 4891–4920. https://doi.org/10.1007/s00024-021-02852-6

Damanik, R., Supendi, P., Widiyantoro, S., Rawlinson, N., Ardianto, A., Gunawan, E., Husni, Y. M., Zulfakriza, Z., Sahara, D. P., & Shiddiqi, H. A. (2021). Earthquake monitoring of the Baribis Fault near Jakarta, Indonesia, using borehole seismometers. *Geoscience Letters*, *8*(1), 38. https://doi.org/10.1186/s40562-021-00209-4

Garini, S. A., Madlazim, & Rahmawati, E. (2014). Relokasi Hiposenter Gempa Bumi Di Sulawesi Tengah Dengan Menggunakan Metode Geiger Dan Coupled Velocity-Hypocenter. *Jurnal Fisika*, *3*(2), 107–112. https://doi.org/10.26740/ifi.v3n2.p%25p

Gunawan, E., & Widiyantoro, S. (2019). Active tectonic deformation in Java, Indonesia inferred from a GPS-derived strain rate. *Journal of Geodynamics*, *123*, 49–54. https://doi.org/10.1016/j.jog.2019.01.004

Hall, R., Clements, B., Smyth, H. R., & Cottam, M. A. (2007). *A new interpretation of Java's structure*. https://archives.datapages.com/data/ipa_pdf/078/078001/pdfs/IPA07-G-035.pdf

Hayes, G. P., Wald, D. J., & Johnson, R. L. (2012). Slab1. 0: A three-dimensional model of global subduction zone geometries. *Journal of Geophysical Research: Solid Earth*, *117*(B1). https://doi.org/10.1029/2011JB008524

Hidayat, W., Sahara, D. P., Widiyantoro, S., Putu Raditya Ambara Putra, I., Shihab, N. H., Amalia, R., Harisandi, A., & Suharsono. (2021). Analysis of Hypocenter Relocation by Using Double Difference Method in a Deep Underground Mining. *IOP Conference Series: Earth and Environmental Science*, *873*(1), 012099. https://doi.org/10.1088/1755-1315/873/1/012099

Hidayat, W., Sahara, D. P., Widiyantoro, S., Suharsono, S., Riyanto, E., Nukman, M., Wattimena, R. K., Melati, S., Sitorus, E., Nainggolan, T., & Putra, I. P. R. A. (2024). 4D time lapse tomography for monitoring cave propagation and stress distribution in Deep Mill Level Zone (DMLZ) PT Freeport Indonesia. *Geomechanics and Geophysics for Geo-Energy and Geo-Resources*, *10*(1), 39. https://doi.org/10.1007/s40948-023-00718-w

Hidayat, W., Sahara, D. P., Widiyantoro, S., Suharsono, S., Wattimena, R. K., Melati, S., Putra, I. P. R. A., Prahastudhi, S., Sitorus, E., & Riyanto, E. (2022). Testing the Utilization of a Seismic Network Outside the Main Mining Facility Area for Expanding the Microseismic Monitoring Coverage in a Deep Block Caving. *Applied Sciences*, *12*(14), 7265. https://doi.org/10.3390/app12147265

Hoffmann-Rothe, A., Ritter, O., & Haak, V. (2001). Magnetotelluric and geomagnetic modelling reveals zones of very high electrical conductivity in the upper crust of Central Java. *Physics of the Earth and Planetary Interiors*, *124*(3–4), 131–151. https://doi.org/10.1016/S0031-9201(01)00196-0

Koulali, A., Mcclusky, S., Susilo, S., Leonard, Y., Cummins, P., Tregoning, P., Meilano, I., Efendi, J., & Wijanarto, A. B. (2017). The kinematics of crustal deformation in Java from GPS observations: Implications for fault slip partitioning. *Earth and Planetary Science Letters*, *458*, 69–79. https://doi.org/10.1016/j.epsl.2016.10.039

Lallemand, S., Heuret, A., & Boutelier, D. (2005). On the relationships between slab dip, back-arc stress, upper plate absolute motion, and crustal nature in subduction zones. *Geochemistry, Geophysics, Geosystems*, *6*(9). https://doi.org/10.1029/2005GC000917

Liu, Y., Gu, Y., & Zhang, H. (2024). Seismic risk assessment and damage analysis: Emerging trends and new developments. *Journal of Safety Science and Resilience*, *5*(3), 365–381. https://doi.org/10.1016/j.jnlssr.2024.04.005

Mase, L. Z., Amri, K., Ueda, K., Apriani, R., Utami, F., Tobita, T., & Likitlersuang, S. (2024). Geophysical investigation on the subsoil characteristics of the Dendam Tak Sudah Lake site in Bengkulu City, Indonesia. *Acta Geophysica*, *72*(2), 893–913. https://doi.org/10.1007/s11600-023-01158-6

Mase, L. Z., Likitlersuang, S., Tobita, T., Chaiprakaikeow, S., & Soralump, S. (2020). Local site investigation of lique-

fied soils caused by earthquake in Northern Thailand. *Journal of Earthquake Engineering*, *24*(7), 1181–1204.

Mase, L. Z., Refrizon, Pakpahan, N. S., Shelina, A., Wu, J., & Chaiyaput, S. (2024). Site Characteristics of Musi Fault Zone in Kepahiang Urban Area, Bengkulu Province, Indonesia. *Transportation Infrastructure Geotechnology*, *11*(4), 2453–2482. https://doi.org//10.1007/s40515-024-00375-w

Mase, L. Z., Tanapalungkorn, W., Anussornrajkit, P., & Likitlersuang, S. (2025). Assessing liquefaction risk and hazard mapping in a high-seismic region: A case study of Bengkulu City, Indonesia. *Natural Hazards*, *121*(6), 6597–6623. https://doi.org/10.1007/s11069-024-07057-3

Mase, L. Z., Tanapalungkorn, W., Ueda, K., & Likitlersuang, S. (2025). Non-linear Site Response Analysis of Liquefaction in the Port Area of Bengkulu City Due to Large Subduction Earthquakes. *Transportation Infrastructure Geotechnology*, *12*(2), 87. https://doi.org/10.1007/s40515-025-00540-9

Muttaqy, F., Nugraha, A. D., Puspito, N. T., Sahara, D. P., Zulfakriza, Z., Rohadi, S., & Supendi, P. (2023). Double-difference earthquake relocation using waveform cross-correlation in Central and East Java, Indonesia. *Geoscience Letters*, *10*(1), 5. https://doi.org/10.1186/s40562-022-00259-2

Novianto, A., Hidayat, W., & Bintarto, B. (2025). Interception of Meratus and Java Trends Structures as Controlling the Emergence of the Purwodadi Mud Volcano Complex. *IOP Conference Series: Earth and Environmental Science*, *1458*(1), 012018. https://doi.org/10.1088/1755-1315/1458/1/012018

Novianto, A., Prasetyadi, C., & Hidayat, W. (2021). Mud Volcano: Revealing the Stratigraphy of Kendeng Basin, Indonesia. *Open Journal of Yangtze Oil and Gas*, *7*(1), 48–64.

Pratama, C., Widjajanti, N., Pinasti, A., Ummi, R., Lestari, D., Sunantyo, T. A., Heliani, L. S., & Ulinnuha, H. (2021). *A possible opak fault segment that caused the 2006 mw 6.3 yogyakarta earthquake and its future implication*. *683*(1), 012059.

Raharja, R., Ito, T., & Meilano, I. (2024). Evaluation of earthquake potential using a kinematic crustal block motion model in Java, Indonesia, based on GNSS observation. *Journal of Asian Earth Sciences: X*, *11*, 100171. https://doi.org/10.1016/j.jaesx.2023.100171

Ramdhan, M., Priyobudi, P., Kristyawan, S., & Sembiring, A. S. (2020). Seismisitas di Wilayah Jawa Tengah dan Sekitarnya Berdasarkan Hasil Relokasi Hiposenter dari Empat Jaringan Seismik Menggunakan Model Kecepatan 3-D. *Eksplorium*, *41*(1), 61. https://doi.org/10.17146/eksplorium.2020.41.1.5828

Saputra, H., Wahyudi, W., Suardi, I., Anggraini, A., & Suryanto, W. (2021). The waveform inversion of mainshock and aftershock data of the 2006 M6. 3 Yogyakarta earthquake. *Geoscience Letters*, *8*(1), 9.

Satyana, A. H. (2008). Mud Diapirs and Mud Volcanoes in Depressions of Java to Madura: Origins, Natures, and Implications to Petroleum System. *Proceedings of Indonesian Petroleum Association, Thirty-Second Annual Convention & Exhibition, 32, IPA08-G 139.*

Soehaimi, A. (2008). Seismotektonik dan Potensi Kegempaan Wilayah Jawa. *Indonesian Journal on Geoscience*, *3*(4), 227–240. https://doi.org/10.17014/ijog.vol3no4.20085

Susanta, F. F., Pratama, C., Aditya, T., Khomaini, A. F., & Abdillah, H. W. K. (2019). Geovisual Analytics of Spatio-Temporal Earthquake Data in Indonesia. *JGISE: Journal of Geospatial Information Science and Engineering*, *2*(2). https://doi.org/10.22146/jgise.51131

Syahbana, A. J., Iqbal, P., Irsyam, M., Asrurifak, M., & Hendriyawan, H. (2021). Smoothed gridded seismicity effect for land-use development, case study: Kalimantan Island, Indonesia. *Rudarsko-Geološko-Naftni Zbornik*, *36*(3).

Tsuji, T., Yamamoto, K., Matsuoka, T., Yamada, Y., Onishi, K., Bahar, A., Meilano, I., & Abidin, H. Z. (2009). Earthquake fault of the 26 May 2006 Yogyakarta earthquake observed by SAR interferometry. *Earth, Planets and Space*, *61*(7), e29–e32. https://doi.org/10.1186/BF03353189

Um, J., & Thurber, C. (1987). A Fast Algorithm for Two-Point Seismic Ray Tracing. *Bulletin of the Seismological Society of America*, *77*(3), 972–986. https://doi.org/10.1785/BSSA0770030972

Upomo, T. C., Chang, M., Kusumawardani, R., Prayitno, G. A., Kuo, C.-P., & Nugroho, U. (2023). Assessment of Petobo Flowslide Induced by Soil Liquefaction during 2018 Palu–Donggala Indonesian Earthquake. *Sustainability*, *15*(6), 5371. https://doi.org/10.3390/su15065371

Wagner, D., Koulakov, I., Rabbel, W., Luehr, B.-G., Wittwer, A., Kopp, H., Bohm, M., Asch, G., & MERAMEX scientists. (2007). Joint inversion of active and passive seismic data in Central Java. *Geophysical Journal International*, *170*(2), 923–932.

Waldhauser, F. (2001). *hypoDD -- A Program to Compute Double-Difference Hypocenter Locations (hypoDD version 1.0—03/2001)*.

Waldhauser, F., & Ellsworth, W. L. (2000). A double-difference earthquake location algorithm: Method and application to the northern Hayward fault, California. *Bulletin of the Seismological Society of America*, *90*(6), 1353–1368.

Xu, S., Fukuyama, E., Ben-Zion, Y., & Ampuero, J.-P. (2015). Dynamic rupture activation of backthrust fault branching. *Tectonophysics*, *644*, 161–183.

Zhang, H. (2003). Double-Difference Tomography: The Method and Its Application to the Hayward Fault, California. *Bulletin of the Seismological Society of America*, *93*(5), 1875–1889. https://doi.org/10.1785/0120020190

Zhang, H., & Thurber, C. (2006). Development and Applications of Double-difference Seismic Tomography. *Pure and Applied Geophysics*, *163*(2–3), 373–403. https://doi.org/10.1007/s00024-005-0021-y

Zulfakriza, Z., Nugraha, A. D., Heryandoko, N., Ry, R. V., Muttaqy, F., Andika, A., Azhari, M. F., Putra, A. S., Palgunadi, K. H., Cummins, P. R., Supendi, P., Lesmana, A., Sahara, D. P., & Puspito, N. T. (2024). Seismic source analysis of the destructive earthquake November 21, 2022, Mw 5.6 Cianjur (Indonesia) from relocated aftershock. *Scientific Reports*, *14*(1), 12142. https://doi.org/10.1038/s41598-024-60408-9

SAŽETAK

Poboljšanje relociranja hipocentra u svrhu evaluacije seizmičkoga hazarda u Središnjoj Javi i Yogyakarti, Indonezija: nalazi iz kataloga potresa BMKG-a za razdoblje kolovoz – listopad 2024.

U radu je predstavljena analiza relociranja hipocentra s ciljem identifikacije raspodjele seizmičnosti u regijama Središnje Jave i Yogyakarte u Indoneziji. Podatci su dobiveni iz baze podataka o potresima BMKG-a za razdoblje od kolovoza do listopada 2024. godine pokrivajući područje između 6,0° – 11,0° J i 108,5° – 111,6° I. Skup podataka podijeljen je u tri mjesečne skupine kako bi se promatrali prostorni i vremenski obrasci izvora potresa u području istraživanja. Analiza je provedena preklapanjem pomaknutih hipocentara, karata aktivnih rasjeda i obrazaca subdukcije u Južnoj Javi, što je omogućilo jasniju karakterizaciju izvora potresa. Podatci od kolovoza do listopada 2024. godine, koji obuhvaćaju 393, 424 i 276 potresnih događaja, analizirani su metodom dvostruke razlike na temelju 26 610 – 19 429 parova P-valova i 21 447 – 15 933 parova S-valova zabilježenih na 28 seizmičkih postaja. Rezultati su pokazali znatnu aktivnost duž rasjeda Baribis – Kendeng, struktura Kebumen – Meratus i lineamenta Progo – Muria, pokazujući raznolike mehanizme rasjeda i dubine hipocentara, od plitkih do srednjih. Grupiranje u blizini zone rasjeda Opak i pridruženih struktura upućuje na složene interakcije rasjeda s potencijalnim prijenosom naprezanja između segmenata, dok seizmičnost na moru upućuje na strmo nagnutu subdukcijsku ploču s događajima srednjega do dubokoga fokusa (50 – 250 km). Kombinirana pojava plitkih, srednjih i dubokih unutarpločnih potresa proširuje regionalni spektar hazarda ističući rizike od jakoga podrhtavanja tla, povećanja intenziteta potresnih valova i lokalnih tsunamija. Rezultati potvrđuju važnost integriranja karakteristika potresa s više izvora i više mehanizama u probabilističke modele hazarda kako bi se poboljšalo prostorno planiranje, otpornost infrastrukture i spremnost zajednice.

Ključne riječi:
seizmički hazard, relociranje hipocentra, dvostruka razlika, aktivni rasjed

Author's contribution

Wahyu Hidayat: conceptualization, supervision, methodology, writing and interpretation, **Nanda Agustina** validation, processing and visualitation, **Ekalia Ardenti** data curation, software, resources supervision, validation, **Suharsono** original draft and writing, review and editing. **Ardian Novianto** project administration and review and editing. **Uli Ulfa** review and editing. **Maman Rohaman** software, resources supervision, **Herry Riswandi** writing and interpretation. All authors have read and agreed to the published version of the manuscript.

RGNZ/MGPB

Ore Genesis and Hydrothermal Evolution of the Cheshmeh-Hadi Stratabound (Manto-type) Copper Deposit in the Volcanic-Plutonic Belt North of the Doruneh Fault, East of the Sepid-Sarve copper deposit (NW Bardeskan, Central Iran): Evidence from Geology, Geochemistry, Fluid Inclusions, and Stable S and O Isotopes

Rudarsko-geološko-naftni zbornik
(The Mining-Geology-Petroleum Engineering Bulletin)
DOI: 10.17794/rgn.2026.3.11

Original scientific paper

Morteza Esform[1] ✉, Hasan Zamanian[2]* ✉, Alireza Zarasvandi[3] ✉, Alireza Almasi[1] ✉, Mahya Manouchehry Nia[1] ✉

[1] *Department of Geology, Faculty of Science, Lorestan University, Khorramabad, Iran.*
[2] *School of Geology, College of Science, University of Tehran, Tehran, 1417935840, Iran.*
[3] *Department of Geology, Faculty of Earth Sciences, Shahid Chamran University of Ahvaz, Ahvaz, Iran.*

Abstract

The Cheshmeh-Hadi copper deposit is part of an Eocene volcano-sedimentary sequence located in the southern Sabzevar Zone. The lithostratigraphic sequence, from oldest to youngest, comprises basalt, basaltic andesite, andesite and pyroxene andesite, conglomerate, limestone, siltstone, gypsiferous marl, and Pliocene conglomerate. The mineralized zone occurs within the conglomerate and at the contact between the conglomerate and andesite. The ore minerals consist of malachite-azurite, chalcocite, bornite, covellite and occasionally native copper. The associated hydrothermal fluids show moderate to high salinities, ranging from 3.09 to 13.39 wt.% NaCl equivalent, with homogenization temperatures between 89 and 387°C, indicating fluid mixing during ore formation. Chalcocite is rarely accompanied by quartz, suggesting low silica content in the ore-forming fluids. The $\delta^{34}S$ values of sulfide samples from the study deposit range from –24.1‰ to –2.6‰, while $\delta^{34}S$ values of hydrothermal H_2S range from –24.3‰ to –2.6‰. The $\delta^{18}O$ values of hydrothermal fluids associated with mineralization fall within the range of basaltic rocks, meteoric waters, and sedimentary rocks. Geochemical variations in major and trace elements suggest the involvement of continental crustal contamination in the magmatic evolution. The studied volcanic rocks fall within the calc-alkaline to shoshonitic fields, formed in a continental arc setting, and are derived from an enriched mantle source influenced by subduction-related fluids. These rocks are characterized by HREE depletion, moderate LREE enrichment, and a weak negative Eu anomaly. Based on the results, the Cheshmeh-Hadi deposit is classified as a stratabound copper sulfide deposit, formed in a volcano-sedimentary setting associated with a subduction-related magmatic arc environment.

Keywords:
Cheshmeh-Hadi, Stratabound Copper, Volcanic-Plutonic Belt, Stable Isotopes, Central Iran

1. Introduction

Numerous copper deposits and mineral occurrences are hosted in the uppermost Eocene volcanic sequences of Iran. Understanding these types of mineralization can offer new insight into the geology and copper resource potential of the region. Most stratabound (manto-type) copper deposits are hosted within stratigraphic sequences predominantly composed of andesitic to basaltic volcanic rocks. These sequences are associated with various geological eras, including the Mesozoic (in Chile and Iran), Proterozoic to Triassic (in North America), Late Silurian to Early Devonian (in China), and the Cenozoic (in Iran) (see **Figure 1**). To date, more than 30 significant manto-type copper deposits and numerous copper occurrences, ranging in age from the Cretaceous to the Eocene, have been identified in Iran. To date, more than 30 major Manto-type copper deposits and numerous copper occurrences ranging in age from Cretaceous to Eocene have been identified in Iran (e.g. the Veshnaveh deposit (**Fazeli, 2002**), Keshtmahaki (**Boveiri Konari et al., 2011**), Koshkoiye (**Abolipour et al., 2015**), the Vorezg-Qayen copper deposit (**Alizadeh et al., 2013**), the Abbas Abad copper deposit (**Maghfouri and Movahednia, 2015**), the Mari Cu(Ag) Manto copper deposit (**Maghfouri et al., 2017**), the Kahak Manto-Type copper deposit (**Kaboodi et al., 2019**), the Narbaghi deposit (**Fazli et al., 2021**), the Yamaghan Manto-Type Cu(Ag) deposit (**Jilba et al., 2021**) and the Madan Bozorg Cu deposits, Abbas Abad (**Salehi and Rasa, 2016**). Some of these deposits were historically exploited in ancient times – for example, the Veshnaveh deposit (**Fazeli, 2002**) and the Narbaghi deposit (**Fazli et al., 2021**) (see **Figure 1**). Some of these deposits, such as Veshnaveh and Eastern Narbaghi (in Qom and Saveh), were exploited during ancient times (see **Figure 1**).

* Corresponding author: Hasan Zamanian
e-mail address: hasanzamanian@ut.ac.ir
Received: 31 August 2025. Accepted: 2. December 2025.
Available online: 14 May 2026

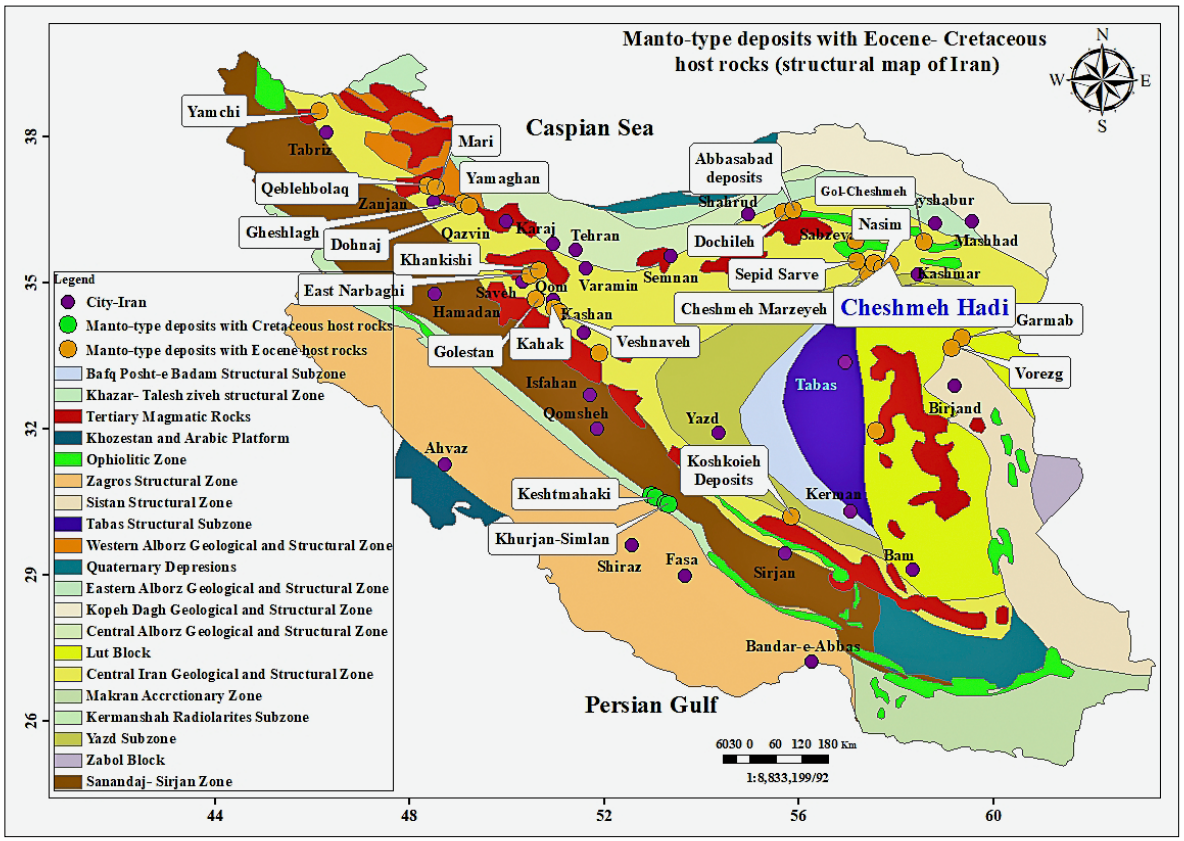


Figure 1. Location of Manto-type copper deposits in Iran and distribution map of these deposits based on the age of host rocks within the main tectonic zones of the country (**Aghanabati, 2004; Alavi, 1991**)

Manto-type deposits in Iran are typically associated with andesitic lava flows. The Eocene host rocks (Eocene volcano-sedimentary sequences) are the most common host lithologies for manto-type copper–silver deposits in Iran. These deposits are mainly concentrated within the Urumieh–Dokhtar Magmatic Arc (UDMA) (**Fazli et al., 2021**), the Alborz Magmatic Arc (AMA), the Sabzevar Zone, and the Lut Block. Approximately 85% of Iran's manto-type copper deposits occur within the UDMA, the Sabzevar Zone (north of the Doruneh Fault), and the AMA. Notable examples include the Abbasabad deposit in the Alborz range, Keshkuiyeh in the UDMA, and (e.g. Abri, Rahbari, and the Cheshmeh Marzeyeh Cu deposit (**Soltani, 2016**), the Bornaward plutonic complex (**Monazzami et al., 2018-2019**), the Baharieh copper deposit (**Rezaeihamid and Tale Fazel, 2019**), the Kal Abri copper deposit (**Jabari et al., 2016**), the Nasim copper deposit (**Ramezaniabbakhsh et al., 2023**), the Sharifabad copper deposit (**Ebrahimi et al., 2020**), Madan Bozorg (**Heidari, 2012**), Grik and Gukhab (**Taefi et al., 2014**), Golcheshmeh (**Entezari Harsini, 2017**), Cheshmeh-Hadi (**Rezapanah Khour, 2016**) in the southern Sabzevar Zone (north of the Doruneh Fault). The majority of the deposits are being actively explored. The Cheshmeh Marzeyeh copper deposit (**Soltani, 2016**), Kal Abri copper deposit (**Jabari et al., 2016**), the Nasim copper deposit (**Ramezaniabbakhsh et al., 2023**), Madan Bozorg (**Heidari, 2012**) and Cheshmeh-Hadi (**Rezapanah Khour, 2016**) deposits are presently mined (see **Figure 1**). The Cheshmeh-Hadi copper deposit is located in the southwest of Khorasan Razavi Province, approximately 46 km west of Bardeskan and 4 km from the village of Qaleh-Dahaneh (see **Figure 2**).

Volcano-sedimentary zones possess significant potential for the formation of Manto-type copper deposits. In the Cheshmeh-Hadi copper deposit area, Manto-type mineralization is associated with Eocene volcanic rocks and is controlled by specific geological horizons. The Doruneh sheet, located along the northern margin of Central Iran and the southern Sabzevar Zone, has acquired a distinctive geological position due to intense Cenozoic magmatic activity and the presence of the active Doruneh Fault. Consequently, a wide range of lithological units, from the Precambrian to the present, are exposed in this region.

The occurrence of vein-type mineralization within andesitic lava flows indicates that stratigraphic control plays a significant role in the deposition and formation of metals in Iran's Manto-type copper deposits. Thus, stratigraphic control is considered one of the major factors in ore formation. Moreover, both the lateral and vertical continuity of mineralization is strongly influenced by lithology, extensional fault systems, and the degree of rock fracturing.

This study characterizes the geological setting and mineralization style of the Cheshmeh-Hadi deposit, and

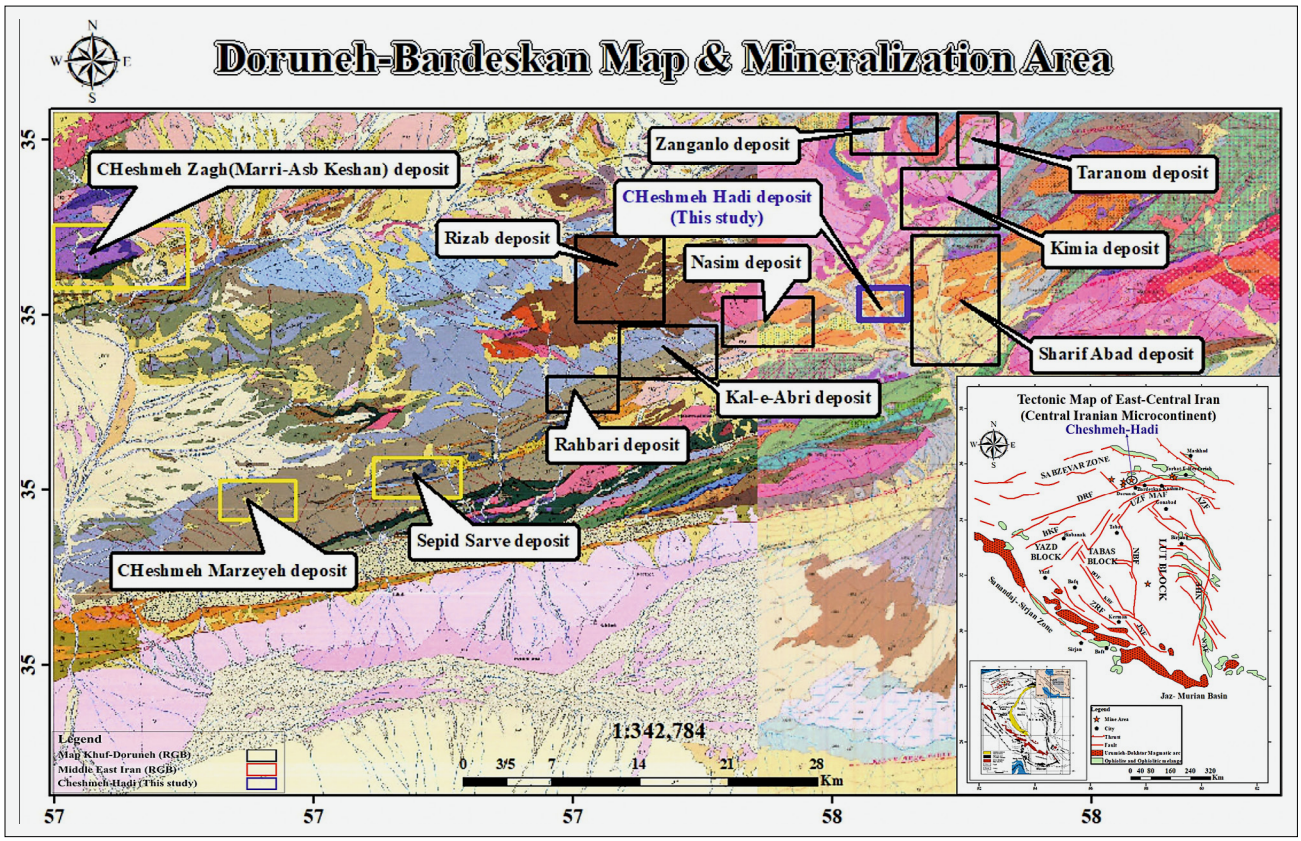


Figure 2. Location of the Cheshmeh-Hadi copper deposit in the southern part of the Sabzevar Zone (north of the Doruneh Fault)

proposes a large-scale mineralization model integrated with the tectono-magmatic evolution of the region, based on newly acquired field and analytical data. The results provide a refined exploration framework for identifying new manto-type copper targets in similar volcano-sedimentary settings, improve the understanding of ore-forming processes in the Sabzevar Zone, and offer practical guidelines for more effective exploration and resource development strategies in Iran's metallogenic provinces.

This research provides a comprehensive review of the Cheshmeh Hadi Manto-type copper deposit, highlighting its unique characteristics and formation processes. The findings contribute to a better understanding of metallogenic evolution in the southern part of the Sabzevar Zone (north of the Doruneh Fault) and emphasize the role of burial diagenesis in ore formation. The results are significant for mineral exploration and resource assessment in numerous Manto-type copper sulfide deposits distributed across the Sabzevar Zone, where the host rocks are predominantly volcanic sequences of Cretaceous to Tertiary age.

2. Materials and Methods

2.1. Geochemical analysis

As part of this study, and following an extensive literature review, a total of 134 samples were collected during fieldwork from intrusive and volcanic igneous units, as well as from mineralized veins and altered zones of the Cheshmeh-Hadi copper deposit. Sampling was conducted from the surface down to a depth of 56.2 meters to facilitate petrographic and lithological investigations. Corresponding thin sections were prepared for detailed analysis. Among these, 20 intrusive rock samples exhibiting minimal alteration were selected for whole-rock geochemical (lithochemical) analysis. Major elements in these samples were measured using X-ray fluorescence (XRF), following the processes of crushing, pulverizing, drying, homogenizing, powder preparation, pressing with boric acid, and finally fusion with lithium metaborate or tetraborate. For the analysis of rare earth elements (REEs) and trace elements, 0.2 grams of each sample was digested with diluted nitric acid and subsequently analyzed using inductively coupled plasma mass spectrometry (ICP-MS), based on ionization and separation of ions according to their mass-to-charge ratios. The analytical procedures were carried out at the Zar Azma Laboratory in Tehran. Multi-elemental analysis (56 elements) was performed using an Inductively Coupled Plasma Mass Spectrometer (ICP-MS) at Zar Azma Laboratory (Tehran, Iran). The analytical precision, evaluated through internal quality control and certified reference materials (NIST SRM 2709, 2710, and 2711), was approximately 3% for most elements and up to 10% for major elements. Calibration

and signal correction were conducted using multi-element calibration standards and internal standards (Sc, Ge, Rh, In, Bi), ensuring high analytical accuracy and reproducibility.

2.2. Fluid inclusions measurements

Five double-polished thin sections with a thickness of 80–100 μm were prepared from quartz and calcite (carbonate) veins and veinlets. Petrographic observations of fluid inclusion evidence were conducted, followed by microthermometric analyses on 40 fluid inclusions. These studies were carried out using a Linkam THMSG600 heating–freezing stage with a temperature range of −196°C to +600°C and a precision of ±1°C, at the Department of Geology, Tarbiat Modares University, Tehran. Temperature calibration was performed using Synflinc synthetic standards. During the freezing and heating procedures, the rates were controlled within the range of 1–10°C/min, before being decreased to 0.5–1°C/min in the vicinity of phase transition points. Salinities (wt.% NaCl equiv.) and densities (g/cm^3) of the aqueous (NaCl-H_2O) inclusions were determined using the computer program HOKIEFLINCS_H2O-NaCl Excel developed by **Steel-MacInnis et al. (2012)** based on the final ice melting temperatures.

2.3. Stable isotope measurements

2.3.1. Oxygen isotope analysis

Two quartz and calcite samples were selected from the same vein locations where fluid inclusion samples were collected, for stable oxygen isotope ($\delta^{18}O$) analysis. The samples were first crushed to mesh 60 at the University of Tehran and then manually purified under a binocular microscope to achieve a purity of over 99%. After separation, the samples were powdered, sieved to remove contaminants, and rinsed with ethanol to ensure cleanliness. Isotopic analyses were performed at the Stable Isotope Research Center, Arak University, Iran. For $\delta^{18}O$ analysis in solid samples, high-temperature pyrolysis was conducted at 1450°C using an elemental analyzer, where all oxygen atoms in the molecular structure were converted to carbon monoxide (CO) gas in the presence of carbon black and glassy carbon. The resulting CO gas passed through a series of purification systems, including a water trap to remove moisture and a purge-and-trap column to eliminate CO impurities. After complete removal of interfering gases, the desorption column was heated to 150°C, and the purified CO gas was transferred through a secondary water trap into the isotope ratio mass spectrometer (IRMS). For calibration and calculation, the isotopic composition of the reference CO gas was determined by comparison with international or laboratory secondary standards. The mass ratio of 30.28 was measured to determine the $\delta^{18}O$ values. In this process, $\delta^{18}O$ is measured by converting the sample to CO gas via pyrolysis at 1450°C, followed by purification and subsequent analysis by IRMS, using the 30/28 mass ratio and calibrated against international standards. δ18O values exhibit a precision of 0.1‰ and are reported in reference to V-SMOW (Vienna Standard Mean Ocean Water, δ18O = 0, with uncertainties of 0.02‰; International Atomic Energy Agency, (2017).

2.3.2. Sulfur isotope analysis

Three representative chalcocite samples from mineralized veinlets were selected for sulfur isotope ($\delta^{34}S$) analysis. The samples were first powdered and sieved to obtain grain sizes between 0.1–0.5 mm. Clean mineral grains were handpicked under a binocular microscope to ensure purity. For isotopic analysis, the samples were combusted at 1150°C in an elemental analyzer, producing sulfur dioxide (SO_2) gas. The generated SO_2 gas was directed through a purification system consisting of a water trap to remove moisture and a purge-and-trap column to eliminate residual impurities. The adsorption column was subsequently heated to 220°C to release the accumulated SO_2 gas, which was then transferred into the isotope ratio mass spectrometer (IRMS). Within the IRMS, the sulfur isotopic composition was determined by measuring the mass ratio 66/64, corresponding to the $^{34}S/^{32}S$ ratio of the sample. To ensure the accuracy and reproducibility of the measurements, repeated calibrations were performed using the IAEA-S-4 international standard ($\delta^{34}S = +16.9 \pm 0.2$‰ VCDT) and a laboratory secondary standard ($\delta^{34}S = -6.3 \pm 0.2$‰ VCDT).

3. Geology

The Cheshmeh-Hadi copper deposit is part of an Eocene volcano-sedimentary sequence located in the southern Sabzevar Zone. This sequence comprises intermediate to mafic volcanic units (including porphyritic to megaporphyritic andesite, pyroxene andesite, and basalt), pyroclastic units (such as tuff and agglomerate), and a range of sedimentary rocks including fossiliferous limestone (with Nummulites, Plesiopoda, and Brachiopods), calcareous sandstones, detrital limestones, conglomerate, siltstone, shale, gypsiferous marl, and alluvial terraces (see **Figure 3**). The lithostratigraphic sequence, from oldest to youngest, comprises basalt, basaltic andesite, andesite and pyroxene andesite, conglomerate, limestone, siltstone, gypsiferous marl, and Pliocene conglomerate. The Cheshmeh Hadi copper deposit is located on the southern limb of an anticline. In this area, the youngest unit is a nummulitic limestone that overlies the conglomerate, cropping out along the outermost part of the anticline limb. The mineralized zone at Cheshmeh Hadi occurs within the conglomerate and at the contact between the conglomerate and andesite.

A distinctive feature of this region is the widespread development of Cretaceous volcanic–tuffaceous rocks

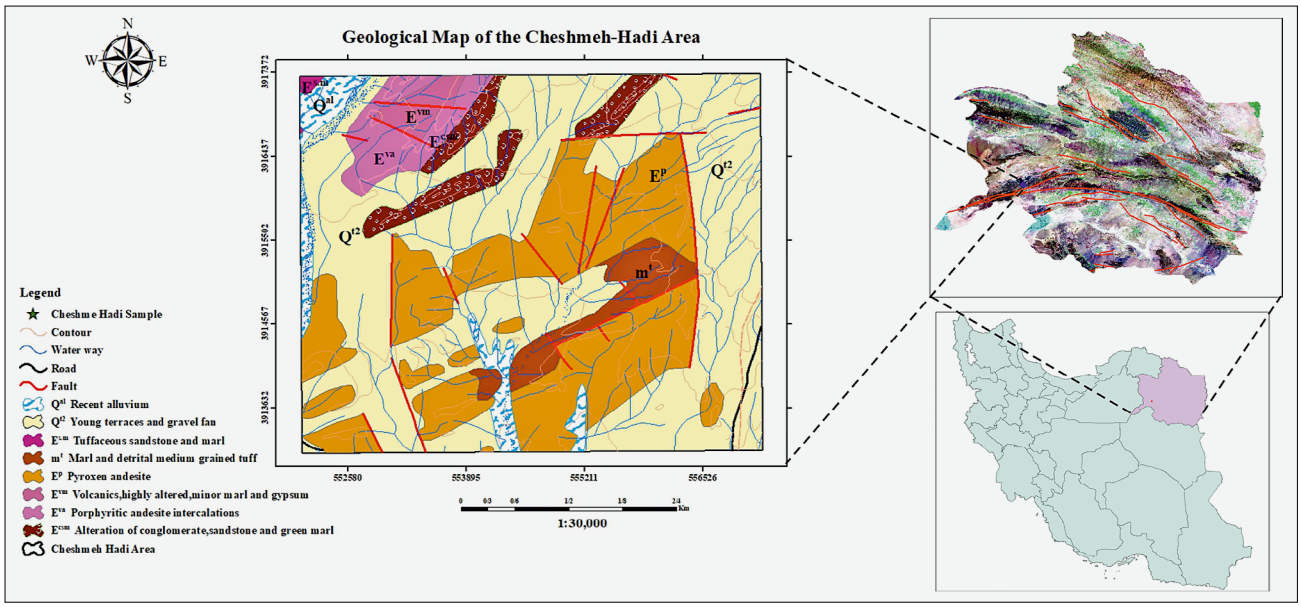


Figure 3. Detailed 1:1000 Geological Map of the Eastern Part of the Cheshmeh-Hadi Copper Deposit

and Eocene volcanic and pyroclastic units, reflecting significant volcanic activity in the area. In the central parts of the study area and within Middle Eocene sediments, a complex of volcanic and pyroclastic rocks is extensively exposed. This complex begins with volcanic rocks comprising andesite, pyroxene andesite, basaltic andesite, and basalt, typically dark green to black in colour. Most exposures display distinct bedding and banding. In some locations, agglomerates with green to red hues are interbedded within this volcanic sequence. Copper mineralization, mainly in the form of malachite, is observed along fractures within the andesitic rocks. Overlying the volcanic complex is a pyroclastic sequence consisting of alternating layers of agglomerate, tuff, lapilli tuff, and andesitic tuff with colours ranging from red to green (see **Figure 3**).

The Upper Eocene sediments are composed of alternating layers of sandstone, siltstone, silty marl, and thin-bedded limestone, typically light green to cream in colour. The Upper Eocene volcanic and pyroclastic rocks in the Cheshmeh-Hadi deposit area are subdivided into four distinct units. The first unit includes volcanic rocks such as andesite, porphyritic andesite, and pyroxene andesite, with green to dark gray colouration. Due to the alteration of phenocrysts in the andesites, an amygdaloidal texture has developed in many parts of these rocks (see **Figure 4A**). The vesicles are commonly filled with secondary minerals, such as calcite. Overlying this unit is a volcanic complex consisting of basalt and basaltic andesite with black colouration. Above this volcanic–pyroclastic complex, Oligo–Miocene sedimentary deposits are present. Therefore, this volcanic assemblage may be regarded as representing the final phase of Eocene volcanic activity. The main volcanic rocks of the area exhibit gentle morphology and are locally vesicular, with vesicles typically filled by calcite, silica, and occasionally zeolite.

3.1. Conglomerate

The highest stratigraphic unit in the Cheshmeh Hadi deposit area is the Pliocene–Pleistocene conglomerate, which represents the thickest and most extensive sedimentary unit at the uppermost horizon. Its characteristic features include a gray to reddish-brown colouration, lack of induration, weak cementation, polymictic clast composition, presence of clay–iron oxide cement with very low strength, and the development of relatively subdued topography. The conglomerate associated with mineralization in the Cheshmeh Hadi copper deposit is composed of rounded clasts with an average size of 3–4 cm, predominantly derived from volcanic rocks such as andesite (see **Figure 4A**), pyroxene andesite (see **Figure 4B**), trachyte, trachyandesite, dacite, and andesitic tuff. In addition, clasts of intrusive units (monzonite, diorite, and pyroxene diorite) as well as subvolcanic rocks (porphyritic diorite, porphyritic monzodiorite, and porphyritic monzonite) are also observed. This conglomerate contains volcanic cement in proximity to volcanic units (andesite), whereas toward the limestone contact, the clast size decreases and the cement becomes carbonate in composition, reflecting deposition in a marine setting alongside the limestone unit. Furthermore, in conglomerates adjacent to limestone, sedimentary clasts such as shale are also present. Mineralization occurs mainly as chalcocite within the conglomerate, where effective porosity is available, and occurs sporadically within andesite and limestone as well. The timing of mineralization postdates the formation of the conglomerate and the limestone in the area. No sedimentary units are developed within the volcanic sequence, and the observed

structures and textures indicate a non-marine environment. The volcanic cement at the base of the conglomerate contains magnetite. Since the volcanic rocks themselves contain approximately 3–5% magnetite, the presence of magnetite in the conglomerate cement does not indicate paragenesis with chalcocite; rather, as noted, the ore-forming fluid responsible for chalcocite was iron-deficient at the time of mineralization. The magnetite present is attributed to the erosion and redeposition of volcanic rock fragments during conglomerate formation.

3.2. Andesitic and basaltic andesite

The Eocene andesitic and basaltic andesite volcanic units show mineralogical, textural, and lithological diversity. These lava flows are conformable and parallel to adjacent units. Fresh andesites are dark gray, weathered to grayish-brown, with some areas stained reddish by iron oxides. Hand samples reveal porphyritic, megaporphyritic, vesicular, amygdaloidal, and flow textures, featuring phenocrysts of plagioclase, pyroxene, and opaque minerals (see **Figure 4C**). Vesicles are often filled with secondary silica, calcite, and chlorite minerals, giving amygdaloidal and vesicular textures.

3.3. Pyroxene andesite

The pyroxene andesite unit appears as low-relief hills with a light gray colour and displays porphyritic and amygdaloidal textures (see **Figure 4D**). Hand specimens contain rounded pyroxene crystals and coarse plagioclase crystals (27–36%). Secondary minerals like chlorite and calcite are present as veinlets and vesicle-fillings, with carbonate veins measuring 1.5–2.5 mm clearly visible (see **Figure 4E**). Phenocrysts constitute approximately half of the rock's volume. Plagioclase makes up about 75–80% of the phenocrysts, pyroxene 15–20%, and alkali feldspar 2–3%. The plagioclase phenocrysts range in size from 1 to 2 mm, pyroxene from 300 micrometers to 2 mm, and alkali feldspar phenocrysts are approximately 200–300 micrometers in size (see **Figure 4E**). Some plagioclase crystals exhibit oscillatory zoning (see **Figure 4E**), indicative of intermediate composition (andesine). Plagioclase phenocrysts also display sieve texture. Pyroxene frequently exhibits oxidized rims, suggesting that the rock erupted at the Earth's surface (see **Figure 4F**). The groundmass consists of fine-grained feldspar crystals and volcanic glass (see **Figure 4G**). The feldspars are unaltered, while the pyroxene is partially altered to secondary iron oxides (iddingsite) (see **Figure 4H**). The glomeroporphyritic texture is observed in the rock due to the aggregation of phenocrysts. Minor amounts of alkali feldspar phenocrysts, measuring approximately 200 micrometers, are also present. The groundmass consists of feldspar microlites and iron oxides (see **Figure 4H**). Scattered carbonate fragments are observed in the rock, resulting from weak carbonation alteration (see **Figure 4I**). The mineral celadonite is green and similar in appearance to malachite (see **Figure 4K**). Scattered green grains and crystals (often associated with carbonate minerals) are observed in the rock (see **Figure 4I**).

3.4. Marl and siltstone

The E^{csm} unit consists of thinly bedded marl and siltstone layers, ranging from light gray to cream, overlying the fossiliferous limestone. It forms hilly terrain, with greater thickness and lateral extent in the western sector compared to the east. This unit is conformably overlain by a red marl layer. Notably, limestone beds analogous to E^{csm} occur within the northern part of the western sector, hosting malachite mineralization, and have been structurally emplaced into the marl via thrust faulting.

The E^{vm} unit includes marls with transparent gypsum layers, gray to white in colour, present in both eastern and western sectors. It locally overlies older units discontinuously, with wider distribution in the east and beyond the study area. The unit hosts multiple high-quality gypsum layers currently under extraction, displaying rugged topography and limited thickness.

3.5. Alteration

Magmatic and hydrothermal fluids derived from volcanic eruptions generally cause very weak alteration within the host rock units, mostly resulting in chloritic and iron oxide alterations (see **Figure 4I**). Chlorite can form either through alteration of mafic minerals present in the rock or by the introduction of iron and magnesium via hydrothermal fluids (see **Figure 4N**). Zeolitic alteration is observed locally within the Cheshmeh-Hadi copper deposit; the formation of zeolites in intermediate to basic rocks is related to hydrothermal alteration (see **Figure 4L**), low-grade metamorphism, and alteration by meteoric waters. Iron oxide staining, chloritization, and iddingsitization occur with weak to moderate intensity in andesitic units, while carbonate and clay alteration are weakly developed (see **Figure 4M**). Iron oxide alteration is likely due to the transformation of pyrite to goethite–hematite (see **Figure 4M**), which facilitates the release of sulfur and its combination with sulfide ions, promoting the formation of sulfide minerals, such as chalcocite and digenite. Secondary processes have transformed copper oxide minerals like malachite from primary sulfides. Alteration in the Cheshmeh-Hadi deposit, similar to much of the northwest Bardeskan region, can be divided into two stages: pre-mineralization and syn-mineralization. Pre-mineralization alteration includes celadonite, carbonate, silicification, and propylitic (epidote and chlorite) assemblages (see **Figure 4N**), whereas syn-mineralization alteration mainly consists of carbonate, zeolite, calcite, minor chlorite, and subordinate argillic alteration. The pre-mineralization alteration corresponds to regional propylitic alteration, while syn-mineralization alteration is characterized by localized

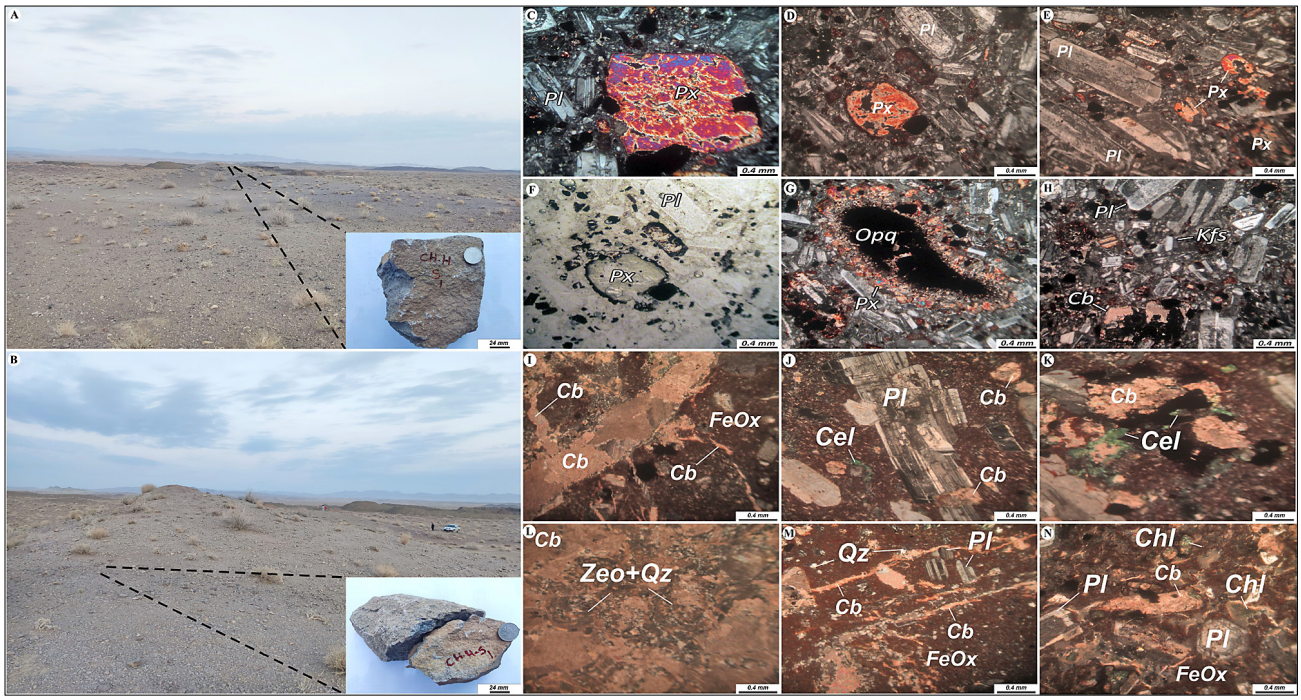


Figure 4: Overview of the Cheshmeh-Hadi copper deposit area: (**A**) Andesite unit. (**B**) Pyroxen andesite unit. (**C**) Pyroxene and plagioclase phenocrysts. (**D**) Pyroxene and plagioclase phenocrysts. (**E**) Pyroxene and plagioclase phenocrysts. (**F**) Pyroxene crystal with oxidized margins, indicating volcanic eruption at the Earth's surface. (**G**) Aggregate of opaque minerals replacing the margins of pyroxene. (**H**) Alkali feldspar occurring as a minor constituent in the rock. (**I**) Alkali feldspar together with plagioclase in basaltic andesite. (**J**) Plagioclase phenocryst and carbonate fragments within the rock. (**K**) Chlorite mineral associated with celadonite (green in colour) and carbonate in andesite. (**L**) Plagioclase phenocryst accompanied by quartz crystals. (**M**) Plagioclase phenocryst with carbonate veinlets within an iron oxide-rich matrix. (**N**) Plagioclase phenocryst showing a sieve texture in a groundmass composed of iron oxides and carbonate minerals, with chlorite occurring as interlocking fragments, while carbonate veinlets cut across the rock matrix. (Px: pyroxene, Cel: Celadonite, Pl: plagioclase, Chl: Chlorite, Qz: Quartz, Zeo: Zeolite, Opq: Opaque, Cb: Carbonates, Kfs: K-feldspar, Feo_x: Fe-oxides) (Mineral abbreviations are taken from **Warr, 2021**).

carbonate, calcite, zeolite, and minor argillic alteration. Hydrothermal alteration in the Cheshmeh Hadi copper deposit can be divided into two groups: pre-conglomerate alterations and post-conglomerate alterations (the latter being synchronous with and related to mineralization). Pre-conglomerate alterations include those observed in volcanic rock fragments – zeolitization, kaolinitization, carbonatization, and celadonitization – as well as alterations in subvolcanic bodies such as monzonite and porphyritic diorite (in the form of dikes), which include propylitic alteration (epidote and occasionally chlorite) and silicification. Zeolitization, dominated by natrolite, is most common in megaporphyritic andesites and porphyritic trachyandesites, formed through multiple stages. In many cases, cavities between grains and large plagioclase phenocrysts are filled with radial natrolite zeolites. This alteration unit represents the basal part of the stratigraphic sequence and its fragments are observed within the conglomerate along with other volcanic rock clasts. Zeolitization is especially prominent in the northern part of the Cheshmeh Hadi deposit. Chloritization, and locally iddingsitization, occurs in porphyritic andesites, pyroxene andesites, and, to a lesser extent, in basalts and basaltic andesites outcropping in the western and northwestern parts of the area. Hydrothermal fluids altered mafic minerals such as pyroxene and olivine to chlorite, forming chloritic alteration, while the breakdown of olivine produced iddingsite. These alterations impart a dark green colouration to the affected rocks. Since these processes are observed in andesite, basaltic andesite, and pyroxene andesite units that constitute the clasts of the conglomerate, the same alteration features can clearly be identified within the conglomerate clasts as well.

4. Results and discussion

4.1. Structural Geology

In general, several fault systems can be recognized in the study area, including E–W and N–S trending faults, as well as dextral strike-slip faults trending NW–SE and NE–SW, which are the most dominant fault types in the Cheshmeh-Hadi copper deposit. These faults have, in some areas, displaced the mineralized zones. In the easternmost part of the area, overturned limestone units are observed in certain locations, indicating intense tectonic activity in this part of the deposit. In this section, several

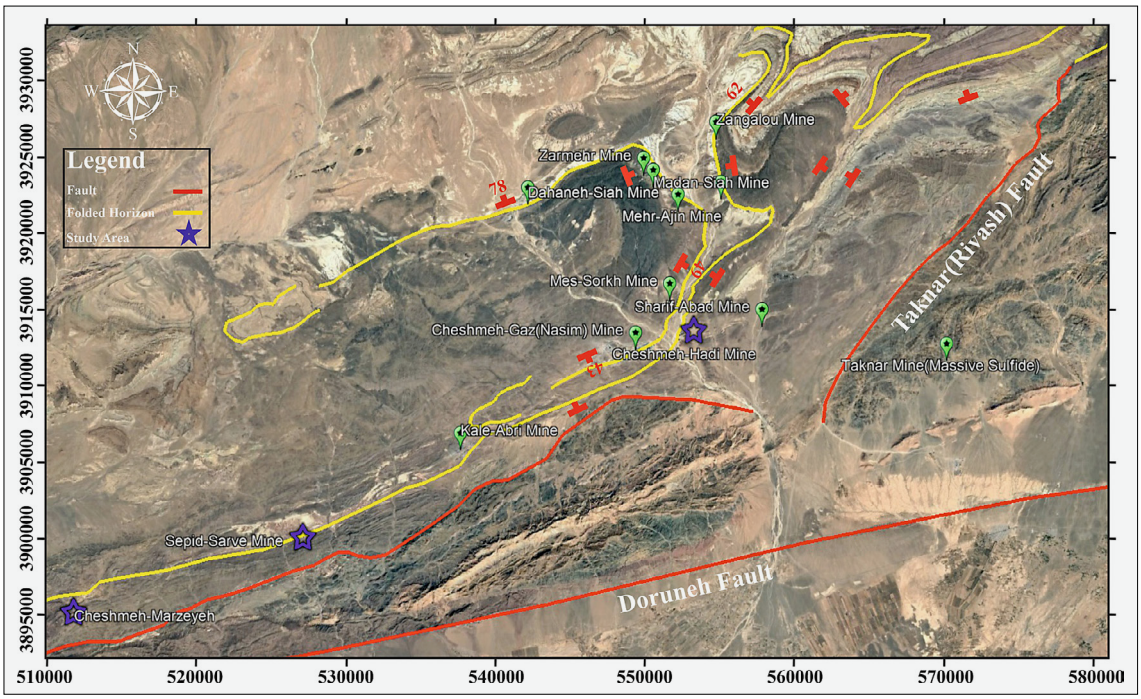


Figure 5. View of the fault and Folded Horizon systems present in the eastern part of the Cheshmeh-Hadi copper deposit

strike-slip faults with approximately NW–SE orientation have disrupted the limestone layers and displaced copper mineralization that occurs at the contact between limestone and volcanic units (see **Figure 5**).

4.2. Economic Geology

4.2.1. Mineralization

Copper mineralization in the Cheshmeh-Hadi deposit has developed along the contact zones between pyroclastic and volcanic units and overlying carbonate sequences (including marly, fossiliferous, and clastic limestones). Mineralization is predominantly located below the carbonate horizon and within the upper portions of volcanic and volcaniclastic units composed of conglomerate, andesite (see **Figure 6A**), and agglomerate (see **Figure 6B**). In some localities, oxide copper mineralization occurs at the upper boundary of the limestone in contact with shale and marl. The mineralized zones vary in thickness and dip steeply to nearly vertical. The ore minerals include malachite (see **Figure 6B**), azurite, chalcocite (see **Figure 6C**), digenite, cuprite, covellite, and locally native copper. Mineralization occurs as veinlets (see **Figure 6D**), cavity-fillings, disseminations (see **Figure 6E**) and impregnation textures. The host rocks for veinlet-style mineralization mainly consist of andesitic and pyroclastic rocks, with limestone playing a lesser role. The high porosity and permeability of conglomerates provided favourable pathways for hydrothermal fluids or metamorphic-derived brines, facilitating mineral precipitation as open-space fillings and disseminated textures. These conglomerates commonly contain fragments of volcanic and agglomeratic rocks. The Cheshmeh-Hadi deposit is situated at the southeastern termination of the Khaf–Kashmar–Bardeskan magmatic belt, within the Sabzevar subzone. The dominant lithology comprises Eocene to Miocene volcano-sedimentary sequences. Intense compressional tectonics have produced a series of anticlines and synclines, with the mineralized zones hosted along the limbs of these structures. The high permeability of the conglomerates promoted fluid circulation and metal precipitation. The ore mineral assemblage includes chalcocite, minor chalcopyrite and bornite, covellite, pyrite, malachite (see **Figure 6I**), and chrysocolla. Chalcocite, bornite (see **Figure 6F**), and pyrite are interpreted as primary sulfides that were later altered to secondary minerals such as malachite, covellite (see **Figure 6G**), and iron hydroxides during supergene enrichment (see **Figure 6H**). The dominant alteration types include chloritic, carbonatic, and zeolitic alterations, with limited zones of argillic alteration. Chalcocite is considered the most important primary copper mineral in manto-type deposits, characterized by high copper content and the absence of iron (**Movahednia et al., 2022**). In contrast, chalcopyrite, the principal copper mineral in porphyry, VMS, and other systems, contains less copper and a higher proportion of iron. The presence of chalcocite without iron-bearing gangue minerals and the absence of quartz indicates that the mineralizing fluids were copper-rich, iron-poor, and silica-deficient, suggesting highly reducing conditions (**Rameza-niabbakhsh et al., 2023**). The lack of epidote – a mineral associated with oxidizing conditions and high iron – supports this interpretation. Although the volcanic host rocks contain up to 5% primary magnetite (see **Fig-**

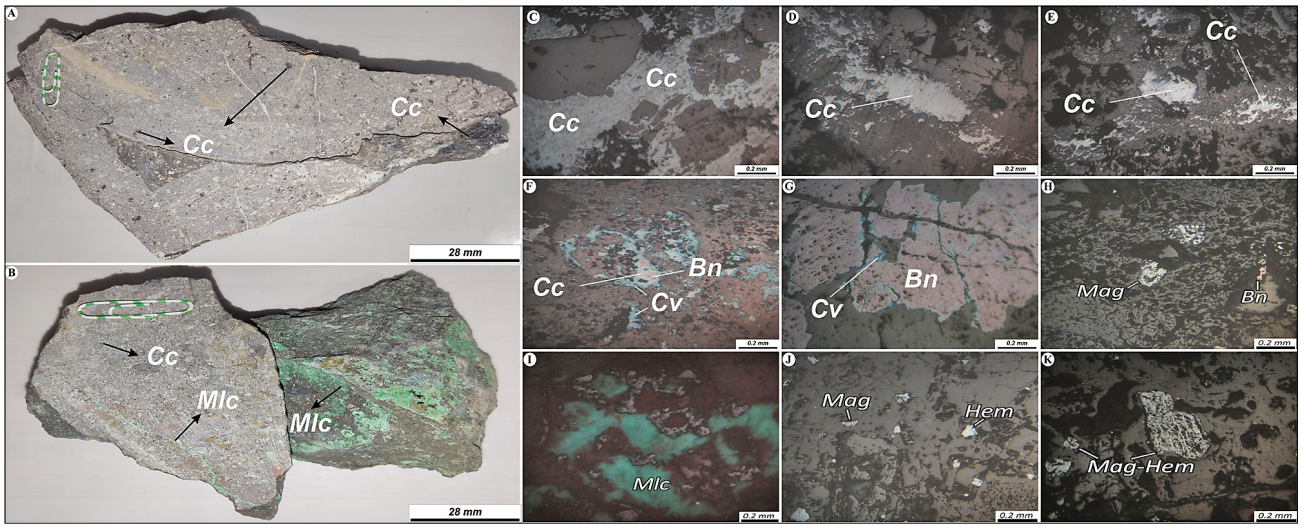


Figure 6. (**A**) Hand specimen showing oxide and sulfide copper mineralization. (**B**) Hand specimen with oxide and sulfide copper mineralization. (**C**) Section of a thick chalcocite vein cut by a second generation of chalcocite veinlets. (**D**) Thin chalcocite veinlets accompanied by fine disseminated grains. (**E**) Chalcocite occurring as disseminated crystalline grains. (**F-G**) Bornite altered to covellite and chalcocite along grain boundaries and fractures. (**H**) Magnetite and disseminated bornite grains. (**I**) Malachite vein under polarized light, appearing green in colour. (**J**) Magnetite crystals, some of which are partially replaced by hematite. (**K**) Hematitized magnetite minerals. (Cc: Chalcocite, Cv: Covellite, Bn: Bornite, Mag: Magnetite, Mlc: Malachite, Hem: Hematite) (Mineral abbreviations are taken from **Warr, 2021**).

ure 6J), there is no evidence of iron-rich mineralization, such as widespread chalcopyrite or pyrite in the deposit, implying that the volcanic rocks are unlikely to be the metal source (see **Figure 6K**). These rocks also show no significant alteration. Likewise, if intrusive bodies were the metal source, the hydrothermal fluids would be expected to be rich in silica, iron, and aluminum. However, the absence of quartz associated with chalcocite suggests otherwise.

In recent decades, several studies have emphasized the role of framboidal pyrite and bitumen in the genesis of mantle-type copper deposits (**Zentilli et al., 1997; Wilson, 2000; Herazo et al., 2020**). Framboidal pyrite is a common pre-ore reducing agent in Iranian stratabound copper deposits (**Movahednia et al., 2022**). For example, in the Keshkuiyeh deposit, the highest copper grades are found in veins and zones closely associated with pyrobitumen and framboidal pyrite. These pyrite textures are widespread and typically occur as fine-grained aggregates in close proximity to copper mineralization, suggesting their critical role in ore formation. In Iranian mantle-type deposits, the pre-ore mineral assemblage typically includes framboidal pyrite and pervasive propylitic alteration affecting andesitic host rocks (see **Figures 7A, B and C**). This assemblage, reported from other stratabound deposits as well, is often interpreted as a product of early diagenesis or pre-hydrothermal processes (**Maghfouri et al., 2017**). Framboidal pyrite formed during early diagenesis may be partially replaced by Cu-(Fe) sulphides, such as chalcocite and bornite, during burial diagenesis (see **Figure 7D**). The presence of zeolite minerals during later burial suggests continued diagenetic evolution (**Maghfouri et al., 2017**). These findings indicate that metal-bearing hydrothermal fluids may have interacted with pre-existing pyrite, which acted as a reducing agent, triggering the precipitation of copper sulfides (**Dissanayake, 1993; Herazo et al., 2020**). Such pyrite replacement processes have also been proposed for stratabound copper deposits in central Chile (**Zentilli & Wilson, 1999; Merinero et al., 2019**).

The ore minerals primarily formed in the cavities and fractures of the host rock, as well as in the micro-fractures and voids of minerals such as pyroxene, plagioclase, and hornblende. The primary hypogene minerals in the Cheshmeh Hadi deposit include chalcopyrite, pyrite, chalcocite (see **Figure 7B**), and hematite. Chalcocite is the most abundant copper sulfide mineral, occurring disseminated and in veinlets within fractures and voids of the host rock and minerals, and in some cases, it has altered to covellite (see **Figure 7I**). Calcite veinlets, and to a lesser extent quartz veinlets, are more widespread at this stage, and minerals like chalcocite commonly occur within these veinlets. Pyrite and chalcocite are present in very small amounts, typically less than 60 microns, and are dispersed in the host rock cavities. Hematite forms as a replacement of magnetite nodules in the cavities; the magnetite crystals belong to the andesitic unit and are unrelated to copper mineralization (see **Figure 7K**). Upon exposure to surface conditions, the copper sulfide minerals undergo oxidation, leading to the formation of secondary supergene minerals such as malachite, azurite (see **Figure 7A**), and covellite. Malachite, the most abundant supergene mineral (see **Figure 7E**), and azurite generally form as replacements of primary copper sulfides like chalcocite, filling fractures and

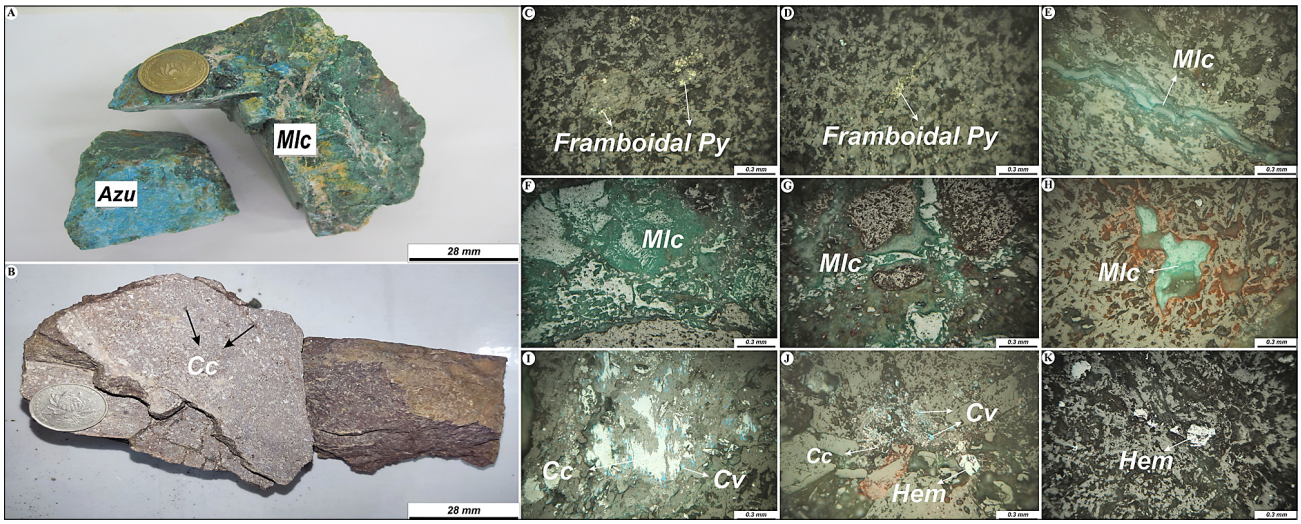


Figure 7. (**A**) Occurrence of chalcocite with disseminated texture, filling interstitial spaces within the rock, accompanied by malachite with a cavity-filling habit. (**B**) Malachite filling voids and grain boundaries, together with chalcocite occurring as irregular fragments dispersed throughout the rock. (**C-D**) Pyrite occurring as fine grains with spherical and framboidal (clustered) textures, disseminated in the host rock. (**E**) Chalcocite as fine- to medium-grained fragments, scattered within the rock and associated with malachite; in some cases, chalcocite is replaced by covellite. (**F-G-H**) Malachite as the only copper-bearing mineral filling fractures in a vein-like manner, accompanied by hematite as irregular fragments disseminated in the rock, apparently formed contemporaneously with the host andesitic rocks. (**I-J-K**) Hematite occurs as scattered grains, chalcocite is present as aggregates ranging from fine- to relatively coarse-grained (mostly associated with covellite), and malachite is distributed as smaller dispersed fragments within the rock. (Cc: Chalcocite, Cv: Covellite, Azu: Azurite, Py: Pyrite, Mlc: Malachite, Hem: Hematite) (Mineral abbreviations are taken from **Warr, 2021**).

cavities (see **Figure 7F**). Covellite is present in very minor amounts and forms from the alteration of chalcocite (see **Figure 7I**). Goethite results from the alteration of iron oxides such as hematite and magnetite (see **Figure 7J**). Based on microscopic studies of texture, structure, and mineralogy, the mineralization can be divided into hypogene and supergene stages. During the hypogene stage, pyrite, chalcocite, and chalcopyrite formed along with minor quartz and calcite. Hematite, resulting from the alteration of magnetite, formed in the late hypogene stage (see **Figure 7G**). In the supergene stage, upon exposure to surface conditions, secondary minerals such as malachite (see **Figure 7H**), azurite, and covellite formed from the oxidation of copper sulfides, while goethite formed from the oxidation of iron-bearing minerals such as hematite and magnetite (see **Figure 7K**).

4.2.2. Paragenesis

Given that chalcocite is the hallmark mineral of the Manto type and is dominant within the Cheshmeh-Hadi copper deposit, lesser amounts of bornite, pyrite, digenite, magnetite, and hematite are sporadically observed as primary metallic minerals. Secondary minerals including malachite, azurite, secondary chalcocite, covellite, and hematite have formed in various parts of the Cheshmeh-Hadi deposit (see **Figure 8**). These minerals exhibit textures such as disseminated grains, cavity-filling (amygdaloidal), martitization, replacement, and skeletal structures. Most of these minerals occur as veinlets of varying lengths and thicknesses, as well as disseminated grains.

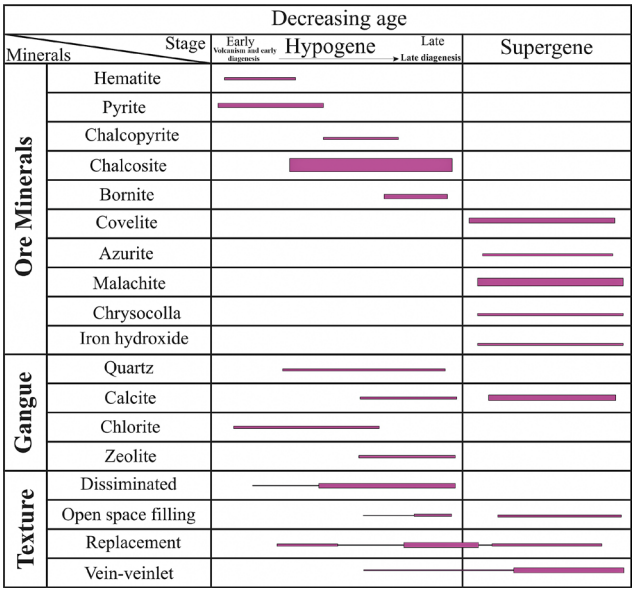


Figure 8. Paragenesis diagram of selected minerals in the Cheshmeh-Hadi copper deposit

4.3. Fluid Inclusions

Fluid inclusions are commonly used to determine temperature, solute type, and salinity of mineralizing solutions in various deposits. In the Cheshmeh-Hadi copper deposit, fine-crystalline calcite is the most abundant and significant mineral associated with the main mineralizing fluid. The studied fluid inclusions occur as mono-phase (liquid, L; vapor, V), and two-phase liquid-rich (see **Fig-**

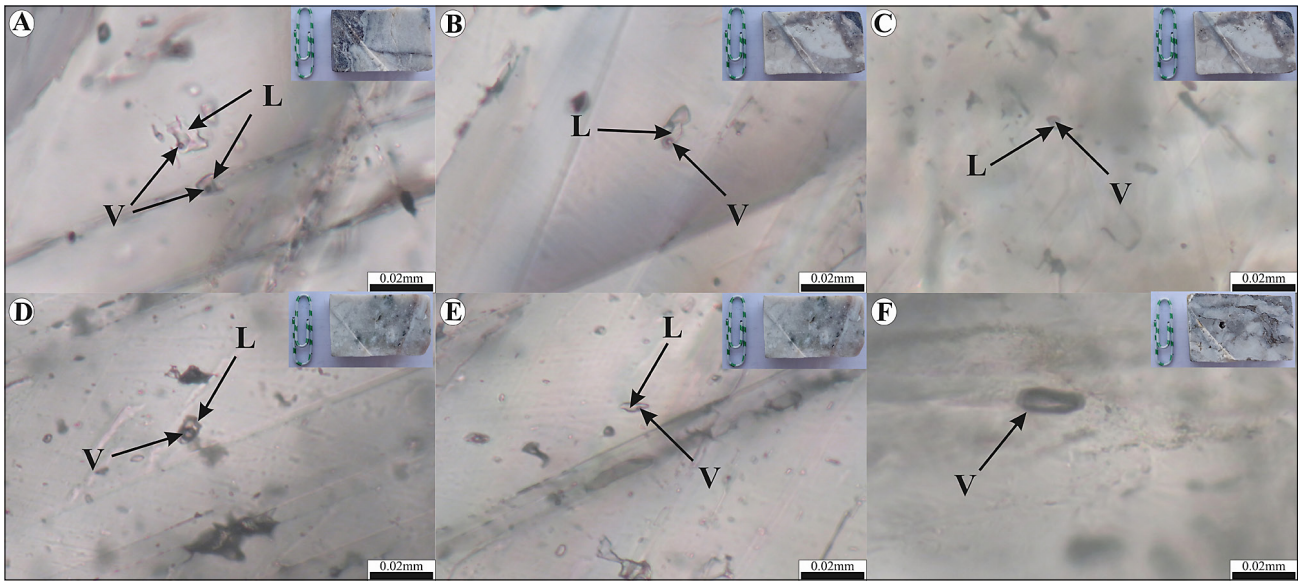


Figure 9. (**A**) Two-phase fluid inclusion enriched in liquid (L+V). (**B**) Two-phase fluid inclusion enriched in vapour (V+L). (**C**) Two-phase fluid inclusions enriched in liquid phase (L+V). (**D**) Mono-phase gaseous fluid inclusion. (**E**) Mono-phase gaseous fluid inclusions. (**F**) Mono-phase gaseous fluid inclusions.

Table 1. Microthermometric data of fluid inclusions in the Cheshmeh-Hadi copper deposit

Sample N.	Mineralization Type	Mineral	phase	Tutec (°C)	Tice(°C)	salinity	Th V-L (°C)	Th L-V (°C)	THT (°C)
S08	Mlc+Az+Cal	Calcite	L+V	-36.5	(-2.2)-(-5.6)	3.36-9.07	133-212		133-212
S11	Cct+Cal	Calcite	L+V	-41	(-2.8)-(9.1)	4.46-12.61	174-332		174-332
S11	Cct+Cal	Calcite	V+L		(-7.7)-(-8.18)	11.21-11.61		263-343	263-343
S13A	Mlc+Az+Cal	Calcite	L+V	-49.7	(-1.9)-(-9.3)	3.09-13.19	89-387		89-387
S17A	Cct+Bn+Ccp+Mag+Qtz	Quartz	L+V	-39.5	(-1.8)-(-9.4)	3.38-13.39	102-235		102-235
S17A	Cct+Bn+Ccp+Mag+Qtz	Quartz	L+V+S		-7.9	11.53	279		279
S14B	Mlc+Az+Cal	Calcite	L+V	-37.1	(-2.1)-(-5.2)	3.37-7.84	147-273		147-273
S14B	Mlc+Az+Cal	Calcite	V+L		(-5.5)-(-5.6)	8.78-8.99		282-302	282-302

ures 9A, C) plus vapour-rich (L+V) types (see **Figure 9B**), mostly irregular, rectangular, spherical, or elliptical in shape and dark in colour. mono-phase vapor inclusions range from 2 to 10 microns, predominantly irregular in shape. In liquid–vapor (L+V) inclusions where the liquid phase occupies a larger volume, the vapor (gas) phase transforms into the dominant liquid phase upon homogenization. Conversely, in vapour–liquid (V+L) inclusions where the vapour occupies a greater volume, the liquid phase transforms into the dominant vapour phase during homogenization. The homogenization temperature to the liquid phase (TH_{V+L}) represents the temperature at which the vapour phase becomes completely homogenized into the liquid phase. The homogenization temperature to the vapour phase (TH_{L+V}) denotes the temperature at which the liquid phase becomes homogenized into the vapour phase. The temperature of the first ice melting (Tu) indicates the closure of the system. The halite melting temperature (THH) reflects the salinity of the fluid, which can be calculated from the measured value. The final ice melting temperature (THT) also represents fluid salinity in the absence of a halite phase; it is measured as a negative value but is conventionally reported as a positive number in calculations. In the studied samples, mono-phase gas-rich inclusions are the most common type, ranging in size from 2 to 15 microns and mostly occurring in irregular and oval shapes. Two-phase, liquid-rich inclusions are very rare, with the vapour phase making up approximately 10–35% of the total inclusion volume. Their sizes range from 5 to 15 microns, and they are mostly irregular in shape. Two-phase, vapour-rich inclusions are around 14 microns in size, with shapes varying from spherical to flattened. Overall, fluid inclusion sizes in the deposit range from a few microns upward. Mono-phase vapour inclusions occur sporadically and individually within the host (see **Figures 9D, E,** and **F**), while two-phase, liquid-rich inclusions are mostly isolated (see **Figures 9A** and **C**) (see **Table 1**).

The first melting temperature is directly related to the salt composition of the hydrothermal fluid (**Shepherd et**

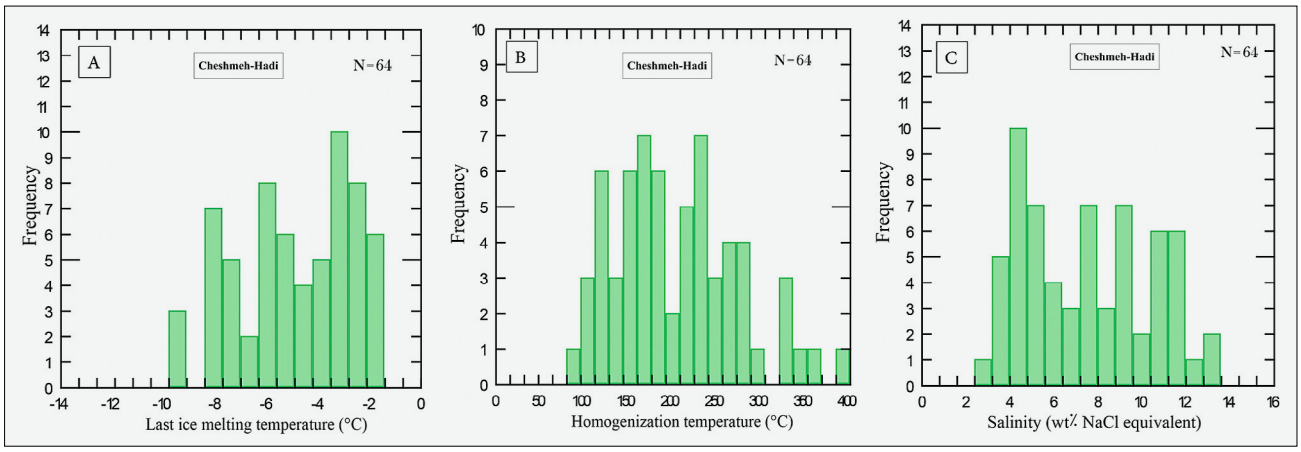


Figure 10. Histograms of fluid inclusion data: (**A**) Final ice-melting temperature. (**B**) Homogenization temperature. (**C**) Salinity

al., 1985) (see **Figure 10A**). Homogenization temperatures (Th) of vapour + liquid (L+V) inclusions range from 89 to 387°C, averaging 194.75°C, while for liquid + vapour (V+L) inclusions Th ranges from 263 to 343°C, averaging 304.6°C (see **Figure 10B**). Salinity varies from 3.08 to 13.38 wt.% NaCl equiv., with an average of 7.56 wt.% (see **Figure 10C**).

Based on fluid inclusion studies, the formation temperature of the Cheshmeh-Hadi copper deposit ranged between 90 and 386°C, originating from a solution containing 3.09 to 13.39 wt.% NaCl. The final ice melting temperatures of fluid inclusions vary from –6.9 to –8.18°C. Salinity, a key factor influencing fluid density, was evaluated using homogenization temperature versus salinity plots for mineralizing inclusions from Cheshmeh-Hadi (**Bodnar, 1983**). Fluid densities vary between 0.7 and 1 g/cm³ (see **Figure 11**). A decrease in homogenization temperature from 387 to 89°C corresponds to a density increase from below 0.7 to 1 g/cm³, resulting in reduced fluid velocity and enhanced mineral precipitation.

The increase in salinity in fluid inclusions over the 89 to 387°C range is accompanied by rising density. This process is linked to boiling phenomena whereby, due to cooling or pressure drop, fluids evolve toward a denser, more saline phase compared to the initial fluid. However, salinity increase with decreasing temperature cannot be solely explained by simple boiling. **Hedenquist and Henley** (**1985**) argued that boiling-induced salinity increases are relatively small compared to the larger salinity variations observed here (see **Figure 11**). With decreasing pressure and temperature during fluid ascent, the physical state of the hydrothermal solution undergoes substantial modification. Among the most critical of these changes is boiling, which leads to the separation of liquid and vapour phases. This process plays a key role in ore-forming systems, as it alters the chemical composition of the hydrothermal fluid and creates favourable conditions for metal precipitation. Primary boiling refers to the initial phase separation or vapour formation that occurs due to a reduction in hydrostatic or

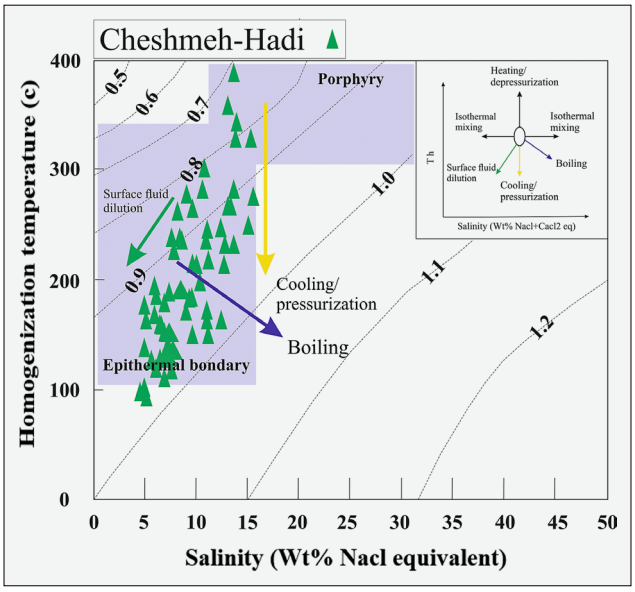


Figure 11. Homogenization temperature-salinity plot showing fluid densities (The fluid densities are shown with dashed lines) ranging from 0.7 to 1.0 g/cm³ in the Cheshmeh-Hadi copper deposit (**after Zhang and Frantz, 1987**), Homogenization temperature-salinity diagram (**Bodnar, 1983**) indicating boiling and cooling processes in the studied deposit, Homogenization temperature-salinity plot delineating the magmatic to epithermal fluid range in the deposit (**after Lattanzi, 1991**).

lithostatic pressure as the hydrothermal fluid ascends from deeper crustal levels. This phenomenon commonly takes place in systems characterized by steep thermal gradients, such as volcanic environments and hydrothermal vein systems. In contrast, secondary boiling develops when the hydrothermal fluid re-enters an unstable state as a consequence of fluid–rock interaction, structural discontinuities (e.g. fractures), or changes in temperature and fluid chemistry. Under these conditions, a new vapour phase may form without a significant large-scale pressure drop. This type of boiling is primarily driven by internal chemical reactions or fluid mixing

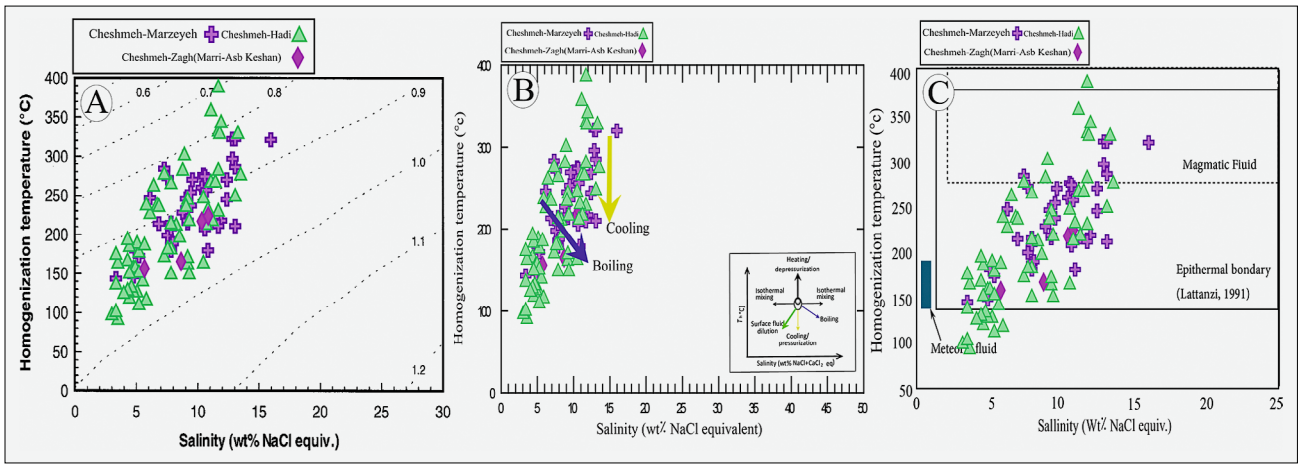


Figure 12. (**A**) Homogenization temperature versus salinity diagram for determining dominant metal complexes (after **Pirajno, 2009**). (**B**) Homogenization temperature versus salinity plot of various deposit types (**Wilkinson, 2001**), with the Cheshmeh-Hadi copper deposit samples falling within the epithermal deposit field. (**C**) Salinity versus homogenization temperature diagram of fluid inclusions showing different fluid-type fields (**after Beane, 1983**)

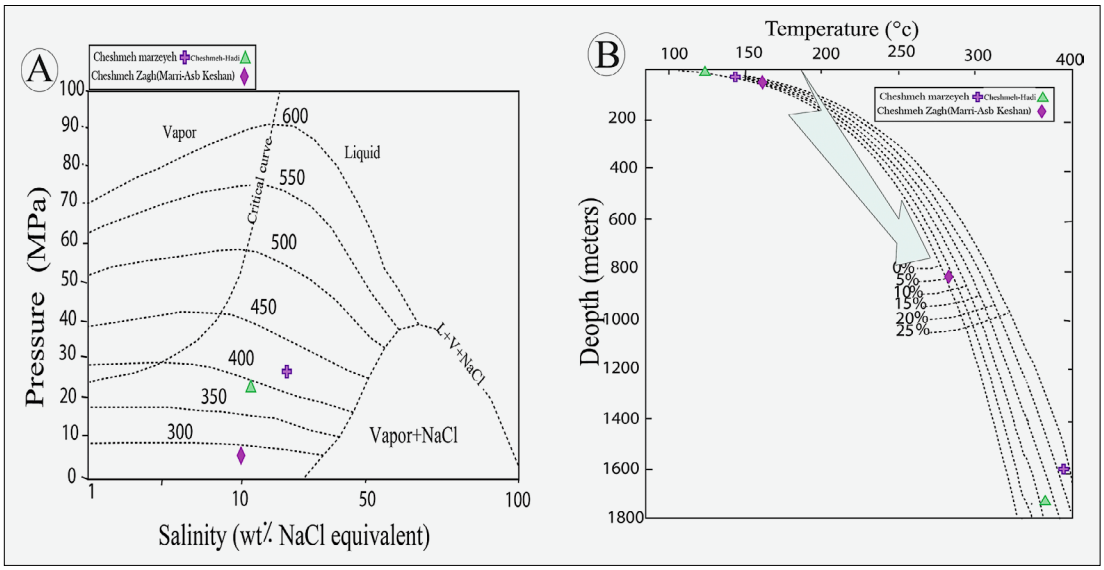


Figure 13. (**A**) Pressure versus salinity diagram showing fluid inclusion pressures of 26/5–28/5 MPa in the Cheshmeh-Hadi copper deposit (**after Zang and Frantz, 1987**). (**B**) Homogenization temperature versus depth diagram for estimating trapping depth of fluids in the Cheshmeh-Hadi copper deposit (**after Haas, 1971**)

processes. It typically occurs where hydrothermal fluids interact or mix with cooler or meteoric waters, or where water–rock reactions induce chemical disequilibrium and vapour generation.

The homogenization temperature–salinity diagram reflects a progressive cooling and dilution of the mineralizing fluid, with both temperature and salinity declining during late-stage deposition (see **Figure 11**). Hydrothermal systems dominated by hydrostatic pressure commonly experience boiling, and vapour pressure can be used to estimate trapping depths. Such systems generally relate to near-surface environments within the upper ~3 km of the crust (**Kant et al., 2012; Wilkinson, 2001**).

To identify the dominant metal-bearing complex, fluid inclusion data were plotted on **Pirajno's (2009)** diagram, showing that Cheshmeh-Hadi fluids fall within the sulfide complex field (see **Figure 12A**). According to **Wilkinson's (2001)** classification of ore-forming systems based on salinity and homogenization temperature, the Cheshmeh-Hadi samples fall within the epithermal deposit range (see **Figures 12B, C**). Origin determination using **Kesler's (2005)** diagram indicates that the fluids derive from magmatic waters, metamorphic waters, and meteoric waters, which likely reacted with host rocks during ascent, migrating along faults and fractures to deposit metals at the contact between conglomerate, andesite, agglomerate, and numulitic limestone.

The coexistence of liquid-rich, vapour-rich, two-phase inclusions with varying fill volumes, as well as some homogenized vapour inclusions, confirms boiling

Table 2. Sulfur isotopic composition ($\delta^{34}S$ ‰) of sulfide minerals in the Cheshmeh-Hadi copper deposit

Chalcopyrite<=>H_2S(**Li & Liu, 2006**)									
Sample Point	Mineral	$\delta^{34}S$min(‰)	T(°C)*-Min	T(°C)*-Ave	T(°C)*-Max	1000 Ln α-T(min)	1000 Ln α-T(Ave)	1000 Ln α-T(max)	$\delta^{34}SH_2S$fluid(‰)
CH-H-S17B	Chalcocite-Bornite-Chalcopyrite-Covellite-Silica(Quartz)	-23.8 ± 0.3	102	193.79	279	0.4	0.2	0.2	-24.0 ± 0.3
Galena<=>H_2S(**Li & Liu, 2006**)									
Sample Point	Mineral	$\delta^{34}S$min(‰)	T(°C)*-Min	T(°C)*-Ave	T(°C)*-Max	1000 Ln α-T(min)	1000 Ln α-T(Ave)	1000 Ln α-T(max)	$\delta^{34}SH_2S$fluid(‰)
CH-H-S17B	Chalcocite-Bornite-Chalcopyrite-Covellite-Silica(Quartz)	-23.8 ± 0.3	102	193.79	279	-4.6	-2.9	-2.1	-21.1 ± 0.3
Galena<=>Chalcopyrite(**Li & Liu, 2006**)									
Sample Point	Mineral	$\delta^{34}S$min(‰)	T(°C)*-Min	T(°C)*-Ave	T(°C)*-Max	1000 Ln α-T(min)	1000 Ln α-T(Ave)	1000 Ln α-T(max)	$\delta^{34}SH_2S$fluid(‰)
CH-H-S17B	Chalcocite-Bornite-Chalcopyrite-Covellite-Silica(Quartz)	-23.8 ± 0.3	102	193.79	279	-3.3	-1.5	-0.6	-22.3 ± 0.3

processes in the study area. Using the **Hass (1971)** diagram, the depth of mineralization in Cheshmeh-Hadi was estimated based on homogenization temperatures ranging from 90 to 386°C. The most frequent homogenization temperature range (100–300°C) corresponds to trapping depths between ~100 and 1580 meters (see **Figure 13A**). This suggests sulfate (SO_4^{2-}) or bisulfide (HS^-) as the dominant anions, consistent with the presence of minerals such as chalcocite and bornite. Using homogenization temperatures and boiling point data, and applying **Hass (1971)**, the trapping pressure of fluid inclusions was calculated via $P = H\rho g$, yielding pressures between 235 and 265 bar (see **Figure 13B**). The relationship between homogenization temperature and pressure is illustrated in **Figure 13**.

4.4. Stable Isotopes

4.4.1. Sulfur Isotopes

In order to investigate the origin and nature of ore-forming and alteration-related fluids in the Cheshmeh-Hadi copper deposit, sulfur and oxygen isotope analyses were performed. One sulfide mineral sample and two silica mineral samples were selected. Sample preparation was carried out at the laboratory in Tehran, and the specimens were subsequently sent to the Stable Isotope Research Laboratory at Arak University for isotopic analysis (see **Table 2**). Sulfur isotope fractionation occurs via two principal mechanisms that result in natural variations of $\delta^{34}S$ values in different environments and materials (**Hoefs, 2004**): (a) Abiotic isotopic fractionation, which takes place through various chemical exchange reactions between sulfate and sulfide species, or among different types of sulfides;

(b) Biological (kinetic) isotopic fractionation, which occurs through microbial metabolic processes, leading to the preferential incorporation of lighter sulfur isotopes (^{32}S) into biologically-derived products. In hydrothermal systems, sulfur is primarily present in reduced forms such as H_2S, HS^-, and S^{2-}, which play key roles in ore deposition processes (**Meheut et al., 2007**). The most stable sulfur species in reducing and alkaline environments are H_2S and HS^-. Under these conditions, the oxygen fugacity (fO_2) and pH of the hydrothermal fluids tend to be low, and the $\delta^{34}S$ values of deposited sulfide minerals generally reflect those of the total sulfur in the fluid (**Li and Liu, 2006**).

The sulfide minerals in the Cheshmeh-Hadi copper deposit exhibit a relative depletion in the heavy sulfur isotope (^{34}S). One of the plausible explanations for this isotopic depletion is the derivation of hydrothermal sulfur from the leaching of sulfide minerals in reduced sedimentary environments (**Hoefs, 2004**). The $\delta^{34}S$ values of H_2S in the ore-forming hydrothermal fluid are estimated to range from –22.6‰ to –2.7‰. In comparison, the $\delta^{34}S$ values in peridotitic kimberlites of mantle origin are approximately 0 ± 1‰, and in basaltic rocks typically vary between 0‰ and 5‰ (**Hoefs, 2004**). However, the recy-

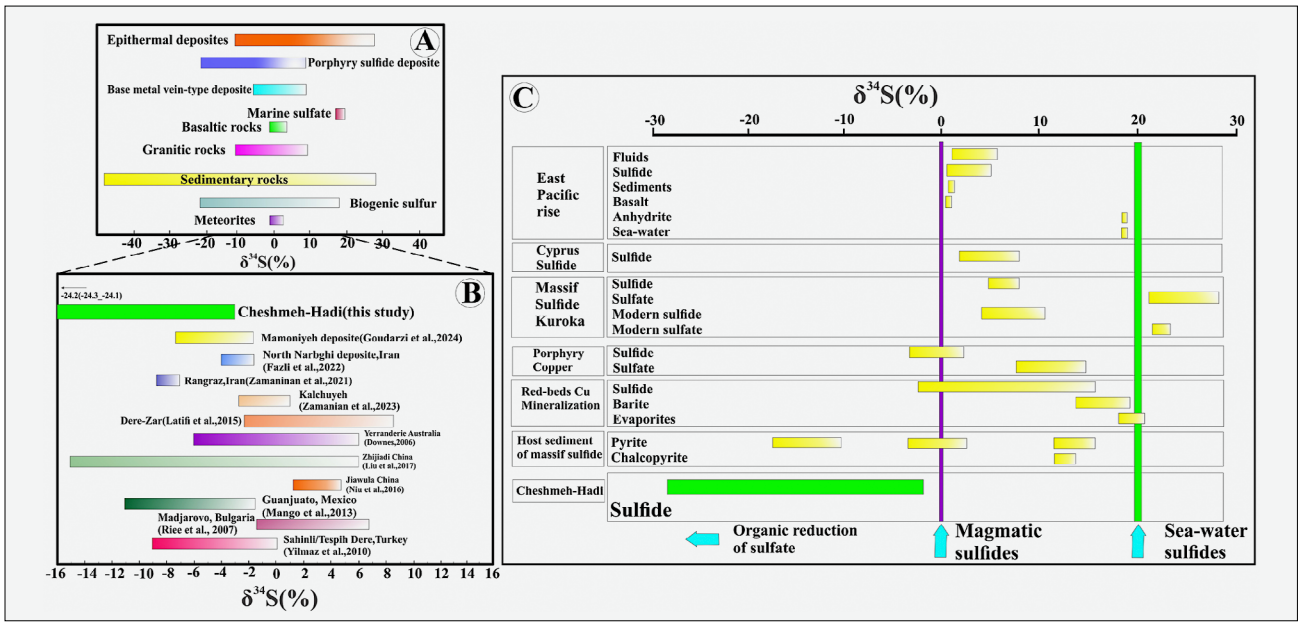


Figure 14. (**A**) Comparison of $\delta^{34}S$ values of sulfur in sulfides from various rock types (**Marini et al., 2011; Hoefs, 2021**). The data illustrate the typical sulfur isotope compositions for mantle-derived, magmatic, and crustal sources, showing distinct isotopic fields. (**B**) Sulfur isotopic compositions ($\delta^{34}S$) of sulfide minerals from the Cheshmeh-Hadi copper deposit compared to global epithermal deposits and deposits within the Urumieh-Dokhtar magmatic arc. The $\delta^{34}S$ values of Cheshmeh-Hadi sulfides fall within or near the compositional fields typical of hydrothermal systems, suggesting a similar fluid evolution pathway. (**C**) Comparison of $\delta^{34}S$ values of sulfides from the Cheshmeh-Hadi deposit with various geological environments (**Rollinson, 1993**). The data suggest that the sulfur isotopic signature of the Cheshmeh-Hadi sulfides is consistent with sources related to ilmenite-series granites and volcanic-hosted hydrothermal systems

cling of crustal materials (e.g. sulfides and marine sulfates) in subduction zones, as well as mantle contamination, can lead to significant heterogeneity in mantle sulfur isotopic values ranging from –10‰ to +10‰ (**Ohmoto and Goldhaber, 1997**). Therefore, the isotopic composition of the hydrothermal fluid may suggest a magmatic origin. Sulfur in the Cheshmeh-Hadi deposit may have been derived either from the leaching of primary volcanic-hosted sulfide minerals or directly from magmatic-hydrothermal fluids. One contributing factor to the ^{34}S depletion could be the preferential leaching of ^{32}S (due to its higher reactivity compared to ^{34}S; (**Hoefs, 2004**) from volcanic and pyroclastic host rocks by meteoric-dominated hydrothermal fluids. Another factor may be isotopic fractionation between sulfate and sulfide species in the hydrothermal fluid. Following isotopic equilibrium fractionation, and subsequent ^{34}S-depletion in sulfides, two potential scenarios could have occurred:

(a) During sulfide mineralization, the hydrothermal fluid expelled and dispersed the sulfate phase away from the vein system. The scarcity of sulfate minerals alongside sulfides may support this removal of sulfate-bearing fluids during or after mineralization. This scenario is consistent with acidic and oxidizing conditions facilitating sulfide precipitation from sulfur complexes and promoting sulfate phase separation.

(b) Prior to the current stage of sulfide deposition, the sulfate phase may have been precipitated at greater depths, allowing the upward migration of a sulfide-dominant hydrothermal fluid into the vein system, where it precipitated ^{34}S-depleted sulfide minerals.

Another mechanism possibly responsible for the observed ^{34}S depletion is the derivation of sulfur from sedimentary sequences containing biogenic sulfides, leached by meteoric-dominated hydrothermal fluids. However, given the fluid inclusion temperatures and the absence of sulfur-bearing sedimentary host rocks, a biogenic sulfur source and bacterial reduction processes are unlikely. Instead, the mixing of meteoric and magmatic waters likely produced a system in which both sulfate and reduced sulfur were generated. The $\delta^{34}S$ values of sulfide minerals in the Cheshmeh-Hadi deposit, when compared to various geological environments and sulfur sources, closely resemble those from ilmenite-series granites and hydrothermal sulfides (see **Figure 14A, B, C**). Additionally, **Figure 15** compares the $\delta^{34}S$ values of Cheshmeh-Hadi with those from other deposits in Central Iran, the Urumieh–Dokhtar belt, and other global analogues. These comparisons suggest that sulfide mineralization in the Cheshmeh-Hadi deposit was formed from fluids that derived sulfur predominantly via the reduction of seawater sulfate.

4.4.2. Oxygen Isotopes

The oxygen isotope compositions ($\delta^{18}O$) of hydrothermal fluids associated with altered and mineralized carbonate samples from the Cheshmeh Hadi copper deposit are presented in **Table 3**. The $\delta^{18}O$ values of mineralized samples fall within or close to the compositional fields of

meteoric water, basalts, and sedimentary rocks, suggesting that the hydrothermal fluids involved in ore deposition were primarily of magmatic origin but underwent mixing with meteoric waters. The $\delta^{18}O$ values of altered but barren carbonate samples plot entirely within the meteoric water range, slightly shifting toward magmatic compositions, indicating that carbonate alteration may have resulted from interaction between magmatic and meteoric fluids. This isotopic transition is consistent with the fluid inclusion microthermometry data, which indicate decreasing fluid temperatures due to fluid mixing and dilution. The evolution from a magmatic-dominated fluid to cooler, oxidizing, and more diluted meteoric waters is characteristic of hydrothermal systems where ore precipitation is triggered by fluid mixing, cooling, and changes in redox conditions (see **Figure 15**).

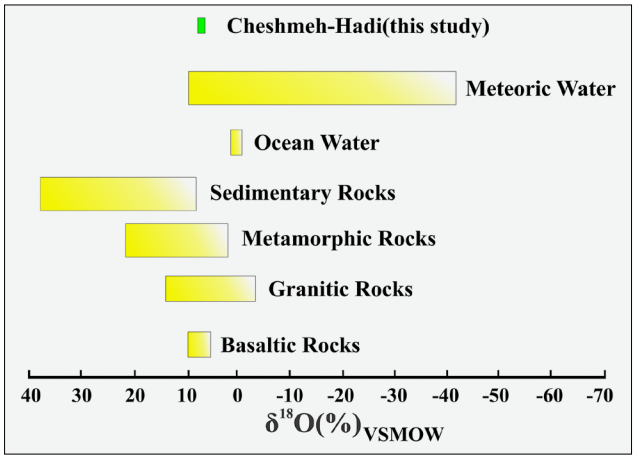


Figure 15. Comparison of $\delta^{18}O$ values from the Cheshmeh-Hadi copper deposit with various geological environments (**after Hoefs, 2004**)

The $\delta^{34}S$ values for three chalcopyrite samples from the main mineralization stage, after temperature correction, range narrowly between –24.3‰ and –2.6‰. These samples are located within evaporitic or sedimentary units containing sulfides of organic origin (**Oyarzun et al., 1998**). Oxygen isotope data from the Cheshmeh Hadi deposit indicate that the hydrothermal fluid responsible for mineralization had a meteoric origin. As it passed through sedimentary rocks, its heavy oxygen content increased (**Kojima et al., 2009**). The fluid became warmer as it moved downward, and the possible presence of cooling intrusive bodies at depth may also have contributed to fluid heating. During its downward circulation through sedimentary and volcanic units, the hydrothermal fluid leached copper from the host rocks and transported it. Isotopic data suggest that the sulfide necessary for mineralization was derived from the reduction of sulfate present in marine and evaporitic sediments; therefore, sulfate- and carbonate-bearing rocks played a key role in mineralization (carbonate-rich environments provided reducing conditions favourable for the conversion of sulfate to sulfide). Subsequently, as the hydrothermal fluid moved upward, copper-bearing minerals- mainly chalcopyrite and minor amounts of chalcocite- were deposited in fractures and cavities of the host rocks in primary or hypogene form. Upon exposure to near-surface conditions, these sulfide minerals were partially oxidized to secondary oxide minerals such as malachite, azurite, and covellite, forming a supergene enrichment zone.

4.5. Geochemistry of Major and Trace Elements

Eight samples from volcanic outcrops and drill cores were selected for petrographic and geochemical analyses of major and trace elements (see **Table 4**).

Table 3. Oxygen isotope compositions of hydrothermal fluids in equilibrium with host rocks in the Cheshmeh-Hadi copper deposit

Muscovite<=>H_2O(**Zheng, 1993b**)									
Sample Point	Mineral	$\delta^{18}O$min(‰)	T(°C)*-Min	T(°C)*-Ave	T(°C)*-Max	1000 Ln α-T(min)	1000 Ln α-T(Ave)	1000 Ln α-T(max)	$\delta^{18}OH_2O$fluid(‰)
CH.H-S13A	Silica(Quartz)	+7.6 ± 0.0	89	177.3	387	12.4	5.6	0.1	+2.0 ± 0.0
CH.H-S17A	Chalcocite-Bornite-Chalcopyrite-Covellite-Silica(Quartz)	+7.7 ± 0.3	102	193.69	279	11.3	4.8	1.9	+2.9 ± 0.3
Quartz<=>H_2O (**Meheut et al., 2007**)									
Sample Point	Mineral	$\delta^{18}O$min(‰)	T(°C)*-Min	T(°C)*-Ave	T(°C)*-Max	1000 Ln α-T(min)	1000 Ln α-T(Ave)	1000 Ln α-T(max)	$\delta^{18}OH_2O$fluid(‰)
CH.H-S13A	Silica(Quartz)	+7.6 ± 0.0	89	177.3	387	24.4	13.5	2.8	-6.2 ± 0.0
CH.H-S17A	Chalcocite-Bornite-Chalcopyrite-Covellite-Silica(Quartz)	+7.7 ± 0.3	102	193.69	279	22.9	12.1	6.5	-4.6 ± 0.3

Table 4. Chemical Analysis Results of the Studied Samples from the Cheshmeh-Hadi Copper Deposit (major elements in wt.%, trace ppm)

Sample	SiO_2	Al_2O_3	Na_2O	MgO	K_2O	TiO_2	CaO	Fe_2O_3	Ag	Pb	Cu	Mo	Bi	Fe	Co	Ni	Ti	Sb
CH.H-18	63.98	18.01	3.94	0.45	3.67	0.59	2.97	5.21	0.59	14.98	1069	2.21	0.06	35894	8.21	30	4466	1.11
CH.H-19	64.01	17.66	3.78	0.25	3.18	0.64	2.75	7.12	31.8	23.05	576	3.81	0.06	35758	4.21	19	3149	2.21
CH.H-21	57.94	16.83	3.47	0.02	4.13	0.75	2.35	5.45	0.18	37.98	1275	6.83	0.47	41600	4.91	13.89	3810	1.34
CH.H-26	61.43	17.21	5.47	1.45	3.68	0.64	5.74	4.27	0.41	21.95	545	3.03	0.18	38900	8.42	19.74	4010	0.57
CH.H-32	60.87	16.76	5.03	0.04	4.67	0.66	6.84	4.98	0.42	19.96	581	3.79	0.14	35700	6.23	16.27	3910	0.83
CH.H-33	60.11	18.18	5.19	1.65	3.78	0.67	6.03	4.75	0.44	22.1	465	3.28	0.15	31958	4.25	17.38	3410	0.85
CH.H-35	60.98	18.81	6.01	0.04	4.98	0.74	5.27	3.25	0.48	14.1	1067	2.14	0.06	3524	2.34	29.9	3225	1.48
CH.H-37	63.66	18.58	4.78	0.34	4.05	0.57	2.71	6.14	0.13	17.2	401	2.82	0.12	32354	9.91	18.84	0.49	1.82

Table 4. (continued)

Tl	Li	Be	Na	K	Ca	Mg	Al	Ga	Cs	Rb	Ba	Sr	Th	U	Y	Zr	Hf	Nb	Ta
0.54	11.02	4.92	31398	34735	24984	2869	7471	15.18	4.82	94.1	614	317	4.35	1.26	14.39	119.5	3.09	5.49	0.39
0.4	10.1	3.92	27589	28341	18036	1854	6503	15.19	3.92	79.2	421	316	4.29	1.55	14.49	18.5	3.13	4.59	0.3
0.59	15.87	1.12	32795	35286	13581	2397	2.67	15.17	5.41	74.4	255	133	2.7	0.35	8.69	109.6	3.79	4.68	0.45
0.5	22.69	1.43	36787	36297	47742	2386	4.18	18.58	5.69	78.3	369	224	3.9	0.34	17.99	128.5	3.67	5.39	0.42
0.57	18.54	1.24	35883	38176	34536	1396	2.59	17.28	6.71	101.3	401	185	3.2	0.26	14.98	110.6	3.16	4.88	0.36
0.55	17.35	1.51	35852	37609	35087	1288	2.38	16.18	6.8	122.2	362	191	3.2	0.24	14.99	110.5	3.16	5.29	0.24
0.38	10.1	3.91	30426	36678	23252	2779	7373	14.37	4.2	802.3	514	313	3.9	1.33	13.98	100.4	3.1	5.19	0.25
0.55	20.68	1.42	29138	42154	32243	4097	3459	17.76	5.61	86.4	399	174	4.5	0.24	20.59	142.35	4.17	5.97	0.47

Table 4. (continued)

P	La	Ce	Pr	Nd	Sm	Eu	Er	Gd	Tb	Dy	Ho	Tm	Yb	Lu
1095	12.05	29.9	3.92	13.71	2.97	0.97	1.67	3.27	0.48	3.05	3.38	0.28	1.81	0.3
1242	11.04	25.95	3.6	12.62	2.88	0.94	1.62	3.28	0.47	3.04	3.37	0.28	1.72	0.27
1006	4.64	9.88	1.3	5.82	1046	0.61	1.31	3.21	0.28	1.83	3.38	0.23	1.42	0.24
1010	8.93	19.48	2.55	11.01	3.01	1.01	2.35	3.1	0.52	3.36	3.67	0.34	2.31	0.37
802	5.61	13.49	1.84	8.03	2.34	0.94	1.78	3.22	0.43	2.76	0.56	0.31	1.83	0.32
904	6.12	12.48	1.72	9.27	2.34	0.76	1.81	3.12	0.34	2.43	0.57	0.23	2.05	0.24
1036	12.04	31.99	2.88	12.83	2.68	0.99	1.57	3.14	0.43	2.79	0.33	0.26	1.61	0.31
1014	7.44	17.96	2.29	10.86	2.23	1.01	2.63	3.37	0.51	3.28	0.73	0.34	2.6	0.42
1095	12.05	29.9	3.92	13.71	2.97	0.97	1.67	3.27	0.48	3.05	3.38	0.28	1.81	0.3
1242	11.04	25.95	3.6	12.62	2/88	0.94	1.62	3.28	0.47	3.04	3.37	0.28	1.72	0.27
1006	4.64	9.88	1.3	5.82	1046	0.61	1.31	3.21	0.28	1.83	3.38	0.23	1.42	0.24

For rock classification and minimizing alteration effects, immobile elements were used. Based on the Nb/Y vs. Zr/Ti diagram (**Pearce, 1996**), the volcanic rocks are classified mainly as andesite, basaltic andesite, basalt, and alkali basalt (see **Figure 16A**). Using the Nb/Y vs. Zr/TiO_2 plot (**Winchester and Floyd, 1977**), the samples are sub-alkaline basalt, basaltic andesite, and andesite (see **Figure 16B**). The Zr/TiO_2 vs. SiO_2 plot indicates compositions ranging from andesite to dacite and rhyodacite (see **Figure 16C**). Based on Co vs. Th (**Hasite et al., 2007**), the samples fall within the calc-alkaline basalt–andesite–andesite series (see **Figure 16D**).

To distinguish between continental arc and island arc settings, Ta/Yb vs. Th/Yb (see **Figure 16E**) and Zr vs. Zr/Y (see **Figure 16F**) diagrams (**Pearce, 1983**) were used. The samples plot in the continental arc field, indicating a source in enriched mantle influenced by subduction-zone fluids. High Th contents likely result from crustal contamination and subducted slab-derived fluids. Magmas from active continental margins typically show stronger enrichment in incompatible LREEs compared to island arc magmas, likely due to a combination of enriched mantle sources and crustal assimilation. The Zr vs. Zr/Y plot further confirms their placement within the continental volcanic arc field.

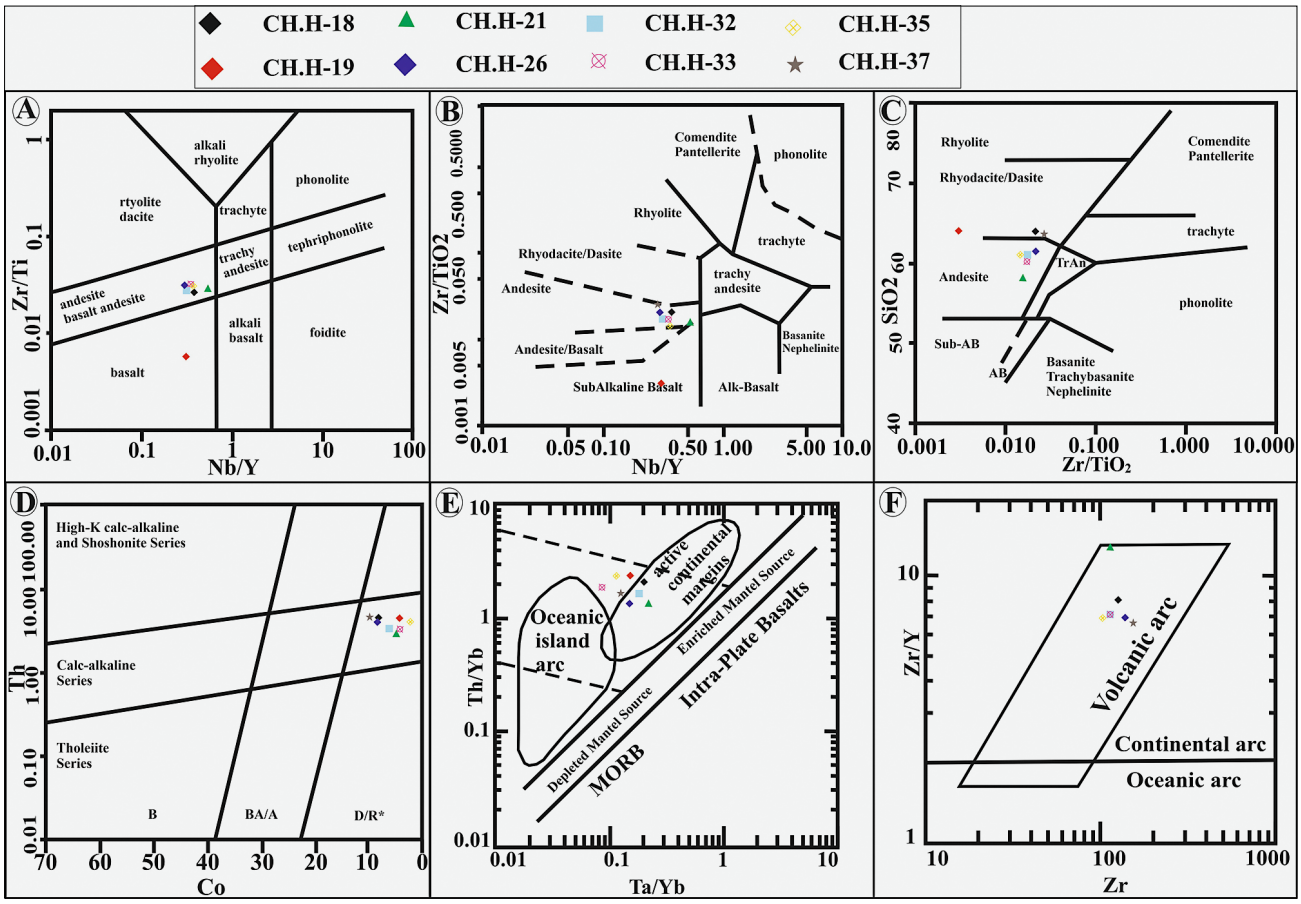


Figure 16. Geochemical discrimination diagrams used to identify the magma series and tectonomagmatic nature of the volcanic rocks in the Cheshmeh-Hadi copper deposit: (A) Nb/Y vs. Zr/Ti (**Pearce, 1996**), (B) Nb/Y vs. Zr/TiO_2 (**Winchester and Floyd, 1977**), (C) Zr/TiO_2 vs. SiO_2 (**Winchester and Floyd, 1977**), (D) Co vs. Th (**Hasite et al., 2007**), (E) Ta/Yb vs. Th/Yb (**Pearce, 1983**), (F) Zr vs. Zr/Y (**Pearce, 1983**)

The SiO_2 content in the volcanic rocks ranges from 57.94 to 64.01 wt%, with an average of 61.62 wt%. Al_2O_3 varies between 16.76 and 18.81 wt%, CaO from 2.35 to 6.84 wt%, Na_2O from 3.47 to 6.01 wt%, K_2O from 3.18 to 4.98 wt%, MgO from 0.02 to 1.65 wt%, TiO_2 from 0.57 to 0.75 wt%, and total Fe_2O_3 (Fe_2O_3T) from 3.25 to 7.12 wt%. To understand the processes influencing magma evolution, such as fractional crystallization, binary plots of oxide- oxide, oxide- element, and element- element Harker diagrams (**Harker, 1909**) were utilized. Generally, linear or negatively correlated trends suggest the influence of processes like fractional crystallization, magma mixing, or crustal assimilation. However, significant scattering may reflect crystal accumulation, alteration, or crustal contamination (**Willson, 2007**). Among the major oxides, Na_2O and Al_2O_3 show increasing trends (see **Figure 17C, E**). K_2O versus SiO_2 lacks a clear trend and shows scattered values (see **Figure 17F**). In calc-alkaline suites, the concentrations of MgO, CaO, Fe_2O_3, and TiO_2 decrease with increasing SiO_2, which aligns with the volcanic rocks of the Cheshmeh-Hadi deposit (**Feely et al., 2002**), reflecting the crystallization of ferromagnesian minerals and plagioclase, amphibole, and clinopyroxene fractionation (see **Figure 17A, B**). The decreasing CaO trend corresponds to plagioclase crystallization from anorthite to albite (see **Figure 17D**). The increasing trends in Na_2O and possibly K_2O may be attributed to the presence of alkali feldspar in the final stages of crystallization or potassium addition during hydrothermal alteration (**Feely et al., 2002**). These trends overall highlight the role of continental crust in the magmatic evolution. In the SiO_2 vs. Sr diagram (see **Figure 17G**), Sr shows a decreasing trend consistent with plagioclase fractionation at low pressure. Since Sr is compatible in plagioclase but not in clinopyroxene, this trend also matches the decreasing CaO pattern due to plagioclase evolution. Europium (Eu) first increases with increasing SiO_2 and then decreases, reflecting plagioclase involvement in magma evolution, further supported by a positive correlation between Sr and Eu (see **Figure 17H**). The Dy/Yb ratio shows a slight decrease with increasing SiO_2, indicating hornblende or clinopyroxene fractionation (see **Figure 17I**). The Sr content also decreases with MgO, suggesting plagioclase removal (see **Figure 17J**). The Rb/Sr ratio first decreases and then increases with increasing Sr, displaying an almost linear trend consistent with plagioclase, hornblende, and clinopyroxene fractionation (**Davidson**

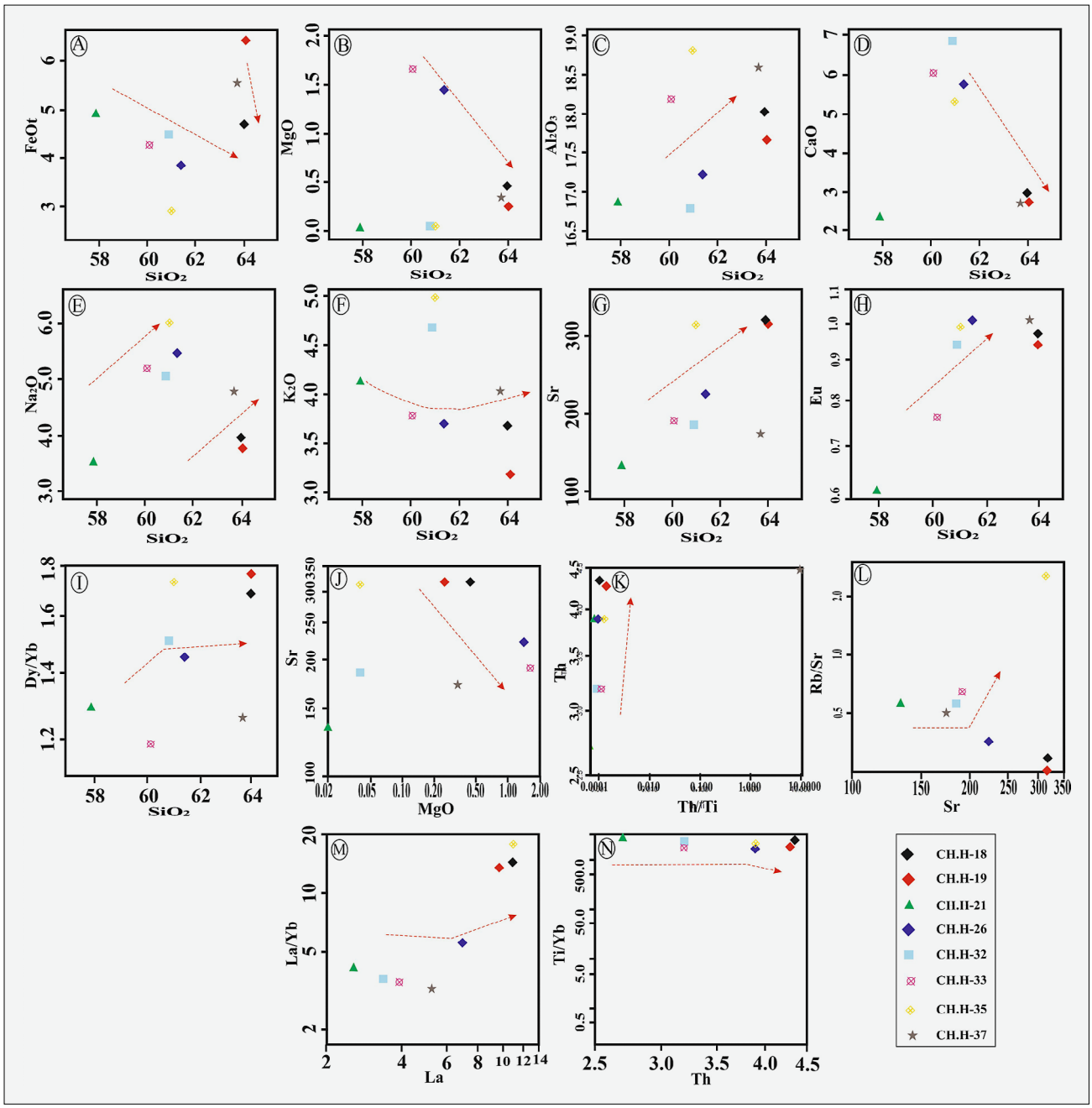


Figure 17. Harker variation diagrams used for petrogenetic interpretation of the volcanic rocks from the Cheshmeh-Hadi copper deposit: (A) SiO_2 vs. FeOt, (B) SiO_2 vs. MgO, (C) SiO_2 vs. Al_2O_3, (D) SiO_2 vs. CaO, (E) SiO_2 vs. Na_2O, (F) SiO_2 vs. K_2O, (G) SiO_2 vs. Sr, (H) SiO_2 vs. Eu, (I) SiO_2 vs. Dy/Yb, (J) MgO vs. Sr, (K) Th/Ti vs. Th, (L) Sr vs. Rb/Sr, (M) La vs. La/Yb, (N) Th vs. Ti/Yb. (**Stepanov et al., 2014; Klimm et al., 2008; Davidson et al., 2007; Wilson, 2007**)

et al., 2007) (see **Figure 17L**). The Th/Ti vs. Th (see **Figure 17K**), La vs. La/Yb (see **Figure 17M**), and Th vs. Ti/Yb (see **Figure 17N**) diagrams (**Schiano et al., 2010**) indicate crustal contamination during magmatic differentiation in the Cheshmeh-Hadi region. Spider diagrams normalized to primitive mantle (**Sun and McDonough, 1989**) show negative slopes with enrichment of LILEs over HFSEs, and depletion in HREEs, all features characteristic of calc-alkaline magmas. The observed positive Pb anomaly is indicative of crustal contamination during magma evolution (see **Figure 18A**). In the chondrite-normalized REE diagram, the volcanic rocks from Cheshmeh-Hadi exhibit moderate LREE enrichment, HREE depletion, and weak negative Eu anomalies, further reflecting plagioclase fractionation and a continental arc signature (see **Figure 18B**).

4.6. Tectono-Magmatic Model

Most of the known Manto-type copper deposits in Iran formed during the Eocene period – a time characterized by intense tectonic and magmatic activity, especially within the Urumieh-Dokhtar Magmatic Arc (UDMA),

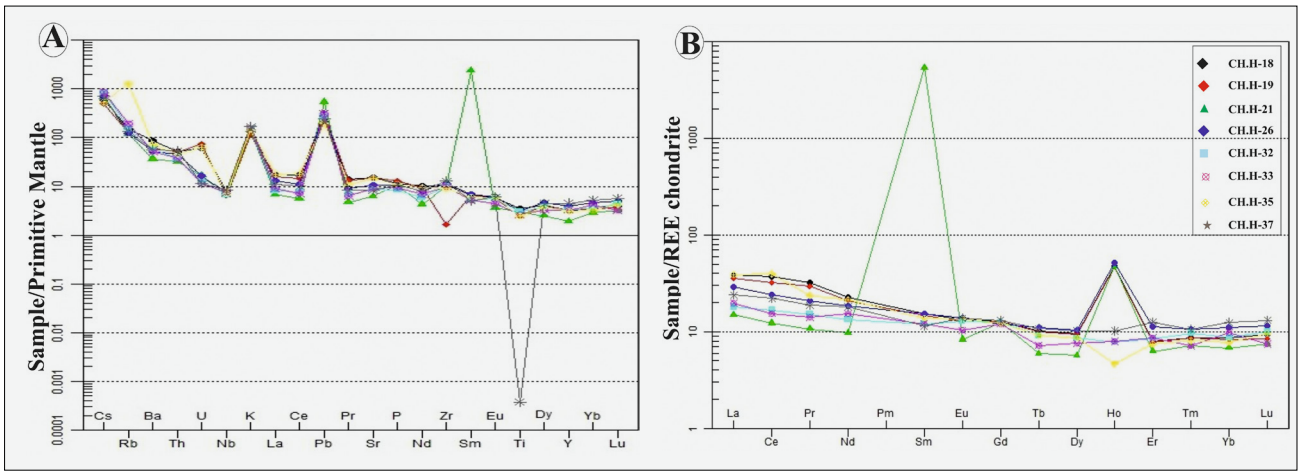


Figure 18. (**A**) Primitive mantle–normalized trace element patterns for rock samples from the Cheshmeh-Hadi deposit. Normalization values are from **Sun and McDonough (1989)**. (**B**) Chondrite-normalized rare earth element (REE) patterns for samples from the Cheshmeh-Hadi deposit, with chondrite values from **Boynton (1984)**

Alborz Magmatic Arc (AMA), and the Sabzevar region. The Eocene is considered a key metallogenic epoch due to the closure of the Neo-Tethys Ocean. Many of Iran's mineral deposits, including Manto-type copper deposits, are closely related to the evolution of the Neo-Tethys Ocean. These deposits typically form in arc-related or subduction zone settings and are generally associated with volcano-sedimentary environments along plate boundaries. They are often hosted by basaltic to andesitic rocks. The general formation process of Manto-type copper deposits involves the generation of calc-alkaline magma in the subduction zone, heat-induced alteration due to intrusive bodies, and the precipitation of copper along fractures and rock porosity through hydrothermal fluids derived from the mantle and lower crust. The Khaf–Doruneh Belt (in the southern Sabzevar Zone, northwest of Bardeskan) hosts Manto-type copper mineralization due to its tectonically active setting related to the subduction of Neo-Tethyan oceanic crust beneath the Central Iranian continental crust and the concurrent Eocene magmatic activity (see **Figure 19A**). These deposits are typically stratabound and hosted in volcanic and sedimentary sequences. The Sabzevar Ocean, situated between the Lut Block to the south and the Turan Block to the north, remained open since at least the mid-Cretaceous. Intra-oceanic subduction in the Sabzevar Basin likely began before the Albian, as evidenced by the presence of high-pressure metamorphic rocks (**Rossetti et al., 2010**). Similar to UDMA magmatism, the Eocene–Oligocene magmatic rocks in the Kashmar region of the Sabzevar area formed during Eocene extensional tectonics (**Shafaii Moghadam et al., 2015**). The Eocene volcanic activity in Davarzan–Abbasabad (Sabzevar) began with continental to shallow marine Paleogene–Eocene sediments and was followed by widespread subaqueous to subaerial basaltic and andesitic volcanism, volcaniclastic rocks, and sedimentary sequences during the middle to late Eocene (**Ghasemi and Rezaei-Kahkhaei, 2015**). These E–W-trending magmatic rocks were generated in response to the subduction of Neo-Tethyan oceanic lithosphere beneath the eastern Alborz (see **Figure 20B**). The mid-Eocene volcanic rocks of the Davarzan–Abbasabad area formed in a back-arc extensional setting and are associated with post-Eocene subduction-related magmatism (see **Figure 19B**). This region experienced collisional and post-collisional tectonic events during the Oligocene to Miocene (**Berberian and King, 1981; Ghasemi and Talbot, 2006; Asiabanha et al., 2012; Asiabanha and Foden, 2012; Ghasemi and Rezaei-Kahkhaei, 2015**). In western Sabzevar (Davarzan–Abbasabad area), these Eocene volcanic rocks host Manto-type Cu–Ag mineralization, including the Bozorg Mine, Damanjala, Asiadeyu, Labkalu, North Choghandarsar, South Choghandarsar, Elhak, and Dochileh deposits. Three main hypotheses have been proposed for the formation of Manto-type deposits: Syn-volcanic or syngenetic formation concurrent with volcanic activity (**Sato, 1984; Ruiz et al., 1971; Tosdal and Munizaga, 2003**). Formation through the action of intrusive bodies and their derived hydrothermal fluids (**Palacios, 1986, 1990; Oliveros et al., 2008**). Formation via leaching of copper from volcanic units during diagenetic processes (**Sato, 1984; Wilson and Zentilli, 2006; Wilson et al., 2003a, b; Kirkham, 1996; Tosdal and Munizaga, 2003**). The formation of the Cheshmeh Hadi deposit can be divided into two main stages: Hypogene stage – associated with volcanic activity, early diagenesis, and diagenetic alteration and Supergene stage – related to uplift and the influence of meteoric fluids.

4.6.1. Early Diagenesis

During the Eocene, a rift-related extensional environment developed behind the Sabzevar magmatic arc. As a result of volcanic activity, volcanic and pyroclastic rocks were deposited over the basement of this rifted setting.

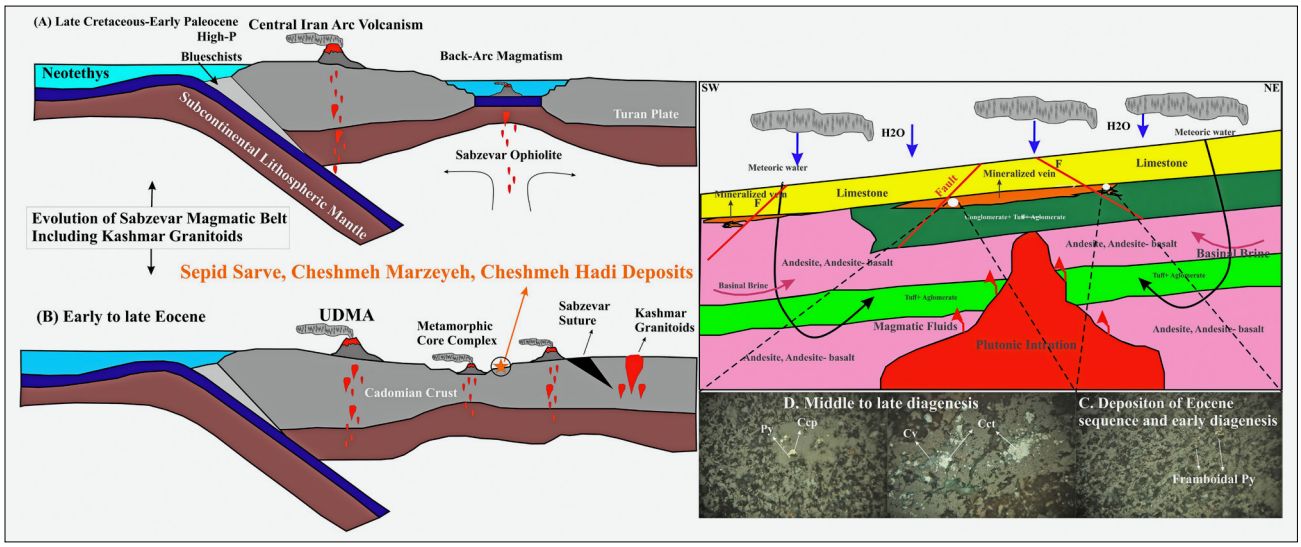


Figure 19. Schematic model illustrating the formation and evolution of the Sabzevar region: (**A**) Oblique subduction of the Neo-Tethyan lithosphere beneath the Iranian plate from Middle–Late Jurassic to Late Cretaceous, followed by the development of back-arc sedimentary and magmatic basins in the Sabzevar area. (**B**) From early to late Eocene, the Kashmar granites and associated volcanic rocks formed above a north-dipping subduction zone during a phase of magmatic flare-up triggered by regional extension (**Shafaii Moghadam et al., 2015**). These Eocene volcanic rocks host Manto-type Cu deposits in the Sepidsarv, Cheshmeh Marzih, and Cheshmeh Hadi areas. (**C-D**) The formation of the Cheshmeh Hadi deposit can be divided into two main stages: Hypogene stage – associated with volcanic activity, early diagenesis, and diagenetic alteration. Supergene stage – related to uplift and the influence of meteoric fluids.

These rocks contain minor amounts of copper, with Cu adsorbed at the surface of their silicate mineral networks. During this stage, along with the formation of the host rocks and early diagenesis, framboidal pyrites formed sporadically within the andesitic-tuffaceous matrix. In many mantle-type copper deposits, the sulfur necessary for pyrite formation is supplied by bacterial reduction of seawater sulfate, which reacts with available iron in the basin, ultimately producing pyrite in the host rock matrix (**Zentilli et al., 2009; Wilson et al., 2003a,b; Wilson and Zentilli, 1999; Corrillo-Rosua et al., 2014**). Since the Cheshmeh Hadi deposit formed in a shallow marine environment, this mechanism is likely applicable here as well. In this setting, pyrite formation plays a key role in establishing reducing conditions in the mineralized host rock. Following volcanic activity, limestone and shale sediments began to accumulate immediately in the subaqueous environment (see **Figure 19C**).

4.6.2. Intermediate and Late Diagenesis

In rift-related extensional environments, extensive volcanic activity leads to the formation of a thick volcanic-sedimentary sequence, which retains high amounts of heat (**Kirkham, 1996**). During this stage, pressure from diagenesis and dehydration of the underlying pyroclastic units generates hydrothermal fluids. The presence of zeolites in the host rock units indicates the progression of burial diagenesis. The mechanical breakdown of pyroclastic units in oxidizing coastal environments leads to silicate dissolution, forming clay minerals. During this reaction, Cu and Fe hydroxides are released, and Cu is adsorbed on clay minerals and Fe hydroxides. Due to the high ambient temperature and circulation through the volcanic sequence- especially the red layers- these fluids become enriched in copper, leaching it from the units and transporting it upward. Upon reaching porous and reducing andesitic-tuff units (where pyrite is present), the copper-bearing fluids precipitate Cu as sulfide. The oxidizing Cu-bearing fluid reacts with unstable pyrite, and sulfur from the pyrite reduces the fluid, resulting in copper sulfides replacing pyrite. Part of the pyrite's iron enters the sulfide network, and the remainder forms hematite (**Zentilli et al., 2009; Corrillo-Rosua, 2014**). The high concentration of hematite around Cu sulfides in the host rock supports this mechanism. Some copper also precipitates due to cooling of the hydrothermal fluid, as high-temperature hydrothermal fluids interact with trapped seawater in the host rock. This cooling destabilizes the chloride complexes transporting copper, leading to Cu sulfide precipitation. During this stage, copper sulfides form as disseminated grains, cavity-filling, and thin veins or veinlets within the host rock. The formation of these small veins is facilitated by the high burial pressure in the host rock during diagenetic mineralization (see **Figure 19D**).

4.6.3. Supergene Stage

This stage involves the uplift of the host rock units, tectonic processes, and weathering. With the onset of uplift, the andesitic host rock of the ore deposit becomes fractured along faults, creating abundant open spaces. During this stage, meteoric fluids leach copper from the

andesite-Conglomerate-Aglomerate host units and concentrate it in fractures and fault-related cracks. The veins formed at this stage typically have greater thickness due to the low confining pressure and are restricted to the mineralized host units. Additionally, primary sulfide minerals are altered into secondary sulfides such as digenite, covellite, malachite, as well as oxidized copper minerals (see **Figure 19D**).

5. Conclusion

The Cheshmeh-Hadi copper deposit is a strata-bound (Manto-type) sulfide system hosted in volcanic-sedimentary sequences formed in a subduction-related magmatic arc setting. The volcanic succession, predominantly comprising basalt, basaltic andesite, and andesite, developed in a non-marine environment, followed by deposition of sedimentary conglomerates and limestone. Mineralization is mainly associated with chlorite, zeolite, and calcite alteration zones. Copper mineralization occurs predominantly as fine-grained chalcocite within permeable conglomerates and, to a lesser extent, in limestones. The ore-forming fluids, characterized by low silica content and reducing conditions, ascended along faults, depositing copper in fractures and pore spaces. Geochemical and isotopic data suggest that the mineralizing fluids originated primarily from a magmatic source but underwent mixing with meteoric waters, promoting sulfide precipitation. Fluid inclusions indicate moderate salinities (3.09–13.39 wt.% NaCl eq.) and highlight boiling and fluid mixing as key mineralization mechanisms. Sulfur isotope values ($\delta^{34}S$ between –2.6‰ and –24.1‰) and oxygen isotope signatures support a model of magmatic-meteoric fluid interaction. Geochemical analyses confirm a calc-alkaline to shoshonitic affinity of volcanic rocks derived from an enriched mantle source influenced by subduction-related fluids and crustal contamination. Mineralogy is dominated by primary chalcocite, bornite, and pyrite, with supergene malachite, azurite, and hematite. Alteration includes regional zeolite–carbonate and localized chlorite and hematite zones. The Cheshmeh-Hadi deposit exemplifies copper mineralization in an active continental margin, where subduction-related magmatism, structural controls (notably the Doruneh Fault), and hydrothermal processes converge to form significant Manto-type deposits in volcano-sedimentary environments.

6. References

Abolipour, M., Rastad, E., Rashidnejad Omran, N. (2015). Manto-type copper mineralization in pyrobitumen-bearing porphyritic andesite, Koshkoiye district of Rafsanjan, Dehaj-Sardoiye subzone. *sciences. Q. J. Geosciences*. 24 (95), 123–144.

Aghanabati, A. (2004). Geology of Iran. *Geological Survey of Iran, Tehran, Iran*, 586 p.

Alavi, M. (1991). Sedimentary and structural characteristics of the Paleo Tethys remnants in northeastern Iran. *Geological Society of America Bulletin*, 103:983-992, https://doi.org/10.1130/0016-7606(1991)103<0983:SASCOT>2.3.CO;2.

Alizadeh, V., Momenzadeh, M., Emami, M.H. (2013). Petrography, geochemistry, mineralogy, fluid inclusions and mineralization study of Vorezg-Qayen copper deposit. *Sciences – Quarterly Journal of Geosciences*. 22 (86), 47–58.

Beane, R.E. (1983). The magmatic-meteoric transition. Geothermal Resources Council, *Special Report* 13, 245–253.

Bodnar, R.J. (1983). A method of calculating fluid inclusion volumes based on vapor bubble diameters and P-V-T-X properties on inclusion fluids. *Economic Geology* 78, 534–542, https://doi.org/10.2113/gsecongeo.78.3.535.

Boveiri Konari, M., Rastad, E., Rashidnejad Omran, N. (2011). Volcanic redbed-type copper mineralization in the Keshtmahaki, Southern Sanandaj-Sirjan Zone, southeastern Iran. *11 th SGA Biennial Meeting Let's Talk Ore Deposits.* 26-29 Sept, Antofagasta, Chile.

Boynton, W.V. (1984). Cosmochemistry of the rare earth elements, Meteorite studies. In: Henderson, P. (Ed.), Rare Earth Element Geochemistry. *Developments in Geochemistry. Elsevier, Amsterdam*, pp. 115–1522, https://doi.org/10.1016/B978-0-444-42148-7.50008-3.

Carrillo-Rosua, F.J. Morales-Ruano, S., Morata Cespedes, D., Boyce, A. J., Belmar, M., Fallick, A. E., Fenoll Hach-Ali, P., Munizaga, F., (2006). Sulfur isotope studies in Chilean "Manto"-type Cu–(Ag) deposits in coastal range of central Chile (area de la serena y Melipilla), *vol. 2, Actas XI Congreso Geologico Chileno, Antofagasta*, 199- 202.

Davidson, J., Turner, S., Handley, H., Macpherson, C. and Dosseto, A. (2007). Amphibole "sponge" *in arc crust Geology* 35: 787–790, https://doi.org/10.1130/G23637A.1.

Dissanayake, C.B. (1993). Gold and other metals in graphite. In: Parnell, J., Kucha, H. and Landais, P. (eds.), Bitumen in Ore Deposits. *Society for Geology Applied to Mineral Deposits*, SP. 9, 138–152, https://doi.org/10.1007/978-3-642-85806-2_9.

Downes, P. M., Yerranderie. (2007). a Late Devonian silver–gold–lead intermediate sulfidation epithermal district, eastern Lachlan Orogen, New South Wales, *Australia. Resource Geology*. 57(1), 1–23, https://doi.org/10.1111/j.1751-3928.2006.00001.x

Ebrahimi. S., Arab-Amiri. A., Ghanbari. H. (2020). Mineralogy, alteration, fluid inclusion and stable isotopes studies of the Sharifabad-Bardeskan copper deposit, NE Iran., *Scientific Quarterly Journal, GEOSCIENCES*. Vol. 30, No. 117, p:135-146.

Entezari Harsini, A. (2017). Geology, Geochemistry, Mineralization, Genesis and Isotope studies of Golcheshmeh deposit, South Neyshabour, Northeastern Iran. *Unpublished Ph.D. thesis, Ferdowsi University of Mashhad, Iran*. 310 p. (in Persian with English abstract).

Fazeli, A. (2002). Type of the copper mineralization at Veshnaveh deposit, south of Qom. [Unpublished M.Sc. thesis], *Tehran, Kharazmi university, Iran*. p. 157.

Fazli, N., Ghaderi, M., Movahednia, M., Maghfouri, S. (2021). Manto-type copper mineralization in the central part of the Urumieh-Dokhtar magmatic arc (Qom-Saveh region) with

emphasis on the East Narbaghi deposit, northeast Saveh. *Iranian Journal of Geology*. 15 (59), 69–90, https://doi.org/10.22059/ijg.302909.1072.

Fazli, N., Ghaderi, M., Movahednia, M., Li, J.W., Lentz, D.R., Yan, S. (2022). Geology and genesis of the North Narbaghi Cu-Ag deposit in the Urumieh-Dokhtar magmatic arc, Iran: fluid inclusion and stable isotope constraints. *Ore Geology Reviews.* 144, 104801, https://doi.org/10.1016/j.oregeorev.2022.104801.

Feely, T. C; Cosca, M. A. and Lindsay, C. R. (2002). Petrogenesis and implications of calc-alkaline cryptic hybrid magmas from Washburn volcano, Absaroka volcanic province, *U.S.A. Journal of Petrology*, 43(4), https://doi.org/10.1093/petrology/43.4.663.

Jabari, A., Malekzadeh Shafaroudi, A., & Karimpoor, M. H. (2016). The stratabound (mantle-type) copper deposit of Kal Abri in the Eocene volcano-sedimentary complex, NW Bardaskan, NE Iran. *Journal of Advanced Applied Geology*. 23.

Jiba, Z., Ghaderi, M., Maghfouri, S. (2021). Geology, mineralogy, and fluid inclusion studies of the Yamaghan Manto-type Cu (Ag) deposit, southeast Zanjan, NW Iran. *Advanced Applied Geology*. 11 (3), 594–615.

Haas, J.L. (1971). The effect of salinity on the maximum thermal gradient of a hydrothermal system at hydrostatic pressure. *Economic Geology* 66, 940-946, https://doi.org/10.2113/gsecongeo.66.6.940.

Harker, A. (1909). The Natural History of Igneous Rocks. *Macmillam*, https://doi.org/10.2307/1777000.

Hasite, A.R., Kerr, A.C., Pearce, J.A. and Mitchell, S.F. (2007). Classification of altered volcanic island arc rocks using immobile trace elements: development of the Th-Co discrimination diagram, *Journal of Petrology*, v. 48, p. 2341-2357, https://doi.org/10.1093/petrology/egm062.

Hedenquist J.W. and Henley R.W. (1985). The important of CO2 on freezing point measurements of fluid inclusion: evidence from active geothermal system and implication for epithermal ore deposition. *Economic Geology*., 80: 1379-1406, https://doi.org/10.2113/gsecongeo.80.5.1379.

Heidari, M. (2012). Study of Geochemistry, Sulfur Stable isotopes, and Genesis of Madan Bozorg Copper Deposit (Abbasabad, East of Shahroud). *Unpublished M.Sc. thesis, Bu-Ali Sina University, Iran*. 169 p. (in Persian with English abstract).

Herazo, A., Reich, M., Barra, F., Morata, D., Real, I.D., Pag` es, A. (2020). Assessing the role of bitumen in the formation of stratabound Cu-(Ag) deposits: Insights from the Lorena deposit, Las Luces district, northern Chile. *Ore Geology Reviews*. 124, 103639, https://doi.org/10.1016/j.oregeorev.2020.103639.

Hoefs, J. (2004). Stable Isotope Geochemistry, *Springer- Verlog, Berlin*, 287p, https://doi.org/10.1007/978-3-662-05406-2.

Hoefs, J. (2021). Stable Isotope Geochemistry (8th ed.). *Cham, Switzerland: Springer,* https://doi.org/10.1007/978-3-030-77692-3.

Ghasemi, H., Rezaei-Kahkhaei, M. (2015). Petrochemistry and tectonic setting of the Davarzan-Abbasabad Eocene Volcanic (DAEV) rocks, NE Iran. *Miner. Petrol*. 109, 235–252, https://doi.org/10.1007/s00710-014-0353-3.

Goudarzi M, Zamanian H, Kloetzli U, Lentz D. (2024). Eocene Magmatism and Ore forming Processes of copper at Mamuniyeh Area (Central Iran): *Using Trace Element and Isotopic Geochemistry of Zircon*, P.366, https://doi.org/10.1016/j.oregeorev.2024.106279.

Kaboodi, Z., Ghaderi, M., Rastad, E. (2019). Mineralogy, texture and structure and genetic model of Kahak Manto-type copper deposit in the Eocene volcano-sedimentary sequence, south Qom. *Geosciences – Scientific Quarterly Journal*. 29 (113), 145–154.

Kant, W., Warmada, W., Idrus, A., Setijadji, L.D., Watanabe, K. (2012). Fluid inclusion study of the polymetalic epithermal quartz veins at Soripesa Prospect Area, Sumbawa island, Indonesia. *Journal of Applied Geology* 4, 77-89, https://doi.org/10.22146/jag.7199.

Kesler S. E. (2005). Ore-forming fluids. Elements. 1(1), pp. 13-18, https://doi.org/10.2113/gselements.1.1.13.

Kirkham, R. V. (1996). Volcanic Red Bed copper. In: Geology of Canadian Mineral Deposit Types, (ed.) Eckstrand, O. R., Sinclair, W. D. and Thorpe, R. I.. *Geological Survey of Canada*, No. 8: 241- 252.

Klimm, K., Holtz, F., King, P.L. (2008). Fractionation vs. magma mixing in the Wangrah suite A-type granites, Lachlan Fold Belt. *Australia: experimental constraints. Lithos* 102, 415–434, https://doi.org/10.1016/j.lithos.2007.07.018.

Kojima, S., Tristá-Aguilera, D. and Hayashi, K. I. (2009). Genetic aspects of Manto type copper deposits based on geochemical studies of north Chilean deposits. Resource Geology 59: 87- 98, https://doi.org/10.1111/j.1751-3928.2008.00081.x.

Latifi Saii, F., Mirnejad, H., Alipour Asl, M., & Niroomand, S. (2014-2015). Evaluating the Au mineralization in the Darrehzar vein system (Pariz area – Kerman Province), with emphasis on fluid inclusion and sulfur isotope studies. *Advanced Applied Geology*, 4(4), 65–75.

Lattanzi, P. (1991). Applications of fluid inclusions in the study and exploration of mineral deposits. *Europian Journal of Mineral* 3, 689–697, https://doi.org/10.1127/ejm/3/4/0689.

Liu, Y., Zhang, J., & Li, Y. (2017). Genesis of the Zhijiadi Ag–Pb–Zn Deposit, Central North China Craton: Constraints from Fluid Inclusions and Stable Isotope Data. *Geofluids. Article ID 4153618,* https://doi.org/10.1155/2017/4153618.

Li YB, Liu JM. (2006). Calculation of sulfur isotope fractionation in sulfides. *Geochimica et Cosmochimica Acta* 70: 1789 – 1795, https://doi.org/10.1016/j.gca.2005.12.015.

Maghfouri, S., Movahednia, M. (2015). Investigation of geology and mineralization of Abbas Abad copper deposit and comparison with manto-type deposit. *18 th Symposium of the Geological Society of Iran, Tarbiat Modares University, Tehran, Iran* (in Persian with English abstract).

Maghfouri, S., Hosseinzadeh, M.R., Moayyed, M., Movahednia, M., Choulet, F. (2017). Geology, mineralization and sulfur isotopes geochemistry of the Mari Cu (Ag) Manto-type deposit, northern Zanjan, Iran. *Ore Geology Reviews*. 81, 10–22, https://doi.org/10.1016/j.oregeorev.2016.12.007.

Mango, H., Oreskes, N., & Zantop, H. (2013). Origin of epithermal Ag–Au–Cu–Pb–Zn mineralization in Guanajuato, Mexico. *Mineralium Deposita.* 49(1), 119–143, https://doi.org/10.1007/s00126-013-0502-2.

Marini, L., Moretti, R., Accornero, M. (2011). Sulfur isotopes in magmatic-hydrothermal systems, melts, and magmas. *Rev. Mineral. Geochem*. 73, 423–492. https://doi:10.1515/9781501508370-014.

Méheut M, Lazzeri M, Balan E, Mauri F. (2007). Equilibrium isotopic fractionation in the kaolinite, quartz, water system: Prediction from first-principles density-functional theory. *Geochimica et Cosmochimica Acta* 71: 3170-3181, https://doi.org/10.1016/j.gca.2007.04.012.

Merinero, R., Ortega, L., Lunar, R., Pi˜na, R., C´ardenes, V. (2019). Framboidal chalcopyrite and bornite constrain redox conditions during formation of their host rocks in the copper stratabound mineralization of Picachos, north-central Chile. *Ore Geology Reviews*. 112, 103037, https://doi.org/10.1016/j.oregeorev.2019.103037.

Monazzami Bagherzadeh, R., Karimpour, M. H., Farmer, J. L., Stern, C., Santos, J. F., Ribeiro, S., Rahimi, B., and Haidarian Shahri, M. R. (2018-2019): Geochronology, petrology and geochemistry of intermediate and mafic Rocks of the Bornaward plutonic complex (northwest of Bardeskan, Iran). *Journal of Economic Geology*. Vol. 10, No. 2, P: 425–448.

Movahednia, M., Maghfouri, S., Fazli, N., Rastad, E., Ghaderi, M., Gonzalez J.F. (2022). "Metallogeny of Manto-type stratabound Cu-(Ag) mineralization in Iran: Relationship with Neo-Tethyan evolution and implications for future exploration." *Ore Geology Reviews*, 149, 1064.

Niu, S.-D., Li, S.-R., Santosh, M., Zhang, D.-H., Li, Z.-D., Shan, M.-J., Lan, Y.-X., & Gao, D.-R. (2016). Mineralogical and isotopic studies of base metal sulfides from the Jiawula Ag–Pb–Zn deposit, Inner Mongolia, NE China. *Journal of Asian Earth Sciences*. 115, 480–494, https://doi.org/10.1016/j.jseaes.2015.10.020.

Ohmoto, H., & Goldhaber, M.B. (1997). Sulfur and Carbon Isotope: In Barnes, H.L., (ed), Geochemistry of Hydrothermal Ore Deposits, 3rd ed., New York, John Wiley & Sons, p. 517- 611.

Oliveros, V., Feraud, G., Aguirre, L., Ramirez, L., Fornary, M., Palacios, C. and Parada, M. (2008). Detailed 40Ar/39Ar dating of geologic events associated with the Mantos Blancos copper deposit, northern Chile. Mineralium Deposita. 43(2): 281–293, http://dx.doi.org/10.1007/s00126-007-0146-2.

Oyarzum, R., Ortega, L., Sierra, J., Lunar, R. and Oyarzn, J. (1998). Cu, Mn and Ag mineralisation in the Quebrada Marquesa quadrangle, Chile: the Talcuna and Arqueros districts. *Mineralium Deposita* 33: 547- 559.

Palacios, C. (1986). Subvolcanic copper deposits in the Coastal Range of northern Chile. Zentralblatt für Geologie und Pal¨aontologie, Teil I, 1985, H.9/10, Stuttgart. p. 1605–1615, https://doi.org/10.1127/zbl_geol_pal_1/1985/1986/1605.

Pearce, J.A. (1996). A user's guide to basalt discrimination diagrams. In: Trace element geochemistry of volcanic rocks: Applications for massive sulfide exploration (Ed. Wyman, D.A.) Short Course Notes. *Geological Association of Canada*. 12, p79-113.

Pearce, J.A. (1983). Role of the Sub-Continental Lithosphere in Magma Genesis at Active Continental Margins. In: Hawkesworth, C.J. and Norry, M.J., Eds., Continental Basalts and Mantle Xenoliths, Shiva Cheshire, UK, 230-249.

Pirajno, F. (2009). Hydrothermal Mineral Deposits, Principle and Fundamental Concept for the Exploration Geologist». *Springer*, 706 p.

Ramezaniabbakhsh, T., Karimpour, M. H., Azizi, H., Rahimi, B., and Saadat, S. (2023). Metallogeny of mantle-copper deposits, special view in Nasim copper deposit, northwest of Bardaskan, Khorasan Razavi, Iran. *Journal of Economic Geology*, 2023. Vol. 15. No. 1, PP: 143-174, DOI: 10.22067/ECONG.81591.1071.

Rezaeihamid, R., Tale Fazel, A. (2019). Mineralogy, mineralschemistry and sulfur isotope geochemistry of Baharieh copper deposit (NE Kashmar): implications for ore genesis. *Journal of Petrology*, 10 Year. No.39, PP: 53–78.

Rezapanah Khour, H. (2016). Investigation of Geology, Alteration and the Cu Mineralization in Cheshmeh-Hadi Area, Bardaskan (Khorasan Razavi Province, Northeast Iran). Unpublished M.Sc. thesis. Shahid Bahonar University of Kerman, Iran. 148 p. (in Persian with English abstract).

Rice, C. M., McCoyd, R. J., Boyce, A. J., & Marchev, P. (2007). Stable isotope study of the mineralization and alteration in the Madjarovo Pb–Zn district, south-east Bulgaria. *Mineralium Deposita*. 42(7), 691–713, https://doi.org/10.1007/s00126-007-0130-x.

Rollinson, H. (1993). Rising geochemical data: evaluation, presentation, interpretation. Longman John Wiley and Sons, New York, 352 p.

Ruiz, C., Aguilar, A., Egert, E., Espinoza, W., Peebles, F., Quezada, R. and Serrano, M. (1971). Strata-bound copper sulphide deposits of Chile. *Society of Mining Geology of Japan*, 39(2): 252–260, https://doi.org/10.1007/978-3-642-88282-1.

Sato, T. (1984). Manto type copper deposits in Chile: a review. Bull. Geol. Surv. Jpn. 35, 565–582.

Schiano, P., Monzier, M., Eissen, J. P., Martin, H. and Koga, K. T. (2010). Simple mixing as the major control of the evolution of volcanic suites in the Ecuadorian Andes. *Contributions to Mineralogy and Petrology* 160, 297–312, https://doi.org/10.1007/s00410-009-0478-2.

Shafaii Moghadam, H., Hua Li, X., Ling, X.X., Santos, J.F., Stern, R.J., Li, Q.L., Ghorbani, G. (2015). Eocene Kashmar granitoids (NE Iran): Petrogenetic constraints from U-Pb zircon geochronology and isotope geochemistry. Lithos 216–217, 118–135, https://doi.org/10.1016/j.lithos.2014.12.012.

Sheppherd. T.J., Rankin. A.H., Alderton. D.H.M. (1985). A Practical Guide to Fluid Inclusion Studies, Blackie and Son, 239 pp.

Soltani, A. (2016). Mineralogy, geochemistry and genesis of the Abri, Rahbari, and Cheshmeh Marziyeh cu deposit, NW Darooneh. M.Sc. Thesis, Shahrood University of Technology, Iran. 191 p.

Steele-MacInnis, M., Lecumberri-Sanchez, P., Bodnar, R.J. (2012). HokieFlincs_H2O-NaCl: a Microsoft Excel

spreadsheet for interpreting microthermometric data from fluid inclusions based on the PVTX properties of H_2O-NaCl. Comput. Geosci. 49, 334–337, https://doi.org/10.1016/j.cageo.2012.01.022.

Stepanov, A., Mavrogenes, J.A., Meffre, S., Davidson, P. (2014). The key role of mica during igneous concentration of tantalum. *Contributions to Mineralogy and Petrology*. 167, 1009, https://doi.org/10.1007/s00410-014-1009-3.

Sun, S. S., and McDonough, W. F. (1989). Chemical and isotopic systematics of oceanic basalts: implications for mantle composition and processes. *Geological Society, London, Special Publications*, 42(1), 313-345, https://doi.org/10.1144/GSL.SP.1989.042.01.19.

Taefi, N., Mousivand, F., Sadeghian, M. (2014). Mineralogy, geochemistry, and genesis of copper mineralization in the Grik and Gurkhan Southeast of Shahrood. *6 th Symposium of Iranian Society of Economic Geology*, University of Birjand, Birjand, Iran. (in Persian with English abstract).

Tosdal, R.M., Munizaga, F. (2003). Lead sources in Mesozoic and Cenozoic Andean ore deposits, north-central Chile (30–34 ◦ S). Mineral. Deposita. 38, 234–250, https://doi.org/10.1007/s00126-002-0307-2.

Warr, L.N. (2021). IMA-CNMNC mineral symbols. Mineralogical Magazine, 85, 291–320.

Wilkinson, J.J. (2001). Fluid Inclusions in Hydrothermal Ore Deposits. Lithos 55, 229-272, https://doi.org/10.1016/S0024-4937(00)00047-5.

Wilson, N.S.F., Zentilli, M. (1999). The role of organic matter in the genesis of the El Soldado volcanic-hosted manto-type Cu deposit, Chile. *Economic Geology*. 94, 1115–1136, https://doi.org/10.2113/gsecongeo.94.7.1115 .

Wilson, N.S.F. (2000). Organic petrology, chemical composition, and reflectance of pyrobitumen from the El Soldado Cu deposit, Chile. *International Journal of Coal Geology*. 43, 53–82, https://doi.org/10.1016/S0166-5162(99)00054-3.

Wilson, N.S.F., Zentilli, M., Reynolds, P.H. (2003a). Age of mineralization by basinal f luids at the El Soldado manto-type Cu deposit. Chile: 40 feldspar. *Chemical Geology*. 197, 161–176, https://doi.org/10.1016/S0009-2541(02)00350-9.

Wilson, N.S.F., Zentilli, M. (2006). Association of pyrobitumen with copper mineralization from the Uchumi and Talcuna districts, central Chile. *International Journal of Coal Geology*, 65, 158–169, https://doi.org/10.1016/j.coal.04.012.

Wilson, M. (2007). Igneous Petrogenesis. Unwin Hyman, London, 461 p.

Winchester, J. A. and Floyd, P. A. (1977). Geochemical discrimination of different magma series and their differentiation products using immobile elements. *Chemical geology*. 20: 325-343, https://doi.org/10.1016/0009-2541(77)90057-2.

Yilmaz, H., Oyman, T., Nuran Sonmez, F., Arehart, G., Zeki, B. (2010). Intermediate sulfidation epithermal gold-base metal deposits in Tertiary subaerial volcanic rocks, Sahinli/Tespih Dere (Lapseki/Western Turkey), *Ore Geology Reviews*. 37, 236–258, https://doi.org/10.1016/j.oregeorev.2010.04.001.

Zamanian, H., Dolatshahi, S., Yang, X., Karimzadeh S.A,m., Meshkani, S.A. (2021). Geochemical, fluid inclusion and O-H-S isotope constraints on the origin of the Rangraz copper deposit, Central Iran. *Ore Geology Reviews*, Volume 128, January, 103877, https://doi.org/10.1016/j.oregeorev.2020.103877.

Zamanian, H.; Tale Fazel, E.; Sameti, M.; Asadi Haroni, H.; Yang, X. (2023). The petrogenesis and metallogenesis of the Kalchuyeh epithermal gold deposit, central Iran: Constraints from geochemistry, fluid inclusion, and H–O–S isotopes. *Journal of Asian Earth Sciences*, Article 105505, DOI: 10.1016/j.jseaes.2022.105505.

Zentilli, M., Collins, P.G., Boric, P.R., Wilson, N. F. S. (2009). Diagenetic pyrite in the El Soldado stratabound copper deposit: a link with the petroleum system of the Cretaceous basin of central Chile. XII Congreso Geologico Chileno Santiago.

Zentilli, M., Munizaga, F., Graves, M.C., Boric, R., Wilson, N.S.F., Mukhopadhyay, P.K., Snowdon, L.R. (1997). Hydrocarbon involvement in the genesis of ore deposits: an example in Cretaceous strata-bound (manto-type) copper deposits of central Chile. *International Geology Review*. 39, 1–21, https://doi.org/10.1080/00206819709465257.

Zhang, Y.G., Frantz, J.D. (1987). Determination of the homogenisation temperatures and densities of superficial fluids in the system NaCl-KCl-$CaCl_2$-H_2O using synthetic fluids inclusions. *Chemical geology*. 64, 335–345, https://doi.org/10.1016/0009-2541 (87)90012-X.

Zheng, Y. F. (1993b). Calculation of oxygen isotope fractionation in hydroxyl-bearing silicates. *Earth and Planetary Science Letters*. 120, pp. 247-263, https://doi.org/10.1016/0012-821X(93)90243-3.

SAŽETAK

Rudna geneza i hidrotermalna evolucija slojevitoga (tipa Manto) ležišta bakra Cheshmeh-Hadi u vulkansko-plutonskome pojasu sjeverno od rasjeda Doruneh, istočno od ležišta bakra Sepid-Sarve (sjeverozapadni Bardeskan, središnji Iran): dokazi iz geologije, geokemije, fluidnih inkluzija i stabilnih izotopa S i O

Ležište bakra Cheshmeh-Hadi dio je eocenskoga vulkansko-sedimentnog slijeda smještenoga u južnoj zoni Sabzevar. Litostratigrafski slijed, od najstarijeg do najmlađeg, obuhvaća bazalt, bazaltni andezit, andezit i piroksenski andezit, konglomerat, vapnenac, siltit, gipsoviti lapor i pliocenski konglomerat. Mineralizirana zona javlja se unutar konglomerata i na kontaktu između konglomerata i andezita. Tipični rudni minerali jesu malahit-azurit, halkocit, bornit, kovelit i povremeno samorodni bakar. Povezani hidrotermalni fluidi upućuju na umjeren do visok salinitet, u rasponu od 3,09 do 13,39 težinskih % ekvivalenta NaCl, s temperaturama homogenizacije između 89 i 387 °C, što upućuje na miješanje fluida tijekom stvaranja rude. Halkocit rijetko prati kvarc, što sugerira nizak sadržaj silicija u fluidima koji stvaraju rudu. Vrijednosti $\delta^{34}S$ uzoraka sulfida iz proučavanoga ležišta kreću se od –24,1 ‰ do –2,6 ‰, dok se vrijednosti $\delta^{34}S$ hidrotermalnog H_2S kreću od –24,3 ‰ do –2,6 ‰. Vrijednosti $\delta^{18}O$ hidrotermalnih fluida povezanih s mineralizacijom spadaju u raspon bazaltnih stijena, meteorskih voda i sedimentnih stijena. Geokemijske varijacije glavnih i elemenata u tragovima upućuju na kontaminaciju kontinentalne kore u magmatskoj evoluciji. Istraživane vulkanske stijene spadaju u kalcijsko-alkalna do šošonitna polja, formirana u okruženju kontinentalnoga luka, a koja potječu iz obogaćenoga izvora plašta pod utjecajem fluida povezanih sa subdukcijom. Ove stijene karakterizira osiromašenje HREE-a, umjereno obogaćivanje LREE-a i slaba negativna Eu anomalija. Na temelju rezultata istraživanja ležište Cheshmeh-Hadi klasificirano je kao stratificirano ležište bakrenoga sulfida, nastalo u vulkansko-sedimentarnome okruženju povezanom s magmatskim lukom pod utjecajem subdukcije.

Ključne riječi:
Cheshmeh-Hadi, slojevito vezani bakar, vulkansko-plutonski pojas, stabilni izotopi, središnji Iran

Authors contribution

Morteza Esform (PhD student, Department of Geology at Lorestan University, Khorramabad): conceptualization, data curation, formal analysis, investigation, methodology, project administration, resources, software, supervision, validation, visualization, writing – original draft and writing – review & editing. **Hasan Zamanian** (Full professor of geology, School of Geology, College of Science, University of Tehran): project administration, methodology, review & editing. **Alireza Zarasvandi** (Full professor, Department of Geology, Faculty of Earth Sciences, Shahid Chamran University of Ahvaz): resources. **Alireza Almasi** (PhD, Department of Geology, Faculty of Science, Lorestan University, Khorramabad): resources. **Mahya Manouchehry Nia** (Department of Geology, Faculty of Science, Lorestan University, Khorramabad): resources.
All authors have read and agreed to the published version of the manuscript.

RGNZ/MGPB

Magnetic characteristics and mineralogy of cave sediments from Solek Cave, West Sumatra: Implications for paleoenvironmental processes within the cave

Rudarsko-geološko-naftni zbornik
(The Mining-Geology-Petroleum Engineering Bulletin)
DOI: 10.17794/rgn.2026.3.12

Original scientific paper

Hamdi Rifai[1]* ✉, Rizaldi Putra[1] ✉, Wilda Febi Rahmadhani[1] ✉, Nilam Sari[1] ✉, Dessupri Niarti[1] ✉, Wardina Nasution[1] ✉, Erni Erni[2] ✉, Christopher M. Wurster[3,4] ✉

[1] *Department of Physics, Universitas Negeri Padang, Padang 25131, Indonesia.*

[2] *Department of Physics, Universitas Sriwijaya, Palembang 30662, Indonesia.*

[3] *College of Science and Engineering James Cook University, PO Box 6811, Cairns, Queensland 4870, Australia*

[4] *ARC Centre of Excellence for Australian Biodiversity and Heritage James Cook University, PO Box 6811, Cairns, Queensland 4870, Australia.*

Abstract

Cave sediments are essential as they preserve valuable archives of past environmental and climate conditions that physical and chemical measurements can reveal. In this study, we explore the magnetic characteristics of the cave sediments collected from Solek Cave, West Sumatra, Indonesia to understand environmental processes within the cave. We employed rock magnetic methods, including magnetic susceptibility, isothermal remanent magnetization (IRM), anhysteretic remanent magnetization (ARM), and Curie temperature measurements. Additionally, we used X-ray diffraction (XRD) and scanning electron microscopy (SEM) in order to analyze the magnetic mineralogy and morphology of the cave sediments. The results show a high concentration of magnetic minerals, specifically ferrimagnetic groups, indicated by high magnetic susceptibility ranging between 210.7 and 1301.2 × 10^{-8} m^3/kg, with a mean value of 602.7 × 10^{-8} m^3/kg. The calculated χ_{FD} (%) values ranged from 0.2 to 6.6, mostly less than 2%, indicating coarse-grained, multidomain ferrimagnetic minerals. Moreover, results from IRM, ARM and XRD show that the magnetic minerals are dominated by coarse-grained magnetite with a grain size of around 20 to 110 μm. Curie temperature measurements also exhibit various titanium proportions, forming a titanomagnetite phase. The morphology and chemical compositions of the magnetic minerals, determined by SEM and energy-dispersive X-ray spectroscopy (EDS), also support the previous analyses, showing that titanomagnetite is the dominant phase, characterized by coarse grain size and angular shape. The uniformity of the magnetic characteristics and mineralogy suggests a titanomagnetite mineral source likely driven by lithogenic processes such as erosion and fluvial events.

Keywords:
Cave sediments, West Sumatra, Magnetic characteristics, Titanomagnetite, Lithogenic

1. Introduction

Caves serve as valuable archives of environmental and climatic history due to unique conditions, which allow for the accumulation and preservation of sediments and other geological materials (e.g. **Sasowsky and Mylroie, 2004; White, 2007; González-Lemos et al., 2015; Onac et al., 2025**). Unlike other sedimentary deposits, such as lake, river and marine deposits, which are prone to a wide range of environmental disturbances, cave sediments are relatively protected from erosion, surface weathering and post-depositional processes. This makes them likely to preserve a more precise record (**Karkanas and Goldberg, 2017**). Cave sediments are typically deposited under stable conditions, controlled by a specific range of moisture and temperature. They are often associated with high accumulation rates driven by hydrological events. These deposits can also provide significant archeological information, including artifacts and remains of animals and humans, offering insight into past human activities (e.g. **Hunt et al., 2015; Riordan et al., 2021**).

The characteristics and preservation of environmental records in cave sediments are primarily governed by a variety of physicochemical changes (**El Abani et al., 2011; Epure et al., 2017; Addesso et al., 2022**). These changes are mainly influenced by processes involving water and wind, which result in the formation and alteration of elements and minerals from fragments of pre-existing rocks during sediment transport (**Haldar, 2020**). Magnetic minerals produced by these processes ultimately possess inherent magnetic properties that dictate

* Corresponding author: Hamdi Rifai
e-mail address: rifai.hamdi@fmipa.unp.ac.id
Received: 12 May 2025. Accepted: 17 May 2025.
Available online: 14 May 2026

the past environmental processes. For example, the type of magnetic minerals found within a cave is related to reduction-oxidation (redox) conditions, and the various grain sizes of these magnetic minerals strongly indicate the mechanism of deposition, such as fine grains suggesting wind transport and coarse grains representing water transport (**Hatfield, 2014; Huang et al., 2025**).

Previous studies have explored the magnetic characteristics of the cave sediments to understand the presence and significance of magnetic minerals associated with cave deposits (e.g. **Ellwood et al., 1998; Sroubek et al., 2001; Jaqueto et al., 2016; Hajna et al., 2020; D'Arcangelo et al., 2021**). Iron (Fe), an ubiquitous element in rocks, soils and sediments, plays a crucial role in forming magnetic minerals. Therefore, analysis of magnetic minerals offer a promising avenue for understanding their origin and impact on paleoenvironmental processes within cave settings, as they serve as sensitive recorders of cave conditions and their surrounding environment (**Evans and Heller, 2003**). Furthermore, it has been suggested that the source of magnetic minerals in the cave sediments can be anthropogenic (human-influenced) and lithogenic (sourced from fragments of rock and mineral) (e.g. **Onac et al., 2015; Tiwow et al., 2025**). Rock magnetic methods are commonly employed to investigate the magnetic characteristics of the cave sediments because they are responsive to the presence of magnetic minerals, (e.g. **Onac et al., 2015; Rifai et al., 2018; Putra et al., 2019; Tiwow et al., 2025; Rifai et al., under review**). The techniques also offer the advantage of fast and non-destructive measurements.

Located in a critical equatorial region, Indonesian caves preserve high-resolution records of past climate and environmental shifts (**Ayliffe et al., 2013; Kimbrough et al., 2023; Krause et al., 2024**). Consequently, studying these caves is crucial for providing key insight into tropical climate dynamics and the Asian monsoon, which is vital for understanding global climate. The West Sumatra Province, which contains the karst systems of the Padang Highlands, offers numerous potential sites for conducting cave exploration and study. Some caves in West Sumatra have been studied previously to reconstruct paleoclimate (**Wurtzel et al., 2018**) as well as ecology, biology, and human history (e.g. **Wirkner and Hertler, 2019; Louys et al., 2022, 2024; Anderson et al., 2024**). Nevertheless, many caves in this region remain poorly understood and need to be further investigated.

In this study, we utilize rock magnetic methods to examine the magnetic characteristics of the cave sediments collected from Solek Cave, an unexplored cave in West Sumatra, Indonesia, to understand the source of magnetic minerals and their depositional mechanisms. The preserved magnetic minerals and their characteristics can indicate how they have been transported to the site. Building on a previous study by **Putra et al. (2019)** which only focused on one of magnetic parameters (i.e. magnetic susceptibility) and elemental composition of the cave sediments in Solek Cave, here we employ a comprehensive approach combining magnetic susceptibility, isothermal remanent magnetization (IRM), anhysteretic remanent magnetization (ARM), and Curie temperature measurements with additional analysis, namely X-ray diffraction (XRD) and scanning electron microscopy (SEM). This integrated approach allows us to constrain the magnetic characteristics, the types of magnetic mineralogy, and their morphology.

2. Methods

The typical cave sediments on the floor consisted of soil and were collected vertically in Solek Cave (0° 16′ S, 100° 43′ E). This cave is located within the carbonate host rocks and is part of the Barisan Mountains of West Sumatra (see **Figure 1**). The cave is developed within limestone strata of the Kuantan Formation (**Barber et al., 2005**), a constituent part of the Tapanuli Group within the West Sumatra Block. This formation, which dates to the Lower Carboniferous to Mid-Permian periods, is also known to include metasedimentary rocks in association with the primary limestone. Solek Cave is a dry cave with a floor that slopes slightly upward near the entrance. The fauna is dominated by bat colonies. The inner chambers contain minimal speleothem deposits. The cave's karst system and hydrological processes of Solek Cave have yet to be documented in previous studies. The cave is situated within a wet tropical rainforest ecosystem. This region experiences consistent high rainfall occurs each year, surpassing 150 mm monthly. While precipitation averages rise above 250 mm per month during the September to December peak, the lowest average monthly rainfall is seen in February (**Aldrian and Susanto, 2003**).

Samples were taken from the uniform brownish layers of soil clastic sediments, from the surface to bottom (when bedrock was reached) at 2 cm intervals and stored in Whirl-Pak™ bags. They were then refrigerated at 4°C until lyophilized for further analysis. All samples were subjected to mass-specific magnetic susceptibility measurement via an MS2 susceptibility meter (Bartington Instruments Ltd., Witney, UK). The device is fitted with a sample internal diameter of 35 mm and a MS2B dual-frequency sensor. During measurement, a magnetic field of 80 A/m was applied and the device allows the range of susceptibility to be measured from 1×10^{-6} to 9.999×10^{-6} in cgs or 1.26×10^{-5} to 1.026×10^{-1} in SI unit. Approximately 10 grams of the sample was carefully placed into a cylindrical plastic container with a 25.4 mm diameter and a 22 mm height. Magnetic susceptibility measurements were conducted using 1.0 sensitivity setting at 0.47 kHz for low frequency magnetic susceptibility (χ_{LF}) and at 4.7 kHz high frequency magnetic susceptibility (χ_{HF}), respectively. These two measurements allow for the estimation of the frequency-dependent magnetic sus-

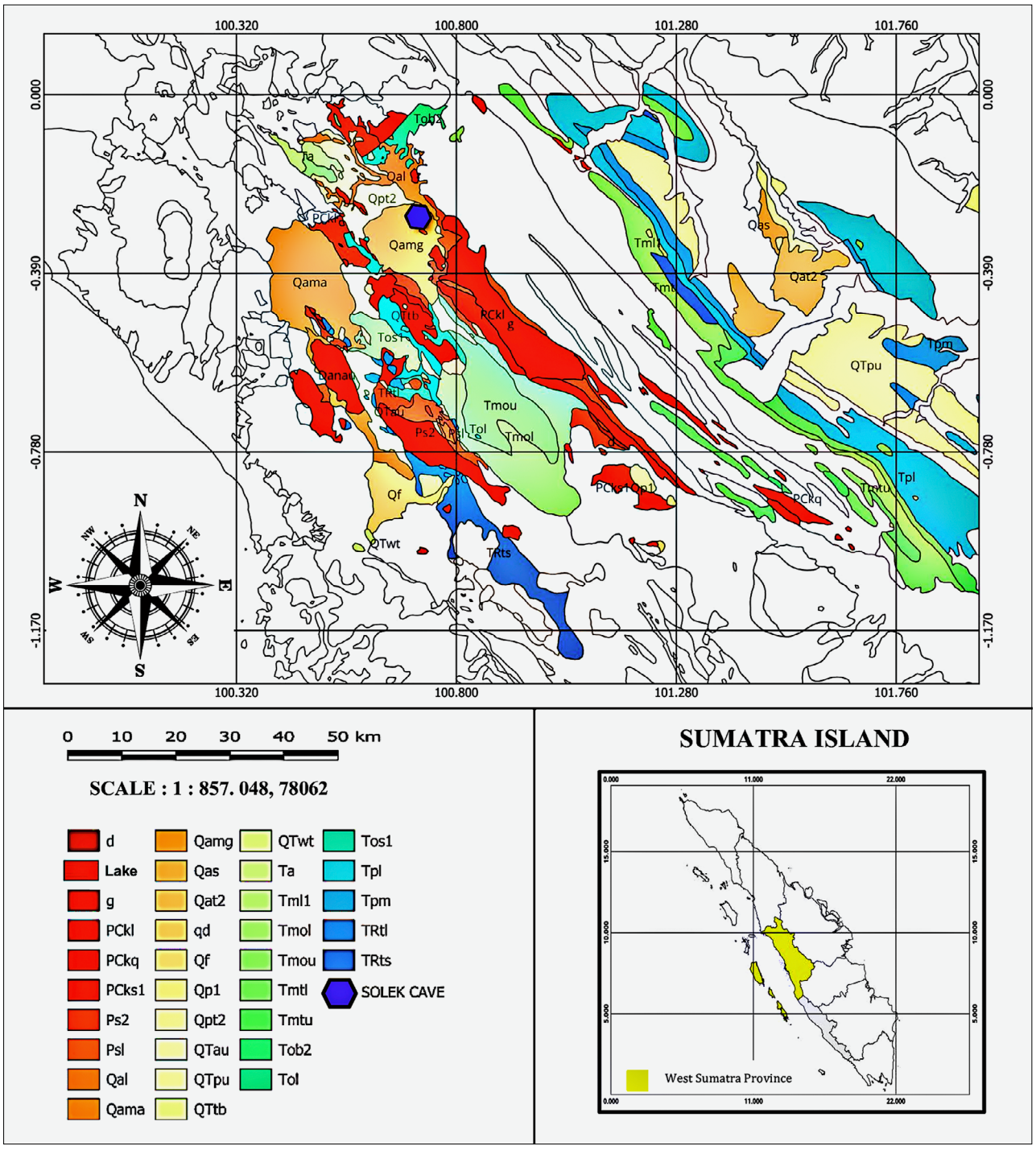


Figure 1. Geological map showing the study site Solek Cave in the West Sumatra Province (blue hexagon), which is located within the PCkl unit (limestone). The inset map shows Sumatra Island. The map legend details the following lithological units and features (abbreviation: lithology): d (intrusive: mafic), Danau (lake), g (intrusive: felsic), PCkl (limestone), PCkq and PCks1 (metasediment), Ps2 (intermediate polymict), Psl (clastic limestone), Qal, Qas, Qat2 (clastic alluvium), Qama, Qamg (intermediate polymict), qd (intrusive: intermediate), Qf (conglomerate), Qp1 (felsic granitoid), Qpt2, QTau, QTtb, QTwt (intermediate pyroclastic), QTpu (felsic pyroclastic), Ta (intermediate polymict), Tml1 (reef limestone), Tmol (sandstone), Tmou (fine claystone), Tmtl (marl), Tmtu (fine shale), Tob2 (conglomerate), Tol, TRtl (evaporite), Tos1 (fine shale), Tpl, Tpm (fine claystone), and TRts (slate).

ceptiblity, χ_{FD} (%), by calculating the ratio between χ_{LF} and χ_{HF} (100% × (χ_{LF} −χ_{HF})/χ_{LF} (**Oldfield et al., 1983**).

The selected samples were analyzed for IRM, ARM and Curie temperature measurements. IRM analysis was performed using an electromagnetic generator that incrementally increased the magnetic field at room temperature. IRM intensity was evaluated by a spinner magnetometer (Minispin magnetometer by Molspin Ltd.,

Newcastle Upon Tyne, UK), reaching a maximum intensity of 1000 mT, defined as saturated isothermal remanent magnetization (SIRM). An electromagnetic generator was also used for determining ARM intensity. Samples were exposed to a 2.5 mT direct current (DC) magnetic field and a 700 mT alternating magnetic field via Molspin AF Demagnetizer (Molspin Ltd., Newcastle Upon Tyne, UK). Selected samples were also extracted for obtaining magnetic minerals and then analyzed for Curie temperature using a Bartington MS2WFP Susceptibility Meter (Bartington Instrument Ltd., Witney, UK). This instrument was equipped with an MS2 Meter, MS2W Water Jacketed, MS2WF Furnace, MS2WFP Power Supply Unit, and a self-contained water coolant supply. The measurement involved heating the sample from a room temperature of 32°C to 750°C, and subsequently cooling it back to 32°C.

XRD type Phillips XD-610 instrument was utilized to identify magnetic mineralogy within extracted samples. The measurement employed CuKα target with a 0.154 nm wavelength (λ). The resulting data included diffraction angles, intensity values and distances between planes, in which these parameters can be related via the Bragg equation ($d = \lambda / 2 \sin \theta$). The magnetic mineral database was used for comparison to determine the types of magnetic minerals (**Cornell and Schwertmann, 2003**). The morphology of magnetic minerals extracted was examined via SEM (Phillips CM 12, PW 6030/10 instrument). Samples were imaged under secondary electron imaging (SEI) using an accelerating voltage of 20 kV and a working distance of 10 mm. Additionally, Energy-Dispersive X-Ray Spectroscopy (EDS) was applied to determine the element compositions.

3. Results and Discussion

3.1. Magnetic characteristics of cave sediment

Results of low magnetic susceptibility measurements (χ_{LF}), sediment samples in Solek Cave have values in the range between 210.7 to 1301.2 × 10^{-8} m^3/kg with a mean value of 602.7 × 10^{-8} m^3/kg (see **Figure 2**). All magnetic susceptibility peaks exhibit an irregular pattern through each depth, yet overall, the observed increasing values correspond to deeper layers. The range of values is in line with previous studies by **Putra et al.** (**2019**) at the order of hundred to thousand × 10^{-8} m^3/kg, which is suggested to have relatively high values, indicating the presence of ferrimagnetic mineral groups (**Tiwow et al., 2025**). The calculated χ_{FD} (%) values ranged from 0.2 to 6.6 with a mean of 1.3. However, most of χ_{FD} values lie in the range of less than 2% and are similar to results from **Putra et al.** (**2019**), except for 6.6%, which might be due to the sensitivity of the instrument during measurement. Values of less than 2% indicate the presence of coarse-grained, multidomain ferrimagnetic minerals (**Dearing et al., 1996; Putra et al., 2019**).

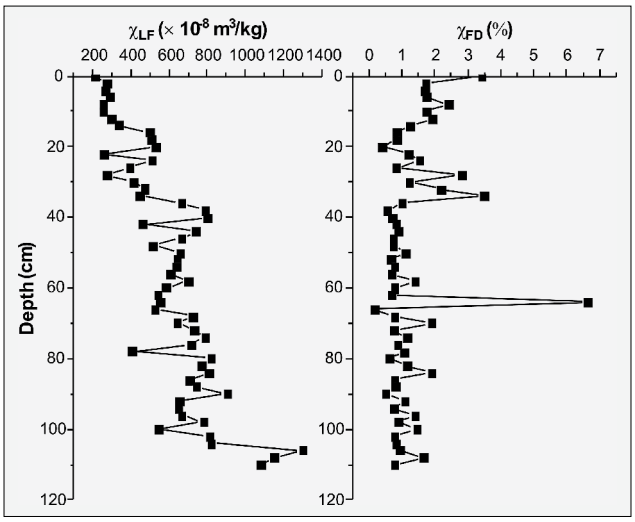


Figure 2. Magnetic susceptibility (left) and frequency dependent magnetic susceptiblity (right) of the cave sediments through each depth.

Figure 3 displays the measured IRM curves of selected samples. Samples undergo saturation at magnetic fields lower than 300 mT, which is indicative of a soft magnetite phase (e.g. **Bijaksana and Huliselan, 2010; Jin et al., 2016; Mariyanto et al., 2019**). Resulting ARM decay curves for selected samples are presented in **Figure 4**. The measured curves are used to approximate the grain size of magnetic minerals by observing MDF_{ARM} (Median Destructive Field) and comparing them with Lowrie-Fuller test graph (**Dunlop and Ozdemir, 1997**). Based on the observation, MDF_{ARM} values are in the range between 8 and 10 mT, where the magnetic minerals are suggested to have coarse grain sizes from around 20 to 110 μm.

Curie temperature curves displayed in **Figure 5** demonstrate the occurrence of iron-titanium oxides such as titanomagnetite with varying titanium proportions based on temperature drops. For both samples measured (GS_0-2 and GS_36-38), two temperature drops are uniquely observed in heating curves at around 300°C and 460°C, respectively, indicating the presence of two Curie temperatures. Instead, there is only one temperature drop in cooling curve observed at less than 500°C.

In heating experiments, magnetic susceptibility values become zero before achieving 580°C and subsequently decrease to negative numbers. Under this condition, magnetic minerals possibly transform from ferrimagnetic to paramagnetic. After switching to cooling experiments, magnetic minerals return to ferrimagnetic with increasing magnetic susceptibility values until maximum values are reached at less than 500°C. Finally, a decrease in magnetic susceptibility values is observed when going back to room temperature. It is noteworthy that the shape of both heating and cooling curves appear to be a bit similar, although cooling curves have only one temperature drop compared to heating curves and there is a higher cooling curve seen in the surface sample

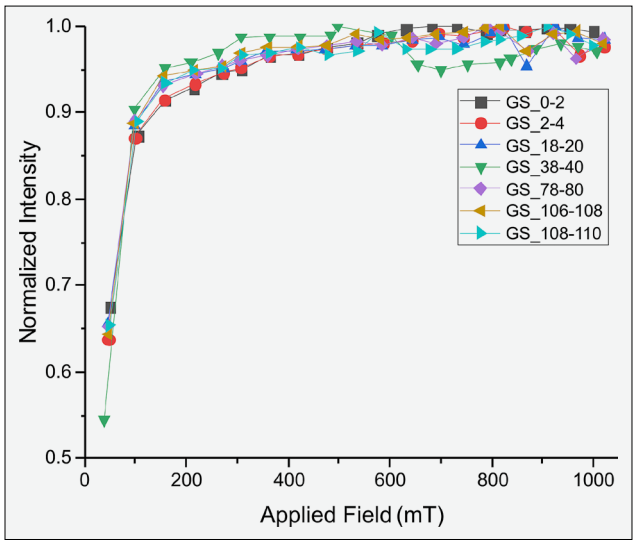


Figure 3: Isothermal remanent magnetization (IRM) curves of selected cave sediment samples.

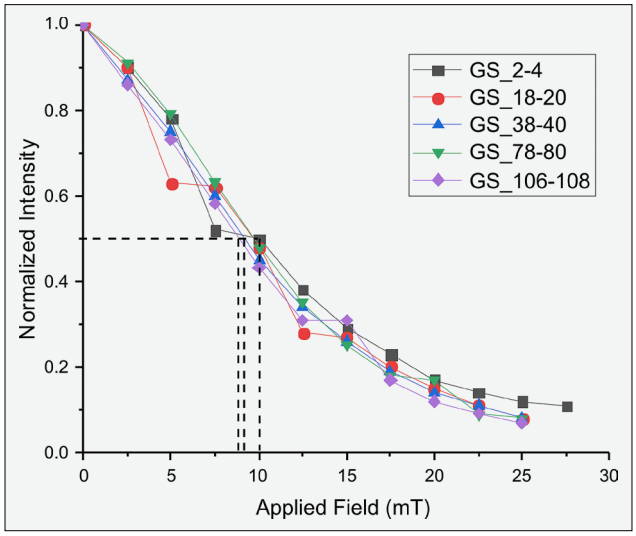


Figure 4. Anhysteretic remanent magnetization (IRM) curves of selected cave sediment samples. The dash lines indicate Median Destructive Field (MDF_{ARM}) at 0.5 corresponding to the applied field.

(GS_0-2) rather than its heating curve. The proportion of Ti content can be estimated using literature data by **Lattard et al. (2006)** and the polynomial expression for Curie temperatures of **Bleil and Peterson. (1982)**. Based on our matching with variations of the Curie temperature in the Fe-Ti-O system as a function of composition in literature data determined by **Brachfeld et al. (2024)**, magnetic minerals within sediments from Solek Cave may contain various titanomagnetite compositions between $Fe_{2.5}Ti_{0.5}O_4$ and $Fe_{2.95}Ti_{0.05}O_4$.

3.2. Magnetic mineralogy and morphology of the cave sediments

Peaks of the XRD diffractogram measured from extracted magnetic minerals indicate that the phase of

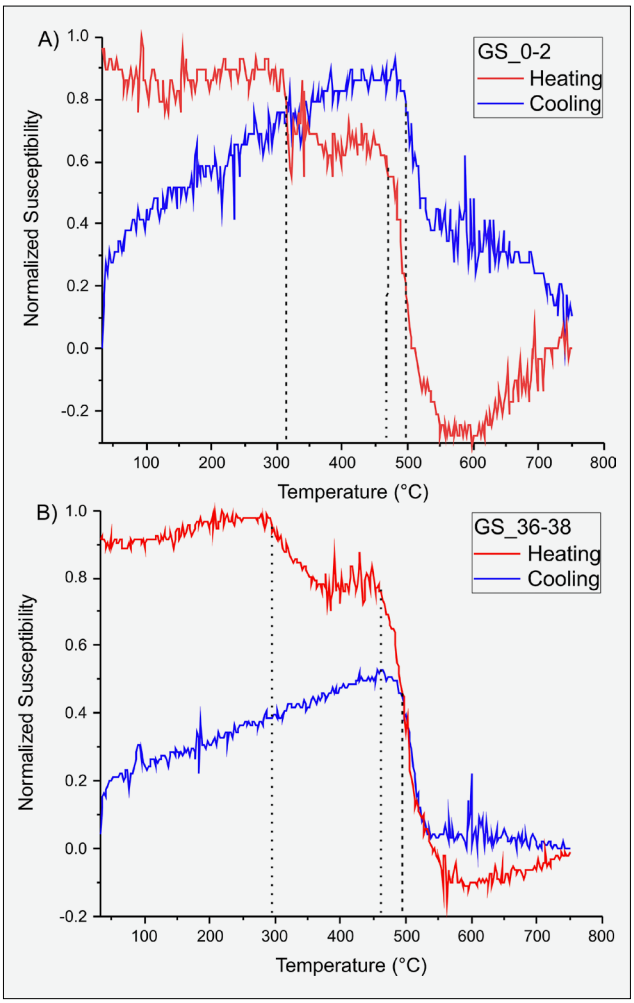


Figure 5. Representative Curie temperature curves based on temperature drops (dash lines) via temperature dependence of magnetic susceptibility (χ–T) measurements.

magnetite dominates within samples (see **Figure 6**). However, only a few peaks of hematite appear, which is suggested to have a small proportion in the cave sediments. Our XRD results thus reinforce IRM analysis, where magnetite is a major phase of magnetic minerals. **Figure 7a-d** shows the morphology of extracted magnetic minerals from selected samples via SEM images. Shapes of magnetic minerals are predominantly angular, with some exhibiting distinct of octahedral morphology. The sizes of the magnetic minerals range from around 20 to 100 μm or larger, implying that the magnetic minerals are predominantly coarse-grained and correspond to multidomain, which further supports ARM and χ_{FD} results.

Both angular and octahedral shapes characterize the presence of titanomagnetite fragments, as supported by previous studies (e.g. **Huliselan et al., 2010; Kirana et al., 2024**). EDS measurements were therefore made in order to quantify elements, including the presence of Fe and Ti within magnetic minerals. **Table 1** provides various element compositions based on selected grains of

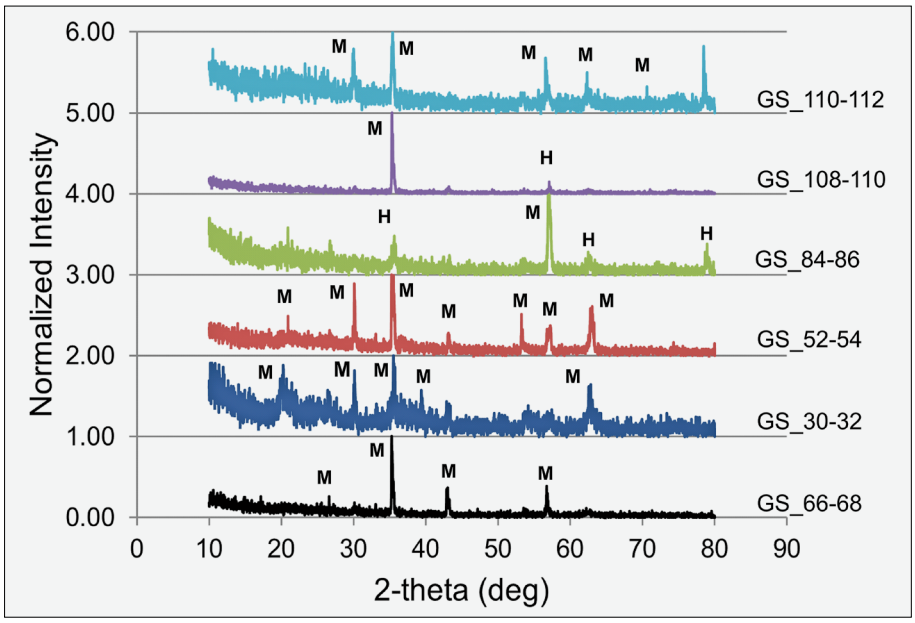


Figure 6. Diffractogram of XRD for representative extracted samples of cave sediment. Peaks indicate that magnetite (M) minerals dominate the diffractogram with minor hematite (H).

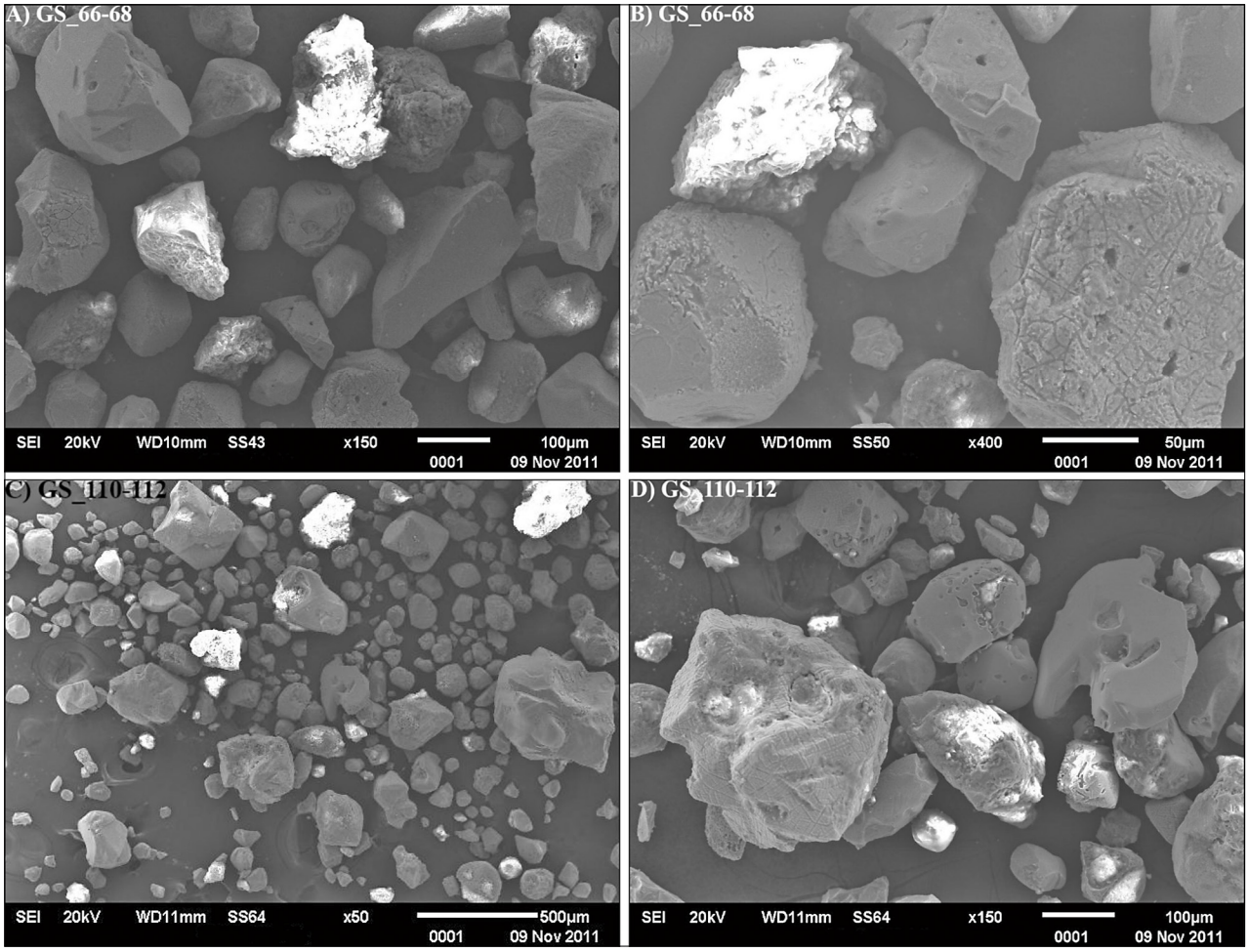


Figure 7. Representative SEM images of extracted samples showing the morphology of magnetic minerals in angular shape.

magnetic mineral from **Figure 7b** and **7d**. Fe is identified as the primary element composing magnetic minerals, followed by some elements such as Ti, Al, and Si. The presence of C might be due to organic abundance associated with sediments. Other elements such as P, Mg and K are considered as minor elements since these ele-

Table 1. Energy-Dispersive X-Ray Spectroscopy (EDS) analytical data (mass%) on selected magnetic mineral grains.

Sampel ID	Element Composition (%)										
	C	O	Al	Si	Mg	P	K	Ca	Ti	Fe	Total
GS_66-68 grain 1	4.65	35.55	5.01	6.45	-	3.46	0.46	11.66	1.68	31.06	99.98
GS_66-68 grain 2	2.66	18.54	3.33	2.02	-	0.28	0.06	0.66	15.44	57.01	100
GS_66-68 grain 3	8.76	28.23	8.65	8.38	-	5.99	5.07	1.27	2.39	31.25	99.99
GS_110-112 grain 1	6.09	46.08	12.64	17.49	0.40	-	0.17	0.94	0.70	15.49	100
GS_110-112 grain 2	3.17	29.11	3.26	1.91	1.15	-	0.08	0.24	6.44	54.65	100.01
GS_110-112 grain 3	3.34	21.59	2.53	2.16	0.41	-	-	0.12	20.67	49.17	99.99

ments either have a small proportion or are undetectable within magnetic mineral grains. Magnetic mineral grains also contain Ca, which is mostly in low concentrations. Since Fe- and Ti- bearing magnetic minerals are present in sediments, we assume that titanomagnetite is the dominant phase, which is also confirmed by the results of the Curie temperature analysis.

3.3. Source of magnetic mineral and its implications for paleoenvironmental processes

Several studies have investigated the magnetic characteristics of clastic sediment in various caves around the world using rock magnetic methods. Some have suggested that the peak of magnetic susceptibility can be related to climate record (e.g. **Sroubek et al., 2001; Ellwood et al., 2004; Benedetti et al., 2019; D'Arcangelo et al., 2021**), while others found that magnetic susceptibility enhancement can be controlled by anthropogenic influence (e.g. **Onac et al., 2015; Rifai et al., 2018; Paar et al., 2025**). In this study, our sampling point in Solek Cave is different compared to a previous study by **Putra et al.** (**2019**), but still in the same cave. Meanwhile, the authors have reported that the magnetic susceptibility signal of sediments in Solek Cave seems to be irregular but in the range of high values, similar to our results. This pattern was also recently confirmed by **Rifai et al.** (**under review**) in studying magnetic characteristics of guano deposits associated with clay from Rantai Cave in West Sumatra with a combination of radiocarbon and organic matter measurements. They suggest that variation in magnetic susceptibility values can be due to detrital influx by fluvial response, which in turn to causes variability in the accumulation rate of magnetic minerals and results in mixing of guano and sediment layers. Radiocarbon dating and organic analysis might be necessary in the future studies to identify potential mixing processes in the cave sediments from Solek Cave.

Our results indicate that titanomagnetite is the dominant phase and has a strong influence on the magnetic characteristics of sediments. Titanomagnetite minerals are ubiquitous in different geological settings, including igneous and metamorphic rocks as well as sedimentary environments. The occurrence of titanomagnetite often serves as an indicator of changes in environmental conditions, implying complex transportation and weathering processes. Moreover, uniformity of magnetic characteristics and mineralogy, namely dominant type, coarse grain size and morphology of magnetic minerals, possibly indicates a common source for titanomagnetite.

We did not find any spherule forms in the morphology of magnetic minerals in **Figure 7**, which commonly originate from anthropogenic sources (**Jordanova et al., 2004; Kirana et al., 2024; Liang and Wang, 2024**). Instead, most of the angular shapes are distinguishable, suggesting that the magnetic minerals in Solek Cave are unlikely to be linked to human activity. If magnetic characteristics are derived from different climate processes, distinctive features in the sediment profile, indicating a heterogeneous source, would be expected. Another recent study by **Onac et al.** (**2025**) explored the presence of Ti in cave sediments and suggested that Ti is an indicator of the lithogenic component that strongly contributes to external environmental conditions, such as past erosional and weathering processes. Ti is also considered to be resistant in its host minerals (e.g. titanomagnetite), which does not readily dissolve or change in chemical processes under normal conditions (**Mbanga et al., 2022**).

The consistent and high concentration of magnetic minerals, particularly titanomagnetite, throughout the sediment profile suggests significant and dynamic depositional processes at play in Solek Cave, likely driven by lithogenic processes such as erosion and fluvial events. This interpretation is supported by variation and erratic pattern of high magnetic susceptibility shown in **Figure 2**, indicating the fluctuating depositional rate of magnetic minerals, which is strongly related to high detrital influx (**Dearing, 1999**). It is also noteworthy that deeper (old) layers exhibit higher susceptibility, implying more intense fluvial transport processes carrying magnetic minerals rather than shallow (younger) layers.

Meanwhile, there is a possibility of magnetic mineral diagenesis in the sediments, which can alter detrital magnetic minerals due to reduction-oxidation (redox) reactions (**Roberts, 2015**). Such processes can transform magnetite into minerals like hematite and goethite

in oxic conditions, or greigite and pyrite in anoxic conditions. Nevertheless, based on the strong detrital magnetic signal, we assume that diagenesis processes have a minor contribution to the magnetic properties of the Solek Cave sediments. To assess the paleoenvironmental implications, future research should aim to obtain high-resolution of geochemical or sedimentological records from the cave. In particular, correlation between magnetic susceptibility signals with regional climate proxies is recommended to reveal climatic controls due to detrital influx.

4. Conclusions

The magnetic susceptibility of the cave sediments from Solek Cave in West Sumatra reveals a high concentration of magnetic minerals, specifically ferrimagnetic groups, with values ranging between 210.7 and 1301.2 × 10^{-8} m^3/kg, with a mean value of 602.7 × 10^{-8} m^3/kg. Further analysis using calculated χ_{FD} (%) values, IRM and ARM curves as well as XRD results, indicates the presence of coarse-grained multidomain magnetite mineral with a size from around 20 to 110 μm. Curie temperature curves also confirm various titanium proportions forming the titanomagnetite phase. Mineralogy and morphology investigation then supports previous methods used where titanomagnetite is the dominant phase of magnetic mineral type, characterized by coarse grain size and angular shape. Uniformity of magnetic characteristics and mineralogy suggests a titanomagnetite mineral source, which is likely driven by lithogenic processes, such as erosion and fluvial events.

Acknowledgement

The authors thank James Cook University's College of Science, Technology and Engineering, National Geographic Society's Scientific Research 8845-10, and Australian Institute of Nuclear Science and Engineering award (ALNGRA11033) to CMW for supporting fieldwork and Research Grants from Hibah Bersaing DIKTI, DIPA Universitas Negeri Padang numbers 1790/UN35.2/PG/2017 and RKAI − PKPTLN No. 1927/UN35.15/LT/2025 to HR for the analysis of magnetic characteristics and mineralogy in this research. The authors also thank Mila Novrilita and Tiwi Olintika for their valuable help during fieldwork.

5. References

Addesso, R., De Waele, J., Cafaro, S., and Baldantoni, D. (2022). Geochemical characterization of clastic sediments sheds light on energy sources and on alleged anthropogenic impacts in cave ecosystems. International Journal of Earth Sciences, 111, 919-927. https://doi.org/10.1007/s00531-021-02158-x.

Aldrian, E., and Susanto, R. D. (2003). Identification of three dominant rainfall regions within Indonesia and their relationship to sea surface temperature. International Journal of Climatology, 23, 1435-1452. https://doi.org/10.1002/joc.950.

Anderson, H. E., Morley, M. W., McAdams, C., Zaim, J., Rizal, Y., Aswan, A., Puspaningrum, M. R., Hascaryo, A. T., Price, G. J., and Louys, J. (2024). The microstratigraphy and depositional environments of Lida Ajer and Ngalau Gupin, two fossil-bearing tropical limestone caves of west Sumatra. Scientific Reports, 14, 259. https://doi.org/10.1038/s41598-023-50975-8.

Ayliffe, L. K., Gagan, M. K., Zhao, J. X., Drysdale, R. N., Hellstrom, J. C., Hantoro, W. S., Griffiths, M. L., Scott-Gagan, H., St Pierre, E., Cowley, J. A., and Suwargadi, B. W. (2013). Rapid interhemispheric climate links via the Australasian monsoon during the last deglaciation. Nature Communications, 4, 2908. https://doi.org/10.1038/ncomms3908.

Barber, A. J., Crow, M. J., and Milsom, J. (2005). Sumatra: Geology, Resources and Tectonic Evolution. Geological Society of London.

Benedetti, M. M., Haws, J. A., Bicho, N. F., Friedl, L., and Ellwood, B. B. (2019). Late Pleistocene site formation and paleoclimate at Lapa do Picareiro, Portugal. Geoarchaeology, 34(6), 698-726. https://doi.org/10.1002/gea.21735.

Bijaksana, S., and Huliselan, E. K. (2010). Magnetic properties and heavy metal content of sanitary leachate sludge in two landfill sites near Bandung, Indonesia. Environmental Earth Sciences, 60, 409-419. https://doi.org/10.1007/s12665-009-0184-4.

Bleil, U., and Petersen, N. (1982). Magnetic properties of natural minerals. In: Angenheister G (ed) Numerical data and functional relationships in science and technology, group V: Geophysics and space research, Springer, New York, pp 308-365.

Brachfeld, S., McCartney, K. N., Hammer, J. E., Shea, T., and Giachetti, T. (2024). Evaluating the role of titanomagnetite in bubble nucleation: Rock magnetic detection and characterization of nanolites and ultra-nanolites in rhyolite pumice and obsidian from Glass Mountain, California. Geochemistry, Geophysics, Geosystems, 25(4), e2023GC011336. https://doi.org/10.1029/2023GC011336.

Cornell, R. M., and Schwertmann, U. (2003). The Iron Oxides: Structure, Properties, Reactions, Occurences and Uses. 2nd Edition, Wiley-VCH, Weinhem.

D'Arcangelo, S., Martín-Hernández, F., and Parés, J. M. (2021). Magnetic properties of cave sediments at Gran Dolina site in Sierra de Atapuerca (Burgos, Spain). Quaternary International, 583, 1-13. https://doi.org/10.1016/j.quaint.2021.02.041.

Dearing, J. A., Dann, R. J. L., Hay, K., Lees, J. A., Loveland, P. J., Maher, B. A., and O'Grady, K. (1996). Frequency-dependent susceptibility measurement of environmental materials. Geophysical Journal International, 124(1), 228-240. https://doi.org/10.1111/j.1365-246X.1996.tb06366.x.

Dearing, J. A. (1999). Holocene environmental change from magnetic proxies in lake sediments. In: Maher, B. A., and Thompson, R. (eds) Quaternary Climates, Environments and Magnetism, Cambridge University Press, pp 231-278.

Dunlop, D. J, and Özdemir, Ö. (1997). Rock Magnetism: Fundamental and Frontiers. Cambridge: Cambridge University Press.

Ellwood, B. B., Zilhão, J., Harrold, F. B., Balsam, W., Burkart, B., Long, G. J., Debenath, A., and Bouzouggar, A. (1998). Identification of the last glacial maximum in the Upper Paleolithic of Portugal using magnetic susceptibility measurements of Caldeirão Cave sediments. Geoarchaeology, 13, 55-71. https://doi.org/10.1002/(SICI)1520-6548(199801)13:1<55::AID-GEA4>3.0.CO;2-7.

Ellwood, B. B., Harrold, F. B., Benoist, S. L., Thacker, P., Otte, M., Bonjean, D., Long, G. J., Shahin, A. M., Hermann, R. P., and Grandjean, F. (2004). Magnetic susceptibility applied as an age–depth–climate relative dating technique using sediments from Scladina Cave, a Late Pleistocene cave site in Belgium. Journal of Archaeological Science, 31(3), 283-293. https://doi.org/10.1016/j.jas.2003.08.009.

El Albani, A., Meunier, A., Macchiarelli, R., Ploquin, F., and Tournepiche, J. -F. (2011). Local environmental changes recorded by clay minerals in a karst deposit during MIS 3 (La Chauverie, SW France). Quaternary International, 241, 26-34. https://doi.org/10.1016/j.quaint.2010.03.007.

Epure, L., Muntean, V., Constantin, S., and Moldovan, O.T. (2017). Ecophysiological groups of bacteria from cave sediments as potential indicators of paleoclimate. Quaternary International, 432, 20-32. https://doi.org/10.1016/j.quaint.2015.04.016.

Evans, M. E., and Heller, F. (2003). Environmental Magnetism: Principle and Applications of Environmagnetics. Elsevier, Amsterdam.

González-Lemos, S., Jiménez-Sánchez, M., and Stoll, H. M. (2015). Sediment transport during recent cave flooding events and characterization of speleothem archives of past flooding. Geomorphology, 228, 87-100. https://doi.org/10.1016/j.geomorph.2014.08.029.

Hajna, N. Z., Bosák, P., Pruner, P., Mihevc, A., Hercman, H., and Horáček, I. (2020). Karst sediments in Slovenia: Plio-Quaternary multi-proxy records. Quaternary International, 546, 4-19. https://doi.org/10.1016/j.quaint.2019.11.010.

Haldar, S. K. (2020). Sedimentary rocks. In: Haldar, S.K. (eds) Introduction to Mineralogy and Petrology (Second Edition), Elsevier, Pages 187-268. https://doi.org/10.1016/B978-0-12-820585-3.00006-5.

Hatfield, R. G. (2014). Particle size-specific magnetic measurements as a tool for enhancing our understanding of the bulk magnetic properties of sediments. Minerals, 4(4), 758-787. https://doi.org/10.3390/min4040758.

Huang, R., Chang, L., Wang, S., Xue, P., Liu, S., Shi, X., Khokiattiwong, S., and Kornkanitnan, N. (2025). Magnetic characterization of sediment source-to-sink processes in the Bengal Fan since 45 ka. Geochemistry, Geophysics, Geosystems, 26, e2024GC011784. https://doi.org/10.1029/2024GC011784.

Huliselan, E. K., Bijaksana, S., Srigutomo, W., and Kardena, E. (2010). Scanning electron microscopy and magnetic characterization of iron oxides in solid waste landfill leachate. Journal of Hazardous Materials, 179, 701-708. https://doi.org/10.1016/j.jhazmat.2010.03.058.

Hunt, C. O., Gilbertson, D. D., Hill, E. A., and Simpson, D. (2015). Sedimentation, re-sedimentation and chronologies in archaeologically-important caves: problems and prospects. Journal of Archaeological Science, 56, 109-116. https://doi.org/10.1016/j.jas.2015.02.030.

Jaqueto, P., Trindade, R. I. F., Hartmann, G. A., Novello, V. F., Cruz, F. W., Karmann, I., Strauss, B. E., and Feinberg, J. M. (2016). Linking speleothem and soil magnetism in the Pau d′Alho cave (central South America). Journal of Geophysical Research: Solid Earth, 121(10), 7024-7039. https://doi.org/10.1002/2016JB013541.

Jin, C., Liu, Q., Hu, P., Jiang, Z., Li, C., Han, P., Yang, H., and Liang, W. (2016). An integrated natural remanent magnetization acquisition model for the Matuyama-Brunhes reversal recorded by the Chinese loess. Geochemistry, Geophysics, Geosystem, 17(8), 3150-3163. https://doi.org/10.1002/2016GC006407.

Jordanova, D., Hoffmann, V., and Fehr, K. T. (2004). Mineral magnetic characterization of anthropogenic magnetic phases in the Danube river sediments (Bulgarian part). Earth and Planetary Science Letters, 221, 71-89. https://doi.org/10.1016/S0012-821X(04)00074-3.

Karkanas, P., and Goldberg, P. (2017). Cave Settings. In: Gilbert, A. S. (eds) Encyclopedia of Geoarchaeology. Encyclopedia of Earth Sciences Series. Springer, Dordrecht. https://doi.org/10.1007/978-1-4020-4409-0_151.

Kimbrough, A. K., Gagan, M. K., Dunbar, G. B., Hantoro, W. S., Shen, C. C., Hu, H. M., Cheng, H., Edwards, R. L., Rifai, H., and Suwargadi, B. W. (2023). Multi-proxy validation of glacial-interglacial rainfall variations in southwest Sulawesi. Communications Earth & Environment, 4, 210. https://doi.org/10.1038/s43247-023-00873-8.

Kirana, K. H., Shalsabila, M. T., Putri, S. U., Fitriani, D., Augustine, E., Hamdan, A. M., Tamuntuan, G. H., Rosandi, Y., and Chaparro, M. A. E. (2024). Topsoil's magnetic and electrical properties in a volcanic and tropical region. Environmental Monitoring and Assessment, 196, 160. https://doi.org/10.1007/s10661-024-12332-8.

Krause, C. E., Gagan, M. K., Dunbar, G. B., Hantoro, W. S., Hellstrom, J. C., Cheng, H., Edwards, R. L., Suwargadi, B. W., Abram, N. J., and Rifai, H. (2019). Spatio-temporal evolution of Australasian monsoon hydroclimate over the last 40,000 years. Earth and Planetary Science Letters, 513, 103-112. https://doi.org/10.1016/j.epsl.2019.01.045.

Lattard, D., Engelmann, R., Kontny, A., and Sauerzapf, U. (2006). Curie temperatures of synthetic titanomagnetites in the Fe-Ti-O system: Effects of composition, crystal chemistry, and thermomagnetic methods. Journal of Geophysical Research, 111, B12S28. https://doi.org/10.1029/2006JB004591.

Liang, M. Y., and Wang, Y. H. (2024). Characteristic changes and environmental indicators of magnetic spherules in the South Yellow Sea mud area for about 7.5 ka. Science of the Total Environment, 918, 170814. https://doi.org/10.1016/j.scitotenv.2024.170814.

Louys, J., Duval, M., Price, G. J., Westaway, K., Zaim, Y., Rizal, Y., Aswan, A., Puspaningrum, M., Trihascaryo, A., Breitenbach, S. F. M., Kwiecien, O., Cai, Y., Higgins, P., Albers, P. C. H., de Vos, J., and Roberts, P. (2022). Speleo-

logical and environmental history of Lida Ajer cave, western Sumatra. Philosophical Transactions of the Royal Society B: Biological Sciences, 377, 20200494. https://doi.org/10.1098/rstb.2020.0494.

Louys, J., Price, G. J., Higgins, P., de Vos, J., Zaim, J., Rizal, Y., Aswan, A., Puspaningrum, M. R., Hascaryo, A. T., Drawhorn, G. M., and Albers, P. C. H. (2024). Geochronology and Palaeoenvironments of Sibrambang and Djambu Caves, Western Sumatra. In Quaternary Palaeontology and Archaeology of Sumatra, edited by J. Louys, P. C. H. Albers, and A. A. E. Geer, 99–119. Australin National University Terra Australis 56. https://doi.org/10.22459/TA56.2024.05.

Mariyanto, M., Amir, M. F., Utama, W., Hamdan, A. M., Bijaksana, S., Pratama, A., Yunginger, R., and Sudarningsih, S. (2019). Heavy metal contents and magnetic properties of surface sediments in volcanic and tropical environment from Brantas River, Jawa Timur Province, Indonesia. Science of the Total Environment, 675, 632-641. https://doi.org/10.1016/j.scitotenv.2019.04.244.

Mbanga, O., Cukrowska, E., and Gulumian, M. (2022). Dissolution of titanium dioxide nanoparticles in synthetic biological and environmental media to predict their biodurability and persistence. Toxicology in Vitro, 84, 105457. https://doi.org/10.1016/j.tiv.2022.105457.

Oldfield, F., Barnosky, C., Leopold, E. B., and Smith, J. P. (1983). Mineral magnetic studies of lake sediments. Hydrobiologia, 103, 37-44. https://doi.org/10.1007/BF00028425.

Onac, B. P., Hutchinson, S. M., Geantă, A., Forray, F. L., Wynn, J. G., Giurgiu, A. M., and Coroiu, I. (2015). A 2500-yr late Holocene multi-proxy record of vegetation and hydrologic changes from a cave guano-clay sequence in SW Romania. Quaternary Research, 83(3), 437-448. https://doi.org/10.1016/j.yqres.2015.01.007.

Onac, B. P., Feurdean, A., Haliuc, A., Hutchinson, S. M., Forray, F. L., Demjén, A., Vulpoi, A., Dumbravă, R., Lőrincz, A., Ghemiş, C., Nae, A., Lascu, V. T., Gogâltan, F., and Meleg, I. N. (2025). Environmental changes in East-Central Europe from a Middle to Late Holocene Romanian cave sediment record. Palaeogeography, Palaeoclimatology, Palaeoecology, 659, 112672. https://doi.org/10.1016/j.palaeo.2024.112672.

Paar, D., Frančišković-Bilinski, S., Buzjak, N., and Maldini, K. (2025). New insight into geochemistry and mineralogy of deep caves in Crotian karst and its implications for environmental impacts. Water, 17(7), 1001. https://doi.org/10.3390/w17071001.

Putra, R., Rifai, H., and Wurster, C. M. (2019). Relationship between magnetic susceptibility and elemental composition of Guano from Solek Cave, West Sumatera. Journal of Physics: Conference Series, 1185, 012011. doi:10.1088/1742-6596/1185/1/012011.

Rifai, H., Putra, R., Fadila, M. R., Erni, E., and Wurster, C. M. (2018). Magnetic susceptibility and heavy metals in guano from South Sulawesi Caves. IOP Conference Series: Materials Science and Engineering, 335, 012001. doi:10.1088/1757-899X/335/1/012001.

Rifai, H., Putra, R., Rahmadhani, W. F., Sari, N., Niarti, D., Nasution, W., Bijaksana, S., Erni, E., Hantoro, W. S., Kimbrough, A. K., and Wurster, C. M. *Under Review*. Identifying magnetic minerals in guano-clay mixed deposits as indicators of past fluvial processes in a Western Sumatran Cave, Indonesia. Open Geosciences.

Riordan, K. J., Field, J. S., and Dudgeon, J. V. (2021). Investigating geoarchaeological deposits from Naihehe cave in the Sigatoka River valley of Viti Levu, Fiji. Journal of Archaeological Science: Reports, 40(B), 103202. https://doi.org/10.1016/j.jasrep.2021.103202.

Roberts, A. P. (2015). Magnetic mineral diagenesis. Earth-Science Reviews, 151, 1-47. https://doi.org/10.1016/j.earscirev.2015.09.010.

Sasowsky, I. D., and Mylroie, J. (2004). Studies of Cave Sediments: Physical and Chemical Records of Paleoclimate (1st ed). Springer US. https://doi.org/10.1007/978-1-4419-9118-8.

Sroubek, P., Diehl, J. F., Kadlec, J., and Valoch, K. (2001). A Late Pleistocene palaeoclimate record based on mineral magnetic properties of the entrance facies sediments of Kulna Cave, Czech Republic. Geophysical Journal International, 147(2), 247-262. https://doi.org/10.1046/j.0956-540x.2001.01527.x.

Tiwow, V. A., Arsyad, M., Palloan, P., Sulistiawaty, S., Rampe, M. J., Rampe, H. L., and Rampengan, A. M. (2025). Estimation of mineralogical, morphological and magnetic properties of the mineral sediments of guano caves in the karst area. Journal of Chemical Technological and Metallurgy, 60(2), 275-285. https://doi.org/10.59957/jctm.v60.i2.2025.9.

White, W. B. (2007). Cave sediments and paleoclimate. Journal of Cave and Karst Studies, 69, 76-93.

Wirkner, M., and Hertler, C. (2019). Feeding ecology of Late Pleistocene Muntiacus muntjak in the Padang Highlands (Sumatra). Comptes Rendus Palevol, 18, 541-554. https://doi.org/10.1016/j.crpv.2019.03.004.

Wurtzel, J. B., Abram, N. J., Lewis, S. C., Bajo, P., Hellstrom, J. C., Troitzsch, U., and Heslop, D. (2018). Tropical Indo-Pacific hydroclimate response to North Atlantic forcing during the last deglaciation as recorded by a speleothem from Sumatra, Indonesia. Earth and Planetary Science Letters, 492, 264-278. https://doi.org/10.1016/j.epsl.2018.04.001.

SAŽETAK

Magnetna svojstva i mineralogija špiljskih sedimenata iz špilje Solek, Zapadna Sumatra: implikacije za paleoekološke procese unutar špilje

Špiljski su sedimenti ključni jer čuvaju vrijedne arhive prošlih okolišnih i klimatskih uvjeta koje fizička i kemijska mjerenja mogu otkriti. U ovoj studiji istražuju se magnetne karakteristike špiljskih sedimenata prikupljenih iz špilje Solek, Zapadna Sumatra, Indonezija, kako bi se razumjeli okolišni procesi unutar špilje. Korištene su metode magnetne analize stijena uključujući magnetnu susceptibilnost, izotermnu remanentnu magnetizaciju (IRM), anhisterezičnu remanentnu magnetizaciju (ARM) i mjerenja Curiejeve temperature. Osim toga, korištena je rendgenska difrakcija (XRD) i skenirajuća elektronska mikroskopija (SEM) kako bi se analizirala magnetna mineralogija i morfologija špiljskih sedimenata. Rezultati pokazuju visoku koncentraciju magnetnih minerala, posebno ferimagnetnih skupina, što je naznačeno visokom magnetnom susceptibilnošću u rasponu između 210,7 i 1301,2 × 10^{-6} m^3/kg, sa srednjom vrijednošću od 602,7 × 10^{-6} m^3/kg. Izračunane vrijednosti χFD (%) kretale su se od 0,2 do 6,6, uglavnom manje od 2 %, što upućuje na grubozrnate, višedomenske ferimagnetne minerale. Štoviše, rezultati IRM-a, ARM-a i XRD-a pokazuju da među magnetnim mineralima dominira grubozrnati magnetit s veličinom zrna od oko 20 do 110 μm. Mjerenja Curiejeve temperature također pokazuju različite udjele titana tvoreći titanomagnetitnu fazu. Morfologija i kemijski sastav magnetnih minerala, određeni SEM-om i energetski disperzivnom rendgenskom spektroskopijom (EDS-om), također podržavaju prethodne analize pokazujući da je titanomagnetit dominantna faza, karakterizirana grubom veličinom zrna i kutnim oblikom. Ujednačenost magnetnih karakteristika i mineralogije sugerira da je izvor titanomagnetitnoga minerala vjerojatno potaknut litogenim procesima poput erozije i fluvijalnih događaja.

Ključne riječi:
špiljski sedimenti, Zapadna Sumatra, magnetna svojstva, titanomagnetit, litogeni

Author's contribution

Hamdi Rifai (PhD, Associate Professor): conceptualization, sampling, funding, acquisition, supervision, interpretation, formal analysis, visualization, writing - original draft, writing - review editing. **Rizaldi Putra** (M.Sc): conceptualization, acquisition, investigation, interpretation, formal analysis, visualization, writing - original draft, writing - review editing. **Wilda Febi Rahmadhani** (B.Sc): acquisition, investigation. **Nilam Sari** (M.Sc): acquisition, investigation. **Dessupri Niarti** (B.Sc): acquisition, investigation. **Wardina Nasution** (B.Sc): acquisition, investigation, visualization. **Erni Erni** (M.Sc): sampling, investigation, supervision, interpretation, resources, writing - review editing. **Christopher M. Wurster** (PhD): sampling, funding, acquisition, supervision, writing - review editing.
All authors have read and agreed to the published version of the manuscript.

RGNZ/MGPB

Fall cone test calibration for slope stability analysis

Rudarsko-geološko-naftni zbornik
(The Mining-Geology-Petroleum Engineering Bulletin)
DOI: 10.17794/rgn.2026.3.13

Preliminary communication

Chalabi Youssouf[1]*, Aissaoui Soufyane[2], Zadjaoui Abdeldjalil[3], Aissa Mamoune Sidi Mohammed[1]

[1] *Smart Structures Laboratory, University of Ain Temouchent, Ain Temouchent 46000, Algeria.*
[2] *Department of Civil Engineering and Publics Works, University of Ain Temouchent, Ain Temouchent 46000, Algeria.*
[3] *EOLE Laboratory, University of Abou-bekr Belkaid, Tlemcen 13000, Algeria.*

Abstract

Undrained shear strength is considered as an essential factor to assess the stability of natural slopes and embankments. Traditionally, this parameter is determined through laboratory tests, which are often costly and time-consuming. Recently, geotechnical research has shifted toward using the Fall Cone Test (FCT) for short-term strength estimation. However, prior studies focusing on pure clay soils have often overlooked the combined impact of soil texture and stress conditions on the reliability of FCT-derived values. To address this gap, undrained shear tests were conducted using both the FCT and pocket vane shear devices on samples exhibiting various degrees of consolidation and different textures. The findings demonstrate that applying a constant cone factor of 0.8 in the FCT yields inconsistent results compared to vane shear tests, as this factor fails to reflect the soil's consolidation state and the texture effect. To overcome this limitation, a new empirical expression for the cone factor, based on the overconsolidation ratio and fines content, is suggested. The results indicate that this approach significantly improves the accuracy of undrained resistance calculations by the FCT, thus providing a refined methodology for better risk management related to slope and embankments instability.

Keywords:
fall cone test, pocket shear vane test, overconsolidation ratio, fines content, undrained shear strength

1. Introduction

Fall cone test (FCT) has emerged as a prominent tool to evaluate the Atterberg limits of clayey materials (**Spagnoli, 2012; Nini, 2014; Niazi et al., 2019; Vardanega et al., 2022; Marušić & Jagodnik, 2023; Malki & Abed, 2024; Marušić & Jagodnik, 2025**). This method provides accuracy comparable to the Casagrande test while offering a key advantage by minimizing the human error associated with subjective blow count measurements (**Shimobe & Spagnoli, 2020**). Since the late 1950s, the FCT has evolved to serve as a valuable tool for estimating undrained shear strength (s_u) and quantifying sensitivity of both disturbed and undisturbed cohesive soils (**Wood, 1985; Tanaka et al., 2012**). The s_u values derived from the FCT align well with those obtained from direct shear tests conducted at low moisture content, as well as from laboratory vane shear tests (**Canelas et al., 2018**).

The efficacy of the FCT performance is intrinsically linked to its physical setup. Factors such as shape and weight of the cone are rigorously studied and defined by established standards (**Shimobe & Spagnoli, 2019**). For example, the commonly used 30° cone weighing 80 grams is prevalent in the United Kingdom, New Zealand, Australia and France, whereas the 60° cone weighing 60 grams is more frequently employed in Scandinavian nations (**Shimobe, 2010**). Beyond these physical specifications, the accurate estimation of s_u relies heavily on the cone factor (K), which is known to be significantly influenced by additional parameters (**Hansbo, 1957; Karlsson, 1961; Wroth & Wood, 1978; Houlsby, 1982; Koumoto & Houlsby, 2001**). Research has demonstrated that these factors include; the shearing rate and clay sensitivity, as well as the cone's surface roughness and the intrinsic cone angle influence, which is explained through fundamental energy conservation principles (**Wood, 1982; Wood, 1985; Sivakumar et al., 2015; Farias & Llano-Serna, 2016; Vardanega et al., 2018; Llano-Serna & Contreras, 2020; Zeng et al., 2020**).

Despite extensive research, the literature presents a wide and inconsistent range of K values (**Karlsson, 1961; Medhat & Whyte, 1986; Brown & Huxley, 1996; Sharma & Bora, 2003; Kyambadde, 2010**). A value of 0.8 is currently recommended by (**EN ISO 17892-6, 2017**). This variability is largely attributed to

* Corresponding author: Chalabi Youssouf
e-mail address: youcef.chalabi@univ-temouchent.edu.dz
Received: 31 October 2025. Accepted: 17 December 2025.
Available online: 14 May 2026

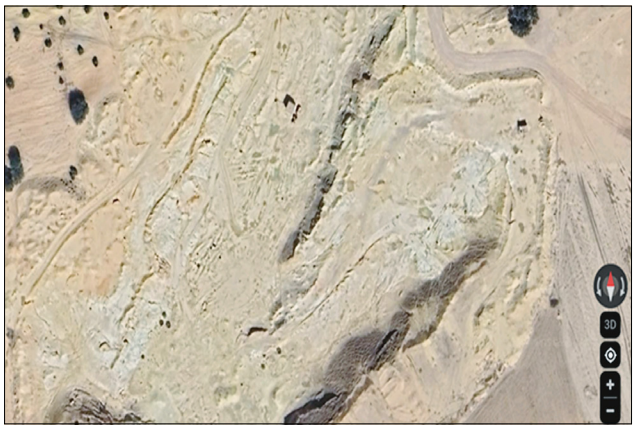


Figure 1. Bouihi quarry (North West of Algeria) – Google Map (34.42166, -1.690772)



Figure 2. Clay deposit (North West of Algeria) – Google Map (35.11198, -1.427161)

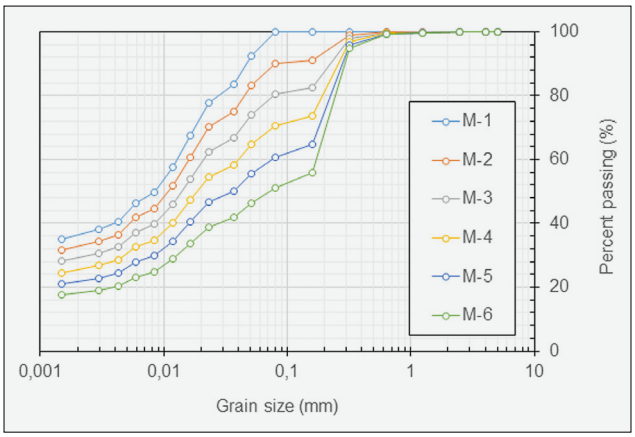


Figure 3. Particle size analysis for all mixtures

Table 1. Geotechnical characteristics of clay and sand

	Clay	Sand
Liquidity limit ω_L (%)	49.75	-
Plasticity limit ω_P (%)	27.30	-
Plasticity index I_P (%)	22.45	-
Specific weight γ_S(kN.m^{-3})	26.30	26.50
Passing 2 mm (%)	100	100
Passing 80 µm (%)	100	1.54
Passing 2 µm (%)	36	/
Coefficient of uniformity Cu	-	2.14
Curvature coefficient Cc	-	0.95

the inexistence of a coherent and standardised methodology of cone factor calibration (**Llano-Serna et al., 2018**). Compounding this issue, the applicability of the Hansbo relationship (**Hansbo, 1957**) is itself questionable for highly consolidated samples (**Stróżyk & Tankiewicz, 2013**), with significant uncertainties remaining in the estimation of s_u for fine-grained soils (**Llano-Serna & Contreras, 2020**), even with proposed modifications to account for strain rate effects (**Hazell, 2008**).

A critical limitation in much of the existing research is the tendency to focus primarily on idealised pure clay samples. This approach fails to capture the complexity of in situ reality, where natural soils often contain varying amounts of silt and sand. This granulometric variability can markedly affect their geotechnical properties (**Terzaghi, 1925; Gilboy, 1928; Lees, 1964; Olson & Mesri, 1970; Abbireddy et al., 2009; Clayton et al., 2009; Göktepe & Sezer, 2010; Cabalar et al., 2013a; Cabalar & Hasan, 2013; Cabalar, 2018**), a challenge particularly evident in studies examining the impact of clay-sand mixtures on s_u (**Cabalar et al., 2020**). Given the research gaps, this investigation intends to examine the combined influence of soil texture (i.e., the fines content) and overconsolidation ratio on cone factor, and their implications for the accuracy of undrained shear strength estimation.

2. Investigated materials and methodology

2.1. Origin and identification

This geotechnical investigation primarily utilised two materials which are identical and reported previously (**Chalabi et al., 2024**). Sand, characterized by its granularity and absence of cohesion, is commonly integrated as a plasticity modulator in geotechnical engineering in line with various established study practices (**Louafi & Bahar, 2012; Amri et al., 2019; Bhardwaj & Sharma, 2020; Meddah et al., 2022; Qusai et al., 2025**). Clay, which is a cohesive, fine-grained material capable of undergoing significant consolidation. The combination of these two types of materials can effectively represent a mixture of clay, silt, and sand as described by (**Gökalp, 2009**).

The sandy material was procured from the Bouihi quarry located North West of Algeria (see **Figure 1**). This poorly graded sand (according to USCS (**ASTM D2487-17e1, 2017**)) is widely employed in construction applications, specifically for wall plastering. Meanwhile, The clayey soil utilised was collected adjacent to a ce-

ramic tile manufacturing facility North West of Algeria (see **Figure 2**). This low plasticity clay (according to USCS (**ASTM D2487-17e1, 2017**)) locally designated as "blue clay," constitutes a base material of ceramic wall tiles. **Figure 3** and **Table 1**, provide a summary of the comprehensive geotechnical properties of the employed materials.

2.2. Specimen formulations

This study employed six distinct mixtures for the experimental investigations in accordance with the protocol defined in **Chalabi et al. (2024)**; M-1 (100% Clay + 0% Sand), M-2 (90% Clay + 10% Sand), M-3 (80% Clay + 20% Sand), M-4 (70% Clay + 30% Sand), M-5 (60% Clay + 40% Sand), and M-6 (50% Clay + 50% Sand). The investigation involved testing clay-sand mixtures at varying water contents (ω %) to pinpoint the optimal moisture level that achieves the required physical properties.

Specimens were meticulously fabricated by gradually incorporating water, subsequently statically compacting the resulting mixture into an oedometer ring with a predefined volume of 7.914×10^{-5} m³ (see **Figure 7**). Later analyses were conducted to assess key characteristics as illustrated in **Figures 4a** to **4c**, which demonstrate the relationship between moisture content and material behaviour.

The findings illustrated in **Figure 4a** and **Figure 4b** reveal that a moisture content ranging from 15% to 20% is optimal for achieving peak density in the various formulations, underscoring the role of a specific amount of moisture in attaining the desired density within these mixtures. Conversely, **Figure 4c** shows that a moisture content of 25% induces full saturation in every specimen. Therefore, this consistent moisture content was selected and applied for the constitution of the testing samples. This decision supports the validation of the consolidation criterion based on Terzaghi's postulate (**Terzaghi & Peck, 1967**), enabling a more accurate observation and analysis of the samples' consolidation behaviour.

2.3. Stress history and consolidation protocols

Following the defined mixture moisture specification, cylindrical samples with a volume of 7.914×10^{-5} m³ were prepared (see **Figure 5**) and subjected to a range of pressure conditions. The procedure implemented as described by (**Chalabi et al., 2020**) comprised imposing a consolidation pressure (σ'_c) to the samples, subsequently releasing this pressure to achieve a targeted vertical effective pressure (σ'_v) corresponding to the desired overconsolidation ratio (*OCR*).

In this regard, consolidation cells were employed (see **Figure 6**), designed with mechanical linkages that magnify the applied load tenfold. The overconsolidation ratios OCR selected were 1, 2, 4, and 8. Their corresponding stress paths, defined by (σ'_c [kPa], σ'_v [kPa]), were

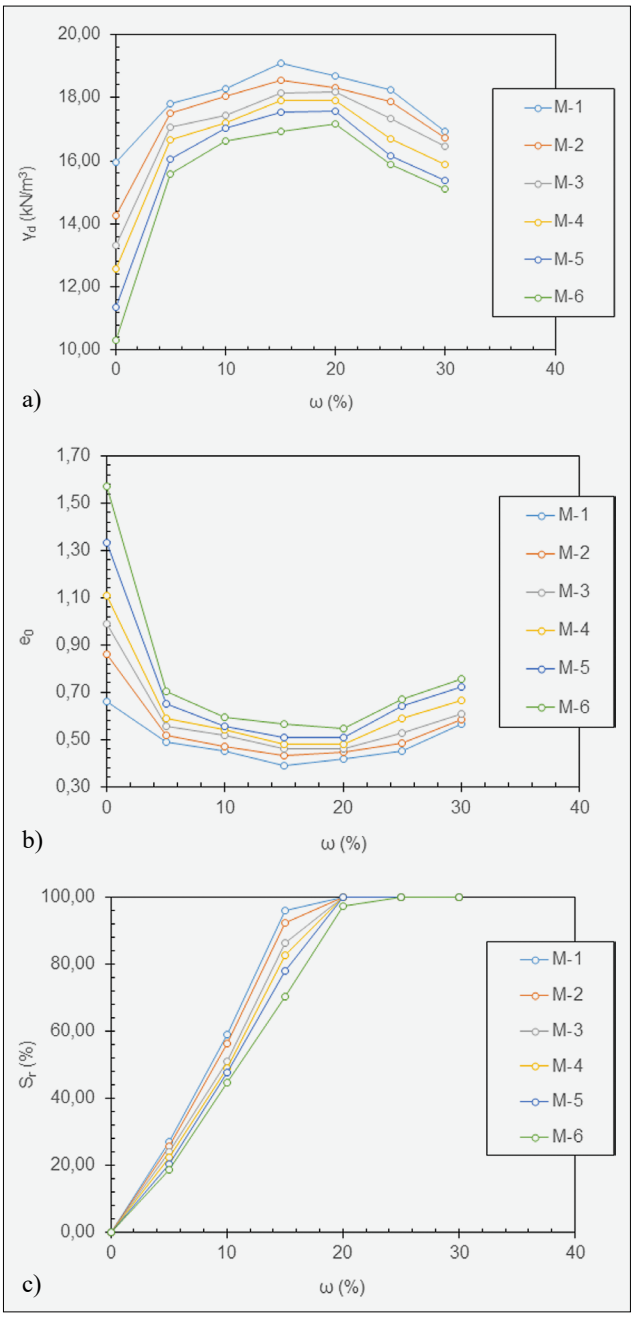


Figure 4. Variation of mixtures behaviour as function of moisture content a) Dry unit weight b) Void ratio c) Degree of saturation.

set as follows; (25,25), (50,25), (100,25), (200,25) as previously established by (**Chalabi et al., 2024**). Throughout the consolidation stage, the imposed pressure exerted upon the soil specimens was systematically incremented by a factor of two at every loading step. This consistent consolidation stress escalation facilitated the meticulous monitoring and evaluation of the soil′s behaviour under elevated stress states.

Each transition between loading and unloading increments within the consolidation cells was allotted a duration of 24 hours. This timeframe was crucial for allowing the samples to stabilise and achieve an equilibrium



Figure 5. Soil filled in the cylindrical mold



Figure 6. Sample under consolidation

condition under the newly imposed load. Throughout this 24-hour period, the specimens experienced consolidation mechanisms, characterised by a reduction in voids between particles and a reorganisation of particles to accommodate the new pressure conditions.

3. Results and discussion

The samples of the six consolidated mixtures were subsequently subjected to two types of laboratory experiments; the pocket shear vane (see **Figure 7**) and the fall cone test (see **Figure 8**). These tests are primarily employed to assess s_u, that is to be considered and further examined in subsequent sections of this paper.

3.1. Influence of overconsolidation ratio and fines content on cone penetration

The FCT (see **Figure 8**) is performed by releasing the standardised steel cone, which then penetrates the soil sample by gravitational force alone. Resulting vertical displacement is measured using an integrated dial gauge. The cone used for this test has a 30° angle and a mass of 80 g.



Figure 7. Pocket shear vane test



Figure 8. Fall cone test

As shown in **Figure 9**, cone penetration decreases with an increase in the overconsolidation ratio, irrespective of the mixture composition. This relationship is found to follow a power law, with greater penetration observed in mixtures containing a lower fine content. Furthermore, the results presented in **Figure 10** corroborate that cone penetration is higher for mixtures with a lower fine content, regardless of the overconsolidation ratio. Specifically, an inverse power-law relationship is demonstrated between cone penetration and the fine content, confirming that increasing the proportion of fines leads to a reduction in penetration.

3.2. Comparison of s_u from pocket shear vane and fall cone tests

The pocket shear vane (see **Figure 7**) is a portable instrument equipped with different-sized vanes designed to adapt various soil consistencies. During testing, the

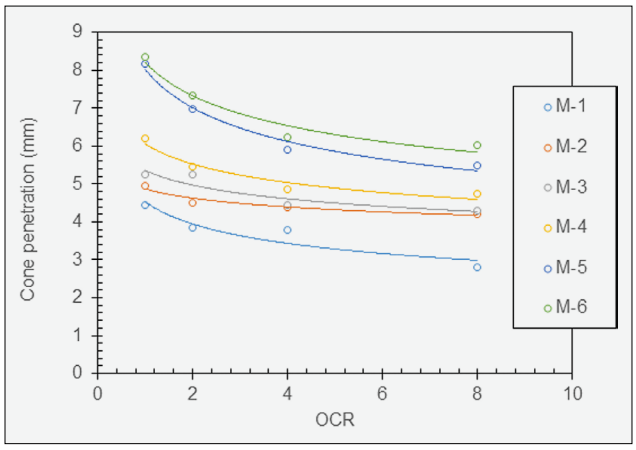


Figure 9. Variation of cone penetration with respect to overconsolidation ratio

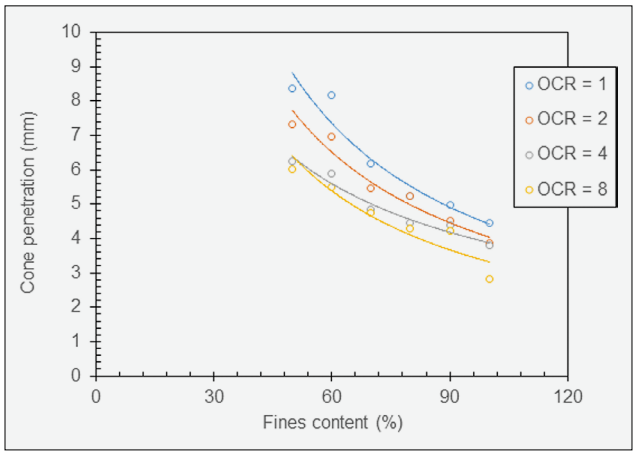


Figure 10. Variation of cone penetration with respect to fines content

selected vane is inserted perpendicularly within the specimen, then subsequently rotated slowly at a uniform speed until failure takes place. The torque at the point of failure is displayed on a dial, and this measurement is then converted to undrained shear strength using a calibration chart.

On the other hand, undrained shear strength by FCT is calculated using the empirical formula (**Equation 1**) proposed by (**Hansbo, 1957**), which correlates it with the penetration depth as follows :

$$s_u = K\, m\, g/H^2 \qquad (1)$$

With:

g – Acceleration due to gravity (9.81 $m.s^{-2}$),

m – Cone masse (80 grams),

H – Penetration (in millimeters),

K – Cone factor.

In this study, *K* is set to 0.8 as recommended by (**EN ISO 17892-6, 2017**).

Figure 11 demonstrates that the undrained shear strength values derived out of FCT are significantly important compared to the measurements yielded by pocket shear vane test. Assuming that the pocket shear vane test provides more appropriate measurements, the RMSE (Root Mean Square Error, as assessed using **Equation 2**) of 1.6 indicates that the estimated values are significantly high, particularly given the narrow range of undrained shear strength (1 to 33 kPa). This discrepancy as quantified by NRMSE (Normalized Root Mean Square Error,estimated using **Equation 3**) of 10%, is attributed to the cone factor *K*, which is typically set at 0.8 – a value deemed inappropriate for overconsolidated soils with varied textures.

$$RMSE = \sqrt{\frac{1}{n}\sum_{i=1}^{n}(A_i - B_i)^2} \qquad (2)$$

Where:

A_i – i^{th} value of derived s_u by FCT,

B_i – i^{th} value of estimated s_u by pocket shear vane test,

n – Total of measurements.

$$NRMSE = \frac{RMSE}{Y_{max} - Y_{min}} \qquad (3)$$

Where:

Y_{max} – Maximum value of s_u by pocket shear vane test,

Y_{min} – Minimum value of s_u by pocket shear vane test.

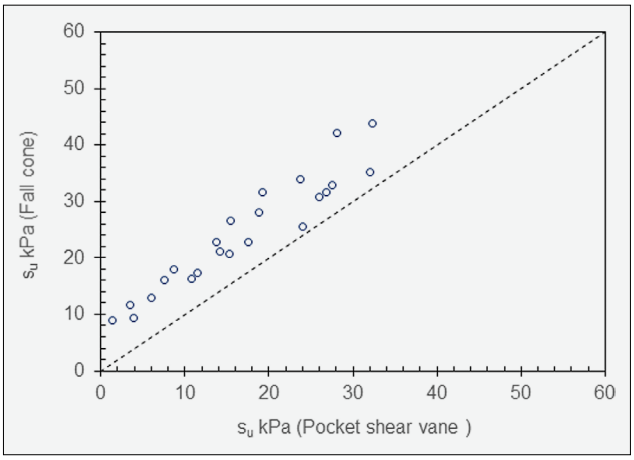


Figure 11. s_u derived by FCT versus pocket shear vane tests.

3.3. Correlation of cone factor with OCR and fines content

As previously observed, FCT significantly overestimates s_u values when compared to the pocket shear vane test. To achieve a reliable estimation of this strength, a back-calculation for *K* factor (see **Equation 6**) is performed for all mixtures, assuming that s_u values estimated by both FCT and pocket shear vane test are equal :

$$s_u(Pocket\ shear\ vane) = s_u(Fall\ cone) \qquad (4)$$

$$s_u(Pocket\ shear\ vane) = K\, m\, g/H^2 \qquad (5)$$

$$K = s_u(Pocket\ shear\ vane)\, H^2/m\, g \qquad (6)$$

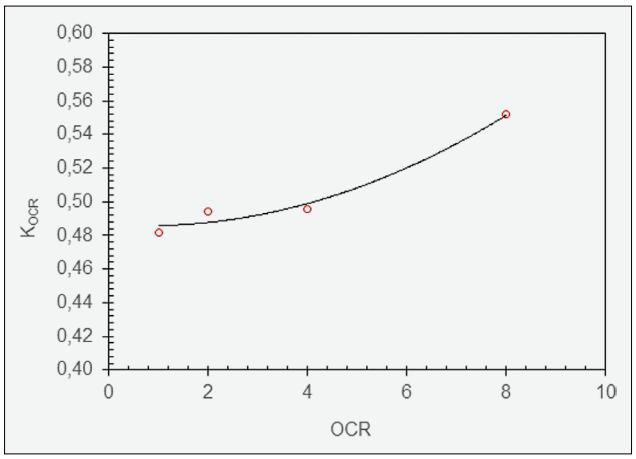


Figure 12. Cone factor expressed by overconsolidation ratio

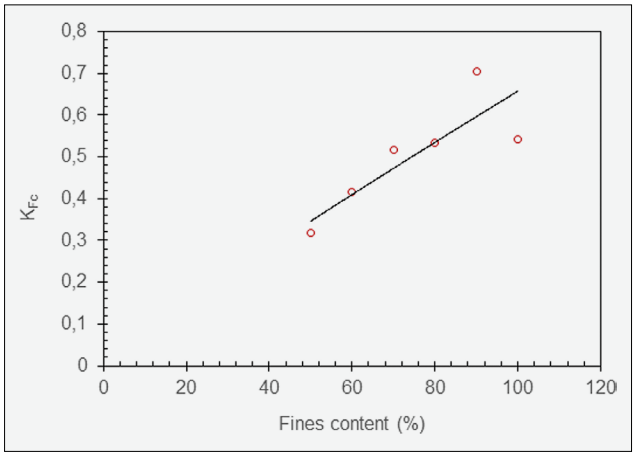


Figure 13. Cone factor expressed by fines content (%)

The back-calculation yielded highly dispersed values, as there are six different cone factor values for each overconsolidation ratio depending on the mixture, making interpretation challenging. Therefore, two specific cone factors are defined. On one hand, the average of the cone factors for all mixtures sharing the same *OCR* is calculated, denoted as K_{OCR}. On the other hand, the average of the cone factors across the entire *OCR* range is calculated for a given mixture, denoted as K_{Fc}.

K_{OCR} is plotted against *OCR* in **Figure 12**. A strong quadratic correlation is observed across the paired parameters, achieving a very good R^2 (coefficient of determination) corresponding to 0.977. The expression for the cone factor as a function of the *OCR* is represented in **Equation 7**. K_{Fc} is plotted against the fines content in **Figure 13**. A good power law correlation is observed among the last enumerated parameters, yielding a R^2 value of 0.782. The resulting empirical expression for the cone factor as a function of fines content is given in **Equation 8**.

$$K_{OCR} = 0.0012\ OCR^2 - 0.0019\ OCR + 0.4864 \quad (7)$$

$$K_{Fc} = 0.0092\ Fc\ (\%)^{0.926} \quad (8)$$

3.4. Application of the proposed cone factors

The evaluation methodology for calculating the undrained shear strength via FCT employed three distinct approaches, incorporating the combinations of K_{OCR} and

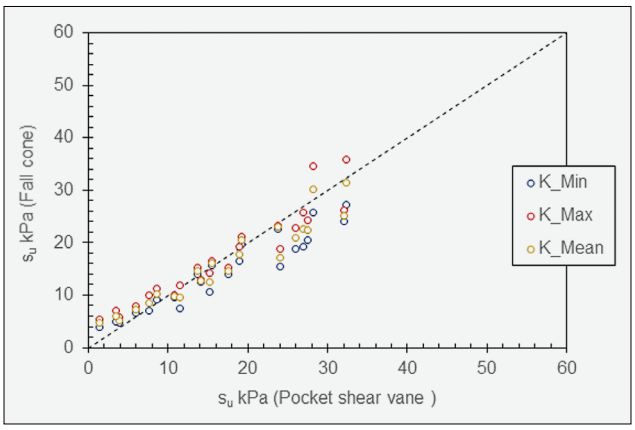


Figure 14. Undrained shear strength by fall cone using combined cone factors versus pocket shear vane tests

K_{Fc}; the minimum (*K_Min*), the maximum (*K_Max*), and the mean (*K_Mean*) of the two factors. The FCT calculations for each approach were performed according to **Equation 1** for other cone penetration measurements. The results of this comparative assessment are presented

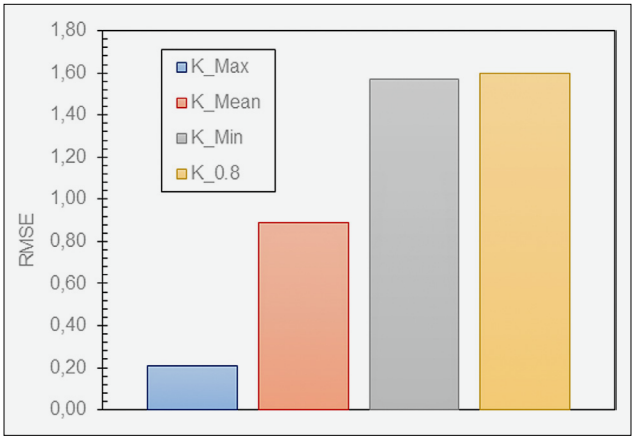


Figure 15. Root Mean Square Error comparison implementing different cone factors

in **Figure 14**, which demonstrates a significant improvement in s_u estimation compared to the use of the conventional constant factor ($K = 0.8$).

Figure 15 shows that the combination utilising the maximum of the two factors (*K_Max*) yields the lowest RMSE among the other combinations with a value of 0.21. This finding is further validated by the NRMSE, which decreased significantly from 10% for the conventional factor to 1.2%. This outcome clearly validates the reliability and significant predictive accuracy of this combined approach.

4. Conclusions

FCT is commonly employed to evaluate the consistency of clayey materials. However, since the late 1950s, scientific studies have increasingly focused on its application to estimate s_u for stability analysis. A notable gap in previous existing literature is rooted in the limited research on estimating s_u for consolidated soils with varied textures. This study aims to address this by proposing a simple and rapid method using the fall cone for the estimation of short-term strength parameters for slope stability analysis. To achieve this, a testing program was conducted on specimens composed of clay and sand, consolidated at various overconsolidation ratios. The subsequent inferences were developed based on the observed findings:

- A decrease in cone penetration is observed with both an increase in the fine content and a rise in the overconsolidation ratio. This reduction occurs irrespective of the soil's consolidation state in the former case and its texture in the latter.
- A quadratic correlation was observed across *OCR* and cone factor. This factor is expressed as a second-degree polynomial equation achieving a very good R^2 corresponding to 0.977.
- A good power law correlation was observed between the fines content and the cone factor with a coefficient of determination of 0.782.
- The proposed cone factors (*K_Max*), derived based on *OCR* and fines content, demonstrably improved estimated s_u values by the FCT method. This enhancement is quantified by a significant reduction in both RMSE (from 1.6 to 0.21) and NRMSE (from 10% to 1.2%) metrics when compared to the conventional approach utilising a constant cone factor of 0.8.

This study did not investigate the effects of unloading or, more broadly, changes in the soil's confinement state. Therefore, future research should focus on exploring the influence of soil sensitivity within this framework. Furthermore, while the pocket shear vane test was used to calibrate the cone factor in FCT approach for undrained shear strength estimation, the implementation of CPTU (Cone Penetration Test with pore water pressure measurement) inside the scope of this analysis, is highly recommended for rigorous geotechnical studies. The *K_Max* combination suggested in this study could be used with reasonable certainty to evaluate s_u for slope stability analysis.

Acknowledgements

The authors gratefully acknowledge the Ceram Divindus-Remchi unit for providing the clay used in this study and the LTPO-West Laboratory for their support during the clay extraction from the site.

5. References

Abbireddy, C. O. R., Clayton, C. R. I., & Huvenne, V. A. I. (2009). A method of estimating the form of fine particulates. Géotechnique, 59(6), 503–511. https://doi.org/10.1680/geot.2008.p.009

American Society for Testing and Materials. (2017). Standard Practice for Classification of Soils for Engineering Purposes: Unified Soil Classification System (ASTM D2487-17e1). West Conshohocken, PA, USA: Author.

Amri, S., Akchiche, M., Bennabi, A., & Hamzaoui, R. (2019). Geotechnical and mineralogical properties of treated clayey soil with dune sand. Journal of African Earth Sciences, 152, 140–150. https://doi.org/10.1016/j.jafrearsci.2019.01.010

Bhardwaj, A., & Sharma, R. K. (2020). Effect of industrial wastes and lime on strength characteristics of clayey soil. Journal of Engineering, Design and Technology, 18(6), 1749–1772. https://doi.org/10.1108/jedt-12-2019-0350

Brown, P. J., & Huxley, M. A. (1996). The cone factor for a 30° cone. Ground Engineering, 29(12), 34–36.

Cabalar, A. F. (2018). Influence of grain shape and gradation on the shear behavior of sand mixtures. Scientia Iranica, 25(6), 3101–3109. https://doi.org/10.24200/sci.2017.4223

Cabalar, A. F., & Hasan, R. A. (2013). Compressional behaviour of various size/shape sand–clay mixtures with different pore fluids. Engineering Geology, 164, 36–49. https://doi.org/10.1016/j.enggeo.2013.06.011

Cabalar, A. F., Dulundu, K., & Tuncay, K. (2013). Strength of various sands in triaxial and cyclic direct shear tests. Engineering Geology, 156, 92–102. https://doi.org/10.1016/j.enggeo.2013.01.011

Cabalar, A. F., Khalaf, M. M., & Isik, H. (2020). A comparative study on the undrained shear strength results of fall cone and vane shear tests in sand–clay mixtures. Arabian Journal of Geosciences, 13(11), 395. https://doi.org/10.1007/s12517-020-05351-5

Canelas, D., Fernandes, I., & Lopes, M. da G. (2018). Use of Fall Cone Test for the determination of undrained shear strength of cohesive soils. MATEC Web of Conferences, 251, 04067. https://doi.org/10.1051/matecconf/201825104067

Chalabi, Y., Mimoune, A. E. h., Aissaoui, S., Mouaissa, M. S., & Brixi, A. (2024). Soil density effects on compressibility and expansion behavior. Journal of Fundamental and Applied Sciences, 16(3), 229–241. https://doi.org/10.4314/jfas.1378

Chalabi, Y., Reiffsteck, P., & Zadjaoui, A. (2020). Applicability of shansep method in evaluation of preconsolidation pressure. Elektronički časopis građevinskog fakulteta Osijek, 13–24. https://doi.org/10.13167/2020.20.2

Clayton, C. R. I., Abbireddy, C. O. R., & Schiebel, R. (2009). A method of estimating the form of coarse particulates. Géotechnique, 59(6), 493–501. https://doi.org/10.1680/geot.2007.00195

EN ISO 17892-6. (2017). Geotechnical investigation and testing – Laboratory testing of soil – part 6 : Fall cone test (EN ISO) [Standard]. Geneva: Author.

Farias, M. M., & Llano-Serna, M. A. (2016). Simple Methodology to Obtain Critical State Parameters of Remolded Clays Under Normally Consolidated Conditions Using the Fall-Cone Test. Geotechnical Testing Journal, 39(5), 855–864. https://doi.org/10.1520/gtj20150207

Gilboy, G. (1928). The compressibility of sand-mica mixtures. Proceedings of the American Society of Civil Engineers, 555–568.

Gökalp, Z. (2009). Engineering characteristics of sand-clay mixtures used for clay cores of earth-fill dams. Clay Minerals, 44(3), 319–326. https://doi.org/10.1180/claymin.2009.044.3.319

Göktepe, A. B., & Sezer, A. (2010). Effect of particle shape on density and permeability of sands. Proceedings of the Institution of Civil Engineers - Geotechnical Engineering, 163(6), 307–320. https://doi.org/10.1680/geng.2010.163.6.307

Hansbo, S. (1957). A New Approach to the Determination of the Shear Strength of Clay by the Fall-Cone Test (Royal Swedish Geotechnical Institute Proceedings No. 14). Stockholm, Sweden.

Hazell, E. (2008). Numerical and experimental studies of shallow cone penetration in clay (Doctoral thesis). University of Oxford, Oxford.

Houlsby, G. T. (1982). Theoretical analysis of the fall cone test. Géotechnique, 32(2), 111–118. https://doi.org/10.1680/geot.1982.32.2.111

Karlsson, R. (1961). Suggested improvements in the liquid limit test, with reference to flow properties of remoulded clays. In Proceedings of the Fifth International Conference on Soil Mechanics and Foundation Engineering. Paris, France.

Koumoto, T., & Houlsby, G. T. (2001). Theory and practice of the fall cone test. Géotechnique, 51(8), 701–712. https://doi.org/10.1680/geot.51.8.701.40475

Kyambadde, B. S. (2010). Strength and Consistency Limits from Quasi-Static Cone Tests (Doctoral dissertation). University of Brighton, Brighton.

Lees, G. (1964). A new method for determining the angularity of particles. Sedimentology, 3(1), 2–21. https://doi.org/10.1111/j.1365-3091.1964.tb00271.x

Llano-Serna, M. A., & Contreras, L. F. (2020). The effect of surface roughness and shear rate during fall-cone calibration. Géotechnique, 70(4), 332–342. https://doi.org/10.1680/jgeot.18.p.222

Llano-Serna, M. A., Farias, M. M., Pedroso, D. M., Williams, D. J., & Sheng, D. (2018). Considerations on the Experimental Calibration of the Fall Cone Test. Geotechnical Testing Journal, 41(6), 1131–1138. https://doi.org/10.1520/gtj20170205

Louafi, B., & Bahar, R. (2012). SAND: An Additive for Stabilzation of Swelling Clay Soils. International Journal of Geosciences, 3(4), 719–725. https://doi.org/10.4236/ijg.2012.34072

Malki, K., & Abed, Y. (2024). Liquid limit determination of medium to high plasticity Algerian soils using fall-cone vs Casagrande percussion cup methods. Acta Geodynamica et Geomaterialia, 21(1), 121–130. https://doi.org/10.13168/agg.2024.0011

Marušić, D., & Jagodnik, V. (2023). Determination of the Atterberg limits using a Fall cone device on low plasticity silty sands. Rudarsko-Geološko-Naftni Zbornik, 38(3), 133–145. https://doi.org/10.17794/rgn.2023.3.11

Marušić, D., & Jagodnik, V. (2025). Atterberg limits determination and soil classification using Fall cone device on the silty sands and sandy silts. International Journal of Geotechnical Engineering, 19(1–3), 78–87. https://doi.org/10.1080/19386362.2025.2454655

Meddah, A., Goufi, A. E., & Pantelidis, L. (2022). Improving Very High Plastic Clays with the Combined Effect of Sand, Lime, and Polypropylene Fibers. Applied Sciences, 12(19), 9924. https://doi.org/10.3390/app12199924

Medhat, F., & Whyte, I. L. (1986). An Appraisal of Soil Index Tests. Geological Society, London, Engineering Geology Special Publications, 2(1), 317–323. https://doi.org/10.1144/gsl.1986.002.01.55

Niazi, F. S., Pinan-Llamas, A., Cholewa, C., & Amstutz, C. (2019). Liquid limit determination of low to medium plasticity Indiana soils by hard base Casagrande percussion cup vs. BS fall-cone methods. Bulletin of Engineering Geology and the Environment, 79(4), 2141–2158. https://doi.org/10.1007/s10064-019-01668-y

Nini, R. (2014). Effect of the silt and clay fractions on the liquid limit measurements by Atterberg cup and fall cone penetrometer. International Journal of Geotechnical Engineering, 8(2), 239–241. https://doi.org/10.1179/193978791 3y.0000000018

Olson, R. E., & Mesri, G. (1970). Mechanisms Controlling Compressibility of Clays. Journal of the Soil Mechanics and Foundations Division, 96(6), 1863–1878. https://doi.org/10.1061/jsfeaq.0001475

Qusai, A., Szendefy, J., & Vásárhelyi, B. (2025). Effect of Changing Sand Content on Liquid Limit and Plasticity Index of Clay. Geotechnics, 5(1), 4. https://doi.org/10.3390/geotechnics5010004

Sharma, B., & Bora, P. K. (2003). Plastic Limit, Liquid Limit and Undrained Shear Strength of Soil – Reappraisal. Journal of Geotechnical and Geoenvironmental Engineering, 129(8), 774–777. https://doi.org/10.1061/(asce)1090-0241(2003)129:8(774)

Shimobe, S. (2010). Determination of index properties and undrained shear strength of soils using the fall cone test. In Proceedings of the 7th International Symposium on Lowland Technology (pp. 51–59). Saga University.

Shimobe, S., & Spagnoli, G. (2019). Some relations among fall cone penetration, liquidity index and undrained shear strength of clays considering the sensitivity ratio. Bulletin of Engineering Geology and the Environment, 78(7), 5029–5038. https://doi.org/10.1007/s10064-019-01478-2

Shimobe, S., & Spagnoli, G. (2020). Fall cone tests considering water content, cone penetration index, and plasticity angle of fine-grained soils. Journal of Rock Mechanics and Geotechnical Engineering, 12(6), 1347–1355. https://doi.org/10.1016/j.jrmge.2020.02.005

Sivakumar, V., O'Kelly, B. C., Henderson, L., Moorhead, C., & Chow, S. H. (2015). Measuring the plastic limit of fine soils: an experimental study. Proceedings of the Institution of Civil Engineers - Geotechnical Engineering, 168(1), 53–64. https://doi.org/10.1680/geng.14.00004

Spagnoli, G. (2012). Comparison between Casagrande and drop-cone methods to calculate liquid limit for pure clay.

Canadian Journal of Soil Science, 92(6), 859–864. https://doi.org/10.4141/cjss2012-011

Stróżyk, J., & Tankiewicz, M. (2013). Undrained shear strength of the heavily consolidated clay. Annals of Warsaw University of Life Sciences - SGGW Land Reclamation, 45(2), 207–216. https://doi.org/10.2478/sggw-2013-0017

Tanaka, H., Hirabayashi, H., Matsuoka, T., & Kaneko, H. (2012). Use of fall cone test as measurement of shear strength for soft clay materials. Soils and Foundations, 52(4), 590–599. https://doi.org/10.1016/j.sandf.2012.07.002

Terzaghi, K. (1925). Erdbaumechanik auf bodenphysikalischer grundlage. Deuticke.

Terzaghi, K., & Peck, R. B. (1967). Soil mechanics in engineering practice (2nd ed.). John Wiley & Sons.

Vardanega, P. J., Haigh, S. K., & O'Kelly, B. C. (2022). Use of fall-cone flow index for soil classification: a new plasticity chart. Géotechnique, 72(7), 610–617. https://doi.org/10.1680/jgeot.20.p.132

Vardanega, P. J., O'kelly, B. C., Haigh, S. K., & Shimobe, S. (2018). Classifying and characterising fine-grained soils using fall cones. ce/papers, 2(2–3), 821–826. https://doi.org/10.1002/cepa.772

Wood, D. M. (1982). Cone penetrometer and liquid limit. Géotechnique, 32(2), 152–157. https://doi.org/10.1680/geot.1982.32.2.152

Wood, D. M. (1985). Some fall-cone tests. Géotechnique, 35(1), 64–68. https://doi.org/10.1680/geot.1985.35.1.64

Wood, D. M., & Wroth, C. P. (1978). Use of the cone penetrometer to determine the plastic limit of soils. International Journal of Rock Mechanics and Mining Sciences & Geomechanics Abstracts, 15(3), 51. https://doi.org/10.1016/0148-9062(78)90033-5

Wroth, C. P., & Wood, D. M. (1978). The correlation of index properties with some basic engineering properties of soils. Canadian Geotechnical Journal, 15(2), 137–145. https://doi.org/10.1139/t78-014

Zeng, X., Li, Y., Liu, X., Yao, J., & Lin, Z. (2020). Relationship between the Shear Strength and the Depth of Cone Penetration in Fall Cone Tests. Advances in Civil Engineering, 2020, 8850430. https://doi.org/10.1155/2020/8850430

SAŽETAK

Kalibracija ispitivanja pomoću padajućega šiljka za analizu stabilnosti kosina

Nedrenirana posmična čvrstoća jedan je od ključnih parametara za procjenu stabilnosti prirodnih kosina i nasipa. Uobičajeno se ovaj parametar određuje laboratorijskim ispitivanjima koja su često skupa i vremenski zahtjevna. U novije vrijeme geotehnička istraživanja sve se više usmjeravaju na primjenu ispitivanja pomoću padajućega šiljka (*Fall Cone Test* – FCT) za procjenu kratkotrajne nedrenirane posmične čvrstoće tla. Međutim, dosadašnja istraživanja, uglavnom provedena na čistim glinovitim tlima, često zanemaruju zajednički utjecaj teksture tla, stanja naprezanja i stanja konsolidacije na pouzdanost vrijednosti nedrenirane posmične čvrstoće dobivenih FCT-om. Kako bi se premostio navedeni nedostatak, provedena su ispitivanja nedrenirane posmične čvrstoće primjenom padajućega šiljka i ispitivanja posmične čvrstoće terenskom krilnom sondom, koja se u normativnoj praksi koristi kao referentna metoda. Ispitivanja su provedena na uzorcima tla različitoga stupnja konsolidacije i različitoga granulometrijskog sastava. Rezultati pokazuju da primjena konstantnoga koeficijenta korelacije vrijednosti o,8 kod ispitivanja pomoću padajućega šiljka dovodi do nepodudarnih rezultata u odnosu na ispitivanje terenskom krilnom sondom jer takav koeficijent ne odražava stanje konsolidacije tla niti utjecaj granulometrijskoga sastava. Radi prevladavanja navedenoga ograničenja predložen je novi empirijski izraz za koeficijent korelacije koji se temelji na omjeru prekonsolidacije (OCR) i udjelu sitnih čestica u tlu. Dobiveni rezultati pokazuju da takav pristup znatno poboljšava točnost određivanja nedrenirane posmične čvrstoće primjenom ispitivanja pomoću padajućega šiljka, čime se osigurava pouzdanija metodologija za analizu stabilnosti kosina i nasipa te učinkovitije upravljanje geotehničkim rizicima u kratkotrajnim (nedreniranim) uvjetima.

Ključne riječi:
padajući šiljak, terenska krilna sonda, koeficijent prekonsolidacije, udio sitnih čestica, nedrenirana posmična čvrstoća

Author's contribution

Youssouf Chalabi (PhD, Associate Professor) defined the overarching research objectives through conceptualisation and designed the specific experimental and analytical framework, alongside conducting the laboratory testing and interpretation. **Soufyane Aissaoui** (PhD, Associate Professor) provided essential equipment and materials, contributed to investigation through meticulous sample preparation, and provided critical intellectual feedback during writing – review & editing. **Abdeldjalil Zadjaoui** (Full Professor) was responsible for data curation, performed the formal analysis of the experimental results, and contributed to the critical review process. **Sidi Mohammed Aissa Mamoune** (Full Professor) managed secondary data curation and generated the initial manuscript draft.
All authors have read and agreed to the published version of the manuscript.

RGNZ/MGPB

Remote sensing of radioactive alteration zones using Sentinel-2 and SPAD chlorophyll measurements in Mamuju, Indonesia

Rudarsko-geološko-naftni zbornik
(The Mining-Geology-Petroleum Engineering Bulletin)
DOI: 10.17794/rgn.2026.3.14

Original scientific paper

Nuraisyiah Pertiwi Kamsir[1], Asep Saepuloh[1]*, Very Susanto[1], Eka Djatnika Nugraha[2]

[1] *Geological Engineering, Faculty of Earth Sciences and Technology, Institut Teknologi Bandung, Jl. Ganesha No. 10 Bandung, Indonesia.*

[2] *Research Center for Safety, Metrology, and Nuclear Quality Technology, Research Organization of Nuclear Technology, The National Research and Innovation Agency of Indonesia (BRIN), Tangerang Selatan 15314, Banten, Indonesia.*

Abstract

This study investigates natural radioactive mineralization (uranium–thorium) in Mamuju, West Sulawesi, particularly within the fault-controlled Adang Volcanics, an area known for anomalous natural radiation. The objective was to evaluate vegetation stress as a proxy for radioactive mineralization by integrating satellite data and field validation. We processed Sentinel-2A data using band ratios (4/2 iron oxide, 4/3 ferric iron, 11/12 clay) and false colour composites to delineate alteration zones. The Red Edge Vegetation Index (REVI; B3, B4, B6) was calculated to detect vegetation stress. Fieldwork in December 2023 collected 68 SPAD chlorophyll measurements from ferns, interpolated with inverse distance weighting, and compared with independent radiation dose rates. The results show a strong correlation between REVI and SPAD (R^2 = 0.76), confirming the sensitivity of red-edge bands to chlorophyll variability. SPAD values decreased significantly in high-radiation zones, showing a strong negative correlation with dose rate (R^2 = 0.90). Values of 4–40 were typical in anomalous radiation areas, while >40 characterized lower exposure. Vegetation stress anomalies and satellite-derived Chlorophyll Index overlapped spatially with alteration zones and were concentrated in the Adang Volcanics along structural controls. Species differences among ferns indicated varied sensitivity to radiation. This integrated approach demonstrates the effectiveness of Sentinel-2 alteration composites, REVI, and SPAD validation as a rapid, low-cost framework for early exploration of radioactive minerals while also contributing to environmental radiation hazard assessment.

Keywords:
Sentinel-2, Red Edge Vegetation Index (REVI), SPAD chlorophyll, radioactive mineralization, Mamuju

1. Introduction

Indonesia has long been recognized as a country with considerable potential for uranium and thorium resources, which are strategically distributed across several major islands, including Sumatra, Kalimantan, and Sulawesi (**Aditya et al., 2025; Saputra et al., 2025**). Among these regions, Mamuju in West Sulawesi stands out as an area with naturally high radiation dose rates compared to its surroundings (**Nugraha et al., 2021**). This anomaly is closely linked to the geological setting, where volcanic rock formations host uranium- and thorium-bearing minerals (**Saepuloh et al., 2023**). These minerals may occur as primary deposits formed via magmatic and hydrothermal processes, or as secondary accumulations derived from sedimentary processes and intense weathering (**Subasinghe et al., 2022**). The natural enrichment of these radioactive elements makes Mamuju an area of dual significance (**Nugraha et al., 2021**). On the one hand, it represents a potential energy resource that could support future nuclear power development as part of a sustainable energy transition. On the other hand, the elevated levels of radiation exposure in the environment pose a serious concern, particularly for local ecosystems and human health (**Bréchignac et al., 2016**). Long-term exposure to ionizing radiation is known to increase risks of cancer, genetic disorders, and other health problems, which underlines the importance of comprehensive studies to better understand the geological and environmental dynamics of this area.

Exploration of radioactive mineralization in such complex environments requires innovative methods that are both effective and practical. Conventional ground-based surveys, although accurate, are often costly, time-consuming, and difficult to implement in regions with rugged terrain or dense vegetation (**Abdulraheem et al., 2023**). Remote sensing has emerged as an alternative approach that can provide broad spatial coverage and detailed information without the need for direct physical access to every location (**Yu & Fang, 2023**). By record-

* Corresponding author: Asep Saepuloh
e-mail address: saepuloh@itb.ac.id

Received: 4 September 2025. Accepted: 28 December 2025.
Available online: 14 May 2026

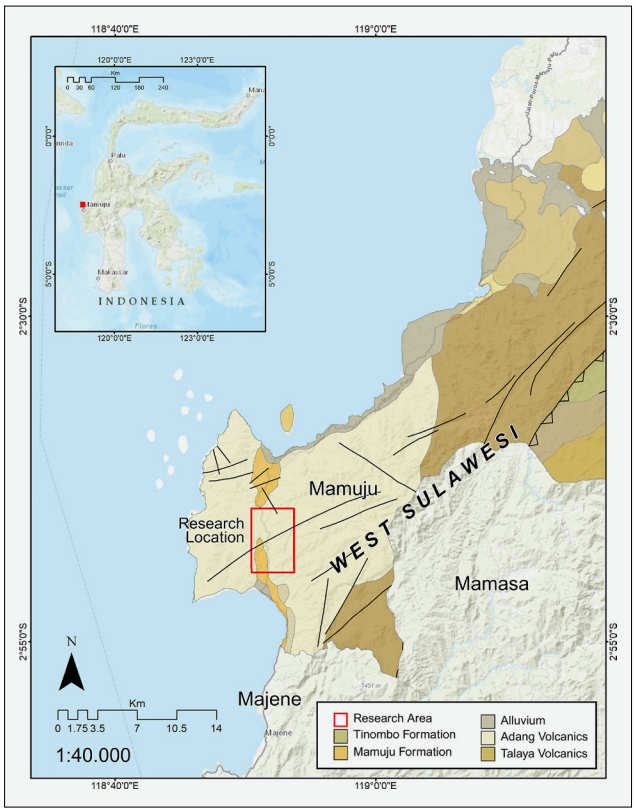


Figure 1. Geological formations in the Mamuju study area showing the distribution of the Mamuju Formation and Adang Volcanics, the only formations present within the study area, along with major faults controlling the structural framework.

ing and analyzing the spectral response of the Earth's surface to solar radiation, satellite sensors are capable of differentiating materials based on their reflectance characteristics. Sentinel-2, for instance, offers high-resolution multispectral data that can highlight zones of mineral alteration and other surface anomalies. However, the interpretation of satellite imagery is not without challenges (**Chen et al., 2023; Hu et al., 2018**). Disturbances from atmospheric particles, cloud cover, and particularly dense vegetation can significantly reduce the clarity of spectral signals, thereby complicating the detection of underlying lithological features (**Meraner et al., 2020; Shebl et al., 2024**). These limitations highlight the necessity of developing techniques that are able to extract meaningful information even under conditions where direct mineral signals are obscured.

Previous studies (**Rosianna et al., 2020; Saepuloh et al., 2023**) have shown that vegetation cover poses a major challenge for mineral exploration using optical satellite imagery, particularly in tropical regions like Mamuju, where a dense canopy often obscures the spectral characteristics of rocks and minerals and reduces the effectiveness of conventional remote sensing methods. A geobotanical approach offers a way to overcome this limitation by leveraging the principle that plants reflect the geochemical conditions of their substrate, as vegetation can absorb metals and radionuclides from the soil, affecting physiological processes such as chlorophyll activity, water uptake, and photosynthesis. Although these stress responses are not always visually apparent, they can be detected through changes in leaf spectral reflectance, particularly in the visible and red-edge regions of the electromagnetic spectrum, making plants potential natural bioindicators of subsurface mineralization.

While the use of vegetation stress as a mineral exploration tool is widely recognized, its application in areas with naturally occurring radioactive minerals in Indonesia remains limited, highlighting opportunities for research that integrates geological, biological, and remote sensing perspectives. By combining remote sensing techniques with vegetation-based indicators, this approach provides an alternative means to investigate regions where direct lithological observation is constrained by forest cover, interpreting vegetation stress as a potential signal of underlying geological conditions associated with radioactive mineralization. The findings are expected to advance both the scientific understanding of geobotanical responses in radioactive environments and practical considerations for natural resource assessment and environmental risk evaluation.

2. Geological Setting

The study area is located in Mamuju, West Sulawesi, within a complex tectonic setting at the junction of the Australian Plate, Sunda Plate, and Philippine Sea Plate, which has produced active faulting and structural deformation (**Sompotan, 2012; Supendi et al., 2021**). The geology of the region is dominated by volcanic and sedimentary formations (**Laode et al., 2025**), with the Mamuju Formation and Adang Volcanics as the primary units in the study area, as shown in **Figure 1**. The Mamuju Formation consists of marl, calcareous sandstone, coral limestone, and tuffaceous sandstone, occasionally interbedded with conglomerate and claystone, reflecting a shallow marine depositional environment characterized by weakly lithified carbonate and volcaniclastic sediments (**Perdana & Amijaya, 2011; White et al., 2017**). The Adang Volcanics comprises volcanic rocks with phonolitic leucite composition containing minerals such as leucite, K-feldspar, plagioclase, pyroxene, and minor opaque minerals, which are generally moderately to strongly weathered (**Shaban et al., 2016**).

Faults are present throughout the study area, controlling the structural framework and influencing the distribution and deformation of both sedimentary and volcanic units (**Meilano et al., 2023; Supendi et al., 2021**). These faults contribute to variations in topography and rock stability, shaping the landscape of Mamuju and affecting the lithological expression of the Mamuju Formation and Adang Volcanics. The combination of volcanic and sedimentary rocks with active fault structures provides a

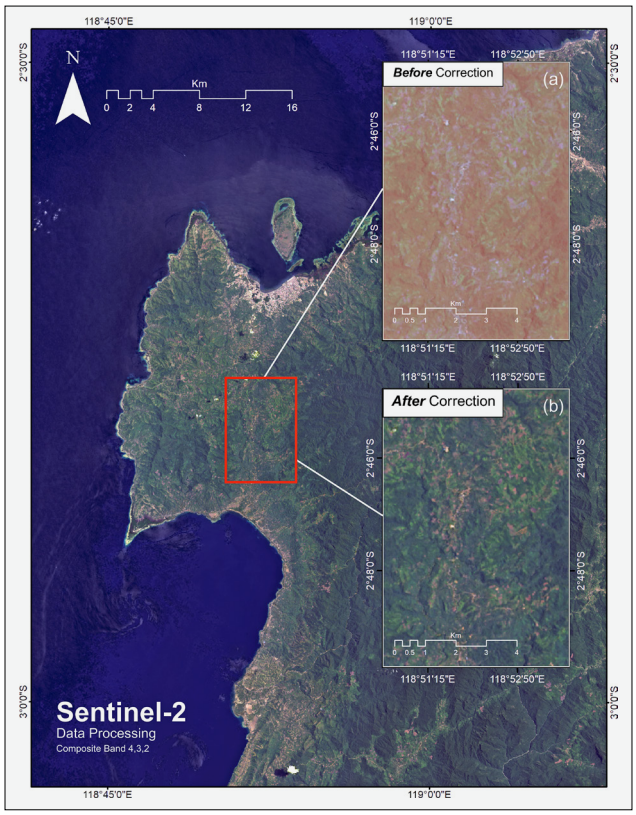


Figure 2. Sentinel-2 imagery before (a) and after (b) correction, showing the improvement in visual quality and spatial alignment.

unique geological setting for examining mineralization patterns, geohazard potential, and the interaction between tectonics and rock properties in the region.

3. Data and Satellite Image Processing

3.1. Data

The primary dataset used in this research is Sentinel-2A multispectral imagery acquired on **October 9, 2019** with less than 10% cloud cover. Sentinel-2 provides 13 spectral bands in the visible, red-edge, near-infrared, and shortwave infrared regions with spatial resolutions ranging from 10 to 60 meters (**Bayle et al., 2019; Liu et al., 2021**). For this study, nine bands were utilized due to their spectral relevance for both mineralogical and vegetation analysis. Details of the spectral bands used are summarized in **Table 1**.

Complementary data included a **geological map of the Mamuju sheet** from Geomap (Indonesian Geological Agency), and a **radiation dose-rate dataset** compiled by **Wijaya (2024)**. These were employed to provide lithological context and independent validation of remote sensing results. The field survey conducted in December 2023 yielded **68 SPAD chlorophyll measurements** on ferns, which served as ground-truth data for vegetation stress evaluation. Each measurement was taken at three points of a leaf (tip, middle, and base) to reduce intra-sample variability.

3.2. Satellite Imagery Data Processing

The Sentinel-2 image was pre-processed through atmospheric and radiometric corrections to convert raw digital numbers into surface reflectance values (**Rumora et al., 2021; Vrdoljak & Kilić Pamuković, 2022**). Geometric correction was conducted to align the image to UTM Zone 50S, WGS84 datum, as shown in **Figure 2**. A pan-sharpening enhancement was also applied to improve the spatial detail of multispectral bands. For mineralogical analysis, band ratio techniques were applied to exploit the spectral differences between absorption and reflectance features of alteration minerals. The following ratios were selected (**Carvalho et al., 2025; Saepuloh et al., 2023**):

- Band 4 / Band 2 → iron oxide (hematite, goethite)
- Band 4 / Band 3 → ferric iron minerals
- Band 11 / Band 12 → clay minerals (illite, kaolinite, smectite)

These ratio layers were subsequently combined into a false-colour composite (R: 4/3, G: 4/2, B: 11/12), allowing the discrimination of alteration zones that are frequently associated with uranium and thorium enrichment. The results of the band ratio composites are presented in **Figure 3**.

3.2.1. Red Edge Vegetation Index (REVI)

Vegetation stress was analyzed using the Red Edge Vegetation Index (REVI), which is particularly sensitive to changes in chlorophyll content and has proven effective in detecting vegetation stress under environmental

Table 1. Summary of the dataset and band features of the Sentinel-2 images employed in this study

Date of acquisition	Band Name	Wavelength range (μm)	Resolution (m)
October 9, 2019	B2 Visible (blue/B)	0.458–0.523	10
	B3 Visible (green/G)	0.543–0.578	10
	B4 Visible (red/R)	0.650–0.680	10
	B5 Red edge-1 (RE-1)	0.698–0.713	20
	B11 Shortwave infrared-1 (SWIR-1)	1.565–1.655	20
	B12 Shortwave infrared-2 (SWIR-2)	2.100–2.280	20

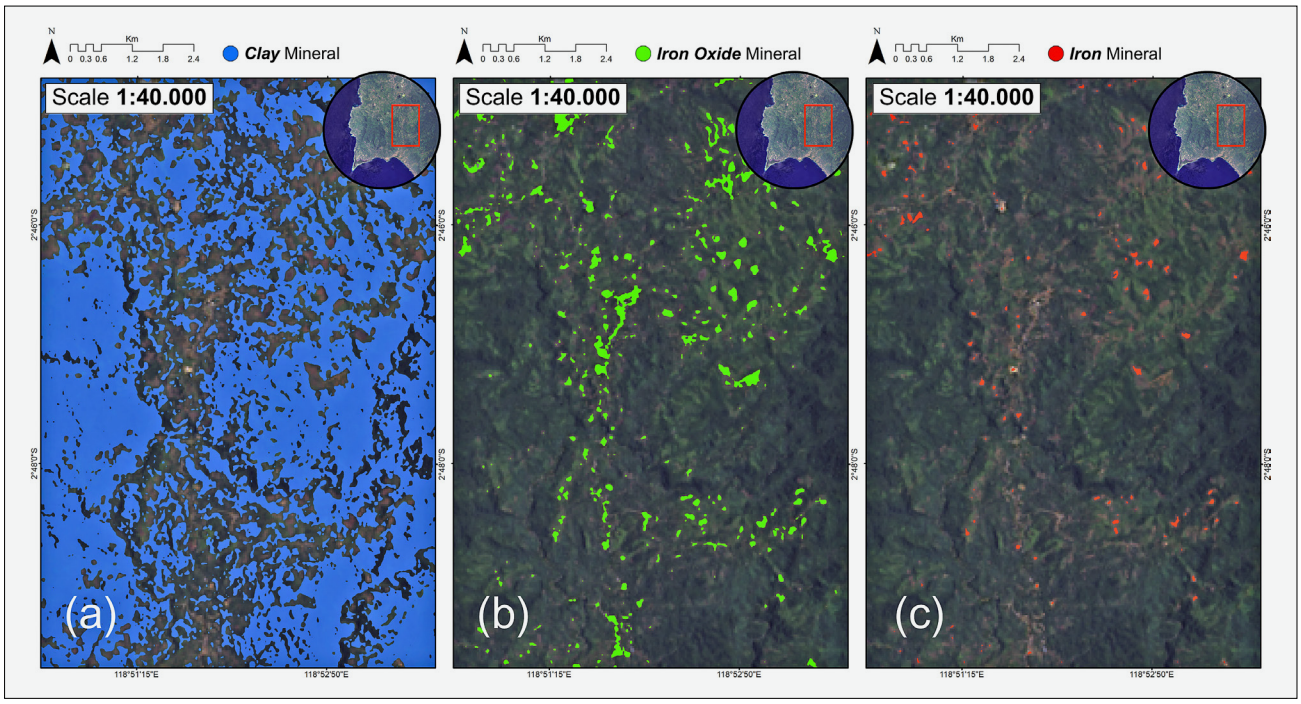


Figure 3. Band ratio composites for hydrothermal alteration mapping: (a) clay minerals (illite, kaolinite, smectite) highlighted using Band 11/Band 12 (blue), (b) iron oxide minerals (hematite, goethite) mapped using Band 4/Band 2 (green), and (c) ferric iron minerals extracted from Band 4/Band 3 (red).

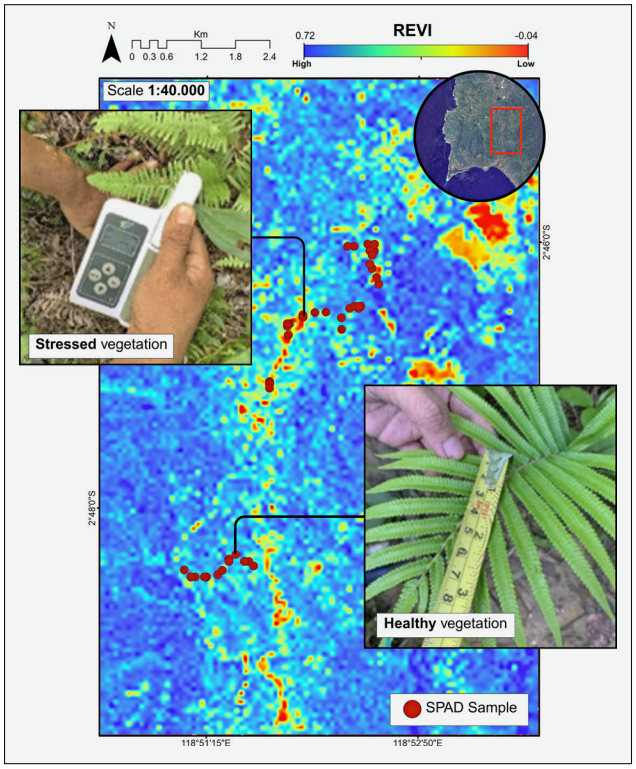


Figure 4. Spatial distribution of the Red Edge Vegetation Index (REVI), where the colour gradient from red to blue reflects variations in vegetation density, with higher values (blue) indicating denser and healthier vegetation cover. The brown dots represent SPAD sampling locations used for ground-truth validation.

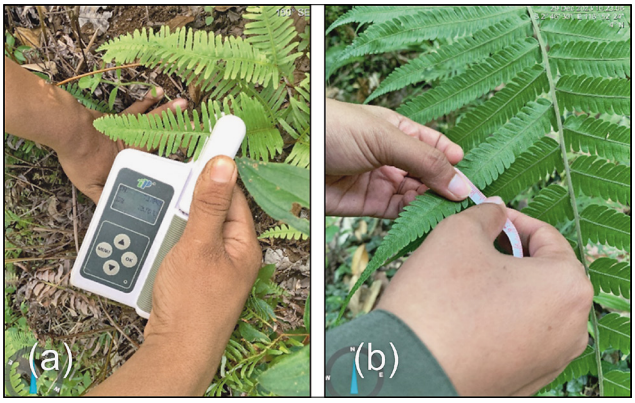


Figure 5. Field documentation of SPAD verification: (a) SPAD measurement on ferns exhibiting stunted growth and pale green colouration; and (b) SPAD measurement on ferns with healthy appearance and greener leaves.

anomalies such as radioactive exposure (**Dong et al., 2019; Sun et al., 2020**). The index was calculated as (**Saepuloh et al., 2023**):

$$\mathrm{REVI} = \frac{\mathrm{B3} - \mathrm{B4}}{\mathrm{B3} + \mathrm{B4}} + \frac{\mathrm{B6} - \mathrm{B4}}{\mathrm{B6} + \mathrm{B4}} \quad (1)$$

Where:

B3 – the green band (0.543–0.578 μm),

B4 – the red band (0.650–0.680 μm),

B6 – the red-edge band (0.733–0.748 μm).

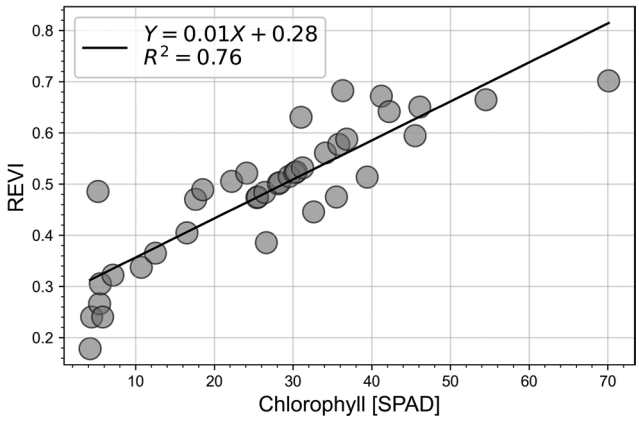


Figure 6. Correlation between field-measured SPAD values and the Red Edge Vegetation Index (REVI), showing a strong positive relationship with R^2 = 0.76, indicating that satellite-based vegetation indices effectively capture chlorophyll variation observed in the field.

The REVI map clearly highlights spatial variations in vegetation health, with lower values indicating stressed vegetation. This index was selected as the primary remote sensing proxy for bioindicator analysis in relation to radioactive mineralization. The results of the REVI analysis are shown in **Figure 4**.

3.3. Field Chlorophyll Measurement

Field surveys were conducted in December 2023 to obtain in-situ validation data. A total of 68 ferns were sampled across Botteng and Salumatti villages. Chlorophyll content was measured using a SPAD chlorophyll meter, which estimates relative chlorophyll concentration by analyzing light transmission in red and near-infrared wavelengths. The collected SPAD values were interpolated spatially using the Inverse Distance Weighting (IDW) method in ArcGIS to generate continuous chlorophyll distribution maps. Morphological observations, such as leaf discolouration and growth inhibition, were recorded to complement quantitative SPAD data, with the sampling locations shown in **Figure 4** and field documentation presented in **Figure 5**.

3.4. Data Integration and Validation

Data integration was performed to link remote sensing results with ground measurements and radiation data. First, alteration mineral composites from band ratios were overlaid with interpolated SPAD maps to examine spatial correspondence between alteration zones and vegetation stress. Second, correlation analysis was conducted between measured SPAD values and radiation dose rates, as well as between SPAD and REVI. As shown in **Figure 6**, REVI exhibited a strong positive correlation with SPAD (R^2 = 0.76), indicating that satellite-based vegetation indices reliably reflect field-measured chlorophyll content. Regression modelling was then applied to derive satellite-based chlorophyll estimates (Chlorophyll Index), enabling the extrapolation of field observations across the study area. This integrative approach ensured that anomalies identified in the satellite imagery corresponded with field-verified vegetation stress and geological context, thereby increasing the reliability of remote sensing for preliminary radioactive mineral exploration.

4. Results and Discussion

4.1. SPAD Measurements and Radiation Dose Rates

Field-based chlorophyll measurements revealed a pronounced physiological response of ferns to elevated natural radiation. Across 68 samples, SPAD values ranged from 4 to 40, with the lowest values consistently recorded in zones of higher radiation dose rates. However, only 38 of these samples had spatially corresponding radiation measurements from the Wijaya (2024) dataset within an acceptable matching distance, and thus this subset (n = 38) was used for correlation and ANOVA analyses to ensure spatial comparability. Conversely, areas characterized by lower radiation levels exhibited markedly higher and more stable SPAD values (>40) (see **Figure 7**). When compared against radiation dose rates reported by **Wijaya (2024)**, the dataset demonstrated a strong negative correlation (R^2 = 0.90), providing robust evidence that increasing radiation levels directly suppress chlorophyll content in vegetation (see **Figure 8**).

To further evaluate whether chlorophyll levels differ systematically across radiation environments, radiation dose rates were grouped into three classes based on the empirical distribution of the dataset: low (< 3206 nSv/h), moderate (3206–4925 nSv/h), and high (> 4925 nSv/h). The summary statistics for these radiation classes are presented in **Table 2**, which clearly shows a monotonic decline in SPAD values with increasing radiation intensity. Mean SPAD decreases from 42.3 ± 10.3 in the low-radiation class to 28.1 ± 2.4 in the moderate class and sharply declines to 10.4 ± 6.3 in the high-radiation class, indicating progressively stronger physiological suppression under elevated radiation conditions.

A one-way ANOVA was conducted to determine whether these observed differences in SPAD among radiation classes were statistically significant. The ANOVA results, summarised in **Table 3**, demonstrate a highly significant effect of radiation class on chlorophyll content ($F(2,35) = 63.84$, $p < 0.0001$). The effect size (η^2 = 0.78) indicates that approximately 78% of the variance in SPAD is attributable to differences in radiation level, underscoring the dominant role of natural radioactivity in shaping vegetation physiological response. Post-hoc Tukey HSD tests confirmed that all three radiation classes differ significantly from one another ($p \leq 0.001$), meaning that SPAD in the high-radiation class is significantly lower than in both the moderate- and low-radia-

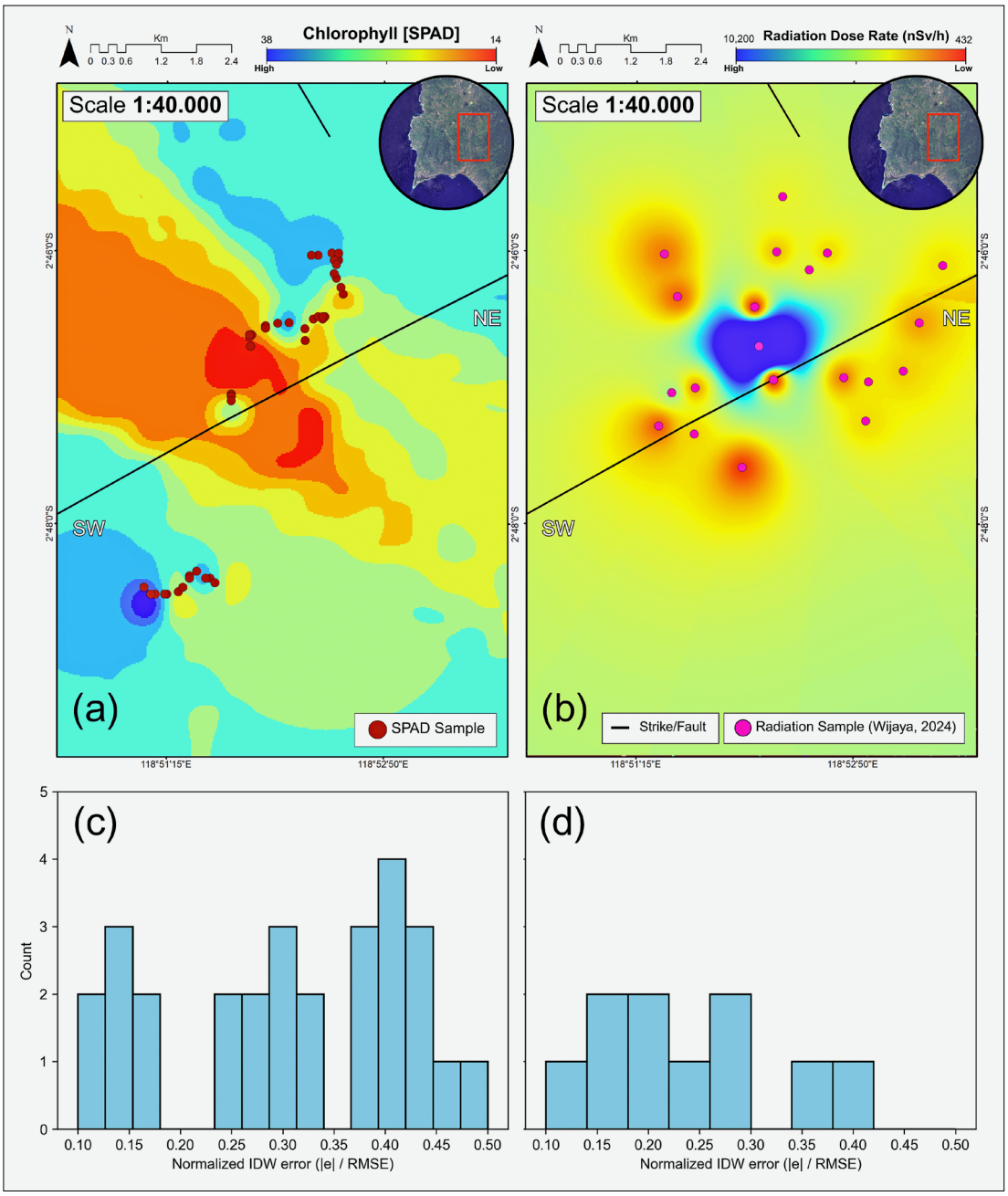


Figure 7. Spatial distribution maps showing (a) interpolated SPAD Chlorophyll Index from 68 fern samples, and (b) natural radiation dose rates adapted from Wijaya (2024). Lower SPAD values (4–40) are associated with zones of higher radiation, while higher values (>40) occur in areas with lower radiation exposure. (c) presents the normalized IDW interpolation error for the SPAD dataset, illustrating the distribution of uncertainty associated with the chlorophyll interpolation surface. (d) The corresponding normalized IDW interpolation error for the radiation exposure rate dataset, providing an assessment of spatial reliability for the radiometric interpolation.

tion classes, and that the moderate class also differs significantly from the low-radiation class.

Assumption checks indicated no significant heterogeneity of variances (Levene's test, $p = 0.11$), while minor deviations from normality were detected in residuals. Given the balanced group sizes, the strong separation of class means, and the large effect size, the ANOVA results are considered robust. Collectively, the regression results and the class-level analysis presented in **Table 2** and **Table 3** provide compelling statistical evidence that elevated natural radiation consistently suppresses chlorophyll content and contributes to measurable physiological stress in vegetation across the study area.

4.2. Chlorophyll Index Distribution and Alteration Mineral Composites

The spatial distribution of Chlorophyll Index was systematically compared with alteration anomalies derived

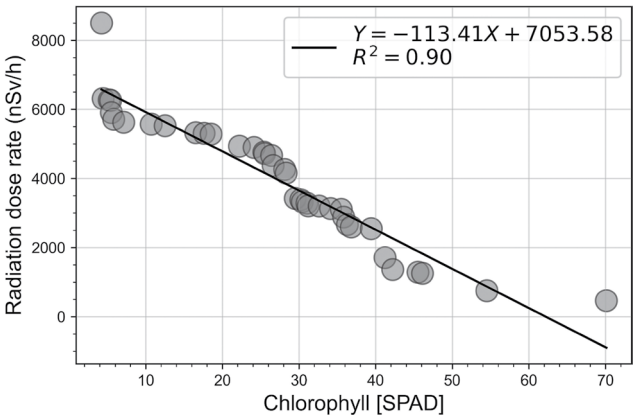


Figure 8. Relationship between SPAD Chlorophyll Index and natural radiation dose rates (**Wijaya, 2024**), showing a strong negative correlation (R^2 = 0.90) that indicates increasing radiation levels directly reduce chlorophyll content in vegetation.

Table 2. Descriptive statistics of SPAD Chlorophyll Index across radiation classes

Radiation Class	Dose-rate Range (nSv/h)	n	Mean SPAD	SD
Low	< 3206	13	42.32	10.30
Moderate	3206–4925	12	28.06	2.43
High	> 4925	13	10.43	6.33

Table 3. One-way ANOVA results for SPAD across radiation classes

Source	SS	df	MS	F	p-value
Between groups	6631.41	2	3315.70	63.84	< 0.0001
Within groups	1817.87	35	51.94	–	–
Total	8449.28	37	–	–	–

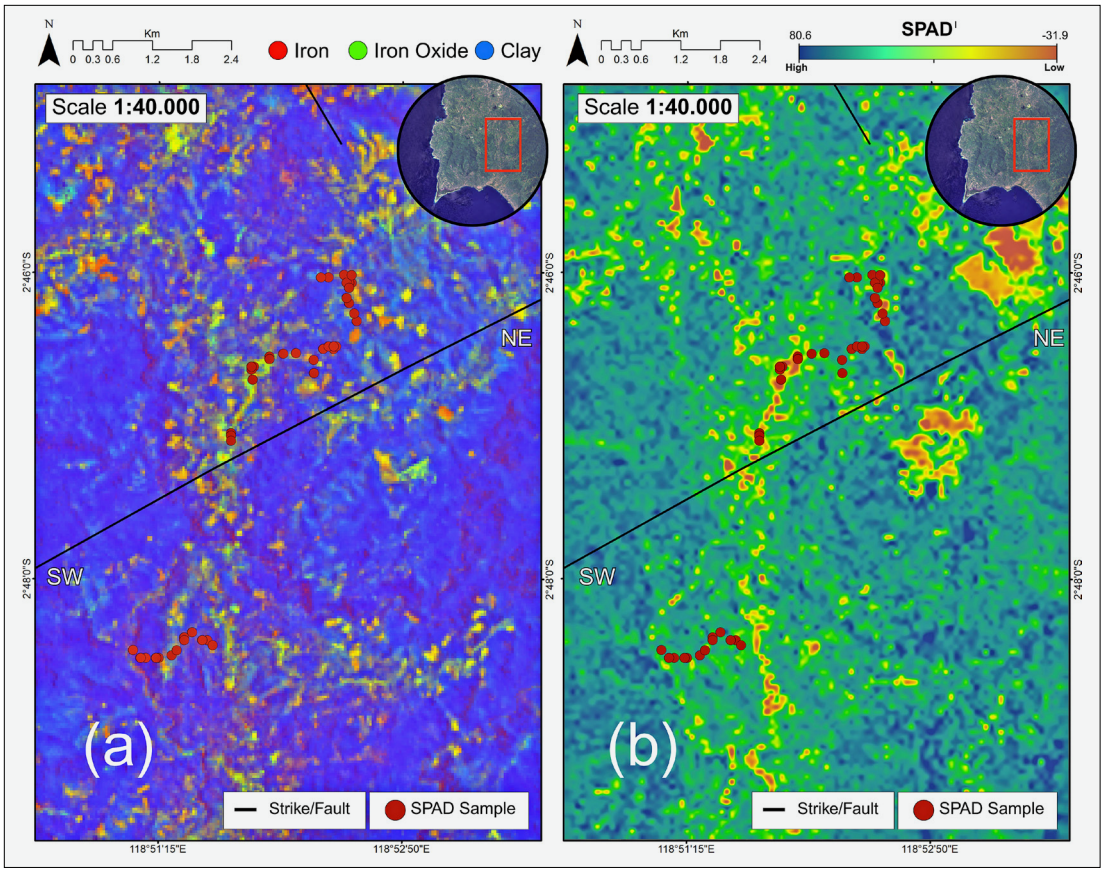


Figure 9. Comparison between vegetation and mineral alteration anomalies. (a) Mineral band ratio composite (R = 4/3, G = 4/2, B = 11/12). (b) spatial distribution of Chlorophyll Index values indicating chlorophyll content, and the black lines indicate mapped faults.

from Sentinel-2 band ratio composites. The false-colour composite (R = 4/3, G = 4/2, B = 11/12) proved effective in delineating three key alteration indicators, namely iron oxides (Band Ratio 4/2), ferric iron minerals (Band Ratio 4/3), and clay minerals (Band Ratio 11/12). These alteration signatures are not randomly distributed but are prominently concentrated in the volcanic rocks of the Adang Formation, which have long been recognized as zones of hydrothermal activity. As shown in **Figure 9**, the composite map reveals that areas characterized by strong alteration signatures correspond closely with zones of reduced Chlorophyll Index values, thereby suggesting a spatial link between mineralogical alteration and vegetation stress.

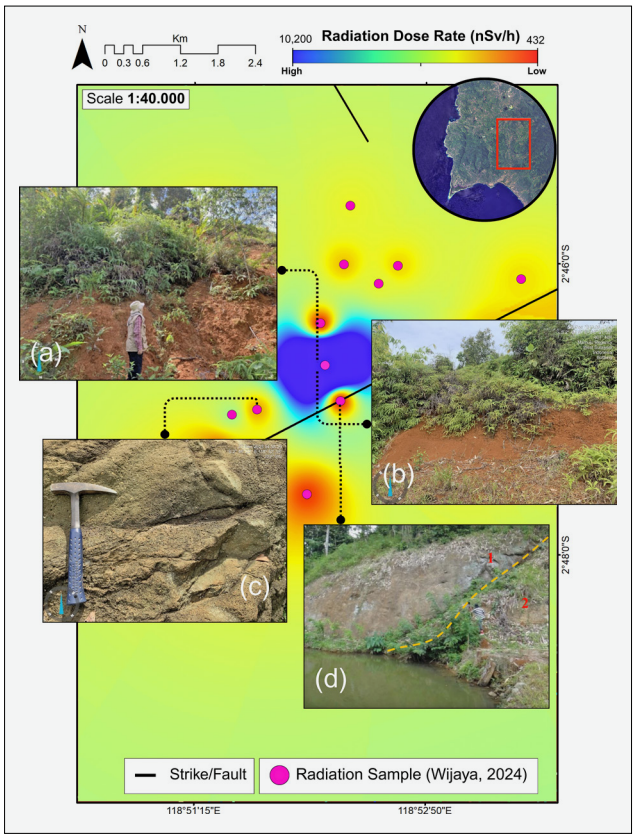


Figure 10. Field verification within the Adang volcanic terrain revealed (a) outcrops showing pervasive hydrothermal alteration of volcanic rocks, (b) vegetation growing on weathered products of altered rocks that exhibited clear stress responses, including low SPAD values and reduced leaf size, (c) basaltic lithology characterized by phenocrysts dominated by leucite minerals, and (d) a distinct lithological contact between phonolitic lava (unit 1) and volcanic breccia (**Rahmaningrum, 2025**).

Ground-based verification provided further confidence in this interpretation (see **Figure 10**). Field surveys conducted within the Adang volcanic terrain revealed rocks that have undergone pervasive hydrothermal alteration. These rocks exhibited clear mineralogical transformations, such as clay replacement and extensive iron oxide staining, which are consistent with processes of alteration linked to fluid–rock interactions in a volcanic setting. Vegetation growing on soils derived from these altered substrates showed distinct stress responses, including markedly low Chlorophyll Index values (commonly below 30), reduced leaf size, and visible discolouration ranging from chlorosis to reddish pigmentation. These symptoms reflect impaired chlorophyll content and overall physiological stress, and they align well with the remote sensing observations of vegetation decline in areas of strong alteration anomalies.

This convergence of remote sensing analysis and field verification underscores the diagnostic strength of integrating Chlorophyll Index measurements with mineral alteration composites. The reduced chlorophyll content observed in vegetation is not merely coincidental but appears to be directly linked to the geochemical environment of radionuclide-bearing alteration zones. The association highlights how vegetation stress indicators can act as a proxy for detecting subsurface mineralogical processes.

In interpreting the REVI patterns, it is important to note that red-edge reflectance is still influenced by several external factors, including thin cloud cover, haze, terrain-induced shadows, and seasonal phenology, all of which may affect the accuracy of chlorophyll estimation. Since this analysis relies on a single-date Sentinel-2 acquisition, part of the observed variability could reflect seasonal changes in pigment concentration or canopy condition rather than purely radiation-driven stress. To address this limitation, NDVI was computed as a complementary vegetation index. Although less sensitive to chlorophyll variation than REVI, NDVI exhibited spatial trends that were consistent with REVI, particularly in high-radiation areas, as shown in **Figure 11**. This agreement strengthens the interpretation that the detected spectral anomalies represent genuine vegetation stress rather than artefacts of illumination or seasonal effects, thereby directly addressing the reviewer's request for clarification of REVI limitations and the inclusion of an alternative index for validation.

4.3. Integrated Overlay of Chlorophyll Index, Radiation, and Geological Framework

The final stage of analysis involved integrating Chlorophyll Index, radiation dose-rate data, and the geological framework to examine spatial controls. The radiation dataset used in this study was derived from **Wijaya (2024)**, who mapped the spatial distribution of natural radiation in the research area. The overlay between Chlorophyll Index distribution and radiation dose-rate maps clearly demonstrates a consistent negative correlation: areas characterized by elevated radiation exposure display markedly low Chlorophyll Index values, whereas zones with lower radiation are associated with higher chlorophyll content. This spatial pattern underscores the direct influence of surface radioactivity on vegetation physiology, particularly its role in reducing chlorophyll concentration. The regions of strong radiation anomalies overlap with vegetation exhibiting stress responses, thereby reinforcing the reliability of Chlorophyll Index as a sensitive biophysical indicator of radiation exposure. These findings are in agreement with the results reported by **Wijaya (2024)**, who observed significant chlorophyll reduction in high-radiation zones. The consistency between this study and previous research strengthens the validity of employing Chlorophyll Index as a physiological proxy for detecting radiation stress in vegetation. Importantly, the correlation highlights the potential of plant-based measurements to serve as an indirect yet effective method for mapping radiation hazards in the field, offering a complementary approach to conventional radiometric surveys.

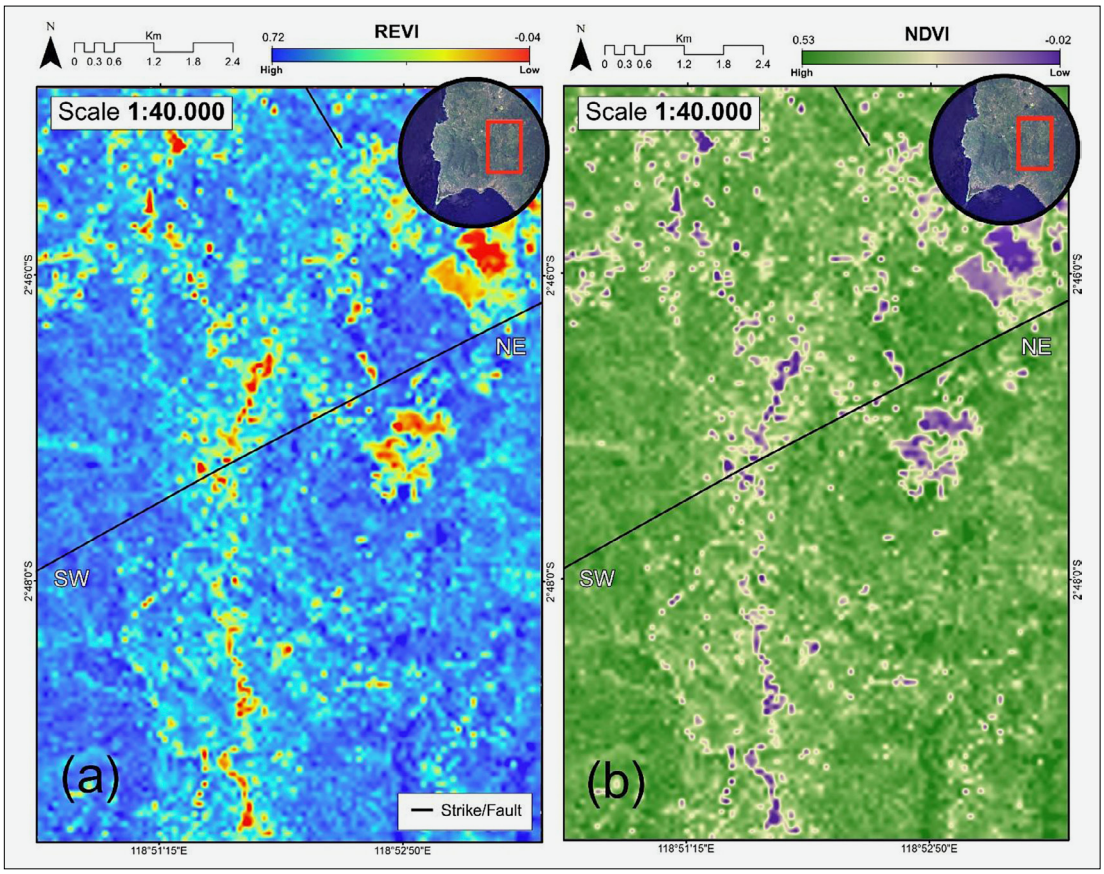


Figure 11. (a) REVI map highlighting vegetation stress zones associated with elevated natural radiation, showing pronounced reductions in red-edge reflectance across the Adang Volcanics. (b) NDVI map derived from the same Sentinel-2 acquisition, which although less sensitive to chlorophyll variation, exhibits spatial patterns consistent with the REVI distribution, particularly in high-radiation areas.

The relationship between Chlorophyll Index and radiation is not only spatially coherent but also strongly linked to the geological setting (see **Figure 12**). Lithological and structural factors exert primary control over the occurrence and intensity of radioactive anomalies. High-radiation zones are predominantly associated with lava flows of Botteng and the Tapalang breccia, both of which belong to the Adang Volcanic Formation. These rocks are dominated by phonolite and leucite-bearing basalt, lithologies with ultrapotassic affinities that are geochemically favorable for the presence of uranium- and thorium-bearing minerals. Consequently, the distribution of Chlorophyll Index values mirrors the underlying lithological variation, with vegetation stress responses most evident on soils derived from radiation-rich volcanic units.

In addition to lithology, structural geology also plays a critical role. Fault zones and remnant topographic highs of the Adang volcanic edifice are interpreted as pathways for hydrothermal fluid mobilization. These fluids likely transported radioactive elements such as uranium and thorium, leading to localized mineral precipitation and the formation of high-radiation zones. Vegetation responses captured through Chlorophyll Index measurements follow this structural control, further supporting the hypothesis that both lithology and tectonic structures dictate the spatial variability of radiation and its ecological impacts.

5. Conclusions

This study demonstrates that the integration of remote sensing and a geobotanical approach provides an effective framework for detecting radioactive mineralization in vegetation-covered regions such as Mamuju, West Sulawesi. By linking Sentinel-2 band ratio composites, red-edge vegetation indices, and in-situ chlorophyll measurements, vegetation stress was shown to reliably reflect the distribution of uranium–thorium–bearing lithologies and hydrothermal alteration zones. The strong spatial correspondence between reduced chlorophyll content, elevated radiation levels, and volcanic units of the Adang Formation underscores the potential of vegetation bioindicators as indirect proxies for subsurface mineralization and environmental radiation hazards.

Despite these promising results, several limitations remain. Environmental factors such as soil moisture, pH, nutrient availability, and micro-topographic shading could not be incorporated due to the lack of spatially matched measurements and may contribute to residual

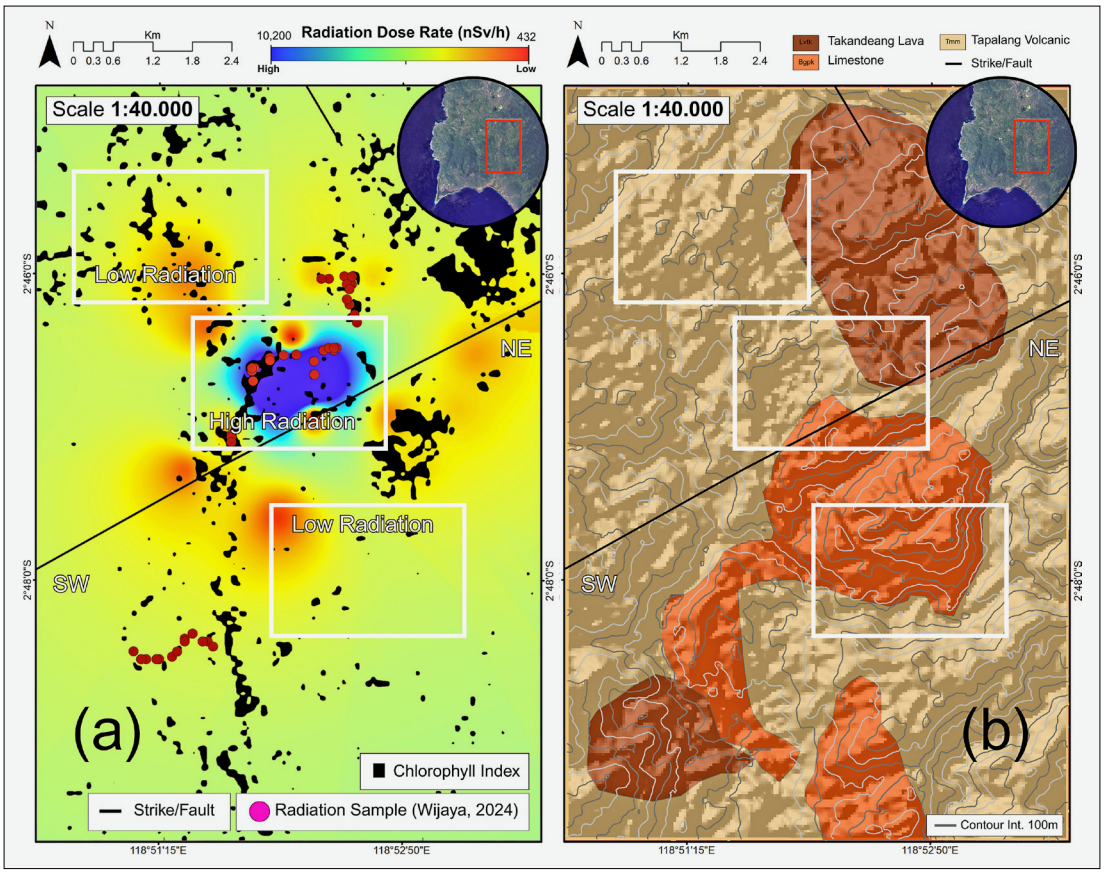


Figure 12. Relationship between vegetation stress and geological controls: (a) overlay of Chlorophyll Index distribution with natural radiation dose rates adapted from **Wijaya (2024)**, showing inverse correlation between radiation intensity and chlorophyll content, and (b) contour and lithological map of the study area illustrating that high-radiation anomalies are primarily concentrated within volcanic units of the Adang Formation

variability in the chlorophyll indicators. In addition, variability in species-specific responses to radiation, seasonal influences on vegetation physiology, and the moderate spatial resolution of Sentinel-2 imagery may constrain the broader applicability of the method. Future research should combine higher-resolution satellite data, expanded species monitoring, and geochemical sampling to improve accuracy and strengthen the interpretative framework. These findings mark an important step toward developing cost-effective exploration and monitoring strategies that address both natural resource potential and environmental health concerns in high-radiation landscapes.

Acknowledgement

This research is funded by the Indonesian Endowment Fund for Education (LPDP) on behalf of the Indonesian Ministry of Higher Education, Science and Technology and managed under the EQUITY Program (Contract No. 4298/B3/DT.03.08/2025), as well as the PPMI FITB Program from the Faculty of Earth Sciences and Technology ITB Research Scheme Number (Contract No. 2235/ IT1.B07.1/TA.00/2026.

6. References

Abdulraheem, M. I., Zhang, W., Li, S., Moshayedi, A. J., Farooque, A. A., & Hu, J. (2023). Advancement of Remote Sensing for Soil Measurements and Applications: A Comprehensive Review. *Sustainability (Switzerland)*, *15*(21). https://doi.org/10.3390/su152115444

Aditya, I. A., Wijayanto, T., & Hakam, D. F. (2025). Advancing Renewable Energy in Indonesia: A Comprehensive Analysis of Challenges, Opportunities, and Strategic Solutions. *Sustainability (Switzerland)*, *17*(5), 2021–2030. https://doi.org/10.3390/su17052216

Bayle, A., Carlson, B. Z., Thierion, V., Isenmann, M., & Choler, P. (2019). Improved mapping of mountain shrublands using the sentinel-2 red-edge band. *Remote Sensing*, *11*(23). https://doi.org/10.3390/rs11232807

Bréchignac, F., Oughton, D., Mays, C., Barnthouse, L., Beasley, J. C., Bonisoli-Alquati, A., Bradshaw, C., Brown, J., Dray, S., Geras'kin, S., Glenn, T., Higley, K., Ishida, K., Kapustka, L., Kautsky, U., Kuhne, W., Lynch, M., Mappes, T., Mihok, S., … Tsukada, H. (2016). Addressing ecological effects of radiation on populations and ecosystems to improve protection of the environment against radiation: Agreed statements from a Consensus Symposium.

Journal of Environmental Radioactivity, *158–159*, 21–29. https://doi.org/10.1016/j.jenvrad.2016.03.021

Carvalho, M., Cardoso-Fernandes, J., González, F. J., & Teodoro, A. C. (2025). Comparative Performance of Sentinel-2 and Landsat-9 Data for Raw Materials' Exploration Onshore and in Coastal Areas. *Remote Sensing*, *17*(2). https://doi.org/10.3390/rs17020305

Chen, Y., Wang, Y., Zhang, F., Dong, Y., Song, Z., & Liu, G. (2023). Remote Sensing for Lithology Mapping in Vegetation-Covered Regions: Methods, Challenges, and Opportunities. *Minerals*, *13*(9), 1–26. https://doi.org/10.3390/min13091153

Dong, T., Liu, J., Shang, J., Qian, B., Ma, B., Kovacs, J. M., Walters, D., Jiao, X., Geng, X., & Shi, Y. (2019). Assessment of red-edge vegetation indices for crop leaf area index estimation. *Remote Sensing of Environment*, *222* (December 2018), 133–143. https://doi.org/10.1016/j.rse.2018.12.032

Hu, B., Xu, Y., Wan, B., Wu, X., & Yi, G. (2018). Hydrothermally altered mineral mapping using synthetic application of Sentinel-2A MSI, ASTER and Hyperion data in the Duolong area, Tibetan Plateau, China. *Ore Geology Reviews*, *101*, 384–397. https://doi.org/10.1016/j.oregeorev.2018.07.017

Koesuma, S., Putera, M. A. H., & Darsono. (2019). A Microtremor Analysis for Microzonation of Seismic Vulnerability Index by Using Horizontal to Vertical Spectral Ratio in The Southern Area of Klaten Regency. *Journal of Physics: Conference Series*, *1153*(1), 1–6. https://doi.org/10.1088/1742-6596/1153/1/012023

Laode, A. M. W., Massinai, M. A., Massinai, M. F. I., & Syamsuddin, E. (2025). Evaluating Liquefaction Susceptibility Through HVSR and MASW Methods: A Case Study in Mamuju, West Sulawesi, Indonesia. *Rudarsko-Geološko-Naftni Zbornik*, *40*(5), 1–18. https://doi.org/10.17794/rgn.2025.5.1

Liu, Y., Qian, J., & Yue, H. (2021). Comprehensive Evaluation of Sentinel-2 Red Edge and Shortwave-Infrared Bands to Estimate Soil Moisture. *IEEE Journal of Selected Topics in Applied Earth Observations and Remote Sensing*, *14*, 7448–7465. https://doi.org/10.1109/JSTARS.2021.3098513

Meilano, I., Salman, R., Susilo, S., Shiddiqi, H. A., Supendi, P., Lythgoe, K., Tay, C., Bradley, K., Rahmadani, S., Kristyawan, S., & Yun, S. H. (2023). The 2021 MW6.2 Mamuju, West Sulawesi, Indonesia earthquake: partial rupture of the Makassar Strait thrust. *Geophysical Journal International*, *233*(3), 1694–1707. https://doi.org/10.1093/gji/ggac512

Meraner, A., Ebel, P., Zhu, X. X., & Schmitt, M. (2020). Cloud removal in Sentinel-2 imagery using a deep residual neural network and SAR-optical data fusion. *ISPRS Journal of Photogrammetry and Remote Sensing*, *166*(July), 333–346. https://doi.org/10.1016/j.isprsjprs.2020.05.013

Nugraha, E. D., Hosoda, M., Kusdiana, Untara, Mellawati, J., Nurokhim, Tamakuma, Y., Ikram, A., Syaifudin, M., Yamada, R., Akata, N., Sasaki, M., Furukawa, M., Yoshinaga, S., Yamaguchi, M., Miura, T., Kashiwakura, I., & Tokonami, S. (2021). Comprehensive exposure assessments from the viewpoint of health in a unique high natural background radiation area, Mamuju, Indonesia. *Scientific Reports*, *11*(1), 1–16. https://doi.org/10.1038/s41598-021-93983-2

Nugraha, E. D., Hosoda, M., Tamakuma, Y., Kranrod, C., Mellawati, J., Akata, N., & Tokonami, S. (2021). A unique high natural background radiation area in Indonesia: a brief review from the viewpoint of dose assessments. *Journal of Radioanalytical and Nuclear Chemistry*, *330*(3), 1437–1444. https://doi.org/10.1007/s10967-021-07908-4

Perdana, M. J., & Amijaya, H. (2011). Source indication of oil seep from Paniki river, Kalukku, Mamuju, West Sulawesi based on geochemical characterization. *Proceedings JCM Makassar 2011*.

Rahmaningrum, A. N. N. (2025). *Karakterisasi mineral Pembawa uranium pada Batuan vulkano-sedimenter kompleks Batuan gunung API adang di daerah botteng dan salumati, Sulawesi Barat*. ITB University.

Rosianna, I., Nugraha, E. D., Syaeful, H., Putra, S., Hosoda, M., Akata, N., & Tokonami, S. (2020). Natural radioactivity of laterite and volcanic rock sample for radioactive mineral exploration in mamuju, indonesia. *Geosciences (Switzerland)*, *10*(9), 1–13. https://doi.org/10.3390/geosciences10090376

Rumora, L., Miler, M., & Medak, D. (2021). Contemporary comparative assessment of atmospheric correction influence on radiometric indices between Sentinel-2A and Landsat 8 imagery. *Geocarto International*, *36*(1), 13–27. https://doi.org/10.1080/10106049.2019.1590465

Saepuloh, A., Ratnanta, I. R., Hede, A. N. H., Susanto, V., & Sucipta, I. G. B. E. (2023). Radioactive remote signatures derived from Sentinel-2 images and field verification in West Sulawesi, Indonesia. *Environmental Monitoring and Assessment*, *195*(10). https://doi.org/10.1007/s10661-023-11868-5

Saputra, A., Abdullah, I., Dahnum, D., Mustika, D., Oktavianto, P., Noor, A. Z., Pamungkas, N. S., & Yusuf, M. (2025). Strategic utilization of covalent organic frameworks for uranium adsorption from high concentrate U–Th monazite sand: a review. *Journal of Radioanalytical and Nuclear Chemistry*, *334*, 3843–3864. https://doi.org/https://doi.org/10.1007/s10967-025-10135-w

Shaban, G., Fadlin, & Priadi, B. (2016). Geochemical signatures of potassic to sodic Adang Volcanics, Western Sulawesi: Implications for their tectonic setting and origin. *Indonesian Journal on Geoscience*, *3*(3), 195–216. https://doi.org/10.17014/ijog.3.3.195-214

Shebl, A., Badawi, M., Dawoud, M., Abd El-Wahed, M., El-Dokouny, H. A., & Csámer, Á. (2024). Novel comprehensions of lithological and structural features gleaned via Sentinel 2 texture analysis. *Ore Geology Reviews*, *168* (March 2023). https://doi.org/10.1016/j.oregeorev.2024.106068

Sompotan, A. F. (2012). *Struktur Geologi Sulawesi*. Bandung Institute of Technology.

Subasinghe, C. S., Ratnayake, A. S., Roser, B., Sudesh, M., Wijewardhana, D. U., Attanayake, N., & Pitawala, J. (2022). Global distribution, genesis, exploitation, applications, production, and demand of industrial heavy miner-

als. *Arabian Journal of Geosciences*, *15*(20). https://doi.org/10.1007/s12517-022-10874-0

Sun, Y., Qin, Q., Ren, H., Zhang, T., & Chen, S. (2020). Red-Edge Band Vegetation Indices for Leaf Area Index Estimation from Sentinel-2/MSI Imagery. *IEEE Transactions on Geoscience and Remote Sensing*, *58*(2), 826–840. https://doi.org/10.1109/TGRS.2019.2940826

Supendi, P., Ramdhan, M., Priyobudi, Sianipar, D., Wibowo, A., Gunawan, M. T., Rohadi, S., Riama, N. F., Daryono, Prayitno, B. S., Murjaya, J., Karnawati, D., Meilano, I., Rawlinson, N., Widiyantoro, S., Nugraha, A. D., Marliyani, G. I., Palgunadi, K. H., & Elsera, E. M. (2021). Foreshock–mainshock–aftershock sequence analysis of the 14 January 2021 (Mw 6.2) Mamuju–Majene (West Sulawesi, Indonesia) earthquake. *Earth, Planets and Space*, *73*(1), 1–10. https://doi.org/10.1186/s40623-021-01436-x

Vrdoljak, L., & Kilić Pamuković, J. (2022). Assessment of Atmospheric Correction Processors and Spectral Bands for Satellite-Derived Bathymetry Using Sentinel-2 Data in the Middle Adriatic. *Hydrology*, *9*(12). https://doi.org/10.3390/hydrology9120215

White, L. T., Hall, R., Armstrong, R. A., Barber, A. J., Boudagher, M., Baxter, A., Wakita, K., Manning, C., & Soesilo, J. (2017). Journal of Asian Earth Sciences The geological history of the Latimojong region of western Sulawesi, Indonesia. *Journal of Asian Earth Sciences*, *138*, 72–91. https://doi.org/10.1016/j.jseaes.2017.02.005

Wijaya, S. (2024). *Identifikasi radionuklida primordial pada tanah dan implikasinya terhadap lingkungan studi kasus : Desa Botteng, Kecamatan Simboro, Kabupaten Mamuju, Sulawesi Barat*. ITB University.

Yu, D., & Fang, C. (2023). Urban Remote Sensing with Spatial Big Data: A Review and Renewed Perspective of Urban Studies in Recent Decades. *Remote Sensing*, *15*(5), 1–34. https://doi.org/10.3390/rs15051307

SAŽETAK

Daljinsko istraživanje radioaktivnih alteracijskih zona korištenjem Sentinel-2 i SPAD mjerenja klorofila u Mamujuu, Indonezija

Ova studija istražuje prirodnu radioaktivnu mineralizaciju (uranij-torij) u Mamujuu, Zapadni Sulawesi, posebno unutar vulkana Adang kontroliranoga rasjedom, područja poznatoga po odstupanjima prirodnoga zračenja. Cilj je bio procijeniti stres vegetacije kao zamjenu za radioaktivnu mineralizaciju integrirajući satelitske podatke i terensku validaciju. Obrađeni su podatci Sentinel-2A koristeći se omjerima pojasa (4/2 željezov oksid, 4/3 ferično željezo, 11/12 glina) i kompozitima lažnih boja kako bi se odredile zone promjena. Indeks vegetacije crvenoga ruba (REVI; B3, B4, B6) izračunan je za otkrivanje stresa vegetacije. Terenskim radom u prosincu 2023. prikupljeno je 68 SPAD mjerenja klorofila iz paprati, interpoliranih s inverznim ponderiranjem udaljenosti i uspoređenih s neovisnim brzinama doze zračenja. Rezultati pokazuju snažnu korelaciju između REVI-ja i SPAD-a (R^2 = 0,76), što potvrđuje osjetljivost pojasa crvenoga ruba na varijabilnost klorofila. Vrijednosti SPAD-a znatno su se smanjile u zonama visokoga zračenja pokazujući snažnu negativnu korelaciju s brzinom doze (R^2 = 0,90). Vrijednosti od 4 do 40 bile su tipične u područjima s odstupanjima zračenja, dok su vrijednosti >40 karakterizirale nižu izloženost. Anomalije vegetacijskoga stresa i indeks klorofila dobiven satelitskim putem prostorno su se preklapali sa zonama alteracija i bili su koncentrirani u vulkanima Adang duž strukturnih kontrola. Razlike u vrstama paprati upućuju na različitu osjetljivost na zračenje. Ovaj integrirani pristup pokazuje učinkovitost kompozita alteracija Sentinel-2, REVI-ja i SPAD validacije kao brzoga i jeftinoga okvira za rano istraživanje radioaktivnih minerala, a istovremeno doprinosi procjeni opasnosti od zračenja okoliša.

Ključne riječi:
Sentinel-2, indeks vegetacije crvenoga ruba (REVI), SPAD klorofil, radioaktivna mineralizacija, Mamuju

Author's contribution

Nuraisyiah Pertiwi Kamsir (M.T.): conceptualization, data curation, investigation, formal analysis, visualization, and writing – original draft. **Asep Saepuloh** (Dr. Eng.): supervision, methodology, validation, resources, and writing – review & editing. **Very Susanto** (Dr. Eng.): software, data curation, formal analysis, visualization, and writing – review & editing. **Eka Djatnika Nugraha** (Dr.): investigation, validation, resources, and writing – review & editing.
All authors have read and agreed to the published version of the manuscript.

RGNZ/MGPB

RAM measure of hydraulic powered roof supports in underground longwall coal mines

Rudarsko-geološko-naftni zbornik
(The Mining-Geology-Petroleum Engineering Bulletin)
DOI: 10.17794/rgn.2026.3.15

Original scientific paper

Mohammad Javad Rahimdel[1]* ✉
[1] *Department of Mining Engineering, Faculty of Engineering, University of Birjand, Birjand, Iran.*

Abstract
Mining operations in underground coal mines, particularly those using the longwall method, require continuous progress and the avoidance of interruptions, as any stoppage can lead to roof collapse. Given the mechanization of coal mining and the underground extraction of this mineral, the use of powered supports is essential to prevent roof collapse. To maintain continuity in mining operations, increase production, and simultaneously control and reduce costs caused by downtime and failures of roof support systems, it is necessary to assess their reliability. This paper aims to analyze the reliability, maintainability, and availability (RAM) of powered support equipment. To achieve this, the hydraulic powered support system was selected for data collection and analysis. The results indicate that the time between failures (TBF) and time to repair (TTR) data of the subsystems followed a renewal process, except for the TBF data of the hydraulic subsystem, which followed a non-homogeneous Poisson process (NHPP). The reliability of the subsystems decreased to 85% after 25 hours. The maintainability analysis showed that most failures of the powered roof supports are repaired within 1 hour. Furthermore, the powered support systems operate under desirable conditions with 99.58% availability. However, in order to create an efficient and easy-to-manage maintenance schedule, it was suggested that preventive maintenance activities be performed at the end of each working day.

Keywords:
coal mining, roof support systems, reliability, maintainability, availability

1. Introduction

Coal is a vital energy source and the first fossil fuel to be widely used. In many countries, conventional resources such as coal continue to play a significant role in energy production. Consequently, coal mines remain highly important, and countries possessing these resources generate substantial profits from their sale. Currently, most of the world's coal is extracted using the longwall mining method. This method employs various machines and equipment, including shearers, armored face conveyors (AFCs), conveyor belts, and power supports (**Bołoz et al., 2022**). Intense competition in the energy raw materials market drives mining companies to reduce production costs. In this context, it is anticipated that increasing production efficiency will help mitigate negative environmental impacts. One approach to achieving this goal is to continuously enhance the efficiency of equipment and machinery (**Uth et al., 2019; Szurgacz et al., 2022a**).

The longwall method is an underground mining technique known for its high production capacity and excellent recovery rates in coal mining. This method has consistently been regarded as the most cost-effective approach for coal extraction (**Kazanin et al., 2022**).

The most important machines used in this method include the drum shearer, AFCs, powered roof supports, and conveyor belt. **Figure 1** shows a view of a longwall mine. In this method, mining operations are conducted beneath the powered supports. The shearer is mounted on the AFC and cuts the coal, dumping it onto the conveyor belt to be transported out of the mine. After the shearer has travelled the entire length of the face, it reverses direction and begins the next cut. As the shearer moves past the powered supports, the supports advance forward, closer to the newly cut surface. The powered supports protect workers and equipment along the working face, while the roof behind the supports is allowed to collapse as the face advances. Mining continues in this manner until the entire coal seam is extracted (**Peng, 2019**).

The primary function of power holders is to protect the mining operation from the adverse effects of the rock mass and its movement, while simultaneously advancing the shearer and AFC. Considering that a large number of units are required to support the roof, the capital invested in powered supports typically accounts for 60–80% or more of the initial investment in a longwall face, depending on the panel width (**Peng, 2019**). Further-

* Corresponding author: Mohammad Javad Rahimdel
e-mail address: rahimdel@birjand.ac.ir
Received: 29 October 2025. Accepted: 28 December 2025.
Available online: 14 May 2026

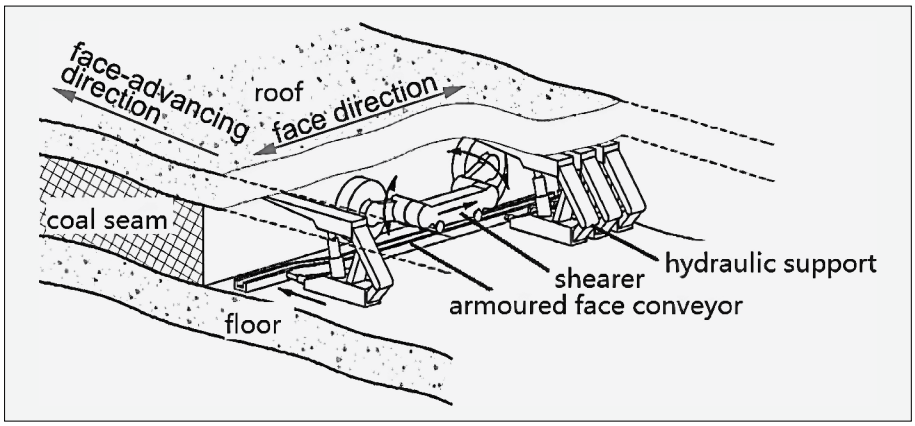


Figure 1. Scheme of the mechanized longwall mining operation (**Guan et al., 2023**)

more, since powered supports in longwall mechanized mines are responsible for ensuring the safety of both equipment and workers, they are among the most critical components of mechanized mining operations and require proper monitoring and control of their operating parameters (**Szurgacz et al., 2022b**).

Any failure or stoppage in powered support systems not only compromises the safety of the mining environment but also leads to the suspension of mining operations and, ultimately, the cessation of mine production. As mentioned earlier, from both economic and technical perspectives, powered supports are crucial pieces of equipment in longwall mining. Therefore, it is essential to study the failure behaviour and analyze the reliability and maintainability of this type of equipment. Focusing on the evaluation of RAM (Reliability, Availability, and Maintainability) in mining operations will enhance production, safety, and maintenance.

Mining equipment and systems comprise multiple interconnected components, and their effective operation is crucial for ensuring uninterrupted production within the mine. Due to the complexity of this equipment, it is essential to conduct research on its RAM. The RAM of mining systems and equipment has been a major emphasis in recent years. To date, considerable research has been conducted on the reliability of a variety of systems in the field of mining engineering. **Table 1** provides a summary of the research articles related to reliability analysis of mining machinery and equipment utilized in underground mining opertion.

Nowadays, reliability and maintainability of mining equipment and systems in underground coal mines such as shearer (**Zhou et al., 2017; Ding et al., 2019; Wang et al., 2025**), roadheader (**Kahraman et al., 2023; Xiaofeng, 2025**), discharge loaders (**Sarkhel and 2015**), and conveyors (**Kumar 2016; Gorai et al., 2017; Masir et al., 2021**) have been analyzed and discussed. Furthermore, numerous attempts have been made to analyze and optimize the load capacity of powered roof supports in longwall mining (**Szurgacz et al., 2022; Szurgacz, 2024; Wang et al., 2023; Borska and Szurgacz, 2024**). However, limited research has been conducted to study the reliability and maintainability of this critical system. **Morshedlou et al. (2014)** studied the reliability of powered supports at the Tabas coal mine using a statistical analysis approach. The results of this study indicate that the powered supports follow a Gamma reliability function. The reliability of the equipment decreases to nearly zero after approximately 520 hours of operation. Furthermore, the failure rate analysis reveals an improving trend, characterized by a decreasing failure rate. **Stebnev et al., (2017)** studied the downtimes of mining machines and equipment in the powered longwall mining systems at SUEK-Kuzbass Company, Russia. This paper analyzes and discusses the output per face, productivity, lifetime, and failure-free operation of mining machines, including shearers, powered roof supports, face conveyors, and electrical equipment. In the study, powered support systems produced by different companies were compared in terms of price, service life, and the unit cost of coal production. Failure analysis of equipment and systems over a seven-year period showed that the overall downtime due to mining machine failures was approximately 12%, with failures of powered support systems accounting for 13% of the total downtime. **Szurgacz (2021)** analyzed the effectiveness of powered roof supports. In this study, the overall equipment effectiveness (OEE) indicator was used to assess the degree of utilization. To achieve this, the availability, performance, and quality of powered roof supports were measured under conditions of tremor hazards and no tremor hazards. The results showed that the OEE of powered roof supports in mining tremor hazard conditions ranged from 55% to 65%, while in conditions without mining tremor hazards, it was estimated to be between 75% and 85%. The study noted that these OEE values indicate low effectiveness in utilizing roof support systems, highlighting the importance of reviewing operation and maintenance policies to improve this indicator.

A review of the aforementioned paper reveals that the reliability of powered support systems has been studied in only a limited number of research efforts. In **Morshedlou et al. (2014)**, powered support systems are considered as a single system. However, breaking down an engineering system into its functional subsystems not only helps identify the subsystems that contribute most

Table 1. A summary of studies on the reliability of underground mining equipment and machinery

Author(s)	Year	Equipment/ system	Modelling method
Prasad and Rao	2008	Dozer Engines	Renewal process and Non-homogeneous Poisson process
Vayenas and Wu	2009	LHD	Non-homogeneous Poisson process
Hoseinie et al.	2013	Shearer machine	Renewal process
Mouli et al.	2014	Dump truck	Renewal process
Thunberg	2016	Underground drilling rigs	Renewal process and Non-Homogeneous Poisson Process
Gorai et al.	2017	Conveyor system	Renewal process
Balaraju et al.	2018	LHD	Non-Homogeneous Poisson Process
Vashistha et al.	2019	LHD	Renewal process
La Roche-Carrier et al.	2020	Rock bolters	Renewal process
Balaraju et al.	2020	LHD	Renewal process
Said	2021	Underground trucks	Non-Homogeneous Poisson Process
Masir et al.	2021	AFC	Non-Homogeneous Poisson Process
Jakkula et al.	2022	LHD	Renewal process
Jakkula et al.	2024	LHD	Renewal process

to system failure but also provides better insights into the failure behaviour of each subsystem. Moreover, this approach supports effective preventive maintenance activities without redundant planning. In **Szurgacz's (2021)** study, the availability, performance, and quality of roof powered supports were addressed by considering only the mean time between failures, mean time to repair, total run time, and ideal cycle time. However, the failure and repair behaviour of the system were neither studied nor discussed. This paper aims to utilize reliability, maintainability, and availability indicators to predict the comprehensive performance of powered support systems, thereby ensuring the safety and continuity of the mining process. These indicators help improve the productivity of mining operations over their life cycle by reducing waste, maximizing profit, and ultimately optimizing overall life cycle costs. The results of this study provide valuable guidance and information to support decision-making related to the design and operation of powered support systems throughout their lifespan.

The paper is organized as follows. Section 2 describes the research methodology, presenting the statistical reliability and maintainability modelling approach. Section 3 details the hydraulic powered supports used in longwall mining operations. In Section 4, the reliability, maintainability, and availability of the powered support system at Parvadeh Tabas Coal Mine, Iran, are analyzed and discussed.

2. Methods

Powered supports emerged following the development and advancement of steel support systems, such as friction and hydraulic supports, used in longwall mining operations. The powered roof support system consists of several hydraulic supports. A solid canopy is positioned on top of these supports, while their bases are connected to AFC components. As the mining face advances, the supports retract and move forward, controlled remotely. **Figure 2** shows a view of a powered support.

The powered support system can be divided into two main subsystems: mechanical and hydraulic. The mechanical subsystem includes the following main components:

- The *canopy* transfers the pressure from the rock mass to the support.
- The *shield support* consists of a gob shield and side shields.
- *Lemniscate tie rods* connect the gob shield to the base in a straight-line system, providing stable support and maintaining an almost constant distance between the canopy end and the face front throughout the entire range of roof support heights.
- *Legs* consists of a double-acting hydraulic ram and a telescopic relay bar.
- *Floor base* to transmit the bearing force of the support to the floor.
- *Shifting system* consists of a ram installed in the body that acts directly on the advancing system's bar, causing the front of the base to lift during support advancement. This system aids in advancing the support.

The hydraulic system operates various rams, including a two-stage telescopic hydraulic leg, tilt ram, correcting ram, support advancing ram, base lifting ram, base correction ram, supporting ram, ram for maintaining the last support on an incline, face sprag ram, and additional devices for operating the support system on inclines.

In modern longwall mining, self-advancing, hydraulically powered supports are used to extract coal at the face. These powered supports hold up the roof, ensuring a safe working environment for miners, face equipment, and

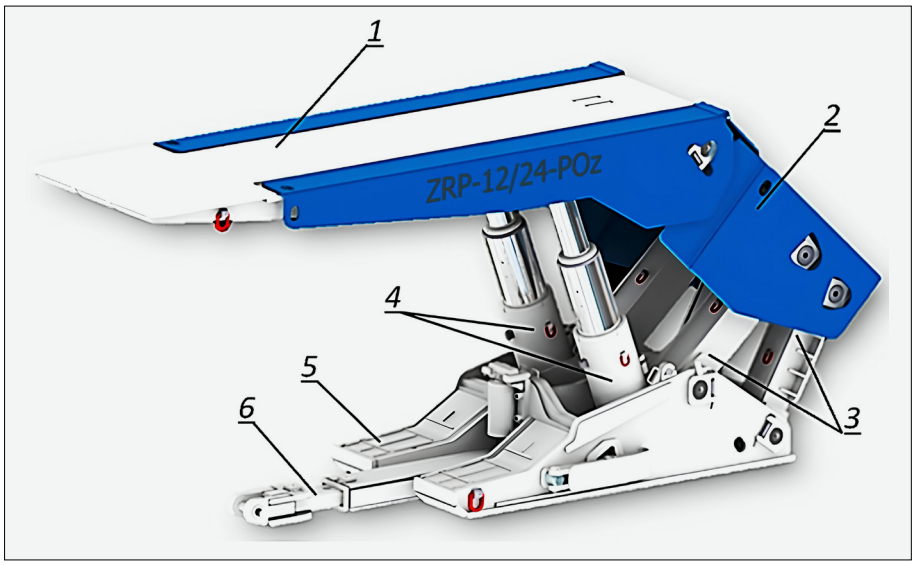


Figure 2. Arrangement of a powered roof support (1: canopy, 2: shield support, 3: lemniscate tie rods, 4: leg, 5: floor base, and 6: shifting system) (**Szurgacz et al., 2022b**).

other mining operations. Additionally, the hydraulically powered supports push the AFC and advance themselves.

There are four basic designs of powered supports: frame, chock, shield and chock shield. The frame support can be considered an extension of the single hydraulic props that are often used underground and it is the first type of powered support designed for modern self advancing hydraulic powered supports. The basic arrangement has two hydraulic props or legs in an vertically arranged series connected at the top with a one or two part canopy, which is frequently referred to as just a canopy (**Peng, 2019**). As opposed to the frame support, chock supports have a solid canopy while the base is composed of two separate pieces that are joined by steel bars, joined at the front or back. This difference is substantial.

Shields are defined as the posterior extension of the caving shield-lemniscate-link system between the base and the canopy. The caving shield is typically pitched and hinged-jointed to the canopy; and the connection with the base is through either the lemniscate assembly or direct. This essentially renders the shield a cinematically stable support, an advantage to frame and chocks. In shields the hydraulic legs are pitched to allow greater range of working height and for more room for traffic. Chock shields have the main advantages of both the chock and shield. Essentially the chock shield is a shield with four legs between the canopy and the base plates. The legs can be oriented vertically or in a V-configurations between the canopy and base, and this is the rationale for the name "chock shield." Chock shields provide the most efficient support and particularly advantageous in hard roof conditions (**Peng, 2019**).

The performance evaluation of powered support systems in underground coal mines is conducted using various criteria. To date, multiple tools have been employed to analyze operational and maintenance performance in equipment and machinery production management. The effectiveness of powered support systems is assessed based on their reliability and ease of maintenance.

Reliability, which can be adequately assessed using failure analysis, is used as a proxy for performance (**Cai et al., 2021**). Reliability (R) is defined as the probability that equipment or processes will perform reliably as designed (and identified) without "failure" when used exactly as intended over a specified time period under stated conditions. The formal mathematical definition of reliability is given by **Equation 1**:

$$R(t) = 1 - F(t) = 1 - \int_0^t f(x)dx \quad (1)$$

Where:

$R(t)$ is the reliability at time t,

$F(t)$ is the cumulative failure distribution function,

$f(x)$ is the failure probability density function.

Complex systems contain numerous mechanical, hydraulic, or electrical subsystems. Each subsystem can fail, which increases the probability of overall system failure. The resulting reliability depends on the reliability of the individual subsystems and their configuration. Series and parallel are two fundamental system arrangements. A series system generally consists of a group of independent subsystems in which the failure of any one component causes the entire system to fail. In contrast, a parallel system fails only if all its subsystems fail. The reliability of series and parallel systems is calculated as **Equations 2** and **3**:

$$R_s = \prod R_i \quad (2)$$

$$R_P = 1 - \prod (1 - R_i) \quad (3)$$

Where:

R_s and R_P are the reliability of the whole system in series and parallel configurations, respectively,

R_i denotes the reliability of the ith independent subsystem.

Maintainability refers to the capability of an item to be kept in, or restored to, a designated state when maintenance is conducted. The **Equation 4** defines the maintainability function.

$$M(t) = 1 - F_r(t) = 1 - \int_0^t f_r(x)dx \quad (4)$$

Where:

M (t) is the maintainability at time t,

$F_r(t)$ is the cumulative repair distribution function,

$f_r(x)$ is the probability density function of the repair time.

If a system contains independent subsystems, the maintainability of a series (M_s) and parallel (M_p) system can be determined as **Equations 5** and **6**:

$$M_s = \prod M_i \quad (5)$$

$$M_P = 1 - \prod (1 - M_i) \quad (6)$$

Where:

M_i is the maintainability of ith subsystem.

Availability is defined as the probability that the equipment or a system can perform its intended function at time t, whereby the time period includes the running time, logistical time, active repair time, and administrative time. Calculating availability (Av) requires obtaining the uptime and downtime, as shown in **Equation 7** (**dos Santos Silva et al., 2016**).

$$Av = \frac{MTBF}{MTBF + MTTR} \quad (7)$$

The *MTBF* represents the average failure time and the *MTTR* denotes average repair time for the machine. The inverse of availability corresponds to unavailability, or the expected downtime ratio, which is crucial for assessing operational risk.

Considering the structure and network of the system's availability, the overall availability of a system with i serial or parallel subsystems (Av_i) can be calculated as follows:

$$Av_s = \prod Av_i \quad (8)$$

$$Av_P = 1 - \prod (1 - Av_i) \quad (9)$$

Where:

Av_s and Av_P represent the availability of the whole system in serial and parallel configurations, respectively.

Since failures cannot be entirely prevented, periodic inspection and measurement can help mitigate the severity of any failure. To ensure a system functions properly, regular maintenance activities are essential. Maintenance tasks can be divided into two main categories: planned and unplanned. Preventive maintenance (PM) consists of preplanned actions aimed at reducing the impact of known causes that could potentially lead to system breakdowns (**Duffuaa and Raouf, 2015, Rahimdel and Ghodrati 2022**). PM activities aim to increase the productivity of equipment and facilities while reducing maintenance and insurance expenses (**e Costa et al., 2012**). In fact, such maintenance operations are performed to ensure the system continues to operate satisfactorily by conducting systematic inspections that identify and address potential failures before they grow into critical issues (**Wang and Pham, 2006**). PM is planned and performed after a specified period or following a certain amount of system usage to reduce the likelihood of failure (**Basri et al., 2017**).

The remainder of this section is devoted to presenting the methodology for estimating reliability and maintainability indicators. Data collection, including failure and repair times, is the first step. After establishing the database, an appropriate method is selected for the statistical modelling of the system's performance indicators.

The step-by-step procedure for reliability modelling of a repairable system is illustrated in **Figure 3**. This detailed flowchart facilitates dataset modelling and serves as a foundation for analyzing failure and repair data.

These processes are commonly known as stochastic point processes (**Andrzejczak, 2015**). For the reliability assessment of repairable systems, three different methods are typically employed:

- Renewal Process (RP)
- Homogeneous Poisson Process (HPP)
- Nonhomogeneous Poisson Process (NHPP)

In repairable systems, the condition of a system after maintenance actions can vary depending on the effectiveness of the repair. In some cases, the system may be restored to a state equivalent to its initial condition, while in others it may retain characteristics of prior deterioration or fall somewhere between these two extremes. When repairs fully restore the system to its original performance level, the failure–repair sequence can be described using a renewal framework. Within this framework, system failures followed by repairs are treated as recurrent events with statistically independent and identically distributed intervals. Analytical expressions for the renewal function are available only for a limited class of probability distributions, including exponential, gamma, and phase-type models (**Arnold et al., 2020**; **Muralidharan, 2008**).

The Homogeneous Poisson Process (HPP) is a special type of renewal process in which the inter-event times are independent and identically distributed (iid) exponential random variables. The HPP is an orderly stochastic point process characterized by stationary and independent increments. In an HPP, the inter-arrival times are independent and exponentially distributed with parameter λ, and the number of events follows a Poisson distribution. In reliability studies, the HPP has been used

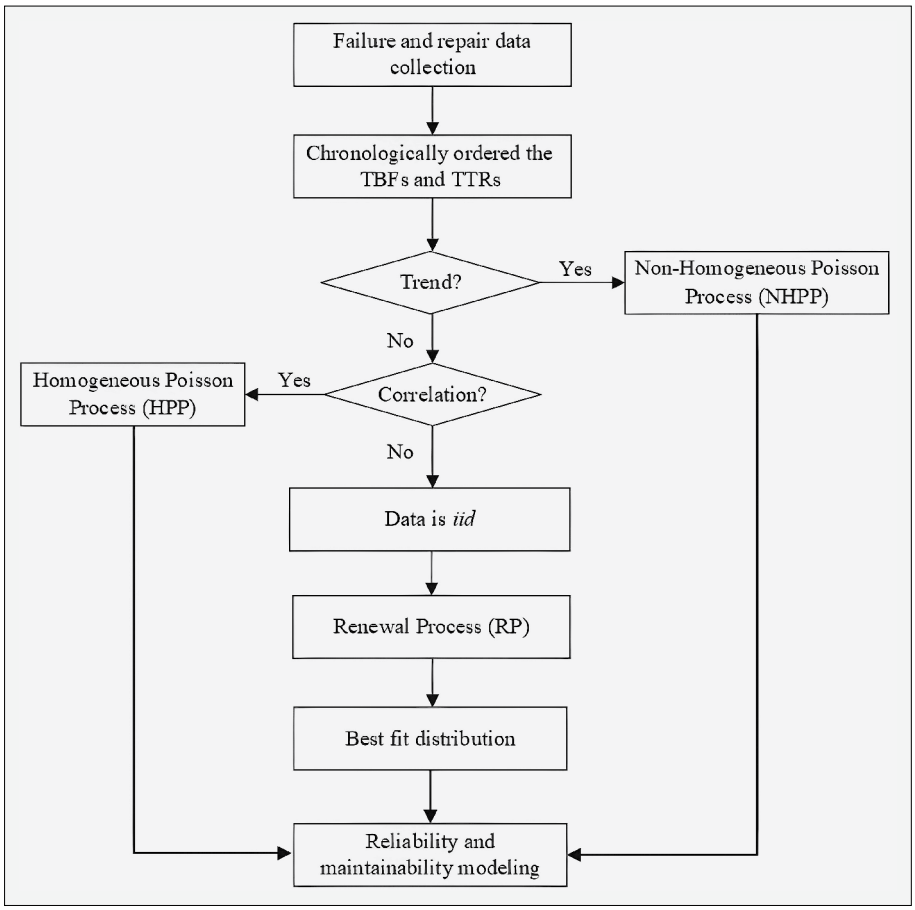


Figure 3. Process flowchart for the reliability and maintainability modelling

to model failures in repairable systems during certain phases of the system's life. However, because the arrival rate in an HPP is constant, it is inadequate for modelling system wear-out or growth, or for developing policies related to maintenance, overhaul, or trade-in (**Muralidharan, 2008**; **Arnold et al., 2020**).

For systems in which maintenance actions do not restore the system to a like-new condition, the non-homogeneous Poisson process provides a more realistic modelling approach. This framework relaxes the assumption of complete renewal by allowing the failure occurrence rate to vary as a function of time, thereby reflecting minimal or imperfect repair scenarios. As a result, NHPP models are particularly effective in representing systems whose failure behaviour evolves due to aging, operational stress, or maintenance interventions. The inclusion of a time-dependent intensity function enables the analysis of changing failure patterns throughout the system's operational life, especially in environments characterized by periodic inspection and maintenance activities (**Saldanha et al., 2001; Asfaw and Lindqvist, 2015; Slimacek and Lindqvist, 2016; Brown et al., 2023; Yarmohammadi et al., 2022**).

The selection of each modelling methodology is based on the type of data being collected. As mentioned in **Figure 3**, a testing procedure is conducted to perform trend and serial correlation tests on the data to assess the attribute and procedure to model the data. If a trend is detected in the failure data, an NHPP approach (e.g. a power-law process) is employed to model the data. If a trend is not present, the data will be analyzed for the testing of the presence or absence of serial correlation. If serial correlation is evidenced, an HPP approach (e.g. a branching Poisson process) is assumed to model the data. If there is neither a trend nor serial correlation, the failure data are considered independent and identically distributed (iid), and the appropriate statistical model is fitted to the data. A Renewal Process (RP) and classical statistical methods treat the data as a counting process where the inter-occurrence times are *iid* with an arbitrary life distribution.

Goodness of Fit (GoF) measures the extent to which a statistical model fits a set of observed data. GoF indices quantitatively summarize the differences between the observed data values and those predicted by the model (**Maydeu-Olivares and Garcı´a-Forero, 2010**). In this test, the decision to reject or fail to reject the null hypothesis for each candidate distribution is made by comparing the test statistic to its critical value at a specified significance level (**Joo et al., 2018**). There are different GoF tests such as Anderson-Darling (**Scholz and Stephens, 1987**), Cramer-von Mises (**Darling, 1957**), chi-square (**Albrecht, 1980**), and Kolmogorov-Smirnov (**Massey, 1951**). In this paper, the Kolmogorov–Smirnov

(K–S) test was employed. This test compares the empirical cumulative distribution function of the data with the theoretical cumulative distribution function of various candidate models. If the *p*-value of the K–S test exceeds the significance level of 0.05 (or, equivalently, if the test statistic is less than the critical value), the null hypothesis is not rejected, and the distribution is considered an acceptable model (**Joo et al., 2018**).

This section continues with methods for assessing trends and correlations in failure data. The failure pattern of a device is referred to as a trend. Various methods exist to examine the presence or absence of trends in failure data. In graphical methods, if the time interval between system failures increases, the system exhibits a decreasing trend. Conversely, if the time interval between failures decreases as the device ages, the system shows an increasing trend. If there are no significant changes in the time between failures throughout the device's life, the device is considered stable and trend-free. Several graphical and analytical tests are available to assess trends in data. In graphical tests, the cumulative failure time is plotted against the cumulative number of failures. A straight line indicates no trend, while convex or concave curves suggest the presence of a trend. However, graphical methods have limited reliability. The **Military Handbook-189 (1986)** analytical method is one of the most widely used techniques for assessing trends in failure data. In this method, the *U* index is calculated using the **Equation 10** to evaluate the trend (**Ascher and Feingold, 1984**; **Kumar and Kelefsjo, 1992**; **Saldanha et al., 2001**):

$$U = 2\sum_{i=1}^{n-1} \ln\left(T_n / T_i\right) \tag{10}$$

Where:

n is the total number of failures,

T_n is the time of the nth failure,

T_i is the time of the ith failure.

Assuming the null hypothesis is a HPP, U has a Chi-squared (Chi^2) distribution with $2(n\text{-}1)$ degrees of freedom. Serial correlation can be visually determined by plotting the ith TBF against the $(i\text{-}1)$th TBF. If the plotted values present as a random scatter with no apparent trend, then the TBFs are free from serial correlation.

4. Results

This part of the study is dedicated to measuring the reliability, maintainability, and availability of powered support systems in Tabas Parvadeh Coal Mine. Parvadeh No. 1 Mine in Tabas has been built as the first mechanized coal mine in Iran, with the annual production capacity value between 1.2 to 1.5 million ton of coal. The Parvadeh coal area is located in an extent of approximately 12,000 square kilometres and consists of a geological reserve of 1.1 billion tons of coking coal. It is one of the four coal regions in Tabas, where it is the largest coking coal deposit in Iran. The location of the area lies 75 km south of Tabas city in the South Khorasan Province. The total number of coal seams in Parvadeh No. 1 is 15 coal seams. Within a 100-meter stratigraphic interval, five main seams of coal designations are identified as D, C1, C2, B1, and B2. **Figure 4** shows the stratigraphic column of Parvadeh coal basin in Tabas.

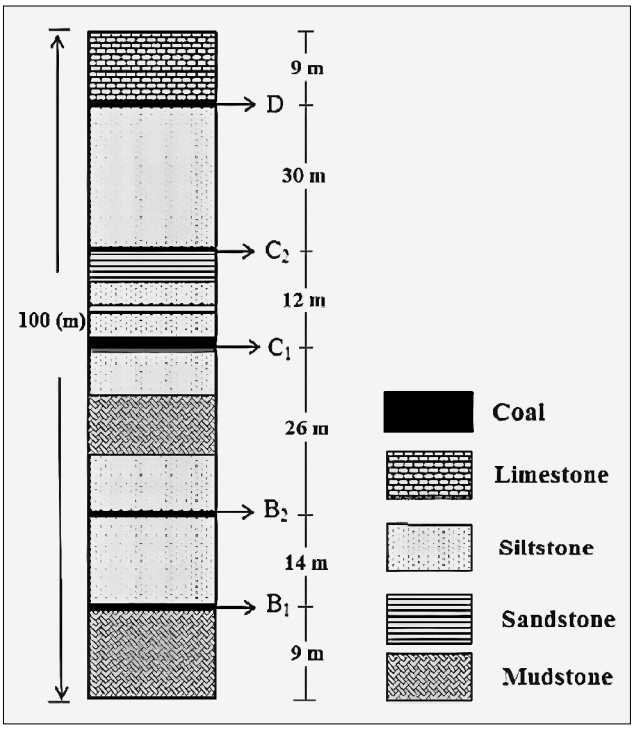


Figure 4. The coal basin stratigraphic column of Tabas Coal Mine (**Molayemat and Mohammad Torab, 2017; Jozanikohan et al., 2021**)

Table 2. The specifications of the panel W3 (**TPCC, 2024**)

The length of tail gate (m)	1934	Extracted tonnage (tons)	1110555
The length of main gate (m)	2005	Date of start of extraction	Feb. 2022
Panel length (m)	207	Coal layer height (m)	2.2

Among the coal seams in this area, only seam C1 is currently being mined. The mining operation utilizes the longwall backward method. This study evaluates the powered support systems used in the W3 panel. The specifications of this mining workshop are presented in **Table 2**. **Figure 5** illustrates the layout of the panels in the mine under study.

This paper aims to conduct a RAM analysis of the hydraulic FAZOS-10/28 POz powered roof supports (manufactured by FAZOS Company) used in the Parvadeh Tabas Coal Mine. In this context, the P means chock support, O refers to shield support, and z refers to roof support designed to operate with the roof caving system.

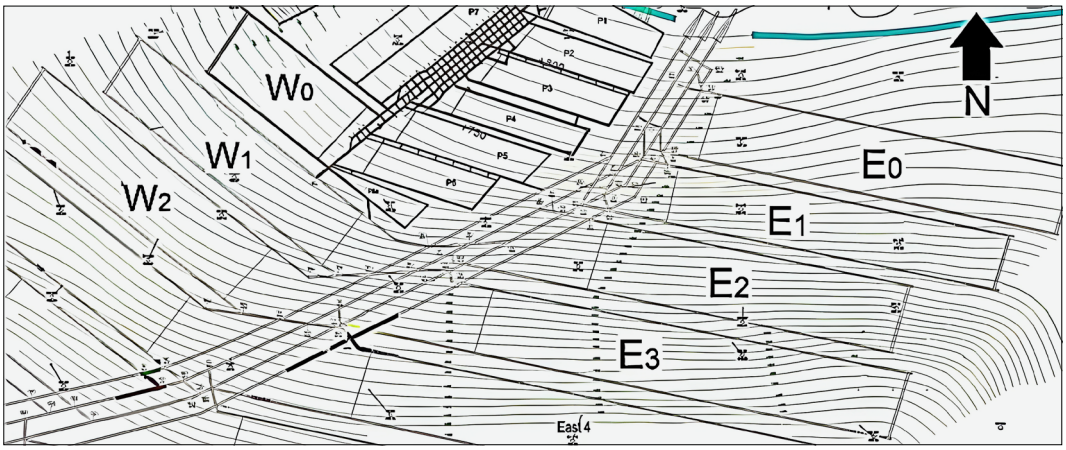


Figure 5. Layout of Various Panels in the Parvadeh-I Coal Mine (Aghababaei et al. 2019)

Table 3. The test statistic *U* at a 95% confidence level for TBF and TTR data

Subsystem	Data type	Mean	DoF	Calculated statistic *U*	Lower Chi² value	Upper Chi² value	Null-hypothesis	Trend	Modelling method
Mechanical	TBF	156.02	76	67.22	56.92	97.35	not rejected	no trend	RP
	TTR	0.50	102	92.12	79.7	126.57	not rejected	no trend	RP
Hydraulic	TBF	350.26	62	24.33	44.89	81.38	rejected	increasing trend	NHPP
	TTR	0.37	78	87.94	58.65	99.62	not rejected	no trend	RP

Table 4. The best-fit distribution for TBF and TTR data

Subsystem	Data type	Best-fit distribution	Estimated parameter
Mechanical	TBF	Lognormal	$\sigma = 1.14$, $\mu = 4.43$
	TTR	Lognormal	$\sigma = 0.85$, $\mu = -1.06$
Hydraulic	TBF	PLP	$\alpha = 0.81$, $\beta = 244.08$
	TTR	Lognormal	$\sigma = 0.77$, $\mu = -1.40$

This support system features a two-leg design, equipped with two telescopic hydraulic legs. The subassemblies of the support system are connected to each other through joint components and powered hydraulic elements.

A database of support system downtimes, collected over an 18-month period, was divided into two subsystems that impeded the machine's ability to operate and progress. The parameters were time between failures (TBF), time to repair (TTR), cumulative TBF and TTR, and total hours of breakdown time for each system. The dataset for RAM Analysis was from daily reports over an 18-month period of mining operations. The data tables were designed to sort and arrays the data chronologically. The TBFs and TTRs when stoppages and repairs were incurred within each subsystem were categorized for reliability and maintainability (RAM) analysis.

After gathering and preparing the failure and repair data, trend and serial correlation tests were carried out with the intent to select suitable reliability and maintainability modelling methods. In consideration of the tests considered, the accompanying computed values of both the test statistic (**Equation 10**) and the Chi² test statistic were used. **Table 3** provides the results. According to **Table 2**, there was no trend in the TBF and TTR data of the mechanical subsystem and the TTR data of the hydraulic subsystem; furthermore, there was no correlation. Thus, these datasets were iid, and the renewal process (RP) method was decided on, for modelling reliability. The TBF data of the hydraulic subsystem did show an increasing trend; thus, the NHPP modelling method, based on the power-law process (PLP), was used for reliability modelling. EasyFit software (**Schittkowski, 2002**) was used to apply the Kolmogorov–Smirnov statistical test to identify the best-fitting distributions and their parameters. The results of the analysis of data and stated parameters are shown in **Table 4**. Using **Table 3** and **Equation 1**, the reliability functions were calculated. The resulting reliability plots for subsystems are presented in **Figure 6**. The reliability of the powered support system as a whole is calculated using **Equation 2** and is shown in **Figure 7**.

Using the calculated parameters for the best-fitted distributions of the TTR data, as shown in **Table 3**, the maintainability of both subsystems was plotted and presented in **Figure 8**. Furthermore, based on the serial configuration of the subsystems, the maintainability of the entire system was calculated using **Equation 5** and illustrated in **Figure 9**.

Availability is the probability that equipment or a system is functioning satisfactorily under specified conditions. Conversely, it represents the likelihood that the system is neither failed nor undergoing repair when it is

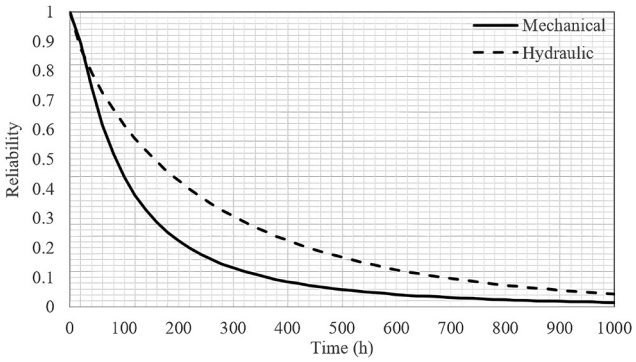


Figure 6. Reliability plots for subsystems of powered support system

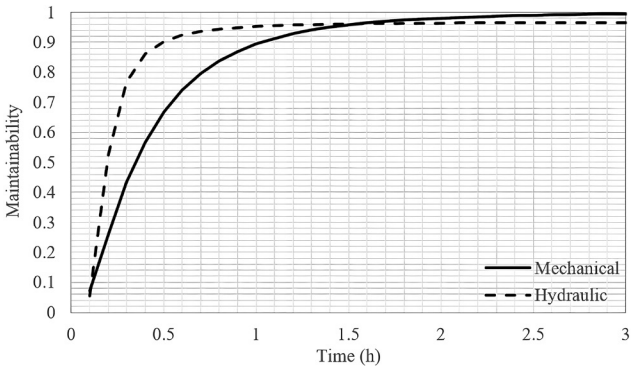


Figure 8. Maintainability plots for subsystems of powered support system

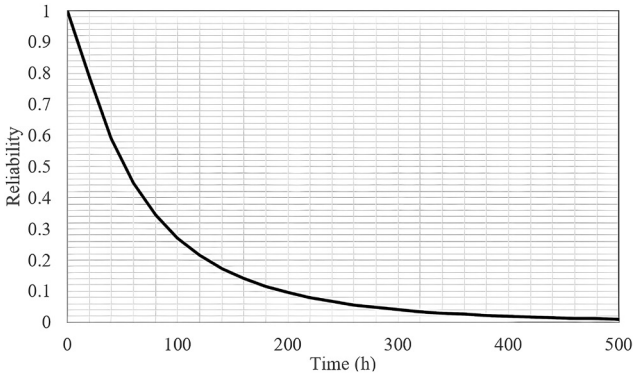


Figure 7. Reliability of the powered support system in Tabas Coal Mine

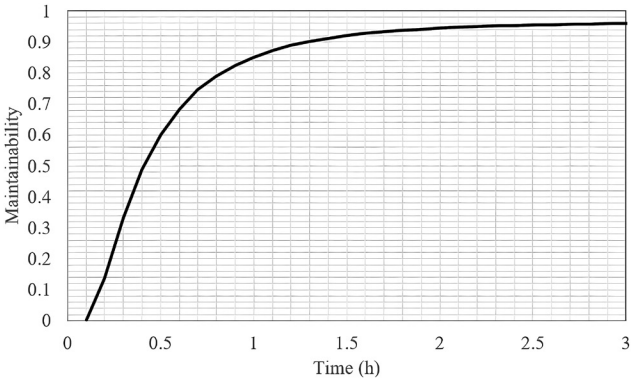


Figure 9. Maintainability of the powered support system in Tabas Coal Mine

Table 5. Availability of powered roof support's subsystems

Subsystem	MTBF (min)	MTTR (min)	Availability (%)
Mechanical	9361.20	60	99.68
Hydraulic	21015.60	22.20	99.89

needed. To calculate the availability index, the mean time between failures and the mean time to repair are first determined. The availability index is then calculated using **Equation 7**. The results are presented in **Table 5**.

5. Discussions

Regarding the reliability analysis, the reliability of both subsystems decreased to 85% after 25 hours. After 25 hours, the reliability of the hydraulic subsystem remains higher than that of the mechanical subsystem throughout all time intervals. This indicates that the service life of the hydraulic subsystem is longer compared to the mechanical subsystem. For instance, the reliability of the mechanical and hydraulic subsystems drops to 50% at 85 hours and 155 hours, respectively. It should be noted that the reliability of both subsystems approaches zero at approximately 1100 hours. Due to the series configuration of the subsystems, failure in any one subsystem halts the overall operation. On the other hand, the powered support system functions only when both subsystems are functioning properly. As seen in **Figure 6**, the failure probability of the powered support system increases to 20% after only 19 hours of operation. The reliability of the entire system decreases to 50% within 52 hours. This downward trend continues until 300 hours, at which point the system reliability falls below 4%.

Referring to maintainability analysis, the maintainability at the beginning of the repair operation steadily increased. The maintainability of the mechanical and hydraulic subsystems reached 90% and 95%, respectively, after one hour of repair. This indicates that most failures in these subsystems are repaired within one hour. The maintainability plot of the whole system (see **Figure 7**) shows that 85% of failures require one hour to be repaired. The maintainability of the powered support systems exceeds 95% at 2.5 hours. Conversely, only 5% of failures require more than 2.5 hours to be repaired and return to their active state.

High availability for both subsystems is reported in **Table 5**. This indicates that both subsystems can operate consecutively at a high level of functioning without interference. Since the availability structure is a series configuration, the availability of the whole system can satisfy **Equation 8** as follows:

$$Av_s = \prod Av_i = Av_{Mechanical} \times Av_{Hydraulic} =$$

$$= 0.9968 \times 0.9989 = 99.58\%$$

The availability analysis of powered roof supports indicates the probability of the powered support systems in Tabas Coal Mine operating under desirable conditions is 99.58%.

The results of the reliability and maintainability study indicate that the powered support system in the Parvadeh Mine operates with a significant probability of failure; however, these failures can be repaired promptly. This suggests that the preplanned tasks are designed to address the known causes of potential failures and reduce the frequency of premature failures. The preventive maintenance (PM) can be either condition-based or based on the historical data of equipment failures. In this study, the PM intervals were estimated using a reliability model. To achieve this, an 80% reliability threshold was considered to ensure both efficiency and performance. On the other hand, the probability that the equipment will continue operating without failure from the start of operation until the next PM action is at least 80%. Equivalently, this means that a maximum failure probability of 20% is accepted before performing preventive maintenance. Regarding the reliability analysis, the reliability of the powered support system in the Parvadeh mine decreased to 80% after approximately 18 hours. This means that if no maintenance is performed before the start of the fourth shift, the failure probability of the powered support system increases to 20%. In this approach the reliability-based maintenance intervals for mechanical and hydraulic subsystems is calculated as about 19 hours. Given that inspecting power retainers during coal mining operations might interrupt the continuity of the mining process, it is recommended that these inspections be conducted at the end of each work period, approximately every 22 hours. Following this schedule, the powered support system will achieve a reliability of approximately 76%. After preventive maintenance, the equipment will operate at full (100%) reliability at the start of the next working day.

6. Conclusions

This research assessed the reliability, maintainability, and availability of powered support systems with a focus on the Parvadeh Tabas Coal Mine in Iran. Initially, all main components and items of the support systems were classified into two serial subsystems: mechanical and hydraulic. Afterward, failure and repair data for each subsystem were collected and analyzed through an 18-month study. Results show that the reliability of both subsystems drops to zero around 1100 hours. Maintainability analysis showed that most failures of the support system are repaired within one hour. Availability analysis revealed that the overall system availability exceeds 99 percent. To establish an effective and manageable maintenance schedule for powered support systems, it was recommended that the preventive maintenance tasks be performed at the end of each working day.

The findings of this study help identify the causes and problems occurring during the operation of roof supports. They provide a basis for implementing improvements and corrective actions to enhance the effectiveness of the coal production process in mechanized longwall mines. Nevertheless, this study has some limitations that can be addressed in future research. The failure behaviour of additional subsystems, such as control systems and sensors—both critical to machine performance—can be incorporated into RAM analysis. Moreover, studying the economic dimensions through the analysis of maintenance costs and coal production losses due to powered systems' failures is proposed for future research. Additionally, environmental factors such as dust, humidity, temperature, and terrain conditions that may affect support systems should also be considered in future studies.

Acknowledgement

The authors would like to acknowledge the financial support of University of Birjand for this research under contract number 1404/D/14597.

Funding

This research was funded by University of Birjand, Birjand, Iran

7. References

Aghababaei, S., Jalalifar, H., & Saeedi, G. (2019). Prediction of face advance rate and determination of the operation efficiency in retreat longwall mining panel using rock engineering system. International Journal of Coal Science & Technology, 6(3), 419-429.

Albrecht, P. (1980). On the correct use of the chi-square goodness-of-fit test. Scandinavian Actuarial Journal, 1980(3), 149-160.

Andrzejczak, K. (2015). Stochastic modelling of the repairable system. Journal of KONBiN, 35(1), 5.

Arnold, R., Chukova, S., Hayakawa, Y., & Marshall, S. (2020). Geometric-like processes: An overview and some reliability applications. Reliability Engineering & System Safety, 201, 106990.

Ascher, H. and Feingold, H. (1984), Repairable System Reliability, Dekker, New York.

Asfaw, Z.G. and Lindqvist, B.H. (2015). Unobserved heterogeneity in the power law nonhomogeneous Poisson process. Reliab Eng Syst Saf., 134, 59–65.

Balaraju, J., Govinda Raj, M., & Murthy, C.H.S.N. (2018). Estimation of reliability-based maintenance time intervals of Load-Haul-Dumper in an underground coal mine. Journal of Mining and Environment, 9(3), 761-770.

Balaraju, J., Govinda Raj, M., & Murthy, C.S. (2020). Performance evaluation of underground mining machinery: A case study. Journal of Failure Analysis and Prevention, 20(5), 1726-1737.

Basri, E. I., Abdul Razak, I. H., Ab-Samat, H., & Kamaruddin, S. (2017). Preventive maintenance (PM) planning: a review. Journal of quality in maintenance engineering, 23(2), 114-143.

Bołoz, Ł., Rak, Z., & Stasica, J. (2022). Comparative analysis of the failure rates of shearer and plow systems—a case study. Energies, 15(17), 6170.

Borska, B., & Szurgacz, D. (2024). Research and Simulation on the Development of a Hydraulic Prop Support System of Powered Roof Support to Increase Work Safety. Methods and Protocols, 7(2), 33.

Brown, B., Liu, B., McIntyre, S., & Revie, M. (2023). Reliability evaluation of repairable systems considering component heterogeneity using frailty model. Proceedings of the Institution of Mechanical Engineers, Part O: Journal of Risk and Reliability, 237(4), 654-670.

Cai, B., Zhang, Y., Wang, H., Liu, Y., Ji, R., Gao, C., ... & Liu, J. (2021). Resilience evaluation methodology of engineering systems with dynamic-Bayesian-network-based degradation and maintenance. Reliability Engineering & System Safety, 209, 107464.

Darling, D. A. (1957). The kolmogorov-smirnov, cramer-von mises tests. The annals of mathematical statistics, 823-838.

Ding, H., Yang, L., & Yang, Z. (2019). A predictive maintenance method for shearer key parts based on qualitative and quantitative analysis of monitoring data. IEEE access, 7, 108684-108702.

dos Santos Silva, F. J., Viana, H. R. G., & Queiroz, A. N. A. (2016). Availability forecast of mining equipment. Journal of Quality in Maintenance Engineering, 22(4), 418-432.

Duffuaa, S. O., & Raouf, A. (2015). Preventive maintenance, concepts, modeling, and analysis. In Planning and Control of Maintenance Systems: Modelling and Analysis (pp. 57-94). Cham: Springer International Publishing.

e Costa, C. A. B., Carnero, M. C., & Oliveira, M. D. (2012). A multi-criteria model for auditing a Predictive Maintenance Programme. European Journal of Operational Research, 217(2), 381-393.

Gorai, A. K., Kumar, P., & Patel, A. K. (2017). Reliability analysis of the main conveyor system in underground coal mine to determine the maintenance schedules. International Journal of Mining and Mineral Engineering, 8(3), 207-233.

Guan, Z., Wang, S., Wang, J., & Ge, S. (2023). Longwall Face Automation: Coal Seam Floor Cutting Path Planning Based on Multiple Hierarchical Clustering. Applied Sciences, 13(18), 10242.

Hoseinie, S. H., Ahmadi, A., Ghodrati, B., & Kumar, U. (2013). Reliability-centered maintenance for spray jets of coal shearer machine. International Journal of Reliability, Quality and Safety Engineering, 20(03), 1340006.

Jakkula, B., Mandela, G. R., & Chivukula, S. M. (2022). Reliability, availability and maintainability (RAM) investigation of Load Haul Dumpers (LHDs): a case study. International journal of system assurance engineering and management, 13(1), 504-515.

Jakkula, B., Mandela, G. R., & Tripathi, A. K. (2024). Reliability analysis of complex repairable systems using artificial neural networks: A case study on underground mining machinery. Precis. Mech. Digit. Fabr, 1(4), 189-200.

Joo, M., Doh, J., & Lee, J. (2018). Determination of the best distribution and effective interval using statistical characterization of uncertain variables. Journal of Computational Design and Engineering, 5(3), 358-367.

Joo, M., Doh, J., & Lee, J. (2018). Determination of the best distribution and effective interval using statistical characterization of uncertain variables. Journal of Computational Design and Engineering, 5(3), 358-367.

Jozanikohan, G., Nosrati Abarghooei, M., & Sedighi, H. (2021). Geochemical study of rare earth elements content in Tabas Coal Ash, Parvadeh Coal Mine. Journal of Mining and Environment, 12(4), 1143-1153.

Kahraman, S., Rostami, M., & Dibavar, B. (2023). Evaluating machine utilization times for roadheaders used in coal mines: Regression and artificial neural network analyses. Scientific Mining Journal, 62(3), 141-151.

Kazanin, O. I., Sidorenko, A. A., Sidorenko, S. A., Ivanov, V. V., & Mischo, H. (2022). High productive longwall mining of multiple gassy seams: Best practice and recommendations. Acta Montan. Slovaca, 27, 152-162.

Kumar, P. (2016). Reliability, availability and maintainability analysis of the main conveyor system in underground coal mine: a case study of Churcha (RO) mine (Doctoral dissertation), National Institute of Technology Rourkela.

Kumar, U. and Kelefsj€o, B. (1992), Reliability analysis of hydraulic system of LHD machine using the power low process model, International Journal of Reliability Engineering and System Safety, Vol. 35 No. 3, pp. 217-224.

La Roche-Carrier, N., Dituba Ngoma, G., Kocaefe, Y., & Erchiqui, F. (2020). Reliability analysis of underground rock bolters using the renewal process, the non-homogeneous Poisson process and the Bayesian approach. International Journal of Quality & Reliability Management, 37(2), 223-242.

Masir, R. N., Ataei, M., Sereshki, F., & Qarahasanlou, A. N. (2021). Availability simulation and analysis of armored face conveyor machine in longwall mining. Rudarsko-geološko-naftni zbornik, 36(2), 69-82.

Massey Jr, F. J. (1951). The Kolmogorov-Smirnov test for goodness of fit. Journal of the American statistical Association, 46(253), 68-78.

Maydeu-Olivares A, and Garcı´a-Forero C. (2010). Goodness-of-Fit Testing, International Encyclopedia of Education (2010), vol. 7, pp. 190-196.

MIL-STD-2173, 1986, Reliability Centered Maintenance, Department of Defense, Washington, DC, USA.

Molayemat, H., & Mohammad Torab, F. (2017). Evaluation of coalbed methane potential in Parvadeh IV coal deposit in central Iran using a combination of MARS modeling and Kriging. Journal of Mining and Environment, 8(2), 305-319.

Morshedlou, A., Dehghani, H., Hoseinie, S.H., (2014). Reliability Analysis of powered supports in Tabas Mechanized Coal Mine, The 2nd National Iranian Coal Congress, Shahrood, Iran.

Mouli, C.; Chamarthi, S.; Chandra, G.; Kumar, V. Reliability Modeling and Performance Analysis of Dumper Systems in Mining by KME Method. International Journal of Current Engineering and Technology. 2014, 255–258

Muralidharan, K. (2008, July). A review of repairable systems and point process models. In *ProbStat Forum*, 1(1), 26-49.

Peng, S. (2019). Longwall mining. CRC Press.)، (Mitchell, G. W. (2009). Longwall mining. Australasian coal mining practice, 340-373.

Prasad, P. V. N., & Rao, K. R. M. (2008, January). A study on optimal age replacement of dozer engines. In 2008 Annual Reliability and Maintainability Symposium (pp. 31-36). IEEE.

Rahimdel, M. J., & Ghodrati, B. (2022). Remaining useful life improvement for the mining railcars under the operational conditions. International Journal of Mining, Reclamation and Environment, 36(1), 46-67.

Said, U. (2021). A Methodology for Maintenance Evaluation and Improvement of Repairable Systems in a Mine (Doctoral dissertation, Toronto Metropolitan University).

Saldanha, P. L., De Simone, E. A., & e Melo, P. F. (2001). An application of non-homogeneous Poisson point processes to the reliability analysis of service water pumps. Nuclear engineering and design, 210 (1-3), 125-133.

Saldanha, P. L., De Simone, E. A., & e Melo, P. F. (2001). An application of non-homogeneous Poisson point processes to the reliability analysis of service water pumps. Nuclear engineering and design, 210(1-3), 125-133.

Saldanha, P. L., De Simone, E. A., & e Melo, P. F. (2001). An application of non-homogeneous Poisson point processes to the reliability analysis of service water pumps. Nuclear engineering and design, 210(1-3), 125-133.

Sarkhel, S., & Dey, U. K. (2015). Reliability modelling of side discharge loader for availability estimation and maintenance planning in underground coal mines. Int J Sci Eng Res, 6, 847-854.

Schittkowski, K. (2002). EASY-FIT: a software system for data fitting in dynamical systems. Structural and Multidisciplinary Optimization, 23(2), 153-169.

Scholz, F. W., & Stephens, M. A. (1987). K-sample Anderson–Darling tests. Journal of the American Statistical Association, 82(399), 918-924.

Slimacek, V. and Lindqvist, B.H. (2016). Nonhomogeneous Poisson process with nonparametric frailty. Reliab Eng Syst Saf., 149, 14–23.

Stebnev, A. V., Mukhortikov, S. G., Zadkov, D. A., & Gabov, V. V. (2017). Analysis of operation of powered longwall systems in mines of SUEK-Kuzbass. Procedia. 2012. No, 16, 1264-1268.

Szurgacz, D. (2021). The effectiveness of the use of a powered roof support in the light of research and analysis. In E3S Web of Conferences (Vol. 278, p. 01007). EDP Sciences.

Szurgacz, D. (2024). Research on the Strain and Stress of Powered Roof Support Construction to Limit Damage. Machines, 12(12).

Szurgacz, D., Borska, B., Diederichs, R., & Zhironkin, S. (2022a). Development of a Hydraulic System for the Automatic Expansion of Powered Roof Support. Energies, 15(3), 680.

Szurgacz, D., Borska, B., Zhironkin, S., Diederichs, R., & Spearing, A. J. (2022). Optimization of the load capacity system of powered roof support: A review. Energies, 15(16), 6061.

Szurgacz, D., Trzop, K., Gil, J., Zhironkin, S., Pokorný, J., & Gondek, H. (2022b). Numerical Study for Determining the Strength Limits of a Powered Longwall Support. Processes, 10(3), 527.

Tabas Parvadeh Coal Company (TPCC). (2024). Report of the Technical Office of the No. 1 Tabas Coal Mine.

Thunberg, H. (2016). Reliability-based Maintenance Plan for Underground Drilling Rigs.

Uth, F.; Polnik, B.; Kurpiel, W.; Baltes, R.; Kriegsch, P.; Clause, E. An innovate person detection system based on thermal imaging cameras dedicate for underground belt conveyors. Min. Sci. 2019, 26, 263–276.

Vashistha, S., Kumar Agrawal, A., Siddiqui, M. A., & Chattopadhyaya, S. (2019, November). Reliability and maintainability analysis of LHD loader at Saoner Mines, Nagpur, India. In IOP Conference Series: Materials Science and Engineering (Vol. 691, No. 1, p. 012013). IOP Publishing.

Vayenas, N., & Wu, X. (2009). Maintenance and reliability analysis of a fleet of load-haul-dump vehicles in an underground hard rock mine. International Journal of Mining, Reclamation and Environment, 23(3), 227-238.

Wang, D., Li, R., Cheng, J., Zheng, W., Shen, Y., Zhao, S., & Wu, M. (2023). Research on the calculation model and control method of initial supporting force for temporary support in the underground excavation roadway of coal mine. Axioms, 12(10), 948.

Wang, H., & Pham, H. (2006). Reliability and optimal maintenance. London: Springer London.

Wang, J., Zhang, R., Jiang, R., Zhang, X., Li, K., Song, S., ... & Wu, J. (2025, July). Reliability model and analysis of long wall coal shearer machine. In Third International Conference on Advanced Materials and Equipment Manufacturing (AMEM 2024) (Vol. 13691, pp. 497-510). SPIE.

Xiaofeng, L. I. U. (2025). Fault diagnosis and maintenance of electromechanical equipment of coal mine roadheader. Coal Mine Modernization, 34(1), 47-51.

Yarmohammadi, M., Afshar, A., Mahmoudvand, R., & Nasiri, P. (2022). Predicting intensity function of nonhomogeneous Poisson process. Journal of Statistical Modelling: Theory and Applications, 3(2), 39-50.

Zhou, D., Zhang, X., & Zhang, Y. (2017). Reliability analysis of the traction unit of a shearer mechanism with response surface method. Journal of Mechanical Science and Technology, 31(10), 4679-4689.

SAŽETAK

RAM analiza hidrauličkih samohodnih sustava podgrade u podzemnim ugljenokopima sa širokočelnim otkopavanjem

Rudarske aktivnosti u podzemnim ugljenokopima, osobito pri primjeni metode širokočelnoga otkopavanja, zahtijevaju neprekidno odvijanje proizvodnoga procesa i izbjegavanje zastoja jer svako neplanirano zaustavljanje može dovesti do gubitka stabilnosti i urušavanja krovine. S obzirom na visoku razinu mehanizacije u podzemnoj eksploataciji ugljena primjena hidrauličkih samohodnih sustava podgrade predstavlja osnovnu sigurnosnu mjeru za osiguranje stabilnosti radnoga prostora. Kako bi se osigurala kontinuirana proizvodnja, povećala učinkovitost rada te istodobno smanjili troškovi uzrokovani zastojima i kvarovima opreme, nužno je provesti sustavnu procjenu pouzdanosti, održivosti i dostupnosti (RAM) sustava podgrade. Cilj ovoga rada jest provedba RAM analize hidrauličkih samohodnih sustava podgrade u stvarnim radnim uvjetima. U tu svrhu analiziran je hidraulički sustav samohodne podgrade kao tehnički sustav sastavljen od više funkcionalnih podsustava. Rezultati pokazuju da podatci o vremenu između kvara (TBF) i vremenu popravka (TTR) većine podsustava slijede obnovljivi (*renewal*) proces, dok podatci o TBF-u hidrauličkoga podsustava slijede nehomogeni Poissonov proces (NHPP). Pouzdanost analiziranih podsustava smanjila se na približno 85 % nakon 25 sati rada. Analiza održivosti pokazala je da se većina kvarova hidrauličke samohodne podgrade otklanja unutar jednoga sata. Nadalje, izračunana dostupnost sustava iznosi 99,58 %, što upućuje na vrlo povoljne radne uvjete. Ipak, radi uspostave učinkovitoga, normativno utemeljenoga i operativno jednostavnoga plana održavanja preporučuje se provođenje preventivnoga održavanja na kraju svakoga radnog dana.

Ključne riječi:
podzemna eksploatacija ugljena, hidraulička samohodna podgrada, pouzdanost, održivost, raspoloživost

Author's contribution

The author prepared the whole work.

RGNZ/*MGPB*

Radovi/*Papers*

1.	Predicting the weight and type of drilling mud by machine learning method *(Amin Tohidi, Alireza Afradi)*	1-20
2.	Integrated Mathematical and Physical Modelling of Salt Ions Leaching from Coal-Mining Waste: Implications for Ecological Safety and Civil Protection *(Vasyl Karabyn, Iryna Kochmar, Oksana Karabyn, Clint Sutherland, Valentyna Loboichenko, Andrii Khorolskyi)*	21-36
3.	Data-driven and knowledge-driven MARCOS method to Cu porphyry prospectivity modelling, a case study, Shahr-e-Babak area, southeastern Iran *(Moslem Jahantigh, Hamidreza Ramazi)*	37-54
4.	Experimental Investigation of the Effects of Temperature and Oil Composition on CO_2-Crude Oil Swelling, Extraction Mechanisms, and Displacement Performance *(Kartika Hartono, Asep K. Permadi, Ucok W. R. Siagia, Andri L. Hakim, Sumadi Paryoto, Ahlul H. Resha, Syaeful A. Satya, Reno Pratiwi, Maman Djumantara, Dina A. Chusniah)*	55-67
5.	Seismogenic Analysis of the 2023 Mw6.9 Murghob Earthquake, Tajikistan, based on Multi-Track InSAR and Modelling *(Rana Jaladara, Naufal Setiawan, Erlan Sumanjaya)*	69-80
6.	Geographic Information System Application for Prospecting the Sandstone-type Uranium Deposit in the Melawi Region, West Kalimantan, Indonesia *(Tyto Baskara Adimedha, Roni Cahya Ciputra, Frederikus Dian Indrastomo, I Gde Sukadana, Heri Syaeful, Yoshi Rachael)*	81-97
7.	Stress Transfer and Seismicity Along the Southern Great Sumatran Fault: Insights from the 1994 Liwa Earthquake *(Andri Kurniawan, Nicolas Silaen, Khalil Ibrahim, Arsy Nurrochman, Ridho Destawan, Nanda Hanyfa Maulida, Irfan Prasetyo, Ahmad Zaenudin, Adhi Wibowo)*	99-113
8.	Enhanced desorption of Cobalt from contaminated sandy silty-clay soils *(Tamás Bacsó, Márton Tóth)*	115-126
9.	Geochemistry and genesis of the manganese ores in the Nawagai ophiolitic melange, Mohmand District, Khyber Pakhtunkhwa, Pakistan *(Irfan Ullah, Aamir Khan, Mohammad Tahir Shah, Liaqat Ali, Asad Khan, Muhammad Mustafa)*	127-141
10.	Enhancing Hypocenter Relocation for Seismic Hazard Evaluation in Central Java and Yogyakarta Indonesia: Findings from the BMKG Earthquake Catalog of August-October 2024 *(Wahyu Hidayat, Nanda Agustina, Ekalia Ardenti, Suharsono, Ardian Novianto, Uli Ulfa, Maman Rohaman, Herry Riswandi)*	143-158
11.	Ore Genesis and Hydrothermal Evolution of the Cheshmeh-Hadi Stratabound (Manto-type) Copper Deposit in the Volcanic-Plutonic Belt North of the Doruneh Fault, East of the Sepid-Sarve copper deposit (NW Bardeskan, Central Iran): Evidence from Geology, Geochemistry, Fluid Inclusions, and Stable S and O Isotopes *(Morteza Esform, Hasan Zamanian, Alireza Zarasvandi, Alireza Almasi, Mahya Manouchehry Nia)*	159-184
12.	Magnetic characteristics and mineralogy of cave sediments from Solek Cave, West Sumatra: Implications for paleoenvironmental processes within the cave *(Hamdi Rifai, Rizaldi Putra, Wilda Febi Rahmadhani, Nilam Sari, Dessupri Niarti, Wardina Nasution, Erni Erni, Christopher M. Wurster)*	185-195
13.	Fall cone test calibration for slope stability analysis *(Chalabi Youssouf, Aissaoui Soufyane, Zadjaoui Abdeldjalil, Aissa Mamoune Sidi Mohammed)*	197-205
14.	Remote sensing of radioactive alteration zones using Sentinel-2 and SPAD chlorophyll measurements in Mamuju, Indonesia *(Nuraisyiah Pertiwi Kamsir, Asep Saepuloh, Very Susanto, Eka Djatnika Nugraha)*	207-218
15.	RAM measure of hydraulic powered roof supports in underground longwall coal mines *(Mohammad Javad Rahimdel)*	219-231

ISSN 0353-4529